



SAKARYA ÜNİVERSİTESİ

FEN BİLİMLERİ ENSTİTÜSÜ DERGİSİ

Sakarya University Journal of Science (SAUJS)



SAKARYA
ÜNİVERSİTESİ

e-issn: 2147-835X

Volume: 28

Issue: 1

February 2024

VOLUME: 28 ISSUE: 1
E-ISSN 2147-835X

February 2024
<https://dergipark.org.tr/tr/pub/sofenbilder>

SAKARYA UNIVERSITY JOURNAL OF SCIENCE



SAKARYA
ÜNİVERSİTESİ

The Owner on Behalf of Sakarya University

Prof. Dr. Hamza Al
Sakarya University, Sakarya-Türkiye

Publishing Manager

Hüseyin Özkan Toplan
Department of Engineering
Sakarya University, Sakarya-Türkiye
toplano@sakarya.edu.tr

Editor in Chief

Ömer Tamer
Department of Physics
Sakarya University, Sakarya-Türkiye
omertamer@sakarya.edu.tr

Associate Editors

İhsan Hakan Selvi
Department of Information Systems Engineering
Sakarya University, Sakarya-Türkiye
ihselvi@sakarya.edu.tr

Managing Editor

Hüseyin Yasin Uzunok
Department of Physics
Sakarya University, Sakarya-Türkiye
hyuzunok@sakarya.edu.tr

Statistical Editor

Önder Gökmen Yıldız
Department of Mathematics
Bilecik Şeyh Edebali University, Bilecik-Türkiye
ogokmen.yildiz@bilecik.edu.tr

English Language Editor

Seçkin Arı
Department of Computer Engineering
Sakarya University, Sakarya-Türkiye
ari@sakarya.edu.tr

Technical Editor

Hatice Vural
Department of Electrical and Electronics Engineering
Amasya University, Amasya-Türkiye
hatice.vural@amasya.edu.tr

Editorial Board

Abderrahmane Benbrik
Department of Mechanical Engineering
M'hamed Bougara University
Algeria
abderrahmane.benbrik@univ-boumerdes.dz

Abdullah Oğuz Kızılcay
Department of Electrical Electronics Engineering
Bülent Ecevit University
Zonguldak-Türkiye
oguzkizilcay@yyu.edu.tr

Ali Cemal Benim
Department of Mechanical and Process Engineering
Duesseldorf University of Applied Sciences
Germany
alicemal@prof-benim.com

Ali Demir
Department of Mathematics
Kocaeli University
Kocaeli-Türkiye
ademir@kocaeli.edu.tr

Aligholi Niaie
Department of Chemical Engineering
University of Tabriz
Iran
aniaei@tabrizu.ac.ir

Aslı Uçar
Department of Nutrition and Dietetics
Ankara University
Ankara-Türkiye
aucar@ankara.edu.tr

Asude Ateş
Department of Environmental Engineering
Sakarya University
Sakarya-Türkiye
aates@sakarya.edu.tr

Bahadır Başyigit
Department of Electrical Electronics Engineering
Isparta Applied Sciences University
Isparta-Türkiye
bahadirbasyigit@isparta.edu.tr

Bahadır Saygi
Department of Physics
Ankara University
Ankara-Türkiye
bsaygi@ankara.edu.tr

Barış Yüce
Department of Industrial Engineering
University of Exeter
England
b.yuce@exeter.ac.uk

Benjamin Durakovic
Department of Industrial and Mechanical Engineering
International University of Sarajevo
Bosnia and Herzegovina
bdurakovic@ius.edu.ba

Berrin Denizhan
Department of Industrial Engineering
Sakarya University
Sakarya-Türkiye
denizhan@sakarya.edu.tr

Can Serkan Keskin
Department of Chemistry
Sakarya University
Sakarya-Türkiye
ckeskin@sakarya.edu.tr

Caner Erden
Department of Computer Engineering
Sakarya Applied Science University
Sakarya-Türkiye
cerden@subu.edu.tr

Cansu Akbulut
Department of Biology
Sakarya University
Sakarya-Türkiye
cansua@sakarya.edu.tr

Ceren Tayran
Department of Physics
Gazi University
Ankara-Türkiye
c.tayran@gazi.edu.tr

Ece Ümmü Deveci
Department of Environmental Engineering
Niğde Ömer Halisdemir University
Niğde-Türkiye
eudeveci@ohu.edu.tr

Edgar Perez Esteve
Department of Food Sciences
Polytechnic University of Valencia
Spain
edpees@upv.es

Elif Ağcakoca
Department of Civil Engineering
Sakarya University
Sakarya-Türkiye
elifd@sakarya.edu.tr

Elif Eker Kahveci
Department of Mechanical Engineering
Sakarya University
Sakarya-Türkiye
eeker@sakarya.edu.tr

Erman Aslan
Department of Mechanical Engineering
Kocaeli University
Kocaeli-Türkiye
erman.aslan@kocaeli.edu.tr

Fahrettin Horasan
Department of Computer Sciences and Engineering
Kırıkkale University
Kırıkkale-Türkiye
fhorasan@kku.edu.tr

Faruk Fırat Çalim
Department of Civil Engineering
Adana Alparslan Türkeş Science and Technology
University
Adana-Türkiye
ffcalim@atu.edu.tr

Feyza Gürbüz
Department of Industrial Engineering
Erciyes University
Kayseri-Türkiye
feyza@erciyes.edu.tr

Francesco De Paulis
Department of Mathematics
University of L'Aquila
Italy
francesco.depaulis@univaq.it

Gökhan Dok
Department of Construction Mechanics
Sakarya University of Applied Sciences
Sakarya-Türkiye
gokhandok@subu.edu.tr

Grażyna Simha Martynková
Department of Chemistry Education
Vsb-Technical University of Ostrava
Czech Republic
grazyna.simha@vsb.cz

Grzegorz Jaworski
Department of Physics
University of Warsaw
Poland
grzegorz.jaworski@pwr.edu.pl

Hakan Alp
Department of Geophysical Engineering
İstanbul University-Cerrahpaşa
İstanbul-Türkiye
hakanalp@iuc.edu.tr

Hatice Esen
Department of Industrial Engineering
Kocaeli University
Kocaeli-Türkiye
hatice.eris@kocaeli.edu.tr

Herman Nied
Department of Solid Mechanics
Lehigh University
USA
hfn2@lehigh.edu

Hüseyin Aksoy
Department of Biology
Sakarya University
Sakarya-Türkiye
haksoy@sakarya.edu.tr

Issa Al-Harthy
Department of Civil and Architectural Engineering
Sultan Qaboos University
OMAN
aissa@squ.edu.om

İsmail Hakkı Demir
Department of Architectural Design
Sakarya University
Sakarya-Türkiye
idemir@sakarya.edu.tr

Jamal Khatib
Department of Civil Engineering
University of Wolverhampton
England
j.m.khatib@wlv.ac.uk

Kamaruzzaman Sopian
Department of Mechanical Engineering
Universiti Kebangsaan
Malaysia
ksopian@ukm.edu.my

Kevser Ovaz Akpınar
Department of Cyber Security
Rochester Institute of Technology of Dubai
Dubai
kxocad1@rit.edu

Khalifa Al-Jabri
Department of Civil and Architectural Engineering
Sultan Qaboos University
Oman
aljabri@squ.edu.om

Luan Hoang
Department of Math Analysis
Texas Tech University
USA
luan.hoang@ttu.edu

Luis Materon
Department of Biology
The University of Texas Rio Grande Valley
USA
luis.materon@utrgv.edu

Mehmet Emin Aydın
Department of Machine Learning
University of the West of England Bristol
England
mehmet.aydin@uwe.ac.uk

Mehmet Uysal
Department of Metallurgical and Materials Engineering
Sakarya University
Sakarya-Türkiye
mehmetu@sakarya.edu.tr

Mesut Baran
Department of Electrical and Computer Engineering
North Carolina State University
USA
baran@ncsu.edu

Miraç Alaf
Department of Metallurgical and Materials Engineering
Bilecik Şeyh Edebali University
Bilecik-Türkiye
mirac.alaf@bilecik.edu.tr

Mohammad Sukri Bin Mustapa
Department of Mechanical Engineering
Universiti Tun Hussein Onn Malaysia
Malaysia
sukri@uthm.edu.my

Muhammed Fatih Adak
Department of Computer Engineering
Sakarya University
Sakarya-Türkiye
fatihadak@sakarya.edu.tr

Muhammed Maruf Öztürk
Department of Computer Engineering
Süleyman Demirel University
Isparta-Türkiye
muhammedozturk@sdu.edu.tr

Muhammet Hilmi Nişancı
Department of Electrical Electronics Engineering
Sakarya University
Sakarya-Türkiye
nisanci@sakarya.edu.tr

Murat Güzeltepe
Department of Mathematics
Sakarya University
Sakarya-Türkiye
mguzeltepe@sakarya.edu.tr

Murat Sarduvan
Department of Mathematics
Sakarya University
Sakarya-Türkiye
msarduvan@sakarya.edu.tr

Murat Tuna
Department of Chemistry
Sakarya University
Sakarya-Türkiye
tuna@sakarya.edu.tr

Mustafa Akpınar
Department of Computer Engineering
Higher Collages of Technology
United Arab Emirates
mustafakpinar@gmail.com

Mustafa Gülfen
Department of Chemistry
Sakarya University
Sakarya-Türkiye
mgulfen@sakarya.edu.tr

Nahit Gencer
Department of Biochemistry
Balıkesir University
Balıkesir-Türkiye
ngencer@balikesir.edu.tr

Nazan Deniz Yön Ertuğ
Department of Biology
Sakarya University
Sakarya-Türkiye
nkoc@sakarya.edu.tr

Necati Olgun
Department of Statistics
Gaziantep University
Gaziantep-Türkiye
olgun@gantep.edu.tr

Nihan Akıncı Kenanoğlu
Department of Biology
Çanakkale Onsekiz Mart University
Çanakkale-Türkiye
nakinci@comu.edu.tr

Oğuz Kurt
Department of Hydrobiology
Manisa Celal Bayar University
Manisa-Türkiye
oguz.kurt@cbu.edu.tr

Osman Sönmez
Department of Fluid Mechanics
Sakarya University
Sakarya-Türkiye
osonmez@sakarya.edu.tr

Ozan Erdinç
Department of Electrical-Electronics Engineering
Yıldız Teknik University
İstanbul-Türkiye
oerdinc@yildiz.edu.tr

Raja Mazuir Bin Raja Ahsan Shah
Department of Mechanical Engineering
Coventry University
United Kingdom
ac9217@coventry.ac.uk

Rıfki Terzioğlu
Department of Electrical and Electronics Engineering
Bolu Abant İzzet Baysal University
Bolu-Türkiye
rifkiterzioglu@ibu.edu.tr

Selma Özçağ
Department of Statistics
Hacettepe University
Ankara-Türkiye
sozcag@hacettepe.edu.tr

Seong Jin Park
Department of Mechanical Engineering
Pohang University of Science and Technology
Korea
sjpark87@postech.ac.kr

Serap Coşansu
Department of Food Engineering
Sakarya University
Sakarya-Türkiye
scosansu@sakarya.edu.tr

Shi-Chune Yao
Department of Energy technologies
Carnegie Mellon University
USA
sy0d@andrew.cmu.edu

Syed Abbas
Department of Grain Technology
Curtin University
Australia
s.abbas@curtin.edu.au

Şenay Çetin Doğruparmak
Department of Environmental Engineering
Kocaeli University
Kocaeli-Türkiye
senayc@kocaeli.edu.tr

Tahsin Turgay
Department of Civil Engineering
Sakarya University
Sakarya-Türkiye
turgay@sakarya.edu.tr

Tauseef Aized
Department of Industrial Engineering
Uet Lahore
Pakistan
aized@uet.edu.pk

Tuba Tatar
Department of Civil Engineering
Sakarya University
Sakarya-Türkiye
ttatar@sakarya.edu.tr

Ufuk Durmaz
Department of Mechanical Engineering
Sakarya University
Sakarya-Türkiye
udurmaz@sakarya.edu.tr

Editorial Assistant

Ahmet Erhan Tanyeri
Department of Sociology
Institute of Science, Sakarya University
Sakarya-Türkiye
tanyeri@sakarya.edu.tr

Evrin Yüksel
Department of Environmental Engineering
Institute of Sciences, Sakarya University
Sakarya-Türkiye
eyuksel@sakarya.edu.tr

Layout Editor

Mehmet Emin Çolak
Scientific Journals Coordinatorship
Sakarya University
Sakarya-Türkiye
mehmetcolak@sakarya.edu.tr

Yakup Beriş
Scientific Journals Coordinatorship
Sakarya University
Sakarya-Türkiye
yakupberis@sakarya.edu.tr

Indexing



Contents

Research Article

- 1 Investigation of the Effects of Cutting Fluid Application with Minimum Quantity Lubrication (MQL) Method on the Machinability of Pure Titanium
Yunus Kartal, Ali Osman Er 1-9
- 2 Drag Reduction on Microstructure Surfaces
Ahmet İlyas Kodal, Şule Kapkın, Hasan Rıza Güven 10-19
- 3 Application and Performance Evaluation of Chemical Coagulation, Electrocoagulation, Electro-Fenton and Anodic Oxidation Processes in the Treatment of Glass Fiber Manufacturing Wastewater
Buket Kar, Özkan Görmez, Belgin Gozmen 20-29
- 4 Identifying Critical Success Factors of Public Private Partnership Projects in Türkiye
Elif Durna, Beliz Özorhon, Semih Caglayan 30-50
- 5 Immobilization of Lipase on Agarose Beads for Enzymatic Hydrolysis/Transesterification of Castor Oil
Semra Yilmazer Keskin, Kübra Karakaya 51-57
- 6 Effect of Sampling Orientation on the Mechanical Properties of Glass Fiber Reinforced Epoxy Nanocomposites
Gökhan Demircan 58-72
- 7 Designing Hollow Brick Waste Based Alkali Activated Composites by Taguchi Method
Mine Kurtay Yıldız 73-84
- 8 Developing and Implementing an Iot Managed by Electronic Devices for Covid Patient Monitoring via a Secured Communication System
Alaa Abdulaal, A F M Shahen Shah, Muhammet Ali Karabulut 85-100
- 9 Heart Disease Prediction with Machine Learning-Based Approaches
Ayhan Küçükmanisa, Zeynep Hilal Kilimci 101-107
- 10 The Impact of Inclined Magnetic Field on Streamlines in a Constricted Lid-Driven Cavity
Merve Gürbüz Çaldağ, Ebutalib Çelik 108-116
- 11 Modeling and Evaluation of Ömerli Basin (Mardin, Southeastern Türkiye) Groundwater Potential Using the Gis-Based Analytical Hierarchy Process (AHP) Approach
Veysel Aslan 117-132
- 12 Ameliorative Effect of a Vanadium-Thiosemicarbazone Complex on Oxidative Stress in Stomach Tissue of Experimental Diabetic Rats
Fatma Gülnaz Karakuş, Sevim Tunalı, Tülay Bal-Demirci, Bahri Ülküseven, Refiye Yanardağ 133-144
- 13 Use of Two-Dimensional and Three-Dimensional Reactors in Oxidative Electrochemical Degradation Studies of Malachite Green
Canan Şamdan 145-154
- 14 Investigation of Light Baryons in Hot *QCD*
Gülşah Bozkır 155-166
- 15 Distributed Control of a Vibrating String in Response to Pointwise Force Application
Şule Kapkın, Mehmet Şirin Demir, Erol Uzal 167-173

16	Evaluation of the Effect of Outer Skin Slope on Fire Safety in Double-Skin Façade Systems <i>Mehmet Akif Yıldız, Figen Beyhan</i>	174-186
17	A Rapid DMeyer-CWT Method Application to The Spectrophotometric Data for the Quantification of Losartan Potassium And Hydrochlorothiazide in a Binary Mixture <i>Özgür Üstündağ, Erdal Dinç</i>	187-194
18	Development of NGR-GelMA Hydrogels for <i>PC3</i> Prostate Cancer Cells <i>Ziysan Buse Yaralı Çevik, Meryem Zeybekoğlu, Ozan Karaman</i>	195-203
19	Analysis of Türkiye's Cybersecurity Strategies: Historical Developments, Scope, Content and Objectives <i>Hasan Çifci</i>	204-219
20	Effect of Adhesion and Corrosion Performance of Geomet Basecoat (321)- Topcoat (ML Black) Applications on Cataphoretic Coating <i>İbrahim Usta, Oğuz Yılmaz, Minel Gül, Ahmet Can, Harun Gül</i>	220-236

Investigation of the Effects of Cutting Fluid Application with Minimum Quantity Lubrication (MQL) Method on the Machinability of Pure Titanium

Yunus Kartal^{1*} , Ali Osman Er² 

^{1*} Kırıkkale University, Faculty of Engineering and Natural Sciences, Department of Mechanical Engineering, Kırıkkale, Türkiye, y.kartal@kku.edu.tr

² Kırıkkale University, Faculty of Engineering and Natural Sciences, Department of Mechanical Engineering, Kırıkkale, Türkiye, er@kku.edu.tr

*Corresponding Author

ARTICLE INFO

ABSTRACT

Keywords:

Minimum quantity lubrication (MQL)
Surface roughness
Cutting force
Sustainable manufacturing
Pure Ti



Article History:

Received: 22.07.2023

Accepted: 27.10.2023

Online Available: 27.02.2024

Machining is one of the widely used methods in today's technology and there are many parameters that affect the machinability of the produced product. In the machining process, the machinability of the product depends on parameters such as feed rate, depth of cut, cutting speed and cutting fluid. The use of cutting fluid during the process has advantages such as improving surface quality, but also disadvantages such as increased cost and environmental damage. Due to these disadvantages of cutting fluid in manufacturing processes, alternative methods have been developed. The method called minimum quantity lubrication (MQL) not only reduces cost but also improves machinability. In this study, the machinability of titanium turning was evaluated with main cutting force, surface roughness and temperature measured in the primary cutting zone data. MQL method was used in the study and Taguchi L9 model was applied. The results were compared between dry cutting and MQL atmospheres. The reliability of the data and the degree of influence of the parameters were analyzed by ANOVA. In this study, the shear force data obtained in the dry shear atmosphere were higher than the data obtained in the MQL method. In addition, the surface roughness values obtained in dry cutting atmosphere were also relatively high. The optimum cutting speed, feed rate and depth of cut values for the process were determined as 60 m/min, 0.05 mm/rev and 0.5 mm, respectively.

1. Introduction

In the manufacturing industry, technology is developing day by day to a degree that is difficult to follow. The manufacturing method to be chosen for the production of the object to be manufactured is decided by considering its advantages and disadvantages. Machining process is one of the most preferred methods in the manufacturing sector due to its advantages as well as its disadvantages such as the formation of residual parts we call chips and high temperature. To remove heat generated during the machining process, The Minimum Quantity Lubrication (MQL) method is the application of the minimum amount of cutting fluid to the cutting zone with

sustainability in mind, is becoming widespread day by day. In this method, the cutting fluid is sprayed through a nozzle tip and applied to the cutting zone. By aiming to minimize the consumption of cutting fluid, the MQL method prioritizes environmental sensitivity and reduces costs. With all these advantages, MQL method improves machinability. Studies using the MQL technique have generally investigated the effect of cutting atmosphere on machinability.

The MQL technique has been used in machining processes such as drilling [1], turning [2, 3], milling [4, 5]. In the studies, the effect of machining cutting atmosphere has been investigated by considering factors such as

machinability properties of the materials, tool wear [6, 7], surface roughness [8], cutting temperature [9], cutting oil [10]. In addition, the effect of cutting atmosphere on energy consumption, carbon emission [11], chip morphology [12] has also been studied. In addition, in another study, a region was named as a shadow zone in the MQL technique and the characteristics of the manufacturing process performed in this region were investigated [13]. In addition to the experimental studies, there are also review articles in which current studies are reviewed and future trends are given [14]. Studies using the MQL technique have achieved relatively better results than studies in dry cutting atmosphere [15].

It has been determined that there are studies in the literature using the MQL system and that it is still a subject worthy of further study. The studies were mostly completed using alloyed metallic materials. Since the MQL system is current in the literature and pure metallic materials are used relatively less, this study investigated the processability of pure titanium with the MQL system. The reason why the study was carried out with pure titanium is that titanium is used especially in machining production areas such as ships and submarines, and the coolant we use does not react with pure titanium.

2. Material Method

The study was carried out on a Goodway GLS-150 computer aided (CNC) lathe. Pure titanium material was used in the study and Kistler 9257b dynamometer, FLIR I50 thermal camera, Mitutoyo SJ-201 surface roughness measuring device, Werte Mikro STN 15 potentiometer controlled pulverized lubrication system and Trim E950 cutting fluid were used for the MQL system. The appearance of the system in which the study was carried out is given schematically in Figure 1.

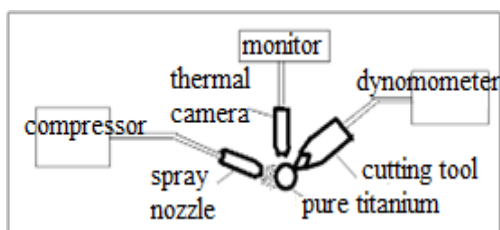


Figure 1. Schematic view of production

Technical specifications of pure titanium used in the study are given in Table 1.

Table 1. Technical properties of pure titanium

Density (g/cm ³)	4.51
Melting point (°C)	1668
Thermal conductivity (W/mK)	21.4
Modulus of elasticity (GPa)	105
Poisson's ratio	0.34
Hardness (BHN)	120

In the study, an MQL system with 0.1 s lubrication interval and 0.1 s lubrication time and bar pressure was used. Trim E950 cutting fluid was used in the study because it is relatively environmentally friendly vegetable-based and has a flash temperature above 160°C. In addition to these features, Trim E950 cutting fluid has a pH value of 8.8 - 9.4 and a refractometer coefficient of 1.0. In the study, Sandvik CNMG 12 04 08-SM 1105 grade PVD TiAlN coated insert and DCLNR 2020K 12 coded lathe tool holder were used.

Three three different depths of cut, three different feeds and three different cutting speeds were used in the study. The selected machining variables are cutting speed 60, 90, 120 m/min, feed 0.05, 0.15, 0.25 mm/rev and depths of cut 0.5, 1, 1.5 mm as given in Table 2. Since 27 experiments will be performed for each machining method in total, Taguchi method orthogonal array was used in order to save both cost and time. Using this method, 9 experiments were performed instead of 27 experiments. The least best approximation was used to evaluate results of the temperature, surface roughness and cutting force.

Table 2. Processing parameters

Parameters	Levels		
	Level 1	Level 2	Level 3
Cutting speed (m/min)	60	90	120
Feed rate (mm/rev)	0.05	0.15	0.25
Depth of cut (mm)	0.5	1	1.5

Since we will apply 3 levels and 3 factors in Taguchi method, L9 array was used. The factors and levels of this array are given in Table 3.

Table 3. Factors and levels of experiment numbers

No.	Factors and levels		
	A	B	C
1	1	1	1
2	1	2	2
3	1	3	3
4	2	1	2
5	2	2	3
6	2	3	1
7	3	1	3
8	3	2	1
9	3	3	2

3. Results and Discussion

In this study, in order to investigate the effect of machining parameters and cutting atmosphere on the machinability of pure titanium material in the machining process, two different cutting environments, dry cutting environment and MQL method, were realized by applying vegetable-based cutting fluid to the cutting zone. The results obtained were compared in terms of cutting force, temperature measured during the process and surface roughness measured after the process. For each result, the optimal machining parameters were determined according to the signal-to-noise ratios of the results by applying the least-best approach and the effect of processing parameters on the results was determined by analysis of variance.

3.1. Cutting force

The cutting force values obtained in different cutting environments are given in Table 4. The results can be followed visually in Figure 2, which was created with the data in Table 4. As can be seen from Table 4, the effect of the cutting atmosphere was affected by the process parameter values.

Table 4. Cutting force values and percentage of difference

No.	DRY (N)	MQL (N)	Difference (%)
1	134	88	34,33
2	423	326	22,93
3	875	835	4,57
4	451	158	64,97
5	820	450	45,12
6	310	252	18,71
7	575	536	6,78
8	248	183	26,21
9	560	511	8,75

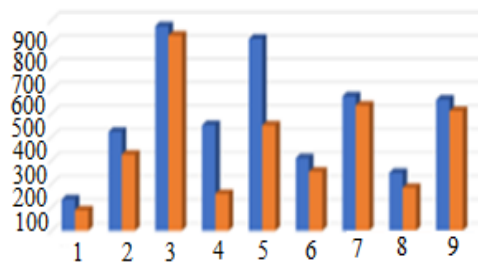


Figure 2. Cutting force values (blue: dry, orange: MQL)

The average of the cutting force values obtained in dry cutting atmosphere is 488 N and 371 N in conditions where cutting fluid is used. Considering the resulting cutting force data, the cutting forces are higher in dry cutting atmosphere.

Minitab application was used to examine the effect of processing parameters. Minitab application was used separately for each atmosphere condition. Signal-to-noise ratio was obtained through Minitab application and the most appropriate machining values were obtained. The Signal to Noise ratio graph obtained for shear force under dry cutting and cutting fluid conditions is given in Figure 3 and the ratio table is given in Table 5.

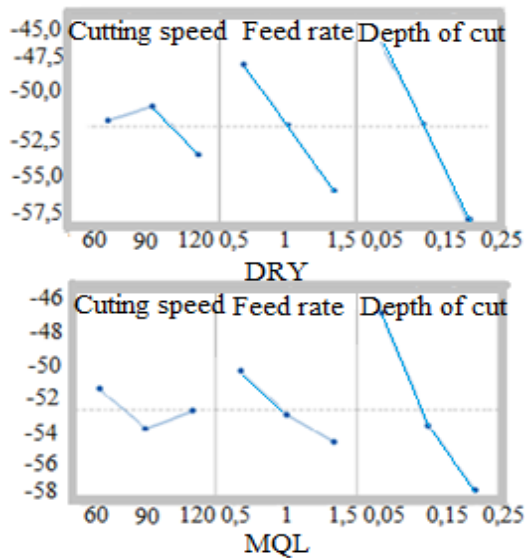


Figure 3. Signal to noise ratio plot of cutting force values for dry cutting and cutting fluid conditions

Table 5. Signal to noise ratio values of cutting force in dry cutting and cutting fluid conditions

DRY			
No.	Cutting speed (%)	Feed rate	Depth of cut
1	-49,20	-45,82	-44,06
2	-48,36	-49,53	-49,47
3	-51,33	-53,54	-55,36
MQL			
1	-51,30	-20,27	-46,75
2	-53,73	-52,90	-53,52
3	-52,68	-54,54	-57,44

Signal to Noise Ratio values in dry machining experiments were defined by selecting the smallest best option when performing Taguchi analysis in Minitab application. Therefore, according to the Signal to Noise Ratio data, the optimum values for cutting force are 60 m/min, 0.05 mm/rev and 0.5 mm for cutting speed, feed rate and depth of cut, respectively. In 10% cutting fluid and water solution atmosphere experiments, the optimum values for cutting force according to Signal to Noise Ratio are 90 m/min, 0.05 mm/rev and 0.5 mm for cutting speed, feed rate and depth of cut, respectively.

ANOVA analyses were performed to examine the effect of machining parameters on the cutting force data obtained under dry cutting conditions. The degree of influence of process parameters under dry cutting and cutting fluid conditions is shown in Table 6.

Table 6. Degree of influence of process parameters on the cutting force under dry cutting and cutting fluid conditions

DRY	
Parameter	Impact ratio (%)
Cutting speed	7,2
Feed rate	27,58
Depth of cut	64,61
MQL	
Parameter	Impact ratio (%)
Cutting speed	1,44
Feed rate	11,64
Depth of cut	84,29

Table 6 shows that the depth of cut is the most effective parameter on the cutting force in the study carried out under cutting fluid and dry cutting conditions.

The reliability rate of the study carried out in dry cutting atmosphere was found to be 97.37% by ANOVA analysis. In the study using cutting fluid, the reliability rate was found to be 99.4%.

Similar to our result, Akgün M., et al. reported that the most effective parameter on cutting force is feed rate [16].

3.2. Temperature

The temperature values obtained in dry cutting and MQL and vegetable cutting fluid spraying atmospheres are given in Table 7. The results can be followed visually in Figure 4, which was created with the data in Table 7. As can be seen from Table 7, the effect of the cutting atmosphere was affected by the process parameter values.

Table 7. Temperature values and percentage of difference

No.	DRY	MQL	Difference (%)
1	125	71,8	42,56
2	188	48,1	74,41
3	292	215	26,37
4	146	70	52,05
5	252	159	36,90
6	144	144	0
7	197	142	27,92
8	194	152	21,65
9	188	118	37,23

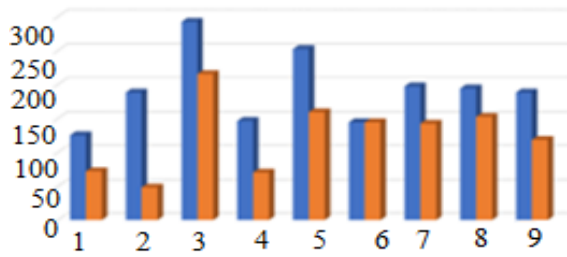


Figure 4. Temperature values (blue: dry, orange: MQL)

All of the measured temperature values of the parts processed in dry cutting environment during the process are higher than the temperature values measured in the cutting fluid atmosphere. This is actually an expected result; it is thought that the cutting fluid used removes the heat generated in the cutting zone.

Minitab application was used to examine the effect of processing parameters. Minitab application was used separately for each atmospheric condition. Signal-to-noise ratio was obtained through the Minitab application and the most appropriate processing values were obtained. The Signal to Noise ratio table obtained for cutting force under dry cutting and cutting fluid conditions is given in Table 8 and the ratio graph is shown in Figure 5.

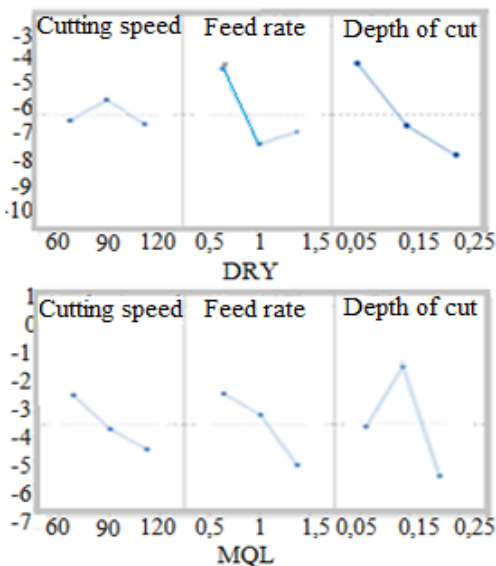


Figure 5. Signal to noise ratio plot of temperature values in dry machining and cutting fluid atmosphere

Table 8. Temperature signal-to-noise ratio values in dry machining and cutting fluid atmosphere

DRY			
No.	Cutting speed	Feed rate	Depth of cut
1	-39,14	-39,02	-41,31
2	-41,37	-40,44	-37,33
3	-42,71	-43,75	-44,57
MQL			
1	-45,58	-43,70	-43,62
2	-44,83	-46,20	-44,75
3	-45,71	-45,99	-47,74

In dry atmosphere tests, the optimum values for temperature according to the Signal to Noise Ratio are 90 m/min, 0.05 for mm/rev and 0.5 mm for cutting speed, feed rate and depth of cut, respectively. In the environment where cutting fluid is used, the optimum values for temperature according to Signal to Noise Ratio are 60 m/min, 0.05 to mm/rev and 1 mm for cutting speed, feed rate and depth of cut, respectively.

ANOVA analyses were performed to examine the degree of influence of process parameters on the temperature data obtained under dry cutting conditions. Table 9 shows the effect of process parameters under dry cutting and cutting fluid atmosphere conditions.

Table 9. Effect of process parameters on temperature in dry cutting and cutting fluid atmosphere

DRY	
Parameter	Impact ratio (%)
Cutting speed	4,41
Feed rate	28,16
Depth of cut	58,23
MQL	
Parameter	Impact ratio (%)
Cutting speed	2,96
Feed rate	25,60
Depth of cut	63,37

In the experiments carried out in dry cutting and cutting fluid atmosphere, the most effective parameter on the temperature values was the depth of cut in both working environments (Table 9).

The reliability ratio study performed with the measured temperature data was found to be 91.93% in dry cutting ANOVA analysis and

90.80% in the environment where cutting fluid was used.

3.3. Surface roughness

Surface roughness values measured at different cutting atmospheres are given in Figure 6.

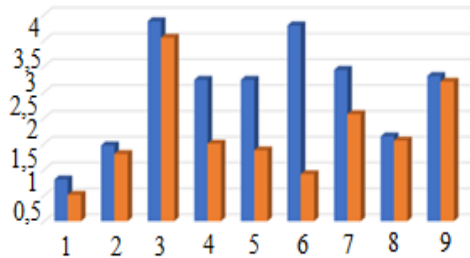


Figure 6. Surface roughness values (blue: dry, orange: MQL)

When the surface roughness values obtained from different cutting environments were analyzed, it was determined that the values measured in dry cutting atmosphere were higher.

Minitab application was used to examine the effect of processing parameters. Minitab application was used separately for each atmosphere condition. Signal-to-noise ratio was obtained through the Minitab application and the most appropriate machining values were obtained. The Signal to Noise ratio graph obtained for surface roughness values under dry cutting and cutting fluid conditions is given in Figure 7 and the ratio table is given in Table 10.

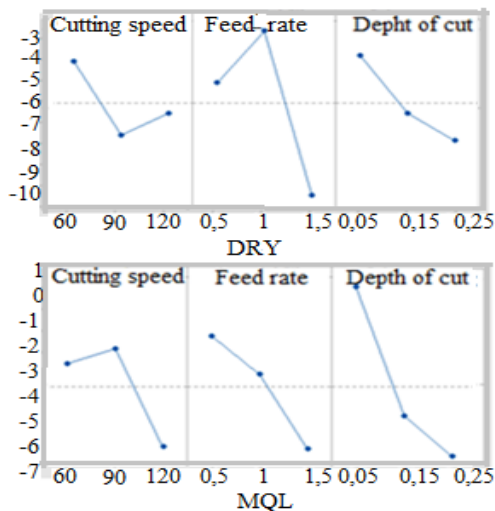


Figure 7. Signal to Noise ratio plot generated from surface roughness data obtained from dry cutting and machining in cutting fluid atmosphere

Table 10. Surface roughness signal to noise ratio values in dry cutting and cutting fluid atmosphere

DRY			
No.	Cutting speed	Feed rate	Depth of cut
1	-4,41	-4,15	-5,40
2	-7,89	-6,80	-3,03
3	-6,78	-8,04	-10,54
MQL			
1	-2,47	-0,94	-1,24
2	-1,81	-4,80	-2,95
3	-6,19	-6,60	-6,27

In dry atmosphere experiments, the optimum values for surface roughness according to Signal to Noise Ratio are 600 m/min, 0.05 mm/rev and 1 mm for cutting speed, feed rate and depth of cut, respectively. In cutting fluid atmosphere experiments, the optimum values for surface roughness according to Signal to Noise Ratio are 90 m/min, 0.05 mm/rev and 0.05 mm for cutting speed, feed rate and depth of cut, respectively.

ANOVA analyses were performed to examine the degree of influence of the process parameters on the surface roughness data obtained under dry cutting conditions. Table 11 shows the degree of influence of process parameters in dry cutting and cutting fluid atmosphere conditions

Table 11. Effect of process parameters on surface roughness in dry cutting and cutting fluid atmosphere

DRY	
Parameter	Impact ratio (%)
Cutting speed	5,50
Feed rate	62,05
Depth of cut	8,72
MQL	
Parameter	Impact ratio (%)
Cutting speed	15,37
Feed rate	45,91
Depth of cut	38,72

The most effective parameter for the surface roughness values obtained in both dry cutting atmosphere and MQL cutting conditions is the feed rate. Similarly, in their study, Subbaiah K.V., et al [17]. determined that the most effective parameter on surface roughness was feed rate (Table 11).

The reliability rate of the study was found to be 76.27% with the ANOVA analysis and 83.92% in the cutting fluid atmosphere.

4. Conclusion

The effects of the machining parameters used in the machining of pure titanium material in different cutting atmospheres on surface roughness, cutting force and temperature were investigated and the following results were obtained:

- It was found that the cutting force values were affected by the cutting conditions and the measured cutting force value was higher in dry cutting atmosphere. The difference between the cutting force data obtained in different cutting atmospheres is 64.97% and the smallest difference is 4.57%.

- It was determined that the most important effect on the cutting force data in dry cutting atmosphere was 84.29% of the depth of cut and the most important effect on the cutting force data in MQL cutting atmosphere was 64.6% of the depth of cut.

- The effect of feed rate on cutting force increased from 11.64% to 27.58% with MQL. For cutting speed, it increased from 1.44% to 7.20%.

- Due to the good wetting achieved with MQL, the average improvement in cutting force values was 23.98%.

- In the analysis of the parameters affecting the cutting force, the measured results were obtained with a high probability of accuracy. The overall probability of accuracy of the obtained results is around 97%.

- It was found that the temperature measured in the primary cutting zone increased with increasing depth of cut values and MQL was more effective on the temperature reduction rate. It is thought that fluid velocity, pressure and removal of heat from the environment with chips are effective in the temperature reduction of MQL.

- The most influential machining parameter on temperature data is depth of cut with 63.37% in dry cutting atmosphere, while The most effective machining parameter in the MQL machining atmosphere is the depth of cut with 58.23%.

- As cutting speed and the depth of cut increase, the temperature also increases and this has a negative effect on the surface roughness. In dry cutting atmosphere, when the results obtained from the surface roughness measured at the end of machining are analyzed, the most effective parameter is the feed rate with 62.05%.

- The accuracy data of the temperature values measured in the cutting zone are on average 85% accurate. This means that the results are highly reliable.

- When the surface roughness values measured after machining were analyzed, the most effective parameter was determined as feed rate by ANOVA analysis. As the feed rate, which refers to the movement of the cutting tip on the material to be cut in one cycle during production in the machining process, increases, the roughness on the material will increase due to the increase in the distance between the two feed steps.

Article Information Form

Acknowledgments

The author wants to thank Kırıkkale University.

Funding

This study was supported by Kırıkkale University Scientific Research Projects Unit with project number 2021/050. Kırıkkale, Türkiye.

Authors' Contribution

The authors contributed equally to the study.

The Declaration of Conflict of Interest/ Common Interest

No conflict of interest or common interest has been declared by the authors.

The Declaration of Ethics Committee Approval

This study does not require ethics committee permission or any special permission.

The Declaration of Research and Publication Ethics

The authors of the paper declare that they comply with the scientific, ethical and quotation rules of SAUJS in all processes of the paper and that they do not make any falsification on the data collected. In addition, they declare that Sakarya University Journal of Science and its editorial board have no responsibility for any ethical violations that may be encountered, and that this study has not been evaluated in any academic publication environment other than Sakarya University Journal of Science.

Copyright Statement


Authors own the copyright of their work published in the journal and their work is published under the CC BY-NC 4.0 license.

References

- [1] P. Krishnan, S. Raj, "Machinability and tribological analysis of used cooking oil for MQL applications in drilling AISI 304 using a low-cost pneumatic operated MQL system," *Journal of Manufacturing Processes*, vol. 104, pp. 348-371, 2023.
- [2] R. Maruda, N. Szczotkarz, M. Michalski, K. Arkusz, S. Wojciechowski, P. Niesłony, N. Khanna, G. M. Królczyk, "Evaluation of tool wear during turning of Ti6Al4V alloy applying MQL technique with Cu nanoparticles diversified in terms of size," *Wear*, vol. 532, no.533, pp. 205111, 2023.
- [3] M. Danish, M. K. Gupta, S. Rubaiee, A. Ahmed, M. E. Korkmaz, "Influence of hybrid Cryo-MQL lubri-cooling strategy on the machining and tribological characteristics of Inconel 718," *Tribology International*, vol. 163, pp. 107178, 2021.
- [4] L. Li, J. Xu, G. Guo, M. K. Gupta, M. Chen, "Wear behavior of different coated tools in MQL-assisted high-speed milling of magnesium-based rare-earth alloys," *Journal of Materials Research and Technology*, 2023.
- [5] H. Sun, B. Zou, P. Chen, C. Huang, G. Guo, J. Liu, L. Li, Z. Shi, "Effect of MQL condition on cutting performance of high-speed machining of GH4099 with ceramic end mills," *Tribology International*, vol.167, pp. 107401, 2022.
- [6] V. Kharka, S. Mujumdar, S. Shukla "Study on helical milling of SS 304 with small diameter tools under the influence of minimum quantity lubrication (MQL)," *Manufacturing Letters*, vol. 35, pp.1312-1317, 2023.
- [7] L. Tu, J. Chen, Q. An, W. Ming, J. Xu, M. Chen, L. Lin, Z. Yang, "Machinability improvement of compacted graphite irons in milling process with supercritical CO₂-based MQL," *Journal of Manufacturing Processes*, vol. 68, no. A, pp. 154-168, 154–168, 2021.
- [8] A. Roushan, U. S. Rao, K. Patra, P. Sahoo, "Performance evaluation of tool coatings and nanofluid MQL on the micro-machinability of Ti-6Al-4V," *Journal of Manufacturing Processes*, vol. 73, pp. 595–610, 2022.
- [9] A. Uysal, "Ferritik paslanmaz çeligin çok duvarli karbon nanotüp katkili kesme sivisi kullanılarak minimum miktarda yağlama yöntemi ile frezelenmesinde kesme sicakliginin incelenmesi," *Journal of the Faculty of Engineering and Architecture of Gazi University*, vol. 32, no. 3, pp. 645–650, 2017.
- [10] P. K. Nishad, "An investigation on performance of castor oil and Pongamia oil based cutting fluid in MQL milling of aluminium alloy 6061," *Materials Today: Proceedings*, 2023.
- [11] B. K. Mawandiya, H. V. Patel, M. A. Makhesana, K. M. Patel, "Machinability investigation of AISI 4340 steel with biodegradable oil-based MQL system," *Materials Today: Proceedings*, vol. 59, no. 1, pp. 1-6, 2021.
- [12] M. E. Korkmaz, M. K. Gupta, M. Boy, N. Yaşar, G. M. Krolczyk, M. Günay, "Influence of duplex jets MQL and nano-

- MQL cooling system on machining performance of Nimonic 80A,” *Journal of Manufacturing Processes*, vol. 69, pp. 112–124, 2021.
- [13] S. Saha, S. Deb, P. P. Bandyopadhyay, “Shadow zone in MQL application and its influence on lubricant deficiency and machinability during micro-milling,” *International Journal of Mechanical Sciences*, vol.220, pp. 107181, 2022.
- [14] D. Panda, K. Kumari, N. Dalai, “Performance of Minimum Quantity Lubrication (MQL) and its effect on Dry Machining with the addition of Nano-particle with the biodegradable base fluids: A review,” *Materials Today: Proceedings*, vol. 56, no.3, pp. 1298-1301, 2022.
- [15] A. Panday, G. S. Goindi, N. Singh, “Evaluation of effect of oil viscosity in MQL turning of aluminium 6061,” *Materials Today: Proceedings*, vol. 48, no. 5, pp. 1740–1747, 2021.
- [16] M. Akgün, B. Özlü, “Optimization of Cutting Parameters Affecting Cutting Force and Surface Roughness in Machining of AISI P20 Die Steel”, *Open Journal of Nano*, vol. 7, no.1, pp. 2147, 2022.
- [17] K.V. Subbaiah, C. Raju, C. Suresh, (2020) “Parametric analysis and optimization of hard turning at diferent levels of hardness using wiper ceramic insert,” *Measurement*, vol.158, no.1, pp.107712, 2020.

Drag Reduction on Microstructure Surfaces

Ahmet Ilyas Kodal¹ , Şule Kapkın^{1*} , Hasan Rıza Güven¹ 

¹ Istanbul University – Cerrahpaşa, Faculty of Engineering, Department of Mechanical Engineering, Istanbul, Türkiye, ahmetilyas.kodal@ogr.iuc.edu.tr, skapkin@iuc.edu.tr, hrguven@istanbul.edu.tr

*Corresponding Author

ARTICLE INFO

ABSTRACT

Keywords:

Bird Feather
CFD
Drag Reduction
Surfaces
Riblet.

In this study, experimental work in the literature about friction on bird-feather like structures has been reviewed and one of these was modeled by using CFD (Computational Fluid Dynamics) to obtain minimum grid parameters. Coupled with obtained optimal grid parameters, the shear stresses of the two-dimensional models were investigated at the values of Reynolds number 110,000-470,000. Based on the concluded previous study, three-dimensional geometries were modeled with reference to two-dimensional models and analyzed with the determined grid structure. The results of the analysis are compared with those of the previous experimental study in the literature. In the final phase of the study, a drag reduction was found to be approximately 30% on the surfaces inspired by bird feathers.

Article History:

Received: 17.08.2023

Accepted: 17.10.2023

Online Available: 27.02.2024

1. Introduction

Reducing the friction at surfaces is an important problem for many industries especially in transportation where fuel consumption and speed are both important parameters. Total drag can be reduced not only by optimizing the form of the body, but also by changing the surface structure so as to reduce viscous friction. In this regard, there have been studies conducted with the inspiration coming from shark skin and bird feathers. Shark skin inspired surfaces reduce drag by up to 10%, while bird feather inspired surfaces are up to 20%.

Reducing drag allows the objects to spend less energy, move faster and cover a longer distance and have higher efficiency. For example, the fuel consumption of land vehicles, air crafts and ships can be reduced by reducing drag. It was reported

that covering 70% of the surfaces of Boeing and Airbus planes with the rough surface structures reduced fuel consumption by 1% [1].

Friction at surfaces can be reduced greatly by making micro-scale changes at the surface. Many methods have been developed for accomplishing this; micro-grooved surface structures employed by Pulles (1988), and micro-ballonet structures made by Kodama et al. (2005) can be given as examples. Many similar methods have been developed and each method reduces drag at various levels [2, 3].

It is a known fact that the surfaces of flying organisms evolved in the form of microstructures which would give the most appropriate shape for drag reduction. For example, microstructures of shark skin influence reducing turbulence and drag on which much work has been done [4].

Longitudinal prominent and discrete surfaces at unusual sizes and angles which were designed and used at oil-channel experiments by Bechert et al. (1997) achieved maximum 8,7% drag reduction [1]. Walsh and Lindemann (1984) found that 8% drag reduction occurred by copying the microstructure of shark skin to the surfaces (at the value of $s^+=15$) by his work which was also called the effect of shark skin. This s^+ is the dimensionless distance among the micro riblets and calculated with the formula $s^+ = s\sqrt{\tau}/\nu$. s refers to the distance among the riblets, $\sqrt{\tau}$ refers to the friction velocity and the ν denotes viscosity. Friction velocity is expressed as $\sqrt{\tau} = \sqrt{(\tau_0/\rho)}$, it is related to shear stress on smooth surfaces [5].

To examine the effect of the surface shape on the friction resistance, Bourisli and Al-Sahhaf (2008) analyzed friction coefficient and velocity by a series of simulation tests using riblets in three different directions, square, triangular and semi-circular. As a result, they found that three of the rough surfaces gave less resistance to smooth surfaces and that the triangular riblets provided the greatest drag reduction [6]. Using the simulation software, El-Samni et al. (2007) determined the pressure gradient to compensate for mass flow on smooth surfaces such as curved surfaces at different protrusions and grooves. This system was used to geometrically optimize gaps between protrusions and protrusions in relation to drag reduction, and a reduction of 11% drag was achieved in these studies [7]. Ren et al. (2005) studied bionic smooth surface evaluation in bending surface design [8]. In different sizes, smooth surfaces carrying a convex body, pits and protrusions were subjected to low speed, subsonic and supersonic wind tunnel tests. The results show that all of the tested smooth surfaces give reduced resistance and the highest drag reduction rate is about 5%. To illuminate the mechanisms underlying drag reduction on smooth surfaces, Sirovich and Karlsson (1997) tested the change in drag reduction on V-shaped grooved surfaces in the wind tunnel. They have found that turbulence energy distribution is reduced by drag reduction and that a reduction in turbulence energy distribution may be a mechanism used by the rough surface approaches [9]. In their study,

Bullen and McKenzie (2008) observed that 23 of bat species living in Western Australia could reduce the drag resistance of rough-surfaced areas on the head and body skin of high-speed flying species by 10% [10].

Birds are another class of organisms with microstructured surfaces. It is known that flight movements and soaring patterns of birds are in the form to minimize the drag force. The microstructure of birds feathers reduces drag significantly. Birds have developed excellent structures by means of evolution along millions of years such as hollow feather shafts and an aerodynamic shape for increasing the flying performance. The alignment of the riblets along the shafts on each wing is a typical feature of bird feathers. This provides the nerds of birds feathers to be attached perfectly especially for major and minor feathers of wings. It is assumed that riblets on such microstructures on feathers reduce drag strongly [11].

Much work has been done on the prepared surfaces which have been inspired by the microstructures of the feathers. In the experimental work made by Tucker and Parrott (1970), Harris falcons floated freely in the air tunnel and they measured the minimum drag with trimming or without trimming the tip feathers of falcons. As a result, they found that trimmed falcons increased drag by 70-90% [12].

Nachtigall (1998) found that, the smooth starling model he used experimentally in the air tunnel has 14% lower drag than the starling model [13]. Figure 1 shows the Starling's position in the wind tunnel. In an experiment in the water tunnel, Chen et al. (2014) observed that the height/width ratio of the drag in three different geometric shapes and dimensions that was inspired by bird feather is the best at 0.6 and reduces the drag up to 21% [14]. Zhou (2006) examined the rough surface of pigeon feather. The placement of the smooth surfaces with protrusions behind the rotary gantry has resulted in a drag reduction of 16.56% as measured by the simulation test [15].

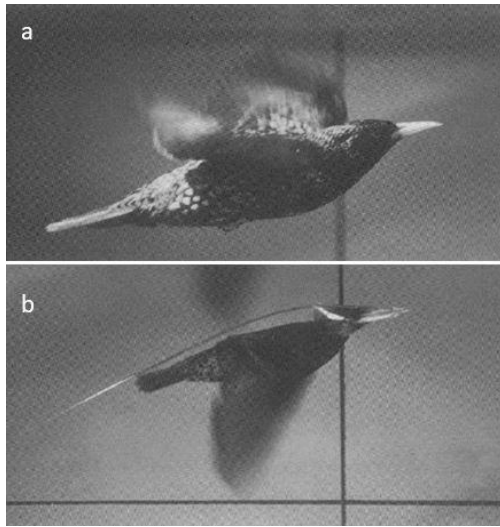


Figure 1. (a) Starling, flying horizontally in wind tunnel, (b) same starling and wind tunnel conditions, the starling wearing a respiration mask [13]

The present study aims to examine micro-grooved structures in varied sizes. The change in drag is examined in three stages on artificial surfaces inspired by the structure of pigeon feather. In the first stage, the experiment by Chen et al. (2013) were modeled in the CFD environment under the same inception and boundary conditions. The purpose of this step is to determine the differences between the experiment and CFD results [16]. In the second step, the effect of geometric dimensions and shapes of riblets on drag is examined by changing height, width and geometric shapes and dimensions, and the optimum parameters are determined. Finally, the change in drag by changing s^+ rate is computed for this optimum shape. This study shows that designing new models of various sizes and geometries can further reduce the drag.

1.1. The Structure of bird feathers

Although the structure of bird feathers changes according to the species, the general features are similar. Feather geometry evolved according to the environmental conditions in different geographical regions and reached the most suitable structure. The wings covered with feathers are flying mechanisms of birds. The wings have changing drag values on different wing surface and wing width ratios [17].

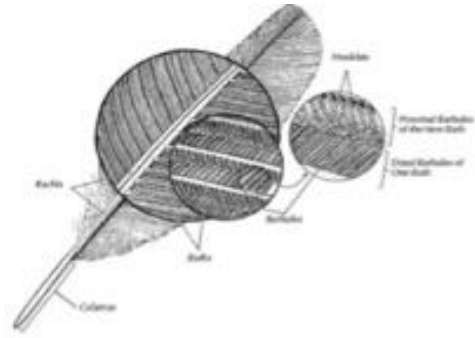


Figure 2. Microscopic appearance of flight feather [18]

Microscopic examination of the feather structure shows that feather nerds are aligned bilaterally along the shaft. The strings between the adjacent nerds run correspondingly along the nerd. As seen in Figure 2 by locating the inner and outer sides up to the shaft, the microstructure strings form the feather riblets. Due to the micro grooved protruding structures on the feather, riblets interact with the flow and crossflow velocity fluctuations occur through riblet holes. These fluctuations affect surface shear stress and momentum transfer positively and reduce drag. Although the distance between the strings, s , is the same everywhere, the height of strings, h , goes down as one moves away from the nerd. Generally, the rate of h/s of the feathers changes between 0.2 and 0.9.

2. Numerical Methods

2.1. Turbulence model

The turbulence model has immense importance in computational studies. The choice of turbulence model changes depending on flow geometry. A study comparing results obtained by using different turbulence models with the experimental results was carried out by Shi et al. (2016). The mentioned study concluded that RNG turbulence model with $k-\varepsilon$ equations was the one that gave the closest results to the experimental values [19].

RNG turbulence model with $k-\varepsilon$ equations gives better results for rapidly strained flows and swirling flows [19]. RNK $k-\varepsilon$ model can be written as

$$\frac{\partial}{\partial t} (\rho k) + \frac{\partial}{\partial x_i} (\rho k u_i) = \frac{\partial}{\partial x_j} \left(\alpha_k \mu_{eff} \frac{\partial k}{\partial x_j} \right) + G_k + G_b - \rho \varepsilon - Y_M + S_k \quad (1)$$

$$\frac{\partial}{\partial t} (\rho \varepsilon) + \frac{\partial}{\partial x_i} (\rho \varepsilon u_i) = \frac{\partial}{\partial x_j} \left(\alpha_\varepsilon \mu_{eff} \frac{\partial \varepsilon}{\partial x_j} \right) + C_{1\varepsilon} \frac{\varepsilon}{k} (G_k + C_{3\varepsilon} G_b) - C_{2\varepsilon} \rho \frac{\varepsilon^2}{k} - R_\varepsilon + S_\varepsilon \quad (2)$$

$C_{1\varepsilon}$, $C_{2\varepsilon}$ and $C_{3\varepsilon}$ are model constants. G_k represents the kinetic energy due to the average velocity. G_b represents the contribution of the fluctuating dilatation in compressible turbulence to the overall dissipation rate, the quantities αk and $\alpha \varepsilon$ are the inverse effective Prandtl numbers for k and ε , respectively. S_k and S_ε are user-defined source terms.

2.2. Drag calculations

The drag reduction is characterized by the surface friction coefficient differences between the selected reference surface and the tested surface. The drag reduction ratio (DR) is calculated by using the experimental value of Chen et al. (2013) and CFD value by the formula [16]:

$$\%DR = \frac{\Delta \tau}{\tau} = \frac{F_c - F_r}{F_r} \quad (3)$$

Here, F_c is the friction coefficient of structured surface, F_r is the friction coefficient of reference surface (smooth surface). The difference between the shear stress on the reference surface and the shear stress on the tested surface is denoted $\Delta \tau$. The negative value of DR shows that drag decreases, while the positive value shows that drag increases.

3. Numerical Methods

3.1. Comparing the results of experiment and CFD

This section compares the experimental data of Chen et al. (2013) using water tunnel with the CFD results under the same boundary and initial conditions which the structural parameters of bio-inspired herringbone was set as following values [16]: $s=100\mu\text{m}$, $h/s=0.6$, $\theta=60^\circ$. And, the length of horizontal empirical surface 0.04 with the generated riblet surface which 0.03 riblet surface along. The water tunnel which was used for the experiment, the total test tube length was 0.6 m and the distance between the two-low

pressure measuring holes was 0.5 m, and the test surface was covered in the tube as bonding the skins.

The turbulent tube flow that comes to the test room at constant temperature is completely improved. Figure 3 shows the computational environment of the models used along with representative figure experimental skin which was used in conducted tests. Also, the model test surface is considered flat and other boundary conditions were practically identical. The 1.5% margin of error inflicted of bending the test surface in the experiment is considered in the analysis results and while calculating this difference is also considered.

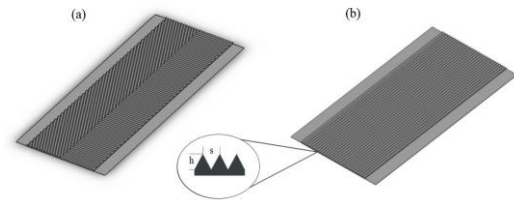


Figure 3. Bird feather model (a) and traditional model, (b) used in Chens experiment

For the different s values from the result of the analysis, changing the drag reduction values of the three models was compared with the results of the experiment. There is a 1-2% difference between the experimental results and the analysis results, this difference consists of the mesh number and variations inflicted on bonding the test surface in the experimental setup. Furthermore, the difference could occur due to an adverse effect of surface wrinkling. In this preliminary study, since the grid structure of the model captures the experimental results, this grid structure is also used in the newly developed models.

The results obtained from two different models show that the amount of drag reduction changes depending on the surface skin riblet replacements. It has been evidently concluded that V-shaped skin has greater influence at reducing the drag force as calculated data derived with the same input values other than skin replacement. Consequently, with a higher value of drag reduction, V-shaped riblet skin is employed in subsequent analyses. In the work by

Dean and Bhushan (2010) the effects of variation of the h/s ratio on riblets were examined. Based on the result obtained by Dean and Bhushan (2010), h/s ratio critical impact, as well as skin replacement, led the research to focus in examination to various h/s ratio model with the same riblet adjustment as a support that the total amount of drag reduction can be increased by regenerating ratio [20]. The results of CFD and H. Chens experiment in Figure 4.

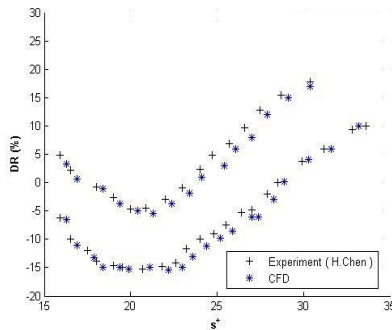


Figure 4. The results of CFD and H. Chens experiment

3.2. The effects of surface feature’s size and shapes on Drag - Dimension effects

At this stage, firstly, models are designed as 2 dimensional in varied sizes and shapes. According to the results obtained from 2-dimensional analysis, the value of apical angle being kept constant, the effects of the dimensions and shapes of riblets on drag reduction is evaluated at the second stage. Models that gave reliable results at the end of analysis are redesigned as 3 dimensional models. Designed 3 dimensional models were analyzed in computer environment and the reduction in drag for different $s+$ values examined.

3.3. Examination on 2 dimensional geometries

On prepared models inspired by the bird feather structure, drag values change by the geometric measures of the feather structure. The change in shear stress due to the geometric shape of the riblet, its height h and width s , was studied. The geometric features that would be used in 3 dimensions were determined by optimizing geometries that were created on two dimensions (Figure 5). The geometric shapes of the models

used are shown below. The total length of the models is all 0.0022 m.

The change in shear stress with width and height are examined initially by changing width values s at constant height values h , and then with constant width and changing height of different prepared geometric shapes of models. Dimensions of the models are shown in Table 1.

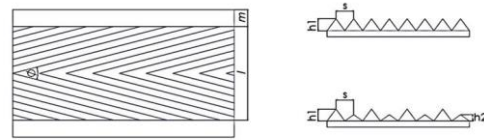


Figure 5. The schematic view of the 3D model

3.4. 3D models

E2 and B2 models which gave appropriate results in two-dimensional analysis were carried onto 3 dimensional models and were analyzed using the Fluent program. The E2 model which was chosen among two-dimensional models was shaped identically and in different dimensions with the riblet of the micro-grooved V-shaped model used in Chen et al. (2013) experiment [16]. The B2 model which gave the best results was formed in different geometric shapes and dimensions. The length and width of the models are taken as 0.035 m. The type of the models are given in Figure 6 and the dimensions are given in Table 2. The riblet of the apical angle in both models is 60 degrees. The riblets were mutually aligned, and the angle denoted as ϕ is 60 degrees. The height of flow area was taken 20 times more than the height of riblet.

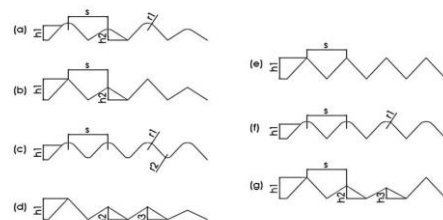


Figure 6. (a) type A model (b) type B model (c) type C model (d) type D model (e) type E model (g) type G model

3.5 Mesh resolution

Models were meshed by observing the y^+ value was less than 1 with the analysis mesh and ICFM CFD. All 2-dimensional models are made up of about 100.000 calculation elements while 3 dimensional models are made up of 5 million. The height of the calculation area was taken 20 times more than the height of riblet of the model. The general mesh view of the models is shown in Figure 7 and the shear stresses of two-dimensional models are shown in Figure 8.

3.5.1 Mesh structure in two-dimensional model

The Ansys-Mesh program was used for meshing the two-dimensional models. The mesh was created in two stages, first the large cells forming the control volume and then the small cells near

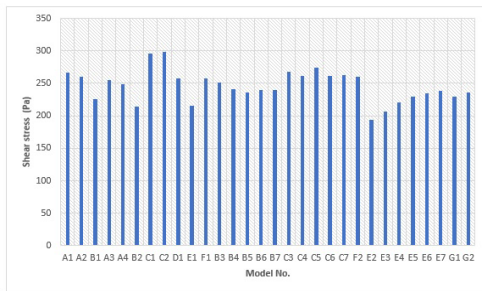


Figure 8. Shear stresses of two-dimensional models

The mesh structure has an average mesh quality of 0.72, with a maximum quality of 1 and a minimum quality of 0.0260. Cells with low mesh quality will have no effect on the analysis since they are not on or near the walls of the flow volume, i.e. on or near the surface to be analyzed.

3.5.2. Mesh structure of the three-dimensional mode

The dimensions of the flow volume were chosen small enough not to disturb the flow in order to reduce the computation time. At the same time,

the surface. The inlet, outlet and outer surfaces of the flow volume were formed by triangular cells. The middle volume of the flow volume was formed with rectangular cells. The numerical mesh structure was prepared with smaller and denser cells on the surface to be analyzed and larger and sparser cells towards the walls of the flow volume. The reason for creating cells with different sizes and shapes in the flow volume is to ensure faster convergence of the analysis.

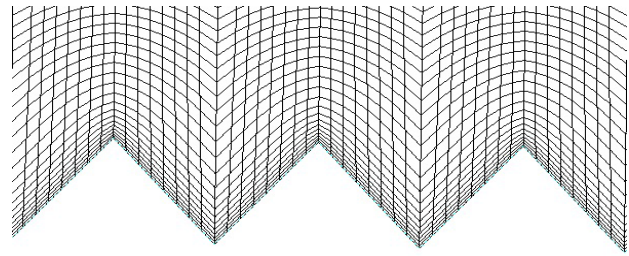


Figure 7. Mesh view of two-dimensional model

the side walls of the flow volume were taken as symmetry to reduce the computation time. Thus, the number of meshes was halved. Most of the cells in the numerical mesh structure were placed in the boundary layer of the surface to be analyzed.

Mesh structures have an average mesh quality of 0.6-0.7, with a maximum quality of 1 and a minimum quality of 0.00267. Cells with low mesh quality will have no effect on the analysis since they are not on the walls of the flow volume, i.e. on or near the surface to be analyzed (Figure 8).

3.6. Analysis of models

Models were analyzed in the ansys-fluent program as time-independent. RNG k- ϵ was chosen as the turbulence model with enhanced wall treatment. Water has taken as fluid with the velocity of 1-5 m/s and analyzed separately for each case. The turbulence density taken 5% and the turbulence viscosity ratio taken 5.

Table 1 2D Dimensions of the models

Constant s											
Model No.	$h1(\mu m)$	$h2(\mu m)$	$h3(\mu m)$	$s(\mu m)$							
A1	50	20	—	100							
A2	50	26	—	100	10	—	B4	80	60	30	
A3	55	25	—	100	5	—	B5	90	60	30	
A4	55	31	—	100	5	—	B6	110	60	30	
B1	60	30	—	100	—	—	B7	120	60	30	
B2	60	36	—	100	—	—	C3	70	50	—	
C1	50	—	—	100	10	5	C4	80	50	—	
C2	55	—	—	100	5	10	C5	90	50	—	
D1	60	58	—	100	—	—	C6	110	50	—	
E1	60	—	—	100	—	—	C7	120	50	—	
E2	70	—	—	100	—	—	E3	70	60	—	
F1	50	—	—	100	10	—	E4	80	60	—	
F2	70	—	—	100	—	—	E5	90	60	—	
G1	60	30	30	100	—	—	E6	110	60	—	
G2	60	36	30	100	—	—	E7	120	60	—	

Table 2. 3D models dimension table

Models	L(m)	$s(\mu m)$	$h1(\mu m)$	$h2(\mu m)$
E2-3D	0.03	100	70	—
B2-3D	0.03	100	60	36

Fluid particles do not slip because the velocity of the fluid contacting parts of the wall is zero. For this reason, a no-slip condition is preferred for the flow volume walls and the surface to be analyzed. In 3D models, the sides are symmetrical and the outlet pressure is equalized to the atmospheric pressure (Figure 9). The SIMPLE algorithm was chosen as the solution method and the convergence criterion was taken as 10^{-5} ($C1_\epsilon = 0,43$; $C2_\epsilon = 1,92$; $C3_\epsilon = 0,09$). The shear stresses of the models were investigated at the values of Reynolds number 110,000-470,000. Simulate the 3D geometry is shown in Figure 10.

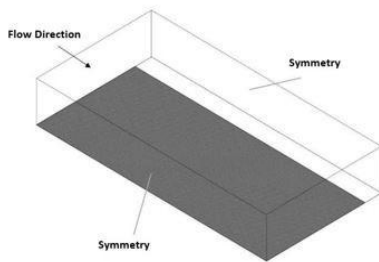


Figure 9. Simulation model of 3D geometries

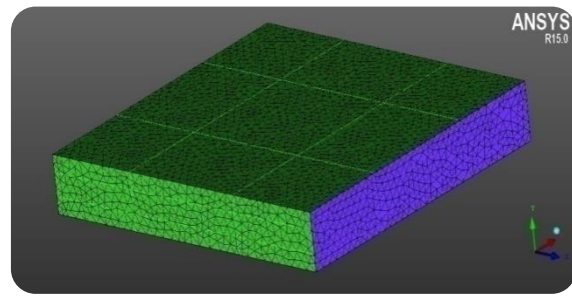


Figure 10. General cross-sectional image of 3D models

4. Results

The validity of the CFD study has been demonstrated by comparison with the experimental work in the literature. Shear stresses, one of the drag reduction parameters, were investigated in 2D models of 30 different sizes and shapes. The comparison of surface shear stresses in models from the analysis is given in Figure 9. It is found that the shear stresses of E2 and B2 models are lower than other models. The velocity vectors of E2 and B2 models near the wall are shown in Figure 11. As seen in the figures swirls interact with the points of riblet and create low-velocity areas in the spaces of holes. These low-velocity areas create low shear stress with the cross-flow velocity fluctuations [3].

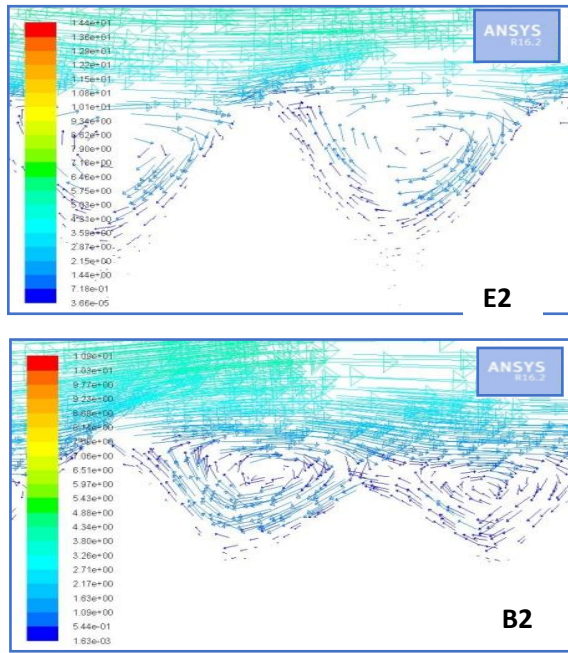


Figure 11. Velocity of E2 and B2 models at the sections near the wall

If these stress values are much at the points of riblet, they stay only in a very small area. Most of the surface area has low surface stress. In this study, in the analysis which has different parameters on geometries shear stresses, initially with the values of geometries which has constant width s , changing height h and constant height h , changing width s are examined. According to the results, it was pointed geometry gave the best results. It has been observed that, the analysis made on this geometry with the constant width and changing height by decreasing the value h provides better results on reducing drag of geometry. It has been observed that, as the height value increases, it affects negatively, and the best result has been taken on 60-70 micrometers.

For the width values as the width increases better results increases parallelly while s value was found to give worse results than values were greater than 120 micrometers. On the prepared B2-3d and E2-3d models which inspired of 2 dimensional models, alternately from 18% to 30% drag reduction has been found. In Figure 12, the results of Bechert et al. (1997) experimental work with the results of this study about how different s^+ values change the drag was compared [1]. The drag reduction for both

models was observed to be maximum at $s^+ \approx 15$ value.

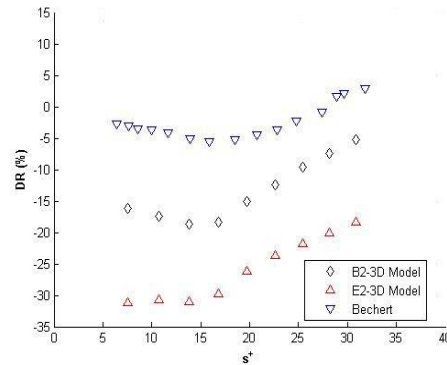


Figure 12. DR/ s^+ comparison of CFD and Bechert's experiment

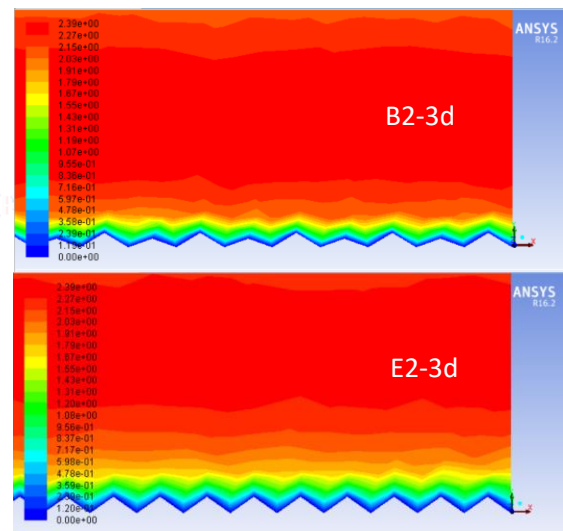


Figure 13. Cross-section velocity contour graphics of the B2-3d and E2-3d models near the wall

As it observed in the cross-section velocity contour, the viscous substratum of the E2-3d model is thicker than the B2-3d model. Consideration of the viscous lower layer removes turbulent swirls from the surface and it works as a drawing compound for the surface drag reduction. B2-3d and E2-3d near wall section velocity contour plots are shown in Figure 13.

5. Conclusion

The CFD studies which were made by using $k-\epsilon$ turbulence model are close to the experimental results. 2-dimensional studies show that riblets that have pointed geometry give better results than the rounded models. In 3-dimensional models drag was reduced by up to 30%. This

study shows that optimizing surface shapes and dimensions achieves good drag reduction.

Article Information Form

Funding

The authors have not received any financial support for the research, authorship or publication of this study.

Authors' Contribution

The authors contributed equally to the study.

The Declaration of Conflict of Interest/ Common Interest

No conflict of interest or common interest has been declared by the authors.

The Declaration of Ethics Committee Approval

This study does not require ethics committee permission or any special permission.

The Declaration of Research and Publication Ethics

The authors of the paper declare that they comply with the scientific, ethical and quotation rules of SAUJS in all processes of the paper and that they do not make any falsification on the data collected. In addition, they declare that Sakarya University Journal of Science and its editorial board have no responsibility for any ethical violations that may be encountered, and that this study has not been evaluated in any academic publication environment other than Sakarya University Journal of Science.

Copyright Statement




Authors own the copyright of their work published in the journal and their work is published under the CC BY-NC 4.0 license.

References

- [1] D. W. Bechert, M. Bruse, W. Hage, J. G. T. V. D. Hoeven, G. Hoppe, "Experiments on drag-reducing surfaces and their optimization with an adjustable geometry," *Journal of Fluid Mechanics*, vol. 338, pp. 59–87, 1997.
- [2] C. Pulles, "Drag reduction of turbulent boundary layers by means of grooved surfaces," [Ph.D. Thesis 1 (Research TU/e / Graduation TU/e), Applied Physics and Science Education]. Technische Universiteit, 1988.
- [3] Y. Kodama, T. Takahashi, M. Makino, T. Hori, T. Ueda, N. Kawamura, M. Shibata, H. Kato, T. Inoue, T. Suzuki, Y. Toda, K. Yamashita, "Practical application of microbubbles to ships --- Large scale model experiments and a new full scale experiment," *Int. Sympos. Smart Contr. Turbul.*, Jan. 2005.
- [4] M. Sasamori, H. Mamori, K. Iwamoto, A. Murata, "Experimental study on drag-reduction effect due to sinusoidal riblets in turbulent channel flow," *Experiments in Fluids*, vol. 55, no. 10, p. 1828, 2014.
- [5] M. Walsh, A. Lindemann, "Optimization and application of riblets for turbulent drag reduction," in *22nd Aerospace Sciences Meeting*, in *Aerospace Sciences Meetings*, American Institute of Aeronautics and Astronautics, 1984.
- [6] R. I. Bourisli, A. A. Al-Sahhaf, "CFD modeling of turbulent boundary layer flow in passive drag-reducing applications," presented at the *Advances In Fluid Mechanics 2008*, The New Forest, UK, May 2008, pp. 79–90.
- [7] O. A. El-Samni, H. H. Chun, H. S. Yoon, "Drag reduction of turbulent flow over thin rectangular riblets," *International Journal of Engineering Science*, vol. 45, no. 2, pp. 436–454, 2007.
- [8] L. Q. Ren, C. C. Zhang, L. M. Tian, "Experimental study on drag reduction for bodies of revolution using bionic non-smoothness," *Journal of Jilin University (Engineering and Technology Edition)*, vol. 35, no. 4, pp. 431–436, 2005.
- [9] L. Sirovich, S. Karlsson, "Turbulent drag reduction by passive mechanisms," *Nature*, vol. 388, no. 6644, Art. no. 6644, 1997.

- [10] R. D. Bullen, N. L. McKenzie, "The pelage of bats (Chiroptera) and the presence of aerodynamic riblets: the effect on aerodynamic cleanliness," *Zoology (Jena)*, vol. 111, no. 4, pp. 279–286, 2008.
- [11] S. G. Martin, "Fluid Flow Modeling of Biomimetic Structures," Ph.D. Thesis, Department of Mechanical and Aerospace Engineering at The Ohio State University", 2013.
- [12] V. A. Tucker, G. C. Parrott, "Aerodynamics of gliding flight in a falcon and other birds," *Journal of Experimental Biology*, vol. 52, no. 2, pp. 345–367, 1970.
- [13] W. Nachtigall, "Starlings and starling models in wind tunnels," *Journal of Avian Biology*, vol. 29, no. 4, pp. 478–484, 1998.
- [14] H. Chen, F. Rao, X. Shang, D. Zhang, I. Hagiwara, "Flow over bio-inspired 3D herringbone wall riblets," *Experiments in Fluids*, vol. 55, no. 3, p. 1698, 2014.
- [15] C. Zhou, L. Tian, L. Ren, W. Zhao, R. Zhang, S. Zhang, "Research on non-smooth surface morphology and bionic technology of columba livia feather," *Transactions of the Chinese Society For Agricultural Machinery*, vol. 37, no. 11, pp. 180–183, 2006.
- [16] H. Chen, F. Rao, X. Shang, D. Zhang, I. Hagiwara, "Biomimetic drag reduction study on herringbone riblets of bird feather," *Journal of Bionic Engineering*, vol. 10, no. 3, pp. 341–349, 2013.
- [17] C. J. Pennycuick, "A wind-tunnel study of gliding flight in the Pigeon *Columba Livia*," *Journal of Experimental Biology*, vol. 49, no. 3, pp. 509–526, 1968.
- [18] I. J. Lovette W. Fitzpatrick, "Handbook of bird biology, 3rd Ed. | Bird Academy • The Cornell Lab." 2016.
- [19] Z. Shi, J. Chen, Q. Chen, "On the turbulence models and turbulent Schmidt number in simulating stratified flows," *Journal of Building Performance Simulation*, vol. 9, no. 2, pp. 134–148, 2016.
- [20] B. Dean, B. Bhushan, "Shark-skin surfaces for fluid-drag reduction in turbulent flow: a review," *Philosophical Transactions of the Royal Society A: Mathematical, Physical and Engineering Sciences*, vol. 368, no. 1929, pp. 4775–4806, 2010.

Application and Performance Evaluation of Chemical Coagulation, Electrocoagulation, Electro-Fenton and Anodic Oxidation Processes in the Treatment of Glass Fiber Manufacturing Wastewater

Buket Kar¹ , Özkan Görmez^{1*} , Belgin Gözmen¹ 

¹ Mersin University, Faculty of Science, Department of Chemistry, Mersin, Türkiye, karbuket@gmail.com, ozkan.grmz@gmail.com, bgozmen@yahoo.com

*Corresponding Author

ARTICLE INFO

ABSTRACT

Keywords:

Advanced oxidation process
Wastewater treatment
Electro-Fenton
Electrocoagulation
Anodic oxidation

Article History:

Received: 06.04.2023

Accepted: 27.10.2023

Online Available: 27.02.2024

This study investigated the oxidation of wastewater generated during the production of glass fiber manufacturing material, which contains high organic carbon (18.32 g/L) and has a pH of 8.8, by chemical coagulation, electrocoagulation and electro-advanced oxidation techniques. It was determined that the total organic content (TOC) of wastewater was reduced by 53% using the chemical coagulation method. After electrocoagulation with Al/Al electrode pair for 300 minutes at 500 mA, 73% TOC removal was achieved at pH 8.8. While 50% TOC removal was completed in 2 h at 400 mA in electrocoagulation with Fe/Fe electrode pair, 71% TOC removal was obtained in the combined electrocoagulation/electro-Fenton process by adding hydrogen peroxide to the medium under the same conditions. In addition, it was also observed that the success of the anodic oxidation methods alone was lower. The electro-Fenton application after electrocoagulation was effective and provided 78% TOC but required work at pH 3 and a longer treatment time.

1. Introduction

Glass fiber-based insulations are widely used in all areas of industry for thermal, acoustic and fire protection. In producing these products, phenol-formaldehyde resins are used as binders and add mechanical strength [1]. Depending on the application, the binder content of such insulation products is between 4.5 and 13.8% phenolic resin by weight of fiber [2]. The presence of phenol-based organic pollutants encountered in the production effluent created by such enterprises is a significant problem. Phenol is toxic to fish (1-2 ppm) and aquatic organisms (10-100 ppm) even at the lowest dosages [3]. The presence of phenol in the environment is also a cause of acute toxicity for humans [4].

Water is one of the most essential and fundamental resources for the sustainability of life on Earth. However, drinkable or usable water

resources (in agriculture) are decreasing daily due to population growth, rapid industrialization, and urbanization. Water pollution affects the environment and poses a problem in reducing biological diversity. It causes severe diseases and even loss of life in humans and living things [5, 6]. Therefore, the protection of aquatic resources is one of the foremost priorities.

The reports published by the World Economic Forum (Weforum) in 2019 and 2020 stated that water scarcity would be the most significant global risk in the next decade. To overcome this problem, it is essential to convert industrial wastewater into reusable properties, at least in the process or irrigation [7]. Purification and reuse of wastewater in the world have been becoming more and more important every year. For example, only 860 Mm³/year of treated wastewater was reused in California in 2010, whereas more than 80% (3440 Mm³/year) of total

wastewater (4300 Mm³/year) was discharged into the ocean. It is planned to reuse 2470 Mm³/year in 2030 [8]. More than 500 Mm³ of treated wastewater per year in Spain is currently reused and is expected to reach 1000 Mm³/year [9]. More than 80% of treated wastewater effluent in Israel is reused mainly for agricultural irrigation. In Singapore, a significant part of the country's current water needs is provided by the water obtained from the national treatment project they created to process wastewater, and this value is expected to increase over 50% by 2060 [10]. In this context, it is important to design effective and low-cost treatment processes for the treatment of industrial wastewater containing persistent organic pollutants.

Chemical coagulation-flocculation processes, which include various chemical and natural coagulants, are frequently used in conventional water treatment processes. Natural (or biocoagulant), inorganic and organic polymers can be used as coagulants. The most effective inorganic coagulants are generally divalent and trivalent metallic ions (usually Fe(II)/(III) and Al(III)) [11]. Many developed electrochemical technologies have been used frequently in the last few decades to remove various pollutants from wastewater.

The high energy efficiency, cost-effectiveness, and application ease of these techniques make them remarkable in different wastewater applications [12]. Electrocoagulation and electro-oxidation have an important place in these electrochemical processes [13, 14]. In electrochemical coagulation, Al³⁺ and Fe²⁺/Fe³⁺ ions are formed in situ by metal anode oxidation such as Fe or Al, while hydrogen gas and hydroxide ions are released at the cathode. Thanks to the coagulation agents formed by hydroxide ions and metal ions, the pollutants in the wastewater are effectively precipitated and removed [15].

Electrochemical advanced oxidation processes (EAOPs) are a method based on using radical oxidizing agents to oxidize pollutants. Among the strongest oxidizing radicals used is the hydroxyl radical ($\cdot\text{OH}$, $E^\circ=2.80$ V/SHE). Recently, studies for removing organic pollutants

from wastewater by sulfate radical ($\text{SO}_4^{\cdot-}$, $E^\circ=2.50-3.10$ V/SHE) have increased remarkably [16]. Two of the methods that have an important place among EAOPs are the electro-Fenton (EF) and anodic oxidation (AO) processes used in this study. In the EF process, hydroxyl radicals are produced by the Fenton reaction between Fe²⁺ ions and hydrogen peroxide which is produced in situ by oxygen reduced on the cathode in an acidic environment [17]. In the AO process, hydroxyl radicals are produced on the surface (quasi-free) of the anode with a high O₂ evolution overpotential, such as Boron Doped Diamond (BDD) [18].

The aim of this study is to design treatment processes that will reduce the organic and inorganic pollution content of wastewater with high phenol content and evaluate them together with their performance. For this purpose the treatment of the wastewater was achieved by chemical coagulation (CC), electrocoagulation (EC) (using Al/Al and Fe/Fe electrode pairs), electrocoagulation/electro-Fenton (EC/EF) combined system, electro-Fenton (EF) and anodic oxidation (AO) processes. The effectiveness of the applied methods was determined by calculating the total organic carbon (TOC) and inorganic carbon (IC) removal.

2. Experimental

2.1. Material

Wastewater was obtained from a company that produces insulation materials in Mersin province. Hydrogen peroxide and iron(III) chloride were purchased from Merck.

2.2. Methods

2.2.1. Chemical coagulation process

Different volumes (2.5, 5.0, and 10 mL) of FeCl₃ solution (10 mg/mL) were added to the 100 mL wastewater sample and mixed rapidly for 2 min at a stirring speed of 150 rpm. Then it was kept for 25 min at 40 rpm for flocculation. The solution (mixture) was left to rest for 25 minutes and after the precipitation was complete, it was filtered with Whatman 54 filter paper.

2.2.2. Electrocoagulation processes

The electrocoagulation process was performed using Al/Al electrode pair (7 × 3 cm) or Fe/Fe electrode pair (10 × 5 cm) with a distance of 2 cm. The wastewater was kept at 8.8 which is its own pH value. If necessary, the pH value of the wastewater was adjusted with a 3 M H₂SO₄ solution. In the EC processes using Al/Al and Fe/Fe electrode pairs, 200 and 400 mL of wastewater were used, respectively. After EC methods were carried out using a DC power supply (MHC, China) at different currents, the precipitated part was separated by a filter and weighed, and the total organic carbon and inorganic carbon content of the filtrate were determined.

2.2.3. The simultaneous process: electrocoagulation and electro-Fenton

Electrocoagulation experiments with Fe/Fe electrode pair (10 × 5 cm) with a distance of 2 cm were performed in 400 mL wastewater. If necessary, the pH value of the wastewater was adjusted with a 3 M H₂SO₄ solution. The wastewater sample was filtered after 2 h of EC and then used in the EF process. For the combination of the electrocoagulation and the electro-Fenton process, H₂O₂ was added to the solution with a molar ratio of H₂O₂/Fe to 5 [19]. The total amount of hydrogen peroxide to be added, determined for each experiment, was added to the solution in parts every ten minutes. Before the total organic carbon analysis, the excess H₂O₂ remaining in the environment was removed by adding Na₂SO₃. Before each use of the electrodes, they were washed in 35% (v/v) HCl acid solution for 2 min and dried in an oven.

Fe ion mass passing into solution during EC was determined by Eq.(1) according to Faraday's law.

$$m_{Fe} = \frac{IM_A t}{nF} \quad (1)$$

where I : current (A), t : time (s), M_A : Fe atomic mass (55.85 g/mol), n : number of electrons (2), F : Faraday constant (96487 C) [19].

2.2.4. The sequential process: electro-Fenton after electrocoagulation

The Electro-Fenton experiments were performed using the filtrate-obtained EC with Fe/Fe pairs at 400 mA. In EF process, edge plane pyrolytic graphite (EPPG, Momentive PG plate UEK, USA) was used as the cathode, while Pt (Aldrich, 9 cm²) was used for the anode with a distance of 2 cm. The 400 mL solution pH was adjusted to 3.0 with 3 M H₂SO₄ solution and a constant current of 400 mA was applied for 4h. Starting 10 min before EF application, the wastewater was saturated with O₂ gas throughout the process.

2.2.5. Anodic oxidation method

In the AO method, 316L stainless steel cathode and BDD anode (Condias, 5×7 cm) electrodes were used. The electrodes were placed in the cell containing 400 mL of wastewater at a distance of 2 cm from each other. In addition, 3 different currents were used, 180, 350 and 530 mA, respectively, during the AO processes, which lasted 8 h. Energy consumption due to TOC removal in AO was calculated [20] using the following Eq. (2):

$$\text{Energy consum. (kWh/L)} = \frac{E_{cell} I t}{1000 V_{ww}} \quad (2)$$

In equation 1, current (A); E_{cell} is cell potential (V); t is the electrolysis time (h); V_{ww} represents the volume (m³) of wastewater.

2.3. Analyses

The organic and inorganic content of glass fiber manufacturing wastewater were analyzed and its physicochemical properties are given in Table 1.

Table 1. The physicochemical properties of the wastewater

Parameters	Value
pH	8.5-8.8
Temperature	25-35 °C
Total solid matter	24.75% (w/w)
Ash	2.11% (w/w)
Conductivity	18.83 mS/cm
Solved organic carbon	18.32 g/L
Solved inorganic carbon	8.19 g/L
Total phenol	0.3-0.5% (w/w)
Free phenol	0.02-0.08% (w/w)
Formaldehyde	0.04-0.12% (w/w)
Ammonia	0.07-0.20% (w/w)
Others (oil, etc)	0.6-0.8% (w/w)
Cl ⁻	13.94 mg/L
NO ₃ ⁻	0.74 mg/L
PO ₄ ³⁻	0.61 mg/L
SO ₄ ²⁻	25.05 mg/L
Na ⁺	50.96 mg/L
NH ₄ ⁺	22.39 mg/L
K ⁺	0.33 mg/L
Ca ²⁺	0.74 mg/L
Mg ²⁺	3.82 mg/L

Ion analysis in wastewater was determined by Metrohm Brand Ion chromatography device with a conductivity detector and Metrosep A Supp 5 (150/4.0) column. Na₂CO₃ (6 mM) / NaHCO₃ (12 mM) mobile phase was used for anion analysis at a flow rate of 0.70 mL/min, and the HNO₃ (1M) mobile phase at a flow rate of 0.90 mL/min for cation analysis.

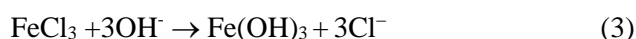
Total phenol determination in wastewater was performed spectrophotometrically. In summary, 2.5 mL of NH₄OH (0.5 N) solution was added to 100 mL of phenol standard solutions and the sample, and the pH was adjusted to 7.9±0.1 with phosphate buffer. 1 mL of 4-amino antipyrine (2 g/100 mL) solution and 1.0 mL of K₃Fe(CN)₆ (8 g/100 mL) were added to the mixture, respectively. After waiting for 15 min, phenol content was determined at 500 nm (ASTM D1783-01).

A total organic carbon analyzer (Shimadzu, TOC-L) was used in the carbon analysis of wastewater and samples taken after the applied processes. Samples were taken at different times, and after filtering, the total organic carbon (TOC) and inorganic carbon (IC) contents were analyzed.

3. Results and Discussion

3.1. Chemical coagulation results

The decrease in TOC and IC values in chemical coagulation experiments performed by adding different volumes of FeCl₃ solution with a concentration of 10 mg/mL to the wastewater is given in Figure 1. In this method, the removal of organic and inorganic species due to adsorption is carried out on Fe(OH)₃ flocs, which are formed depending on the pH value of the wastewater with Eq. (3) [21].



After 2.5, 5, and 10 mL of coagulant were added in the chemical coagulation process, 0.9765, 1.3542, and 1.7265 g of solid waste were obtained for 100 mL of wastewater, respectively.

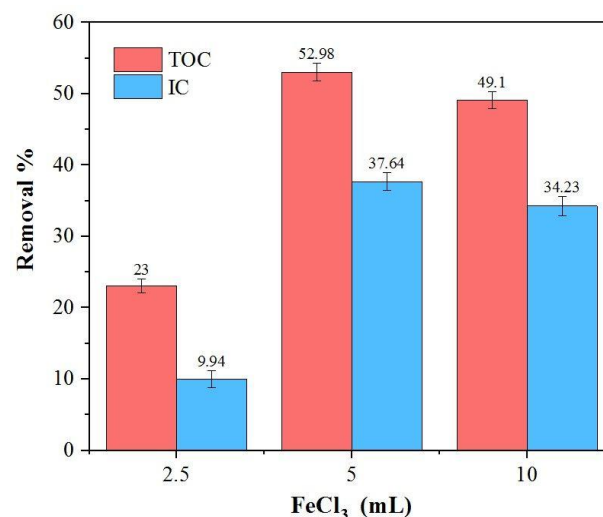


Figure 1. TOC and IC removal by chemical coagulation method (pH= 8.8, V=100 mL)

When 5 mL of FeCl₃ is used as a coagulation agent, it is seen that 53% and 38% of dissolved TOC and IC content in wastewater can be removed. However, while 2.5 mL of coagulation agent is not sufficient, the addition of 10 mL of coagulant does not seem to have a positive effect on TOC removal.

When Gasmi et al. (2022) compared textile wastewater treatment with EC and CC processes, they stated that although the EC operation cost is high, the treated water is more in line with Tunisian environmental discharge standards. EC technology can also be integrated into different

wastewater management systems for the complete mineralization of wastewater [21].

3.2. Electrocoagulation and the simultaneous process: electrocoagulation and electro-Fenton results

In the EC method, Al and Fe electrodes were used as sacrificial electrodes. Since the conductivity of the wastewater was at the appropriate value, it was carried out without adding any electrolyte. TOC removals in wastewater after EC with Al/Al electrode pair were obtained as 55, 67, 73, and 76% at 200, 300, 500, and 800 mA, respectively (Figure 2).

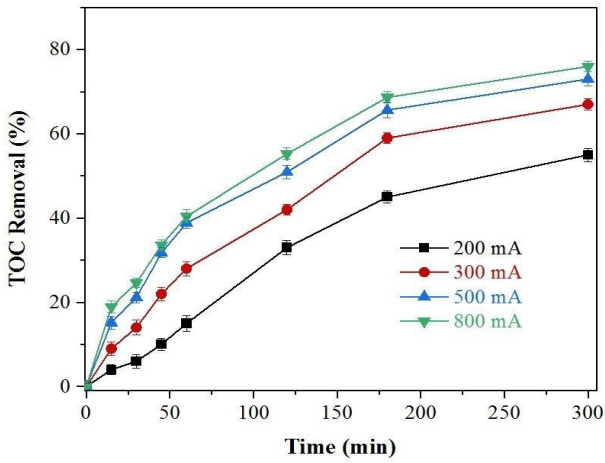
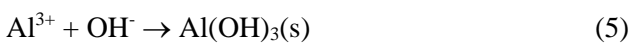
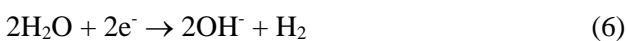


Figure 2. TOC removal results by electrocoagulation method with Al/Al electrode pair (pH=8.8, V= 200 mL)

As a result of oxidation at the anode due to the applied current, Al^{3+} ions pass into the solution. Since the pH value of the wastewater is basic, the $\text{Al}(\text{OH})_3$ structures formed cause coagulation/flocculation and then collapse (Eq. (4,5)). In this way, pollutants including suspended solids in the wastewater are separated by precipitation. TOC removal was determined as 73% and 76% for 500 and 800 mA, respectively.



The reaction at the cathode (in alkaline solution) is given as follows [22]:



The amount of solid that precipitates out of the wastewater as a result of the applied EC method and the amount of Al that is oxidized on the Al anode surface and passed into the solution are shown in Table 2.

Table 2. Solid amount and energy consumption values depending on the method applied

Method	Solid (g)	Energy Consumption (kWh/m^3)
EC-Al/Al, 5h pH 8.8, 200 mA	1.542	0.0120
EC-Al/Al, 5 h pH 8.8, 300 mA	2.673	0.0225
EC-Al/Al, 5 h pH 8.8, 500 mA	5.228	0.0438
EC-Fe/Fe, 2 h pH 8.8, 400 mA	5.280	0.0054
EC/EF-Fe/Fe, 2 h pH 8.8, 400 mA	4.681	0.0050
EC-Fe/Fe, 2 h pH 5.0, 400 mA	5.182	0.0055
EC/EF-Fe/Fe, 2 h pH 5.0, 400 mA	6.700	0.0054

As the amount of applied current increased, the amounts of solid precipitates and Al increased. Similarly, 70-77% TOC and complete color removal were achieved in the previous studies performed EC with Al/Al pair for olive mill wastewaters. This method allowed lower energy consumption with lower sludge formation than chemical coagulation [22, 23].

TOC removals after EC and combined EC/EF methods using Fe/Fe electrode pair as electrode pair are shown in Figure 3. While iron ions are formed at the anode, $\text{Fe}(\text{OH})_3$ flocs are formed depending on the basic property of the wastewater with Eqs. (7) and (3) [24]. TOC removal in wastewater after 2 h of EC at pH 5.0 and 8.8 were determined as 18.8% and 49.8%, respectively.

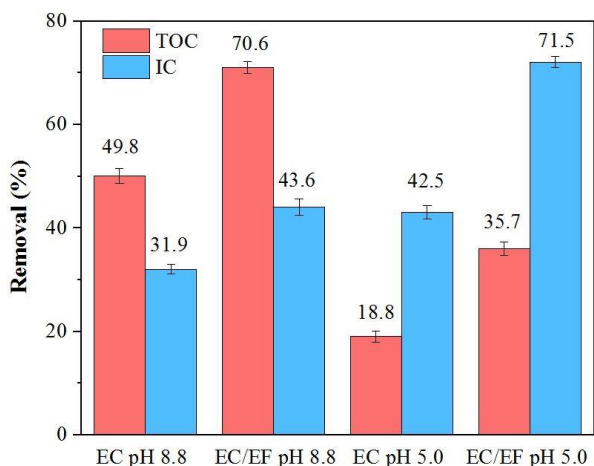
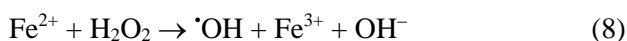


Figure 3. The efficiencies of electrocoagulation and electrocoagulation/electro-Fenton methods using Fe/Fe electrode pair ($I=400$ mA, $t=2$ h)

Recently, the general view of using the EC process is to employ it as an integrated step combined with other methods [14, 19, 25]. In the combined EC/EF method with the addition of hydrogen peroxide, the TOC removal efficiencies at the same pH values increased to 35.7 and 70.6, respectively. In the EF method, as a result of Fenton reaction (Eq. (8)), hydroxyl radicals were formed and increased mineralization.



In the EC process, the types of iron hydroxocomplexes show different distributions depending on the pH of the solution [12, 14]. When the $\text{pH} > 5.5$, $\text{Fe}(\text{OH})_2$ and $\text{Fe}(\text{OH})_3$ begin to precipitate, and as the pH increases, their formation rate increases. Therefore, more effective TOC removal was achieved as a result of EC at pH 8.8. On the other hand, as the EC efficiency decreases at pH 5.5 and the possibility of Fenton and Fenton-like reactions between $\text{Fe}^{2+}/\text{Fe}^{3+}$ ions and H_2O_2 increases. TOC removal occurs mostly through radical species ($\cdot\text{OH}/\text{HO}_2\cdot$), but the TOC removal efficiency was obtained lower. Also, the higher IC removal percent was observed at more acidic pH values, as the decomposition of inorganic species in wastewater occurred more easily.

It is seen that the energy consumption values are close to each other in EC and EC/EF combined methods (Table 2).

3.3. The sequential process: electro-Fenton after electrocoagulation results

After EC treatment at 400 mA for 2 h, the obtained wastewater was filtered. The filtrate pH value was adjusted to 3.0 and oxidation was carried out by EF method at 400 mA using Pt/EPPG anode/cathode pair (Figure 4). The hydroxyl radicals are produced as a result of the Fenton reaction between hydrogen peroxide (formed from the reduction of O_2 at the cathode) and Fe ions (formed by EC methods) due to Eqs. (8,9) [26].



While 49.8% TOC removal was achieved as a result of the EC process, a total TOC removal of 78.2% was achieved after 4 h of oxidation with the EF method. With the EC/EF combined system with external H_2O_2 added, 70.8% TOC removal was achieved at pH 8.8 and after 2 h of electrolysis. In addition to the higher TOC removal, the energy consumption increased in the EF application following the EC method. In addition to 0.0054 kWh/m³ energy consumption in the two-hour EC application, 0.0170, 0.0341, 0.0510, and 0.0680 kWh/m³ energy consumption in the EF method after 1, 2, 3, and 4 h of electrolysis, respectively, was calculated.

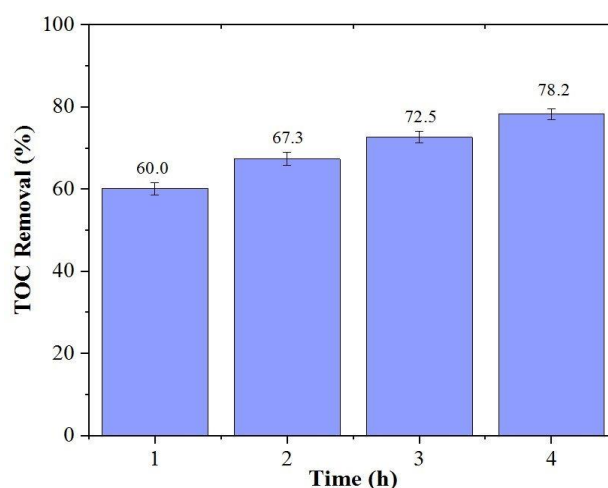


Figure 4. TOC removal by electro-Fenton method after electrocoagulation ($I=400$ mA, pH 8.8, pH 3)

The effectiveness of the electro-Fenton method for different pollutant groups containing phenol has been demonstrated by many previous studies. These studies have shown that effective oxidation of phenol and phenol-derived organic

pollutant groups can be achieved in low-concentration synthetic solutions with the EF process under appropriate operating parameters, but the time and energy requirement is high for the full mineralization of aliphatic products formed as a result of aromatic ring decomposition [26-28]. Similarly, in this study, after reducing the organic carbon load and suspended solids amount of wastewater with EC, 78% TOC removal was achieved with the EF process, but more time was needed for 100% efficiency.

3.4. Anodic oxidation results

The AO method was directly performed with the BDD anode and 316L cathode as a final method. Figure 5a depicted a rapid decrease in TOC value in the first two hours but then slowed down.

It is seen that TOC removal does not change much when the currents were applied as 180, 350, and 530 mA. For these applied currents, 48%, 51%, and 55% TOC removal were achieved, respectively (Figure 5b).

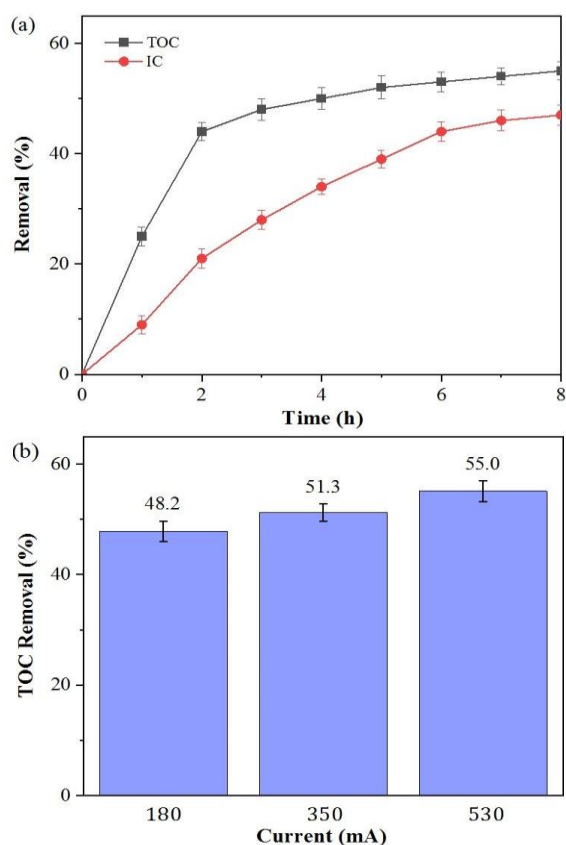
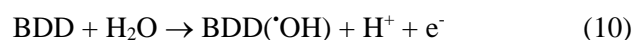


Figure 5. (a) Time-dependent TOC removal in anodic oxidation ($I = 530$ mA, pH 8.8), (b) the effect of current

As in all electrochemical methods, the selection of the suitable current amount or density is an important parameter for effective organic pollutant removal and low energy consumption in the AO process. As the applied current value increases, TOC removal by the AO process is significantly accelerated. However, the reaction rate decreased at a high current values, due to the rapid consumption of reactants and the side reaction of oxygen evolution [29].

In addition, it should be noted that the high performance results to be obtained in the AO process are too complex to be explained through a single parameter. It should not be forgotten that the synergistic effect of many parameters such as the type of pollutants, the preferred electrode material, the type of electrolyte, and the applied current or potential will affect the efficiency obtained as a result of the AO process. Therefore, increasing the applied current alone may not be sufficient to dramatically increase the degradation performance of pollutants [16].

While quasi-adsorbed hydroxyl radicals are formed on the BDD electrode surface (Eq. (10)), chlorine ions and sulfate ions in wastewater can be converted into oxidants such as persulfate and chlorine gas by oxidation (Eqs. (11,12)) [30, 31]. In this study, anodic oxidation did not provide sufficient mineralisation although the wastewater contained sulphate and chloride ions. This may be because the anode surface becomes passive due to different species in the waste.



4. Conclusions

This study investigated chemical coagulation and various electrooxidation methods to treat a real wastewater sample with high total organic carbon and suspended solids content. It was observed that chemical and electrochemical coagulation methods reduced the total suspended solids content and a significant amount of TOC content in the wastewater. In addition, the electrocoagulation method was kept shorter and

tested together and sequentially with the electro-Fenton process. Without changing the wastewater's alkaline pH value (8.8), 71% TOC removal efficiency was achieved in a short period (2 h) when H₂O₂ was added from the outside for the simultaneous implementation of the Fe/Fe electrode pair and the EC/EF method. The same energy consumption was spent with the EC method alone, while more organic pollution was removed. When the EF method was applied in the filtrate after the EC process at pH 3 to produce in situ H₂O₂, 4 h of processing time and an extra 0.0680 kWh/m³ energy consumption were required for 78% TOC removal. The anodic oxidation method did not give an effective result in wastewater treatment, and it revealed the necessity of EC as a pre-treatment. When the data obtained as a result of these studies are evaluated, it is seen that the simultaneous or sequential use of different electrochemical method such as EC and electro-Fenton process will increase the yield of real wastewater with high organic pollution load.

Article Information Form

Funding

The authors has no received any financial support for the research, authorship or publication of this study.

Authors' Contribution

The authors contributed equally to the study.

The Declaration of Conflict of Interest/ Common Interest

No conflict of interest or common interest has been declared by the authors.

The Declaration of Ethics Committee Approval

This study does not require ethics committee permission or any special permission.

The Declaration of Research and Publication Ethics

The authors of the paper declare that they comply with the scientific, ethical and quotation rules of SAUJS in all processes of the paper and that they do not make any falsification on the data collected. In addition, they declare that Sakarya University Journal of Science and its editorial board have no responsibility for any ethical violations that may be encountered, and that this

study has not been evaluated in any academic publication environment other than Sakarya University Journal of Science.

Copyright Statement

Authors own the copyright of their work published in the journal and their work is published under the CC BY-NC 4.0 license.

References

- [1] S. Joseph, M. S. Sreekala, Z. Oommen, P. Koshy, S. Thomas, "A Comparison of the Mechanical Properties of Phenol Formaldehyde Composites Reinforced with Banana Fibres and Glass Fibres," *Composites Science and Technology*, vol. 62, pp. 1857–1868, 2002.
- [2] M. M. Quinn, T. J. Smith, T. Schneider, E. A. Eisen, D. H. Wegman, "Determinants of Airborne Fiber Size in the Glass Fiber Production Industry," *Journal of Occupational and Environmental Hygiene*, vol. 2, pp.19–28, 2005.
- [3] J. Arana, E. Tello Rendon, J. M. Dona Rodriguez, J. A. Herrera Melian, O. Gonzalez Diaz, J. Perez, "Highly concentrated phenolic wastewater treatment by the Photo-Fenton reaction, mechanism study by FTIR-ATR," *Chemosphere*, vol. 44, pp. 1017-1023, 2001.
- [4] H. Ma, X. Zhang, Q. Ma, B. Wang, "Electrochemical catalytic treatment of phenol wastewater," *Journal of Hazardous Materials*, vol. 165, pp. 475-480, 2009.
- [5] X. W. Zhuang, Y. P. Li, S. Nie, Y. R. Fan, G. H. Huang. "Analyzing Climate Change Impacts on Water Resources under Uncertainty using an Integrated Simulation-Optimization Approach," *Journal Hydrology*, vol. 556, pp. 523-538, 2018.
- [6] F. Zhang, H. Xue, H. Wang, H. Dong, "Industrial Growth Path Under the Restriction of Water Resources in China,"

- Procedia Engineering, vol. 174, pp. 934-940, 2017.
- [7] The Global Risks Report. (2020). Available: <https://www.weforum.org/reports/the-global-risks-report-2020>.
- [8] G. Tchobanoglous, H. Leverenze, M. H. Nellor, J. Cook, "Direct Potable Reuse: A Path Forward" in *Water Reuse Research*, Foundation: Alexandria, VA, USA, 2011.
- [9] S. Mudgal, L. Von Long, N. Saidi, R. Haines, D. McNeil, P. Jeffrey, H. Smith, J. Knox, "Optimization Water Reuse in EU: Final Report", BIO by Deloitte: Brussels, Belgium, 2015, p.199-200.
- [10] A. N. Angelakis, P. Gikas, "Water reuse: Overview of current practices and trends in the world with emphasis in EU," *Water Utility Journal*, vol. 6, pp. 67-78, 2014.
- [11] A. T. A. Baptista, P. F. Coldebella, P. H. F. Cardines, R.G. Gomes, M. F. Vieira, R. Bergamasco, A. M. S. Vieira, "Coagulation-Flocculation process with ultrafiltered saline extract of *Moringa Oleifera* for the treatment of surface water," *Chemical Engineering Journal*, vol. 276, pp. 166-173, 2015.
- [12] S. Pulkka, M. Martikainen, A. Bhatnagar, M. Sillanpää, "Electrochemical methods for the removal of anionic contaminants from water – A Review, *Separation and Purification Technology*, vol. 132, pp.252–271, 2014.
- [13] Y. Feng, L. Yang, J. Liu, B. E. Logan, "Electrochemical technologies for wastewater treatment and resource reclamation," *Environmental Science: Water Research & Technology*, vol. 2, pp. 800–831, 2016.
- [14] D. Ghernaout, N. Elboughdiri, "Electrocoagulation process intensification for disinfecting water – A Review," *Applied Engineering*, vol. 3, pp. 140-147, 2019.
- [15] J. Rumky, W. Z. Tang, M. Sillanpää, "Statistical analysis of anode efficiency in electrochemical treatment of wastewater and sludge," *Environmental Processes*, vol. 7, pp. 1041–1064, 2020.
- [16] R. Fu, P. Zhang, Y. Jiang, L. Sun, X. Sun, "Wastewater treatment by anodic oxidation in electrochemical advanced oxidation process: Advance in mechanism, direct and indirect oxidation detection methods," *Chemosphere*, vol. 311, 136993, 2023.
- [17] L. Tirado, O. Gökkus, E. Brillas, I. Sirés, "Treatment of cheese whey wastewater by combined electrochemical processes," *Journal of Applied Electrochemistry*, vol. 48, pp. 1307–1319, 2018.
- [18] Y. Aktaş, B. Gözmen, M. A. Oturan, "Degradation of phthalic acid by anodic oxidation in acidic aqueous solutions with high chromium content using Boron doped diamond anode," *Separation and Purification Technology*, vol. 293, 121098, 2022.
- [19] H. Olvera-Vargas, X. Zheng, O. Garcia-Rodriguez, O. Lefebvre, "Sequential "Electrochemical peroxidation e electro-Fenton" Process for Anaerobic Sludge Treatment," *Water Research*, vol. 154, pp. 277–286, 2019.
- [20] F. Görmez, Ö. Görmez, E. Yabalak, B. Gözmen, "Application of the Central Composite Design to Mineralization of Olive Mill Wastewater by the Electro/FeII/Persulfate Oxidation Method," *SN Applied Sciences*, vol. 2, pp. 178, 2020.
- [21] A. Gasmi, S. Ibrahim, N. Elboughdiri, M. A. Tekaya, D. Ghernaout, A. Hannachi, A. Mesloub, B. Ayadi, L. Kolsi, "Comparative study of chemical coagulation and electrocoagulation for the

- treatment of real textile wastewater: Optimization and operating cost estimation,” *ACS Omega*, vol. 7, pp. 22456–22476, 2022.
- [22] H. Hanafi, O. Assobhei, M. Mountadar, “Detoxification and discoloration of Moroccan olive mill wastewater by electrocoagulation,” *Journal of Hazardous Materials*, vol. 174, pp. 807-812, 2010.
- [23] S. Khoufi, F. Feki, S. Sayadi, “Detoxification of olive mill wastewater by electrocoagulation and sedimentation processes,” *Journal of Hazardous Materials*, vol. 142, pp. 58-67, 2007.
- [24] Ü. Tezcan Ün, S. Uğur, A. S. Koparal, Ü. Bakır Öğütveren. “Electrocoagulation of olive mill wastewaters,” *Separation and Purification Technology* vol. 52, pp. 136–141, 2006.
- [25] X. Wang, J. Zhao, C. Song, X. Shi, H. Du, “An eco-friendly iron cathode electro-Fenton system coupled with a pH-regulation electrolysis cell for p-nitrophenol degradation,” *Frontiers in Chemistry*, vol. 9, 837761, 2022.
- [26] P. V. Nidheesh, R. Gandhimathi, “Trends in electro-Fenton process for water and wastewater treatment: An overview,” *Desalination* vol. 299, pp. 1–15, 2012.
- [27] M. Pimentel, N. Oturan, M. Dezotti, M. A. Oturan, “Phenol Degradation by advanced electrochemical oxidation process electro-Fenton using a carbon felt cathode,” *Applied Catalysis B*, vol. 83, pp. 140–149, 2008.
- [28] Y. Song-hu, L. Xiao-hua, “Comparison treatment of various chlorophenols by electro-Fenton method: Relationship between chlorine content and degradation,” *Journal of Hazardous Materials*, vol. B118, pp. 85–92, 2005.
- [29] Y. Jiang, H. Zhao, J. Liang, L. Yue, T. Li, Y. Luo, Q. Liu, S. Lu, A. M. Asiri, Z. Gong, X. Sun, “Anodic oxidation for the degradation of organic pollutants: Anode materials, operating conditions and mechanisms. A mini review,” *Electrochemistry Communications*, vol. 123, 106912, 2021.
- [30] S. O. Ganiyu, M. G. El-Din, “Insight into in-situ radical and non-radical oxidative degradation of organic compounds in complex real matrix during electrooxidation with Boron doped diamond electrode: A case study of oil sands process water treatment,” *Applied Catalysis B*, vol. 279, 119366, 2020.
- [31] L. W. Matzek, M. J. Tipton, A. T. Farmer, A. D. Steen, K. E. Carter, “Understanding electrochemically activated persulfate and its application to ciprofloxacin abatement,” *Environmental Science and Technology*, vol. 52, pp. 5875–5883, 2018.

Identifying Critical Success Factors of Public Private Partnership Projects in Türkiye

Elif Durna¹ , Beliz Ozorhon² , Semih Çağlayan^{3*} 

¹ Boğaziçi University, Dept. of Civil Engineering, Istanbul, Türkiye, elifdurna87@gmail.com

² Boğaziçi University, Dept. of Civil Engineering, Istanbul, Türkiye, beliz.ozorhon@boun.edu.tr

^{3*} Sakarya University of Applied Sciences, Dept. of Civil Engineering, Sakarya, Türkiye, semihcaglayan@subu.edu.tr

*Corresponding Author

ARTICLE INFO

ABSTRACT

Keywords:

Public Private Partnerships
Construction Industry
Critical Success Factors
Factor Analysis
Project Management



Article History:

Received: 29.07.2023

Accepted: 30.10.2023

Online Available: 27.02.2024

Public private partnerships (PPPs) have become increasingly common as a result of states' shifting roles in infrastructure services from service providers and operators to policymakers and regulators. PPPs have been established as a prominent technique of public service procurement in both developed and developing countries. PPPs give the parties the opportunity to split the costs and risks of providing a public service or building a public infrastructure. Successful project management is crucial, especially in light of PPP projects' size and complexity. This study investigates the critical success factors (CSFs) of PPP investments in developing countries. In this regard, 23 CSFs were selected based on a thorough literature review, and a questionnaire survey was run to examine the impact of those factors on PPP performance. The information is gathered from 82 different companies in Türkiye that represent both the public and private sectors. The statistical analysis results show that favorable legal framework, detailed and clear project identification, and extensive cost-benefit assessment are the most significant drivers of success. Additionally, factor analysis is used on the data to investigate and identify underlying correlations between the factors, as well as to categorize them into fewer, more focused, and more thorough factors. The results of factor analysis suggest five dimensions; namely project finance, project management, operational factors, procurement, and organizational factors. The study's findings are anticipated to benefit both the public sector in its focus on legal concerns to permit better operation and the contractors in its examination of their capacity to manage big projects more effectively.

1. Introduction

The state's role in providing infrastructure services has undergone some changes in the last quarter of the 20th century as a result of changes and interactions in economic, social, and political meaning; this transformation involves moving from the state's understanding as a service producer and operator to that of a policy maker and regulator [1]. Public-private partnerships (PPPs), which account for the majority of capital project spending in the public sector, rose to prominence as a result of the search for novel methods of project procurement [2]. PPPs enable the public and private sectors to jointly bear the

risks and benefits. A PPP is described as a “contractual arrangement between a public sector agency and a for-profit private sector developer, whereby resources and risks are shared for the purpose of delivery of a public service or development of public infrastructure” by the National Council for Public-Private Partnership [3].

Numerous empirical and non-empirical research have been undertaken on various PPP features in light of the growing interest in PPP since the late 1990s [4]. Relationship management, risk management, and financing models have all received the greatest attention among these. The

need to successfully complete PPP projects is essential because of their complexity. Finding the critical success factors (CSFs) was the subject of a different set of studies [5–9]. The critical success factors were identified for various PPP projects such as build-own-operate-transfer, build-operate-transfer, transfer-operate-transfer from different parts of the world including Australia, United Kingdom, China, and India. Studies on CSFs are more recent than those on other studies on PPPs, but they are still quite important, particularly in developing countries where PPPs are heavily invested in.

The literature has identified a number of variables that affect capital project success [10]. When applied to public projects, it is critical to identify those critical aspects that may help lead to a profitable outcome for the stakeholders [11]. This study's main goals are to (i) identify the CSFs and quantify their impact on PPP success in Türkiye, a developing country, and (ii) investigate the underlying characteristics of the CSFs. In order to create CSFs for construction projects, a thorough assessment of the literature was undertaken. These factors were then modified to create a distinct set of CSFs for PPPs. Then, a questionnaire survey was created and distributed to Turkish construction industry specialists. In order to understand the industry's practices and perceptions about PPP adoption, the collected data were evaluated. The underlying causes of PPP success were categorized using factor analysis. The results of this study are anticipated to serve as a roadmap for the public and private sectors in terms of financing and managing prosperous PPP initiatives.

1.1. The role of PPPs in construction

The contract value of PPP projects, which include privatization, has risen rapidly in the 1990s, reaching its greatest level (107 billion US dollars) in 1997, according to World Bank data for developing countries. The annual sum continued to increase once more and reached the record level in 2010 (186.4 billion US Dollars) after declining to 48.7 billion US Dollars in 2002. In total, 5783 PPP projects in the energy, transportation, telecom, and sewage sectors have received funding, with a combined cost of 2.026

billion US dollars. The total number of PPP projects completed in the European Union between 1990 and 2013 was 1626, or 67 per year on average. The total project value was 310.57 billion euros, or 12.94 billion euros per year on average, and the projects were in the transportation, environment, education, healthcare, general public services, and public order and safety sectors [12].

The PPP experience in various nations was described by Gurgun and Touran [13], who also highlighted Türkiye's potential for PPP initiatives as a developing country. Practices of cooperation between the public and private sectors in Türkiye extend back to the time of the Ottoman Empire. Public service concessions were given legal status in 1910, and the first application of PPP - in its current form - to the production of electricity came in 1984. Public infrastructure investment is crucial in Türkiye as the country strives to rank among the top ten largest economies in the world by 2023, the year of the 100th anniversary of the Turkish Republic. In the 1980s, a model of development led by the private sector was embraced. Public investments in industry thus declined, while infrastructure projects took center stage in the central investment budget. Concession, Build-Operate-Transfer (BOT), Build-Operate (BO), Build-Lease-Transfer (BLT), and Transfer of Operating Rights (TOR) are the PPP models now in use. Examining the contract value by year reveals that after 2012, there was a significant uptick. PPP contract value reached 46.14 billion USD at the end of 2013. When PPP projects in Türkiye that are in operation and under construction are combined, the total value reaches 87.5 billion USD for 167 projects in the urban infrastructure, healthcare, energy, seaport, airport, and marina sectors [1].

Various factors have been defined as assisting the successful delivery of projects in many studies. Chua et al. [10] and Morledge and Owen [11] have pointed out that determining those key components, which may directly affect the profitable conclusion for the stakeholders is crucial. In their study, Osei-Kyei and Chan [14] reported that most of the studies on the CSFs of PPP projects had concentrated on developed countries including Australia, United Kingdom,

Singapore, and Hong Kong. Studies on the USA market have mainly focused on other areas such as improving value for money, risk management, financial viabilities, and relationship management [15]. However, less is known about the developing countries. CSFs have been identified for Lebanon [16], China [17], and India [18]. A couple of studies have focused on other countries such as Malaysia [19] and Uganda [20]. Even though a number of studies have addressed the situation for Türkiye [21-29], few of them have focused on the critical success factors of key performance indicators. Considering the high potential of PPPs and fewer number of studies in the developing countries, this study aims to determine the CSFs in Türkiye, as a significant example, where there is a vast amount of investment on PPPs.

1.2. Critical success factors of PPPs

Tang et al.'s [4] analysis of the literature revealed many PPP study types. They categorized the studies in their paper as either empirical or non-empirical. While the non-empirical studies concentrate on funding, project success factors, risks, and the concession period; the empirical research are more concerned with risks, relationships, and finance. The CSFs of PPPs in developing countries are the subject of this study. Without putting much focus on project type, the majority of the literature discusses characteristics that contribute to the success of building projects in general (Table 1). Most studies on project delivery systems focused on design-bid-build projects.

2. Method

The methodology is composed of three parts: (i) literature review, (ii) questionnaire design, and (iii) descriptive statistics.

2.1. Critical success factors of PPPs

To list the success determinants for PPP projects, a thorough literature analysis was done. A preliminary list of 73 criteria was created. Three experts - two experienced civil engineers and a professor of civil engineering - participated in a pilot study. The goal of the pilot study was to prevent repetition of factors with similar

meanings and create a compact final list. In this direction, participants of the pilot study identified the factors with overlapping meanings in the initial list. These factors were either merged or removed. Through conversations with the experts, the original 73 criteria were reduced to 23 factors. There are no overlaps in the final list of components, which is displayed in Table 2.

2.2. Questionnaire design

An appropriate method for examining the CSFs of PPP projects in Türkiye from the perspectives of both public and private sector actors is a questionnaire survey. The questionnaire is divided into three sections: Part 1 covers general information about the respondents; Part 2 covers CSFs of PPP; and Part 3 covers projects the respondents have (if any have) done. Experts from the private, semi-public, and public sectors, including owners, project managers, consultants, contractors, financiers, and operators in the construction industry, were the target audience. The Turkish Contractors Association was mostly used to recruit survey participants. A total of 82 fully completed questionnaires out of the 365 that were sent out were returned for the online survey, yielding a response rate of 22%.

The profile of respondents is shown in Figure 1. Most of the respondents are engineers and architects. Majority of the respondents are employed by large companies with more than 200 employees. Just 32% of the organizations have participated in PPP projects. The average age of the respondents is 34, and they have an average of 10.96 years of industry experience. 22 PPP initiatives have so far involved the respondents in some capacity. The procurement types for PPP projects are listed in Table 3. Out of 22 cases, 45% of the projects are obtained through a BOT agreement. TOR comes in second place with a share of 18% and 4 cases. In the "other" category, which includes revenue sharing, 4 examples have been implemented with a share of 18%, and BO and BLT models have 2 cases with a share of 9%. Based on their project construction costs and operation NPV, the majority of the instances can be categorized as medium and large size; only three transportation projects can be categorized as mega projects (>1 billion USD). Most projects take 1-2 years or less

to develop, 1-3 years to build, and 20–25 years to operate under the control of private contractors.

Table 1. Critical success factors mentioned in certain studies

Critical Success Factors	Sources
Structure of the project organization	[30-33]
Project manager capabilities and experience	[30-31, 34-37]
Executive commitment of project management	[31-32, 35-41]
Commitment to planning and control	[31-32, 34-35, 38, 41-42]
Project team motivation and goal orientation	[33-36, 38, 41]
Scope and work definition	[34-35, 38, 43]
Control systems	[32, 34, 36, 42]
Technical uncertainty and risk management	[34-35, 38]
Client consulting	[35-36, 38]
Communication and relationship	[32, 35-39, 43]
Client acceptance	[36, 38]
Monitoring and feedback	[34-36, 38, 42, 44-45]
Achieving design and environmental objectives	[32, 35]
Benefit to the customer	[44-45]
Simple, flexible, phased stage/gate process	[32, 43]
Competency of the contractor	[34, 36, 38, 41]
Adequate funding for the entire project	[35, 42]
Thorough contract documentation	[31, 35, 43]
A stable political and economic environment	[34, 38]
Competitive procurement process	[32, 36, 40, 43]
An appropriate legal framework	[34, 38, 43]
A strong and good private consortium	[32, 35, 37, 39, 41-42]
Qualified project management consultants	[30, 34, 36]
Value for money analysis	[35, 38]
Return on investment for lenders and sponsors	[35, 38, 44-45]
An effective approval procedure	[32, 43]
Realistic planning and implementation	[31, 34, 41-42]
Risk and liability assessment	[34-35, 38]
Presence of international financial institutions	[34]

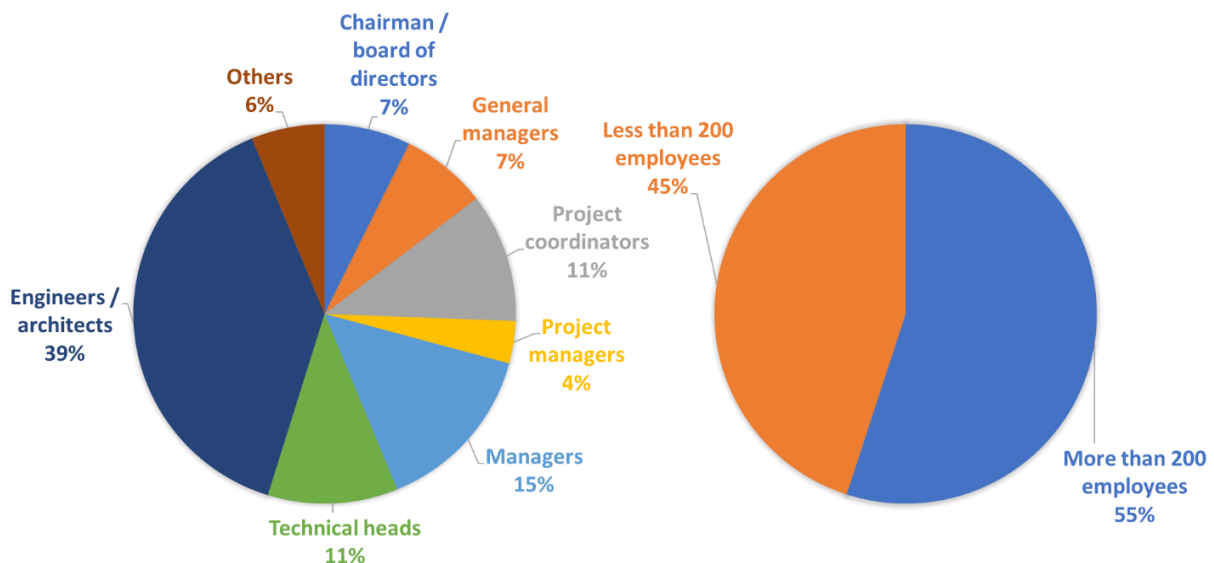


Figure 1. Profile of respondents

Table 2. List of critical success factors

#	Variable	Sources
V1	Strong Private Consortium	[5, 46-54]
V2	Detailed Cost and Benefit Analysis	[35-36, 55]
V3	Solid Investment Climate	[28, 54]
V4	Inspiring Financial Package	[5, 17, 27, 35, 37, 55]
V5	Political and Economic Stability	[17, 26]
V6	Favorable Legal Framework	[27, 33, 54]
V7	Executive Support from Public and Private Sectors	[17, 22-23, 25-29, 54, 56]
V8	Optimal Stakeholder Relations and Communication	[26-29, 34, 52-53, 56-57]
V9	Effective Procurement Process	[22, 25, 54]
V10	Rational and Practical Project Manager	[21-22, 26-28, 32, 57]
V11	Successful Client Consultation	[26, 29, 56]
V12	Wide Client Acceptance	[26, 29, 56, 58]
V13	Competent Client and Contractor	[5, 17, 26-29, 37, 53, 56]
V14	Comprehensive Technical Feasibility	[26, 29, 53-54, 56]
V15	Dedicated and Skilled Project Team	[25-27, 29, 32, 37, 56]
V16	Detailed and Clear Project Identification	[17, 21, 25-26, 29, 34, 56]
V17	Achieving Design Objectives	[25, 27, 35-36, 55]
V18	Proper and Systematic Project Control	[23, 25, 27, 33, 53]
V19	Regular Monitoring and Feedback	[26-27, 29, 56]
V20	Extensive Risk Analysis and Risk Sharing	[17, 25, 37, 54, 59]
V21	Strong Public Entit	[54]
V22	Complete Project Management Methodologies	[24, 28, 60-61]
V23	Simple Organizational Structure	[21-24, 27, 34, 61-62]

Table 3. PPP project procurement arrangement by sector

Sector	Type				
	BOT	BLT	BO	TOR	Other
Hospital	2	2	1	0	0
Power & Energy	1	0	0	0	0
Highway	3	0	1	0	0
Airport	2	0	0	0	0
Industrial Plants & Urban Infrastructure	1	0	0	1	0
Railways	0	0	0	3	1
Other	1	0	0	0	3
Total (22 projects)	10	2	2	4	4

2.3. Descriptive statistics

The importance of each of the 23 CSFs was rated by the respondents on a five-point Likert scale. The followings are the meanings of the scores: According to the scale, 1 indicates "Not Significant," 2 "Fairly Significant," 3 "Significant," 4 "Very Significant," and 5 "Extremely Significant." The data were subjected to various statistical analyses, including factor analysis using SPSS, analysis of

variance (ANOVA), mean ranking, descriptive analysis, reliability tests using Cronbach's alpha, and reliability tests using mean scores. The study's findings suggested that, in accordance with Nunally's [63] recommendations, a Cronbach's alpha score of 0.873- which is higher than 0.7- is appropriate. Based on 82 responses, Table 4 provides the descriptive statistics.

The results point to the most important drivers of success as a favorable legal framework (V6),

detailed and clear project identification (V16), and detailed cost and benefit analysis (V2); while less important factors include successful client consultation (V11), simple organizational structure (V23), and wide client acceptance (V12).

Table 4. Descriptive statistics

Variable	Priv. Client		Publ. Client		Contractor		Total		F	Sig. (%5)
	Mean	Rank	Mean	Rank	Mean	Rank	Mean	Rank		
V6	4.52	1	4.75	1	4.13	8	4.33	1	2.047	0.136
V16	4.48	2	4.42	6	4.23	1	4.33	2	0.450	0.639
V2	4.30	6	4.58	3	4.21	2	4.29	3	0.258	0.773
V13	4.39	3	4.50	5	4.17	6	4.28	4	0.228	0.797
V14	4.39	4	4.75	2	4.06	10	4.26	5	0.565	0.571
V15	4.26	10	4.25	9	4.19	4	4.22	6	0.099	0.906
V4	4.30	7	3.92	15	4.13	7	4.15	7	2.428	0.095
V10	4.26	9	4.25	8	4.06	9	4.15	8	0.240	0.788
V3	3.87	16	4.33	7	4.17	5	4.11	9	0.314	0.732
V18	4.35	5	4.00	14	3.96	12	4.07	10	0.048	0.953
V5	4.00	12	4.50	4	3.94	13	4.04	11	0.525	0.593
V19	4.00	13	4.17	12	4.02	11	4.04	12	0.713	0.493
V1	3.52	20	4.17	11	4.19	3	4.00	13	1.608	0.207
V8	4.26	8	4.00	13	3.83	15	3.98	14	0.953	0.390
V17	4.09	11	3.92	16	3.91	14	3.96	15	0.062	0.940
V21	3.96	14	3.58	20	3.74	17	3.78	16	2.076	0.132
V22	3.70	18	3.75	19	3.77	16	3.74	17	0.065	0.937
V7	3.78	17	3.83	17	3.68	18	3.73	18	0.176	0.839
V20	3.57	19	4.25	10	3.64	19	3.71	19	0.244	0.784
V9	3.91	15	3.75	18	3.47	20	3.63	20	2.210	0.116
V11	3.43	21	3.50	21	3.34	21	3.39	21	0.613	0.544
V23	3.26	22	3.25	22	3.34	23	3.30	22	0.215	0.807
V12	3.04	23	3.08	23	2.94	22	2.99	23	0.499	0.609

3. Results and Discussion

The results of this study and those of earlier studies can be compared to demonstrate how the CSFs differ based on the country. Additionally, the ranks of the factors may vary depending on the respondents. “legal framework” has been rated as the most significant aspect in this study (4.33). According to Cheung et al. [64], this factor was discovered to be the most important CSF for PPP projects carried out in Hong Kong and China (4.06-4.36, respectively); yet, it was placed eighth (2.98) and ninth (3.63) in Singapore [65] and the UK [53], respectively.

There are eleven primary laws in force to establish five PPP models, as there is no one PPP law in Türkiye due to several line ministries' attempts to introduce various legislations for the use of identical PPP models in their respective sectors [66]. The Turkish government's Tenth

Development Plan mentions the need for a stronger judicial system. In the UK, which was one of the first countries to use PPPs and has made significant progress in resolving its legal challenges, “strong and good private consortium” was ranked first, while Türkiye came in fourth.

“Detailed and clear project identification” (4.33) is another crucial feature. Might and Fisher [30], Ashley et al. [34], Pinto and Slevin [38], Pinto and Prescott [55], Pinto and Covin [35], Clarke [43], Qiao et al. [17], and Jamali [16] all made reference to this factor. However, its impact hasn't been measured in prior research. The importance of “appropriate project identification” for BOT projects in China was highlighted by Qiao et al. [17]. According to Jefferies [67], creating a precise project brief is associated with project success in Australia. Compared to the conventional procurement

approach, PPP projects place a greater emphasis on the need for precise project identification. Due to the way business is done in Türkiye, specifications for projects frequently alter even after the bidding process.

“Detailed cost and benefit analysis” (4.29) is the third most crucial component. According to Cheung et al. [64], it was ranked fifth (3.95) in the UK [53], thirteenth in both Hong Kong (3.65) and China (3.79). The Turkish building industry clearly benefits from it, although mean values in other countries are generally low. Due to the fact that costs and benefits are derived from predictions that are predicted across time periods ranging from three to thirty years throughout the project development stage [6], how uncertainty is handled in such assessments is of utmost importance.

Türkiye is a developing country with an unstable political and economic climate, and interest rates, which directly affect project costs, can change significantly. The climate for investing is made unstable by this circumstance, which raises the risk for the investors. Potential investors strive to protect themselves by extending the operational duration in order to manage the higher level of risks.

Previous research by Li et al. [53], Cheung et al. [64], and Hwang et al. [65] have demonstrated that distinct success variables are crucial to PPP projects in the construction industry in both developing and wealthy nations. The CSFs for PPP/PFI projects in the UK construction industry were examined by Li et al. [53], and it was discovered that “a strong and good private consortium,” “appropriate risk allocation,” and “available financial market” were extremely important.

These all have financial implications, and unlike Türkiye, there are no political or legal obstacles to PPPs in the UK. The main CSFs, according to Cheung et al. [64], are “favorable legal framework”, “proper risk distribution and risk sharing”, “strong and good private consortium”, commitment and “responsibility of public and private sectors”. Similar to Türkiye, China and Hong Kong also experience legal difficulties while implementing PPP projects, and the duties

and obligations of both public and private partners are not clearly defined. In a different study, Hwang et al. [65] investigated the CSFs for PPP projects in Singapore from the viewpoint of contractors and highlighted “well-organized public agency”, “appropriate risk allocation”, and “strong private consortium” as crucial factors in project success. Similar to the UK, Singapore's building industry is more dependent on financial concerns.

CSFs appear to vary for each party when the results are analyzed in depth based on the survey respondents (private clients, public clients, and contractors). From the perspective of the private clients, favorable legal framework (4.52), detailed and clear project identification (4.48), and competent client and contractor (4.39) are crucial for the successful delivery of PPP projects in Türkiye; however, for the public client, favorable legal framework (4.75), comprehensive technical feasibility (4.75), detailed cost and benefit analysis (4.58), detailed and clear project identification (4.23), and competent client and contractor (4.39) are crucial.

“Favorable legal framework” was cited as the top CSF by respondents from the private and public client sectors. On the other side, the contractors placed it eighth. Despite the observed ranks discrepancies between the three groups, all three groups' mean values are relatively high (above 4). This indicates that it is crucial to the successful completion of a PPP project in the eyes of both clients and contractors. The foundation of sustained private sector participation is the legal and political environment; as a result, the client must have a clear knowledge of the evaluation that has to be conducted and the conclusions that need to be drawn. For this reason, clients place a higher value on favorable legal frameworks. A clear and solid legal foundation is necessary for the contracts and agreements to be bankable. Additionally, it is anticipated that the creation of an efficient system would help to guarantee the continuity of PPP policies and implementations [64]. Establishing a legal and regulatory framework is crucial to improving the appeal of PPP project investments for private partners.

“Detailed and clear project identification” was the second CSF that both the contractors and private clients rated highly. This CSF was ranked second and first by contractors and private clients, respectively, but only sixth by public clients while having a high mean score (4.42). These findings demonstrate the significance of this element for all parties. The disparity in rankings may be due to the viewpoint of the public and private sectors rather than that of the client and contractor. Objectives must be defined and agreed upon with a shared understanding by all parties. When the project's objectives are specified clearly at the outset, success can be measured more precisely, and the project will stay within its designated boundaries and not deviate too far from the original plan [17, 30, 34–35, 38, 55].

Private clients, public clients, and contractors placed “competent client and contractor” fifth, third, and sixth, respectively. One with goals This aspect was shown to be extremely important for the public clients (4.5). The clients should assess the various credentials of potential subcontractors and choose that are similar to their own, experience working on PPP projects, technical expertise in the areas needed, an appropriate management style, and reliability and financial credibility. Choosing qualified contractors has a beneficial impact on the project's outcome [17].

Private clients, public clients, and contractors scored “comprehensive technical feasibility” fourth, second, and tenth, respectively. Respondents from the private and public clients gave this CSF reasonably high ratings, with mean scores of 4.39 and 4.75, respectively, and 4.06 for the contractors. This conclusion suggests that although contractors have not given it the same weight as clients, this component is very important for a project's success. This may be because the customer has a responsibility to oversee the project's financial audit, but it is more crucial for the client to base its investment decisions on trustworthy feasibility studies. There must be a clear need for the services to be supplied since, given the market conditions, the level of demand for the products and services to be offered is crucial to PPP projects' long-term viability.

It is essential to getting the private sector to approve a PPP project as a result [68]. Some PPP law provisions charge the government with predicting market demand in order to ensure a certain amount of income to the contractor in the event that pre-specified levels of services are provided, regardless of the degree of demand realized in the market. A thorough investigation must be used prior to defining the minimal demand/revenue because the study's sequential steps have an impact on the project's size, cost, and revenues [66].

The private clients, the public clients, and the contractors scored “detailed cost and benefit analysis” sixth, third, and second, respectively. Private clients placed it sixth, although the average score is still very high (4.3). Cost-benefit analysis is obviously important for all stakeholders. Before a project is put through the procurement process, the public client should carefully evaluate all of the alternative options that are advantageous to the government and end users [53].

However, clients and contractors have different perspectives on thorough, reasonable cost-benefit analyses because, unlike clients, contractors are only profit-driven and assume all financial risks in a PPP project. As a result, cost-benefit analyses have a direct impact on contractors' initial attitudes toward the project.

The private clients ranked “strong private consortium” twenty, the public clients eleven, and the contractors third. This result demonstrates that contractors believe a strong private consortium is crucial to the success of PPP projects (4.19). On the other hand, particularly private consumers rated it poorly, indicating just a medium level of relevance with a mean value of 3.52. Due to the connection between project viability and the private consortium participants' eligibility and financial capacity, stakeholders evaluate each participant's strong and weak points and, if deemed appropriate, join forces to form consortia that combine and capitalize on each participant's individual strengths. Additionally, it is crucial for partners to get along well because they must share the project's risks and advantages [5, 46–47, 69–71]. A project is more likely to be

completed effectively if it has the correct partners and shared objectives [6].

“Wide client acceptance” was identified as the least significant factor (less than 3.00). In a long-term partnership contract each party must appreciate and respect each other’s goal; in other words, the project itself, apart from being technically implementable, must satisfy different participants’ objectives as well. The objectives of the government are those of reduction in financial restraints, public finance limitations, provision of public goods and services (detailed by specific project), achievement of value for money, while the private sector’s objectives are profit generation and market penetration, however the objectives of the communities are to receive better services or occupy a better environment. The fierce competition for cost-effectiveness in Türkiye could be the main reason behind the lack of appreciation of the other’s goals.

The goal of factor analysis is to investigate and uncover hidden connections between the variables, and to categorize them into a smaller number of more focused but thorough variables. Table 5 presents the correlation matrix for the 23 variables. The population correlation matrix might not be an identity matrix, according to the big value of the sphericity test statistics (Barlett test of sphericity = 1301.78) and the small significance level that goes along with it (p.000). According to the correlation matrix, all of the variables have a significant correlation at the 5% level, indicating that none of the variables need to be dropped for the principal component analysis. The KMO statistic has a value of 0.710, which is suitable for factor analysis, in Kaiser's opinion [72].

A couple of studies have conducted factor analysis to explore the main components for CSFs of PPPs. Sanni [73] identified three factors explaining 59.72% of the variance. The factors were identified as leadership focus, risk allocation and economic policy, and projects feedback. In a similar way, Dithebe et al. [74] found three factors that account for 69.00% percent of of the variance. The factors were determined as public cooperation, project

viability, and policy and legislation enhancement.

In this study, a five-factor solution with eigenvalues greater than 1.000 was produced via principal component analysis, accounting for 68.15% of the variance. Table 6 displays the factor grouping based on varimax rotation. Only one of the factors is assigned to each variable, and the loading on each factor is greater than 0.50. As can be seen, “inspiring financial package” is not one of the components.

The components were named based on the intersection of the meanings of the factors under that component. It is possible to interpret the five components as follows: Factor 1 stands for project financing; Factor 2 for project management; Factor 3 for operational aspects; Factor 4 for procurement; and Factor 5 for organizational factors.

Factor 1- Project Finance:

16.12% of the overall variations in the CSFs are explained by this component. Project financing includes sound investment climate, extensive risk analysis and risk sharing, strong private consortium, political and economic stability, and detailed cost and benefit analysis.

Numerous factors contribute to the project financing component, including sound climate environment (4.11) and extensive risk analysis and risk sharing (3.71). The highest loadings are for these two sub-factors, which have significance values of 0.808 and 0.765, respectively. This shows that the financial market is crucial for the growth of PPP projects because it depends heavily on share and debt contributions. The best party to handle the risks is chosen to receive the risks, according to the concept of appropriate risk allocation. The management of PPP project implementation is made simple by this type of allocation system. In summary, creating a sound finance structure is crucial for project success [53]. Before committing to a project, the private sector should fully understand the risks involved and ensure that risks are managed effectively [17, 37]. The government should make sure that mechanisms are in place to control risks in all circumstances.

Strong private consortium and stable political and economic environment are the other two high loading sub-factors with significance values of 0.634 and 0.632, respectively. This recommends that private businesses should research the strengths and shortcomings of other players and, where appropriate, team up to form a consortium that can leverage and capitalize on their particular strengths [5, 52, 46–47, 51–52, 69–70]. The presence of a stable political and economic climate is crucial for project financing. This encourages both domestic and foreign investors to participate in PPP projects, and the availability of financially stable partners who share the same objectives will increase the number of PPP projects that are most likely to be successfully implemented [17, 35, 53].

Detailed cost and benefit analysis is identified as the third most important factor for a PPP project (4.33). It has a significant loading of 0.599 and a rather high loading in terms of project finance. The public client should make sure that the whole project feasibility study is completed before a project is put up for procurement and that all viable solutions that are advantageous to the government and end users are considered [53]. Project financial analysis is seen differently by the public and private sectors [49]. Cost-benefit analysis would therefore be preferable for project evaluation. The alternative that maximizes the gap between benefits and costs to society as a whole is found using a cost-benefit analysis [44-45, 54]. PPPs offer a wide range of potential project finance choices. Cost-benefit analysis is not intended to distinguish between different funding choices; rather, it is used to support decisions about resource allocation [49]. Although Turkish contractors and public clients ranked this criterion third, it was not deemed essential in earlier studies. This may be due to disparities in cultural perceptions and customs between the nations.

Factor 2- Project Management:

15.088% of the total variances in the critical success factors can be attributed to the project management factor. This category contains five elements: rational and practical project manager, favorable legal framework, competent client and

contractor, executive support from public and private sectors, regular monitoring and feedback. Two essential elements in project management are a rational and practical project manager, as well as favorable legal framework with a significance of 0.765. The most important factor in creating PPPs is having a supportive legal environment. Its mean value is 4.33, which is high. Bennett [75] stated that the foundation for sustainable private sector participation in urban infrastructure services is an enabling regulatory, legal, and political environment. All projects acquired under the PPP are based on a wide variety of law blended together, including planning and environment, employment, corporate commercial, construction, finance, and insurance [76]. In Türkiye, there is no coherent law on PPP; instead, there are different legislations like BOT laws. The government ought to release a number of formal PPP procurement guidelines that lay out the entire procurement process in detail and specify what evaluations and choices must be made at each stage. A successful project also requires a favorable legal framework, according to Dvir et al. [36] and Kerzner [42]. Türkiye has a sporadic selection of PPP laws available.

There is a growing need for a legal framework as PPPs become more significant. Infrastructure provision is challenging in Türkiye. It is necessary to have a solid understanding of PPP models and to put models established on reliable principles into practice in order to fast close this investment gap. Therefore, creating a uniform PPP law is part of the government's growth plans. Although one-way ANOVA study revealed this component to be the most important element for the Turkish construction sector, it was only briefly highlighted in the literature.

The need for a rational and practical project manager (4.15) to assure project delivery on time, within acceptable standards, and within a predetermined budget is another significant sub-factor. The influence of a project manager's experience on a project's success or failure was looked at by Rubin and Seelig [77]. Success was determined by technical performance. They concluded that, in contrast to the size of the previously, a project manager's prior experience had little bearing on the project's performance. In

other investigations, this characteristic has also been identified as a crucial element [30–31, 35–37, 41, 53, 56, 78].

Table 5. Correlation matrix

Variables	V1	V2	V3	V4	V5	V6	V7	V8	V9	V10	V11	V12	V13	V14	V15	V16	V17	V18	V19	V20	V21	V22	V23	
V1	1.00																							
V2	0.34	1.00																						
V3	0.51	0.47	1.00																					
V4	-0.02	0.19	0.29	1.00																				
V5	0.25	0.44	0.59	0.18	1.00																			
V6	-0.04	0.22	0.07	0.04	0.31	1.00																		
V7	0.08	0.35	0.19	0.01	0.41	0.42	1.00																	
V8	0.11	0.32	0.20	-0.03	0.28	0.40	0.27	1.00																
V9	0.06	0.29	0.24	0.18	0.35	0.24	0.32	0.14	1.00															
V10	-0.01	0.29	0.08	0.06	0.21	0.54	0.41	0.47	0.07	1.00														
V11	-0.01	0.14	0.05	0.06	0.15	0.21	0.39	0.12	0.38	0.40	1.00													
V12	0.04	0.26	0.08	0.09	0.38	0.03	0.42	0.01	0.49	0.09	0.64	1.00												
V13	0.02	0.30	0.20	-0.01	0.38	0.45	0.40	0.49	0.10	0.70	0.32	0.16	1.00											
V14	0.25	0.71	0.39	0.23	0.51	0.46	0.23	0.60	0.36	0.43	0.14	0.09	0.43	1.00										
V15	0.10	0.46	0.28	-0.12	0.42	0.30	0.23	0.46	0.22	0.68	0.14	0.11	0.62	0.53	1.00									
V16	0.27	0.54	0.38	0.01	0.37	0.15	0.20	0.50	0.33	0.37	0.17	0.17	0.37	0.50	0.71	1.00								
V17	0.04	0.32	0.04	-0.08	0.20	0.49	0.35	0.58	0.05	0.65	0.21	0.01	0.48	0.49	0.59	0.58	1.00							
V18	0.33	0.66	0.31	0.11	0.38	0.22	0.36	0.45	0.28	0.38	0.04	0.01	0.21	0.62	0.37	0.52	0.50	1.00						
V19	0.38	0.41	0.43	0.03	0.32	0.42	0.18	0.51	0.04	0.49	0.14	-0.19	0.44	0.57	0.50	0.40	0.52	0.58	1.00					
V20	0.34	0.58	0.53	0.09	0.55	0.16	0.41	0.06	0.27	0.12	0.13	0.22	0.11	0.38	0.28	0.32	0.10	0.49	0.40	1.00				
V21	0.18	0.33	0.41	0.06	0.50	0.17	0.43	0.20	0.24	0.25	0.36	0.37	0.21	0.14	0.34	0.56	0.29	0.38	0.30	0.48	1.00			
V22	0.14	0.23	0.28	-0.07	0.38	0.24	0.45	0.06	0.29	0.33	0.35	0.35	0.19	0.08	0.36	0.47	0.49	0.37	0.22	0.45	0.67	1.00		
V23	0.33	0.28	0.32	-0.04	0.21	0.07	0.17	0.15	0.18	0.20	0.09	0.10	-0.03	0.12	0.40	0.58	0.29	0.31	0.24	0.52	0.47	0.61	1.00	

Table 6. Rotated component matrix

Common Factors	Variables	Components				
		1	2	3	4	5
Project Finance	Solid Investment Climate	0.808				
	Extensive Risk Analysis and Risk Sharing	0.765				
	Strong Private Consortium	0.634				
	Political and Economic Stability	0.632				
	Detailed Cost and Benefit Analysis	0.599				
Project Management	Rational and Practical Project Manager		0.765			
	Favorable Legal Framework		0.765			
	Competent Client and Contractor		0.735			
	Executive Support from Public and Private Sectors		0.567			
	Regular Monitoring and Feedback		0.518			
Operational Factors	Detailed and Clear Project Identification			0.783		
	Dedicated and Skilled Project Team			0.684		
	Comprehensive Technical Feasibility			0.664		
	Optimal Stakeholder Relations and Communication			0.644		
	Achieving Design Objectives			0.575		
Procurement	Wide Client Acceptance				0.882	
	Effective Procurement Process				0.714	
	Successful Client Consultation				0.681	
Organizational Factors	Complete Project Management Methodologies					0.779
	Simple Organizational Structure					0.722
	Strong Public Entity					0.612
Initial Eigenvalues		7.851	2.666	2.283	1.760	1.114
Percentage of Variance		16.120	15.088	14.972	11.380	10.589
Cumulative Percentage of Variance		16.120	31.207	46.180	57.560	68.149
Kaiser-Meyer-Olkin Measure (KMO) of Sampling Adequacy:			0.710			
Bartlett's Test of Sphericity:						
		Approx. chi-square	1301.783			
		df	253			
		Sig.	0.000			
Extraction Method: Principal Component Analysis.						
Rotation Method: Varimax with Kaiser Normalization.						
Rotation converged in 8 iterations.						

Competent client and contractor (4.28) is crucial in coming up with creative ideas to achieve the goals of the government for PPP projects. In a typical PPP project, the special purpose vehicle will outsource the construction, operations, and equipment supply to qualified suppliers to manage its design, construction, operational, and maintenance obligations. The significance of hiring a qualified contractor has also been mentioned by Pinto and Slevin [38], Baker et al. [52], Pinto and Covin [35], Dvir et al. [36], Ghosh et al. [37], Qiao et al. [17], and Jefferies et al. [5].

The fourth crucial factor has a significance of 0.567 and a mean value of 3.73 and is the executive support from public and private sectors. To ensure a successful PPP project, Kerzner [31], Ashley et al. [34], Pinto and Slevin [38], White and Patton [32], Dvir et al. [36], Ghosh et al. [37], and Qiao et al. [17] all emphasized the importance of managing the relationships. The attitude of the actors affects the caliber of the final product. This implies that this issue must also be considered when assessing the project's viability [53].

The fifth crucial factor, regular monitoring and feedback (4.04), has a rather high loading and a significance of 0.518. A monitoring process is necessary to ensure an efficient operation; it includes performance monitoring, determining if the contracted services are provided in accordance with the contracted standards, and analyzing the corrective measures implemented by the PPP provider. The information must be factual, pertinent, and quantitative. Numerous research [35-36, 38, 55] have highlighted the significance of this characteristic.

Factor 3- Operational Factors:

14.972% of all CSF deviations are accounted for by the operational factors. This primary aspect has six components: detailed and clear project identification, dedicated and skilled project team, comprehensive technical feasibility, optimal stakeholder relations and communication, achieving design objectives, proper and systematic project control.

With a significance of 0.783, detailed and clear project identification (4.33) has the highest loading. The project identification step is crucial because it ensures that all involved parties have a shared knowledge of the project's goals. The team becomes committed to and in agreement with the project goals when there are only a few primary goals [79]. As a result, a project's progress may be efficiently tracked. Because the project's objectives are made explicit from the outset, success may ultimately be assessed more precisely [17, 30, 34–35, 38, 43, 55].

If the project's scope is established at the outset, it should remain within those boundaries and avoid growing to encompass more than was originally intended. This element was discussed in earlier studies, and it was believed to be crucial for success in the end result. However, it was discovered in this study that it is extremely important for the Turkish building industry.

The second crucial factor is a dedicated and skilled project team (4.22), which has a high loading and a significance of 0.684. The success of the project depends on understanding the contractor and consultant teams involved in PPP delivery [34, 36, 38, 41]. A team-based

management approach is typically justified by the complexity and size of the majority of PPP projects in order to ensure that all necessary abilities are successfully utilized. The team's experience spans a wide range of areas, including management, previous work on related projects, public relations, leadership skills, and many more.

Comprehensive technical feasibility, the third operational component, has a mean value of 4.26 and a significance level of 0.664. For the private sector to win a PPP contract, comprehensive technical feasibility is necessary [35, 38, 46, 52]. Technical challenges are typically one of the most crucial factors in a project feasibility assessment. This implies that it is crucial to analyze the related technical issues while thinking about PPP procurement choices.

Another important component is optimal stakeholder relations and communication (3.98). When used efficiently, communication can cut down on ineffective work, prevent duplication, and aid in error-free operations. This can aid in managing uncertainty, help identify issues earlier, or spark ideas for better solutions [36–38, 43, 51, 56].

Functional and technical specifications, schedule goals, and budget goals are components of achieving design objectives with a significance of 0.575 (3.96). Both the consultant and the contractor have a responsibility to collaborate amicably in order to accomplish these objectives for a successful project completion. Numerous researchers have highlighted the significance of this component [34, 36, 44–45, 54].

The final operational factor with a loading of 0.524 is proper and systematic project control (4.07). For a project to be delivered successfully, adherence to the initial requirements - including those related to schedule, budget, quality, and environmental concerns - is crucial. Over the years, the construction sector has regularly failed to deliver successful projects on schedule, within budget, and with the required level of quality [80]. All parties are required to follow the timelines, finances, quality, safety, and environmental criteria set forth at the project's inception [32, 34, 52]. To produce a successful

project, all parties must work together in coordination to complete tasks within the allotted time frames [36, 42]. The fact that the results were provided in this manner is not unexpected given that the literature research indicates a moderate loading for this element. In addition, the criticality level for proper and systematic schedule, cost, quality, and budget control has been noted to be near to moderate. It is related to elements like a realistic and logical project manager and an enthusiastic and skilled project crew. Unfortunately, in Türkiye, the planning stage is typically kept very brief, making it impossible to accurately estimate the time and cost of construction. Eventually, the contractors request an extension to finish the projects because, in these conditions, the needed quality cannot be achieved.

Factor 4- Procurement:

11.380% of all CSF deviations are attributable to the procurement component. Three things fall under this category: wide client acceptance, effective procurement process, and successful client consultation.

Wide client acceptance (2.99) indicates that the final project's sale to its intended users has the maximum loading, with a significance of 0.882. Client satisfaction with the goods and services the industry has been delivering in recent years has increased pressure on service providers to increase performance [2]. While the communities' goals are to receive better services or live in a better environment, the private sector's typical goals are profit production and market penetration [53]. Additionally, it has been noted by Pinto and Slevin [38], Pinto and Prescott [55], and Pinto and Covin [35] that client acceptance is one of the essential elements for a project's effective completion.

Effective procurement process (3.63) must be present throughout the whole procurement process. With a significance of 0.714, this sub-factor has a significant loading. A quick and effective procurement procedure is crucial for reducing transaction costs and expediting the negotiation and closing of the purchase. To achieve competitive neutrality, or the objective and uniform treatment of public and private

parties in their rivalry for public works and services, the government must establish the relevant policies or legal procedures [81]. Maintaining the integrity of the procurement process, sustaining competition, fostering technological and financial advances, optimizing resource allocation, boosting productivity, and cutting costs are all significant goals of a competitively neutral procurement process. Most of the time, competitive bidding processes based only on price may not be able to help achieve a strong private consortium and obtain value for the public. When looking for the ideal partner, the government should have a long-term perspective [5, 17, 53, 67, 71]. Despite its relatively high mean value, effective procurement process was ranked 20th by the respondents. A few studies [31, 34] have also shown the importance of this aspect.

Another crucial element is successful client consultation, which has a factor loading of 0.681 and a mean value of 3.39. A construction project needs to comprehend and meet the needs of the clients. Client consultation is the initial phase of a program to execute change, according to Kolb and Frohman [82]. In their investigations, Pinto and Covin [35], Pinto and Slevin [38], and Manley [83] also highlighted the significance of this aspect.

Factor 5- Organizational Factors:

10.589% of the overall variance in CSFs can be attributed to organizational factors. This factor consists of three parts: complete project management methodologies, simple organizational structure, and strong public entity. Complete project management methodologies are related to higher loading (3.73).

According to Schultz and Slevin [84], Jaselskis and Ashley [59], Wong and Maher [33], and Ghosh et al. [37], managerial support for projects, or indeed for any implementation, has long been seen to be extremely important in determining whether they would ultimately succeed or fail. According to Beck [85], project management is ultimately responsible for carrying out executive management's plans or goals for the organization. It is dependent on executive management for authority, direction,

and support. The project manager's confidence in management's support during a crisis as well as the allocation of enough resources (money, people, time, etc.) are both examples of how management may help the project.

One of the organizational variables related to organizational outcomes revealed in this study is the simple structure of the project organization (3.30). It has a favorable relationship with project management success, as determined by cost effectiveness or overall evaluations of project performance. The organizational structure of a project has also been deemed essential for the project's success by Nahapiet and Nahapiet [61], Might and Fisher [30], Kerzner [31], White and Patton [32], Wong and Maher [33], Dvir et al. [36], and Clarke [43].

Finally, for PPP projects to be financially viable and appealing investment prospects for private sector developers, a strong public entity (3.78) is required. The loading for this sub-factor is 0.612. This affirms the institutional framework of a PPP project, which holds that policymakers, government agencies, and its agency are essential for the execution of PPPs [53].

4. Conclusion

This study examines the CSFs of PPP projects in developing nations using the results of a questionnaire survey. In this regard, data from the Turkish construction industry was gathered. The 23 CSFs' underlying factor groupings were discovered by factor analysis, and they are denoted by the following names: project finance, project management, operational factors, procurement, and organizational factors. Based on a one-way ANOVA analysis, the relative significance of the CSFs was assessed. The three elements "favorable legal framework," "detailed and clear project identification," and "detailed cost and benefit analysis" are deemed to be the most important for the Turkish building industry.

According to the analysis' findings, a favorable legal framework is the most important component for the success of PPP projects. Given the complexity of the country's legal system and the lack of a unified PPP law, the scenario is not unexpected in the case of Türkiye.

The government's development plans also refer to the requirement for a supportive legal environment. Detailed and precise project identification is the second most important component of a successful project delivery. Construction time and operating time must be carefully scrutinized, particularly throughout the tendering process.

Due to the national culture and business practices of Türkiye, project specifications frequently change even after the bidding process. In the Turkish construction sector, clients frequently request numerous project adjustments since they don't give themselves enough time to plan. The third most crucial success criterion for PPP projects in the Turkish construction industry is a thorough, acceptable cost-benefit analysis. Both the public and private sectors should thoroughly evaluate the benefits and drawbacks, risks, expenses, and other factors of a PPP project before moving forward.

Cost-benefit analysis is crucial because the majority of PPP projects are intricate and highly regulated. Since Türkiye is a developing nation with an unstable political and economic climate, borrowing rates that directly affect project costs might fluctuate sharply far too frequently. The climate for investing is made unstable by this circumstance, which raises the risk for the investors. Potential PPP project partners prefer to prolong the operation period and take precautions to manage this risk.

Learning from past mistakes and experiences, the Turkish government should support the PPP technique as it will enable the timely and high-quality completion of public projects. The findings of the analysis indicated that the Turkish government should resolve legal matters first in order to draw in investors and the private sector. Second, each partner should devote an appropriate amount of time to preparation in order to correctly identify the project's purpose, objectives, and requirements.

The results of the study reflect the perceptions and experiences of the Turkish construction professionals. Even though they are well-experienced in international arena, this should be considered as a limitation. Based on the unique

circumstances of the nations where PPP projects are done, the results could differ. Türkiye serves as an example of a developing nation. In contrast, in a developed nation with a well-established legal system, the outcomes would be different.

Article Information Form

Funding

The authors have not received any financial support for the research, authorship, or publication of the study.

Authors' Contribution

The authors contributed equally to the study.

The Declaration of Conflict of Interest/ Common Interest

No conflict of interest or common interest has been declared by the authors.

The Declaration of Ethics Committee Approval

This study does not require ethics committee permission or any special permission.

The Declaration of Research and Publication Ethics

The authors of the paper declare that they comply with the scientific, ethical and quotation rules of SAUJS in all processes of the paper and that they do not make any falsification on the data collected. In addition, they declare that Sakarya University Journal of Science and its editorial board have no responsibility for any ethical violations that may be encountered, and that this study has not been evaluated in any academic publication environment other than Sakarya University Journal of Science.

Copyright Statement

Authors own the copyright of their work published in the journal and their work is published under the CC BY-NC 4.0 license.

References

- [1] Ministry of Development. "Advances in PPP in Türkiye and in the World", Republic of Türkiye Ministry of Development Memorandum, Ankara, Türkiye, 2012.
- [2] C. T. Amponsah, "Public-Private Partnerships: Critical Success Factors for Procurements of Capital Projects," Ph.D. dissertation, Capella University, 2010
- [3] B. Li, A. Akintoye, An Overview of Public-Private Partnership. Public-Private Partnerships: Managing Risks and Opportunities, Blackwell Science Ltd, 2003.
- [4] L. Y. Tang, Q. Shen, E. W. L. Cheng, "A review of studies on Public-Private Partnership projects in the construction industry," International Journal of Project Management, vol. 28, pp. 683-694, 2010.
- [5] M. C. Jefferies, R. Gameson, S. Rowlinson, "Critical success factors of the BOOT procurement system reflections from the stadium Australia case study," Engineering Construction and Architectural Management, vol. 9, no 4, pp. 352-361, 2002.
- [6] C. Hardcastle, P. J. Edwards, A. Akintoye, B. Li, "Critical success factors for PPP/PFI projects in the UK construction industry: a factor analysis approach," Construction Management and Economics, vol. 23, no 5, pp. 459-471, 2005.
- [7] Z. Y. Zhao, J. Zuo, G. Zillante, X. W. Wang, "Critical success factors for BOT electric power projects in China: Thermal power versus wind power," Journal of Renewable Energy, vol. 35, pp. 1283-1291, 2010.
- [8] X. Meng, Q. Zhao, Q. Shen, "Critical success factors for transfer-operate-transfer urban water supply projects in China," Journal of Construction Engineering and Management, vol. 27, no 4, pp. 243-251, 2011.
- [9] A. Gupta, M. Gupta, R. Agrawal, "Identification and ranking of critical success factors for BOT projects in India," Management Research Review, vol. 36, no 11, pp. 1040-1060, 2013.

- [10] D. K. H. Chua, Y. C. Kog, P. K. Loh, "Critical success factors for different project objectives," *Journal of Construction Engineering and Management*, vol. 125, no 3, pp. 142-150, 1999.
- [11] R. Morledge, K. Owen, "Critical success factors in PFI projects," in 14th Annual ARCOM Conference, University of Reading, Association of Researchers in Construction Management, 1998, pp. 565-74.
- [12] European PPP Expertise Centre, "Market update - First half of 2013", Luxembourg, 2013.
- [13] A.P. Gurgun, A. Touran, "Public-private partnership experience in the international arena: Case of Türkiye," *Journal of Management in Engineering*, vol. 30, no 6, pp. 04014029, 2014.
- [14] R. Osei-Kyei, A. P. C. Chan, "Review of studies on the critical success factors for public-private partnership (PPP) projects from 1990 to 2013," *International Journal of Project Management*, vol. 33, no 6, pp. 1335-1346, 2015.
- [15] A. M. Algarni, D. Arditi, G. Polat, "Build-operate-transfer in infrastructure projects in the United States," *Journal of Construction Engineering and Management*, vol. 133, no 10, pp. 728-735, 2007.
- [16] D. Jamali, "Success and failure mechanisms of public private partnerships (PPPs) in developing countries: Insights from the Lebanese context," *International Journal of Project Management*, vol. 17, no 5, pp. 414-430, 2004.
- [17] L. Qiao, S. Q. Wang, R. L. K. Tiong, T. S. Chan, "Framework for critical success factors of BOT projects in China," *The Journal of Project Finance*, vol. 7, no 1, pp. 53-61, 2001.
- [18] R. Agrawal, "Successful Delivery of Public-Private Partnerships for Infrastructure Development," Ph.D. dissertation, Jaypee Institute of Information Technology, Noida, India, 2010.
- [19] S. Ismail, "Critical success factors of public private partnership (PPP) implementation in Malaysia," *Asia-Pacific Journal of Business Administration*, vol. 5, no 1, pp. 6-19, 2013.
- [20] H. Alinaitwe, R. Ayesiga, "Success factors for the implementation of public-private partnerships in the construction industry in Uganda," *Journal of Construction in Developing Countries*, vol. 18, no 2, pp. 1-14, 2013.
- [21] B. Acikgoz, "Public-Private partnership—the case of Türkiye," in *Public Financial Management Reforms in Türkiye: Progress and Challenges*, Singapore, 2020, Volume 1, pp. 105-118.
- [22] O. Okudan, C. Budayan, "Determination of the critical success criteria for public-private partnership (PPP) projects in Türkiye," *Politeknik Dergisi*, vol. 24, no 4, pp. 1675-1689, 2020.
- [23] M. Balcilar, G. Uzuner, C. Nwani, F. V. Bekun, "Boosting energy efficiency in Türkiye: The role of public-private partnership investment," *Sustainability*, vol. 15, no 3, pp. 2273, 2023.
- [24] M. Top, C. Sungur, "Opinions and evaluations of stakeholders in the implementation of the public-private partnership (PPP) model in integrated health campuses (city hospitals) in Türkiye," *The International Journal of Health Planning and Management*, vol. 34, no 1, pp. e241-e263, 2019.
- [25] H. Oge, T. Bas, "Public-private partnership healthcare projects in Türkiye," *The Journal of Business Science*, vol. 4, no 2, pp. 105-119, 2016.

- [26] D. Bulbul, "Evaluation of the public private partnership practices in terms of financial transparency in Türkiye," *The Journal of International Scientific Researches*, vol. 2, no 7, pp. 93-108, 2017.
- [27] C. Budayan, O. Okudan, I. Dikmen, "Identification and prioritization of stage-level KPIs for BOT projects—evidence from Türkiye," *International Journal of Managing Projects in Business*, vol. 13, no 6, pp. 1311-1337, 2020.
- [28] C. Budayan, "Evaluation of delay causes for BOT projects based on perceptions of different stakeholders in Türkiye," *Journal of Management in Engineering*, vol. 35, no 1, pp. 04018057, 2019.
- [29] K. Kuru, D. Artan, "A canvas model for risk assessment and performance estimation in public–private partnerships," *International Journal of Construction Management*, vol. 20, no 6, pp. 704-719, 2020.
- [30] R. J. Might, W. A. Fisher, "The role of structural factors in determining project management success," *IEEE Transactions on Engineering Management*, vol. 32, no 2, pp. 71-77, 1985.
- [31] H. Kerzner, "In search of excellence in project management," *Journal of Systems Management*, vol. 38, no 2, pp. 30-39, 1987.
- [32] D. E. White, J. R. Patton, "Metrics and critical success factors for managing organizations by projects," *IEEE Transactions on Engineer Management*, vol. 37, no 4, pp. 252-253, 1990.
- [33] Y. Y. Wong, T. E. Maher, "New key success factors for China's growing market," *Business Horizons*, vol. 30, no 2, pp. 43-52, 1997.
- [34] D. B. Ashley, C. S. Laurie, E. J. Jaselskis, "Determinants of construction project success," *Project Management Journal*, vol. 18, no 2, pp. 69-79, 1987.
- [35] J. K. Pinto, J. G. Covin, "Critical factors in project implementation: A comparison of construction and R&D projects," *Technovation*, vol. 9, pp. 49-62, 1989.
- [36] D. Dvir, S. Lipovetsky, A. Tishler, A. J. Shenhae, "In search of project classification: A non-universal approach to project success factors," *Research Policy*, vol. 27, pp. 915-935, 1998.
- [37] B. C. Ghosh, T. W. Liang, T. T. Meng, B. Chan, "The key success factors, distinction capabilities and strategic thrusts of top SMEs in Singapore," *Journal of Business Research*, vol. 51, pp. 209-221, 2001.
- [38] J. K. Pinto, D. P. Slevin, "Critical factors in successful project implementation," *IEEE Transactions on Engineering Management*, vol. 34, no 1, pp. 22-27, 1987.
- [39] M. K. Parfitt, V. E. Sanvido, "Checklist of critical success factors for building projects," *Journal of Management in Engineering*, vol. 9, no 3, pp. 243-249, 1993.
- [40] P. Galilea, F. Medda, "Does the political and economic context influence the success of a transport project? An analysis of transport public-private partnerships," *Research in Transportation Economics*, vol. 30, pp. 102-109, 2010.
- [41] D. K. H. Chua, Y. C. Kog, P. K. Loh, E. J. Jaselskis, "Neural networks for construction project success," *Expert Systems with Applications*, vol. 13, no 4, pp. 317-328, 1997.
- [42] H. Kerzner, "In Search of Excellence in Project Management: Successful Practices in High Performance Organizations," Van Nostrand Reinhold, New York, USA, 1998.
- [43] A. Clarke, "A practical use of key success factors to improve the effectiveness of project management," *International*

- Journal of Project Management, vol. 17, no 3, pp. 139-145, 1999.
- [44] J. Shenhar, D. Dvir, O. Levy, "Mapping the dimensions of project success," *Project Management Journal*, vol. 28, no 2, pp. 5-13, 1997.
- [45] D. Dvir, T. Raz, A. J. Shenhar, "An empirical analysis of the relationship between project planning and project success," *International Journal of Project Management*, vol. 22, pp. 24-30, 2002.
- [46] R. L. K. Tiong, "CSFs in competitive tendering and negotiation model for BOT projects," *Journal of Construction Engineering and Management*, vol. 122, no 3, pp. 205-211, 1996.
- [47] J. Birnie, "Private finance initiative (PFI) – UK construction industry response," *Journal of Construction Procurement*, vol. 5, no 1, pp. 5-14, 1999.
- [48] M. J. Brodie, "Public/private joint ventures: The government as partner-bane or benefit?" *Real Estate Issues*, vol. 20, no 2, pp. 33-39, 1995.
- [49] S. G. Hambros, *Public-Private Partnerships for Highways: Experience, Structure, Financing, Applicability and Comparative Assessment*, Hambros SG, Canada, 1999.
- [50] G. Zantke, B. Mangels, "Public sector client-private sector project: Transferring the state construction administration into private hand," *Engineering, Construction and Architectural Management*, vol. 6, no 1, pp. 78-87, 1999.
- [51] D. C. Murphy, B. N. Baker, D. Fisher, *Determinants of Project Success*, Boston College School of Management, Boston, 1974.
- [52] N. Baker, D. C. Murphy, D. Fisher, *Factors Affecting Project Success: Project management handbook* (2nd ed.), John Wiley & Sons, New York, USA, 1988.
- [53] Li, A. Akintoye, P. J. Edwards, C. Hardcastle, "Critical success factors for PPP/PFI projects in the UK construction industry," *Construction Management and Economics*, vol. 23, pp. 459-471, 2005.
- [54] S. Lipovetsky, A. Tishler, D. Dvir, A. Shenhar, "The relative importance of defense project success dimensions," *R&D Management*, vol. 27, no 2, pp. 97-106, 1997.
- [55] J. K. Pinto, J. P. Prescott, "Variation in critical success factors over the stages in the project life cycle," *Journal of Management*, vol. 14, no 1, pp. 5-18, 1988.
- [56] T. Kayworth, D. Leidner, "The global virtual manager: A prescription for success," *European Management Journal*, vol. 18, no 2, pp. 183-194, 2000.
- [57] M. A. Tas, E. Cakir, "Green supplier selection using game theory based on fuzzy SWARA," *Sakarya University Journal of Science*, vol. 25, no 4, pp. 885-897, 2021.
- [58] S. C. Turan, M. A. Cengiz, "Determining the factors that influence the effectiveness of the health sector in the OECD countries," *Sakarya University Journal of Science*, vol. 24, no 5, pp. 1094-1104, 2020.
- [59] J. Jaselskis, D. B. Ashley, "Optimal allocation of project management resources for achieving success," *Journal of Construction Engineering and Management*, vol. 117, no 2, pp. 321-340, 1991.
- [60] L. F. Alarcon, D. B. Ashley, "Modeling project performance for decision making," *Journal of Construction Engineering and Management*, vol. 122, no 3, pp. 265-273, 1996.
- [61] J. Nahapiet, H. Nahapiet, "A comparison of contractual arrangements for building projects," *Construction Management and Economics*, vol. 3, no 3, pp. 217-231, 1985.

- [62] O. Gun, P. Y. Kumru, Z. Aladag, "Developing a model for measuring project performance with software life cycle process metrics and calculating project success score," *Sakarya University Journal of Science*, vol. 24, no 3, pp. 536-554, 2020.
- [63] J. C. Nunnally, *Psychometric Theory*. (2nd ed.), McGraw-Hill, New York, 1978.
- [64] Cheung, A. P. C. Chan, S. Kajewski, "Factors contributing to successful public private partnership projects, comparing Hong Kong with Australia and the United Kingdom," *Journal of Facilities Management*, vol. 10, no 1, pp. 45-58, 2012.
- [65] B. G. Hwang, X. Zhao, M. J. S. Gay, "Public private partnership projects in Singapore: Factors, critical risks and preferred risk allocation from the perspective of contractors," *International Journal of Project Management*, vol. 31, no 3, pp. 424-433, 2013.
- [66] U. Emek, "Turkish experience with public private partnerships in infrastructure: Opportunities and challenges," *Utilities Policy*, vol. 37, pp. 120-129, 2015.
- [67] M. C. Jefferies, "Critical success factors of public private sector partnerships: A case study of the Sydney SuperDome," *Engineering, Construction and Architectural Management*, vol. 13, no 5, pp. 451-462, 2006.
- [68] J. Mota, A. C. Moreira, "The importance of non-financial determinants on public-private partnerships in Europe," *International Journal of Project Management*, vol. 33, no 7, pp. 1563-1575, 2015.
- [69] C. M. Tam, W. Y. Li, A. P. C. Chan, "BOT applications in the power industry of South East Asia: A case study in China," in *CIB W92 Procurement Systems Symposium*, University of Hong Kong, 175, Hong Kong, 1994, pp. 315-322.
- [70] A.A. Abdul-Rashid, S. J. K. Puteri, U. A. Ahmed, J. Mastura, "Public Private Partnerships (PPP) in Housing Development: The Experience of IJM Malaysia in Hyderabad, India," in *World Conference on Accelerating Excellence in the Built Environment*, Birmingham, UK, 2006.
- [71] P. Corbett, R. Smith, "An Analysis of the Success of the Private Finance Initiative as the Government's Preferred Procurement Route," *Accelerating Excellence in the Built Environment Conference*, Birmingham, UK, 2006.
- [72] M. J. Norusis, *SPSS for Windows, Professional Statistics, Release 5*, SPSS Inc., Chicago, 1992.
- [73] A.O. Sanni, "Factors determining the success of public private partnership projects in Nigeria," *Construction Economics and Building*, vol. 16, no 2, pp. 42-55, 2016.
- [74] K. Dithebe, C. O. Aigbavboa, W. D. Thwala, A. E. Oke, "Factor analysis of critical success factors for water infrastructure projects delivered under public-private partnerships," *Journal of Financial Management of Property and Construction*, vol. 24, no 3, pp. 338-357, 2019.
- [75] Bennett, *Public Private Co-Operation in the Delivery of Urban Infrastructure Services (water and waste)*, UNDP/Yale Collaborative Program, United Nations Development Program, New York, 1998.
- [76] Payne, "Key legal issues in projects procured under the private finance initiative," *Engineering, Construction and Architectural Management*, vol. 4, no 3, pp. 195-202, 1997.
- [77] J. Rubin, W. E. Seelig, "Experience as a factor in the selection and performance of project managers," *IEEE Transactions on*

Engineering Management, vol. EM-14, no 3, pp. 131-135, 1967.

- [78] A. Mustafa, "Public-private partnership: An alternative institutional model for implementing the private finance initiative in the provision of transport infrastructure," *Journal of Project Finance*, vol. 5, no 2, pp. 64-79, 1999.
- [79] T. Richardson, "Project management pitfalls," *Business Management Review*, vol. 25, no 8, pp. 49-51, 1995.
- [80] P. W. G. Morris, G. H. Hough, *The Anatomy of Major Projects: A study of the Reality of Project Management*, Wiley, Chichester, UK, 1987.
- [81] X. Zhang, S. Chen, "A systematic framework for infrastructure development through public private partnerships," *IATSS Research*, vol. 36, no 2, pp. 88-97, 2013.
- [82] D. A. Kolb, A. L. Frohman, "An organization development approach to consulting," *Sloan Management Review*, vol. 12, no 1, pp. 51-65, 1970.
- [83] T. Manley, "Have you tried project management?" *Public Personnel Management*, vol. 12, pp. 180-188, 1975.
- [84] R. L. Schultz, D. P. Slevin, "Behavioral considerations in the implementation of marketing decision models," in *Spring and Fall AMA Conference*, Wilmington, Delaware, 1972, pp. 494-498.
- [85] D. R. Beck, *Implementing Top Management Plans Through Project Management*, *Project Management Handbook* (eds. D. I. Cleland and W. R. Kings), New York, 1983.

Immobilization of Lipase on Agarose Beads for Enzymatic Hydrolysis/Transesterification of Castor Oil

Semra Yilmazer Keskin^{1*}, Kübra Karakaya²

^{1*} Sakarya University, Faculty of Science, Department of Chemistry, Sakarya, Türkiye, syilmazer@sakarya.edu.tr

² Sakarya University, Institute of Natural Sciences, Sakarya, Türkiye, kubraozdemir54@gmail.com

*Corresponding Author

ARTICLE INFO

ABSTRACT

Keywords:
Agarose beads
Biocatalysis
Castor oil
Lipase
Ricinoleic acid

Lipase was immobilized onto agarose beads and used for enzyme-catalyzed hydrolysis/transesterification of castor oil at room temperature without surfactants and salts. The immobilization yield was evaluated by reacting *p*-nitrophenyl butyrate and immobilized lipase. The reaction was performed in a 25 mL phosphate buffer medium (pH 7.0) and incubated for 2 hours. The absorbance of the formed *p*-nitrophenol was measured at 346 nm. The highest immobilization rate was obtained using 5.0 mg lipase with 2.5 mL glyoxal agarose beads. The reaction was performed in 25.0 mL sodium bicarbonate buffer pH 10 for 12 h. The hydrolysis/transesterification of castor oil was performed in phosphate buffer (pH 7) – ethanol medium. The main products were ricinoleic acid and ethyl ricinoleate. The highest hydrolysis/transesterification yield was 87% using 1.0 g castor oil and 2.5 mL of lipase immobilized agarose beads in the phosphate buffer (pH 7): ethanol (1: 9, V: V) at 72 hours. The reaction products were analyzed using a Fourier Transform Infrared spectrometer (FTIR) and Reversed-Phase High-Performance Liquid Chromatography (RP-HPLC).

Article History:

Received: 12.09.2023

Accepted: 01.11.2023

Online Available: 27.02.2024

1. Introduction

Most industrial processes about oil hydrolysis or transformation to produce valuable products such as free fatty acids (FFAs) or their esters are carried out in harsh conditions. Enzymatic reactions can be performed under more favorable conditions than complicated processes. Lipases, triacylglycerol acylhydrolases, are mainly derived from microorganisms and have been used for many applications, such as enzymatic oil hydrolysis, modifying flavor via fatty acids, producing alcohols, etc [1].

They can catalyze transformations of various organic reactions via esterifications and transesterifications [2]. Lipases are usually used for hydrolysis and transesterification of castor oil under mild conditions. Castor oil is a

triglyceride of fatty acids, and ricinoleic acid is the main hydrolysis reaction product. Ricinoleic acid has anti-inflammatory and bactericidal properties [3]. Therefore, it has received significant interest in the pharmaceutical industry. Also, its ester derivatives are used in many industrial processes, such as emulsifiers and soaps [4].

Some studies investigated the effect of solution mediums on hydrolysis and transesterification of castor oil by lipases. Yamamoto and Fujiwara used sodium phosphate buffer (pH 7.0) as the reaction medium and reported that isooctane, Triton X-100, or PEG-6000 addition slightly improved hydrolysis yields using free lipase [5]. Kulkarni and Pandit investigated the effect of *n*-hexane, *n*-heptane, isooctane, and diethyl ether solvents and reported that they all enhanced hydrolysis yield by using free lipase [6]. Jeon et

al. achieved 100% hydrolysis yield via isopropyl ether–water mixture (1:1) by free lipase [7]. Malhotra et al. investigated lipase-catalyzed castor oil transesterification [8]. The reported conversion rates were 95%, 90%, and 80% for hexanol, octanol, and dodecanol. Narwal et al. used lipase-immobilized silica gel for castor oil transesterification [9].

The highest yield obtained was 78%. In the present work, 90% ethanol was used as a reaction medium, and hydrolysis and transesterification products were obtained via catalysis of lipase-immobilized agarose beads.

As can be seen from the literature studies, researchers have performed hydrolysis and transesterification of castor oil using different reaction media by free and immobilized lipase. This study aims to show the availability of agarose as a support material for lipase immobilization and the ability of lipase-immobilized agarose beads to obtain both ester and hydrolysis products in an alcohol/phosphate buffer (pH 7) medium.

Using agarose as a support material provides high immobilization efficiency, easy immobilization, and increased enzyme stability. Both hydrolysis and transesterification products were obtained in mild conditions using lipase-immobilized agarose beads and ethanol-phosphate buffer (pH 7) medium.

2. General Methods

2.1. Materials

All of the used chemicals were of analytical grade. High-density glyoxal 6BCL agarose (ABT) was used as supporting material. Lipase from *Burkholderia (Pseudomonas) cepacia* was purchased from Sigma. Ricinoleic acid, as standard, was purchased from TCI chemicals. Ethanol, NaOH, acetonitrile, acetone, p-nitrophenyl, and p-nitrophenyl butyrate (PNB) were purchased from Merck Chemicals. Before HPLC analysis, the solutions were filtered with a 0.45 μm mesh cellulose esters filter(CHMLAB).

2.2. Immobilization of lipase

The lipase immobilization was carried out according to the previously described method

by Bolivar et al [10]. The glyoxal agarose beads (2.5 mL) were added to the 25.0 mL of 0.1 M sodium bicarbonate solution (pH 10) containing 2.5 – 7.5 mg lipase. The suspension was shaken with an orbital shaker at a 150 rpm agitation rate for 2 – 12 h intervals. At the end, 20.0 mg NaBH_4 was added to the suspension and stirred for 30 min. Then, it was washed with distilled water and stored in phosphate buffer (pH 7.0). The immobilization degree was evaluated with the hydrolysis of pNB.

2.3. Hydrolysis of pNPB

Hydrolysis of p-nitrophenyl butyrate (as substrate, 40 μM) was investigated using 2.5 mL of the immobilized enzyme. The reaction was performed in a 25 mL phosphate buffer medium (pH 7.0) and incubated for 2 hours. The absorbance of the product, p-nitrophenyl, was measured at 346 nm by a UV-Vis spectrophotometer (Shimadzu, UV-2600), and the concentrations were calculated using the calibration curve in the range of 10 – 40 μM p-nitrophenyl concentrations.

2.4. Hydrolysis/transesterification reaction

The hydrolysis/transesterification experiments were carried out in a 1:9 volume ratio of phosphate buffer (pH 7)-ethanol medium with different reaction times (2 – 72 h), shaking rates (30 – 200 rpm), enzyme immobilized agarose beads amount (1 – 5 mL in phosphate buffer, pH 7) and castor oil amount (0.1 – 2.0 g) in a closed erlenmeyer flask. First, an appropriate amount of castor oil was dissolved in ethanol, and then the immobilized enzyme in the buffer solution was added to the reaction medium. The total reaction volume was made up to 25 mL. Approximately 100 μL of the sample was collected with the help of an automatic pipette at the specified times. The samples were filtered with a 0.45 μm cellulose filter before HPLC analysis. All experiments were performed in three replicates. The total (hydrolysis and transesterification) conversion rates were calculated using the peak areas of TAG in HPLC analysis before and after reaction with castor oil and immobilized enzyme. The concentrations of formed ricinoleic acid and

ethyl ricinoleate were calculated using the calibration curve (4 – 80 µg/mL).

2.5. Analysis of products

The hydrolysis/transesterification products were analyzed by an RP-HPLC (Shimadzu model LC-20AD, SPD-M20A diode array detector). The acetonitrile and acetone (V/V, 2:1) mixture was used as the mobile phase. The C18 column was used (5 µm, 4.6 mm × 250 mm Intersustain) for the analysis. The flow rate was 1.0 mL/min, and the injection volume was 3.0 µL. FTIR analyses of castor oil and the products were carried out with a Perkin Elmer Spectrum Two FTIR with ATR attachment. After the reactions, the solutions were filtered with a 0.45 µm cellulose filter paper and dried in a vacuum oven at 30 °C before FTIR analysis.

3. Results and Discussion

3.1. Lipase immobilization

Enzyme immobilization experiment was carried out in 1, 2, 4, 8, and 12 hours to provide maximum immobilization. Immobilization occurred between amine groups of lipase and aldehyde groups of glyoxal agarose beads and resulted in the formation of imine groups. With the addition of NaBH₄, these groups were reduced, and stable multi-covalent bonds formed between lipase and glyoxal agarose beads [10, 11]. The immobilization degree was evaluated by *p*NPB hydrolysis [12]. The absorbance of the product, *p*-nitrophenyl, was measured at 346 nm. The occurred reaction is shown in Figure 1. The hydrolysis rate increased from 56% to 99% by raised times from 2 to 12 h (Figure 2). Immobilization was also tried with different enzyme amounts to reach maximum hydrolysis yields. The lipases (2.5, 5.0, and 7.5 mg) were used for immobilization with 2.5 mL of agarose. Nearly 100% hydrolysis yield was achieved using 5.0 mg of the enzyme (Figure 2.). As can be seen from the results, maximum immobilization was obtained with a 12 h reaction using 5 mg enzyme and 2.5 mL agarose beads. Further experiments were carried out with immobilized lipase obtained in a reaction of 5 mg lipase with

2.5 mL glyoxal agarose beads in 25 mL sodium bicarbonate buffer pH 10 for 12 h.

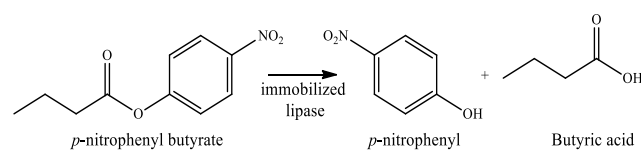


Figure 1. The catalytic reaction of *p*-nitrophenyl butyrate

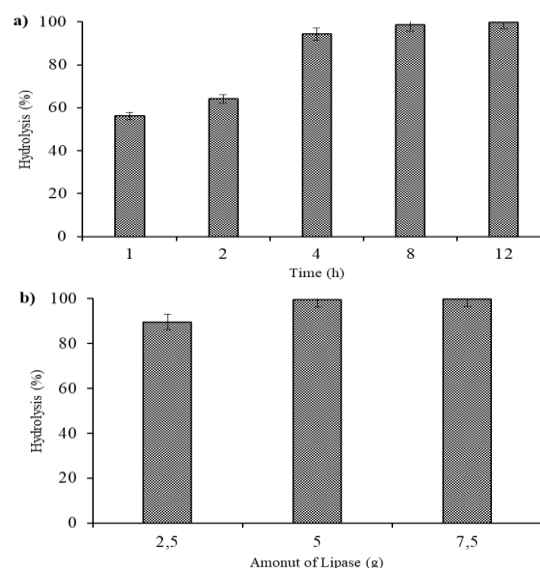


Figure 2. The immobilized enzyme activities in different immobilization times (a) (5.0 mg of lipase, 2.5 mL of glyoxal agarose) and amounts of lipase (b) (2.5 mL of glyoxal agarose, 12 h)

3.2. Characterization of lipase

RP-HPLC and FTIR analyses were performed for the identification of products. RP-HPLC chromatograms are shown in Figure 3. As can be seen from the figure, castor oil is mainly triacylglycerol (TAG)(~%70), and a large proportion of TAG remained unhydrolyzed at the reaction in the buffer. The hydrolysis increased with the rising ethanol ratio, and transesterification products were also formed in the reaction. The primary hydrolysis and transesterification products were ricinoleic acid and ethyl ricinoleate. The obtained highest amounts were 0.41 g for ricinoleic acid and 0.47 g for ethyl ricinoleate using 2.5 mL of lipase-immobilized agarose beads. The reaction was performed using 1.0 g of castor oil at 150 rpm agitation rate for 72 hours in a 25 mL 1: 9 (V: V) ratio of phosphate buffer (pH 7): ethanol medium. The retention times of ricinoleic acid and ethyl ricinoleate were 3.47 minutes and 4.72

minutes. The other observed peaks were probably castor oil hydrolysates such as linoleic, oleic, palmitic, stearic, and linolenic acids and their esters.

The FTIR spectra of castor oil and product are shown in Figure 4. The 3380 and 3009 cm^{-1} peaks in the castor oil spectrum were attributed to the $-\text{OH}$ and $=\text{CH}$ vibrations. The 1743 and 1162 cm^{-1} peaks were assigned to $\text{C}=\text{O}$ and $\text{C}-\text{O}$ symmetric stretching vibrational bands, respectively. The product spectrum supports that the product was a mixture of FFAs and esters. A split band was obtained at around 1700 cm^{-1} from FFAs and esters. The $\text{C}-\text{O}$ vibration bands of FFAs and esters appeared at 1179 and 1034 cm^{-1} , respectively. These results were agreed with Khaskheli et al [13].

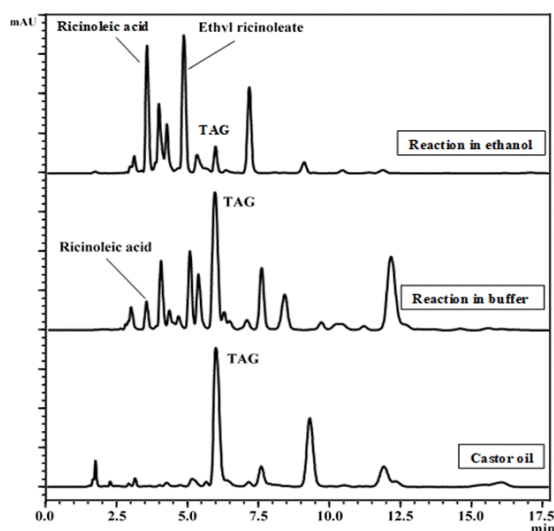


Figure 3. HPLC chromatograms of castor oil and products after hydrolysis/transesterification reactions. (72 h, 150 rpm, 2.5 mL lipase immobilized agarose beads, 1.0 g castor oil, 25 mL reaction volume)

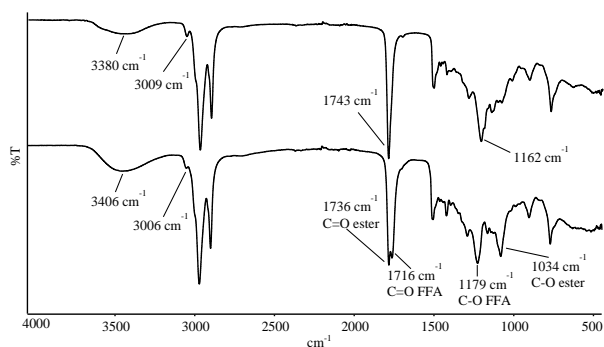


Figure 4. FTIR spectra of castor oil and product

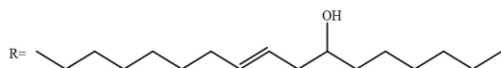
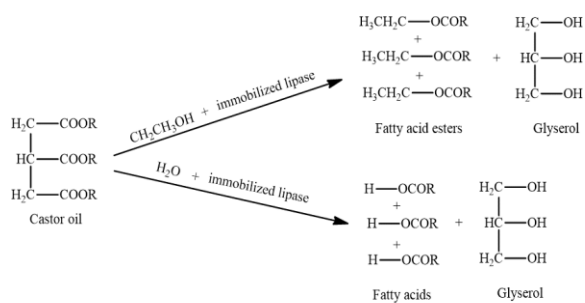
3.3. Optimization of substrates ratio

The hydrolysis/transesterification reactions were carried out in different ethanol/buffer ratios. The enzyme-substrate interactions were feeble when only water was used as solvent due to the low solubility of oil. The ricinoleic acid (1.0%) formed when the reaction was performed in the phosphate buffer solution (pH 7).

Although the solubility problem could be overcome using surfactants, salts, or higher temperatures, there are also some disadvantages. The use of alcohols could be a solution to oil solubility but decrease yields of the hydrolysis reaction due to the occurring transesterification reaction. Both hydrolysis and transesterification efficiency increased with more dissolved castor oil by raising the ethanol ratio in the solution (Table 1). Also, ethanol acted as a substrate for transesterification and increased the reaction efficiency. The obtained maximum alcohol ratio was 90% because the synthesized lipase immobilized agarose was stored in the buffer and added to the reaction medium in buffer solution. In 1:9 (phosphate buffer (pH 7): ethanol, V: V) reaction medium, the result of the hydrolysis and transesterification reactions (Figure 5) FFAs and ester products were formed. The main products were ricinoleic acid and ethyl ricinoleate. In the enzyme: oil ratio experiments, the reaction yields decreased with the increased castor oil due to insufficient immobilized lipase in the solution (Table 2). The reaction yields were calculated from total TAG conversion rates obtained by HPLC analysis. The conversion percentage decreased from 87% using 1.0 g of castor oil to 43% using 2.0 g of castor oil with 2.5 mL lipase immobilized agarose beads at 150 rpm agitation speed and 72 h. Also, the decrease in efficiency may be due to the increased viscosity of the solution at higher oil content. As expected, the reaction yield increased when the amount of lipase-immobilized agarose beads was raised, and the castor oil was kept constant (1.0 g). The obtained efficiencies were 31% and 99% using 1 mL and 5 mL of immobilized lipase at 150 rpm agitation speed and 72 h.

Table 1. The effect of ethanol concentration on the hydrolysis/transesterification of castor oil with immobilized lipase

Ratio of phosphate buffer (pH 7):ethanol (V:V)	Ricinoleic acid (g)	Ethyl ricinoleate (g)
1:0	0.1	-
1:3	0.15	0.17
1:6	0.27	0.31
1:9	0.40	0.47

**Figure 5.** Hydrolysis and transesterification reactions of castor oil**Table 2.** The effect of castor oil amount on the hydrolysis/transesterification of castor oil with immobilized lipase

Ratio*	Hydrolysis / transesterification(%)
2.5:0.1	99
2.5:0.5	90
2.5:1.0	87
2.5:1.5	70
2.5:2.0	43
1.0:1.0	31
2.0:1.0	70
3.0:1.0	90
4.0:1.0	96
5.0:1.0	99

*Lipase immobilized agarose beads (mL): castor oil (g) in phosphate buffer (pH 7): ethanol (1:9, V:V)

3.4. Optimization of other parameters

The optimization experiments were performed at room temperature (20 °C), and yields were calculated from total TAG conversion rates obtained by HPLC analysis. The effect of temperature was not investigated due to the low boiling point of ethyl alcohol. As shown in Figure 6, the hydrolysis/transesterification yield increased with raised time from 35% (2 hours) to 87% (72 hours) due to more enzyme-substrate interaction. Similarly, the yields were increased by the agitation rate. A liquid film was formed around the beads in the solution,

and film diffusion rates of the substrate were low at the lower agitation speed. The diffusion rate of the substrate was raised by eliminating film resistance at higher agitation speeds [14]. The obtained yield increased from 30% to 87% with raised agitation speeds from 30 to 150 rpm.

In the present study, lipase was used as an immobilization agent for glyoxal agarose beads. Easy and direct lipase immobilization occurred in an alkaline medium via multi-covalent attachment. Therefore, a stable structure is formed against the various external effects. The synthesized lipase immobilized agarose beads can be used for castor oil hydrolysis and transesterification. The reaction products, ricinoleic acid, and its derivatives could be used as a surfactant, plasticizer, emulsifier, soap ingredient, etc [15]. The obtained results were compared to the literature study in Table 3. It is seen that the obtained results are compatible with the literature. No study has been found on the hydrolysis of castor oil using lipase-immobilized glyoxal agarose beads in phosphate buffer(pH 7)-ethanol medium.

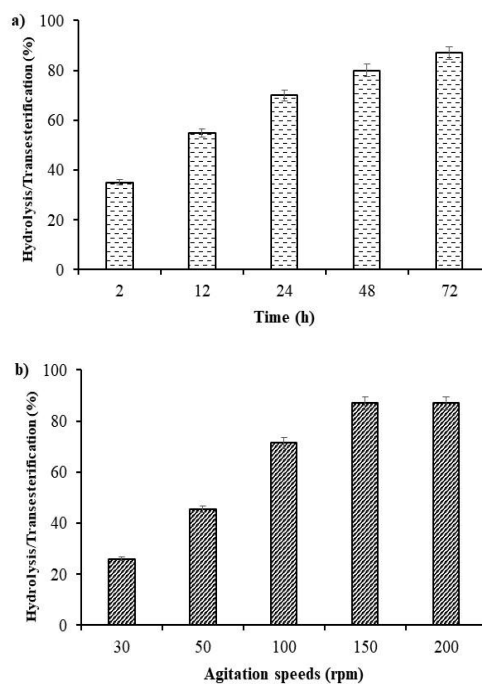
**Figure 6.** The effect of reaction time (1.0 g castor oil, 2.5 mL of immobilized lipase, 150 rpm), agitation speed (1.0 g castor oil, 2.5 mL of immobilized lipase, 72 h) on the reaction yields

Table 3. Comparison of the obtained results with the literature studies

Method	Reaction	Conditions	Yield
Free lipase [5]	Hydrolysis	Phosphate buffer (pH 7.0), 40 °C, 72 h, 1 g lipase	71.3%
Free lipase [6]	Hydrolysis	Isooctane, pH 7, 55°C, 24 h 175U lipase	~90%
Free lipase [7]	Hydrolysis	Isopropyl ether:water(1:1), 30 °C, 24 h, pH 6, 4% lipase	~100%
Immobilized [8]	Transesterification	1-hexanol, 50 °C, 48 h, RMIM+Novozym 435 (2.5%+5% w/w oil)	95%
Immobilized [9]	Transesterification	Methanol, 55 °C, 96 h, 84 U lipase	78.13%
Immobilized [this study]	Hydrolysis / transesterification	Ethanol:phosphate buffer(9:1) pH 7, 72 h, 2.5 mL immobilized lipase suspension	87%

4. Conclusion

An enzymatic procedure was evaluated for hydrolysis/transesterification of castor oil by lipase-immobilized glyoxal agarose beads. Immobilization efficiency improved at a 12-hour reaction using 5.0 mg enzyme and 2.5 mL agarose beads. A nearly 100% hydrolysis yield was achieved against the p-NPB using lipase-immobilized agarose beads. The highest conversion yield was obtained using 2.5 mL of lipase immobilized agarose beads and 1.0 g of castor oil at a 150 rpm agitation rate, 72 hours in 25 mL 1: 9 (V: V) ratio of phosphate buffer(pH 7): ethanol medium. The obtained main products were ricinoleic acid and ethyl ricinoleate. The other reaction products probably were linoleic, oleic, palmitic, stearic, and linolenic acids and their esters. The reaction products were analyzed using RP-HPLC and FTIR.

Article Information Form

Funding

This study was supported by a part of the project number 2017-50-01-035 of Sakarya University.

Authors' Contribution

S. Yilmazer Keskin: Supervision, Project administration, Conceptualization, Writing-Original Draft.

K. Karakaya: Performed the experiments and collected data.

The Declaration of Conflict of Interest/ Common Interest

No conflict of interest or common interest has been declared by the authors.

The Declaration of Ethics Committee Approval

This study does not require ethics committee permission or any special permission.

The Declaration of Research and Publication Ethics

The authors of the paper declare that they comply with the scientific, ethical and quotation rules of SAUJS in all processes of the paper and that they do not make any falsification on the data collected. In addition, they declare that Sakarya University Journal of Science and its editorial board have no responsibility for any ethical violations that may be encountered, and that this study has not been evaluated in any academic publication environment other than Sakarya University Journal of Science.

Copyright Statement

Authors own the copyright of their work published in the journal and their work is published under the CC BY-NC 4.0 license.

References

- [1] K. D. Mojsov, "Aspergillus enzymes for food industries", *New and Future Developments in Microbial Biotechnology and Bioengineering*, vol. 16, pp. 215–222, 2016.
- [2] G. Brahmachari, "Lipase-Catalyzed Organic Transformations-A Recent Update", *Biotechnology of Microbial Enzymes*, pp. 325–346, 2017.
- [3] V. S. Gamayurova, M. E. Zinov'Eva, H. T. T. Tran, "Features of the enzymatic hydrolysis of castor oil", *Catalysis in Industry*, vol. 5, no. 3, pp. 269–273, 2013.

- [4] M. S. Puthli, V. K. Rathod, A. B. Pandit, “Enzymatic hydrolysis of castor oil: Process intensification studies”, *Biochemical Engineering Journal*, vol. 31, no. 1, pp. 31–41, 2006.
- [5] K. Yamamoto, N. Fujiwara, “The hydrolysis of castor-oil using a lipase from *Pseudomonas* sp. F-B-24: Positional and substrate-specificity of the enzyme and optimum reaction conditions”, *Bioscience, Biotechnology, and Biochemistry*, vol. 59, no. 7, pp. 1262–1266, 1995.
- [6] S. R. Kulkarni, A. B. Pandit, “Enzymatic hydrolysis of castor oil: An approach for rate enhancement and enzyme economy”, *Indian Journal of Biotechnology*, vol. 4, no. 2, pp. 241–245, 2005.
- [7] G. J. Jeon, J. W. Yang, B. K. Hur, “Hydrolysis of castor oil with lipases and organic solvents”, *Korean Journal of Biotechnology and Bioengineering*, vol. 14, no. 6, pp. 696–701, 1999.
- [8] D. Malhotra, J. Mukherjee, M. N. Gupta, “Lipase catalyzed transesterification of castor oil by straight chain higher alcohols”, *Journal of Bioscience and Bioengineering*, vol. 119, no. 3, pp. 280–283, 2015.
- [9] S. K. Narwal, N. K. Saun, P. Dogra, G. Chauhan, R. Gupta, “Production and Characterization of Biodiesel Using Nonedible Castor Oil by Immobilized Lipase from *Bacillus aerius*”, *BioMed Research International*, pp. 1-6, 2015.
- [10] J. M. Bolivar, F. Cava, C. Mateo, J. Rocha-Martín, J. M. Guisán, J. Berenguer, R. F. Lafuente, “Immobilization–stabilization of a new recombinant glutamate dehydrogenase from *Thermus thermophilus*”, *Applied Microbiology and Biotechnology*, vol. 80, no. 1, pp. 49–58, 2008.
- [11] S. Y. Keskin, C. S. Keskin, “Quantitative Determination of Glycine in Aqueous Solution Using Glutamate Dehydrogenase-Immobilized Glyoxal Agarose Beads”, *Applied Biochemistry and Biotechnology*, vol. 172, no. 1, pp. 289–297, 2014.
- [12] A. N. Zaid, N. Zohud, B. E'Layan, T. Aburadi, N. Jaradat, I. Ali, F. Hussein, M. Ghanem, A. Qaddomi, Y. A. Zaaror, “Pharmacodynamic testing and new validated HPLC method to assess the interchangeability between multi-source orlistat capsules”, *Drug Design, Development and Therapy*, vol. 11, pp. 3291–3298, 2017.
- [13] A. A. Khaskheli, F. N. Talpur, M. A. Ashraf, A. Cebeci, S. Jawaid, H. I. Afridi, “Monitoring the *Rhizopus oryzae* lipase catalyzed hydrolysis of castor oil by ATR-FTIR spectroscopy”, *Journal of Molecular Catalysis B: Enzymatic*, vol. 113, pp. 56–61, 2015.
- [14] N. Ertugay, Y. K. Bayhan, “Biosorption of Cr (VI) from aqueous solutions by biomass of *Agaricus bisporus*”, *Journal of Hazardous Materials*, vol. 154, no. 1–3, pp. 432–439, 2008.
- [15] D. Goswami, J. K. Basu, S. De, “Lipase applications in oil hydrolysis with a case study on castor oil: A review”, *Critical Reviews in Biotechnology*, vol. 33, no. 1, pp. 81-96, 2013.

Effect of Sampling Orientation on The Mechanical Properties of Glass Fiber Reinforced Epoxy Nanocomposites

Gökhan Demircan^{1*} 

^{1*} Harran University, Faculty of Engineering, Department of Mechanical Engineering, Şanlıurfa, Türkiye, gdemircan@harran.edu.tr

*Corresponding Author

ARTICLE INFO

ABSTRACT

Keywords:
Glass Fiber
Polymer
Nanocomposite
Mechanical Properties
Sampling Orientation

Article History:
Received: 16.09.2023
Accepted: 08.11.2023
Online Available: 27.02.2024

Fiber-reinforced polymer composites are manufactured using various methods, with vacuum-assisted resin transfer molding (VARTM or VARIM). This study's primary focus lies in assessing how the orientation of sampling impacts the mechanical properties of glass fiber-reinforced pure and nanocomposites. 2 wt.% nano Al₂O₃-doped and non-doped composites were produced using the VARTM process. Tensile, flexural, and density test specimens were extracted from three distinct zones and two distinct direction those aligned horizontally to the resin flow (HRF) and those oriented vertically to the resin flow (VRF). Remarkably, results showed up to a 3.91% increase in values from samples in the third zone, particularly on the vacuum outlet side. To facilitate precise stress value comparisons across plates, uniform sample orientation and consistent zone selection are essential.

1. Introduction

Composite materials have brought a new age in materials engineering science, allowing engineers to create superior materials with outstanding mechanical characteristics. Fiber-reinforced polymer composites (FRP) are one of them and are made up of two major components: a load-bearing component, such as fibers, and a polymer medium that acts as a binding and protection for the fibers [1-3]. The polymer matrix plays a pivotal role in ensuring the fibers maintain their orientation and structural integrity, while also facilitating the transfer of loads. Typically, thermoset or thermoplastic materials are chosen for the polymer matrix [4, 5]. Meanwhile, the fibers primarily shoulder the load transmitted from the matrix, imparting macroscopic stiffness and strength to the structure. Commonly used reinforcing fibers include glass, aramid, and carbon fibers. Such FRP composites are gaining prominence due to their exceptional resistance to corrosion,

impressive thermo-mechanical characteristics, and high strength-to-weight ratio [6, 7]. Their diverse range of properties makes them indispensable in a wide array of industries, including aerospace, marine, construction, biomedical, automotive, and many others [8-10].

The performance of composite materials is predominantly influenced by the quality of their constituent elements and the precision of their manufacturing processes. The manufacturing processes need to be investigated to determine the material's optimal properties for the specific purpose. Various approaches are viable, depending on the chosen reinforcement category and the intended product application [11, 12]. Some of them are as follows; hand layup [13], compression molding [14], filament winding [15], pultrusion [16], spray-up [17], resin transfer molding (RTM) [18], vacuum-assisted resin infusion method (VARIM) [19]. Since the 1950s, vacuum-assisted resin infusion method (VARIM) has been utilized to create fiber

reinforced polymer composites in different shapes [20-23]. This method is also referred to as vacuum assisted resin transfer molding (VARTM) in the literature [24]. The technique is a closed mold method for producing high-performance and large-scale fiber reinforced polymer (FRP) products with minimal tooling costs. Although large and complex composite parts can be produced in high quality with this method, there are some disadvantages. The possibility of air leakage is considerable, and this is highly dependent on the worker's ability, training, and the consumables (peel ply, vacuum bag, distribution medium etc.) condition of each VARIM operation. Dry spots and inadequate resin infusion might result from air leakage and can ruin the composite production [25]. Factors such as mold filling, fiber compaction, dry spot and micro-voids are the related processing issues to be considered in order to produce a stable composite.

The VARIM technique is also a key method in the production of nanoparticle enhanced FRP composites [26-28]. To create nanocomposite, nano-enhanced polymers can be injected into fiber mats composed of fibers such as carbon, aramid or glass fibers. Due to its unique through-thickness flowing profile the VARIM process has been recognized as a potential approach for producing nano-enhanced FRP among several production methods. However, through-thickness flow may not reduce the traveling distance of the nano resin flow along the fiber preform to the desired level [29]. As a result, the possibility of nanoparticles being filtered by the fiber preform increases. This nanoparticle filtration affects the distribution of nano-enhanced polymer blend in composite. This imperfection can also affect the mechanical properties of the nanocomposite. The porosity of the fiber preform also has an impact on nanoparticle filtering. Fan et al. [30] developed a new injection and double vacuum assisted resin transfer molding (IDVARTM) technique to decrease the impacts of porosity. The infusion is assisted by capillary pressure in this approach. This provided a high void formation, allowing the nano-doped resin to pass through the fiber with less nanoparticle filtration. Another VARTM-based technique to incorporating carbon nanofibers (CNFs) into FRP was

investigated by Movva et al. [31]. They used a solvent guided spray method to pre-bond the CNFs to the glass fiber matting. This technique may lower the risk of CNF filtering during resin infusion.

The literature review revealed that the VARTM or VARIM method was improved with different modifications to minimize nanoparticle filtration for nanocomposite production. However, the mechanical stability of the sample extraction zones of the nanocomposite plate produced by the traditional VARTM method is an important issue that needs to be investigated in detail. In this study, nano alumina (Al_2O_3) reinforced epoxy composites were produced by VARIM. Samples were taken from the composites in the directions horizontal to the resin flow (HRF) and vertical to the resin flow (VRF), and the mechanical properties of these directions were determined by tensile, three point bending and density tests. Also, ANOVA analysis was performed to determine the significance of the variables and to see if each variable has or not significant effect on tensile and flexural strength values.

2. Experimental Procedure

2.1. Materials

The nanoparticle to be used for nano reinforcement was aluminum oxide (Al_2O_3) with 78 nm average particle size (Nanografi). The purity of nanoparticles is 99.55%. MGS L285 epoxy resin and H287 hardener were used for obtaining nano-enhanced polymer (HEXION). It was chosen because it has a low viscosity (600-900 mPas). The resin-to-hardener ratio is 100:40 by weight. Plain weave-type glass fiber with an area weight of 200 gr/m² was used as the fiber reinforcement. A table type circular saw bench with water cooling system was used to cut the samples.

2.2. Production of glass fiber reinforced epoxy nanocomposite

Two different composites were produced by using the conventional VARTM method. One plate was produced in pure form and the other was produced using nano Al_2O_3 particles to study

the dispersion of the nanoparticle in polymer resin. The representation of the method is shown in Fig 1.

The following steps were applied for production.

- Release film was applied to prevent the composite plate from sticking to the bench.
- 16 layers of glass fiber were laid on the release film.
- A peel ply was applied for easy removal of the composite plate.
- Infusion mesh was applied on the top of the peel ply.
- A spiral hose was used to provide a fast resin supply in the resin injection line.

- Ventilation ports are placed in the resin inlet and outlet region.
- The assembly was surrounded with sealing tape, which is a double-sided sticky adhesive.
- The vacuum bag was carefully laid on the assembly.
- Resin injection port was closed, and vacuum port opened to apply the vacuum.
- Pure resin and nano-enhanced resin were infused into the resin reservoir.
- After the vacuum port was closed, the system was left to cure at 80 °C for 15 h (bench heater) as mentioned by resin manufacturer.
- Demolding the composite part from the bench was successfully made. Fig. 2 shows a cured composite plate on the bench.

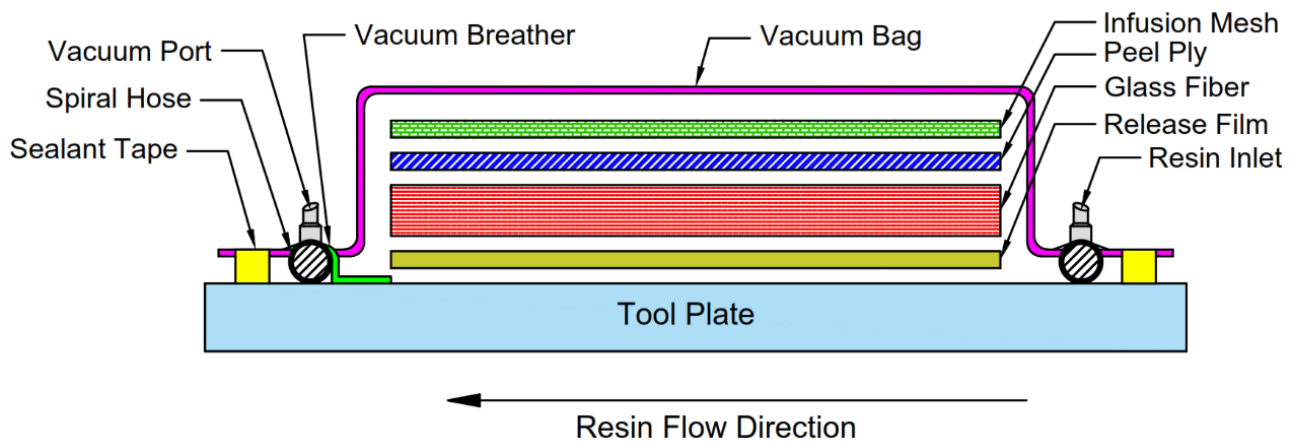


Figure 1. Schematic representation of VARTM

2 wt.% of Al_2O_3 nanoparticles was used to form nano-enhanced epoxy resin using the ultrasonic dual mixing method (UMM) [32]. Ultrasonic dual mixing is the employment of ultrasonic vibration and mechanical stirring at the same

time to shear the resin matrix. It has the ability to modify resin matrix and provide a homogeneous distribution of nanoparticles that is nearly cluster-free.

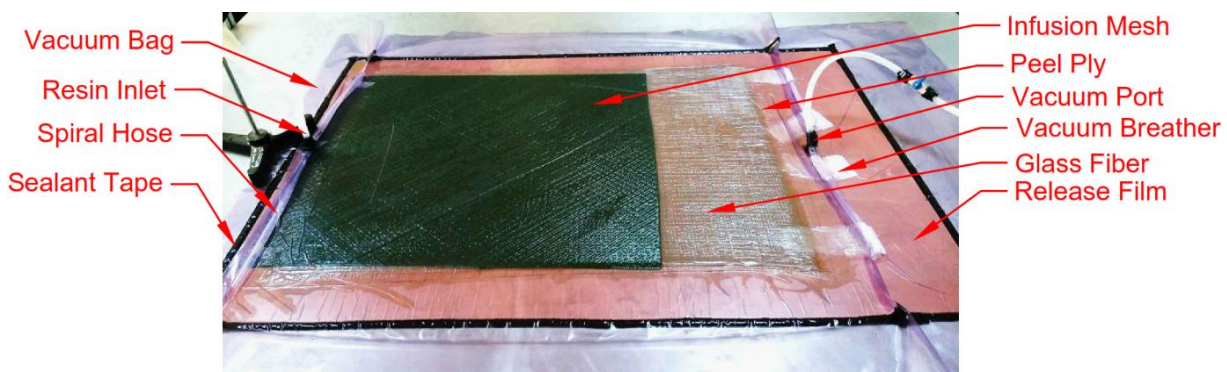


Figure 2. Cured composite plate on the bench

This was important in significantly improving the mechanical and physical characteristics of the polymeric basis composites. The ultrasonic

mixing was done with an ultrasonic stirrer (VCX 500, Sonics, USA) with a maximum power output of 750 W and a steady frequency of 20

kHz and a 50 mm diameter titanium alloy tip. A pulse of 2 s on and 3 s off was used to apply sonication with a 70% amplitude for 2 h. During sonication process a magnetic mixer (MR Hei-Tech, Heidolph, Germany) was used simultaneously at 400 rpm [5, 19, 26]. To achieve a successful dispersion, precautions were taken during UMM to ensure that the temperature of the polymer mixture did not rise throughout the mixing time. The mixing was done in a bowl bordered by an ice bath, and the temperature of the bath is tracked by immersing a temperature probe connected to the ultrasonic mixer to prevent an extreme increase in temperature during mixing. The schematic representation of UMM method is shown in Fig 3. Finally, two composite plates were produced for comparison purposes. One is pure plate without nanoparticle additive, and the other is nanoparticle doped plate.

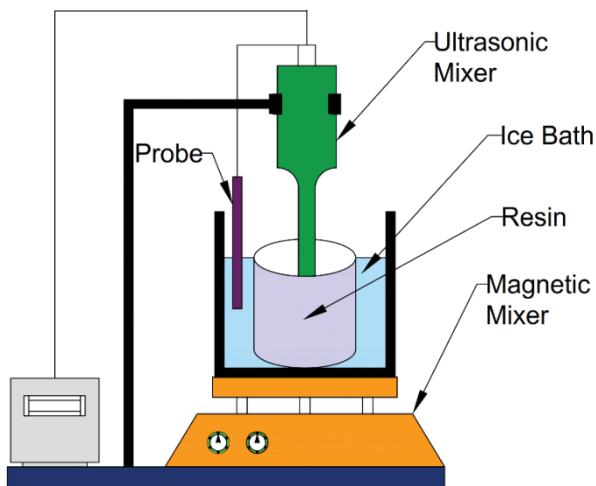


Figure 3. Schematic representation of UMM method

2.3. Mechanical tests and sampling orientation

Tensile and bending tests were performed in accordance with ASTM D3039/D3039M-17 [33] and ASTM D790-17 [34] using a Shimadzu AGS-X Plus Universal test machine. Density Measurement was carried out with Archimedes' principle with samples having $15 \times 15 \times 3.2 \text{ mm}^3$ dimensions. The bending test specimen's dimensions were determined to be $127 \times 12.7 \times 3.2 \text{ mm}^3$ and the dimensions of tensile test specimen were $250 \times 25 \times 3.2 \text{ mm}^3$. The strain rate was 2

mm/min for tensile test and 1 mm/min for bending test. Samples and dimensions were shown in Fig. 4.

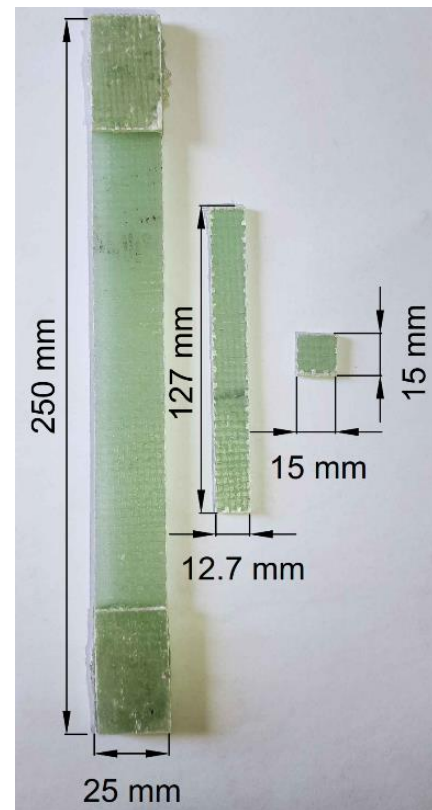


Figure 4. Test samples and dimensions

Two different plates were produced to examine the effect of nanoparticle filtration on the mechanical properties of the composite. One plate has no nanoparticles, while the other has 2 wt.% of nanoparticles. The plates were divided into 3 different zones to determine in which zones the filtration is effective along the vacuum line. In addition, to examine the effect of sample extraction directions, samples were extracted both vertical to the resin flow (VRF) and horizontal to the resin flow (HRF). Sample notations are given in Fig. 5. Sample extraction zones and orientations are shown in Fig. 6.

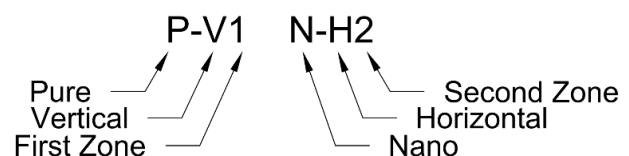


Figure 5. The notation of samples

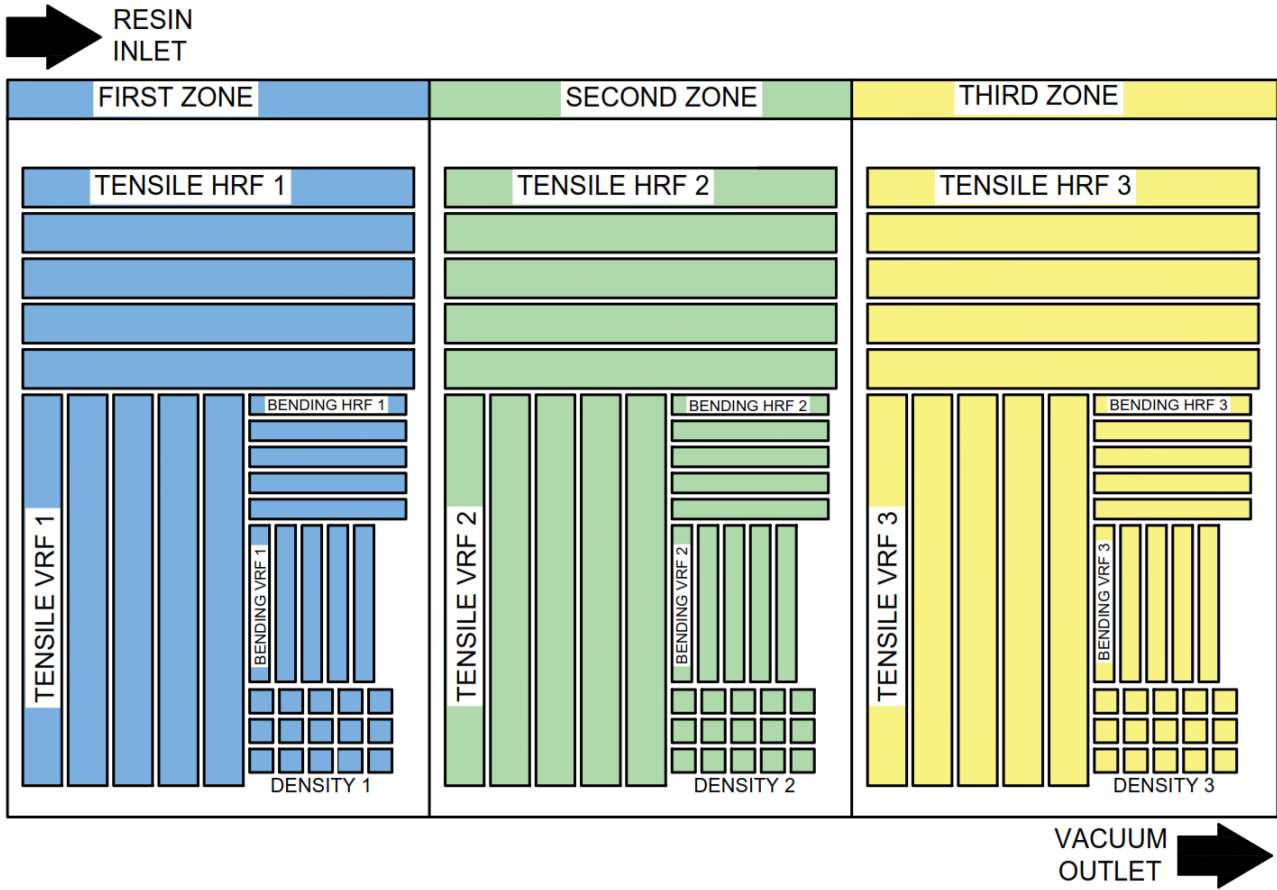


Figure 6. Sampling orientation of composite

3. Results and Discussion

3.1. Mechanical test results

Tensile, flexural and density tests were carried out using 5 samples of each parameter and the average results were taken as a basis in the graphics. Fig. 7 shows all test results. Considering the Fig. 7, it is observed that the tensile, bending and density values for both pure and nano composite increase from the 1st zone to the 3rd zone. This result is valid for both HRF and VRF samples. Normally, test results are expected to be very close to each other in pure composite. But the highest change was observed in bending.

VRF samples have an increase rate of 3.23%. This is because the resin line of the plate is long. The fact that the length of this line was around 1 m caused the compaction ratio at the vacuum side to be higher than the compaction ratio at the resin inlet. It can be concluded that the VARIM or VARTM technique was effective in compacting the fiber reinforcement under vacuum pressure,

resulting in samples with a high fiber volume percentage, consistent thickness, and minimal voids content [35]. Furthermore, the compaction pressure is restricted to the pressure of atmosphere, prohibiting the vacuum infusion process from attaining greater fiber volumetric levels [36]. Since the thickness values of the composite plate shown in Table 1 are thinner in the region where the compaction is high, stress values increase due to the cross-sectional area difference in the experimental stress calculation. Density results also confirm this phenomenon. The density values increased from the 1st zone to the 3rd zone for both composite plates. The fact that the compaction is more on the vacuum side has reduced the possible void amount, which has caused the density values to increase towards the 3rd zone.

Considering the Fig.7-b, it is seen that the nanocomposite exhibits a similar behavior like pure one. Since the phenomena described above are also valid for this composite, all test results increased from 1st zone to the 3rd zone. However, when increase percentages in Table 2

are examined, it is seen that the increase in the test results in nanocomposite for each region is higher than in pure composite. The percentage increase rates were calculated based on how much the test results in zone 2 and 3 increased compared to zone 1. Based on the tensile test

result, an increase of 2.82% was observed in NV-3, while this rate was 1.49% in PV-3. Similarly, in bending test results, an increase of 3.31% in NV-3 and 3.23% in PV-3 was observed. Results demonstrate a consistent pattern in regions aligned horizontally with the resin flow.

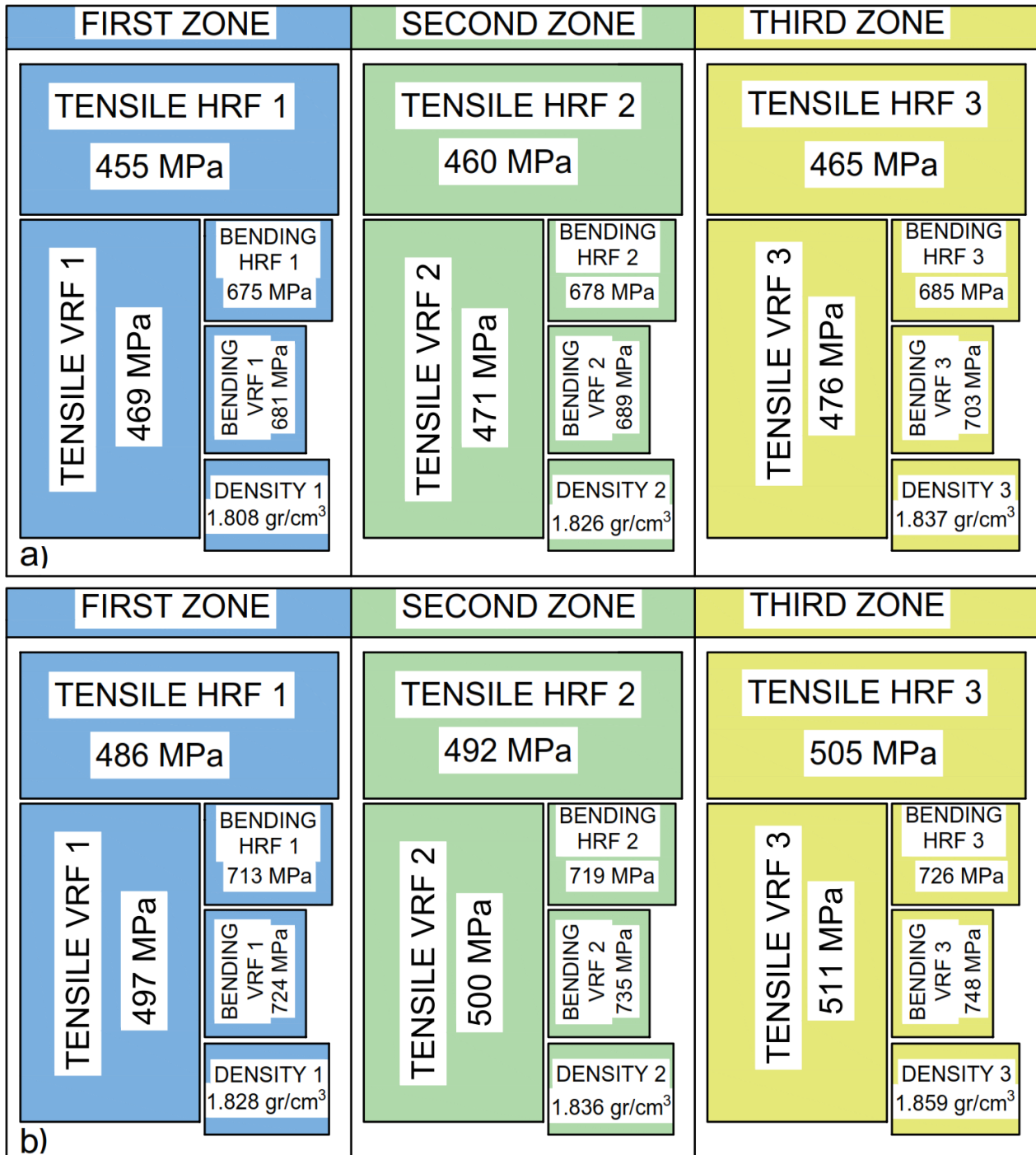


Figure 7. Test results of nanocomposite plates a) pure composite b) nanocomposite

2 wt.% of Al₂O₃ nanoparticles increased the tensile and flexural strength of glass fiber reinforced epoxy composites. Although there is variation between regions, an improvement in tensile strength from 5.97% to 8.61% was

observed. This improvement varied between 5.62% and 6.41% in flexural strength. If a comparison is made between HRF and VRF directions, it is seen that HRF values are higher than VRF values both for pure and nano

composite. This is because the thickness is more stable in the HRF direction than in the VRF direction.

Table 1. Thickness values of zones of composite plates

Zone	Thickness (mm)
Pure Zone 1	2.404
Pure Zone 2	2.374
Pure Zone 3	2.341
Nano Zone 1	2.556
Nano Zone 2	2.515
Nano Zone 3	2.476

Table 2. Percentage increase of tensile and bending test results

No.	Tensile Strength (MPa)	Perc. Increase (%)	Flexural Strength (MPa)	Perc. Increase (%)
P-V1	469±1.5	---	681±2.5	---
P-V2	471±2.6	0.43	689±3.2	1.17
P-V3	476±3.2	1.49	703±3.1	3.23
N-V1	497±1.7	---	724±2.6	---
N-V2	500±1.3	0.60	735±3.3	1.52
N-V3	511±2.4	2.82	748±2.7	3.31
P-H1	455±1.6	---	675±2.4	---
P-H2	460±1.3	1.10	678±2.8	0.44
P-H3	465±2.8	2.20	685±3.1	1.48
N-H1	486±2.2	---	713±3.2	---
N-H2	492±1.9	1.23	719±3.1	0.84
N-H3	505±2.1	3.91	726±3.4	1.82

2 wt.% of Al₂O₃ nanoparticles increased the tensile and flexural strength of glass fiber reinforced epoxy composites. Although there is variation between regions, an improvement in tensile strength from 5.97% to 8.61% was observed. This improvement varied between 5.62% and 6.41% in flexural strength. If a comparison is made between HRF and VRF directions, it is seen that HRF values are higher than VRF values both for pure and nano composite. This is because the thickness is more stable in the HRF direction than in the VRF direction. The reason why the increase between regions in nanocomposite is higher than in pure composite depends on the compaction ratio. Since compaction ratio is more on the vacuum port, the movement of the resin in the through-thickness direction is shortened in this port. Since

the nano-doped resin will travel less distance in vacuum port, the nanoparticle filtration is less in this line, resulting in relatively higher mechanical properties of the region close to the vacuum line [27]. In other words, the mechanical properties are affected by the resin flow direction. The first resin flow occurs horizontally through the infusion mesh, while the second resin flow occurs within the fiber through thickness. Hsiao et al. [37] presented an analytical solution for this and stated that a dimensionless approach with the expression given in Equation 1 is an important approach in determining the main production parameters.

$$\frac{Q_x}{Q_y} \sim \frac{K_{2xx}h_2^2}{K_{2yy}d^2} \ll 1 \quad (1)$$

The structural layer's permeabilities in the x and y directions are K_{2xx} and K_{2yy}, respectively. h₂ is the thickness of fiber preform and d is the length of flow front region.

Tensile and flexural test results were also given as stress-strain graphics in Fig.8 and Fig.9, respectively. Tensile and bending forces represent fundamental aspects of mechanical loading, constituting two of the five primary types of loads in the field. The stress-strain curves of fiber-reinforced polymer composites under tensile and bending forces are different from each other. Since FRP composites are in a brittle structure, they do not have yield points [38]. When the tensile stress-strain curves (Fig.8) are examined, the curves demonstrate a linear relationship and the sample is suddenly broken without any yielding. The rupture happens without any obvious difference in the rate of elongation [39]. The curves obtained in this study are similar to the typical curves observed in FRP composites. No abnormality was found between the curves of pure and nanocomposite or between the curves of VRF and HRF zones. A similar trend occurred in bending (flexural) curves. But here, when the stress reaches its maximum point, the fracture does not occur suddenly, as in tensile test. Once stress reaches its peak, the sample sustains bending load until a specific threshold, as bending stress is highest at the specimen's surface and zero at the neutral axis. This behavior reflects the material's capacity to withstand bending forces and highlights the distribution of

stress across the specimen. The normal bending stress changes linearly according to the distance from the neutral axis in the elastic range. Therefore, the surface of the sample is subjected to maximum stress and the fibers on the surface begin to rupture first. The rupture of fibers continues gradually from the surface to the neutral axis. This means that the fracture event

occurs with a long strain and this causes the flexural stress-strain curves to form as in Fig. 9. Fig. 10 shows the damage mechanism of tested samples. The reason for the behavior of flexural stress-strain curves is more clearly understood with this figure. The fiber ruptures on the surface of the sample are clearly visible.

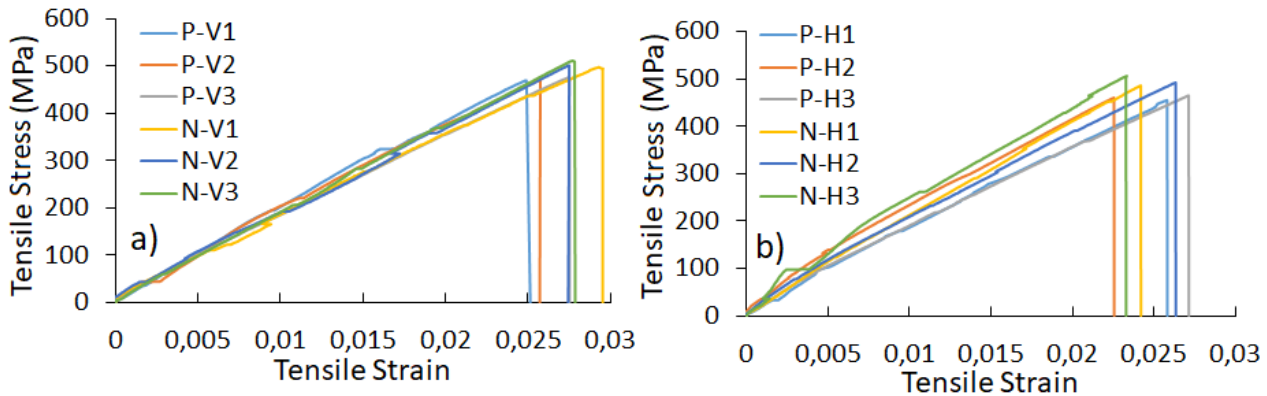


Figure 8. Tensile strength-strain curves of composite plates a) vertical to the resin flow (VRF) b) horizontal to the resin flow (HRF)

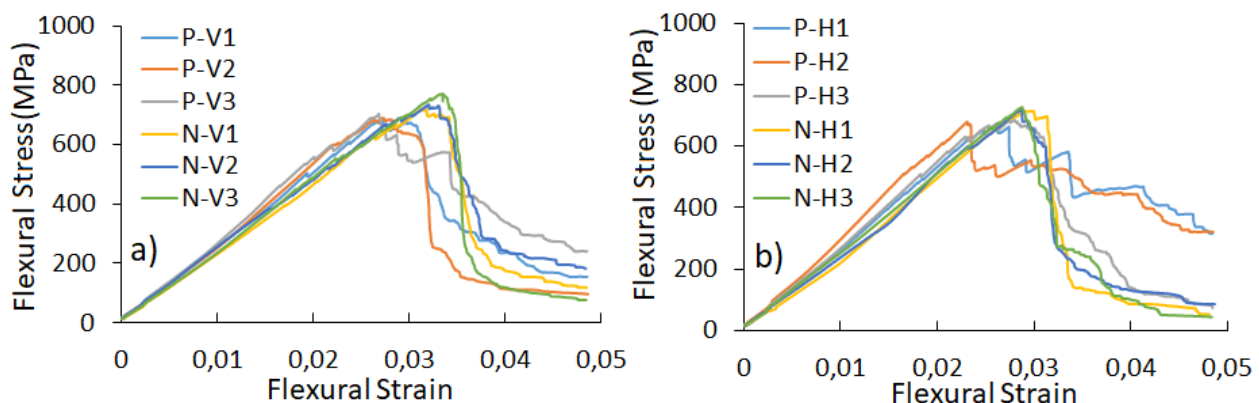


Figure 9. Flexural strength-strain curves of composite plates a) vertical to the resin flow (VRF) b) horizontal to the resin flow (HRF)

In tensile test samples, failure modes should be analyzed according to ASTM D3039 standard. In this standard three-character coding is used to identify failure modes. The first character represents the failure type, the second character represents the failure area, and the third character represents the failure location. The failure types with respect to coding system were shown in Fig. 10. The first character "L" represents the lateral failure type observed similarly in all samples. The second character "M" and "A" are the failure area codes of "multiple areas" and "at grip", respectively. These two failure areas were observed predominantly in all samples. The third character, "V" and "T" are failure location codes of "various" and "top", respectively. These two

failure locations are valid for all samples. Damage mechanisms with the above codes were observed in all samples regardless of nanoparticle contribution and sampling orientation.

The first character "L" represents the lateral failure type observed similarly in all samples. The second character "M" and "A" are the failure area codes of "multiple areas" and "at grip", respectively. These two failure areas were observed predominantly in all samples. The third character, "V" and "T" are failure location codes of "various" and "top", respectively. These two failure locations are valid for all samples. Damage mechanisms with the above codes were

observed in all samples regardless of nanoparticle contribution and sampling orientation. The SEM images of nanocomposite tensile test samples are shown in Fig.11. The homogeneous distribution of nanoparticles is shown in the surface image in Figure 11-a. The

various damage modes, encompassing fiber fracture, matrix breakage, and delamination are demonstrated in Fig. 11b and Fig. 11c. It can be seen in Fig.11b that nano Al_2O_3 particles strengthen the matrix-fiber bonding



Figure 10. Damage mechanism of tensile and flexural test samples

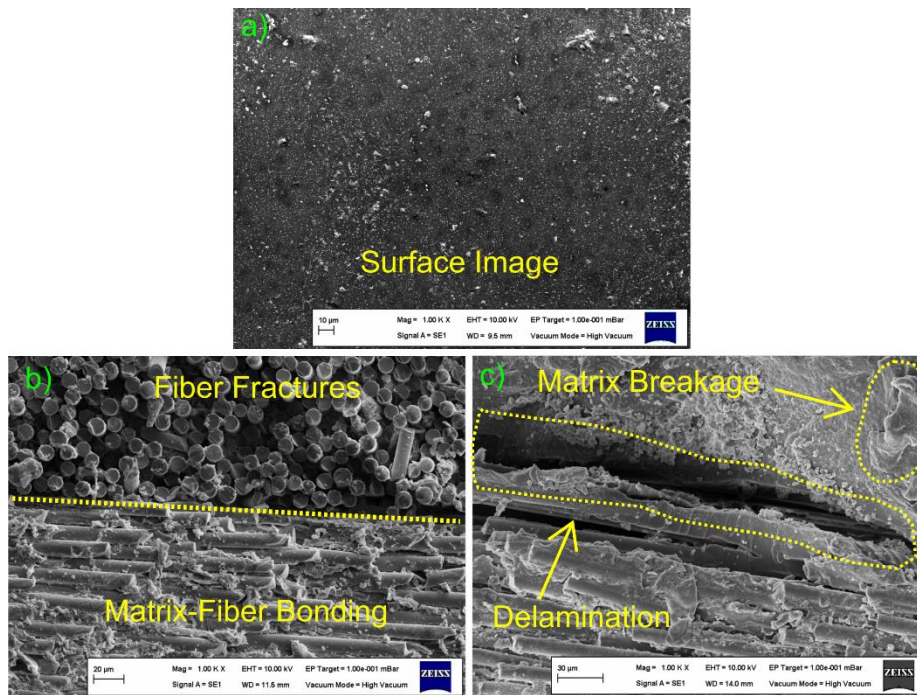


Figure 11. SEM images of test sample

3.2. Statistical analysis (ANOVA)

One-way ANOVA analysis was used to determine whether the means of three independent variables were statistically significant [40]. The three different variables are the first, second and third zones from which the samples are extracted. A null hypothesis (H_0) is needed to use the ANOVA test. In this study, the H_0 hypothesis was considered as “there is no difference between the means for three different regions.” To test this hypothesis, strength values was used as dependent variable and three different regions were used as factor variables. First, to test the hypothesis, the data of the PV samples were tested using the IBM SPSS Statistics 22. Table 3 shows the descriptives of PV samples for tensile strength. N represents the number of samples and tests were performed at the 95% Confidence Interval for the Mean.

After determining the descriptives, the one-way ANOVA analysis was performed. Table 4 shows

the results of PV samples for tensile strength. df means degree of freedom and F is the variance of the group means. The value in the last column indicates statistical significance. It's generally represented by P-Value. The null hypothesis should be assessed by comparing the P-value to the significance level to see if any of the comparison of means are statistically significant. A significance score of 0.05 is usually sufficient. With a significance level of 0.05, there's a 5% chance of determining that a difference exists. The null hypothesis is rejected if the P-value is below or equal to the significance level [41]. If the P-value is greater, the null hypothesis is accepted. In Table 4, the P-value is 0.104, which is greater than 0.05 and the hypothesis is accepted. It means that there is no difference between the means for three different regions. Although the experimental results show an increase from the first zone to the third zone for PV samples, statistical analysis indicates that this change is not significant.

Table 3. Descriptives of PV (Pure-Vertical) samples

	N	Mean	Std. Deviation	Std. Error	95% Confidence Interval for Mean			
					Lower Bound	Upper Bound	Minimum	Maximum
PV-1	5	469.4306	5.15650	2.30606	463.0280	475.8332	463.33	475.41
PV-2	5	471.1172	4.96969	2.22251	464.9465	477.2879	465.77	476.62
PV-3	5	476.0494	3.63552	1.62585	471.5353	480.5635	470.47	480.50
Total	15	472.1991	5.18457	1.33865	469.3279	475.0702	463.33	480.50

Table 4. One way ANOVA of PV (Pure-Vertical) samples

	Sum of Squares	df	Mean Square	F	P
Between Groups	118.300	2	59.150	2.751	0.104
Within Groups	258.017	12	21.501		
Total	376.316	14			

Normally, if the null hypothesis is accepted, the analysis is not continued. Because the result already indicates that the mean of the independent variables is not significant. However, Tukey test from post hoc analysis is

given in Table 5 to show that the results between groups are not significant. Tensile stress variables of PV-1, PV-2 and PV-3 samples were evaluated among themselves and P-values were higher than 0.05 in all comparisons. This means that although there is an experimental difference between the stress values of the tensile samples extracted from three different zones, this difference is not statistically significant. The above-mentioned analysis was performed for only one parameter. Since it is meaningless to give each table in detail for each parameter, the results of ANOVA analysis, which is the most important table for all parameters, are given in Table 6. All p-values for each parameter are greater than 0,05. This shows that in all samples, from the first region to the third region, the test

results are not statistically significant in terms of tensile and flexural stress for both pure and nanocomposite. The fact that group comparisons do not show a statistically significant difference does not mean that the experimental results are insignificant. According to McLean and Ernest [42], significance tests may not give information regarding the practical importance of an event or whether the result can be replicated. Slight differences between experimental results make sense in the test evaluation. In the realm of experimental applications, it is of paramount

importance to meticulously extract the samples from precisely the same orientation. This meticulous approach ensures that the samples being compared are not only consistent but also align perfectly, thereby enhancing the accuracy and reliability of the results obtained. This critical step serves as the cornerstone for the entire experimental process, laying the foundation for meaningful and robust evaluations that can lead to invaluable insights and scientific advancements.

Table 5. Multiple comparisons (Tukey) of PV (Pure-Vertical) samples

Groups (I)	Groups (J)	Mean Difference (I-J)	Std. Error	P	95% Confidence Interval	
					Lower Bound	Upper Bound
PV-1	PV-2	-1.68660	2.93267	.836	-9.5106	6.1374
	PV-3	-6.61880	2.93267	.101	-14.4428	1.2052
PV-2	PV-1	1.68660	2.93267	.836	-6.1374	9.5106
	PV-3	-4.93220	2.93267	.252	-12.7562	2.8918
PV-3	PV-1	6.61880	2.93267	.101	-1.2052	14.4428
	PV-2	4.93220	2.93267	.252	-2.8918	12.7562

Table 6. One-way ANOVA test results of all parameters

Groups	Types	Sum of Squares	df	Mean Square	F	P
PV (Tensile)	Between Groups	118.300	2	59.150	2.751	.104
PH (Tensile)	Between Groups	248.914	2	124.457	1.986	.180
NV (Tensile)	Between Groups	521.307	2	260.654	3.041	.085
NH (Tensile)	Between Groups	970.601	2	485.301	2.344	.138
PV (Flexural)	Between Groups	1199.749	2	599.874	1.190	.338
PH (Flexural)	Between Groups	267.103	2	133.551	.540	.597
NV (Flexural)	Between Groups	1430.553	2	715.276	.366	.432
NH (Flexural)	Between Groups	482.234	2	241.117	1.038	.384

4. Conclusion

The VARTM or VARIM method employed in the production of nanocomposites is a subject that demands examination from various perspectives, particularly concerning nanoparticle filtration. In this study, two types of materials were manufactured: pure glass fiber-reinforced composites and glass fiber-reinforced nanocomposites with a 2 wt.% Al₂O₃ doping. The study investigated the effects of extracting samples from different zones and orientations within both the pure and nanocomposite materials. Samples were collected from three

distinct zones: the resin inlet zone (First), the middle zone (Second), and the vacuum outlet zone (Third). Additionally, two directions were considered: horizontal to the resin flow (HRF) and vertical to the resin flow (VRF) to provide a comprehensive assessment of the mechanical properties of the composites. Mechanical property assessments were conducted, including tensile, three-point bending, and density tests. As a result, there was a notable increase in tensile, bending, and density values when moving from the first zone to the third zone in both pure and nanocomposites. This increase can be attributed to the slightly higher pressure at the

vacuum outlet compared to the pressure at the resin inlet. It is worth noting that the plates used in this study had a length of approximately 1 meter. The pressure differential led to variations in thickness, resulting in stress value differences of up to 3.91%, with the nanocomposites exhibiting more pronounced variations compared to the pure composites.

The reduction in nanoparticle filtration through-thickness in the vacuum outlet region can be explained by the thinner thickness of the vacuum outlet compared to the resin inlet due to compaction. This shorter travel distance for the nano-doped resin in the vacuum outlet resulted in enhanced mechanical properties in the vicinity of the vacuum outlet, as supported by the density measurements. Notably, the density values of both composite plates increased from the first to the third zone due to reduced potential voids caused by higher compaction on the vacuum side. In the context of nanocomposite production, using smaller-sized plates has proven to yield more consistent outcomes. It's also important to mention that the horizontal to the resin flow (HRF) values consistently exceeded the vertical to the resin flow (VRF) values, highlighting the greater thickness stability in the HRF direction. To ensure accurate comparisons between stress values of samples across different plates, it is essential to extract samples with the same orientation and from the same zone.

To assess the statistical significance of the means of three independent variables, a one-way ANOVA analysis was conducted. The null hypothesis (H₀) posited that there was no difference in means across three different regions. The null hypothesis was accepted, as the calculated p-value of 0.104 exceeded the significance level of 0.05. This result indicates that there is no statistically significant difference in means among the three distinct regions.

While experimental observations may suggest an increase in test results from the first to the third zones, the statistical analysis reveals that this shift is not significant. However, it's important to note that a lack of statistical significance does not render experimental results meaningless. Instead, it indicates the absence of a clear correlation. Nonetheless, for a more precise interpretation of

the results, it remains crucial to consistently extract samples from the same zone and orientation in experimental tests.

Article Information Form

Funding

The author has not received any financial support for the research, authorship, or publication of this study.

Authors' Contribution

The author confirms sole responsibility for the following: study conception and design, data collection, analysis and interpretation of results, and manuscript preparation.

The Declaration of Conflict of Interest/ Common Interest

The author declares that they have no known competing financial interests or personal relationships that could have appeared to influence the work reported in this paper.

The Declaration of Ethics Committee Approval

This study does not require ethics committee permission or any special permission.

The Declaration of Research and Publication Ethics

The author of the paper declares that he complies with the scientific, ethical, and quotation rules of SAUJS in all processes of the paper and that they do not make any falsification on the data collected. In addition, he declares that Sakarya University Journal of Science and its editorial board have no responsibility for any ethical violations that may be encountered and that this study has not been evaluated in any academic publication environment other than Sakarya University Journal of Science.

Copyright Statement

The author owns the copyright of their work published in the journal and their work is published under the CC BY-NC 4.0 license

References


- [1] G. Demircan, M. Kisa, M. Ozen, A. Acikgoz, Y. İşiker, E. Aytar, "Nanogelcoat application of glass fiber reinforced

- polymer composites for marine application: Structural, mechanical, and thermal analysis,” *Marine Pollution Bulletin*, vol. 194, p. 115412, 2023.
- [2] T. Singh, B. Gangil, L. Ranakoti, A. Joshi, “Effect of silica nanoparticles on physical, mechanical, and wear properties of natural fiber reinforced polymer composites,” *Polymer Composites*, vol. 42, no. 5, pp. 2396–2407, 2021.
- [3] G. Demircan, M. Ozen, M. Kisa, A. Acikgoz, Y. Işiker, “The effect of nanogelcoat on freeze-thaw resistance of glass fiber-reinforced polymer composite for marine applications,” *Ocean Engineering*, vol. 269, p. 113589, 2023.
- [4] K. Srinivasan, W. C. Jackson, B. T. Smith, J. A. Hinkley, “Characterization of damage modes in impacted thermoset and thermoplastic composites,” *Journal of Reinforced Plastics and Composites*, vol. 11, no. 10, pp. 1111–1126, 1992.
- [5] G. Demircan, M. Kisa, M. Ozen, A. Acikgoz, “Quasi-Static Penetration behavior of glass-fiber-reinforced epoxy nanocomposites,” *Mechanics of Composite Materials*, vol. 57, no. 4, pp. 503–516, Sep. 2021.
- [6] A. Siddika, M. A. Al Mamun, R. Alyousef, Y. H. M. Amran, “Strengthening of reinforced concrete beams by using fiber-reinforced polymer composites: A review,” *Journal of Building Engineering*, vol. 25, p. 100798, 2019.
- [7] J. J. Kenned, K. Sankaranarayananasamy, J. S. Binoj, S. K. Chelliah, “Thermo-mechanical and morphological characterization of needle punched non-woven banana fiber reinforced polymer composites,” *Composites Science and Technology*, vol. 185, p. 107890, 2020.
- [8] M. Özen, G. Demircan, M. Kisa, Z. Ilik, “Investigation of usability of waste textile fabrics in composites,” *Emerging Materials Research*, vol. 9, no. 1, pp. 1–6, Mar. 2020.
- [9] T. D. Tavares, J. C. Antunes, F. Ferreira, H. P. Felgueiras, “Biofunctionalization of natural fiber-reinforced biocomposites for biomedical applications,” *Biomolecules*, vol. 10, no. 1, p. 148, Jan. 2020.
- [10] Y. Li, N. Li, J. Gao, “Tooling design and microwave curing technologies for the manufacturing of fiber-reinforced polymer composites in aerospace applications,” *The International Journal of Advanced Manufacturing Technology*, vol. 70, no. 1–4, pp. 591–606, 2013.
- [11] D. K. Rajak, D. D. Pagar, P. L. Menezes, E. Linul, “Fiber-reinforced polymer composites: Manufacturing, properties, and applications,” *Polymers (Basel)*, vol. 11, no. 10, p. 1667, Oct. 2019.
- [12] A. T. Bhatt, P. P. Gohil, V. Chaudhary, “Primary manufacturing processes for fiber reinforced composites: History, development & future research trends,” *IOP Conference Series: Materials Science and Engineering*, vol. 330, p. 12107, 2018.
- [13] J. P. Davim, P. Reis, C. C. António, “Experimental study of drilling glass fiber reinforced plastics (GFRP) manufactured by hand lay-up,” *Composites Science and Technology*, vol. 64, no. 2, pp. 289–297, 2004.
- [14] S. G. Advani C. L. Tucker, “A numerical simulation of short fiber orientation in compression molding,” *Polymer Composites*, vol. 11, no. 3, pp. 164–173, 1990.
- [15] N. O. Cabrera, B. Alcock, E. T. J. Klompen, T. Peijs, “Filament winding of

- co-extruded polypropylene tapes for fully recyclable all-polypropylene composite products,” *Applied Composite Materials*, vol. 15, no. 1, pp. 27–45, 2008.
- [16] X. Peng, M. Fan, J. Hartley, M. Al-Zubaidy, “Properties of natural fiber composites made by pultrusion process,” *Journal of Composite Materials*, vol. 46, no. 2, pp. 237–246, 2011.
- [17] J. H. Jeon, C. K. Yoon, S. H. Park, W. Il Lee, S. M. Kim, “Assessment of long fiber spray-up molding of chopped glass fiber reinforced polydicyclopentadiene composites,” *Fibers and Polymers*, vol. 21, no. 5, pp. 1134–1141, 2020.
- [18] M. A. Agwa, S. M. Youssef, S. S. Ali-Eldin, M. Megahed, “Integrated vacuum assisted resin infusion and resin transfer molding technique for manufacturing of nano-filled glass fiber reinforced epoxy composite,” *Journal of Industrial Textiles*, vol. 51, no. 3_suppl, pp. 5113S-5144S, 2020.
- [19] M. Ozen, G. Demircan, M. Kisa, A. Acikgoz, G. Ceyhan, Y. Işiker, “Thermal properties of surface-modified nano-Al₂O₃/Kevlar fiber/epoxy composites,” *Mater. Materials Chemistry and Physics*, vol. 278, p. 125689, Feb. 2022.
- [20] U. K. Vaidya, M. V Kamath, H. Mahfuz, S. Jeelani, “Low velocity impact response of Resin Infusion Molded foam filled honeycomb sandwich composites,” *Journal of Reinforced Plastics and Composites*, vol. 17, no. 9, pp. 819–849, 1998.
- [21] G. Demircan, M. Kisa, M. Özen, A. Açikgöz, B. Aktaş, M. Ali Kurt, “A bio-based epoxy resin from rosin powder with improved mechanical performance,” *Emerging Materials Research*, vol. 9, no. 4, pp. 1076–1081, Dec. 2020.
- [22] M. Sánchez, M. Campo, A. Jiménez-Suárez, A. Ureña, “Effect of the carbon nanotube functionalization on flexural properties of multiscale carbon fiber/epoxy composites manufactured by VARIM,” *Composites Part B: Engineering*, vol. 45, no. 1, pp. 1613–1619, 2013.
- [23] Z. A. Oguz, A. Erklig, Ö. Y. Bozkurt, “Degradation of hybrid aramid/glass/epoxy composites hydrothermally aged in distilled water,” *Journal of Composite Materials*, vol. 55, no. 15, pp. 2043–2060, 2020.
- [24] A. Hindersmann, “Confusion about infusion: An overview of infusion processes,” *Composites Part A: Applied Science and Manufacturing*, vol. 126, p. 105583, 2019.
- [25] R. Matsuzaki, S. Kobayashi, A. Todoroki, Y. Mizutani, “Full-field monitoring of resin flow using an area-sensor array in a VaRTM process,” *Composites Part A: Applied Science and Manufacturing*, vol. 42, no. 5, pp. 550–559, 2011.
- [26] G. Demircan, M. Kisa, M. Ozen, B. Aktas, “Surface-modified alumina nanoparticles-filled aramid fiber-reinforced epoxy nanocomposites: preparation and mechanical properties,” *Iranian Polymer Journal*, vol. 29, no. 3, pp. 253–264, Mar. 2020.
- [27] M. Özer, H. Ulus, H. B. Kaybal, “Enhanced out-of-plane loading performance of multi-scale glass/epoxy composites doped with HNTs,” *International Journal of Pioneering Technology and Engineering*, vol. 2 no. 01, pp. 99-102, 2023.
- [28] H. Ulus, “The impact of seawater aging on basalt/graphene nanoplatelet-epoxy composites: performance evaluating by Dynamic Mechanical Analysis (DMA) and

- short beam shear (sbs) tests” Niğde Ömer Halisdemir Üniversitesi Mühendislik Bilimleri Dergisi, vol.10 no.1, pp. 412-419, 2021.
- [29] K.-T. Hsiao D. Heider, “Vacuum assisted resin transfer molding (VARTM) in polymer matrix composites,” *Manufacturing Techniques for Polymer Matrix Composites (PMCs)*. Elsevier, pp. 310–347, 2012.
- [30] Z. Fan, M. H. Santare, S. G. Advani, “Interlaminar shear strength of glass fiber reinforced epoxy composites enhanced with multi-walled carbon nanotubes,” *Composites Part A: Applied Science and Manufacturing*, vol. 39, no. 3, pp. 540–554, 2008.
- [31] S. Movva, G. Zhou, D. Guerra, L. J. Lee, “Effect of carbon nanofibers on mold filling in a vacuum assisted Resin Transfer Molding system,” *Journal of Composite Materials*, vol. 43, no. 6, pp. 611–620, 2009.
- [32] H. B. Kaybal, H. Ulus, O. Demir, Ö. S. Şahin, A. Avcı, “Effects of alumina nanoparticles on dynamic impact responses of carbon fiber reinforced epoxy matrix nanocomposites,” *Engineering Science and Technology, an International Journal*, vol. 21 no.3, pp. 399-407, 2018.
- [33] “Test Method for Tensile Properties of Polymer Matrix Composite Materials.” ASTM International. ASTM D3039/D3039M-17, West Conshohocken, PA, 2017.
- [34] “Test Methods for Flexural Properties of Unreinforced and Reinforced Plastics and Electrical Insulating Materials.” ASTM International. ASTM D790-17, West Conshohocken, PA, 2017.
- [35] U. R. Hashim, A. Jumahat, M. Jawaid, “Mechanical properties of hybrid graphene nanoplatelet-nanosilica filled unidirectional basalt fibre composites,” *Nanomaterials (Basel, Switzerland)*, vol. 11, no. 6, p. 1468, Jun. 2021.
- [36] G. Francucci, S. Palmer, W. Hall, “External compaction pressure over vacuum-bagged composite parts: Effect on the quality of flax fiber/epoxy laminates,” *Journal of Composite Materials*, vol. 52, no. 1, pp. 3–15, 2017.
- [37] K.-T. Hsiao, R. Mathur, S. G. Advani, Gillespie J. W., B. K. Fink, “A closed form solution for flow during the vacuum assisted Resin Transfer Molding Process,” *Journal of Manufacturing Science and Engineering*, vol. 122, no. 3, pp. 463–475, 1999.
- [38] S. Cao, Z. WU, X. Wang, “Tensile Properties of CFRP Hybrid FRP Composites at Elevated Temperatures,” *J Journal of Composite Materials*, vol. 43, no. 4, pp. 315–330, 2009.
- [39] A. C. N. Singleton, C. A. Baillie, P. W. R. Beaumont, T. Peijs, “On the mechanical properties, deformation and fracture of a natural fibre/recycled polymer composite,” *Composites Part B: Engineering*, vol. 34, no. 6, pp. 519–526, 2003.
- [40] R. M. Heiberger E. Neuwirth, “One-Way ANOVA,” *R Through Excel*. Springer New York, pp. 165–191, 2009.
- [41] J. P. Verma, “One-Way ANOVA: Comparing Means of More than Two Samples,” *Data Analysis in Management with SPSS Software*. Springer India, pp. 221–254, 2012.
- [42] J. E. McLean, J. M. Ernest, “The role of statistical significance testing in educational research,” *Research in the Schools*, vol. 5 no. 2, 1998.

Designing Hollow Brick Waste Based Alkali Activated Composites by Taguchi Method

Mine Kurtay Yıldız^{1*} 

^{1*} Sakarya University, Faculty of Engineering, Department of Civil Engineering, Sakarya, Türkiye, miney@sakarya.edu.tr
*Corresponding Author

ARTICLE INFO

ABSTRACT

Keywords:

Alkali Activated Composite
Hollow Brick Waste
Taguchi
ANOVA



Article History:

Received: 14.06.2023

Accepted: 09.11.2023

Online Available: 27.02.2024

The use of waste materials in alkali-activated material technologies is important in terms of sustainability. The production of alkali-activated composites (AAC) with hollow brick waste (HBW) as a binder may contribute to solving existing environmental problems related to the depletion of natural resources. In this study, mortars were produced using different concentrations (6 M, 8 M, and 10 M NaOH) and Alkaline Activator/Powder Material (AA/PM) ratios of 0.30, 0.35, and 0.40 through the alkali activation method. The hollow brick waste (HBW) powder was obtained by grinding inactive bricks in brick factories. The prepared mortars were cured separately for each mixture at 90°C for 24 hours. Compressive and flexural strength tests were performed on the prepared perforated hollow brick waste-based composites. The Taguchi method was used to determine the optimum mixing ratios by conducting compressive and flexural strength tests on the produced AAC. To optimize the parameters determined using the Taguchi method, the best mixing ratios were determined using the L9 (3²) orthogonal index. The compressive and flexural strengths of the mixtures were evaluated considering the signal to noise ratio "larger the better" and the highest compressive strength value was 63.669 MPa and the highest flexural strength value was 6.629 MPa according to the optimum values. According to the obtained results, it was determined that the AAC produced at 6 M NaOH and 0.30 AA/PM ratio exhibited the highest compressive and flexural strength values.

1. Introduction

The most widely used engineering material in the world is concrete. Cement, on the other hand, is the most costly, least environmentally friendly, and energy-intensive material of traditional concrete, despite being suitable and readily available for construction applications [1]. The cement industry accounts for 5-8% of human-induced CO₂ emissions, resulting in significant carbon emissions [2]. In terms of sustainability and environmental awareness, the design, production, and use of eco-friendly building materials that will contribute to reducing the use of cement-based materials by using recycled or waste materials to minimize energy and natural resource consumption has become a topic of interest [3]. Therefore, in recent years, there has

been an increased interest in alternative studies aiming to produce building materials without using cement. The fact that alkali-activated composite materials produced using industrial waste products and/or recycled products have much lower CO₂ emissions compared to Portland cement has become an important issue in materials science [4-7]. Therefore, the production of alkali-activated materials has contributed to both the reduction of carbon dioxide emissions and the development of sustainable building materials with adequate mechanical parameters [8-10].

With the increase in urbanization, significant amounts of waste are generated each year as a result of infrastructure improvement, repair and demolition [11]. The waste generated after

construction and demolition activities has become a major problem for society [12]. Therefore, the use of construction and demolition waste in various construction processes is being encouraged in specific locations around the world. Construction and demolition waste is used in concrete production as recycled coarse and fine aggregates according to their sizes [13, 14]. Recycled coarse aggregates are currently applied in the production of non-structural concrete and sub-base foundations [15].

Numerous studies have shown that concrete can be produced by binding materials such as fly ash and blast furnace slag, which contain alumina and silica, with alkali activators without the use of cement [16, 17]. As a result of the activation of fly ash and blast furnace slag with alkalis, calcium silicate hydrate (C-S-H) structures similar to cement-based binders are formed [18]. When the properties and performance of cement-free and alkali-activated fly ash or blast furnace slag binders are evaluated, it has been revealed that they can be used as an alternative to cement through research studies [19]. In this regard, studies on the use of various agricultural and industrial wastes as well as construction and demolition wastes activated with alkali activators have increased when environmental problems and factors such as the decrease of natural resources are taken into account [20, 21]. The production of alkali-activated composites involves the utilization of waste materials, contributing to recycling and the production of sustainable and environmentally friendly building materials [22-24].

The results obtained in the study where recycled fine powder was used as a partial replacement of fly ash at different substitution rates (10%, 20%, 30%, 40% and 50%) as a partial replacement of fly ash showed that the replacement of recycled fine powder up to 30% improved the strength and durability properties of geopolymer mortar mixtures [25]. In the study investigating the effect of activator type, usage rates and combinations on the rheological and workability performance of CDW-based geopolymer matrix, wall and roof elements containing recycled aggregates such as brick, glass waste, tile and concrete waste were prepared and it was

recommended that the activator selection should be made according to the application needs [26].

In the study conducted by Yurt (2020), alkali-activated concrete (AAC) samples produced using ground granulated blast furnace slag (GGBFS) were tested for capillary water absorption, density, Dynamic Elasticity Modulus (DMoE), compressive strength, tensile strength in splitting, wear resistance tests and microstructure analyzes. The study determined that GGBFS can be used entirely in AAC production, and high-strength cement-free concrete with a compressive strength of 82.32 MPa was achieved [27]. In the study conducted by Yıldırım et al. (2021), as different wall units, red clay brick, hollow brick and tile were used in binary combinations with a total weight of binder in 75-25%, 50-50% and 25-75% ratios. According to the results obtained from the study, it was observed that alkali-activated binders with compressive strength up to 80 MPa can be produced [28].

In a study examining the strength and wear properties of geopolymer concrete prepared with zeolite-incorporated high-temperature furnace slag at weight percentages of 5%, 10%, and 15% over time, it was stated that the highest compressive strength value of 88 MPa was obtained at 60 °C water curing [29]. It was observed that the increase in the amount of zeolite added to geopolymer concrete resulted in an increase in wear resistance. In the study where recycled clay brick, recycled ceramic wall tile and recycled concrete wastes were used, the relationship between fresh and mechanical properties such as fluidity, setting time, compressive strength and microstructure and design factors were comprehensively investigated. According to the results obtained, it was confirmed that recycled clay brick, recycled concrete wastes and recycled ceramic wall triple combinations significantly increased the sustainability of geopolymer binders compared to their individual use [30].

Alkali-activated mortar specimens were produced by adding different ratios (5%, 10% and 15%) of marble powder and 0.5% of glass fiber to ferrochrome slag ground to the same fineness as cement. Compressive strength,

flexural strength, unit weight, ultrasonic transmission rate and capillarity coefficient determination tests were applied to the produced geopolymer mortar samples and the results of the experiments were analyzed by Taguchi method. The highest compressive strength value of 24.27 MPa was obtained with Elazığ ferrochrome slag without cement and the optimum levels of the parameters were determined by analysis of variance [31].

In the study where the Taguchi-Grey relational analysis method was used for the systematic evaluation and efficient recycling of blast furnace slag and paper production waste (PPW) for reuse, the setting time, compressive strength, flexural strength, and tensile strength of the produced mortar were analyzed. Four types of PPW-blast furnace slag specimens were prepared: lime mud, primary sludge, fly ash and bottom ash. It was found that PS content affected the setting time, bottom ash content affected the flexural and compressive strengths, and bottom ash and lime mud content affected the degree of shrinkage and the most suitable PPW-BFS mortar composition was lime mud: 5%; primary sludge: 5%; fly ash: 30%; bottom ash: 10% [32].

The Taguchi method is efficiently used for fractional factorial design of materials. This method is based on the principles of using orthogonal arrays [33, 34]. The optimum combination is determined based on the signal-to-noise ratio (S/N) and is used to understand the effects of each parameter on the responses.

Several studies have been conducted using the Taguchi method to convert complex waste compositions into construction materials [32, 35, 36]. The Taguchi method is efficiently utilized for examining waste materials with complex compositions, but its disadvantage is that it can only be used to optimize a single objective. Therefore, this limitation restricts the application possibilities of the method. Upon reviewing the literature, it can be observed that there is a limited number of studies focusing on the use of brick waste through alkali activation method.

In this study, mortar production was carried out using the alkali activation method with different concentrations of NaOH (6 M, 8 M, and 10 M) and AA/PM ratios (0.30, 0.35, 0.40) of hollow

brick powder waste. The compressive and flexural strength tests were applied to the samples. The optimum mixture ratios were determined using the Taguchi L9 (3^2) orthogonal array design based on the obtained experimental results. There is a need for new approaches for the reuse of waste materials generated after construction and demolition applications [37].

Recycling of demolition wastes is one of the important subjects with high added value and has been studied in recent years. In addition, the utilization of building demolition wastes in this way is environmentally effective. Therefore, it is believed that this research will contribute to the existing literature with the use of Taguchi method in determining the mixing ratios of BFS and HBW based AAC systems.

1. Material and Method

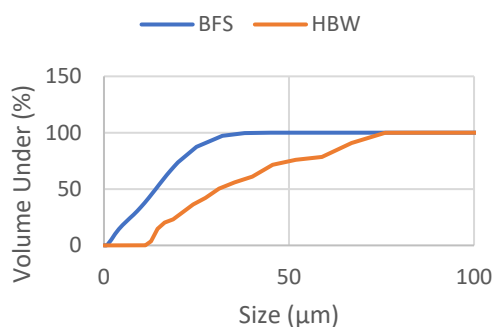
1.1. Materials and mixture ratios

In the preparation stage of alkali-activated mortar samples, finely ground blast furnace slag (BFS) obtained from Oyak Bolu Çimento Ereğli Facility was used. The chemical and physical properties of the BFS and HBW used in the study are shown in Table 1. AFS 30-35 silica sand was used in the mixtures. HBW obtained from the Duzce region were ground and used after passing through a 4 mm sieve in the laboratory. In addition, the sieve analysis of the BFS and HBW are shown in Figure 1. Sika ViscoCrete SF-18 high-performance superplasticizer (brown; density: 1.25 g/cm^3) obtained from Sika Construction Chemicals was used to increase the workability of composite mixtures. In addition, liquid Sodium Hydroxide (NaOH) (colorless; density: 1.507 g/cm^3) and liquid Sodium Silicate

Table 1. Chemical properties of BFS and hollow brick powder waste

	SiO ₂	Fe ₂ O ₃	TiO ₂	Al ₂ O ₃	CaO	MgO	Na ₂ O	K ₂ O	SO ₃	Mn ₂ O ₃	Cr ₂ O ₃
BFS	38.86	0.71	2.03	13.23	37.71	4.15	0.47	0.54	0.01	0.74	0.01
HBW	59.78	9.04	1.02	21.24	1.92	1.73	0.67	2.97	0.00	0.19	0.03

(Na₂SiO₃) (colorless; density: 1.431 g/cm³) were used as alkali activators.

**Figure 1.** Sieve analysis of the BFS and HBW

Na₂SiO₃ was added to the mixture at a ratio of 2 for the prepared mortar. The mixture ratios of the produced alkali-activated composites are given in Table 2.

1.2. Preparation of mortar samples

For the compressive strength tests, molds with dimensions of 50x50x50 mm were used, and for the flexural strength tests, molds with dimensions of 40x40x160 mm were used (Fig. 2). NaOH solutions prepared as 6M, 8M and 10M were mixed until homogeneous. The materials to be used for the mortar specimens were weighed separately in individual containers and prepared. For the prepared mortar, sodium silicate (Na₂SiO₃) was added to achieve a Na₂SiO₃/NaOH ratio of 2 [38, 39].

**Figure 2.** Beam and cubic molds used in experiments

While the powder materials were mixed in the mixer at low speed (62.5 rpm) for 60 seconds, a homogeneous mixture of alkali activator and super plasticizer was ensured during this time. After 60 seconds, the alkaline activators were added to the powdered samples, and the mixtures were mixed at a high speed (125 rpm) for 150 seconds. After mixing, the homogeneity of the mortar was checked, and if necessary, it was mixed again for 60 seconds (Fig. 3). The mortar was placed in lubricated molds and compacted thoroughly on the shaking table. After the mortars placed in the molds were covered with stretch film, they were kept in an oven at 90°C for 24 hours and when the samples reached room temperature, compressive and flexural strength tests were conducted.

1.3. Compressive strength tests

Compressive strength tests were carried out according to the ASTM C109 (2020) standard. Compressive strength tests were performed on the prepared cube specimens with an application rate of 0.5 MPa/s (Fig. 4a). The averages of the obtained results were calculated, and the compression strength values were determined using Equation 1.

Table 2. Mixing ratios of alkali-activated composite samples

Mix Type	BFS (%)	HBW (%)	Silica sand (%)	SP* (%)	NaOH (%)	Na ₂ SiO ₃ (%)	AA/PM
6 M NaOH	21.90	32.80	21.90	0.40	7.60	15.20	0.30
	24.57	24.57	24.57	0.50	8.60	17.20	0.35
	23.70	23.70	23.70	0.50	9.50	19.00	0.40
8 M NaOH	21.90	32.80	21.90	0.40	7.60	15.20	0.30
	24.57	24.57	24.57	0.50	8.60	17.20	0.35
	23.70	23.70	23.70	0.50	9.50	19.00	0.40
10 M NaOH	21.90	32.80	21.90	0.40	7.60	15.20	0.30
	24.57	24.57	24.57	0.50	8.60	17.20	0.35
	23.70	23.70	23.70	0.50	9.50	19.00	0.40

* Super Plasticizer

$$R_c = \frac{F_c}{Area} \tag{1}$$

In the formula, R_c represents the compressive strength (MPa), F_c represents the maximum load reached at the point of failure (N), and Area represents the cross-sectional area of the specimen (expressed in mm²).



Figure 3. Mixing materials and mixer

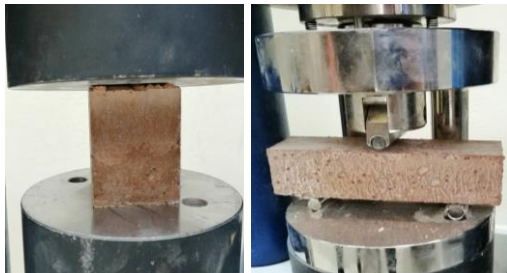


Figure 4. a) Compressive and b) Flexural strength test specimens

1.4. Flexural strength tests

Flexural strength tests were conducted according to the TS EN 1015–11/A1 (2013) standard. The three-point bending test method based on the simple beam principle was used in the study. Flexural strength tests were conducted at a loading rate of 0.05 MPa/s (Fig. 4b). The flexural strength calculation was made according to the results obtained by using the formula in Equation 2. In the formula, σ : the flexural strength (N/mm²), P: the force acting at the moment of fracture (N), L: the distance between the two supports (mm), b: the beam width (mm), and d: the beam height (mm).

$$\sigma = \frac{3PL}{2bd^2} \tag{2}$$

1.5. Taguchi method

The Taguchi method is a statistical approach based on the principle of determining the most suitable parameter to achieve a high-quality product or process design. In this method, the most significant factors that affect product quality are identified during the product development stage, and the optimum parameters are determined by statistical analysis of these factors in order to obtain the desired result [33]. The Taguchi method allows for the reduction of the number of experiments required to obtain the desired quality product by identifying the most important parameters. This contributes positively in terms of both time and cost [34].

In the Taguchi method, the Signal-to-Noise (S/N) ratio is a measure that determines the

performance of a product or process and ensures that the targeted output quality is achieved at the desired level. The S/N ratio is selected as the smallest-the better, the largest-the better, or the target value-the better, depending on the desired objective, in order to reach the desired goal. When calculating the S/N ratios, the smallest-the better is preferred when the output values need to be minimized, the largest-the better when they need to be maximized, and the target value-the better when they need to match a specific nominal value [40]. In this study, optimization was performed using the Taguchi method with the predetermined parameters and levels, and the best mixing ratios were determined. The L9 (3²) Taguchi orthogonal index was chosen with 3 concentrations of NaOH of 6M, 8M and 10M and AA/PM 0.30, 0.35 and 0.40 ratios with 3 levels (Table 3).

Table 3. Experimental parameters and levels

Parameter	Level	Value
NaOH	3	6M, 8M, 10M
AA/PM	3	0.30, 0.35, 0.40

2. Result and Discussion

When examining Table 4, it can be observed that an increase in NaOH molarity and AA/PM ratio leads to a decrease in compressive strength values [41]. The amount of Na₂O present in the NaOH solution plays an important role in the development of compressive strength. 6 M and higher NaOH concentration increases the amount of Na⁺ cation and causes higher alkalinity [42]. However, specimens with high alkali content show a decrease in compressive strength due to the rapid precipitation of aluminosilicates at early ages and the formation of a porous microstructure. In addition, higher NaOH concentration leads to a weakening of the gel structure due to excess hydroxide ions and a decrease in the availability of Si, Al and Ca [43]. During the analysis of compressive strength values using the Taguchi method, Equation 3 was preferred by considering the larger-the-better case since it is desired to have high compressive strength values for the specimens in the calculation stage of the S/N ratios.

2.1. Compressive strength results

The test results of compressive strength for the prepared AACs are shown in Table 4.

Table 4. Compressive strength results

NaOH	AA/PM	Compressive Strength Results (MPa)*	*SD
6 M	0.30	63.669	±4.930
	0.35	45.906	±6.004
	0.40	34.284	±5.221
8 M	0.30	38.216	±2.962
	0.35	37.405	±2.691
	0.40	37.996	±2.795
10 M	0.30	30.603	±2.248
	0.35	29.219	±1.648
	0.40	26.461	±2.127

*Standard Deviation

$$S/N = -10 \log\left(\frac{1}{n} \sum_{i=1}^n \frac{1}{y_i^2}\right) \quad (3)$$

The highest S/N graph and S/N ratios in the response table obtained using the Taguchi method to achieve the optimum parameter (NaOH and AA/PM) values for Figure 4 and Table 5 are shown. According to Figure 4, the highest S/N ratio was obtained at a parameter level of 6 M NaOH and an AA/PM ratio of 0.30.

Table 5. S/N ratios obtained according to compressive strength values

NaOH	AA/PM	S/N
6 M	0.30	36.078
	0.35	33.237
	0.40	30.701
8 M	0.30	31.645
	0.35	31.458
	0.40	31.594
10 M	0.30	29.715
	0.35	29.313
	0.40	28.452

Furthermore, Variance (ANOVA) analysis was conducted to determine the effect of the pressure resistance experimental parameters (Table 6).

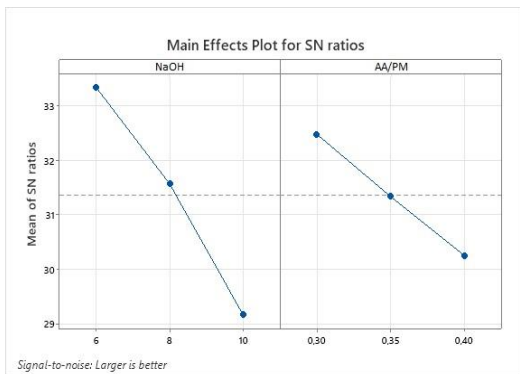


Figure 4. S/N ratios compressive strength according to parameter levels

When Table 6 is examined, the fact that the P value for NaOH is lower than that of AA/PM shows that it is a more influential parameter. The parameter with the higher F value is again the NaOH parameter. When analyzing the impact ratios of the parameters on the compressive strength results, it can be observed that the most influential parameter is NaOH with a percentage of 55.28%.

2.2. Flexural strength results

The average values of the flexural strength results obtained from 9 series activated with alkali prepared using different ratios of NaOH and AA/PM are given in Table 7. It is seen that

the flexural strength values decrease with the increase in the NaOH ratio in Table 7. The flexural strength follows a similar trend to the compressive strength, with a significant decrease observed when the NaOH concentration rises from 6 M to 10 M. This decrease in the flexural strength values may be attributed to the change in the microstructure of HBW-based samples due to the increase in NaOH concentration. While the analysis of flexural strength values using the Taguchi method, Equation 3 was preferred, considering the larger-the-better case, as higher flexural strength values for the mortars were desired during the calculation stage of the S/N ratios.

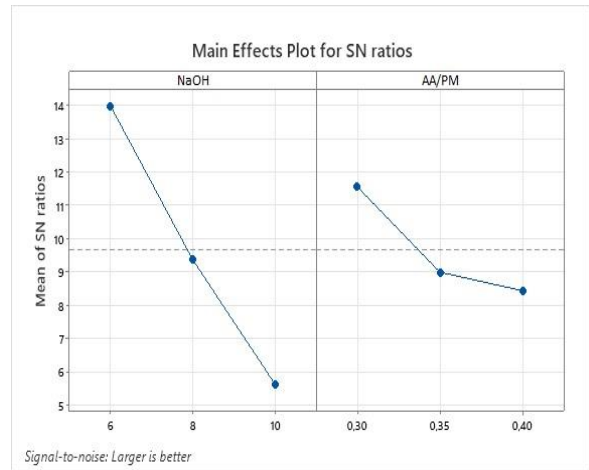


Figure 5. S/N ratios flexural strength by parameter levels

The graph of the flexural strength values analyzed using the Taguchi method according to parameter levels is given in Figure 5, and the S/N ratios are provided in Table 8. When examining Table 8, the lower P-value for NaOH compared to AA/PM indicates that NaOH is a more influential parameter. The parameter with a high F-value is also NaOH. When analyzing the impact ratios of the parameters on the flexural strength results, it can be observed that the most influential parameter is NaOH with a percentage of 75.47%.

Table 6. Analysis of variance results for compressive strength values

Parameter	Degree of Freedom	Effect Ratio	Sum of Squares	Mean of Squares	F-Value	P-Value
NaOH	2	55.28%	553.0	276.48	4.33	0.100
AA/PM	2	19.19%	192.0	95.98	1.50	0.302
Error	4	25.53%	255.3	63.84		
Total	8	100.00%				

Table 7. Flexural strength results

NaOH	AA/PM	Flexural Strength Results (MPa)*	*SD
6 M	0.30	6.629	±0.588
	0.35	5.079	±0.939
	0.40	3.721	±0.910
8 M	0.30	3.602	±0.315
	0.35	2.894	±0.341
	0.40	2.437	±0.472
10 M	0.30	2.266	±0.573
	0.35	1.518	±0.235
	0.40	2.030	±0.259

*Standard Deviation

Table 8. S/N ratios according to flexural strength values

NaOH	AA/PM	S/N
6 M	0.30	16.428
	0.35	14.115
	0.40	11.413
8 M	0.30	11.129
	0.35	9.229
	0.40	7.736
10 M	0.30	7.103
	0.35	3.625
	0.40	6.148

The highest S/N ratio was obtained at the parameter levels of 6 M NaOH and an AA/PM ratio of 0.30. Additionally, Variance analysis was conducted to determine the effect of the flexural strength experimental parameters (Table 9).

3. Conclusion

In this study, the compressive and flexural strength of alkali-activated mortars produced using high furnace slag and hollow brick waste were investigated. The parameters determined using the Taguchi method were optimized for the best mixture ratios using the L9 (3²) orthogonal array. The following data were obtained as a result of the study:

- The lowest compressive strength was obtained from 10M NaOH with 26.461 MPa, and the highest compressive strength was obtained from 6M NaOH with 63.669 MPa. It was observed that as AA/TM increased from 0.30 to 0.40, the compressive strength of 6M NaOH, 8M NaOH and 10M NaOH decreased by 46%, 0.5% and 14%, respectively.
- The highest flexural strength was obtained from 6M NaOH with 6.629 MPa, and the lowest flexural strength was obtained from 10M NaOH, 1.518 MPa. It was observed that as AA/TM increased from 0.30 to 0.40, the flexural strength of 6M NaOH, 8M NaOH and 10M NaOH compressive strength decreased by 44%, 32% and 11%, respectively.
- When evaluating the compressive and flexural strength results according to the AA/PM ratios used (0.30, 0.35, and 0.40), it was observed that the highest value was obtained at a ratio of 0.30.
- According to the experimental results of compressive and flexural strength, it was observed that the highest strength values were obtained at 6 M, while the lowest values were obtained at 10 M.

Table 9. Analysis of variance results for flexural strength values

Parameter	Degree of Freedom	Effect Ratio	Sum of Squares	Mean of Squares	F-Value	P-Value
NaOH	2	75.47%	16.044	8.0222	16.37	0.012
AA/PM	2	15.31%	3.255	1.6276	3.32	0.141
Error	4	9.22%	1.960	0.4090		
Total	8	100.00%				

- Optimum values were determined by conducting a variance analysis using the Taguchi method based on the obtained compressive and flexural strength results. According to this analysis, it was observed that the best values were obtained at 6 M NaOH and an AA/PM ratio of 0.30.
- Additional research can be conducted with alkaline activated mortar mixtures by changing the parameters and levels determined in this study. It is also possible to improve the study by using different waste materials, changing activator types or additives.

Article Information Form

Acknowledgments

The author would like to thank Prof. Dr. Mehmet EMİROĞLU for his contributions.

Funding

This study is supported by TÜBİTAK Project Number: 121C378.

Authors' Contribution

The author confirms sole responsibility for the following: Study conception and design, data collection, analysis and interpretation of results, and manuscript preparation

The Declaration of Conflict of Interest/ Common Interest

No conflict of interest or common interest has been declared by the author.

The Declaration of Ethics Committee Approval

This study does not require ethics committee permission or any special permission.

The Declaration of Research and Publication Ethics

The author of the paper declares that he complies with the scientific, ethical, and quotation rules of SAUJS in all processes of the paper and that they do not make any falsification on the data collected. In addition, he declares that Sakarya University Journal of Science and its editorial board have no responsibility for any ethical violations that may be encountered and that this study has not been evaluated in any academic publication environment other than Sakarya University Journal of Science.

Copyright Statement

The author owns the copyright of their work published in the journal and their work is published under the CC BY-NC 4.0 license

References




- [1] E. Özçelikci, "İnşaat yıkıntı atığı içeren jeopolimer beton tasarımlarının geliştirilmesi," Yüksek Lisans Tezi, Hacettepe Üniversitesi Fen Bilimleri Enstitüsü, Ankara, 2020.
- [2] E. Gartner, "Industrially interesting approaches to 'low-CO₂' cements," Cement and Concrete Research, vol. 34, no. 9, pp. 1489–1498, 2004.
- [3] A. Petek Gürsel, Ç. Meral, "Türkiye'de çimento üretiminin karşılaştırmalı yaşam döngüsü analizi," 2. Proje ve Yapım Yönetimi Kongresi, İzmir, 2012.
- [4] A. Heath, K. Paine, M. McManus, "Minimising the global warming potential of clay based geopolymers," Journal of Cleaner Production, vol. 78, pp. 75-83, 2014.

- [5] I. K. Jeon, A. Azzam, H. Al Jebaei, Y. R. Kim, A. Aryal, J. C. Baltazar, "Effects of alkali-activated slag binder and shape-stabilized phase change material on thermal and mechanical characteristics and environmental impact of cementitious composite for building envelopes", *Journal of Building Engineering*, vol. 76, 107296, 2023.
- [6] J. Fořt, M. Mildner, M. Keppert, R. Černý, "Waste solidified alkalis as activators of aluminosilicate precursors: Functional and environmental evaluation", *Journal of Building Engineering*, vol. 54, 104598, 2022.
- [7] A. Palomo, O. Maltseva, I. Garcia-Lodeiro, A. Fernández-Jiménez, "Portland versus alkaline cement: continuity or clean break: a key decision for global sustainability", *Frontiers in Chemistry*, vol. 9, 705475, 2021.
- [8] J. Fort, E. Vejmelkova, D. Konakova, N. Alblova, M. Cachova, M. Keppert, P. Rovnanikova, R. Cerny, "Application of waste brick powder in alkali activated aluminosilicates: functional and environmental aspects", *Journal of Cleaner Production*, vol. 194, pp. 714–725, 2018.
- [9] A. Komaei, A. Soroush, S. M. Fattahi, H. Ghanbari, "Influence of environmental stresses on the durability of slag-based alkali-activated cement crusts for wind erosion control", *Science of The Total Environment*, vol. 902, 166576, 2023.
- [10] G. Habert, J.B.D. de Lacaillerie, N. Roussel, "An environmental evaluation of geopolymer based concrete production: reviewing current research trends", *Journal of Cleaner Production*, vol. 19, no. 11, pp. 1229–1238, 2011.
- [11] P. Ren, B. Li, J.-G. Yu, T.-C. Ling, "Utilization of recycled concrete fines and powders to produce alkali-activated slag concrete blocks," *Journal of Cleaner Production*, vol. 267, 122115, 2020.
- [12] N. Cristelo, A. Fernández-Jiménez, C. Vieira, T. Miranda, Á. Palomo, "Stabilisation of construction and demolition waste with a high fines content using alkali activated fly ash," *Construction and Building Materials*, vol. 170, pp. 26–39, 2018.
- [13] P. Zhu, M. Hua, H. Liu, X. Wang, C. Chen, "Interfacial evaluation of geopolymer mortar prepared with recycled geopolymer fine aggregates," *Construction and Building Materials*, vol. 259, 119849, 2020.
- [14] M. A. Nawaz, L. A. Qureshi, B. Ali, "Enhancing the performance of recycled aggregate mortars using alkali-activated fly ash," *KSCE Journal of Civil Engineering*, vol. 25, no. 2, pp. 552–560, 2021.
- [15] R. Cardoso, R. V. Silva, J. de Brito, R. Dhir, "Use of recycled aggregates from construction and demolition waste in geotechnical applications: A literature review," *Waste Management*, vol. 49, pp. 131–145, 2016.
- [16] M. Sarıdemir, "Alkali ile aktive edilmiş öğütülmüş diatomitli harçların dayanım özellikleri," *Nigde University Journal of Engineering Sciences*, vol. 5, no. 2, pp. 124–134, 2016.
- [17] A. Aldemir, S. Akduman, O. Kocaer, R. Aktepe, M. Sahmaran, G. Yildirim, H. Almahmood, A. Ashour, "Shear behaviour of reinforced construction and demolition waste-based geopolymer concrete beams," *Journal of Building Engineering*, vol. 47, 103861, 2022.
- [18] S. Aydın, "Alkalilerle aktive edilmiş yüksek fırın cürufu bağlayıcılı lifli kompozit geliştirilmesi," *Doktora Tezi, Dokuz Eylül Üniversitesi Fen Bilimleri Enstitüsü, İzmir*, 2010.
- [19] Ü. Yurt, "Kür sıcaklığının alkali aktivasyonlu lifli betonunun kırılma özelliklerine etkisi," *OKU Fen Bilimleri*

- Enstitüsü Dergisi, vol. 5, no. 1, pp. 176–188, 2022.
- [20] C. Luan, X. Shi, K. Zhang, N. Utashev, F. Yang, J. Dai, Q. Wang, “A mix design method of fly ash geopolymer concrete based on factors analysis,” *Construction and Building Materials*, vol. 272, 121612, 2021.
- [21] P. Cong, Y. Cheng, “Advances in geopolymer materials: A comprehensive review,” *Journal of Traffic and Transportation Engineering*, vol. 8, no. 3, pp. 283–314, 2021.
- [22] C. Arenas, C. Leiva, L. F. Vilches, F. Arroyo, R. Villegas, C. Fernández-Pereira, “Development of a fly ash-based geopolymeric concrete with construction and demolition wastes as aggregates in acoustic barriers,” *Construction and Building Materials*, vol. 134, 433–442, 2017.
- [23] B. A. Tayeh, A. M. Zeyad, I. S. Agwa, M. Amin, “Effect of elevated temperatures on mechanical properties of lightweight geopolymer concrete,” *Case Studies in Construction Materials*, vol. 15, e00673, 2021.
- [24] H. İlcan, O. Sahin, A. Kul, G. Yildirim, M. Sahmaran, “Rheological properties and compressive strength of construction and demolition waste-based geopolymer mortars for 3D-Printing,” *Construction and Building Materials*, vol. 328, 127114, 2022.
- [25] A. Sharma, P. Singh, K. Kapoor, “Utilization of recycled fine powder as an activator in fly ash based geopolymer mortar,” *Construction and Building Materials*, vol. 323, 126581, 2022.
- [26] H. İlcan, “İnşaat yıkıntı atıkları kullanılarak tasarlanan jeopolimer bağlayıcı harçların reolojik ve işlenebilirlik özelliklerinin incelenmesi,” *Yüksek Lisans Tezi, Hacettepe Üniversitesi Fen Bilimleri Enstitüsü, Ankara, 2021.*
- [27] Ü. Yurt, “High performance cementless composites from alkali activated GGBFS,” *Construction and Building Materials*, vol. 264, 120222, 2020.
- [28] G. Yıldırım, A. Kul, E. Özçelikci, M. Şahmaran, A. Aldemir, D. Figueira, A. Ashour, “Development of alkali-activated binders from recycled mixed masonry-originated waste,” *Journal of Building Engineering*, vol. 33, 101690, 2021.
- [29] Ü. Yurt, M. Emiroğlu, “Zeolit ikameli jeopolimer betonlarda kür şartlarının etkileri,” *Academic Platform Journal of Engineering and Science*, vol. 8–2, pp. 396–402, 2020.
- [30] O. Mahmoodi, H. Siad, M. Lachemi, S. Dadsetan, M. Şahmaran, “Optimized application of ternary brick, ceramic and concrete wastes in sustainable high strength geopolymers,” *Journal of Cleaner Production*, vol. 338, 130650, 2022.
- [31] M. N. Mısıır, “Elazığ Ferrokrom cürufu ile alkali aktive edilmiş cam lifi ve atık mermer tozu katkılı harçların mühendislik özelliklerinin belirlenmesi,” *Yüksek Lisans Tezi, Fırat Üniversitesi Fen Bilimleri Enstitüsü, Elazığ, 2021.*
- [32] T. Yi, S. R. Liou, W. Y., Kuo, “Optimizing a hybrid mortar for an alkali-activated material using Taguchi–Grey relational analysis of paper production wastes,” *Case Studies in Construction Materials*, e02116, 2023.
- [33] S. V. Dave, A. Bhogayata, “The strength oriented mix design for geopolymer concrete using Taguchi method and Indian concrete mix design code,” *Construction and Building Materials*, vol. 262, 120853, 2020.
- [34] C. Y. Chang, R. Huang, P. C. Lee, T. L. Weng, “Application of a weighted Grey-Taguchi method for optimizing recycled

- aggregate concrete mixtures,” *Cement and Concrete Composites*, vol. 33, no. 10, pp. 1038–1049, 2011.
- [35] N. C. Sukmana, M. I. Khifdillah, A. S. Nurkholil, U. Anggarini, “Optimization of non-autoclaved aerated concrete using phosphogypsum of industrial waste based on the taguchi method,” *IOP Conference Series: Materials Science and Engineering*, vol. 509, 012095, 2019.
- [36] H. J. Chen, H. C. Lin, C. W. Tang, “Application of the Taguchi method for optimizing the process parameters of producing controlled low-strength materials by using dimension stone sludge and lightweight aggregates,” *Sustainability*, vol. 13, no. 10, 5576, 2021.
- [37] M. Alhawat, A. Ashour, G. Yildirim, A. Aldemir, M. Sahmaran, “Properties of geopolymers sourced from construction and demolition waste: A review”, *Journal of Building Engineering*, vol. 50, 104104, 2022.
- [38] C. L. Wong, K. H. Mo, U. J. Alengaram, S. P. Yap, “Mechanical strength and permeation properties of high calcium fly ash-based geopolymer containing recycled brick powder,” *Journal of Building Engineering*, vol. 32, pp. 1–11, 2020.
- [39] N. Youssef, A. Z. Rabenantoandro, Z. Dakhli, C. Chapiseau, F. Waendendries, F.H. Chehade, Z. Lafhaj, “Reuse of waste bricks: A new generation of geopolymer bricks,” *SN Applied Sciences*, vol. 1, pp. 1–10, 2019.
- [40] A. Uğur, E. Nas, H. Gökkaya, “Investigation of the machinability of SiC reinforced MMC materials produced by molten metal stirring and conventional casting technique in die-sinking electrical discharge machine,” *International Journal of Mechanical Sciences*, vol. 186, 105875, 2020.
- [41] P. Delgado-Plana, A. García-Díaz, S. Bueno-Rodríguez, D. Eliche Quesada, “Influence of NaOH molarity and Portland cement addition on performance of alkali activated cements based in silicomanganese slags”, *Construction and Building Materials*, vol. 407, 133544, 2023.
- [42] P. Delgado-Plana, A. García-Díaz, S. Bueno-Rodríguez, D. Eliche Quesada, “Influence of NaOH molarity and Portland cement addition on performance of alkali activated cements based in silicomanganese slags”, *Construction and Building Materials*, vol. 407, 133544, 2023.
- [43] Z. Yahya, M. M. A. B. Abdullah, K. Hussin, K. N. Ismail, R. A. Razak, A. V. Sandu, “Effect of solids-to-liquids, Na₂SiO₃-to-NaOH and curing temperature on the palm oil boiler ash (Si + Ca) geopolymerisation system”, *Materials*, vol. 8, pp. 2227-2242, 2015.

Developing and Implementing an IoT Managed by Electronic Devices for Covid Patient Monitoring via a Secured Communication System

Alaa Hussein Abdulaal¹ , A. F. M. Shahan Shah^{2*} , Muhammet Ali Karabulut³ 

¹ Al-Iraqia University, Department of Electrical Engineering, Iraq, engineeralaaahussein@gmail.com

^{2*} Yildiz Technical University, Electronics and Communication Engineering, İstanbul, Türkiye, shahan.shah@hotmail.com

³ Kafkas University, Electrical and Electronics Engineering Department, Kars, Türkiye, karabulutmali@gmail.com

*Corresponding Author

ARTICLE INFO

ABSTRACT

Keywords:
Communication system
Covid 19
IoT
Microcontroller
Sensors

End of 2019 had seen global spread of the deadly coronavirus (SARS-CoV-2) pandemic, which kills people, puts a large portion of the world in danger, and poses a serious threat to all of the world's nations. Leading medical professionals are working extremely hard to identify the virus, develop treatments for it, and create the vaccines that are required to stop and limit its spread. This study intends to develop a low-cost electronic health system to observe patients with covid infections and lessen the work required of clinicians. An enhanced approach for remote health monitoring in hospitals or detention facilities is offered by the internet of things (IoT). The IoT keeps and displays the patient's medical data via a web browser or through specialized apps that offer remote treatment once the sensors collect it. When a patient is in danger, the system offers immediate action to send alarms by email and SMS and to rapidly provide drugs to the patient. Doctors will be updated on each patient's condition thanks to this message.

Article History:

Received: 24.11.2022

Accepted: 10.11.2023

Online Available: 27.02.2024

1. Introduction

More than 213 nations throughout the world were affected by the coronavirus (COVID 19), which spread quickly and became a highly hazardous outbreak. More than 23 million cases have been officially stated to the world health organization (WHO), and over 800,000 individuals have passed away as a result [1, 2]. The global economy, public health, and several other facets of daily life are now at risk due to the emergence of the coronavirus. Frequently, COVID 19 produces lung issues that first manifest as respiratory signs that might turn into pneumonia, which rapidly worsens the patient's clinical condition. Three classifications of COVID 19 infection severity exist: mild infection, high-risk

(fatal) infection, and infection without clinical signs [3].

The worldwide threat posed by the coronavirus epidemic to healthcare systems makes it more difficult to treat individuals who are not directly affected by the virus pandemic but who still have health issues that are unrelated to this epidemic. Patients who are admitted to the hospital in critical condition are quarantined from the injured based on the severity of their Coronavirus infection. To relieve the strain on hospitals, patients with minor symptoms were instead sent home to receive care. However, in these circumstances, medical intervention is not necessary until the patient's condition rapidly deteriorates.

One of the most important things to consider when fighting the virus is how to improve healthcare delivery methods and develop medical platforms to observe patients distantly as well as sustain the health of medical workforce and healthcare service providers. Decreased direct patient contact also helps to stop the epidemic from spreading. The next generation health monitoring and controlling technologies created by current technology makes it necessary to move healthcare from hospitals to homes or detention facilities in order to give medical gadgets to patients who need them most.

Medical technology advancements, including sensors and remote monitoring, provide patients control and offer doctors a viable way to combat the COVID 19 outbreak. Due to the low cost of its component parts, which encourages the development of more innovative technologies, internet-connected devices provide enormous promise for the transition to remote medical care. There are several devices and sensors that make up the Internet of Things (IoT) [4]. Today, health care is seen as a crucial concern due to the possibility of clinical collapse. A patient is remotely monitored via the IoT when they are admitted to a hospital or a place of quarantine, and their anxious family is also kept informed at all times of the patient's status.

Monitoring is done at a minimal cost with Raspberry Pi and IoT using a collection of sensors. The suggested system gauges body movement, heart rate, temperature, blood pressure, and blood oxygenation. The medical staff's burden is reduced, and physicians' lives are also preserved since they can monitor numerous patients at once thanks to the capacity to transmit information instantaneously, particularly when they are at the top of their profession and more susceptible to harm. By communicating with the patient's family, the medical system can work preventing from collapsing.

On the other side, we can accomplish this utilizing the IoT' sensor platform. We have created a health monitoring system to keep tabs on patients and communicate data to the accountable medical professionals via remote monitoring. In order to do this, a microcontroller gathers health data from the sensors, sends it to the cloud, and then displays it on PCs and mobile

applications while following a security policy to safeguard patient information. The body area system, which is run by a Raspberry Pi and features a special upgraded communication for low-energy sensors, aims to give comprehensive patient information.

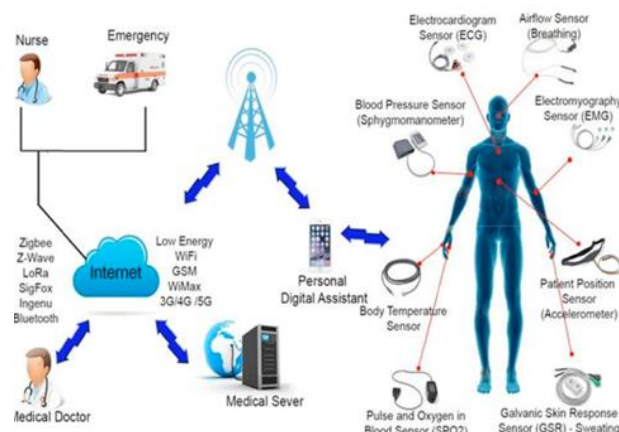


Figure 1. Application scenarios of wearable sensor [5]

Monitoring a variety of accessible physiological parameters such as respiratory parameters, blood oxygen saturation (SpO₂), heart rate, blood pressure, and body temperature via wearable devices and unobtrusive sensing can also provide more accurate alerts to anomalous physiological changes, which can potentially identify deteriorating health or the onset of serious medical problems. It has the potential to be used to continuously monitor personal health at home, public places, residential care, or hospitals, with application scenarios including providing screening and real-time triage of patients with suspected infection, monitoring diagnosed patients with mild severity while in isolation, and enabling real-time health surveillance of patients in improvised hospital and established hospital settings. Figure 1 depicts a non-exhaustive list of application possibilities.

During the COVID-19 pandemic, wearable technologies and unobtrusive sensing, in conjunction with telemedicine, can monitor COVID-19 symptoms and warning signals, allowing health care clinicians to remotely monitor a patient's health over time. This will enable better management through early diagnosis and monitoring of coronavirus symptoms, reducing the requirement for face-to-face contact even further. If symptoms appear, the data supplied through the secure cloud

platform can enable healthcare authorities to implement effective general population triage, such as quarantining patients, transferring them to care home facilities, or managing high-risk people in their own homes.

2. Materials and Methods

2.1. Related works

One of the most crucial variables causing sudden infant death syndrome, a febrile complication, is an unexpected rise in the baby's temperature during sleep. In [6,] an IoT-based infant monitoring mechanism, specifically a smart cradle structure, is offered, which records the baby's real-time temperature, heart rate, wetness, and sound, and the data obtained from the sensors will be uploaded to a web platform over Wi-Fi and verified in real-time. In the event of weeping, the cradle will swing on its own. If the sobbing does not cease or if there is an abnormal increase in the detected body temperature, heart rate, or humidity level, the alert will sound.

It is critical to improve the standards of the data set for efficient big data management, and filtering methods are being developed for a higher quality data set. Using data cleaning procedures, for example, is a preprocessing approach that simplifies data mining processes. By limiting the production of interference, more controllable data is generated, and large data may be managed more successfully. In [7], we look into the effective operation of IoT and massive data generated by the IoT. Furthermore, real-time anomalous data filtering is conducted on IoT edges using a data collection comprised of six separate real-time data sets.

[8] demonstrated wearable sensor and telemedicine technologies for using covid patients. The usage of sensors and remote health caring systems to tackle the coronavirus epidemic was mentioned in the article. Making healthcare systems portable, they also strive to decrease patient-medical staff interaction to halt the transmission of illness and ensure the security of medical personnel. The use of telemedicine in the battle against COVID 19 is extremely promising [8]. In light of COVID 19, researchers and developers have a definite interest in mobile health and the usage of mobile health apps. Its

excellent and promising outcomes are starting to be adjusted by medical professionals for wider use. [9] planned COVID-19 Pandemic sensors and new technology.

The development and adoption of technologies that can track patients with the newly emergent covid were reviewed and addressed [9]. Figure 1 presents Application scenarios of wearable sensors. An IoT-based patient monitoring system utilizing electrocardiogram (ECG) sensor has been suggested by [10]. Their study covered an ECG sensor-based remote patient monitoring system. It has been proposed to use a mobile health system that can be remotely operated to monitor the patient using an ECG sensor. These datas are transmitted to the cloud which can be accessed by doctors and can track the patient's health, and notify them of any potential health worsening [11].

A real-time health monitoring system that is IoT based was introduced in [11]. The proposed research uses a collection of sensors using mobile and web applications to control the patient's situation. In order for caregivers and medical experts to access the database, provide guidance, and mitigate any harmful effects, data are collected and created [10]. An IoT-based emergency health monitoring system has been proposed by [10]. In addition to gathering information on the patient's temperature, pulse, and number of heart beats per minute, the article suggests a health system that would enable the doctor to inform and keep tabs on the patient's health state every few seconds [12].

[13] makes the suggestion of a health monitoring system that is based on the IoT. This research describes a cost-effective technology for continuous health monitoring and detection of human body fluctuation. During the study, pulse rate, humidity, and temperature were observed using sensors. The data was saved in the cloud after comparing the sensor results to the predefined value. Then, with the aid of the cloud and Node MCU, sends an alarm message to the user or doctor for health fluctuations when the value goes above the predefined value.

The results of the experiment suggest that a health monitoring device is a more convenient and reliable way to identify changes in the human body in a short period of time [13]. [14] have

proposed an IoT based system for health care tracking and monitoring. An IoT is nothing more than the connection of sensors connected to different things to the internet in order to send data to the internet and to make use of data already accessible on the internet. The link has a lot of potential for improving human health.

Each individual is helped to maintain his or her physical well-being by the various equipment that is available. The primary goal of this study was to provide a complete overview of IoT applications in medical care, as well as to report on the wide variety of gadgets and tools that are already available and planned. We have prioritized both research and commercial devices in our survey article in order to explore and investigate present and future technology [14].

A health monitoring system for remote patient has been proposed by [15] which is also IoT-based. With the use of sensors, the proposed system can keep tabs on patients' basic vitals such their body temperature, blood pressure, pulse rate, and ECG data at home or at other places. The user may remotely monitor the patient's current state from any location, with the caveat that the user must have internet access to get real-time information about the patient. The suggested concept would be tremendously beneficial to society and would complement current health monitoring technologies [15].

[16] has proposed a wearable health monitoring device. A wearable health monitoring gadget was presented in this proposal, which would be especially helpful for those with Parkinson's disease. This system offers a thorough way for heart rate monitoring, real-time showing, collecting historical data, and sending crucial data to a mobile phone, in contrast to other options that are now accessible. Other capabilities include step counting, aberrant gesture detection, and falling detection, as well as the ability for users to design their own anomalous gestures and be taught off-line [16]. Figure 2 depicts wearable pulse oximeters.



Figure 2. Wearable pulse oximeters [8]

2.2. Physiological measurements

In this section, different measurements systems will be described. Vital indicators such as oxygen saturation, respiratory rate, heart rate, blood pressure, temperature, glucose, ECG, galvanic skin response (GSR), and body posture are utilized to evaluate the health state of COVID 19 patients.

2.2.1. Oxygen saturations (SPO₂)

One of the fundamental elements for maintaining life is oxygen. A significant sign of the newly developing covid illness is an oxygen deficiency. It refers to how much saturated hemoglobin is present in the blood. Inflammation of the lung's air sacs brought on by COVID 19 impairs oxygen delivery to the blood and harms the lungs [17]. When a patient has respiratory issues, their proportion of Spo₂ falls from 95% to 99%, which is the range for a healthy individual. A key indicator for identifying people with coronaviruses is oxygen saturations.

People with spo₂ levels of over 94% may be able to get home health care, according to the WHO [3]. According to this study, a COVID patient who have a percentage of less than 93% should be hospitalized [18]. Less than 90% of patients had a higher mortality rate [19]. To preserve patients' health and prevent any potential health deterioration, continuous monitoring of oxygen saturation hemoglobin is crucial. It can save a lot of lives, principally as it is portable and available

in any home, mainly in underdeveloped nations [20, 21].

The basis for how pulse oximetry devices operate is optical imaging, or the degree to which arterial blood volume alters light absorption. The oxygen gadget, which is often worn on the finger, has an LED and an infrared beam. The ratio is estimated once the wavelengths are identified based on how much oxygenated and non-oxygenated hemoglobin absorbs each of the two light wavelengths. De-oxy and oxyhemoglobin (HBO₂) are the two kinds of hemoglobin found in red blood cells [22].

2.2.2. Respiratory rate

The respiratory rate (RR) is a crucial marker for managing COVID-19 patients because it may accurately and quickly anticipate conditions like hypoxia (low oxygen levels) and elevated blood carbon dioxide levels. The main determinant of respiratory illness is RR. Additionally, a characteristic of a COVID patient is respiratory rate. Studies on sars-cov-2 patients in Wuhan, China, revealed that 63% of those who passed away from the covid had a greater RR (54) per minute [22]. Therefore, monitoring the evolution of covid and identifying any potential worsening to mediate in a timely way to deliver therapeutic therapy is made feasible by utilizing the IoT to measure the respiratory rate.

There are three techniques to monitor respiratory rate using the IoT:

- By sensing factors such as temperature and carbon dioxide, and then calculating the quantity of respiratory airflow.
- Breathing is accompanied by a sonic and bodily experience of mechanical stress, in the form of respiration and concomitant chest and abdominal motions.
- Based on the modifying impact of breathing on respiratory arrhythmia (RSA) signals, as well as other cardiovascular signals such as the ECG and Photoplethysmography (PPG). Thermal, acoustic, humidity, pressure, resistance, acceleration, inductance, resistance, and electromyography are examples of technologies. These sensors can be found in wearable devices that can be strapped to the chest [23-26], or put on the skin [18, 27].

2.2.3. Airflow

The basis for the airflow approach is Exhaled air is hotter, more humid, and contains more carbon dioxide than inhaled air. According to it, the amount of carbon dioxide and temperature change are used to calculate the respiratory rate. The nose's airways serve as a sensor for the airflow sensor's basic design. The sensor, which is a thermostat in the mouth or nose, determines the quantity of carbon dioxide and humidity present during inhalation and exhalation. It has been stated that a high-sensitivity respiratory sensor is capable of detecting various breathing patterns [18]. According to reports, a multi-air flow sensor electrolyte that can be utilized with a face mask in a COVID -19 scenario has also been created [28]. Figure 3 shows an airflow sensor.

The average healthy adult breathes between 12 and 20 times each minute. This percentage varies based on the patient's health, with low or high respiratory rates indicating a larger or lesser requirement for oxygen, respectively. A serious decline in the patient's health is also indicated by a drop in RR to 9 per minute or less.

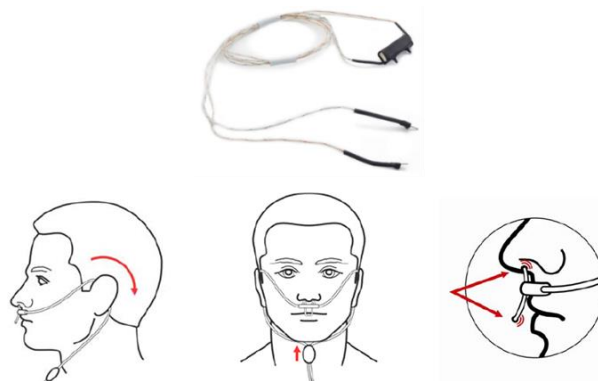


Figure 3. Airflow sensor [29]

2.2.4. ECG for monitoring COVID patients

By observing the heart's actions, the ECG equipment carries out the process of assessing the muscular and electrical function of heart. One of a person's vital signs, it is. Monitoring heart activity has become essential for individuals with cardiovascular issues, particularly with COVID 19 patients. Patients with COVID 19 have reportedly had a considerable alteration in their ECG signals and an increased heart rate [30]. Cardiac functions must be regularly checked in order to avoid any worsening in the patient's

health [31]. The IoT-based ECG sensor also lessens direct patient-doctor contact and guards against dangerous infections. The portable ECG gadget has three ends, each attached to the patient's chest with a circular adhesive and connecting cables. The proposed sensor is quite convenient and cozy to use. The ECG is one of several items that the Food and Drug Administration has approved for use in COVID 19 patient monitoring [32]. Figure 4 presents an ECG sensor.



Figure 4. ECG sensors

2.2.5. Body temperature

It is an essential sign of a healthy physique. By keeping an eye on the temperature, we can determine whether a patient has a fever with precision. In heavily packed public spaces like airports and subway stations, thermal scanning devices such as infrared scanning were utilized during the COV-SARS-2 virus epidemic. As a result, the suggested temperature monitoring device can track changes in body temperature since it can quickly identify individuals with high temperatures who may be infected with the virus [32], particularly those without symptoms who may be treated remotely. In Figure 5, a temperature sensor is shown.



Figure 5. Temperature sensor [31]

2.2.6. Blood pressure monitoring

Blood pressure is a warning sign for heart patients and is thought to be the cause of 10 million deaths globally [33]. It is a reflection of the condition of the heart and blood arteries. According to studies and research done on 5800

Corona epidemic patients, high blood pressure is also a disorder that affects the patient (3090 out of 5800, with a rate of more than 57%) [34]. Recent studies that involved 44,900 patients found that persons with high blood pressure (6.1%) and heart disease (11%) had higher death rates than patients without heart issues (1%) [35].

Blood pressure has been monitored during the previous century using the traditional method, which necessitates the face-to-face presence of medical personnel. However, as the coronavirus outbreak expanded, more patients asked for blood pressure monitors. This put a great deal of strain on medical personnel and raised the danger that they would become infected with the COVID 19 virus, which is extremely infectious. Therefore, we can monitor and supply the medical personnel with the most recent information by using IoT technology and certain wearable sensors. This will result in better blood pressure management related to the coronavirus. A blood pressure sensor is presented in Figure 6.



Figure 6. Blood pressure sensor

2.2.7. GSR

Galvanic skin reaction is what it is. Strong emotions activate the sympathetic nervous system, which causes the sweat glands to release perspiration and allows for the measurement of the skin's electrical conductivity. As seen in Figure 7, linking the polarity of the fingers allows for the monitoring of emotions.



Figure 7. GSR sensor

2.2.8. Glucose

It is a tool for measuring and keeping track of blood glucose levels. A single-use test strip is used to collect a sample of the patient's blood, and after some time, the result is shown, as shown in Figure 8.



Figure 8. Glucose sensors [36]

2.2.9. Body position

The patient is continually monitored, as shown in Figure 9, and the body position sensor is put around the chest to detect the form of the body, for instance (standing, lying down, laying left, right, down). A body position sensor is shown in Figure 10.

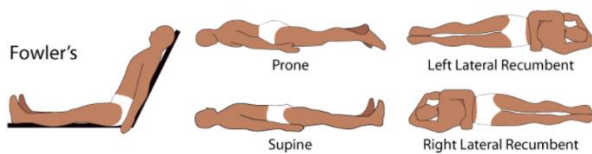


Figure 9. body position



Figure 10. Body position sensor

2.3. Design and working methodology

Before attaching the sensors to the microcontroller device, we'll need a health sensor shield to connect them all together, including the blood pressure sensor, pulse sensor, temperature sensor, oxygen sensor, sugar sensor, and motion sensor (Raspberry Pi or Arduino). After being gathered from the patient by sensors, data is transferred by Wi-Fi or GSM to the database where it is stored. The doctor may obtain the information remotely using a smartphone or

computer device. System work flow is presented in Figure 11.

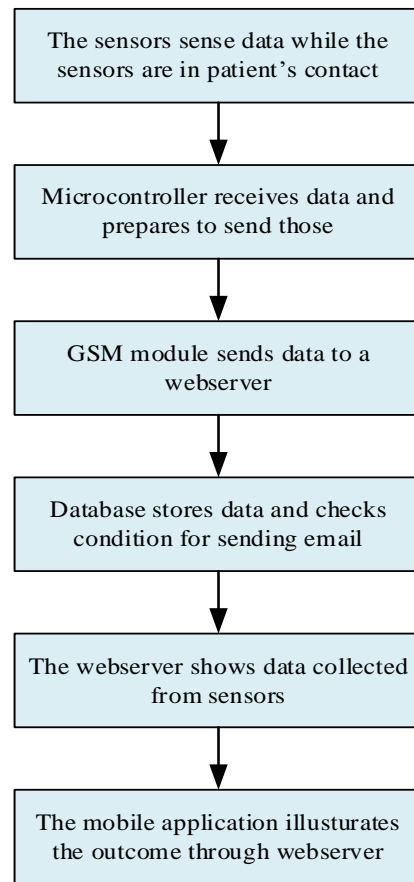


Figure 11. System work flow

2.3.1. System model

The proposal suggests a system in which information is gathered from sensors and delivered to the microcontroller, which then transmits vital signs to the cloud through Wi-Fi or GSM, where a database is produced and saved for use by smartphone and computer devices. System model is presented in Figure 12. Table 1 presents measurement levels of monitoring patients with COVID 19 using wearable technologies.

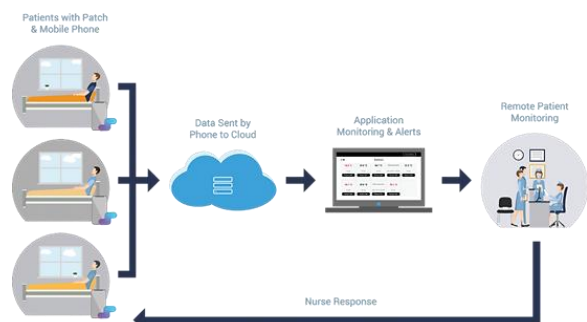


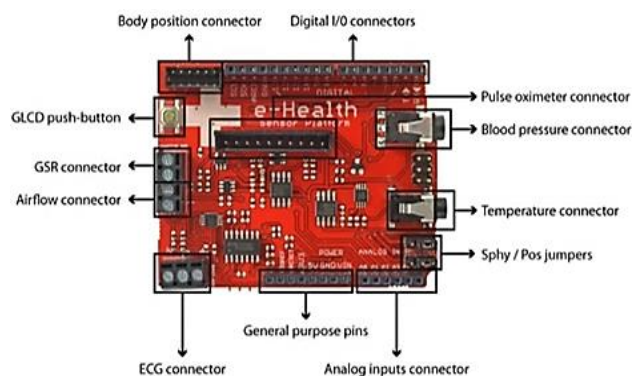
Figure 12. System model

Table 1. Monitoring patients with covid-19 using wearable technologies [8]

Measurements	Warning levels for COVID 19	Normal levels
Oxygen Saturation (SPO2)	< 90 %	95-98 %
Respiratory Rate (RR)	< 25 ppm	12 – 25 ppm
Body temperature	> 100 °F	97.7 – 99.5 °F
Heart Rate (HR)	> 120 < 60	60 – 120 bpm
Blood Pressure	> 120 mmHg systolic > 80 mmHg diastolic	<80 / <120 mmHg
Glucose	> 144 mg/dl < 72 mg/dl	72 – 144 mg/dl
GSR	> 7.0 μ s < 2.0 μ s	2.0 – 7.00 μ s

2.3.1.1. E-health sensor platform shield

As seen in Figure 13, an electronic circuit was created that can control all the sensors at once. The Raspberry Pi is used to collect data from the sensors, which include the glucometer, ECG, body temperature, GSR, airflow (breathing), pulse, SPO2, and patient position (accelerometer).

**Figure 13.** e-health sensors

2.4. Telemedicine technology

Even if e-health and telemedicine are not still in their infancy, they are crucial initiatives in the war against SARS-CoV-2 [37]. Many healthcare systems throughout the world, particularly those in nations with highly developed medical infrastructure like the United States, have declined as a result of Covid-19's fast

proliferation [37]. It is now crucial to design and implement a health system which embrace telemedicine technology and implement the mobile digital system [38].

Through the use of video medical care (videoconferencing services), telemedicine, mobile health, and wearable medical sensors outfitted with IoT and neural networks (NN) technology and big data analysis, can advance dramatically [39]. Additionally, by following up, keeping tabs on patients' health, and delivering the right care remotely.

Reducing the danger of direct patient contact, slowing the transmission of viruses, and preventing the collapse of the medical system due to high infection rates are significant advantages of telemedicine and mobile digital system. The United States of America is one of the nations that has shifted its medical practices to telemedicine [37]. It advised performing remote medical examinations, minimizing direct patient interaction, cutting back on the amount of time needed, and hiring fewer physicians.

This section will highlight cutting-edge telemedicine and mobile health technologies that can treat the newly developing Coronavirus. The focus will be on treating individuals suspected of having the Corona Virus, providing treatment, and utilizing telehealth technologies. Finally, we'll offer an exemplary medical sensor platform that can handle a variety of data.

i. E-Health Monitoring of SARS-CoV-2

Smart devices and wearable sensors are supported by the health platform known as Mobile Health [40]. The suggested system is divided into 3 primary components:

- 1- Wearable sensors for the purpose of gathering the needed data.
- 2- A network with the purpose of sending the gathered data to the main station monitoring, which functions as a central computer.
- 3- A cloud whose job it is to evaluate the sensor-generated data and make use of the valuable information.

The technology can trace infected individuals' interactions and deliver essential medical treatment.

ii. Contact tracking technology

The most crucial tactic for limiting the transmission of the virus is contact tracking [40]. Quarantine, isolation of people infected, and social estrangement will continue to be the most crucial elements in curbing the epidemic's spread in the absence of effective treatment and a vaccine [41]. To stop the spread of the illness, remote surveillance and infection tracking are helpful [42].

To stop the disease from spreading, a contact tracking tool that compiles a list of contacts can inform those individuals. Security issues pertaining to user privacy are brought up by the practice of gathering data from mobile devices from individuals on a broad scale. A peer-to-peer contact tracing normalization has been created to address this issue, employing Ysak's encryption of user identification to protect user privacy in the event of a pandemic [43].

Using bluetooth technology, Google. and Apple have created a contact tracing application that exchanges signals without disclosing the user's identify or sharing data. Users who were in contact with a suspected and diagnosed case can receive notifications from the system [44].

iii. Remote monitoring physiological

It is feasible to transfer treatment from the hospital to the home using the COVID19 mobile health platform, particularly for patients with minor wounds and those with various illnesses who run the risk of contracting an infection from interacting with other patients. Medical instruments like those connected with a temperature sensor platform, blood pressure sensor, and the percentage of oxygen are needed to monitor the patient's health in addition to the very necessary portable ECG equipment to check the patient's tachycardia difficulties.

The mobile medical platform, which depends on a collection of remotely collected sensors, cannot take the role of specialist medical professionals, but it may be a helpful tool in making judgments about treatment that enable the medical unit to act quickly.

iv. Remote imaging

One of the major clinical indicators of COVID 19 illness is acute pneumonia connected with SARS-CoV-2, where medical imaging plays a

crucial role in observing and identifying the condition. COVID 19 disease has the potential to harm the organs and tissues of patients. The medical unit receives the findings of the MRI and CT scans for remote diagnosis. Figure 14 shows portable medical imaging devices.



Figure 14. Portable medical imaging devices [45-46]

There are several medical imaging systems, such as remote x-ray, remote ultrasound, and tomography, that process pictures utilizing neural network methods (artificial intelligence). People who are infected by the virus may be able to receive a CT picture by using a mobile medical imaging center, provided that remote clinicians make the diagnosis and the outcomes and images are preserved in the cloud [45–47].

2.5. Data encryption

The IoT is widely used in telemedicine and medical care. As a result, the IoT came into focus. This provided a significant possibility for growth and higher productivity, which in turn boosted quality as it applied to the delivery of medical treatment for Corona virus patients.

Remote medical treatment is becoming one of the most important components of life, not only for COVID affected people but also for everyone with a chronic condition and the elderly. This is due to the fact that managing, diagnosing, and treating patients remotely is now feasible, saving time and effort while also safeguarding the staff's health.

One of the primary obstacles preventing the IoT and mobile health platforms is the growing user concern over privacy and security due to the worry of harmful attacks and privacy violations [45]. Therefore, there is a pressing need for

greater study in the area of user protection and information security.

Data encryption and app security are required to protect patient data. One of the biggest issues for mobile health apps and cloud services is dealing with security concerns such as patient privacy violations, illegal access, and the manipulation of critical cloud data. We'll go through the two most crucial mobile health safety standards: [48, 23].

- i. Authentication: Using one of the encryption techniques, proving the user's identity and confirming it with the medical professionals if the user is ill.
- ii. Authorization: Following the user's identification has been confirmed, this is the next stage. Depending on the privileges granted to each party, access rights are dispersed.
- iii. Non-repudiation: By employing a unique encryption platform and maybe distinctive symbols or signatures, it confirms that the sender of the communication actually transmitted it.
- iv. Integrity and confidentiality make sure that the message is only viewed by the intended recipient and that the transmission is private.

For a cloud-based mobile health system, a four-layer structure is suggested, each of which is interconnected.

- First layer: It include users in general, such as patients, technicians, doctors, and hospital administrators.
- Second Layer: The computers, smart gadgets, and office equipment found in this layer are used to receive, transmit, and display data for the first layer.
- Third layer: Between the first layer and the fourth layer, communication and data transmission are handled by this layer.
- Fourth layer: In this layer, which is used to monitor patients, direct orders, and provide instructions, are hospitals, health centers, and decision-making centers.

An encryption technique with three stages—authentication, data encryption, and decryption—has been developed to secure data and create a secure link between the user layer (first layer) and the communication layer (third

layer). Figure 15 depicts secure framework for IoT-based medical data.

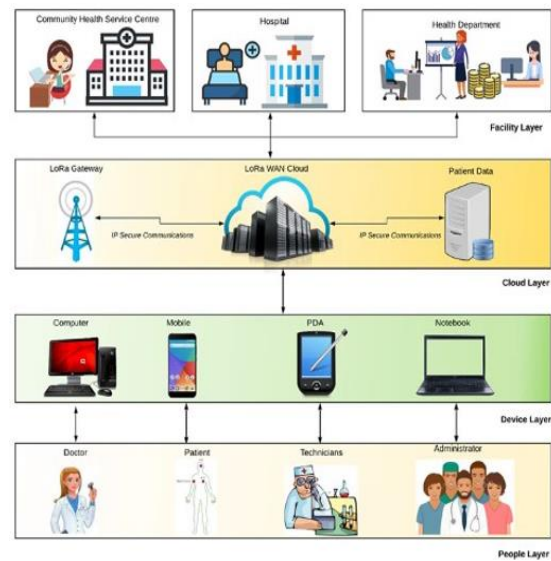


Figure 15. Proposed secure framework for IoT-based medical data [48]

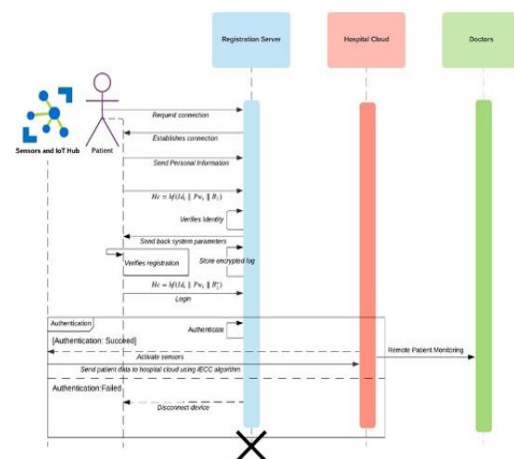


Figure 16. Encryption Scheme [48]

Three processes are involved: data recording, logging in using the entered information, and verification. A user name and password are provided to the user, and all login information is maintained in the cloud. Hash codes are produced using the SHA-512 encryption technique to confirm the patient's identification, and after verification, the sensors are turned on, the e-health platform is engaged, and the data and results are encrypted using Caesar encryption. The text is replaced with the encrypted text as part of the encryption process. Then, an elliptic encryption method is used to further encrypt the data. Figure 16 shows how the cloud sequentially receives encrypted data and starts to decrypt it before assembling it and sending it to the hospital's private layer.

3. Results and Discussion

This study established the use of IoT-driven electronic devices and their integration with secure communication systems for COVID-19 patient monitoring. There are, however, several critical considerations to consider when comparing comparable research. For starters, if IoT devices are unsafe or have flaws, the chance of patients' confidential health data being disclosed increases.

As a result, future research should place a greater emphasis on the security of IoT devices. Furthermore, widespread usage of this technology may result in data management and communication issues between healthcare personnel and patients. As a result of the findings of previous research, appropriate management and user training procedures for IoT-based COVID-19 patient monitoring systems must be established. In conclusion, while this study indicates the promise of IoT technology for monitoring COVID-19 patients, it also underlines the importance of future research on security and data management. Moreover, after the implementation of 5G, a lot of IoT based applications will be available [49].

3.1. Analysis of the results for body temperature

The average body temperature for adults is 98.6 degrees Fahrenheit, with a 24-hour range of 0.5 degrees Celsius (0.9 degrees Fahrenheit). Table 2 and Figure 17 show the body temperature rates and outcomes, respectively.

Table 2. Body temperature rates

Normal	36.5–37.5 °C (97.7–99.5 °F)
Hypothermia	<35.0 °C (95.0 °F)
Fever	>37.5–38.3 °C (99.5–100.9 °F)
Hyperpyrexia	>40.0–41.5 °C (104–106.7 °F)

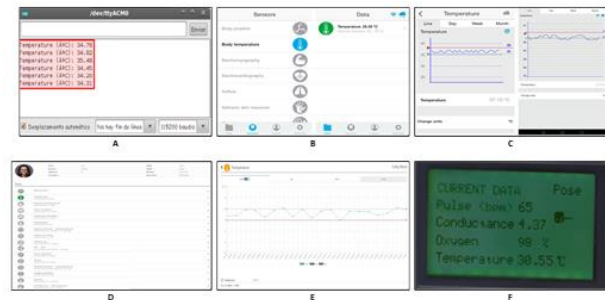


Figure 17. Body temperature results: (a) in serial monitor; (b) in mobile application; (c) waves in the mobile application; (d) in web server; (e) waves in web server; (f) in GLCD

3.2. Analysis of the blood oxygen and pulse test results (SPO2)

Normal rates are between 94% and 99% for healthy individuals, but they fall to 85% or less for COVID 19 patients and patients who are oxygen deficient because the virus targets the patient's respiratory system, which lowers the oxygen level. Figure 18 shows Spo2 results.

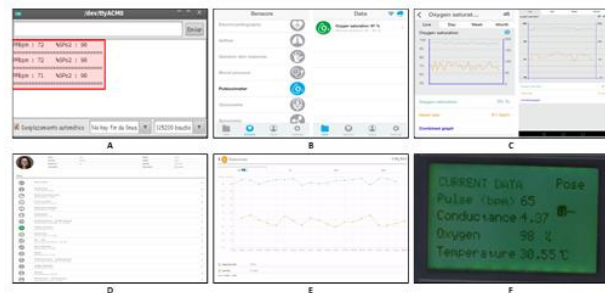


Figure 18. Spo2 results: (a) in serial monitor; (b) in mobile application; (c) waves in the mobile application; (d) in web server; (e) waves in web server; (f) in GLCD

3.3. Analysis for electrocardiogram (ECG)



Figure 19. ECG Schematic

One of the most vital medical devices for diagnosing and determining the functionality of the heart is the ECG machine. ECG system and

results can be depicted in Figure 19 and 20, respectively.

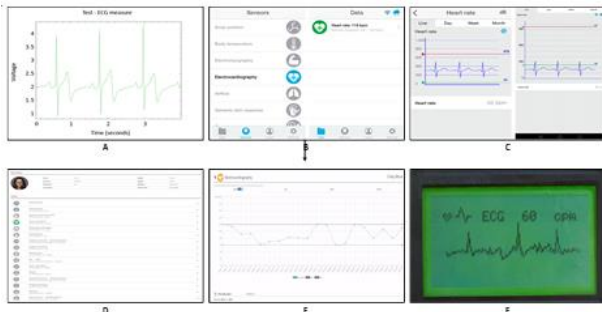


Figure 20. ECG results: (a) in serial monitor; (b) in mobile application; (c) waves in the mobile application; (d) in web server; (e) waves in web server; (f) in GLCD

3.4. Analysis for airflow: Breathing sensor

The newest findings on COVID 19 sickness reveal a shift in respiratory rates as a result of the harm the virus does to the human body, making the respiratory index one of the key indicators of a person's overall health. Airflow results are shown in Figure 21.



Figure 21. Airflow results: (a) in serial monitor; (b) in mobile application; (c) waves in the mobile application; (d) in web server; (e) waves in web server; (f) in GLCD

3.5. Analysis for blood pressure

One of the most important markers of a patient's health is their blood pressure, which is not always steady due to changes in patient's posture, stress levels, and psychological state due to COVID 19 pandemic, especially in patients who have chronic illnesses. Table 3 and Figure 22 show a system for classifying blood pressure and blood pressure results, respectively.

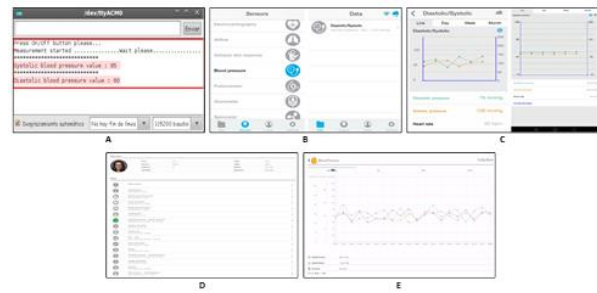


Figure 22. Blood pressure results: (a) in serial monitor; (b) in mobile application; (c) waves in the mobile application; (d) in web server; (e) waves in webserver

Table 3. A system for classifying blood pressure

Bp	Systolic	Diastolic
Ordinary	<120	and <80
High blood pressure	>119 – <140	81–90
Step 1: Hypertension	>141 – <160	91 –98
Step 2: Hypertension	>161	>100

3.6. Analysis for glucometer

It is the level of blood glucose concentration. On the single-use test strip, we place a drop of blood, and then we insert the strip into device. Figure 23 shows glucometer results.

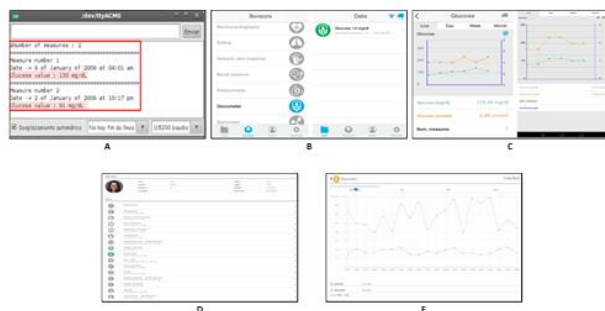


Figure 23. Glucometer results: (a) in serial monitor; (b) in mobile application; (c) waves in the mobile application; (d) in web server; (e) waves in the web server

3.7. Analysis for galvanic skin response (GSR)

The quantity of moisture affects measurement of the skin's electrical conductivity sensor. When skin's electrical resistance varies, the sweat gland regulates the sympathetic nervous system to keep track of the stress. Figure 24 shows GSR results.



Figure 24. GSR results: (a) in serial monitor; (b) in mobile application; (c) waves in the mobile application; (d) in web server; (e) waves in web server; (f) in GLCD

3.8. Analysis for body position

The location of the item is determined using a 3-axis accelerometer (sitting, standing, lying down, prone). Figure 25 shows body position results.



Figure 25. Body position results: (a) in serial monitor; (b) in the mobile application; (c) waves in the mobile application; (d) in web server; (e) waves in web server; (f) in GLCD

4. Conclusion

We provided a thorough real-world picture of wearable sensors and remote medical treatment during the Corona Epidemic in this study. By moving direct care to far-flung locales, it helps ease the strain on medical facilities (i.e., transferring care from the hospital to the home). With the help of the telehealth center, it is possible to keep an eye on patients, make quick diagnoses, and take action to stop any potential worsening and minimize contact between medical professionals and patients. As a result, it will be used to treat epidemics in the future, particularly COVID 19. While wearable devices and telehealth offer tremendous potential to help improve the management of infectious diseases such as COVID-19, overcoming some of the challenges to enable more widespread adoption remains a key concern. Some promising aspects

of the development and introduction of wearable devices, unobtrusive sensing, and telehealth will be studied for future research and applications. Moreover, artificial intelligence-based software will be developed as future work.

Article Information Form

Funding

The authors have no received any financial support for the research, authorship or publication of this study.

Authors' Contribution

The study is done by Alaa Hussein ABDULAAL for his M.Sc. degree from Istanbul Gelisim University under the supervision of A. F. M. Shahan SHAH. Muhammet Ali KARABULUT contributes to writing and editing the manuscript.

The Declaration of Conflict of Interest/ Common Interest

The authors have not disclosed any conflicts of interest or common interests.

The Declaration of Ethics Committee Approval

This study does not require ethics committee permission or any special permission.

The Declaration of Research and Publication Ethics

The authors of the paper declare that they comply with the scientific, ethical and quotation rules of SAUJS in all processes of the paper and that they do not make any falsification on the data collected. In addition, they declare that Sakarya University Journal of Science and its editorial board have no responsibility for any ethical violations that may be encountered, and that this study has not been evaluated in any academic publication environment other than Sakarya University Journal of Science.

Copyright Statement

Authors own the copyright of their work published in the journal and their work is published under the CC BY-NC 4.0 license.

References

- [1] Y. N. Mi, "Estimating instant case fatality rate of COVID-19 in China," International

- Journal of Infectious Diseases, vol. 97, pp. 1-6, 2020.
- [2] G. Onder, "Case-fatality rate and characteristics of patients dying in relation to COVID-19 in Italy," *Jama*, vol. 323, no. 18, pp. 1775–1776, 2020.
- [3] H. Chu, "Comparative replication and immune activation profiles of SARS-CoV-2 and SARS-CoV in human lungs: an ex vivo study with implications for the pathogenesis of COVID-19," *Clinical Infectious Diseases*, vol. 71, no. 6, pp. 1400-1409, 2020.
- [4] A. F. M. S. Shah, M. A. Karabulutand K. Rabie, "Mission-critical internet of things on the 6G network: Services and Apps with Networking Architecture". *TechRxiv*, Sep. 2023, doi: 10.36227/techrxiv.24115869.v1.
- [5] K. Qian, Z. Zhang, Y. Yamamoto, B. W. Schuller, "Artificial intelligence internet of things for the elderly: From assisted Living to health-care monitoring," *IEEE Signal Processing Magazine*, vol. 38, no. 4, pp. 78-88, 2021.
- [6] Ü. Duman, E. Aydin, "IOT based baby cradle system with real time data tracking," 5th International Conference on Computer Science and Engineering, Diyarbakir, Türkiye, 2020, pp. 274-279.
- [7] Ş. M. Kaya, A. Erdem, A. Güneş, "Anomaly detection and performance analysis by using big data filtering techniques for healthcare on IoT edges", *Sakarya University Journal of Science*, vol. 26, no. 1, pp. 1-13, 2022.
- [8] X. Ding, "Wearable sensing and telehealth technology with potential applications in the coronavirus pandemic" *IEEE Reviews in Biomedical Engineering*, vol. 14, pp. 48-70, 2020.
- [9] S. S. Kumar, "Emerging technologies and sensors that can be used during the COVID-19 pandemic," *International Conference on UK-China Emerging Technologies*, 2020, pp. 1-4.
- [10] A. Rahman, T. Rahman, N. H. Ghani, S. Hossain, J. Uddin, "IoT based patient monitoring system using ECG sensor," *International Conference on Robotics, Electrical and Signal Processing Techniques*, 2019, pp. 378-382.
- [11] V. Yeri, D. C. Shubhangi, "IoT based real time health monitoring," *Second International Conference on Inventive Research in Computing Applications*, 2020, pp. 980-984.
- [12] M. R. Ruman, A. Barua, W. Rahman, K. R. Jahan, M. Jamil Roni, M. F. Rahman, "IoT based emergency health monitoring System," *International Conference on Industry 4.0 Technology*, 2020, pp. 159-162.
- [13] V. Tamilselvi, S. Sribalaji, P. Vigneshwaran, P. Vinu, J. Geetha Ramani, "IoT based health monitoring system," 6th International Conference on Advanced Computing and Communication Systems, 2020, pp. 386-389.
- [14] S. S. Mishra, A. Rasool, "IoT health care monitoring and tracking: A survey," 3rd International Conference on Trends in Electronics and Informatics, 2019, pp. 1052-1057.
- [15] P. S. Akram, M. Ramesha., S. A. S. Valiveti, S. Sohail, K. T. S. S. Rao, "IoT based remote patient health monitoring system," 7th International Conference on Advanced Computing and Communication Systems (ICACCS), 2021, pp. 1519-1524.
- [16] H. Fei, M. Ur-Rehman, "A wearable health monitoring system," *International Conference on UK-China Emerging Technologies*, 2020, pp. 1-4.
- [17] Y. Shi, "COVID-19 infection: the perspectives on immune responses" *Cell Death & Differentiation*, vol. 27, pp. 1451-1454, 2020.

- [18] Y. Liu, "Epidermal electronics for respiration monitoring via thermo-sensitive measuring" *Materials Today Physics*, vol. 13, pp. 100199, 2020.
- [19] H. Hui, "Clinical and radiographic features of cardiac injury in patients with 2019 novel coronavirus pneumonia" *MedRxiv* (2020).
- [20] G. MacLaren, F. Dale, B. Daniel, "Preparing for the most critically ill patients with COVID-19: the potential role of extracorporeal membrane oxygenation" *Jama*, vol. 323, no. 13, pp. 1245-1246, 2020.
- [21] X. Ding, "Wearable sensing and telehealth technology with potential applications in the coronavirus pandemic" *IEEE Rev Biomed Engineer*, Preprint posted online on May 11 2020.
- [22] F. Zhou, "Clinical course and risk factors for mortality of adult inpatients with COVID-19 in Wuhan, China: a retrospective cohort study" *The Lancet*, vol. 395, no. 10229, pp. 1054-1062, 2020.
- [23] H. Zhang, "Waist-wearable wireless respiration sensor based on triboelectric effect" *Nano Energy*, vol. 59, pp. 75-83, 2019.
- [24] H. Liu, Z. Dingchang, "Clinical Evaluation of stretchable and wearable Inkjet-Printed strain gauge sensor for respiratory rate monitoring at different body postures," *Applied Science*, vol. 10, no. 2, pp.480 , 2020.
- [25] G.-Z. Liu, "Estimation of respiration rate from three-dimensional acceleration data based on body sensor network" *Telemedicine and e-health*, vol. 17, no. 9, pp. 705-711, 2011.
- [26] A. Yamamoto, "Monitoring respiratory rates with a wearable system using a stretchable strain sensor during moderate exercise" *Medical & Biological Engineering & Computing*, vol. 57, no. 12, pp. 2741-2756, 2019.
- [27] M. Chu, "Respiration rate and volume measurements using wearable strain sensors" *NPJ digital medicine*, vol. 2, no. 1, pp. 1-9, 2019.
- [28] J. Dai, "Ultrafast response polyelectrolyte humidity sensor for respiration monitoring" *ACS applied materials & interfaces*, vol. 11, no. 6, pp. 6483-6490, 2019.
- [29] I. Yoshiaki, S. Miyazaki, T. Tanaka, Y. Shibata, I. Kazuo, "Detection of respiratory events during polysomnography nasal oral pressure sensor versus thermocouple airflow sensor" *Practica oto rhino laryngological*, vol. 129, pp. 60-63, 2010.
- [30] J. He, "Characteristic electrocardiographic manifestations in patients with COVID-19" *Canadian Journal of Cardiology*, vol. 36, no. 6, pp. 966-e1, 2020.
- [31] A. N. Kochi, "Cardiac and arrhythmic complications in patients with COVID-19" *Journal of Cardiovascular Electrophysiology*, vol. 31, no. 5, pp. 1003-1008, 2020.
- [32] J. Abbasi, "Wearable digital thermometer improves fever detection" *Jama*, vol. 318, no. 6, pp. 510-510, 2017.
- [33] P. Pragna, "Standardized hypertension management to reduce cardiovascular disease morbidity and mortality worldwide." *Southern medical journal*, vol. 111, no. 3, pp. 133, 2018.
- [34] S. Richardson, "Presenting characteristics, comorbidities, and outcomes among 5700 patients hospitalized with COVID-19 in the New York City area." *Jama*, vol. 323, no. 20, pp. 2052-2059, 2020.
- [35] Z. Wu, J. M. McGoogan, "Characteristics of and important lessons from the coronavirus disease 2019 (COVID-19) outbreak in China: summary of a report of 72 314 cases from the Chinese Center for Disease Control and Prevention" *Jama*, vol. 323, no. 13, pp. 1239-1242, 2020.

- [36] J. Zhang, K. Hoshino, "Molecular sensors and nanodevices: Principles, designs and applications in biomedical engineering" Academic Press, 2018.
- [37] A. C. Smith, "Telehealth for global emergencies: Implications for coronavirus disease 2019" *Journal of telemedicine and telecare*, vol. 26, no. 5, pp. 309-313, 2020.
- [38] S. Keesara, J. Andrea, K. Schulman, "Covid-19 and health care's digital revolution" *New England Journal of Medicine*, vol. 382, no. 23, pp. e82, 2020.
- [39] E. Z. Barsom, "Coping with COVID-19: scaling up virtual care to standard practice" *Nature medicine*, vol. 26, no. 5, pp. 632-634, 2020.
- [40] R. S. H. Istepanian, E. Jovanov, Y. T. Zhang, "Guest editorial introduction to the special section on m-health: Beyond seamless mobility and global wireless healthcare connectivity" *IEEE Transactions on information technology in biomedicine*, vol. 8, no. 4, pp. 405-414, 2004.
- [41] J. Hellewell, "Feasibility of controlling COVID-19 outbreaks by isolation of cases and contacts" *The Lancet Global Health*, vol. 8, no. 4, pp. e488-e496, 2020.
- [42] M. Ienca, E. Vayena, "On the responsible use of digital data to tackle the COVID-19 pandemic" *Nature medicine*, vol. 26, no. 4, pp. 463-464, 2020.
- [43] T. M. Yasaka, M. L. Brandon, R. Sahyouni, "Peer-to-peer contact tracing: development of a privacy-preserving smartphone app" *JMIR mHealth and uHealth*, vol. 8, no. 4, pp. e18936, 2020.
- [44] A. Greenberg, "How apple and google are enabling covid-19 contact-tracing", <https://www.wired.com/story/apple-google-bluetooth-contact-tracing-covid-19>, Access 20/11/2022.
- [45] K. Matsumura, "Cuffless blood pressure estimation using only a smartphone" *Scientific reports*, vol. 8, no. 1, pp. 1-9, 2018.
- [46] F. Shi, "Review of Artificial Intelligence Techniques in Imaging Data Acquisition, Segmentation, and Diagnosis for COVID-19," in *IEEE Reviews in Biomedical Engineering*, vol. 14, pp. 4-15, 2021.
- [47] P. K. Gupta, T. M. Bodhaswar, R. Malekian, "A novel and secure IoT based cloud centric architecture to perform predictive analysis of users activities in sustainable health centres" *Multimedia Tools and Applications*, vol. 76, no. 18, pp. 18489-18512, 2017.
- [48] L. M. R. Tarouco, "Internet of Things in healthcare: Interoperability and security issues," *IEEE International Conference on Communications*, 2012, pp. 6121-6125.
- [49] A. F. M. S. Shah, "A Survey From 1G to 5G Including the Advent of 6G: Architectures, Multiple Access Techniques, and Emerging Technologies," *IEEE 12th Annual Computing and Communication Workshop and Conference*, Las Vegas, NV, USA, 2022, pp. 1117-1123.

Heart Disease Prediction with Machine Learning-Based Approaches

Ayhan Küçükmanisa^{1*}, Zeynep Hilal Kilimci²

^{1*} Kocaeli University, Faculty of Engineering, Department of Electronics and Communication Engineering, Kocaeli, Türkiye, ayhan.kucukmanisa@kocaeli.edu.tr

² Kocaeli University, Faculty of Technology, Department of Information Systems Engineering, Kocaeli, Türkiye, zeynep.kilimci@kocaeli.edu.tr

*Corresponding Author

ARTICLE INFO

ABSTRACT

Keywords:

Heart Disease Prediction
Machine Learning
Artificial Neural Networks
Gradient Boosting



Article History:

Received: 09.06.2023

Accepted: 12.11.2023

Online Available: 27.02.2024

Heart disease, a global ailment with substantial mortality rates, poses a significant health concern. The prevalence of heart disease has escalated due to the demanding nature of contemporary occupations and inherent genetic predispositions. Hence, timely detection of cardiac disorders is paramount to preserving lives. However, the analysis of routine clinical data presents a formidable challenge in identifying cardiovascular ailments. Leveraging machine learning approaches to scrutinize clinical data can furnish effective solutions for informed decision-making and precise prognostications. This research endeavors to predict heart disease by examining the data of 303 individuals encompassing 14 distinct categories. Several machine learning methodologies, namely K-Nearest Neighbor, Gaussian Naive Bayes, Logistic Regression, Random Forest, Gradient Boosting, and Artificial Neural Networks, are proposed as potential remedies to address the problem. The experimental findings unveil that Gradient Boosting attains a remarkable accuracy of 95% and Artificial Neural Networks exhibit a commendable accuracy of 90.1%, establishing them as the most successful models in this study. These results underscore the superior performance of the proposed techniques vis-à-vis the existing literature.

1. Introduction

The early and precise detection of heart diseases plays a vital role in the preservation of patients' lives, like numerous other medical conditions. It is noteworthy that heart disease accounts for approximately 32% of total fatalities, amounting to 17.9 million deaths annually [1]. For this reason, the applications made in the field of health, the diagnoses made, and the results obtained are of great importance for human life.

Today, artificial intelligence applications have affected many areas of life. Artificial intelligence has also made very useful contributions to the field of medicine in evaluating, classifying, and analyzing data. The investigation and development of prediction methods focused on

heart diseases represent a crucial area of study within the field of medicine. Deep learning and machine learning algorithms, both categorized under artificial intelligence, have the capability to be employed on carefully curated datasets, incorporating specific information gathered from individuals. This approach allows for the development of highly accurate models, yielding exceptional precision rates. By putting the information from the newly arrived patient into these models, it becomes possible to diagnose many patients with high accuracy in a very short time.

Within the existing body of literature, numerous investigations have been conducted in the field of heart disease prediction. A recent study [2] put forward the utilization of six distinct machine

learning techniques to identify the likelihood of heart disease occurrence, aiming to discern the prevalence of this medical condition. The performance of these methods was evaluated over eight different classification metrics. Among the methods proposed in the study, logistic regression provided the highest performance with 85% accuracy, 89% sensitivity and 81% specificity.

Random Forest, Decision Tree and Hybrid version of them are employed to solve disease prediction problem on Cleveland dataset in [3]. Based on the experimental findings, it is revealed that the hybrid model attains an accuracy rate of 88.7% in the prediction task. [4] introduces the Hybrid Random Forest with Linear Model (HRFLM) approach. Many studies use some feature selection techniques to get better performances. The HRFLM technique, in contrast, employs all features from the Cleveland dataset without any limitations on feature selection. In the HRFLM approach, all 13 clinical characteristics are utilized as input to an ANN with back propagation. The proposed method's accuracy is 87%.

In [5], ensemble learning based methods for heart disease prediction are proposed and tested. A classifier that is derived via randomness analysis of distance sequences is used as the base estimation for a bagging strategy. The medical Spectf dataset has successfully tested the approach. In the case of the UCI dataset, known as Statlog, a classifier based on Graph Lasso and Ledoit-Wolf shrinkage techniques is devised. These two methods yield highly satisfactory accuracy outcomes, with Spectf achieving 88.7% accuracy and Statlog achieving 88.8% accuracy.

A hybrid approach utilizing data mining techniques for heart disease prediction is proposed in the study conducted by [6]. Experimental results demonstrate that higher accuracy is achieved by the hybrid approach compared to individual algorithms. The complex relationships between risk factors and heart disease are effectively captured by combining the outputs of multiple algorithms, resulting in improved prediction performance. By applying Naive Bayes, Support Vector Machines, k-NN, ANN, J4.8, Random Forests, and Genetic

Algorithm to the entire dataset, an accuracy rate of 89.2% is achieved, and the feature set is reduced from 14 to 12 without compromising accuracy, as determined through calculations.

In [7], a hybridized approach is introduced to enable early detection of heart disease. The dataset undergoes a feature selection process combining the Genetic Approach (GA) with recursive feature removal, thereby identifying the most relevant features. Pre-processing of the data involves utilizing both SMOTE (Synthetic Minority Oversampling Technique) and traditional scalar methods. The proposed hybrid system incorporates support vector machine, naive Bayes, logistic regression, random forest, and Adaboost classifiers. Experimental results reveal that the random forest classifier achieves the highest accuracy rate of 86.6% within the proposed methodology.

[8] proposes a method based on deep neural networks (DNN). After two convolutional layers, the model has eight dense layers. The 6 layers of the model have 128,128,128,128,64,1 neuron, respectively. The activation function used throughout the network, except for the last layer, is the exponential linear unit (ELU). The proposed DNN model achieved accuracy of 91.7%.

2. Proposed Method

In this work, prediction of heart disease is considered as a classification problem. To solve this classification problem, various machine learning based approaches are proposed.

2.1. Dataset

Heart Disease Dataset [9] is created 1988 with the work of 4 different health institutions, including V.A. Medical Center Long Beach and Cleveland Clinic Foundation, Hungarian Institute of Cardiology Budapest, University Hospital Basel Switzerland, University Hospital Zurich Switzerland. This dataset contains 76 features in 14 different categories. For those who do machine learning studies, especially the Cleveland part has been the only dataset for a long time.

Within the labeled data, the target section contains grading information about the presence of the disease. A scale ranging from 0 to 4 is utilized to denote the absence or presence and severity of the disease. A rating of 0-4 corresponds to the absence of the disease, whereas a rating higher than 4 indicates the presence and increasing severity of the disease. Although the personal information of the patients, such as name and surname, was included in the dataset at first, it was then anonymized. Dataset properties and details are given in Table 1.

Of the 14 features in the dataset, 9 of them are categorical and 5 of them are numerical data. Components of high risk of developing heart disease: weight, high cholesterol, smoking, diabetes, high blood pressure, and family history are stated in the dataset comment sections. The metrics that cannot be changed and that we cannot have an impact on are stated as increasing age, gender, and heredity. Factors that can be found in the data set and changed in a person's life: high blood pressure, smoking, being overweight, high cholesterol, sedentary life, and having diabetes.

2.2. Proposed machine learning methods

In this research investigation, a range of machine learning techniques is employed to address the problem at hand. The utilized methods encompass Artificial Neural Networks (ANN), K-nearest neighbor (kNN), Random Forests, Gaussian Naïve Bayes, Logistic Regression, Gradient Boosting and Support Vector Machine (SVM).

Table 1. Heart disease dataset properties

Feature	Description
Age	Current age of persons
Sex	People's gender
Cp	Chest pain types: Atypical angina, asymptomatic, typical angina, non-anginal pain.
Trestbps	A person's blood pressure is tested at a hospital when they are at rest.
Chol	Measurement of a person's cholesterol

Table 2. Heart disease dataset properties (Continue)

Feature	Description
Fbs	Fasting blood glucose level of a person (if value > 120 mg/dl, 1 means true; 0 means false)
Restecg	Electrocardiographic measurement at rest 0,1,2 normal, wave abnormal and possible hypertrophy, respectively
Thalach	Person's highest heart rate
Exang	Pain formation due to exercise is present or absent, in order of 0 or 1
Oldpeak	ECG position of ST depression at rest
Slope	The slope of the ST segment during peak exercise is categorized into three distinct patterns: upward slope, flat slope, and downward slope, denoted by the values 1, 2, and 3, respectively.
Ca	Main change metric
Thal	Thalassemia is a blood disorder that has three levels: normal (3), fixed (6), and reversible (7).
Target	Heart disease 0 or 1 respectively no, yes

Support Vector Machine (SVM) is a supervised learning approach that can employ various kernel functions depending on the data's characteristics during the algorithm's execution. This flexibility enables it to perform both linear and nonlinear classification tasks effectively. Its main objective is to establish a hyperplane that efficiently separates the data points.

K-nearest neighbor (k-NN) [10] is an example-based learning method without an initial training set of examples based on a full theoretical model. Basically, in this method, the value to be estimated is determined by the value of its neighbors in the sample space. The k-nearest neighbor (kNN) makes its estimations based on two basic measurements (distance and number of neighbors). Distance is expressed as the distance of the state or value from which the estimation will be made to other states or values. Euclidean, Minkowski or Manhattan criteria can be used to calculate the distance. K indicates how many of the nearest neighbors will be selected. The variables in the dataset entering the model are evaluated in space according to the determined K value. Then, input's state or value is determined as the majority of the k neighbors. In this work, Euclidean distance criteria and K=3 are selected.

The utilization of Naive Bayes (NB), a probabilistic machine learning approach grounded in Bayes' theorem, is observed in

various classification tasks. An improvement on naive Bayes, Gaussian Naive Bayes assumes that each class has a Gaussian distribution. A change in the value of one attribute in the algorithm has no direct impact on the value of any other attribute. The Gaussian Naive Bayes method is favored due to its simplicity and effectiveness as an algorithm, as it calculates the mean and standard deviation of the training data. It is built on a probabilistic model with an easy-to-code algorithm that makes predictions in real time. As a result, because it can be designed to reply rapidly to user inquiries, this algorithm is a common choice for solving real-world issues.

Logistic Regression (LR) serves as a predictive analytic method in the domain of statistical analysis used in classification issues that is based on the idea of likelihood. Similar to a linear regression model, logistic regression utilizes a more advanced cost function known as the "sigmoid function" instead of a linear or logistical function. The logistic regression hypothesis limits the cost function to values between 0 and 1.

Decision trees are utilized as models capable of acquiring fundamental decision rules for predicting the class or value of a target variable based on historical information derived from training data. The initiation of prediction takes place at the root node, which serves as the highest decision node. The last nodes of the tree are the leaf nodes when predictions of a category or a numerical value are made. There are intermediate nodes between the root node and the leaf node. Feature-based comparisons are made until the leaf node is reached.

The splits of these nodes are determined according to the entropy value. Random Forest (RF) employs the concept of bagging. A number of models are trained using different dataset subsets in bagging, and the final output is created by integrating the findings of all the models. Gradient Boosting (GB) benefits from the boosting strategy. Boosting is a sequential construction procedure that focuses on lowering prior model faults while increasing the effect of high-performance. The base model for random forests and Gradient boosting is decision trees [11].

Artificial Neural Networks (ANNs) [12] are models inspired by the human brain, designed to simulate learning processes. They mimic the structure and learning capabilities of biological neural networks found in the brain, allowing them to learn, store information, and generalize. In ANNs, artificial neurons are interconnected to form a network of connections. Artificial neural networks employ three primary layers, namely the input layer, the middleware (hidden) layer, and the output layer, which collectively govern the network's operations.

Through the input layer, data is sent to the network. In the hidden layers, it is processed before being transmitted to the output layer. Data processing is the process of transforming data input into output using the network's weight values. In order to ensure accurate output results for the given inputs, the network necessitates the establishment of suitable weights. The ANN model employed in this study is depicted in Figure 1.

3. Experiment Results

The proposed method is trained and evaluated Cleveland Heart Disease Dataset [9]. Parameters of proposed methods are given in Table 2. Proposed methods in this work are evaluated using Precision, Recall, F1-score and Accuracy metrics which of formulas are given in (1), (2), (3) and (4), respectively. These metrics are obtained from the contingency table shown in Table 3. An effective heart disease prediction system will have greater TP and TN while having lower FP and FN.

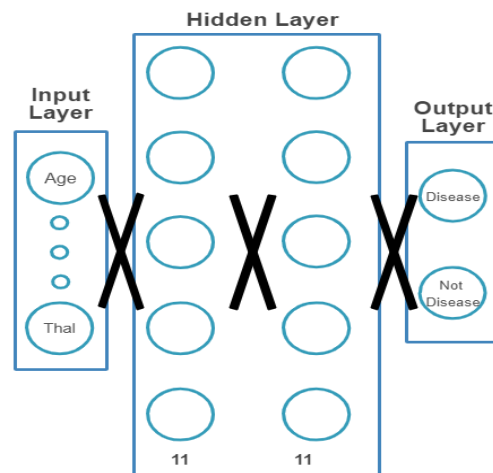


Figure 1. Proposed ANN model

Cleveland dataset contains data of 303 patients in total. These patients are randomly divided into 80% training and 20% test. The performance outcomes of the suggested methodologies on the Cleveland dataset are displayed in Table 4. For general comparison, accuracy is preferred. Table 4 reveals that the proposed Gradient Boosting model exhibits the highest accuracy value. This outcome serves as evidence that machine learning methods generally outperform neural network-based methods (ANN, Deep Neural Network) on smaller datasets. To further explore the capabilities of the proposed methods, an analysis of confusion matrices is conducted. When Figure 2 is examined, it becomes apparent that the Gradient Boosting method displays the least amount of confusion between classes.

Table 2. Experimental parameters of proposed methods

SVM	penalty=2, loss='squared hinge', C=1.0
k-NN	n_neighbors=3, distance_metric = 'Minkowski'
GNB	var_smoothing = 0.1
LR	max_iter=1000, random_state=1, solver='liblinear', penalty='l1'
RF	n_estimators=1000, random_state=1, max_leaf_nodes=20, min_samples_split=15
GB	random_state=1, n_estimators=100, max_leaf_nodes=3, loss='exponential', min_samples_leaf=20
ANN	optimizer = 'adam', loss = 'binary_crossentropy'

$$Precision = \frac{TP}{TP + FP} \quad (1)$$

$$Recall = \frac{TP}{TP + FN} \quad (2)$$

$$F1 - score = \frac{2 * Precision * Recall}{Precision + Recall} \quad (3)$$

$$Accuracy = \frac{TP + TN}{TP + TN + FP + FN} \quad (4)$$

Table 4. Evaluation of proposed methods for heart disease prediction

Model	Precision	Recall	F1-Score	Accuracy
SVM	91.0	92.0	92.0	91.8
k-NN	87.0	88.0	87.0	86.8
GNB	88.0	89.5	88.0	88.5
LR	91.0	92.0	92.0	91.8
RF	88.0	89.5	88.5	91.8
GB	95.0	95.0	95.0	95.0
ANN	90.0	89.5	89.0	90.1

In terms of accuracy, Table 5 showcases a comparison between the proposed method and recent approaches in the literature on the Cleveland dataset. The accuracy results of recent approaches are derived from their original papers. As seen from Table 5, the proposed method outperforms the compared methods. Also, the processing speed performance of the proposed method is analyzed. Processing speed is obtained 16 ms on a PC with 2.80 GHz Quad core CPU, 8 GB RAM.

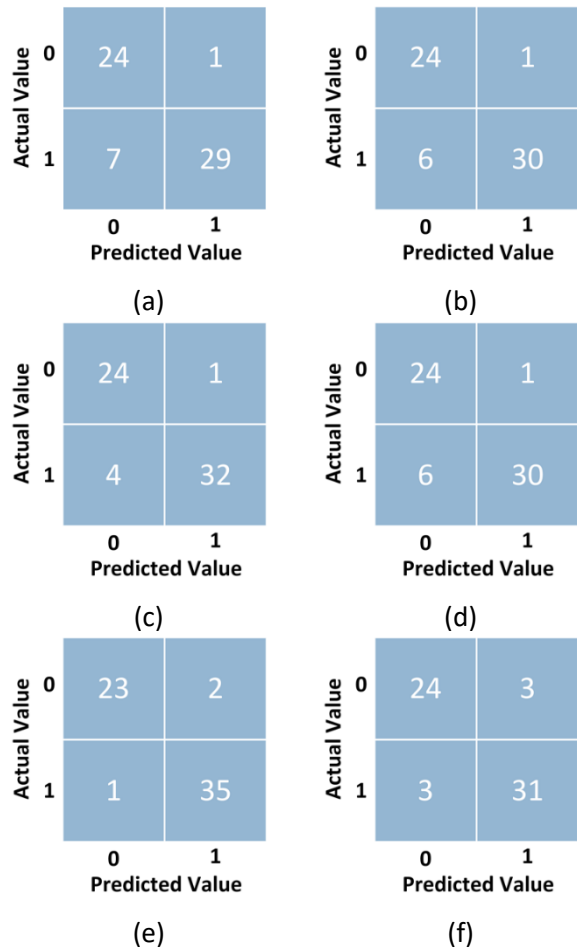


Figure 2. Confusion matrix of proposed methods (a) k-NN (b) GNB (c) LR (d) RF (e) GB (f) ANN

Table 5. Evaluation of proposed method and recent methods

Method	Accuracy
Dwedi et al. [2]	85.0
Kavitha et al. [3]	88.7
Mohan et al. [4]	87.0
Karadeniz et al. [5]	88.7
Tarawneh et al. [6]	89.2
Rani et al. [7]	86.6
Aarof et al. [8]	91.7
Ahamad et al. [13]	87.9
Chandrasekhar et al. [14]	93.4
Proposed Method	95.0

4. Conclusion

Heart disease continues to pose a substantial worldwide health challenge, significantly impacting both morbidity and mortality rates. Recent years have witnessed extensive research endeavors dedicated to diagnosing, predicting, and preventing heart disease. In this study, a range of machine learning techniques is employed to forecast heart disease occurrence. The proposed Gradient Boosting approach exhibits exceptional efficacy in predicting heart disease on the Cleveland dataset, surpassing contemporary methods in terms of accuracy. This investigation contributes to the field of heart disease prediction by introducing a dependable and precise methodology for early detection and prevention of cardiovascular disorders.

Article Information Form

Funding

The authors have not received any financial support for the research, authorship, or publication of this study.

Authors' Contribution

The authors contributed equally to the study.

The Declaration of Conflict of Interest/ Common Interest

No conflict of interest or common interest has been declared by the authors.

The Declaration of Ethics Committee Approval

This study does not require ethics committee permission or any special permission.

The Declaration of Research and Publication Ethics

The authors of the paper declare that they comply with the scientific, ethical and quotation rules of SAUJS in all processes of the paper and that they do not make any falsification on the data collected. In addition, they declare that Sakarya University Journal of Science and its editorial board have no responsibility for any ethical violations that may be encountered, and that this study has not been evaluated in any academic publication environment other than Sakarya University Journal of Science.

Copyright Statement

Authors own the copyright of their work published in the journal and their work is published under the CC BY-NC 4.0 license.

References

- [1] World Health Organization, "Cardiovascular Diseases," World Health Organization, Available: <https://www.who.int/health-topics/cardiovascular-diseases>. Accessed: May 15, 2023.
- [2] A. K. Dwivedi, "Performance evaluation of different machine learning techniques for prediction of heart disease," *Neural Computing & Applications*, vol. 29, pp. 685-693, 2018.
- [3] M. Kavitha, G. Gnaneswar, R. Dinesh, Y. R. Sai, R. S. Suraj, "Heart disease prediction using Hybrid Machine Learning Model," 2021 6th International Conference on Inventive Computation Technologies (ICICT), 2021.
- [4] S. Mohan, C. Thirumalai, G. Srivastava, "Effective heart disease prediction using hybrid machine learning techniques," *IEEE Access*, vol. 7, pp. 81542–81554, 2019.
- [5] T. Karadeniz, G. Tokdemir, H. H. Maraş, "Ensemble methods for heart disease prediction," *New Generation Computing*, vol. 39, no. 3–4, pp. 569–581, 2021.

- [6] M. Tarawneh, O. Embarak, “Hybrid approach for heart disease prediction using data mining techniques,” *Advances in Internet, Data and Web Technologies*, pp. 447–454, 2019.
- [7] P. Rani, R. Kumar, N. M. Ahmed, A. Jain, “A decision support system for heart disease prediction based upon machine learning,” *Journal of Reliable Intelligent Environments*, vol. 7, no. 3, pp. 263–275, 2021.
- [8] S. Arooj, S. ur Rehman, A. Imran, A. Almuhaimeed, A. K. Alzahrani, A. Alzahrani “A deep convolutional neural network for the early detection of heart disease,” *Biomedicines*, vol. 10, no. 11, p. 2796, 2022.
- [9] UCI Machine Learning Repository, “Heart Disease Dataset,” Available: <https://archive.ics.uci.edu/ml/datasets/Heart+Disease>. Accessed: Feb 10, 2023.
- [10] D. W. Aha, “*Lazy Learning*,” Berlin: Kluwer Academic Publishers, 1997.
- [11] A. Cutler, D. R. Cutler, J.R. Stevens, “Random Forests,” in *Ensemble Machine Learning*, C. Zhang and Y. Ma, Eds. New York, NY: Springer, pp. 123-145, 2012.
- [12] H. Ergezer, M. Dikmen, E. Özdemir, “Yapay sinir ağları ve tanıma sistemleri,” *PIVOLKA*, vol. 2, no.6, 11-17
- [13] G. N. Ahamad, H. Fatima, S. M. Zakariya, M. Abbas, “Influence of optimal hyperparameters on the performance of machine”, *Learning Algorithms for Predicting Heart Disease*,” *Processes*, vol. 11, 734, 2023.
- [14] N. Chandrasekhar, S. Peddakrishna, “Enhancing heart disease prediction accuracy through machine learning techniques and optimization,” *Processes*, vol. 11, no. 4, 1210, 2023.



The Impact of Inclined Magnetic Field on Streamlines in a Constricted Lid-Driven Cavity

Merve Gürbüz Çaldağ^{1*}, Ebutalib Çelik²

^{1*} TED University, Faculty of Arts and Science, Department of Mathematics, Ankara, Türkiye, merve.gurbuz@tedu.edu.tr

² Çanakkale Onsekiz Mart University, Çanakkale Technical Sciences Vocational School, Department of Computer Technologies, Çanakkale, Türkiye, e.celik@comu.edu.tr

*Corresponding Author

ARTICLE INFO

ABSTRACT

Keywords:
MHD Flow
Inclination Angle
Constricted Cavity
Radial Basis Function (RBF)

The influence of oriented magnetic field on the incompressible and electrically conducting flow is investigated in a square cavity with a moving top wall and a no-slip constricted bottom wall. Radial basis function (RBF) approximation is employed to velocity-stream function-vorticity formulation of MHD equations. Numerical results are shown in terms of streamlines for different values of Hartmann number M , orientation angle of magnetic field θ and the height of the constricted bottom wall h_c with a fixed Reynolds number. It is obtained that the number of vortices arises as either h_c or M increases. However, the increase in θ leads to decrease the number of vortices. Formation of vortices depends on not only the strength and the orientation of the magnetic field but also the constriction of the bottom wall.

Article History:
Received: 15.09.2023
Accepted: 15.11.2023
Online Available: 27.02.2024

1. Introduction

Flow behaviour in a wavy enclosure has been many industrial applications such as electronic packages, micro-electronic devices, crystal growth, etc. Saidi, Legay-Desesquelles, Prunet-Foch [1] obtained numerical results of the natural convection flow in a sinusoidal cavity by using finite difference method (FDM). They also presented the experimental results of this problem which are good agreement with the numerical ones. Das, Mahmud [2] applied finite volume method (FVM) to solve the Navier-Stokes (N-S) equations coupled with the energy equations. Average Nusselt number and streamlines are depicted for different values of Grashof number and amplitude-wavelength ratios. Layek, Midya [3] studied the impacts of both constriction height and Reynolds number on the incompressible flow in a constricted channel. They implemented the FDM to primitive form of

N-S equations. The influence of wavy top and bottom walls on heat transfer of nanofluids reported in [4]. They showed that including nanoparticle into fluid causes the heat transfer to increase. Mekroussi, Nehari, Bouzit, Chemloul [5] focused on the mixed convection flow in an inclined lid-driven cavity with wavy bottom wall. They indicated that the local Nusselt number attains maximum value at the undulation number is 6 and inclination angle 120° . Natural convection of nanofluids in an inclined cavity with wavy side walls is studied by Ögüt, Akyol, Arıcı [6]. It is found that local Nusselt number decreases with an increase in the inclination angle of the cavity. Azizul, Alsabery, Hashim, Chamkha [7] considered the mixed convection flow in cavity with a wavy bottom wall and moving side walls. Numerical results are depicted for Reynolds, Richardson, Prandtl numbers and the oscillations of the walls by applying finite element method (FEM).

Pirmohammadi, Ghassemi [8] included the magnetic field impact on the heat transfer in a tilted cavity. They solved magnetohydrodynamic (MHD) convection equations for different values of Hartmann and Rayleigh numbers and the inclination angle of the cavity. Öztop, Sakhrieh, Abu-Nada, Al-Salem [9] analyzed the heat transfer of nanofluid in a lid-driven cavity with a hot wavy bottom wall imposed to the horizontal magnetic field. They reported that Hartmann number controls the heat transfer. MHD convection flow in a constricted cavity is studied in [10]. They indicate the contour plots of flow, pressure and temperature for varying the length of the cavity, constriction ratio, Hartmann and Grashof numbers. Khalil, Azzawi, Al-damook [11] performed the MHD free convection in a trapezoidal wavy cavity for various Rayleigh and Hartmann numbers and the number of waves. It is investigated that Rayleigh number increases the heat transfer. Saha, Islam, Yeasmin, Parveen [12] utilized FEM to MHD natural convection flow of nanofluids in an enclosure with wavy top wall exposed to horizontal magnetic field. They obtained that heat transfer is effected by the shape of the nanoparticles.

The impact of magnetic field with an orientation angle on MHD duct flow is analyzed by Aydın, Selvitopi [13]. They implemented the FEM-BEM coupled approach to MHD equations with unbounded external domain. Inclination angle of the magnetic field is considered for MHD mixed convection in parallel plates by Kaladhar, Reddy, Srinivasacharya [14]. Computations carried out for Soret and Hall parameters, Hartmann numbers and inclination angle. They depicted that an increase in the angle decreases the profiles of concentration. Wasif, Mishal, Haque, Haque, Rahman [15] investigated the heat transfer in different cavity shapes subjected to oriented magnetic field.

The effect of the angle of magnetic field on the Nusselt number depends on the aspect ratio of the cavity. Hussain, Öztop [16] focused on the rotation of the magnetic field on power law fluid in a curvilinear cavity with a moving top wall. Influences of various physical parameters on isolines, streamlines and isoconcentration are depicted utilizing FEM. Gürbüz-Çaldağ, Çelik [17] studied the effect of the inclination angle of

magnetic field on Stokes flow in a lid-driven cavity. They showed that the magnitude of the stream function depends on the type of the inclination angle. Selvitopi [18] applied Galerkin FEM to MHD duct flow equations. Impact of the time-varied oblique magnetic field on flow is analyzed. In [19] flow behaviour in a T-Junction is considered under the effect of magnetic field with an angle. Numerical results are obtained in terms of velocity and induced magnetic field by using the stabilized FEM.

To the best of the authors' knowledge the impact of the oriented magnetic field on the flow in a lid-driven cavity with constricted bottom cavity has not been studied yet. We adopt RBF approximation to MHD equations in terms of velocity, stream function and vorticity. The contour plots of stream function are depicted for various values of Hartmann number, orientation of magnetic field and the constriction height of the cavity with a fixed Reynolds number. It is deduced that the constriction causes the formation of new eddies (vortices) with different directions. On the contrary, the augmentation of inclination angle diminishes the number of vortices.

2. Mathematical Formulation

The two-dimensional steady flow of a viscous, incompressible and electrically conducting fluid is considered in a square lid-driven cavity whose bottom wall is constricted using the function g_b such that

$$g_b(x) = \frac{1}{2}h_c(1 + \cos(2\pi(x - \frac{1}{2}))), 0 \leq x \leq 1 \quad (1)$$

where h_c is the constriction height shown in Figure 1. The uniform inclined magnetic field is exposed to the cavity. This problem is modelled by MHD equations which are obtained from the Navier-Stokes equations of fluid dynamics and Maxwell's equations of electromagnetics through Ohm's law. The non-dimensional form of MHD equations is obtained from the transformations such as

$$(x, y) \rightarrow (xl, yl), \quad (u, v) \rightarrow (uU, vU), \quad (2)$$

$$p \rightarrow pv\rho U/l. \quad (3)$$

In these transformations l, U, ρ and ν are characteristic length, characteristic velocity, density and kinematic viscosity of the fluid, respectively. The non-dimensional MHD equations [20-21] are

$$\nabla \cdot \mathbf{u} = 0 \quad (4)$$

$$\nabla^2 \mathbf{u} = Re(\mathbf{u} \cdot \nabla) \mathbf{u} + \nabla p - M^2(\mathbf{u} \times \mathbf{H}) \times \mathbf{H} \quad (5)$$

where \mathbf{H} is the magnetic field. Non-dimensional parameters are the Reynolds number and the Hartmann number given as

$$Re = lU/\nu, \quad M = l\mu H_0 \sqrt{\sigma/\rho\nu}, \quad (6)$$

respectively. In these parameters, μ, H_0 and σ are magnetic permeability, magnetic field intensity and electric conductivity, respectively.

To eliminate pressure terms in the equation (5) MHD equations can be transformed into the stream function-vorticity formulation by using the definition of stream function

$$u = \psi_y, \quad v = -\psi_x \quad (7)$$

and the vorticity

$$\omega = v_x - u_y. \quad (8)$$

Thus, the steady and two-dimensional MHD flow equations in terms of velocity components, stream function and vorticity are

$$\nabla^2 \psi = -\omega \quad (9)$$

$$\nabla^2 \omega = Re \left(u \frac{\partial \omega}{\partial x} + v \frac{\partial \omega}{\partial y} \right) + M^2 \left(-\frac{\partial u}{\partial y} \sin^2 \theta + \left(\frac{\partial v}{\partial y} - \frac{\partial u}{\partial x} \right) \sin \theta \cos \theta + \frac{\partial v}{\partial x} \cos^2 \theta \right) \quad (10)$$

where θ is the inclination angle of the magnetic field.

The boundary conditions are

$$u = 0, \quad v = 0, \quad \psi = 0 \text{ on the left wall}$$

$$(x=0, 0 \leq y < 1), \quad (11)$$

$$u = 0, \quad v = 0, \quad \psi = 0 \text{ on the right wall}$$

$$(x=1, 0 \leq y < 1), \quad (12)$$

$$u = 0, \quad v = 0, \quad \psi = 0 \text{ on the bottom wall}$$

$$(y=g_b(x), 0 \leq x \leq 1), \quad (13)$$

$$u = 1, \quad v = 0, \quad \psi = 0 \text{ on the top wall}$$

$$(y=1, 0 \leq x \leq 1). \quad (14)$$

The unknown vorticity boundary conditions are obtained from the stream function equation by using the discretization matrix G given in the next section.

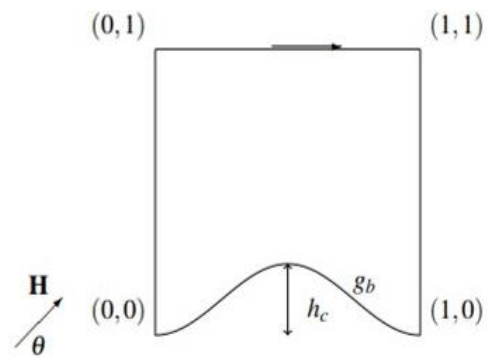


Figure 1. Lid-driven cavity with constricted bottom wall.

3. Numerical Technique

The radial basis function (RBF) approximation method is employed to solve MHD equations (9)-(10). In RBF technique [22], the inhomogeneity term b_1 of Poisson equation ($\nabla^2 \tilde{u} = b_1$), which is the term except for the Laplacian, is approximated by the RBFs $\{f_i\}$ as

$$b_1(x, y) = \sum_{i=1}^{NT} \beta_i f_i(r), \quad (x, y) \in \Omega \quad (15)$$

and the approximate solution \tilde{u} is written

$$\tilde{u}(x, y) = \sum_{i=1}^{NT} \beta_i h_i(r) \quad (16)$$

where $\{h_i\}$ is obtained from the differential equation

$$\nabla^2 h_i(r) = f_i(r) \quad (17)$$

$$\text{and } r = \sqrt{(x - x_i)^2 + (y - y_i)^2}.$$

The approximate solution \tilde{u} is forced to satisfy boundary condition

$$B_c \tilde{u} = b_2, \tag{18}$$

we get

$$\sum_{i=1}^{NT} \beta_i B_c h_i(r) = b_2(x, y), (x, y) \in \partial\Omega. \tag{19}$$

Discretizing the boundary $\partial\Omega$ with NB points and the domain Ω with ND points gives

$$\sum_{i=1}^{NT} \beta_i B_c h_i(r_j) = b_2(x_j, y_j), 1 \leq j \leq NB \tag{20}$$

$$\sum_{i=1}^{NT} \beta_i f_i(r_k) = b_1(x_k, y_k), 1 + NB \leq k \leq NT = NB + ND. \tag{21}$$

The unknown coefficients $\{\beta_i\}$ are obtained from the system

$$C\beta = B \tag{22}$$

which is the combination of equation (20) and (21) where

$$C = \begin{bmatrix} B_c h_1(r_1) & B_c h_2(r_1) & \cdots & B_c h_{NT}(r_1) \\ \vdots & \vdots & \ddots & \vdots \\ B_c h_1(r_{NB}) & B_c h_2(r_{NB}) & \cdots & B_c h_{NT}(r_{NB}) \\ f_1(r_{NB+1}) & f_2(r_{NB+1}) & \cdots & f_{NT}(r_{NB+1}) \\ \vdots & \vdots & \ddots & \vdots \\ f_1(r_{NT}) & f_2(r_{NT}) & \cdots & f_{NT}(r_{NT}) \end{bmatrix}_{NT \times NT},$$

$$B = \begin{bmatrix} b_2(x_1, y_1) \\ \vdots \\ b_2(x_{NB}, y_{NB}) \\ b_1(x_{NB+1}, y_{NB+1}) \\ \vdots \\ b_1(x_{NT}, y_{NT}) \end{bmatrix}_{NT \times 1}, \quad \beta = \begin{bmatrix} \beta_1 \\ \vdots \\ \beta_{NT} \end{bmatrix}_{NT \times 1}.$$

The numerical solution

$$\tilde{u} = A[C^{-1}B] \tag{23}$$

is acquired from equation (16) by substituting the coefficients $\{\beta_i\}$ obtained in the above system (22).

The space derivatives of unknowns are obtained by the discretized matrix

$$G \left(G_{ij} = 1 + r_{ij} \right) \text{ as}$$

$$P_x = G_x G^{-1} P, \quad P_y = G_y G^{-1} P \tag{24}$$

where P denotes u, v, ψ and ω .

In [23], different RBFs such as quadratic polynomial $f(r) = 1 + r + r^2$ and multiquadratics $f(r) = \sqrt{r^2 + c^2}$ with the pre-defined shape parameter c are used to find solution of MHD Stokes flow in a lid-driven cavity problem. It is deduced that the similar results are obtained, and the linear RBF takes less computational time. In our computation, the iteration takes 210.347s CPU time and 709 iteration step with $f(r) = 1 + r$ whereas 211.476s time and 710 step with $f(r) = 1 + r + r^2$ for $h_c = 0.25, M = 0$ and $\theta = 0^\circ$. For that reason, the polynomial RBF $f(r) = 1 + r$ and the corresponding h function $h(r) = \frac{r^2}{4} + \frac{r^3}{9}$ are chosen to find numerical solutions of coupled MHD equations (9)-(10) iteratively.

Iterative procedure is given as:

- Discretized form of the stream function equation (9)

$$\psi^{l+1} = AC^{-1}B \tag{25}$$

is solved by using an initial estimate for the vorticity ω^0 . The right-hand side matrix B is obtained by taking

$$b_2(x, y) = 0 \text{ and } b_1(x, y) = -\omega^l. \tag{26}$$

- Velocity components are obtained from the equation (7) with new stream function value such as

$$u^{l+1} = G_y G^{-1} \psi^{l+1}, \quad v^{l+1} = -G_x G^{-1} \psi^{l+1}. \tag{27}$$

- The unknown boundary values of vorticity are obtained from the definition of the vorticity (8)

$$\omega_{bc}^{l+1} = G_x G^{-1} v^{l+1} - G_y G^{-1} u^{l+1}. \tag{28}$$

- We solve the vorticity equation (10)

$$\omega^{l+1} = AC^{-1}B \tag{29}$$

where B is obtained by taking

$$b_2(x, y) = \omega_{bc}^{l+1} \quad (30)$$

And

$$\begin{aligned} b_1(x, y) = & Re(u_d^{l+1}G_xG^{-1} + v_d^{l+1}G_yG^{-1})\omega^l \\ & - M^2 \sin^2 \theta G_y G^{-1} u^{l+1} \\ & + M^2 \sin \theta \cos \theta (G_y G^{-1} v^{l+1} - \\ & - G_x G^{-1} u^{l+1}) \\ & + M^2 \cos^2 \theta G_x G^{-1} v^{l+1} \end{aligned} \quad (31)$$

u_d and v_d are diagonal matrices of u and v respectively.

- The iteration continues until the preassigned tolerance (ξ) is reached between two successive iterations such that

$$\frac{\|\psi^{l+1} - \psi^l\|_\infty}{\|\psi^{l+1}\|_\infty} < \xi, \quad \frac{\|\omega^{l+1} - \omega^l\|_\infty}{\|\omega^{l+1}\|_\infty} < \xi \quad (32)$$

where ξ is taken 10^{-6} and l is iteration level.

This iteration is coded with Matlab version R20022a and results are visualized with Tecplot 360EX.

4. Numerical Results

The present iterative RBF approximation is adapted to the steady MHD equations (9)-(10) for various values of Hartmann number ($0 \leq M \leq 50$), inclination angle of the magnetic field ($0^\circ \leq \theta \leq 90^\circ$) and the constriction height $h_c = 0.25, 0.5$ to analyze the effects of the strength, direction of the magnetic field and the constriction of the cavity on the flow, respectively. Boundary of the cavity is discretized by taking $NB = 160$ points. x and y coordinates of the points [4] are obtained by

$$x_{i+1} = x_i + \Delta x \text{ and } y_{i+1} = y_i + \Delta y \quad (33)$$

where

$$\Delta x = \frac{1}{NB/4} \text{ and } \Delta y = \frac{1-g_b(x)}{NB/4}. \quad (34)$$

The discretization of the domain is depicted in Figure 2. The numerical results are presented in terms of counter plots of stream function in Figures 3-8.

We validate our proposed technique by taking $M = 0, h_c = 0, Re = 100$. In this case, our governing equations convert to Navier-Stokes equations in a non-constricted lid-driven cavity so we can compare our results with the solutions obtained by Ghia, Ghia, Shin [24]. In Figures 3-4, it is seen that both the streamlines and the velocity profiles are in well agreement with the results in [24].

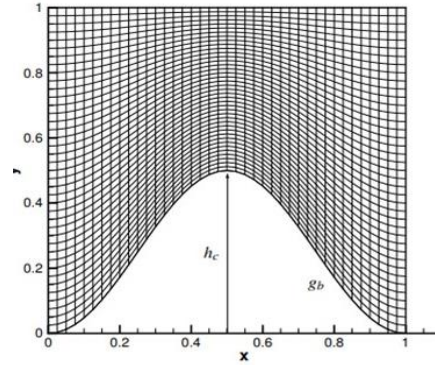


Figure 2. Discretization of the cavity.

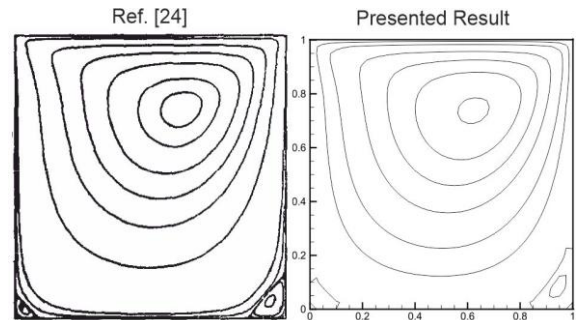


Figure 3. Validation case for $M = 0$.

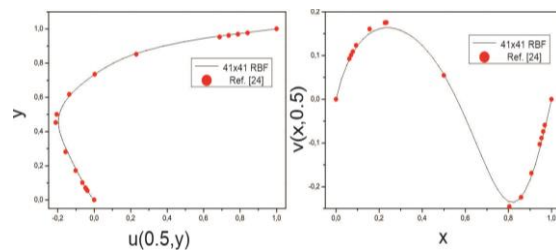


Figure 4. Centerline velocities for $M = 0$ and $Re = 100$.

Also, streamlines are plotted for $h_c = 0.2, M = 50$ with $Re = 100$ and $Re = 200$ as shown in Figure 5. It can be observed that flow patterns are the same. The difference between them is that the position of main vortex as in the Navier-Stokes equations for a single lid driven cavity. More information also can be found in [25].

Besides, our aim is to investigate impact of strength of inclined magnetic field on the streamlines in the cavity with wavy bottom. Thus, we fixed Reynolds number at 100 in our calculations.

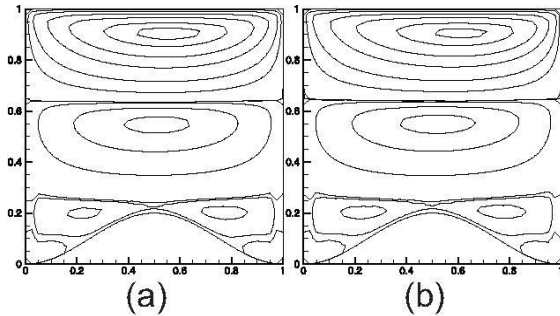


Figure 5. Flow patterns for $h_c = 0.2, M = 50$ with (a) $Re = 100$, (b) $Re = 200$.

After the validation, computations are carried out for different values of h_c in the absence of magnetic field ($M = 0$) to investigate the impact of constriction on the stream function profiles in Figure 6. For small values of h_c main vortex of the fluid is located near the top wall due the effect of moving lid and secondary vortices with an opposite direction are formed at the left and right of the constricted area. As h_c increases to 0.5, the main vortex of the flow shifts through the right part of the cavity. On the other hand, secondary vortices move upward and the formation of new vortex with small value is seen at the left bottom corner.

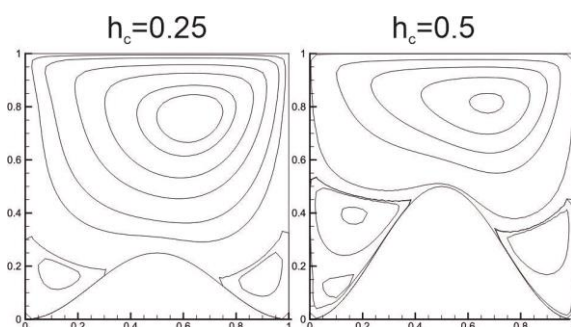


Figure 6. Effect of the constriction of the cavity on streamlines for a fixed $M = 0$.

Figure 7 demonstrates the effects of both strength and the direction of the magnetic field on the streamline profiles for fixed $h_c = 0.25$. When $\theta = 0^\circ$ which means that magnetic field is applied in the x –direction, secondary vortices occur at the left and right corners due to the constriction. As Hartmann number increases, the

secondary vortices in the corners move up and bifurcate into main vortex with each other under the first one. The third vortices circulating opposite direction are formed at the bottom corners.

When the inclination angle of the magnetic field is included, flow behaviour is changed. For $\theta = 45^\circ$ the symmetry of the flow is deformed. The right secondary vortex is larger than the left one due to the direction of the magnetic field. As M increases, new vortices develop at the right corner. On the contrary, the vorticity at the left corner vanishes. As θ reaches to 90° , flow attains symmetric behaviour. For small Hartmann number secondary vortices occur at the bottom corners due the constriction. However, these vortices diminish with an increase in the strength of the magnetic field. Fluid flows in all part of the cavity showing the impact of the moving lid. The augmented in M causes to form a boundary layer regardless of the direction of the magnetic field.

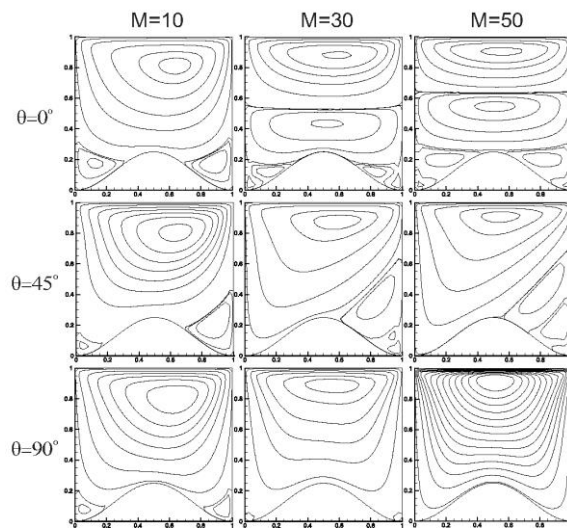


Figure 7. Streamlines for a fixed $h_c = 0.25$.

In Figure 8 the influences of both M and θ on streamlines are analyzed for different values of $h_c = 0.25, 0.5$. In the case of $\theta = 0^\circ$, for $M = 10$ the effect of h_c on the main vortex and the other vortices are the same as in the case of $M = 0$ (Figure 6) which shows that the electromagnetic effect on the flow is small. Flow behaviours obtained for fixed $M = 50$ show that increase in h_c retards the main effect of Hartmann number on the single secondary vortex formation. It is deduced that the higher constriction ratio requires the higher Hartmann number to form a single secondary vortex. When the inclination

angle increases to 45° , for small values of M flow behaviours are the same as in the case of $\theta = 0^\circ$. However, with a further increase in M vortices at the left corner due to the constriction diminish. Thus, the direction of the magnetic field controls the development of the new vortices due the constriction.

Table 1. Maximum value of $|\psi|$.

$h_c=0.25$	$M=0$	$M=10$	$M=30$	$M=50$
$\theta = 0^\circ$	0.09369	0.07358	0.04610	0.03568
$\theta = 45^\circ$		0.06817	0.02945	0.01456
$\theta = 90^\circ$		0.06134	0.01980	0.00703
$h_c=0.5$				
$\theta = 0^\circ$	0.07783	0.06899	0.04727	0.03682
$\theta = 45^\circ$		0.06162	0.03061	0.01758
$\theta = 90^\circ$		0.05596	0.02146	0.01045

Table 1 indicates the effects of physical parameters on the maximum value of $|\psi|$. In the absence of magnetic field the increase in the constriction decreases $|\psi|_{max}$. The same effect is observed for small Hartmann number $M = 10$. However, with a further increase in M as the constriction of the cavity increases, the

maximum value of $|\psi|$ increases regardless of the direction of the magnetic field. On the other hand, for a fixed h_c , $|\psi|_{max}$ decreases due to the augmentation of M .

5. Conclusion

The behaviour of the flow in a lid-driven cavity with a constricted bottom wall under an applied magnetic field with an inclination angle is analyzed for the first time. The governing MHD equations are solved by using RBF approximation for different values of Hartmann number, inclination angle and the constriction of the cavity. It is deduced that the rotation of the magnetic field plays an important role on the formation of the new vortices due to the constriction. As the inclination angle increases the number of new vortices because of the constriction diminishes. An increase in the Hartmann number decreases the maximum value of $|\psi|$ regardless of the direction. The flow structure is controlled by the strength of the magnetic field, direction of the magnetic field and the constriction of the cavity.

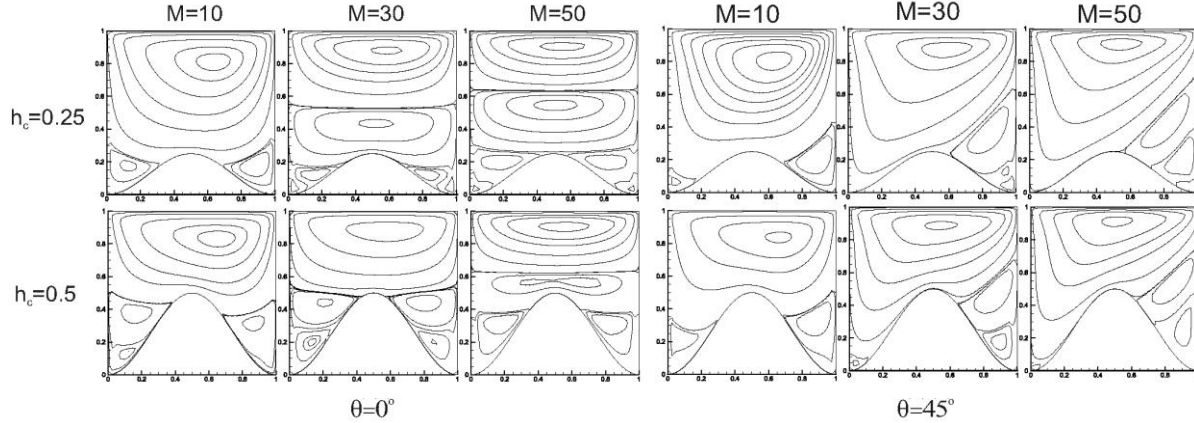


Figure 8. Effects of M and θ on streamlines for $h_c = 0.25, 0.5$.

Article Information Form

Funding

The author (s) has no received any financial support for the research, authorship or publication of this study.

Authors' Contribution

The authors contributed equally to the study.

The Declaration of Conflict of Interest/ Common Interest

No conflict of interest or common interest has been declared by the authors.

The Declaration of Ethics Committee Approval

This study does not require ethics committee permission or any special permission.

The Declaration of Research and Publication Ethics

The authors of the paper declare that they comply with the scientific, ethical and quotation rules of SAUJS in all processes of the paper and that they do not make any falsification on the data collected. In addition, they declare that Sakarya University Journal of Science and its editorial board have no responsibility for any ethical violations that may be encountered, and that this study has not been evaluated in any academic publication environment other than Sakarya University Journal of Science.

Copyright Statement

Authors own the copyright of their work published in the journal and their work is published under the CC BY-NC 4.0 license.

References

- [1] C. Saidi, F. Legay-Desesquelles, B. Prunet-Foch, "Laminar flow past a sinusoidal cavity", *International Journal of Heat and Mass Transfer*, vol. 30, no. 4, pp. 649–661, 1987.
- [2] P. K. Das, S. Mahmud, "Numerical investigation of natural convection inside a wavy enclosure", *International Journal of Thermal Sciences*, vol. 42, no. 4, pp. 397–406, 2003.
- [3] G. C. Layek, C. Midya, "Effect of constriction height on flow separation in a two-dimensional channel", *Communications in Nonlinear Science and Numerical Simulation*, vol. 12, no. 5, pp. 745–759, 2007.
- [4] E. Abu-Nada, H. F. Oztop, "Numerical analysis of Al₂O₃/water nanofluids natural convection in a wavy walled cavity", *Numerical Heat Transfer, Part A: Applications*, vol. 59, no. 5, pp. 403–419, 2011.
- [5] S. Mekroussi, D. Nehari, M. Bouzit, N. E. S. Chemloul, "Analysis of mixed convection in an inclined lid-driven cavity with a wavy wall", *Journal of Mechanical Science and Technology*, vol. 27, pp. 2181–2190, 2013.
- [6] E. B. Ögüt, M. Akyol, M. Arıcı, "Natural convection of nanofluids in an inclined square cavity with side wavy walls", *Isı Bilimi ve Tekniği Dergisi*, vol. 37, no. 2, pp. 139–149, 2017.
- [7] F. M. Azizul, A. I. Alsabery, I. Hashim, A. J. Chamkha, "Heatline visualization of mixed convection inside double lid-driven cavity having heated wavy wall", *Journal of Thermal Analysis and Calorimetry*, vol. 145, pp. 3159–3176, 2021.
- [8] M. Pirmohammadi, M. Ghassemi, "Effect of magnetic field on convection heat transfer inside a tilted square enclosure", *International Communications in Heat and Mass Transfer*, vol. 36, no. 7, pp. 776–780, 2009.
- [9] H. F. Öztop, A. Sakhrieh, E. Abu-Nada, K. Al-Salem, "Mixed convection of MHD flow in nanofluid filled and partially heated wavy walled lid-driven enclosure", *International Communications in Heat and Mass Transfer*, vol. 86, pp. 42–51, 2017.
- [10] M. Tezer, M. Gürbüz, "MHD convection flow in a constricted channel", *Analele Stiintifice Ale Universitatii Ovidius Constanta-Seria Matematica*, vol. 26, no. 2, 2018.
- [11] W. H. Khalil, I. D. Azzawi, A. Al-damook, "The optimisation of MHD free convection inside porous trapezoidal cavity with the wavy bottom wall using response surface method", *International Communications in Heat and Mass Transfer*, vol. 134, p. 106035, 2022.
- [12] T. Saha, T. Islam, S. Yeasmin, N. Parveen, "Thermal influence of heated fin on MHD natural convection flow of nanofluids inside a wavy square cavity", *International Journal of Thermofluids*, vol. 18, p. 100338, 2023.

- [13] S. H. Aydın, H. Selvitopi, “Stabilized FEM-BEM coupled solution of MHD pipe flow in an unbounded conducting medium”, *engineering analysis with boundary Elements*, vol. 87, pp. 122-132, 2018.
- [14] K. Kaladhar, K. M. Reddy, D. Srinivasacharya, “Inclined magnetic field and solet effects on mixed convection flow between vertical parallel plates”, *Journal of Applied Analysis and Computation*, vol. 9, no. 6, pp. 2111–2123, 2019.
- [15] M. Wasif, K. A. Mishal, M. R. Haque, M. M. Haque, F. Rahman, “Investigation of fluid flow and heat transfer for an optimized lid driven cavity shape under the condition of inclined magnetic field”, *Energy and Thermofluids Engineering*, vol. 1, no. 1–2, pp. 47–57, 2021.
- [16] S. Hussain, H. F. Öztöp, “Impact of inclined magnetic field and power law fluid on double diffusive mixed convection in lid-driven curvilinear cavity”, *International Communications in Heat and Mass Transfer*, vol. 127, p. 105549, 2021.
- [17] M. Gürbüz-Çaldağ, E. Çelik, “Stokes flow in lid-driven cavity under inclined magnetic field”, *Archives of Mechanics*, vol. 74, no. 6, 2022.
- [18] H. Selvitopi, “Numerical investigation of damped wave type MHD flow with time-varied external magnetic field”, *Chinese Journal of Physics*, vol. 80, pp. 127-147, 2022.
- [19] H. Selvitopi, “Stabilized FEM solution of magnetohydrodynamic flow in different geometries”, *Journal of Scientific Reports-A*, vol. 49, pp. 105-117, 2022.
- [20] H. Yosinobu, T. Kakutani, “Two-dimensional Stokes flow of an electrically conducting fluid in a uniform magnetic field”, *Journal of the Physical Society of Japan*, vol. 14, no. 10, pp. 1433–1444, 1959.
- [21] M. Gürbüz, M. Tezer-Sezgin, “MHD Stokes flow in lid-driven cavity and backward-facing step channel”, *European Journal of Computational Mechanics*, vol. 24, no. 6, pp. 279–301, 2015.
- [22] C. S. Chen, C. M. Fan, P. Wen, “The method of approximate particular solutions for solving certain partial differential equations”, *Numerical Methods for Partial Differential Equations*, vol. 28, no. 2, pp. 506–522, 2012.
- [23] M. Gürbüz, “Radial Basis Function and Dual Reciprocity Boundary Element Solutions of Fluid Dynamics Problems”, Ph.D. dissertation, Department of Mathematics, Middle East Technical University, Ankara, Türkiye, 2017.
- [24] U. Ghia, K. N. Ghia, C. Shin, “High-Re solutions for incompressible flow using the Navier-Stokes equations and a multigrid method”, *Journal of Computational Physics*, vol. 48, no. 3, pp. 387–411, 1982.
- [25] E. Çelik, M. Gürbüz-Çaldağ, “Streamline analysis of MHD flow in a double lid-driven cavity”, *Proceedings of the Institution of Mechanical Engineers, Part C: Journal of Mechanical Engineering Science*, vol. 238, pp. 64-74, 2024.

Modeling and Evaluation of Ömerli Basin (Mardin, Southeastern Türkiye) Groundwater Potential using the GIS-Based Analytical Hierarchy Process (AHP) approach

Veysel Aslan^{1*} 

^{1*} Harran University, Hilvan Vocational High School, Department of Construction Technology, Sanliurfa, Türkiye, vaslan@harran.edu.tr

*Corresponding Author

ARTICLE INFO

ABSTRACT

Keywords:

AHP Method One
GIS Two
Groundwater Three
MCDM method Four



Article History:

Received: 15.10.2022

Accepted: 18.11.2023

Online Available: 27.02.2024

Water, which is an indispensable element of human life, is also a basic need for living things and nature. Groundwater, which is the world's freshwater source, has low-cost usage opportunities because it is generally of high quality and does not need to be treated. For this reason, there has been an excessive increase in the use of groundwater in recent years due to the low rainfall and limited surface waters. Accordingly, in recent years, the lack of precipitation and the decrease in surface water potential have led to an excessive increase in groundwater use. Nowadays, technology, which is called the information age and finds its place in almost all professional applications, supports practitioners in terms of time, effort, and cost. Among these technological studies, Geographic Information System (GIS) applications are one of the most popular fields of study (detection and monitoring of groundwater resources and application of thematic maps with spatial analysis). The AHP technique, one of the GIS-supported MCDM methods, was used to reveal the groundwater potential of the Ömerli district basin of Mardin province. First of all, raster maps were created in the GIS program ArcGIS ArcMap environment, and then reclassified maps were produced. These data regarding the basin study were obtained from official institutions and private drilling companies that work on groundwater. In the first stage of the study, data related to groundwater potential such as precipitation, static water level, dynamic water level, well yield, depth, and aspect were modeled. In the second stage, these data were weighted in AHP and the resulting map was created and interpreted; It was created and interpreted with very bad, bad, moderate, good and very good values. In the third and last stage, the results and recommendations were discussed.

1. Introduction

Groundwater is the general name for water found in the layers below the earth's surface. This water is stored in underground aquifers and fed from various sources. In our country, the average total rainfall per square meter is measured as 574 mm. However, the amount of precipitation may vary depending on geographical regions. There fore, groundwater can be found at different levels and

quantities depending on the region [1]. Depending on the changing precipitation amounts, the amount of water leaking and stored subsurface also changes. In some regions, water is constantly infiltrating into the ground, and groundwater is fed. However, in today's world, together with the effects of man on nature, water discharges directly into the streams and seas as surface flows, and groundwater level is drawn deeper. The decrease in groundwater in response

to the rapidly increasing water demand in the world has led to the determination of existing resources primarily with a reliable and controllable database.

It is known that the vast majority of usable fresh water in the world and in our country is found in groundwater resources. The use of groundwater resources is usually made possible by drilling wells. Underground water is extracted from these deep water wells with the help of drilling, with deep water well pumps. The number of deep water well pumps, the use of which is increasing every year in our country, has reached 191173 as of 2019 [2].

It is known that well features are as important as the pump in transporting the water to the surface of the wells. Well Properties also lead to the use of the properties of the pump in the well. In this case, it causes the pumping system to be taken [3]. In deep water wells, the feed conditions affect the pumping operation that will be used, such as the water velocity, and the length and width of the well. In addition, it was emphasized that the water level in the deep water well depends on the aquifer type, aquifer depth, reserve and degree of saturation [4-5].

The water levels in the well differ depending on the characteristics of the aquifer and the well. The position of the pump in the well becomes important in response to the water levels formed in the well. In deep water wells, it shows certain heights according to the movement or condition of the water. It is known that water levels in pumping wells affect pump operating characteristics. The height of the pump, when it is not working, is defined as the static water level, and the decreasing water level after a while is defined as the dynamic water level, and the difference between these two heights is expressed as a decrease [6]. Immersion depth, on the other hand, refers to the water level up to the pump suction inlet when the well is at the dynamic water level. The vertical hydraulic head is the water level between the static water level and the pump inlet axis (Figure 1).

Schulz (2013) reported that the immersion depth of deep well pumps should be 5 m below the dynamic water level. In another study, it was

emphasized that determining the dynamic submersion depth of the deep water well pump installation as 2-3 m and placing it according to this level depending on the fixed deep water well equipment and feeding would be more appropriate for the pump. Working conditions [7-8].

Detailed information about the hydraulics of the wells and their water-giving formations (aquifer) are obtained from the pumping tests carried out in the wells. This information, other geological, chemical, etc. Information about the groundwater basins and capacities of the plain is obtained. A good business project can be prepared in proportion to the accuracy of the experiments and values. In this direction, there are different package programs that have emerged with the developing technology in the field of surface and ground waters. Each surface and groundwater program has its own software features and advantages.

In this sense, program selection is a very important issue for such businesses and program selection requires multi-criteria decision making. In this study, the Analytical Hierarchy Process (AHP) technique, which is one of the GIS audio MCDM methods, is discussed by considering the criteria to be considered in choosing the most appropriate package program and finding the most appropriate solution.

2. Material And Method

The location map of the study area has been considered as a map showing both the topographic and geological structure of the Ömerli basin, which has an annual precipitation of approximately 460 mm/year, has a plateau appearance and attracts attention with its simplicity. Surface forms (Fig. 1). The land structure within the boundaries of the district is in the form of consecutive reverse layers with a total surface area of 409 km² [9].

Drilling data obtained from institutions and organizations related to water wells were extracted and those within the borders of the basin were discussed. These data were arranged in the Excel table by giving their coordinates. Subsequently, these data, which were called to

the ArcMap 10.2 environment in the GIS program, were digitized and a thematic map was created. In the same way, a slope map was created with the help of a DEM map. A precipitation map was created with the data related to precipitation received from the meteorology institution. Then, Static Water Level, Dynamic Water Level, Well Yield, Depth, and Aspect thematic maps were created and reclassified maps of these maps were obtained.

2.1. Study area and geographical structure

The Assyrian State was established in the geography called Upper Mesopotamia and including the Ömerli basin. When the Yaylatepe (Hibatok), Göllü, İkipınar, Beşikkaya (Fafit), and Maserati ruins in the district are examined, the region where this settlement is quite old has remained under the rule of Assyrians, Persians, Romans, Byzantines and Turkish-Islamic States 28 km from Mardin. It is in the east of the city center.

Ömerli is adjacent to Midyat in the east, Yesilli in the west, Nusaybin in the south and Savur in the north. The total area of the district is 409 km² [10].



Figure 1. Ömerli Basin Location Map

The south and east of the basin consist of slightly rugged and limestone hills extending in the east-west direction. The Mardin Mountains, sandwiched between the Syrian platform in the south and the Diyarbakır-Siirt pliocene depression in the north; mostly composed of southward inverted anticlines, and their peaks are the southern slopes. The base of the Cretaceous lime stones is seen only on the Sadan-Derik line. The thickness here is close to 400 meters; It continues as an alternation of various hard

massive lime stones, brecciated lime stones and marly lime stones, forming large cliffs on the Derik-Sadan line. It starts with the Cretaceous pedestal conglomerates, and these conglomerates, ranging in size from 10-30 meters, have large elements and include all Paleozoic series stones. The elements include old effusive and intrusive pebbles and all Paleozoic series elements. Conglomerates gradually pass upwards into marls and limestone's [11].

The land structure within the boundaries of the district is in the form of successive reverse layers and consists of hills at an altitude of 800 to 1100 meters around the streams that usually separate in the north-south direction. The land structure is closed and covered with oak vegetation varying between 0.50 meters and 3.5 meters in length. Plant density decreases towards the north. Partially flat lands in the valleys can be irrigated with the help of springs within the boundaries of the district. The district has a continental climate with low temperature and precipitation in summers, and severe cold and snowfall in winter. There are seasons when heavy snow or heavy rain is recorded from time to time [10].

2.2. Method

The Ömerli basin groundwater potential study was determined by GIS. For this, the data obtained from approximately 320 boreholes drilled for irrigation and drinking purposes by drilling companies, as well as relevant institutions and organizations, were used. 130 of them were evaluated in the study area (Figure 2).

2.2.1. Outline of the study

GIS is a system that creates situations such as collecting, storing, querying, controlling, processing, analyzing and displaying the data of the earth for a purpose. With its additional extensions such as Spatial Analyze and Geostatistical Analyze, it has a wide range of uses such as interpolation, modeling, and production of state and forecast maps while performing statistical analyses. Applications such as ARC INFO, TNTmips, Map Info, and Net cad are the most common. In this study, the ArcMap 10.5 program was used. Within the

scope of this information, the following explanations were obtained;

➤ Along with the arrangement and digitization of the well data, these data were classified and results such as well depth, static water level, dynamic water level, well pump efficiency and opening time were obtained in 1/1,000.000 and 1/500.000 scales.

➤ Through the digitization of maps, shape (.shp) files have been created for contour lines, settlements, rivers, and streams. Using digital 1:100.000 and 1:50.000 map data, a Digital Elevation Model (DEM) map has been generated.

➤ In the Net cad program, Ömerli Basin (.ncz) files were first converted to (.shp) format with the ArcGIS Data Interoperability program and then opened in the ArcMap program.

➤ Ömerli basin groundwater data were collected and corrected in the Microsoft Excel program and converted to digital map with a GIS program.

➤ Spatial Analysis → Interpolation → IDW method was used in the ArcMap environment. Thanks to this technique, data belonging to unknown regions were obtained by using the data values in the known region and interpolating the weighted average method.

➤ Annual well data was organized, and separate thematic maps were created for each period. These maps include the Static Water Level map (Figure 3-III), Dynamic Water Level map (Figure 3-IV), Pump Efficiency map (Figure 3-V), and Well Depth map (Figure 3-IV).

➤ Spatial Analysis-evaluation, as seen in Table 1, estimated on pump efficiency; Achieved with 30% impact, 25% impact at low dynamic water level, 20% impact at near-surface static water levels, and 10% impact at depth [11].

➤ These thematic maps were reclassified and converted into raster maps. While preparing data for Optimum Groundwater Potential as shown in Table 1, a Spatial Analysis-assessment was performed with the following effects: 30%

for pump efficiency, 25% for low dynamic water levels, 20% for static water levels, 10% for surface and depth [11].

➤ Geographic Coordinate System GCS_WGS_1984 is used as a projection on the map.

2.2.2. AHP technique approach for determining groundwater potential of ömerli basin

In the study, the AHP method was used to maintain the groundwater processes. Fuzzy AHP is used to determine the preference weights of the evaluation [12].

In order to better express the verbal uncertainty to be encountered in determining the target market, Chang's [4] Order Analysis Technique, which is widely used in fuzzy AHP applications, was used as a solution technique [4].

The AHP method was developed in 1970 by Thomas L. Saaty at the Wharton School of Business to think for the solution of complex multi-criteria decision-making problems. This method is a technique that decision-makers (experts) need to have in determining the degree of importance by considering all criteria. Decision-makers, criteria, and sub-criteria make comparisons with Saaty's criteria 1-9 by filling out the criteria questionnaires. Ranks of alternatives to consider all criteria are found [13-23].

There are several multi-criteria decision-making (MCDM) methods available, among which the Analytic Hierarchy Process (AHP) offers significant advantages. One of its key benefits is its widespread use, which enables it to provide good results for complex decision problems involving both objective and subjective judgments [14].

AHP is a method that collects more than one statement under one heading and includes it. The hierarchical structure of complex numbers consists of binary comparisons, multiple factors and eigenvectors obtained by calculating their weights. Saaty gathered everything together, connected them and found a powerful method, AHP. With this method, the analysis became

easier and improved, and the number of applications using the AHP method increased by introducing the Expert Choice program. The first academic interviews by the International AHP Association were held in Tianjin, China [15].

AHP method is often used to evaluate decision options and solve problems. AHP is used in many studies such as making predictions, comparing, and ranking the factors that differ according to their importance. It is a multi-criteria decision-making formulation that shows the result of

comparisons between factors using the eigenvalue method and reveals the importance of numerical scales. In the AHP method, factors and options are compared in pairs by experts in this method. These comparisons generally use a scale of 1-9 developed by Saaty and given in Table 1 below [16].

The weights to be given to the criteria for groundwater performance in the AHP method by Vaidya and Kumar (2006) are given in Table 1 below.

Table 1. Importance ratings used in comparisons [17-18].

Importance level	Definition	Explanation
1	Equally Important	Both factors are equally important.
3	Moderately Important	According to experience and judgment, one factor is slightly more important than the other.
5	Strongly Important	One factor is strongly more important than the other.
7	Very Strongly Important	One factor is strongly more important than the other.
9	Absolutely Important	One of the factors is much more important than the other.
2, 4, 6, 8	Represents Intermediate Values	They are the intermediate values of the degrees found in the explanations above in the preference between the two factors.
Mutual Values	If a value (x) is assigned when comparing i with j; The value to assign when comparing j with i will be (1/x).	

In order to create a hierarchical structure in decision problems, the values of the criteria are found at each stage and pairwise comparisons are made. In the solution of the AHP method, the following process is followed;

- 1) Defining the decision problem and revealing the purpose,
- 2) Determining the criteria to reveal the purpose,
- 3) Creation of decision options,
- 4) Creation of hierarchical structure,
- 5) Making binary comparisons for each step, creating importance levels by using eigenvalues and eigenvector values,
- 6) Pairwise comparisons of options and priorities based on criteria,
- 7) Finding the compliance ratio,

- 8) Sorting the options and putting the option with the strongest priority first,
- 9) Calculation by sensitivity analysis

While finding W (weight matrix), the result is reached by using pairwise comparison. It is used relatively, that is, in verbal comparisons, as well as in comparisons with numerical data at the decision stage. Comparisons are usually made using Saaty's 1-9 weight scale. All comparison results will be positive. The diagonal values of the comparison matrix are 1. This is because the criterion is compared with itself [14].

If n relative importance weights with criteria a_1, a_2, \dots, a_n and weights w_1, w_2, \dots, w_n are taken into account, the general expression of the pairwise comparison matrix is as in Equation 1;

$$\begin{bmatrix} a_{11} & \dots & a_{1j} & \dots & a_{1n} \\ \vdots & \ddots & \vdots & \ddots & \vdots \\ a_{i1} & \dots & a_{ij} & \dots & a_{in} \\ \vdots & \ddots & \vdots & \ddots & \vdots \\ a_{n1} & \dots & a_{nj} & \dots & a_{nn} \end{bmatrix} \quad (1)$$

It exists as $a_{ij} = 1/a_{ji}$ and $a_{ij} = a_{ik}/a_{jk}$. In the real expression of the problem, W_i/W_j is unknown, therefore, the predicted $a_{ij} \cong W_i/W_j$ in AHP is to determine the result of a_{ij} .

The general expression of the weight matrix is Equation 2;

$$\begin{bmatrix} W_1/W_2 & \dots & W_1/W_j & \dots & W_1/W_n \\ \vdots & \ddots & \vdots & \ddots & \vdots \\ W_i/W_1 & \dots & W_i/W_j & \dots & W_i/W_n \\ \vdots & \ddots & \vdots & \ddots & \vdots \\ W_n/W_1 & \dots & W_n/W_j & \dots & W_n/W_n \end{bmatrix} \quad (2)$$

W (weight matrix) and w (weight values) values are multiplied and the result is;

$$W \cdot w = \begin{bmatrix} W_1/W_2 & \dots & W_1/W_j & \dots & W_1/W_n \\ \vdots & \ddots & \vdots & \ddots & \vdots \\ W_i/W_1 & \dots & W_i/W_j & \dots & W_i/W_n \\ \vdots & \ddots & \vdots & \ddots & \vdots \\ W_n/W_1 & \dots & W_n/W_j & \dots & W_n/W_n \end{bmatrix} \cdot \begin{bmatrix} W_1 \\ \vdots \\ W_i \\ \vdots \\ W_n \end{bmatrix} = n \cdot \begin{bmatrix} W_1 \\ \vdots \\ W_i \\ \vdots \\ W_n \end{bmatrix} \quad (3)$$

The equation takes the form of 2.

There is a base value for each evaluation factor. When we take the arithmetic average of these

values, λ_{max} (eigenvalue) is obtained for comparison [20]. $A \cdot w = \lambda_{max} \cdot w$ and λ_{max} are found together with the eigenvector w considering the relative weight values. λ_{max} is the eigenvalue of the matrix A and the eigenvector w and is calculated with $(A - \lambda_{max}I) \cdot w = 0$. Consistency Index (CI) and Consistency Ratio (CR) are included to find consistency of subjective results and correct relative weights. The Consistency Index (CI) is calculated as follows;

$$CI = \frac{\lambda_{max} - n}{n - 1} \quad (4)$$

Here n represents the total number of features, that is, the number of criteria. For a reliable result, the CI (Consistency Index) value should not exceed 0.1. Otherwise, the study must be repeated until this value (<0.1) is achieved. Consistency Rate (CR) is calculated as follows;

$$CR = CI/RI \quad (5)$$

RI stands for random value index. The RI values that different element values (n) can take are shown in Table 2 below [17].

Table 2 Random value index [17]

n	1	2	3	4	5	6	7	8	9	10	11	12	13	14	15
RI	0	0	0.58	0.90	1.12	1.24	1.32	1.41	1.45	1.49	1.51	1.54	1.56	1.57	1.59

3. Results

The planned management of groundwater resources plays a very important role for the sustainability of life in arid and semi-arid regions at every stage. The southern part of the study basin shows semi-arid climate characteristics. In the study area, the highest precipitation falls in the winter season, and the lowest precipitation falls in the summer season. The annual average temperature of Ömerli District is 19.7°C. The annual average rainfall is 425 mm.

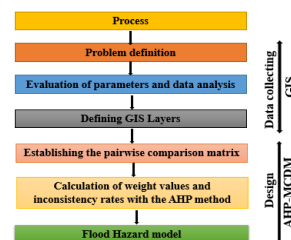


Figure 2. AHP method implementation template with GIS support [19].

First of all, raster thematic maps of the 6 parameters were produced in ArcMap (Figure 3) [3].

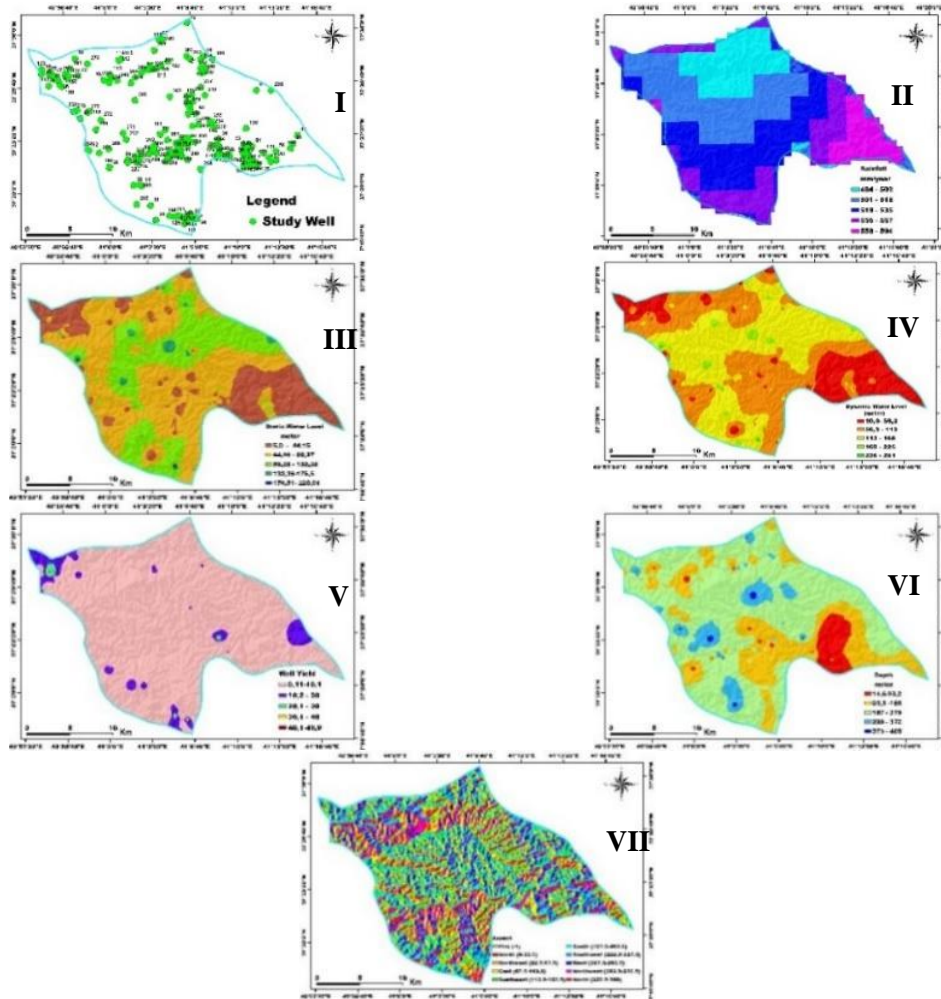


Figure 3. Thematic maps created according to the outline of the study (I. Study well, II. Rainfall, III. Static water level, IV. Dynamic water level, V. Well yield, VI. Depth, VII. Aspect map) After the creation of raster thematic maps, these maps were reclassified (Figure 4) [21-27].

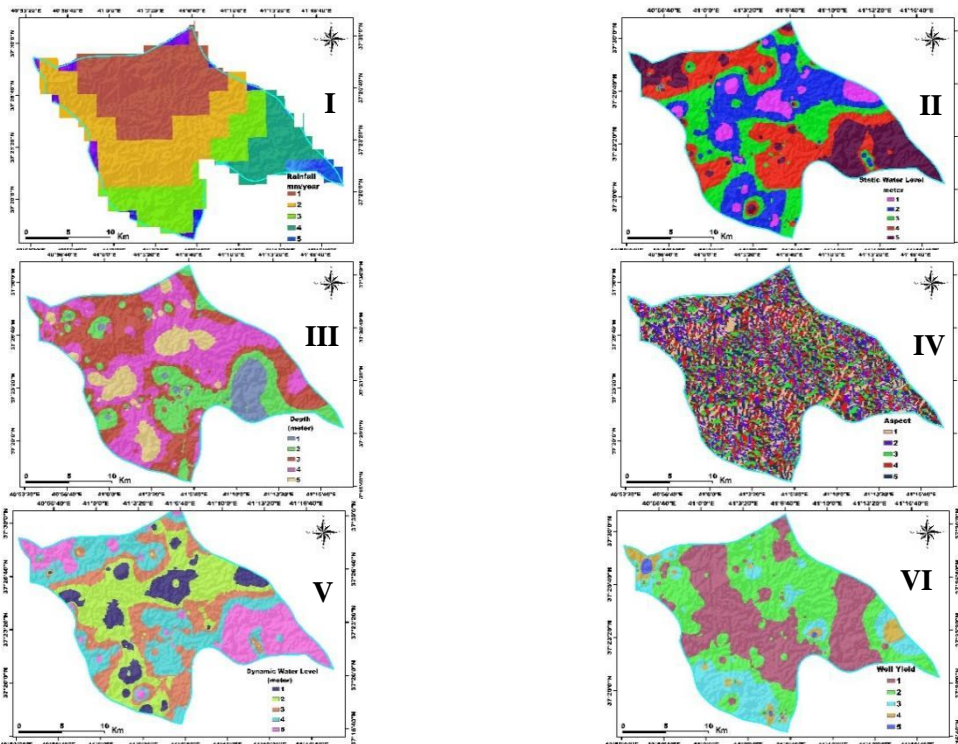


Figure 4. Classified maps created according to the outline of the study (I. Precipitation, II. Static water level, III. Dynamic water level, IV. Well yield, V. Depth map, VI. Aspect map)

Raster thematic maps were produced to create the infrastructure of the AHP method (Figure 2). These 6 parameters were then reclassified in the ArcMap environment (Figure 3).

After raster thematic maps are produced, Water wells are established for various purposes such as water supply, environmental monitoring, and Groundwater treatment. Technical parts related to well hydraulics;

Well Location Map: 220 of the 320 drilling data to be used in the well location map given in Figure 3-I were evaluated. Then, 15 of these data were taken into account as observation wells to be evaluated in the groundwater potential map.

Rainfall: The groundwater Potential Index distribution map is created to analyze the yearly 460-600 mm/year average rainfall, which is one of the crucial parameters. This thematic raster map is divided into five distinct classes during its creation within the ArcMap environment.

As seen in the map (Figure 3-II), the northern parts of the watershed have higher average annual rainfall, while the eastern regions experience lower average annual rainfall. Generally, the region exhibits similar precipitation patterns. It can be noted that not only the quantity of rainfall but also its duration and intensity play a significant role in nourishing the groundwater, in addition to the basin's groundwater potential. Extended periods of low-intensity rainfall will have a positive impact on the groundwater aquifer [6].

Static Water Level (SWL): The height at which the water level remains constant (the height between the surface level and the water level) when water is not drawn from a well. A static water level of 5 m in a well indicates that the water level is stable at 5 m below when pumping is not done. The static water level expressed for the basin is the general static level, not the specific static level in the plain where the well is drilled. If continuous observation is made within the basin boundaries, the average of the daily or monthly lowest levels of the surrounding wells is accepted as the general static level. The second point to be considered about the static level is that

if more than one well is to be drilled in the field, the wells should be wetted outside of each other's area of influence; If there is a necessity in this, static levels should be calculated by taking this effect into account [11]. Spatial Analyst tools/Multiple Value Determination method. The altitude values are recorded in the Excel table and the level of the aquifer is found by subtracting the Static Water Level from the altitude value. The aquifer map was created using Spatial Analyst Tools/Interpolation/IDW methods (Figure 3-III).

Dynamic Water Level (DWL): It is the height at which the water remains constant while the water drawn from a well continues with a certain flow rate. It is the height of the water gushing from the well in an artesian well.

Figure 5 was created inspired by the information of Vaidya and Kumar (2006). In the light of this information, criteria such as static water level, dynamic water level, and well efficiency are explained.

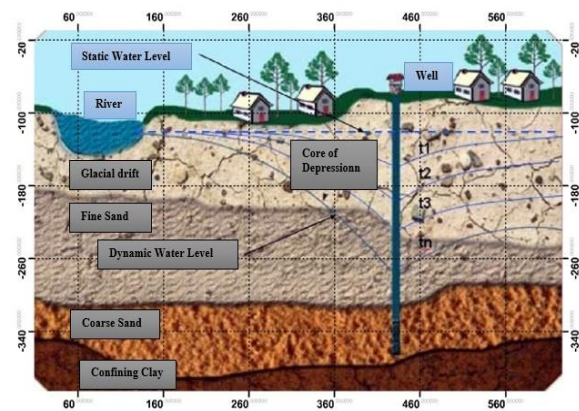


Figure 5. Groundwater and wells [20]

When the dynamic water level map of the groundwater of the basin is examined, it is seen that the groundwater flow is directed from the upper parts to the lower parts. As a natural consequence of this process, groundwater in the upper parts was carried to the lower parts, causing the water level to drop in the upper wells (Figure3-IV).

Well Yield: It is the volume of water drawn from a well per unit time. It is usually calculated in units of m^3/day , liters/hour. It is usually expressed as m^3/day or lt/s (Figure 3-V). The

purpose of water yield tests in wells is to obtain information about the hydraulics of the wells and the formations that give water (aquifers). When this information is combined with geological information, the groundwater situation of the aquifers and the plain can be understood. Obtaining and analyzing this information completely and accurately is especially important for the error-free preparation of business projects and the selection of the appropriate pump. The main purpose of groundwater survey is;

- Determination of aquifer properties
- Revealing well characteristics
- Pump selection suitable for wells

Well productivity for Ömerli plain almost varies between 0.11-11 l/s in most of the basin, while productivity can be between 20-30 l/s in the northwestern parts. It varies between 10-20 lt/s in different parts of the region.

As a result, it is understood that the middle parts of the Ömerli basin are higher in terms of both groundwater potential and productivity. When the maps obtained in the Ömerli basin study were compared with the groundwater maps of the Harran plain made by Aslan, Sepetcioğlu in 2022; It is seen that both basins have an average groundwater potential.

However, in the Ömerli basin, groundwater has been used as alternative drinking and utility water in other water sources as well as irrigation. The upstream part of these sources is Karacadağ. It reaches the historical Sur region with basalt cracks. However, considering the entire basin, these available resources alone are not sufficient to meet the water needs. When there is no mains water, the existing groundwater potential is at a level to meet the drinking water of the region [2].

The water levels in the well differ depending on the characteristics of the aquifer and the well. The position of the pump in the well becomes important in response to the water wells levels formed in the well. In deep water wells, it shows certain heights according to the movement or condition of the water. It is known that water levels in pumping wells affect pump operating characteristics.

The height of the pump, when it is not working, is defined as the static water level, and the decreasing water level after a while is defined as the dynamic water level, and the difference between these two heights is expressed as a decrease [6]. Immersion depth, on the other hand, refers to the water level up to the pump suction inlet when the well is at the dynamic water level. The vertical hydraulic head is the water level between the static water level and the pump inlet axis (Figure 1).

Schulz (2013) reported that the immersion depth of deep well pumps should be 5 m below the dynamic water level. In another study, it was emphasized that determining the dynamic submersion depth of the deep water well pump installation as 2-3 m and placing it according to this level depending on the fixed deep water well equipment and feeding would be more appropriate for the pump. working conditions [7].

Well Depth: The efficiency of a well depends on the specific flow and the reduction achieved.

Since the fall also depends on the thickness of the aquifer, in principle it is most convenient to drill a well at the bottom of the aquifer. If there is wells throughout the aquifer. The depth of the wells varies between 15 meters and 400 meters Since the fall also depends on the thickness of the aquifer, in principle it is most convenient to drill a well at the bottom of the aquifer. If there is no known poor quality or inefficiency in the aquifer layers, each well should be drilled to the (Figure 3-VI).

An inspection of the water surveillance in boreholes and observation wells is required from time to time before and during the pumping test or in various polluting water investigations. Accurate measurements are very important. Water levels in free and country aquifers can be measured by various methods. Measurement in free aquifer with advanced measuring instruments such as steel meter, electric meter, pressure gauge, air pipe. In the pressurized aquifer, the measurement is made with a plastic pipe and a manometer.

Aspect: Aspect refers to the direction of slope or the orientation of the hillside surface with respect to magnetic north, represented by values ranging

from 0 to 360 degrees in a clockwise direction. Additionally, the value for each cell in the dataset encompasses the direction of the cell's sloping surfaces.

Aspect determination possibilities, which have an important place in field analysis, without the direction of flat surfaces defined by the value of -1;

- To calculate the solar illumination of each location and to determine the biodiversity living in the area.
- After determining all the southern slopes of the mountains, finding where the snow will melt first and revealing the settlement areas that will be affected by snow waters,

- Besides recognizing flat areas, it can be used to identify many places of need and to see a kind of compass work.

Parameters are measured at different scales and thus standardized using the GIS reclassification tool. Each parameter is weighted according to its significance level (W_i) and applied as in Equation 5. The GIS technique is not capable of finding these weights (W_i);

For this reason, Analytical Hierarchy Process (AHP), one of the Multi-Criteria Decision Making methods, is used (Saaty, 2008). Each criterion is evaluated using a matrix of pairwise comparisons with the scales shown in Table 1 Table 3).

Table 3. Parameter values according to groundwater potential

Parameters	Values of Parameters for Groundwater (%)	Weighting of Parameters
Static Water Level	20	3
Dynamic Water Level	30	4
Well Yield	40	5
Groundwater Depth	10	2

3.1. AHP Approach for determination of ömerli basin groundwater potential

In the study, the Analytic Hierarchy Process (AHP) analysis method was employed to determine preference weights for the continuation and assessment of groundwater processes. This method is widely used as a solution technique for better expressing the verbal uncertainty encountered in target market identification. Additionally, it is a technique that requires the opinions of decision-makers to determine the relative importance levels concerning all criteria. Below is the AHP Method Sequential Application Working Template (Figure 6). In this study, decision-makers compared the criteria and sub-criteria using Saaty's 1-9 scale. Subsequently, all parameters were taken into consideration, and the priority sequence of alternatives was determined (Figure 4-5-6).

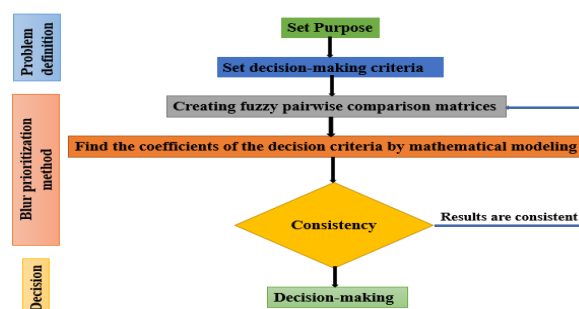


Figure 6. AHP method sequential application working template [12].

In establishing criteria for parameters, comparisons are needed to determine the importance of one criterion relative to another. The importance comparisons of the criteria were made within the framework of the experience gained so far and according to Table 1, which is the criterion comparison scale suggested by Saaty (2008) (Table 4).

Table 4. Used parameters and their weights

Parameters	Grade	Explanation
R	Rainfall	25 Very Strong
SWL	Static Water Level	10 Strong Plus
DWL	Dynamic Water Level	20 Very Strong
WY	Well Yield	30 Very Important
D	Groundwater Depth	9 Extra Important
A	Aspect	6 Important

Thus, a comparison matrix was created by comparing the importance of each criterion with each of the other criteria. In order to create the vector that will indicate the priorities of the criteria, the column total values of the comparison matrix were first calculated (Table 5).

Looking at the results in Table 6, the best the alternative parameters with the best performance are precipitation (22%), static water level (13.3%) and finally aspect sub-criteria (10%).

Table 5. Pairwise comparison matrix

Layers	Assigned Weights	R	SWL	DWL	WY	D	A
R	7	1.000	1.167	0.875	0.778	1.400	1.750
SWL	6	0.857	1.000	0.750	0.667	1.200	1.500
DWL	8	1.143	1.333	1.000	0.889	1.600	2.000
WY	9	1.286	1.500	1.125	1.000	1.800	2.250
D	5	0.714	0.833	0.625	0.556	1.000	1.250
A	4	0.571	0.667	0.500	0.444	0.800	1.000
Total		5.571	6.500	4.875	4.434	7.800	9.750

Table 6. Pairwise comparison matrix (Standardized matrix)

Layers	R	SWL	DWL	WY	D	A	Geometric mean	Normalized weight
R	0.63650	0.17954	0.17949	0.17546	0.17949	0.17949	1.47821	0.22575
SWL	0.15383	0.15385	0.15385	0.15043	0.15385	0.15385	0.93983	0.15328
DWL	0.20517	0.20508	0.20513	0.20049	0.20513	0.20513	1.03875	0.17094
WY	0.23084	0.23077	0.23077	0.22553	0.23077	0.23077	1.38976	0.22991
D	0.12816	0.12815	0.12821	0.12539	0.12821	0.12821	0.65298	0.10682
A	0.10250	0.10262	0.10256	0.10014	0.10256	0.10256	0.62414	0.10216

In establishing criteria regarding parameters, comparisons are needed to determine the degree of importance of one criterion relative to another.

$$\lambda_{\max} = 6.12367$$

$$\text{Consistency Index: CI} = (6.12367 - 6) / 5 = 0.024734$$

$$\text{CI/RI} = 0.057743 / 1.24 = 0.019947$$

If the consistency ratio is less than 0.10, the matrix is considered consistent, implying that the judgments of the decision-makers are consistent [22]. Therefore, the applied AHP technique for the Ömerli Basin is suitable for the research article ($0.1 > (\text{CI/RI} = 0.019947)$).

The values obtained as a result of the applied AHP Method are in ArcMap environment of ArcGIS; The GWPI region map was obtained by applying ArcToolbox → Spatial Analyst Tools → Overlay → Weighted Overlay.

3.2. Production of groundwater potential index distribution map

Six parameters, namely Rainfall (mm/year), Static Water Level (m), Dynamic Water Level (m), Well Pump Efficiency, Well Depth (m), and Aspect, have been classified and used to create the Groundwater Potential Index Distribution map. The calculation for the parameter "P" is defined as $P = (QH) / 200$, where Q represents the discharge of extracted water (m³/hour), and H represents the manometric height (m) (Figure 7).

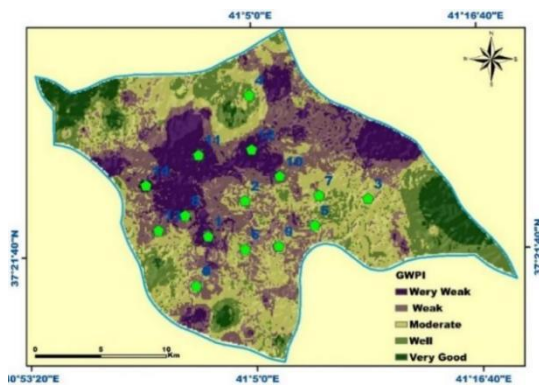


Figure 7. Ömerli basin optimum ground water enterprise map

The values in the GWPI area map of the Ömerli basin range between 454 and 594 and the corresponding percentage area calculations are shown in Table 7. Groundwater is potentially good or even very good, especially at the extreme points of the basin.

It can be said that the groundwater potential is weak or very weak, especially in the middle parts of the basin. It is a normal level in the southeast and northwest regions (Figure 7). Additionally, the green dots shown in Figure 7 represent observation wells [23].

Table 7. Classification according to Ömerli district boundary GWPI distribution values

GWPI Value	Description	Percentage (%)	Total area (409 km ²)
454-500	No bad	12,32	50,59
501-518	Not bad at all	14,27	58,36
519-535	Moderate level	25,35	103,68
536-557	Enough for the area	28,62	117,06
558-594	Pretty good for the county.	19,44	79,51

3.2.1. Validity (Verification)

Data obtained from 15 observation wells within the basin boundaries were utilized to validate the groundwater index area map of the basin. The groundwater study area map, indicating the locations of observation wells, is illustrated in Figure 4 within the GWPZ map. Nearly all the

irrigation pumping wells currently in use are assessed as having very good, poor, (weak), or very weak groundwater potential for the region. Based on this classification, only 1 out of the 15 reference well data showed partial compatibility. Perfect compatibility was achieved for 14 of these wells [24-26] (Table 8).

Table 8. Data from GWPI and wells are compared

RN	Town	X	Y	Z	Depth	SWL	DWL	Yield	GWPI	Evaluation	Rapport
1	Alicli	680992	4134521	250	250	103	112	11	254	Poor	Compatible
2	Gollu	681904	4148060	250	325	123	129	10	239	Good	Compatible
3	Alicli	680926	4138342	225	311	113	129	4	224	Poor	Compatible
4	Salih	677324	4146986	250	271	53	77	3	245	Good	Compatible
5	Kocakuyu	674886	674886	110	197	80	90	2	233	Poor	Compatible
6	Catalyurt	680926	4138342	86	174	45	54	3	227	Poor	Compatible
7	Yesilli	686277	4139659	65	159	43	51	8	212	Good	Compatible
8	Salih	676559	4146844	79	183	60	85	2	203	Good	Compatible
9	Yeni Mahalle	671691	4146078	160	85	22	59	2	208	Good	Compatible
10	Besikkaya	683729	4141036	80	92	43	57	4.9	201	Poor	Compatible
11	Kayaüstü	670137	4146177	200	270	60	85	3	273	Good	Compatible
12	Salih	678596	4149312	160	221	53	71	2	231	Poor	P Compatible
13	Kayadere	669266	4148076	180	200	19	44	2	204	Moderate	Compatible

Partially Compatible: P. Compatible

3.3. Analysis of the study

In the Ömerli basin, annual rainfall generally ranges between 480 mm/year and occasionally reaches 590 mm/year. The majority of this precipitation occurs in the southeastern part of the area, which is the mountainous region. The city center, being a plain area, receives relatively low amounts of rainfall. Instead of relying on surface runoff, groundwater is predominantly used, particularly for irrigation purposes. Static

Water Level (SWL) values vary between 5 m and, to a lesser extent, 220 m. The Dynamic Water Level (DWL) within the basin ranges from around 10 m depth to partially 280 m. Well yield varies between 0.11 and 12 l/s, while well depths range from 22 m up to around 400 meters in certain areas. The Baki map highlights the significance of terrain orientation and groundwater flow directions.

From an operational perspective in the study, pump efficiency was considered significant, and thus assigned a weight of 30%. Subsequently, the

importance of rainfall was evaluated at 25%. The assessment for Dynamic Water Level (DWL) was set at 20%, followed by 12% for Static Water Level, 7% for groundwater depth, and 6% for the Aspect parameter. The groundwater potential within the basin is at a good level. This signifies the region's economic capacity to extract groundwater and its possession of a substantial groundwater potential. While the groundwater potential is lower at the basin's center, it tends to be generally moderate in the eastern and western parts, as well as the northwest region. However, in the northwest and western areas, namely Kocakuyu, Koçak, Çatalyurt, and Kayadere, groundwater management seems to be weaker.

4. Conclusion and Recommendations

Within the scope of this study, a water potential evaluation index was developed by using the GIS-supported AHP method in order to evaluate the groundwater potential within the boundaries of the Ömerli basin in terms of drinking and utility water. In the creation of the water potential index, the results of the analysis of the data obtained from the water wells drilled by the relevant institutions and organizations, and the private sector were used.

The criteria constituting the water potential evaluation index were selected by taking into account the expert opinions and water potential standards, and a weight indicating the water potential status was obtained for each criterion. In this way, an index showing the total water potential suitability ratio was developed. The water potential index for the study area is very good (19.44%), high quality (28.62 %), medium quality (25.35%), low quality (14.27%) and very poor (12.32%) defined in five categories.

A geostatistical method known as the groundwater potential index and the Inverse Distance Weighting (IDW) method was used to generate distribution maps of the water potential of the study area. According to these maps, in the southeast and northwest parts of the study area, which covers an area of approximately 200 km², water quality is seen as very high and high areas.

As a result of this study, the proposed method can be reliably and successfully used for identifying areas with high water potential and in water

potential assessment studies. The utilization of groundwater potential maps indicating areas with high water potential can enhance the productivity of drinking water, irrigation, and agricultural activities. Simultaneously, it can also help mitigate potential economic losses arising from wells in regions with low water potential.

Groundwater potential maps created for the study area can be used by local authorities, engineers, urban and regional planners, further enhancing their decision-making processes. Also, as a recommendation;

Moreover, the findings of this research suggest that the developed groundwater potential assessment method could provide reliable results for identifying areas suitable for water supply and sustainable agricultural practices. The integration of these maps into water resource management and land-use planning strategies could lead to more informed and efficient decision-making processes, benefiting both local communities and regional development efforts [25].

- Penal sanctions should be applied to machines that drill wells without permission.
- In order to make irrigation system transformations on time, regularly and at the desired speed, and to apply drip irrigation systems in pressurized systems instead of flood irrigation, joint funds should be created and resources should be transferred to institutions and organizations.
- Considering that groundwaters are public property, it should be taken into account that the waters in the region are the most important strategic national resource for our country, and ways of transferring the heritage to the future by protecting it in a cleaner and usable way should be sought.
- The equipment and insulation of the wells to be drilled for irrigation, utility, and drinking water should be done in accordance with the standards.
- When the data of the last 10 years are evaluated, it is seen in the graphs that the YES level in the Basin has decreased by

approximately 20-25 m. For this reason, regardless of the number of reservoirs and wells, after deciding at which meter to keep the targeted groundwater level, excess water withdrawal should be prevented.

- First of all, the water drawn from the wells should be taken under control. If gravity is controlled it can be controlled and the management of groundwater will be more effective, easier, and sustainable.
- Considering the certified, undocumented and additional wells, projects at the planning stage, and cooperative irrigation areas in surface irrigation in the enterprise, is it primarily surface water or groundwater? choice must be made [26-27].
- All undocumented wells should be taken under control. It should be ensured that the wells are used in the project by looking at the inventory of the mourning wells opened by the citizens for the groundwater projected in the region.
- The electrification networks of these wells should be projected and transferred to units to be established by the State.
- Underground water wells will be controlled and illegal electricity usage will be prevented.

Funding

The author (s) has no received any financial support for the research, authorship or publication of this study.

Authors' Contribution

Since the author is a person, he equally did the work himself.

The Declaration of Conflict of Interest/ Common Interest

No conflict of interest or common interest is declared by the author.

The Declaration of Ethics Committee Approval

This study does not require ethics committee permission or any special permission.

The Declaration of Research and Publication Ethics

The author of the article declares that they complied with the scientific, ethical and citation rules of SAUJS in all processes of the article and did not falsify the collected data. He also declares that Sakarya University Science Journal and its editorial board have no responsibility for ethical violations that may be encountered, and that this study has not been evaluated in any academic publication environment other than Sakarya University Science Journal.

Copyright Statement

Authors own the copyright of their work published in the journal and their work is published under the CC BY-NC 4.0 license.






References

- [1] (GDM). General Directorate of Meteorology, "Annual Total Area Precipitation Data", 2017.
- [2] D. Yang, Y. Yang, J. Xia, "Hydrological cycle and water resources in a changing world: A review". *Geography and Sustainability*, vol. 2, no. 2, 115-122, 2021.
- [3] M. Özdoğan, A. O. Üstündağ and H. Demirel, "Evaluation of Aydın Province Groundwater in terms of Drinking Water Quality for Livestock". *Adnan Menderes University Journal of the Faculty of Agriculture*, vol. 13, no. 2, 113-122, 2016.
- [4] C. H. Chang, "Evaluating naval tactical missile systems by fuzzy AHP based on the grade value of membership function". *European journal of operational research*, vol. 96, no. 2, 343-350 1997.
- [5] O. Rahmati, A. Nazari Samani, M. Mahdavi, H. R. Pourghasemi, H. Zeinivand, "Groundwater potential mapping at Kurdistan region of Iran using analytic hierarchy process and GIS". *Arabian Journal of Geosciences*, vol. 8, no. 9, 7059-7071, 2015.

- [6] S. Çalşır, “Promotional Facilities in Irrigation”. Chapter 14. Agricultural Machinery Book Editor: Gazanfer ERGUNES, Nobel Publication Distribution, 2009.
- [7] N. Orhan, “Determination of critical immersion depth in submersible pumps”, 2018.
- [8] H. Schulz, “The Pumps: How They Work, Calculation, Construction”. Springer-Verlag, 2013.
- [9] T. Melese, T. Belay, “Groundwater potential zone mapping using analytical hierarchy process and GIS in Muga Watershed”, Abay Basin, Ethiopia. *Global Challenges*, vol. 6, no.1, 2100068, 2022.
- [10] C. Mercan, S. Arpag, “Evaluation of Soil and Land Characteristics Using Geographic Information System Analysis”: Türkiye, Mardin Province Land. *Turkish Journal of Agricultural Research Magazine*, vol. 7, no. 1, 23-33, 2020.
- [11] R. Çelik, "Investigation of groundwater potential in Diyarbakır's historical sur region". *Dicle University Faculty of Engineering Engineering Journal*, vol. 8, no. 2, 319-326, 2017.
- [12] T. Kaya, C. Kahraman, “An integrated fuzzy AHP–ELECTRE methodology for environmental impact assessment”. *Expert Systems with Applications*, vol. 38, no. 7, 8553-8562, 2011.
- [13] O. Günhan, “An Appropriate Methodology Study for the Evaluation of Groundwater Quality”. TR Ministry of Forestry and Water Affairs Specialization Thesis, 113, 2014.
- [14] F. Yıldırım, E. Önder, “Multi-Criteria Decision Making Methods”, Dora Publishing, Istanbul, 2014.
- [15] E. H. Forman, M.A. Selly, “Decision by Objectives: How to Convince Others That You Are Right”, World Scientific, 2001.
- [16] K. C. Chejarla, O. S. Vaidya, S. Kumar, “MCDM applications in logistics performance evaluation: A literature review”. *Journal of Multi-Criteria Decision Analysis*, vol. 29, no. 3-4, 274-297, 2022,
- [17] T. L. Saaty, L. G. Vargas, H. J. Zoffer, “A structured scientific solution to the Israeli–Palestinian conflict: the analytic hierarchy process approach”. *Decision Analytics*, vol. 2, no. 1, 1-53, 2015.
- [18] M. Timor, “Analytical Hierarchy Process, Turkmen Bookstore”, ISBN: 9786054259502, 2011.
- [19] V Aslan, R. Çelik, “Integrated gis-based multi-criteria analysis for groundwater potential mapping in the euphrates’s sub-basin, harran basin, Türkiye”. *Sustainability*, vol. 13, no. 13, 7375, 2021.
- [20] O. S. Vaidya, S. Kumar, “Analytic hierarchy process: An overview of applications”. *European Journal of operational research*, vol. 169, no. 1,1-29, 2006.
- [21] V. Aslan, M. Y. Sepetçioğlu, “Modeling Of Groundwater Potential And Quality Of Harran Plain ByGis Supported Ahp And Topsis Methods”. *Turkish Hydraulic Magazine*, vol. 6, no. 1, 31-41, 2022.

- [22] A. Öner, F. Ülengin, “AHP approach to weapon selection”. Military Academy, 1st Systems Engineering and Defense Applications Symposium, Proceedings-II, 1109, 1122. 1995.
- [23] M. Zeinolabedini, A. Esmaily, “Groundwater potential assessment using geographic information systems and AHP method (Case study: Baft city, Kerman, Iran)”. The International Archives of the Photogrammetry, Remote Sensing and Spatial Information Sciences, vol. 40, 769-774. 2015.
- [24] M. Kavurmacı, A. Üstün, “Evaluation of water quality using multi-criteria decision analysis and Geographic Information System (GIS)”. KSU Journal of Natural Sciences, vol. 19, no. 2, 208-220, 2016.
- [25] H. F. Yeh, Y. S. Cheng, H. I. Lin, C. H. Lee, “Mapping groundwater recharge potential zone using a GIS approach in Hualian River”, Taiwan. Sustainable Environment Research, vol. 26, no. 1, 33-43, 2016.
- [26] M. J. Nasır, S. Khan, H. Zahid, A. Khan, “Delineation of groundwater potential zones using GIS and multi influence factor (MIF) techniques: a study of district Swat, Khyber Pakhtunkhwa, Pakistan”. Environmental Earth Sciences, vol. 77, 1-11, 2018.
- [27] Ö. Arif, M., O. Dengiz, M. Sağlam, A. Erkoçak, F. Türkmen, “Mapping and assessment-based modeling of soil fertility differences in the central and eastern parts of the Black Sea region using GIS and geostatistical approaches”. Arabian Journal of Geosciences, vol. 10, 1-9, 2017.

Ameliorative Effect of a Vanadium-thiosemicarbazone Complex on Oxidative Stress in Stomach Tissue of Experimental Diabetic Rats

Fatma Gülnaz Karakuş¹, Sevim Tunalı^{*1}, Tülay Bal Demirci², Bahri Ülküseven², Refiye Yanardağ¹

¹ Istanbul University-Cerrahpaşa, Faculty of Engineering, Department of Chemistry, Biochemistry Division, Istanbul, Türkiye, f.g.guler@hotmail.com, stunali@iuc.edu.tr, yanardag@iuc.edu.tr

² Istanbul University-Cerrahpaşa, Faculty of Engineering, Department of Chemistry, Inorganic Chemistry Division, Istanbul, Türkiye, tulaybal@iuc.edu.tr, bahseven@iuc.edu.tr

*Corresponding Author,

ARTICLE INFO

ABSTRACT

Keywords:
Diabetes mellitus
Vanadium complex
Stomach tissue
Oxidative stress



Article History:

Received: 28.04.2023

Accepted: 21.11.2023

Online Available: 27.02.2024

Recently, we have shown that oral administrations of an oxidovanadium (IV) complex, VOL, with tetradentate thiosemicarbazone ligand normalizes hyperglycemia of streptozotocin-induced diabetic rats (STZ-rats). For the development of vanadium compounds that exhibit insulin-like behavior, it is essential to know some of the pharmacokinetic properties of these complexes. The goal of the current research is to examine the healing effect of new synthesized VOL complex on the oxidative stress parameters of diabetic stomach tissue. Rats used in the experiments were divided as control, VOL+control, diabetic and diabetic+VOL. The rats were sacrificed after 12 days of the experimental period. The levels of glutathione, lipid peroxidation, non-enzymatic glycosylation, advanced oxidized protein products levels and the activities of some enzymes were measured in stomach tissue of all the experimental animals. Although VOL treatment to diabetic rats increased the stomach glutathione levels; lipid peroxidation, non-enzymatic glycosylation and advanced oxidized protein products levels were decreased. Also, the activities of catalase, superoxide dismutase, glutathione-S-transferase, glutathione peroxidase, glutathione reductase and carbonic anhydrase were increased in VOL treated diabetic group. Whereas, lactate dehydrogenase and xanthine oxidase activities were decreased. According to the obtained outcomes, it can be said that VOL treatment has a healing effect on the stomach tissue of diabetic rats. This effect provided by VOL is most likely due to the insulin-like and antioxidant activity of the complex. In conclusion, we can say that VOL may be a suitable candidate for diabetes treatment

1. Introduction

In recent years, increasing urbanization and deteriorating lifestyle has led to an increasing level of diabetes mellitus (DM), which is estimated to reach 700 million worldwide by 2045 [1]. The main underlying causes are the disruptions in carbohydrate, lipid and protein metabolisms due to insufficient insulin levels or its action on target tissues such as eyes, skin, kidneys, heart, nerve and stomach [2-6]. In

addition to disorders in insulin metabolism, recent reports show that severe acute respiratory syndrome coronavirus 2 (SARS-CoV-2) infection can also induce hyperglycemia and diabetic ketoacidosis as a result of coronavirus disease 2019 (COVID-19) complications even in nondiabetic patients [7].

Although the diffusiveness of diabetic gastroenteropathy has not been fully disclosed, there is shown that the 10-year cumulative

incidence of diabetic gastroparesis is 5.2% for patients with type 1 DM, and 1% for type 2 DM patients [8]. The most common gastrointestinal dysfunctions in diabetic patients are nausea, vomiting, diarrhea, heartburn, constipation, and motor dysfunction in various segments of the system [9].

Hyperglycemia can alter oxidant/antioxidant balance in the biological system, which is an important factor causing oxidative stress [10]. High free radical production and accumulation, which occurs through metabolic reactions and immune cell responses as well as processes such as cell interactions and signaling, cell growth, aging, synaptic plasticity, autoimmune reactions, autophagy and apoptosis, can trigger devastating biological effects. [11].

Streptozotocin (STZ) is a diabetes-inducing agent that acts directly on the islet beta cells of the pancreas, causing an elevation of reactive oxygen species (ROS) levels and weakening of the defense system that neutralizes them [12]. The degeneration of insulin-producing beta cells in the pancreas leads to the pathogenesis of diabetic [13].

There are various oral antihyperglycemics currently available for the treatment of diabetes. From them, sulfonylureas and biguanides have been in use since the 1950s. The sulfonylurea family (glyburide, glimepiride and glipizide) bestows their antidiabetic action via a mechanism that involves stimulating insulin secretion [14-16], while biguanides (metformin) act by increasing insulin activity [17]. Contrary to these traditional agents whose glucose-lowering effects were serendipitously discovered, a new generation of oral antidiabetics such as dipeptidyl peptidase-4 inhibitors have been developed [18]. However, different prospective studies are rapidly underway to find the most effective orally active insulin replacements or insulin mimicking agents.

Vanadium is an ultra-trace element that acts as a cofactor for some intra cellular enzymatic reactions in the biological system. It is also closely related to glucose homeostasis, lipid metabolism, antioxidant functions and regulation of immunity in humans and animals [19]. Initial

findings suggested that vanadium had replaced insulin in living organisms. However, it was later reported to enhance insulin secretion by regenerating pancreatic beta cells [20, 21]. Furthermore, vanadium and some of its complexes have curative effects on hyperlipidemia and hypertension. They are also potential agents to cure malignant tumors, heart and neuronal disorders, influenza and viral infections like human immunodeficiency virus (HIV) and SARS-CoV-2 [19, 22].

Although diabetic gastroenteropathy is often associated with other manifestations of DM, its prevalence is not well documented. The current research is aimed at determining the effects of thiosemicarbazone-based oxidovanadium (IV) complex (VOL) on biochemical changes in stomach tissue of diabetic rats as a candidate for alternative therapies.

2. Materials and Methods

2.1. Synthesis

2,4-dihydroxybenzaldehyde-S-methyl-thiosemicarbazone was used as starting material to obtain 2,4-dihydroxybenzylidene-N (4)-2-hydroxybenzylidene-S-methyl-thiosemicarbazidato-oxidovanadium (IV) (VOL). The compound was prepared according to previously reported methods [21, 23, 24]. 2,4-dihydroxybenzaldehyde (1 mmol) was added to the solution of S-methyl-thiosemicarbazide (1 mmol) in ethanol (50 ml), and refluxed for 4 hours. The cream-colored precipitate formed was filtered, and recrystallized with ethanol (m.p.:180-181 °C, yield: 92%).

Further reactions were proceeded when $\text{VO}_2\text{SO}_4 \cdot 5\text{H}_2\text{O}$ (1 mmol) was dissolved in a balloon flask by adding ethanol (50 ml). The solution of the starting material (1 mmol), 2-hydroxybenzaldehyde (1 mmol) were added to balloon containing the metal solution and then stirred for 5 hours [21, 25]. The brownish-powder product formed was filtered, and its structural confirmation was evaluated by elemental analysis, UV and IR spectra (Fig 1). The characterization data are: Yield 68%, m.p. > 380-381°C. μ_{eff} : 1.64 BM. Anal. Calc. for $\text{C}_{16}\text{H}_{13}\text{N}_3\text{O}_4\text{SV}$ (394.3 g mol⁻¹): Found (calc.): C,

48.77 (48.74); H, 3.30 (3.30); N, 10.69 (10.66); S, 8.12 (8.09). UV-Vis (λ nm in DMSO): 246, 316, 352, 418, 800, 958. IR (ATR, cm^{-1}): $\nu(\text{OH})$ 3411, $\nu(\text{C}=\text{N})$ 1605, 1595, 1578, $\nu(\text{C}-\text{O})$ 1146-1123, $\nu(\text{V}=\text{O})$ 985, $\nu(\text{V}-\text{O})$ 477-434.

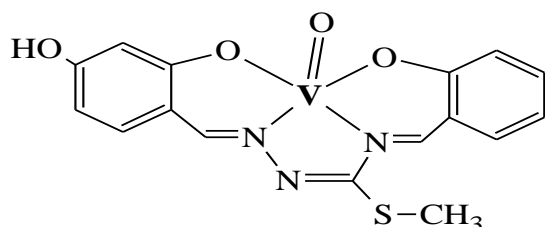


Figure 1. The oxidovanadium (IV) complex, VOL

2.2. Animal groupings

Male Swiss albino rats (between 3.0-3.5 months old and 200 ± 50 g weight) were provided from Animal Care and Use Institute's Committee of Istanbul University. Before starting the study, all rats were housed in the same conditions. Animals, fed with standard pellets, were allowed to access water *ad libitum*. The experimental protocols were reviewed and approved by the Animal Care and Use Institute's Committee of Istanbul University. Animals were randomly selected into four experimental groups as follows: two control groups divided as (Group 1; $n=5$) control group-intact and (Group 2; $n=5$) treated control-which received VOL (0.2 mM/kg/day); two diabetic groups separated as (Group 3; $n=6$) diabetic control-injected with streptozotocin (STZ) (65 mg/kg body weight) and (Group 4; $n=5$) VOL treated diabetic group (received the same doses of STZ and VOL). VOL was given to the rats by gavage technique (upon dissolution in 3% gum arabic solution) for 12 days after the rats became diabetic [26]. On day 12, last day of the experiment, the animals were sacrificed under anesthesia and stomach tissue samples were collected.

2.3. Diabetic model induction

After overnight fasting but allowed free access to water, diabetes was induced via a single intraperitoneal injection (i.p.) of STZ (dissolved in cold citrate buffer (0.1 M, pH 4.5) to the rats (65 mg/kg) [27]. Diabetes was confirmed from tail blood samples after 24 hours of injection. A

blood glucose level above 250 mg/dL was considered a standard for successful diabetic model induction. On the 0, 1, 6 and 12 days, blood glucose and weight of all animals were examined. This section was detailed in the study based on synthesis characterization and antidiabetic properties of the VOL complex [21].

2.4. Sample collection

After intervention for 12 days, the rats in each group were sacrificed and stomach specimens were carefully collected. Stomach tissues were homogenized in a cold saline solution (0.9 %), and centrifuged at $15000 \times g$, $+4^\circ\text{C}$ for 10 minutes. The clear supernatant of each sample was aliquoted into several vials and stored at -76°C for biochemical analysis for later use.

2.5. Analysis of oxidative stress markers and antioxidant enzyme activities

The reduced glutathione (GSH), lipid peroxidation (LPO), advanced oxidized protein products (AOPP), non-enzymatic glycosylation (NEG), and total protein levels of the stomach homogenates were determined according to the methods of Beutler [28] - using Ellman's reagent, Ledwozyw et al. [29], Witko-Sarsat et al. [30], thiobarbituric acid method [31] and Lowry et al. [32], respectively. Catalase (CAT), superoxide dismutase (SOD), glutathione peroxidase (GPx), glutathione reductase (GR) and glutathione-S-transferase (GST) activities were assessed as described by Aebi [33], Mylorie et al. [34], Paglia & Valentine [35] and modified by Wendel [36], Beutler [37] and Habig & Jakoby [38], respectively. The activities of carbonic anhydrase (CA), lactate dehydrogenase (LDH) and xanthine oxidase (XO) were estimated according to Verpoorte et al. [39], Wroblewski [40] and Corte & Stirpe [41], respectively.

2.6. Statistical analysis

Biochemical findings were evaluated using GraphPad Prism Software, version 6.01 (San Diego, USA). Data were expressed as mean \pm standard deviation (SD) using one-way analysis of variance (One-way ANOVA), followed by

Tukey's multiple comparison post hoc test. $p < 0.05$ was considered statistically significant.

3. Results and Discussion

3.1. Synthesis and structural confirmation

Complex VOL was obtained from the template reaction of the starting material and aldehyde in the presence of oxovanadium (II) ion. Formation of the complex was monitored through IR spectrum, by tracking bands attributed to the 2-OH and NH₂ groups on the starting material. The disappearance of these bands and the emergence of bands related to the V=O and VO vibrations were evidence of VOL formation [21].

In IR spectrum of the starting material, the imine groups were observed at 1608 and 1585 cm⁻¹, while the hydroxyl group was monitored at 3495 cm⁻¹. In the infrared spectrum of VOL, bands attributed to C=N1 and N4=C were monitored at 1605, 1595, and 1578 cm⁻¹ respectively. Additionally, while the stretching and bending bands at 3445, 3337 and 1624 cm⁻¹ of amine group of the starting material disappeared, new bands formed at 985, 477-434 cm⁻¹ assigned to V=O and VO groups were observed. The UV-Vis spectrum of VOL showed the charge transfer bands at the 246, 316 and 352 nm assigned to $\pi \rightarrow \pi^*$ and $n \rightarrow \pi^*$, d-d bands at 418, 800 and 958 nm [21].

The structure and purity of the products were checked by elemental and TLC analyses. Before the biological tests, the stability of VOL was investigated in gum arabic solution by monitoring UV-Vis spectrum. The absorptions and λ_{max} values remained unchanged for 20 days.

3.2. Biochemical result

The findings regarding body weight and fasting blood glucose levels of the animals used in the present study has been previously reported [21]. The loss in body weight as well as increased blood glucose levels that arise due to STZ administration were diminished by VOL treatment.

Fig. 2 represents the levels of GSH and LPO parameters in the control and other experimental

groups. An evident decrease in GSH ($p < 0.05$) and significantly increased LPO ($p < 0.05$) was observed in the diabetic group. In contrast, the administration of VOL to the diabetic animals markedly increased ($p < 0.05$) GSH level, whereas the level of LPO significantly decreased ($p < 0.0001$) as compared to non-treated diabetic rats (Fig. 2).

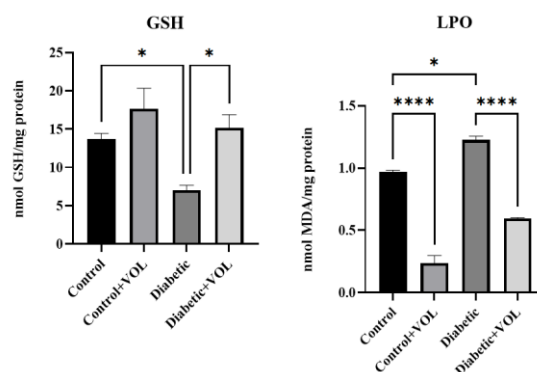


Figure 2. Effects of VOL on gastric tissue GSH and LPO levels in control and experimental animals

* $p < 0.05$; **** $p < 0.0001$; VOL: N (1)-2, 4-dihydroxybenzylidene-N-(4)hydroxybenzylidene-S-methyl thiosemicarbazidato-oxidovanadium (IV); GSH: reduced glutathione; LPO: lipid peroxidation

The levels of AOPP and NEG are presented in Fig. 3. Elevated AOPP and NEG levels were observed in the STZ-treated group when compared to the control group ($p < 0.05$; $p < 0.05$). The 12 days treatment of the diabetic animals with VOL resulted in a significant decline in the levels of both AOPP and NEG when compared to the solely STZ administered rats ($p < 0.05$; $p < 0.05$).

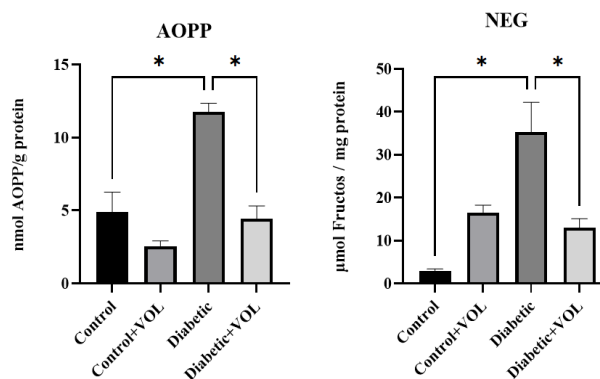


Figure 3. Effects of VOL on gastric tissue AOPP and NEG levels in control and experimental animals

* $p < 0.05$; VOL: N (1)-2, 4-dihydroxybenzylidene-N-(4)hydroxybenzylidene-S-methyl thiosemicarbazidato-oxidovanadium (IV); AOPP: advanced oxidized protein products; NEG: non enzymatic glycolisation

An apparent reduction in the activities, CAT and SOD (though not statistically significant) of diabetic rats in comparison to control was observed (Fig. 4). Moreover, the activities of these enzymes significantly increased upon treatment of the diabetic rats with VOL as compared to non-treated diabetic animals ($p < 0.01$; $p < 0.0001$).

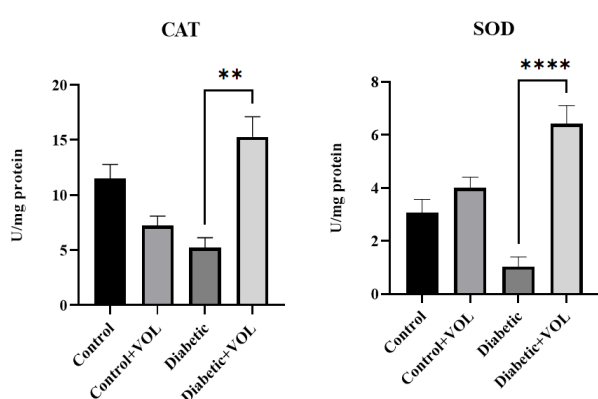


Figure 4. Effects of VOL on gastric tissue CAT and SOD activities in control and experimental animals

** $p < 0.01$; **** $p < 0.0001$; VOL: N (1)-2, 4-dihydroxybenzylidene-N-(4)hydroxybenzylidene-S-methyl thiosemicarbazidato-oxidovanadium (IV); CAT: catalase; SOD: superoxide dismutase

Gastric tissue LDH, XO and CA activities for all the experimental groups are given in Figs. 5, 6. Compared to the control group, significantly higher LDH and XO activities ($p < 0.01$; $p < 0.001$, respectively) were observed in the non-treated diabetic group. The rise in the activity of these enzymes (LDH and XO) due to diabetes was significantly attenuated by VOL ($p < 0.01$; $p < 0.0001$, respectively) (Fig. 5). Similarly, the activity of CA was significantly elevated in the diabetic group as compared to control animals ($p < 0.0001$). The 12 days VOL administration to diabetic animals significantly increased CA activity when compared to the non-treated hyperglycemic group ($p < 0.0001$) (Fig. 6).

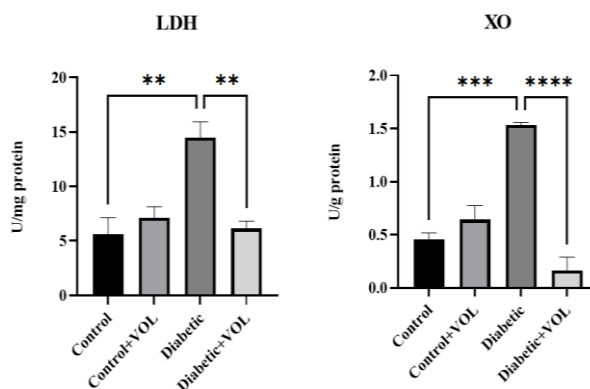


Figure 5. Effects of VOL on gastric tissue LDH and XO activities in control and experimental animals

** $p < 0.01$; *** $p < 0.001$; **** $p < 0.0001$;

VOL: N (1)-2, 4-dihydroxybenzylidene-N-(4)hydroxybenzylidene-S-methyl thiosemicarbazidato-oxidovanadium (IV); LDH: lactate dehydrogenase; XO: xanthine oxidase

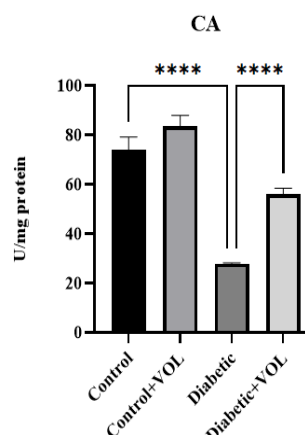


Figure 6. Effects of VOL on gastric tissue CA activity in control and experimental animals

**** $p < 0.0001$; VOL: N (1)-2, 4-dihydroxybenzylidene-N-(4)hydroxybenzylidene-S-methyl thiosemicarbazidato-oxidovanadium (IV); CA: carbonic anhydrase

The activities of GST, GPx and GR of the hyperglycemic group markedly decreased when compared to non-treated control animals ($p < 0.001$; $p < 0.05$; $p < 0.001$). On the other hand, VOL treatment significantly increased the activities of these antioxidant enzymes in the diabetic rats when compared to the hyperglycemic animals ($p < 0.01$) (Figure 7).

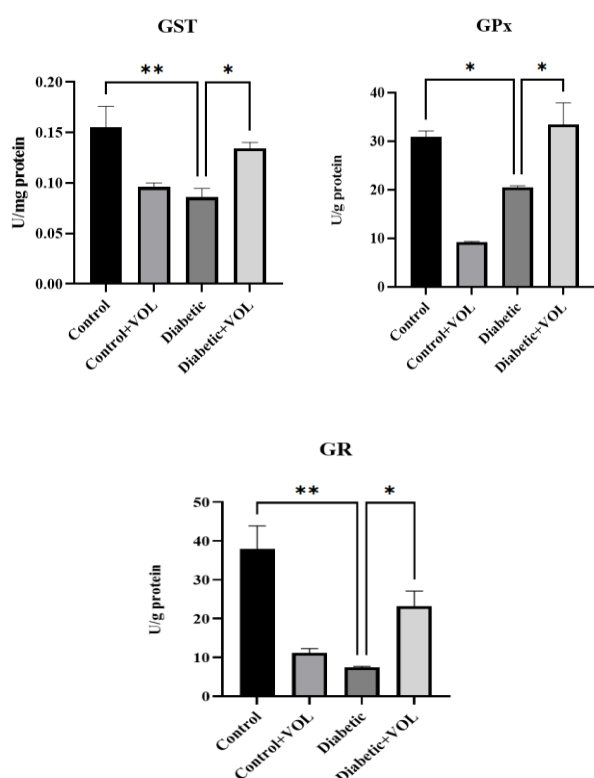


Figure 7. Effects of VOL on gastric tissue GST, GPx and GR activities in control and experimental animals

* $p < 0.05$; ** $p < 0.01$; VOL: N (1)-2, 4-dihydroxybenzylidene-N-(4)hydroxybenzylidene-S-methyl thiosemicarbazidato-oxidovanadium (IV); GST: glutathione-S-transferase; GPx: glutathione peroxidase; GR: glutathione reductase

Oxidative stress has a very common effect on the emergence and the progression of diabetes, as well as its complications [42]. An abnormally increased level of free radicals can compromise the function of the antioxidant defense system. Thus, resulting in damage to the intra-cellular organelles, defective enzyme activities, increased lipid peroxidation levels, and insulin resistance. In general, oxidative stress may trigger the complications observed in the DM.

The present study was undertaken to assess the potential of an oxidovanadium (IV) complex as an antidiabetic and antioxidant agent in order to ameliorate defective biochemical parameters in the stomach tissue of diabetic rats.

The possible antidiabetic mechanism of vanadium and vanadium-based compounds has

been described in several studies [43-45]. Vanadium mimics insulin action, thereby resulting in the mediation of phosphorylation of certain downstream targets, such as the activation of phosphatidylinositol 3'-kinase (PI3K), and the stimulation of phosphatidylinositol phosphate synthesis. In general, the mimic action of these compounds leads to the regulation of glucose transport, glycogen synthesis and gluconeogenesis [22].

It can also restore pancreatic beta cells, as observed in our previous research [20, 21], and by Gao et al. [46]. However, the administration of the VOL complex to diabetic rats resulted in a significant gain of body weight, a decrease in blood glucose levels, as well as significant regeneration of pancreatic beta cells [21]. These findings support the fact that VOL had hypoglycemic property [12].

As a stimulant for insulin secretion, GSH plays an important role in glucose performance. GSH level is relevant for the balance between oxidation and the reduction cycles. In the present study, decreased GSH levels of the diabetic animals might be attributed to changes in the GSH metabolism following increased blood glucose levels [47]. The induction of diabetes either with STZ or alloxan resulted in an increased level of thiobarbituric acid reactive substances (TBARS), which is indirect evidence of increased free radical production [42]. Therefore, preventing the formation of hydroxyl radicals would be an effective way to reduce hydroxyl-induced damage. In the present study, VOL significantly increased stomach GSH levels and decreased LPO formation in diabetic rats. These findings are in agreement with the previous work [48]. This may be due to the effect of the oxidovanadium (IV) complex on blood glucose lowering effect, as well as the increase in gastric antioxidant capacity in diabetic rats.

Diabetes is tightly associated with the formation of glycation end products (AGEs) and AOPP in different tissues [49]. While AGEs are the result of non-enzymatic glucose-protein reactions

alongside lipids and nucleic acids, AOPP is an indicator of albumin damage due to oxidative stress [30].

AGEs and AOPP levels are reported to be elevated in diabetic conditions due to micro/macrovacular complications and albuminuria [50-53]. In the present study, STZ induced diabetes resulted in an increased gastric AOPP levels, as well as NEG level [49]. Vanadium administration normalized the levels of AOPP and NEG via its antidiabetic effect.

Besides high lipid peroxidation, disrupted CAT and SOD activities are associated with increased production of O^{2-} and cellular radical level [53]. High production and the accumulation of free radicals disrupt intracellular antioxidant levels and decrease GSH level. Under such circumstances, the activities of GSH metabolizing enzymes such as GPx, GR and GST are reduced [11]. ROS and other reactive species are directly moped up/scavenged by GSH via the indirect activities of GPx, GR and GST. The proton released as a result of the oxidation of GSH enables the reduction of H_2O_2 to water by GPx.

Therefore, decreased GSH level is accompanied by reduction of H_2O_2 and accumulation of hydroxyl radicals which are responsible for the oxidative damage of cells. On the other hand, accumulating GSSG is reduced to GSH by GR in the presence of NADPH, so as to be reutilized for the detoxification of ROS [54]. The decreased activity in all glutathione-related enzymes (GPx, GR and GST) observed in the hyperglycemic group of the present study, can be either due to decreased intracellular GSH concentration or increased GSH consumption by GPx [55]. In addition to restoring the impaired activities of glutathione metabolizing enzymes, oral VOL treatment also restores CAT and SOD activities in the STZ-induced diabetic group.

CA and its isozymes are found in significant amounts in the stomach tissue because they are related to the secretion of gastric acid. Stomach

Parietal cells are responsible for the production of gastric acid. The hydrochloric acid produced by these cells occurs via a mechanism dependent on the hydration of carbon dioxide to carbonic acid (catalyzed by CA) [56]. Depending on the increase in blood glucose concentration, stomach CA activity decreases. According to Speeckaert et al. [57], hyperglycemia and insulin resistance can increase the level of anaerobic conversion, lactic acid accumulation in red blood cells. This can cause a decrease in the level of CAIII protein, thus preventing oxygen from binding to hemoglobin while triggering increased HbA1c levels. Parallel to these findings, decreased CA activity in stomach tissue of diabetic animals was observed in the present study. VOL significantly increased the activity of CA in the diabetic treated group. On the other hand, LDH and XO levels (two important tissue damage markers) were observed to be elevated in diabetic gastric tissue (Fig 5). While LDH catalyzes the reduction of pyruvate to the lactate without oxygen consumption, XO catalyzes the last two steps modulating the conversion of hypoxanthine to xanthine and then xanthine to uric acid. These metabolic pathways have been associated with oxidative stress and insulin resistance [58, 59]. In line with the current results, previous studies have shown that LDH and XO activities in diabetic stomach tissue increase [5]. In the current research, the increased activities of LDH and XO were significantly diminished in the diabetic + VOL group, to levels near that of the control groups.

4. Conclusion

Diabetic gastroenteropathy is an important complication that can lead to a high risk of death in diabetic patients. For this reason, the diagnosis of diabetic gastroenteropathy should be well observed and its complications outlined. In the present research, an oxidovanadium (IV) complex, VOL which was orally administered to diabetic STZ-rats may have exhibited its beneficial effect in the gastric tissue against oxidative stress damage caused by DM due to its hypoglycemic and antioxidant effects.

Article Information Form

Funding

This research did not receive any specific grant from funding agencies in the public, commercial, or not-for-profit sectors.

Authors' Contribution

Concept: F.G.K., S.T., T.B.D., B.Ü., R.Y., Design: S.T., T.B.D., B.Ü., R.Y., Execution: F.G.K., S.T., T.B.D., B.Ü., R.Y., Material supplying: F.G.K., S.T., T.B.D., Data acquisition: F.G.K., S.T., T.B.D., B.Ü., R.Y., Data analysis/interpretation: F.G.K., S.T., T.B.D., B.Ü., R.Y., Writing: S.T., T.B.D., B.Ü., R.Y., Critical revision: S.T., T.B.D., B.Ü., R.Y.

The Declaration of Conflict of Interest/ Common Interest

No conflict of interest or common interest has been declared by the authors.

The Declaration of Ethics Committee Approval

Experiments were approved by the Animal Care and Use Institute's Committee of Istanbul University, Türkiye.

The Declaration of Research and Publication Ethics

The authors of the paper declare that they comply with the scientific, ethical and quotation rules of SAUJS in all processes of the paper and that they do not make any falsification on the data collected. In addition, they declare that Sakarya University Journal of Science and its editorial board have no responsibility for any ethical violations that may be encountered, and that this study has not been evaluated in any academic publication environment other than Sakarya University Journal of Science.

Copyright Statement

Authors own the copyright of their work published in the journal and their work is published under the CC BY-NC 4.0 license.

References

[1] W. Bielka, A. Przekaz, A. Pawlik, "The Role of the gut microbiota in the

pathogenesis of diabetes," *International Journal of Molecular Sciences*, vol. 23, no. 1, pp. 480, 2022.

[2] A. Yarat, R. Yanardağ, S. Tunalı, O. Sacan, F. GURSOY, N. Emekli, A. Ustuner, G. Ergenekon, "Effects of glibornuride versus metformin on eye lenses and skin in experimental diabetes," *Arzneimittel-Forschung*, vol. 56, no.7, pp. 541–546, 2006.

[3] A. Bajpai, "Universal nerve conduction screening in type 1 diabetes-are we there yet?," *Indian Journal of Pediatrics*, vol. 89, no. 3, pp. 216–217, 2022.

[4] B. B. Bayrak, P. Koroglu, O. Karabulut Bulan, R. Yanardag, "Metformin protects against diabetes-induced heart injury and dunning prostate cancer model," *Human & Experimental Toxicology*, vol. 40, no.2, pp. 297–309, 2021.

[5] I. B. Turkyilmaz, B. B. Bayrak, O. Sacan, O. Mutlu, N. Akev, R. Yanardag, "Zinc supplementation restores altered biochemical parameters in stomach tissue of STZ diabetic rats," *Biological Trace Element Research*, vol. 199, no. 6, pp. 2259–2265, 2021.

[6] H. Liu, V. S. Sridhar, J. Boulet, A. Dharia, A. Khan, P. R. Lawler, D. Z. I. Cherney, "Cardiorenal protection with SGLT2 inhibitors in patients with diabetes mellitus: from biomarkers to clinical outcomes in heart failure and diabetic kidney disease," *Metabolism: Clinical and Experimental*, vol. 126, pp. 154918, 2022.

[7] C. O. de Sá-Ferreira, C. H. M. da Costa, J. C. W. Guimarães, N. S. Sampaio, L. M. L. Silva, L. P. de Mascarenhas, N. G. Rodrigues, T. L. Dos Santos, S. Campos, E. C. Young, "Diabetic ketoacidosis and COVID-19: what have we learned so far?," *American Journal of Physiology. Endocrinology and Metabolism*, vol. 322, no. 1, pp. E44–E53, 2022.

- [8] M. J. Concepción Zavaleta, J. G. Gonzáles Yovera, D. M. Moreno Marreros, L. D. P. Rafael Robles, K. R. Palomino Taype, K. N. Soto Gálvez, L. F. Arriola Torres, J. C. Coronado Arroyo, L. A. Concepción Urteaga, “Diabetic gastroenteropathy: An underdiagnosed complication,” *World Journal of Diabetes*, vol. 12, no.6, pp. 794–809, 2021.
- [9] M. Bulc, S. Gonkowski, J. Całka, “Expression of cocaine and amphetamine regulated transcript (CART) in the porcine intramural neurons of stomach in the course of experimentally induced diabetes mellitus,” *Journal of Molecular Neuroscience*, vol. 57, no. 3, pp. 376–385, 2015.
- [10] A. H. Kurniawan, B. H. Suwandi, U. Kholili, “Diabetic gastroenteropathy: a complication of diabetes mellitus,” *Acta Medica Indonesiana*, vol. 51, no. 3, pp. 263–271, 2019.
- [11] H. Yaribeygi, T. Sathyapalan, S. L. Atkin, A. Sahebkar, “Molecular mechanisms linking oxidative stress and diabetes mellitus,” *Oxidative Medicine and Cellular Longevity*, vol. 2020, pp. 8609213, 2020.
- [12] L. Xu, Z. Li, F. Guo, “Curcumin improves expression of ghrelin through attenuating oxidative stress in gastric tissues of streptozotocin-induced diabetic gastroparesis rats,” *European Journal of Pharmacology*, vol. 718, no. 1-3, pp. 219–225, 2013.
- [13] D. C. Damasceno, A. O. Netto, I. L. Iessi, F. Q. Gallego, S. B. Corvino, B. Dallaqua, Y. K. Sinzato, A. Bueno, I. M. Calderon, M. V. Rudge, “Streptozotocin-induced diabetes models: pathophysiological mechanisms and fetal outcomes,” *BioMed Research International*, vol. 2014, pp. 819065, 2014.
- [14] K. Trerattanavong, P. Tadi, 2021. “Glimepiride,” In: StatPearls [Internet], Treasure Island (FL): StatPearls Publishing; 2022.
- [15] R. Correa, B. S. Quintanilla Rodriguez, T. M. Nappe, “Glipizide.” In: StatPearls [Internet], Treasure Island (FL): StatPearls Publishing; 2022.
- [16] M. D. Hardin, T. F. Jacobs, “Glyburide,” In: StatPearls [Internet]. Treasure Island (FL): StatPearls Publishing; 2022.
- [17] P. Koroglu Aydın, O. Karabulut-Bulan, I. Bugan, I. B. Turkyilmaz, S. Altun, R. Yanardag, “The protective effect of metformin against testicular damage in diabetes and prostate cancer model,” *Cell Biochemistry and Function*, vol. 40, no. 1, pp. 60–70, 2022.
- [18] C. F. Deacon, H. E. Lebovitz, “Comparative review of dipeptidyl peptidase-4 inhibitors and sulphonylureas,” *Diabetes, Obesity & Metabolism*, vol. 18, no. 4, pp. 333–347, 2016.
- [19] D. Tripathi, V. Mani, R. P. Pal, “Vanadium in biosphere and its role in biological processes,” *Biological Trace Element Research*, vol. 186, no. 1, pp. 52–67, 2018.
- [20] S. Bolkent, S. Bolkent, R. Yanardag, S. Tunali, “Protective effect of vanadyl sulfate on the pancreas of streptozotocin-induced diabetic rats,” *Diabetes Research and Clinical Practice*, vol. 70, no. 2, pp. 103–109, 2005.
- [21] R. Yanardag, T. B. Demirci, B. Ulküseven, S. Bolkent, S. Tunali, S. Bolkent, 2009. “Synthesis, characterization and antidiabetic properties of N (1)-2,4-dihydroxybenzylidene-N (4)-2-hydroxybenzylidene-S-methyl-thiosemicarbazidato-oxovanadium (IV),” *European Journal of Medicinal Chemistry*, vol. 44, no. 2, pp. 818–826, 2009.
- [22] S. Semiz, “Vanadium as potential therapeutic agent for COVID-19: A focus

- on its antiviral, antiinflammatory, and antihyperglycemic effects,” *Journal of Trace Elements in Medicine and Biology*, vol. 69, pp. 126887, 2022.
- [23] T. Bal, B. Atasever, Z. Solakoğlu, S. Erdem-Kuruca, B. Ülküseven, “Synthesis, characterisation and cytotoxic properties of the N1, N4-diarylidene-S-methylthiosemicarbazone chelates with Fe (III) and Ni (II),” *European Journal of Medicinal Chemistry*, vol. 42, no. 2, pp. 161-167, 2007.
- [24] B. Atasever, B. Ülküseven, T. Bal-Demirci, S. Erdem-Kuruca, Z. Solakoğlu, “Cytotoxic activities of new iron (III) and nickel (II) chelates of some S-methylthiosemicarbazones on K562 and ECV304 cells,” *Investigational New Drugs*, vol. 28, no. 4, pp. 421-432, 2010.
- [25] T. Demirci, Y. Köseoğlu, S. Güner, B. Ülküseven, “Oxovanadium (IV) complexes of bromo-and methoxy substituted N1, N4-diarylidene-S-methylthiosemicarbazones,” *Open Chemistry*, vol. 4, no. 1, pp. 149-159, 2006.
- [26] M. Melchior, S. J. Rettig, B. D. Liboiron, K. H. Thompson, V. G. Yuen, J. H. McNeill, C. Orvig, “Insulin-enhancing vanadium (III) complexes,” *Inorganic Chemistry*, vol. 40, no. 18, pp. 4686–4690, 2001.
- [27] A. Junod, A. E. Lambert, W. Stauffacher, A. E. Renold, “Diabetogenic action of streptozotocin: relationship of dose to metabolic response,” *The Journal of Clinical Investigation*, vol. 48, no. 11, pp. 2129–2139, 1969.
- [28] E. Beutler, “In a manual of biochemical methods”, 2nd ed. Grune and Stratton, New York, 1975, pp. 112-114.
- [29] A. Ledwozyw, J. Michalak, A. Stepień, A. Kadziółka, “The relationship between plasma triglycerides, cholesterol, total lipids and lipid peroxidation products during human atherosclerosis,” *Clinica Chimica Acta; International Journal of Clinical Chemistry*, vol. 155, no. 3, pp. 275–283, 1986.
- [30] V. Witko-Sarsat, M. Friedlander, C. Capeillère-Blandin, T. Nguyen-Khoa, A. T. Nguyen, J. Zingraff, P. Jungers, B. Descamps-Latscha, “Advanced oxidation protein products as a novel marker of oxidative stress in uremia,” *Kidney International*, vol. 49, no. 5, pp. 1304–1313, 1996.
- [31] K. M. Parker, J. D. England, J. Da Costa, R. L. Hess, D. E. Goldstein, “Improved colorimetric assay for glycosylated hemoglobin,” *Clinical Chemistry*, vol. 27, no. 5, pp. 669–672, 1981.
- [32] O. H. Lowry, N. J. Rosebrough, A. L. Farr, R. J. Randall, “Protein measurement with the Folin phenol reagent,” *The Journal of Biological Chemistry*, vol. 193, no. 1, pp. 265–275, 1951.
- [33] H. Aebi, “Catalase in vitro,” *Methods in Enzymology*, vol. 105, pp. 121-126, 1984.
- [34] A. A. Mylroie, H. Collins, C. Umbles, J. Kyle, “Erythrocyte superoxide dismutase activity and other parameters of copper status in rats ingesting lead acetate,” *Toxicology and Applied Pharmacology*, vol. 82, no. 3, pp. 512–520, 1986.
- [35] D. E. Paglia, W. N. Valentine, “Studies on the quantitative and qualitative characterization of erythrocyte glutathione peroxidase,” *The Journal of Laboratory and Clinical Medicine*, vol. 70, no. 1; pp. 158–169, 1967.
- [36] A. Wendel, “Glutathione peroxidase,” *Methods in Enzymology*, vol. 77, pp. 325-333, 1981.
- [37] E. Beutler, *Red cell metabolism: A manual of biochemical methods*, London: Grune & Stratton, 1971.

- [38] W. H. Habig, W. B. Jakoby, "Assays for differentiation of glutathione S-transferases," *Methods in Enzymology*, vol. 77, pp. 398–405, 1981.
- [39] J. A. Verpoorte, S. Mehta, J. T. Edsall, "Esterase activities of human carbonic anhydrases B and C," *The Journal of Biological Chemistry*, vol. 242, no. 18, pp. 4221–4229, 1967.
- [40] F. Wroblewski, "Clinical significance of serum enzyme alterations associated with myocardial infarction," *American Heart Journal*, vol. 54, no. 2, pp. 219–224, 1957.
- [41] E. D. Corte, F. Stirpe, "Regulation of xanthine oxidase in rat liver: modifications of the enzyme activity of rat liver supernatant on storage at 20 degrees," *The Biochemical Journal*, vol. 108, no. 2, pp. 349–351, 1968.
- [42] A. C. Maritim, R. A. Sanders, J. B. Watkins 3rd, "Diabetes, oxidative stress, and antioxidants: a review," *Journal of Biochemical and Molecular Toxicology*, vol. 17, no. 1, pp. 24–38, 2003.
- [43] I. G. Fantus, G. Deragon, R. Lai, S. Tang, S. "Modulation of insulin action by vanadate: evidence of a role for phosphotyrosine phosphatase activity to alter cellular signaling," *Molecular and Cellular Biochemistry*, vol. 153, no. 1-2, pp. 103–112, 1995.
- [44] J. E. Sprietsma, G. E. Schuitemaker, "Diabetes can be prevented by reducing insulin production," *Medical Hypotheses*, vol. 42, no. 1, pp. 15–23, 1994.
- [45] I. G. Fantus, E. Tsiani, "Multifunctional actions of vanadium compounds on insulin signaling pathways: evidence for preferential enhancement of metabolic versus mitogenic effects," *Molecular and Cellular Biochemistry*, vol. 182, no. 1-2, pp. 109–119, 1998.
- [46] Z. Gao, C. Zhang, S. Yu, X. Yang, K. Wang, K. "Vanadyl bisacetylacetonate protects β cells from palmitate-induced cell death through the unfolded protein response pathway," *Journal of Biological Inorganic Chemistry*, vol. 16, no. 5, pp. 789-798, 2011.
- [47] M. Hadjzadeh, V. Alikhani, S. Hosseinian, B. Zarei, Z. Keshavarzi, "The effect of melatonin against gastric oxidative stress and dyslipidemia in streptozotocin-induced diabetic rats," *Acta Endocrinologica*, vol. 14, no. 4, pp. 453–458, 2018.
- [48] S. Tunali, R. Yanardag, "Effect of vanadyl sulfate on the status of lipid parameters and on stomach and spleen tissues of streptozotocin-induced diabetic rats," *Pharmacological Research*, vol. 53, no. 3, pp. 271–277, 2006.
- [49] F. Heidari, S. Rabizadeh, A. Rajab, F. Heidari, M. Mouodi, H. Mirmiranpour, A. Esteghamati, M. Nakhjavani, "Advanced glycation end-products and advanced oxidation protein products levels are correlates of duration of type 2 diabetes," *Life Sciences*, vol. 260, pp. 118422, 2020.
- [50] A. Piwowar, M. Knapik-Kordecka, M. Warwas, "Comparison of the usefulness of plasma levels of oxidatively modified forms of albumin in estimating kidney dysfunction in diabetic patients," *Clinical and Investigative Medicine*, vol. 3, no 2, pp. E109Ā, 2010.
- [51] V. Jakuš, E. Sándorová, J. Kalninová, B. Krahulec, "Monitoring of glycation, oxidative stress and inflammation in relation to the occurrence of vascular complications in patients with type 2 diabetes mellitus," *Physiological Research*, vol. 63, no. 3, pp. 297–309, 2014.
- [52] K. A. Adeshara, A. G. Diwan, T. R. Jagtap, K. Advani, A. Siddiqui, R. S. Tupe, "Relationship between plasma glycation with membrane modification, oxidative stress and expression of glucose transporter-

- 1 in type 2 diabetes patients with vascular complications,” *Journal of Diabetes and Its Complications*, vol. 31, no. 2, pp. 439–448, 2017.
- [53] S. K. Jaiswal, C. V. Rao, B. Sharma, P. Mishra, S. Das, M. K. Dubey, “Gastroprotective effect of standardized leaf extract from *Argyrea speciosa* on experimental gastric ulcers in rats,” *Journal of Ethnopharmacology*, vol. 137, no. 1, pp. 341–344, 2011.
- [54] A. A. Hosni, A. A. Abdel-Moneim, E. S. Abdel-Reheim, S. M. Mohamed, H. Helmy, “Cinnamaldehyde potentially attenuates gestational hyperglycemia in rats through modulation of PPAR γ , proinflammatory cytokines and oxidative stress,” *Biomedicine & Pharmacotherapy*, vol. 88, pp. 52-60, 2017.
- [55] T. Anwer, Z. A. Alkarbi, A. Hassan Najmi, S. Alshahrani, R. Siddiqui, G. Khan, M. Firoz Alam, “Modulatory effect of zingerone against STZ-nicotinamide induced type-2 diabetes mellitus in rats,” *Archives of Physiology and Biochemistry*, vol. 127, no. 4, pp. 304–310, 2021.
- [56] N. Kılınç, M. M. İşgör. B. Şengül, Ş. Beydemir, “Influence of pesticide exposure on carbonic anhydrase II from sheep stomach,” *Toxicology and Industrial Health*, vol. 31, no. 9, pp. 823–830, 2015.
- [57] M. Speeckaert, W. Van Biesen, J. Delanghe, R. Slingerland, A. Wiecek, J. Heaf, C. Drechsler, R. Lacatus, R. Vanholder, I. Nistor, “European renal best practice guideline development group on diabetes in advanced CKD. Are there better alternatives than haemoglobin A1c to estimate glycaemic control in the chronic kidney disease population?” *Nephrology, Dialysis, Transplantation: Official Publication of the European Dialysis and Transplant Association- European Renal Association*, vol. 29, no. 12, pp. 2167–2177, 2014.
- [58] M. Adeva-Andany, M. López-Ojén, R. Funcasta-Calderón, E. Ameneiros-Rodríguez, C. Donapetry-García, M. Vila-Altesor, J. Rodríguez-Seijas, “Comprehensive review on lactate metabolism in human health,” *Mitochondrion*, vol.17, pp. 76-100, 2014.
- [59] T. E. Omolekulo, O. S. Michael, L. A. Olatunji, “Dipeptidyl peptidase-4 inhibition protects the liver of insulin-resistant female rats against triglyceride accumulation by suppressing uric acid,” *Biomedicine & Pharmacotherapy*, vol. 110, pp. 869-877, 2019.

Use of Two-Dimensional and Three-Dimensional Reactors in Oxidative Electrochemical Degradation Studies of Malachite Green

Canan Samdan^{1*} 

^{1*} Eskisehir Osmangazi University, Faculty of Engineering and Architecture, Department of Chemical Engineering, Eskişehir, Türkiye, caydin@ogu.edu.tr

*Corresponding Author

ARTICLE INFO

ABSTRACT

Keywords:

Electrochemical
oxidative degradation
Microelectrodes
Malachite green



Article History:

Received: 14.05.2023

Accepted: 21.11.2023

Online Available: 27.02.2024

With the developments in treatment technologies, including porous materials in electrochemical systems have recently become the focus of researchers' attention. In electrochemical methods, operating cost is as important as efficiency. It is possible to increase the system performance by increasing the effective electrode surface by incorporating activated carbon, which can be produced from biomass, into electrochemical oxidation systems. This study investigated using activated carbon from walnut shells as a microelectrode in the electrochemical oxidative degradation of malachite green. When potential differences between 2V and 4V are applied to 2DES and 3DES reactors containing MG solution, a higher % MG Removal was obtained in 3DES reactors than in 2DES reactors. When the potential difference is 4V, a value of $0.026 \text{ (min}^{-1}) k_{1,3D}$ and $0.0117 \text{ (min}^{-1}) k_{1,2D}$ are obtained. In 3DES reactors, the rate constant at 0.003 A/cm^2 was achieved as $0.0167 \text{ (min}^{-1}) k_{1,3D}$, while at 0.010 A/cm^2 , it increased by approximately 5 times, reaching a value of $0.0845 \text{ min}^{-1} k_{1,3D}$. Similarly, in 3DES reactors, when the current density increased from 0.003 A/cm^2 to 0.010 A/cm^2 , the mass transfer rate increased from 0.011 (cm/s) to 0.05633 (cm/s) .

1. Introduction

Electro-oxidation is a method by which hydroxyl radicals oxidize and purify pollutants. It is one of the most widely used methods in wastewater treatment as it allows the breakdown of high-toxicity waste [1]. The anode has an essential place in the electro-oxidation method. In studies with electro-oxidation processes (2DES), generally, Ti/Ru TiO₂, Ti/Pt [2], Ti/Ir-Pb, Ti/Ir-Sn, Ti/Ru-Pb, Ti/Pt-Pd and Ti/RuO₂ [3] etc. anodes are widely used. Particle electrodes are essential in designing and operating three-dimensional electrochemical oxidative degradation reactors (3DES). It has many advantages over traditional electrochemical oxidation reactors and has become the focus of interest of researchers since its inception. Recently, many studies have focused on

preparing particle electrodes for 3D electrochemical oxidation [4,5].

Particle electrodes are mainly prepared using highly porous and high-impedance materials. Researchers have used various materials, such as graphite [6], Ti-Sn/ γ -Al₂O₃ [7], CuFe₂O₄ [8], Pd-supported magnetic biochar [9], γ -Fe₂O₃-CNTs [10] and activated carbon [11] in the synthesis of particle electrodes. However, developing such particle electrodes is limited due to the complex preparation process and expensive (or non-abundant) raw materials, which hinders the practical application of the 3-D electrochemical oxidation reactor. Therefore, selecting available and cost-effective raw materials for the preparation of particulate electrodes is crucial. Therefore, synthesizing particle electrodes using local and abundant waste biomass is a very logical method.

The 3D electro-oxidation method, based on traditional electrochemical technology, is developed by filling conductive particles between the anode and the cathode [12]. The 2-dimensional electro-oxidation method is the realization of the electro-oxidation process on a thin film on the surface of an electrode. In the 3D electro-oxidation method, it is possible to increase the surface of the microelectrodes easily by increasing the amount of particle electrodes. In this way, the surface area where direct oxidation will occur is increased. This situation improves the degradation of the pollutant to be removed [8].

This study examined the oxidative degradation of malachite green (MG) using activated carbons produced from biomass kinetically in a 3D electro-oxidation reactor. At the same time, the degradation of malachite green was performed in the 2D electro-oxidation reactor, and the kinetic results were compared with the 3D reactor.

2. Materials And Method

2.1. Devices and chemicals

Phosphoric acid (H_3PO_4) (Merck) was used for the chemical activation process of biomass to produce activated carbon with an acidic character. The pH values of the solutions were brought to the desired value by using 0.1N HCl (Merck) and 0.1N NaOH pellets (Merck EMPLURA®) solutions. The malachite green (basic green 4) was used as an organic compound. UV/vis spectrophotometer (Model: Thermo Electron AquaMete) was used to measure the MG concentration in aqueous solution.

2.2. Production of activated carbons as microparticles

Walnut shells were ground into small pieces. Walnut shells and the appropriate amount of H_3PO_4 were added as a walnut shell/ H_3PO_4 ratio (w/w) of 4/1. This mixture was mixed with a magnetic stirrer at 65 °C for 7 hours; the heating was turned off and left for 17 hours. The filtered sample was dried in an oven. The appropriate amount from the sample, which absorbed the chemical agent, was placed in the reaction vessel.

The vessel was brought to 400 °C in a nitrogen atmosphere. The reactor was kept at the final temperature for 1 hour and was left to cool in the furnace. Micro and mesoporous activated carbon with 1328 m^2/g surface area was produced using 4/1 (w/w) phosphoric acid from the walnut shell. Activated carbon is used as microelectrodes in 3DES reactors.

2.3. Electrochemical oxidative degradation

In this study, a three-dimensional electrode system (3DES) and a two-dimensional electrode system (2DES) were used as electrochemical (EC) oxidative degradation systems. A schematic image of 2DES and 3DES electro-oxidation systems is given in Figure 1. For this purpose, a 5x10x5 mm glass electrolytic cell connected to a DC power source and continuously stirred was used in 2DES and 3DES systems.

Carbon fibre was used as an anode and cathode for 2.5x2.5 cm (6.25 cm^2 surface area). While the 2DES electrochemical cell was designed with an anode and cathode, activated carbon was added between the anode and the cathode in the 3DES cell, and 0.2 g activated carbon was used as particle electrodes. Each 3DES reactor has a surface area of 265.6 m^2 (1328 m^2/g particle electrode x 0.2 g particle electrode) of particulate electrodes. A 3-phase, 3-dimensional electrochemical oxidation system is built in the 3DES cell, where continuous mixing is applied. The voltage during the 2DES and 3DES experiments was varied in the range of 2-4 V.

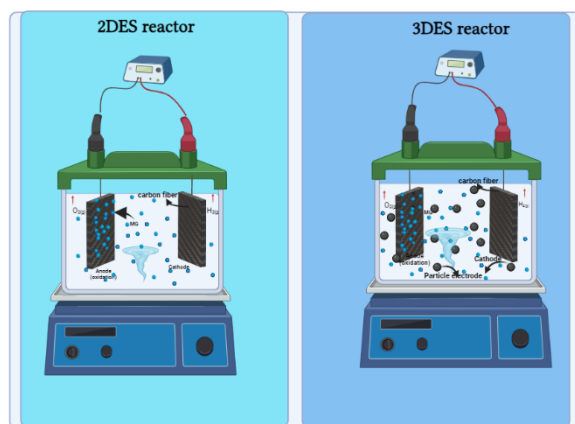


Figure 1. Schematic image of 2DES and 3DES systems

0.003-0.010 (A/cm²) j values were applied. All experiments were carried out under control during the study at 25 °C. MG solutions were loaded into the EC reactor at an initial concentration of 250 ppm in each EC experiment. Sodium chloride was used to adjust the initial conductivity of the solution. During the experiments, 2 ml samples were drawn from the solution and analyzed to determine the amount of MG.

A calibration curve was created in a UV-vis spectrophotometer using MG solutions at different concentrations. The concentration of MG in the solution at any time was calculated using this calibration curve at 621 nm [13]. Using the MG concentration (C) in the solution at any time t and the MG concentration (C₀) at time t = 0, the % MG Removal was calculated using Eq 1.

$$\% \text{ Removal} = \frac{C}{C_0 - C} * 100 \quad (1)$$

If we consider electro-oxidation as a surface treatment, then the kinetics of decay can be represented by the following Eq. 2 in terms of the heterogeneous rate constant, k_h (cm/s) [14],

$$r = - \left(\frac{V}{A_e} \right) \frac{d[C]}{dt} = k_h [C] \quad (2)$$

Where A_e electrode surface area (cm²), V is the reactor volume (cm³), and t is the EC oxidative degradation time (s). Inside the electro-oxidation reactor, the MG removal rate is proportional to the concentration of the contaminant. Therefore, the kinetics for MG removal can be represented by the following pseudo-first-order kinetic model: Eqs. (3 and 4) [15,16]:

$$r = - \frac{d[C]}{dt} = k_{1 \text{ 2D or 3D}} [C] \quad (3)$$

$$-\ln \left(\frac{C}{C_0} \right) = k_{1 \text{ 2D or 3D}} t \quad (4)$$

Where k_{1 2D or 3D} is the pseudo-first-order reaction rate constant (min⁻¹), and k_{1 2D or 3D} is related to k_h as follows Eq. 5. Constants can be determined from ln (C/C₀) vs time graphs.

$$k_h = k_{1 \text{ 2D or 3D}} \left(\frac{V}{A_e} \right) \quad (5)$$

3. Results And Discussion

3.1. Textural properties of particle electrodes

The surface area, micropore volume, mesopore volume and average pore diameter obtained using N₂ adsorption-desorption isotherms of particle electrodes are given in Table 1.

Table 1. The surface pore properties of the particle electrodes

S _{BET} (m ² /g)	V _{mic} (cm ³ /g)	V _{mes} (cm ³ /g)	V _{tot} (cm ³ /g)	D _p (Å)
1328	0.492	0.286	0.778	23.44

The surface area of particle electrodes is 1328 m²/g, and its total pore volume is 0.778 cm³/g. The micropore volume is more than the mesopore volume. The average pore diameter is 23.44 Å. Adsorption-desorption isotherms and pore size distributions of particle electrodes are given in Figure 2.

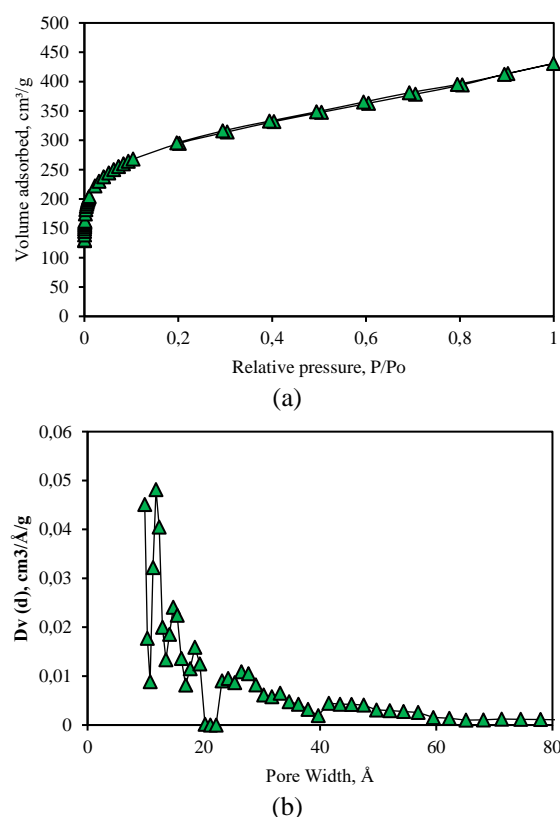


Figure 2. Adsorption-desorption isotherms (a) and pore size distributions (b) of particle electrodes

Considering Figure 2 (a), the adsorption-desorption isotherms of particle electrodes comply with Type I isotherms according to the IUPAC classification [17]. According to Figure 2 (b), the particle electrodes had peaks between 10-20 Å (1-2 nm) and 20-60 Å (2-4 nm). According to IUPAC, the pores of porous materials such as activated carbon are classified as micropores (<2 nm), mesopores (2-50 nm), and macropores (> 50 nm). In this study, particle electrodes consist of micro and mesopores.

2DES and 3DES reactors were used in MG oxidative electrochemical degradation studies. The effects of voltage and current densities applied to the reactors were investigated to determine the reactor efficiency.

3.2. Effect of voltage

In the experiments with 2D and 3D electrochemical (EC) oxidative degradation systems, the MG concentration changes occurring at all potential difference values examined during the reaction were recorded and shown graphically in

. The resulting energy consumption values were calculated with the help of these values and shown graphically in Figure 4. The energy consumption values obtained with the help of the potential difference values that occur during the reaction were calculated with the help of (6) [18].

$$E = \frac{U \cdot I \cdot t}{V} \quad (6)$$

Where E is electrical energy (kWh/m³), U is volts, I is current intensity (A), t is time (hours), and V is solution volume (m³). Energy consumption is also calculated according to (7) per unit mass of decomposed MG [19].

$$E = \frac{U \cdot I \cdot t}{(C_0 - C) \cdot V} \quad (7)$$

Where E is electrical energy (kWh/g MG), U is volt, I is current intensity (A), t is time (hours), V is solution volume (L). While calculating the energy consumption values, the current densities for 2, 3, and 4V potential differences in 2DES reactors were taken as 0.033, 0.044 and 0.057 A/cm², respectively. In 3DES reactors, the

current densities for the same potential differences are 0.060, 0.067 and 0.081 A/cm², respectively.

According to Figure 3, when potential differences between 2V and 4V are applied to 2DES and 3DES reactors containing MG solution, a higher % MG Removal was obtained in 3DES reactors than in 2DES reactors. Direct oxidation of MG takes place in two steps: the first is the diffusion of MG to the anode surface, and the second is the oxidation of MG on the anode surface. In 3DES reactors, microelectrodes provide an extra surface for the oxidation of MG molecules. In this way, more MG molecules are degraded due to electron transfers occurring both on the carbon fibre surface, which is the anode, and on the surface of the microelectrodes. When the 3DES reactors are not subjected to any potential difference (0 V), the MG molecules that come into contact with the particle electrodes are absorbed on the surfaces of the particle electrodes. Without a potential difference, the adsorption mechanism results in a 13.87% MG Removal.

When the potential difference in the 2DES reactor increased from 2V to 4V, the %R value increased from 65.74 to 76.00. Similarly, in 3DES reactors, with the potential difference increase to 3V, the %R value increased from 87.6 to 95.6. When 4V voltage was applied in 3DES reactors, a 96.8 %R value was obtained. The variation of the same potential difference reduced the normalized concentration from 0.34 to 0.20 in 2DES reactors and from 0.12 to 0.032 in 3DES reactors at 120 min. The optimum potential difference was considered 3V since the decomposition efficiencies obtained at the 3V and 4V potential differences were close. However, the results also need to be evaluated from an economic point of view. As seen in Eq. (6), the energy consumption value is expressed as the amount of energy applied per unit of time per unit volume. The potential difference value applied to the system is one of the critical parameters affecting energy consumption. The increase in the value of the potential difference applied causes the energy consumption value to increase. For all the potential differences studied, 3DES reactors consumed more energy than 2DES (Figure 4 (a)).

At 4V volts, where the highest MG removal values were obtained, 11.52 kWh/m³ energy consumption was a requirement in 2DES reactors, while 16.32 kWh/m³ energy was needed in 3DES reactors. The microelectrodes used in 3DES reactors have caused electrical resistance in the system.

The increase in resistance led to an increase in current at a constant voltage. As a result, 3DES reactors have higher energy requirements.

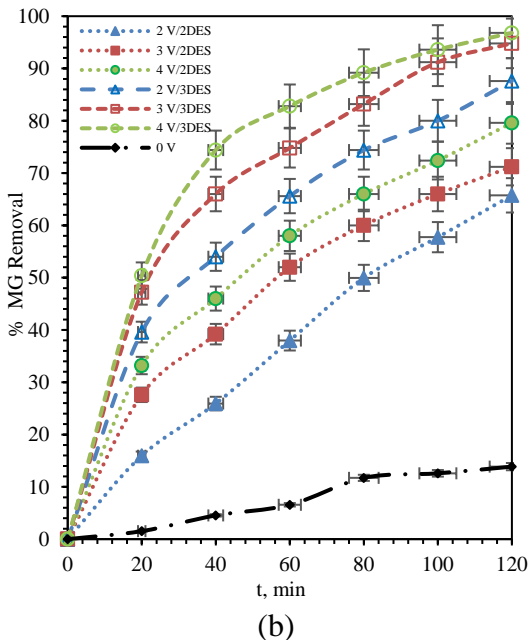
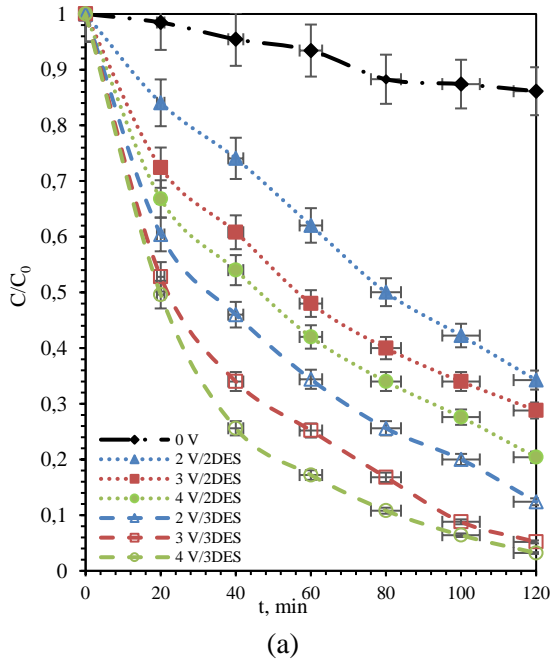
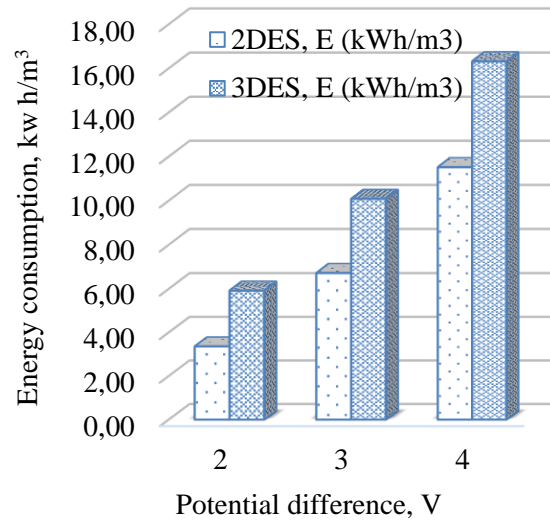
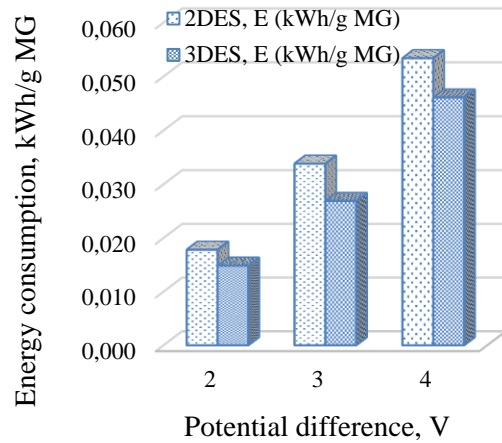


Figure 3. Comparison of normalized concentration vs time (a) and % MG Removal vs time (b) at different potentials in 2DES and 3DES oxidation systems



(a)



(b)

Figure 4. The resulting energy consumption values for 2DES and 3DES reactors

When the energy requirements per gram of the degraded MG are examined (Figure 4 (b)), the energy requirement in 3DES reactors is lower than in 2DES reactors. In 3DES reactors, the energy consumption of 0.015, 0.028 and 0.048 kWh/gMG was realized for potential differences of 2, 3 and 4V. In 2DES reactors, the energy consumption of 0.020, 0.038, and 0.061 kWh/gMG occurred for the same potential differences. From this point of view, 3DES reactors are more economical. When the 3D electrochemical oxidative degradation system

was evaluated regarding energy consumption to determine the optimal potential difference, less energy requirement occurred in 3V than in 4V. Therefore, the 3V potential difference may be the optimum condition for 3DES reactors.

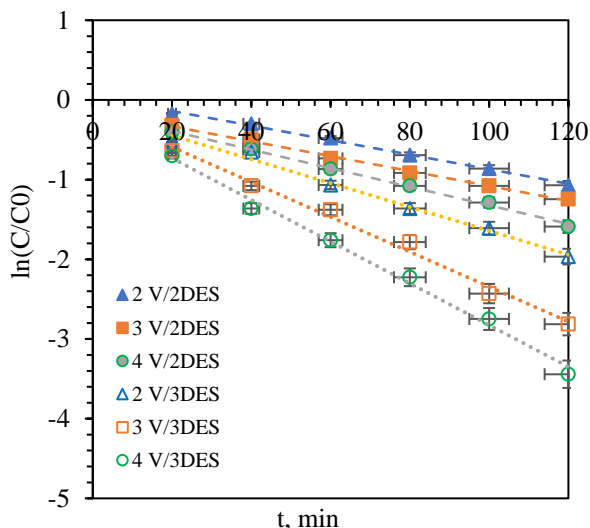


Figure 5. The pseudo-first-order kinetic model for 2DES and 3DES reactors at 2V, 3V and 4V

To kinetically evaluate the data obtained at 2, 3 and 4V potential differences, $\ln(C/C_0)$ - time graphs were drawn for 2DES and 3DES reactors and pseudo-first-order reaction rate constants $k_{1,2D}$ (min^{-1}) and $k_{1,3D}$ (min^{-1}) were calculated. The resulting graphs are shown in Figure . In addition, the k_h (cm/s) values for the MG degradation reactions in the 2DES and 3DES reactors (Eq. (5)) are calculated, and all rate constants are given in Table 2.

As the voltage increased in 2DES reactors, the oxidative degradation rate increased, and the highest values of $k_{1,2D}$ and $k_{h,2D}$ were obtained as 0.0117 (min^{-1}) and 0.0078 (cm/s) at 4V, respectively. In 3DES reactors, when a potential difference of 2V is applied, a value of 0.015 (min^{-1}) $k_{1,3D}$ is obtained, while when the potential difference is increased to 4V, a value of 0.026 (min^{-1}) $k_{1,3D}$ is obtained. In addition, the heterogeneous rate constant increased as the potential difference applied increased.

3.3. Effect of current density

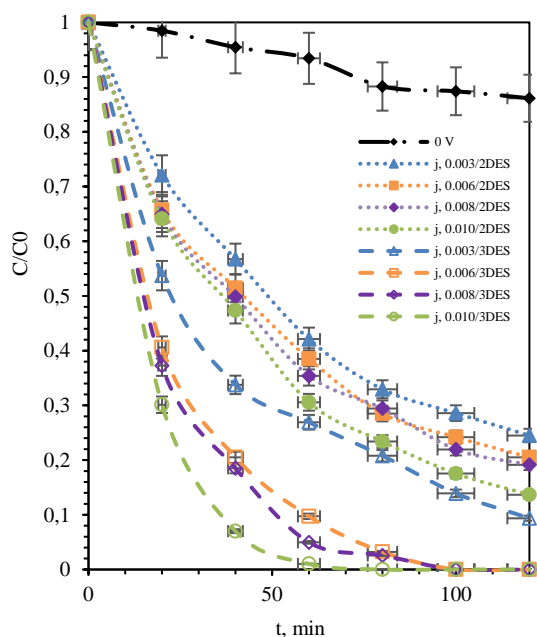
To investigate the effect of current density on the oxidative degradation of MG, experiments were performed in both 2DES and 3DES reactors at

different current densities. Over time, the oxidative degradation rate and % degradation amount of MG were determined, and the results are given in Figure 6. The compatibility of the obtained data with the pseudo-first-order kinetic model was investigated (Figure 7). The pseudo-first-order rate constant ($k_{1,2D}$ (min^{-1}) and $k_{1,3D}$ (min^{-1})) and heterogeneous rate constants ($k_{h,2D}$ (cm/s) and $k_{h,3D}$ (cm/s)) for both reactor types are calculated and given in Hata! Başvuru kaynağı bulunamadı..

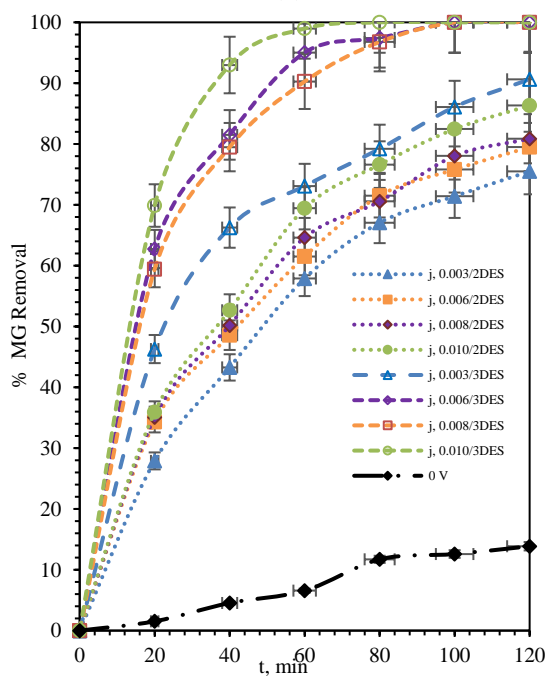
Table 2. Kinetic rate constants for electro-oxidative degradation of MG in 2DES and 3DES reactors

2DES			
V (volt)	$k_{1,2D}$ (min^{-1})	$k_{h,2D}$ (cm/s)	R^2
2V	0.0091	0.00607	0.99
3V	0.0093	0.00620	0.99
4V	0.0117	0.00780	0.99
j (A/cm ²)	$k_{1,2D}$ (min^{-1})	$k_{h,2D}$ (cm/s)	R^2
0.003	0.0110	0.00733	0.98
0.006	0.0118	0.00787	0.99
0.008	0.0125	0.00833	0.98
0.010	0.0157	0.01047	0.99
3DES			
V (volt)	$k_{1,3D}$ (min^{-1})	$k_{h,3D}$ (cm/s)	R^2
2V	0.015	0.0100	0.99
3V	0.022	0.0146	0.98
4V	0.026	0.0173	0.99
j (A/cm ²)	$k_{1,3D}$ (min^{-1})	$k_{h,3D}$ (cm/s)	R^2
0.003	0.0167	0.01113	0.99
0.006	0.0418	0.02787	0.98
0.008	0.0467	0.03113	0.98
0.010	0.0845	0.05633	0.99

As the current density applied in the 2DES and 3DES reactors increased, the normalized concentration value decreased from 0.24 to 0.13 in 2DES reactors and decreased from 0.09 to 0 in 3DES reactors (Figure 6 (a)). Similarly, the % MG Removal value increased (Figure 6 (b)).



(a)



(b)

Figure 6. Comparison of normalized concentration vs time (a) and % MG Removal vs time (b) at different current densities in 2DES and 3DES oxidation systems

At the end of 2 hours in 2DES reactors, 75.50% MG Removal was achieved at 0.003 A/cm² current density, and 86.33% %R value was obtained at 0.010 A/cm². In 3DES reactors, 90.63% MG Removal was achieved at 0.003 A/cm² and 100% %R value was obtained at 0.006 A/cm² j value. The increase in current density

affected the oxidation of 3DES reactors more than in 2DES reactors.

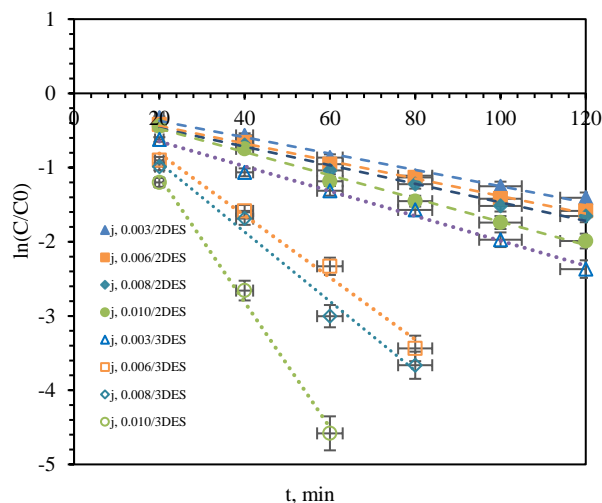


Figure 7. The pseudo-first-order kinetic model for 2DES and 3DES reactors at 0.003, 0.006, 0.008 and 0.010 A/cm² current density

When we evaluate the effect of current density from a kinetic point of view, the data obtained at all current densities were well compatible with the pseudo-first-order kinetic model with an R² value of 0.98-0.99. As the current density increased in 2DES reactors, the oxidative degradation rate increased, and the highest values of $k_{1,2D}$ and $k_{h,2D}$ were obtained as 0.0157 (min⁻¹) and 0.01047 (cm/s) at 0.010 A/cm², respectively. In 3DES reactors, the rate constant at 0.003 A/cm² was achieved as 0.0167 (min⁻¹) $k_{1,3D}$, while at 0.010 A/cm², it increased by approximately 5 times, reaching a value of 0.0845 min⁻¹ $k_{1,3D}$. Similarly, in 3DES reactors, when the current density increased from 0.003 A/cm² to 0.010 A/cm², the mass transfer rate increased from 0.011 (cm/s) to 0.05633 (cm/s).

4. Conclusions

In this study, activated carbon was produced from walnut shells by the chemical activation method. When potential differences between 2V and 4V are applied to 2DES and 3DES reactors containing MG solution, a higher % MG Removal was obtained in 3DES reactors than in 2DES reactors. In 3DES reactors, microelectrodes provide an extra surface for the oxidation of MG molecules. In this way, more MG molecules are degraded due to electron transfers occurring both on the carbon fibre

surface, which is the anode, and on the surface of the microelectrodes. In 3DES reactors, the energy consumption of 0.015, 0.028 and 0.048 kWh/gMG was realized for potential differences of 2, 3 and 4V. In 2DES reactors, the energy consumption of 0.020, 0.038, and 0.061 kWh/gMG occurred for the same potential differences. From this point of view, 3DES reactors are more economical.

When the potential difference is 4V, a value of 0.026 (min^{-1}) $k_{1.3D}$ is obtained. In 3DES reactors, the rate constant at 0.003 A/cm² was achieved as 0.0167 (min^{-1}) $k_{1.3D}$, while at 0.010 A/cm², it increased by approximately 5 times, reaching a value of 0.0845 min^{-1} $k_{1.3D}$. Similarly, in 3DES reactors, when the current density increased from 0.003 A/cm² to 0.010 A/cm², the mass transfer rate increased from 0.011 (cm/s) to 0.05633 (cm/s). The change in current density in 3DES reactors had a more significant effect on the oxidative degradation rate of MG than the potential difference variation.

Article Information Form

Funding

This study was financially supported by Eskişehir Osmangazi University Scientific Research Foundation (Project No: FBA-2021-1591).

Authors' Contribution

Conceptualization, Funding acquisition, Investigation, Methodology, Project administration, Resources, Validation, Visualization, Writing – review & editing.

The Declaration of Conflict of Interest/ Common Interest

The author has declared no conflict of interest or common interest.

The Declaration of Ethics Committee Approval

The author declares that this document does not require ethics committee approval or special permission.

The Declaration of Research and Publication Ethics

The author of the paper declares that he complies with the scientific, ethical, and quotation rules of

SAUJS in all processes of the paper and that she does not make any falsification of the data collected. In addition, she declares that Sakarya University Journal of Science and its editorial board are not responsible for any ethical violations that may be encountered and that this study has not been evaluated in any academic publication environment other than Sakarya University Journal of Science.

Copyright Statement

Authors own the copyright of their work published in the journal and their work is published under the CC BY-NC 4.0 license.

References

- [1] Wang, Z., Qi, J., Feng, Y., Li, K., Li, X., "Preparation of Catalytic Particle Electrodes from Steel Slag and Its Performance in a Three-Dimensional Electrochemical Oxidation System," *Journal of Industrial and Engineering Chemistry*, vol. 20, no. 5, 2014, pp. 3672–3677.
- [2] Tavares, M. G., Da Silva, L. V. A., Sales Solano, A. M., Tonholo, J., Martínez-Huitle, C. A., Zanta, C. L. P. S., "Electrochemical Oxidation of Methyl Red Using Ti/Ru_{0.3}Ti_{0.7}O₂ and Ti/Pt Anodes," *Chemical Engineering Journal*, vol. 204–206, 2012, pp. 141–150.
- [3] Isarain-Chavez, E., Baro, M. D., Rossinyol, E., Morales-Ortiz, U., Sort, J., Brillas, E., and Pellicer, E., "Comparative Electrochemical Oxidation of Methyl Orange Azo Dye Using Ti/Ir-Pb, Ti/Ir-Sn, Ti/Ru-Pb, Ti/Pt-Pd and Ti/RuO₂ Anodes," *Electrochimica Acta*, vol. 244, 2017, pp. 199–208.
- [4] Zhang, T., Liu, Y., Yang, L., Li, W., Wang, W., Liu, P., "Ti-Sn-Ce/Bamboo Biochar Particle Electrodes for Enhanced Electrocatalytic Treatment of Coking Wastewater in a Three-Dimensional Electrochemical Reaction System," *Journal of Cleaner Production*, vol. 258, 2020, p. 120273.

- [5] Xiao, H., Hao, Y., Wu, J., Meng, X., Feng, F., Xu, F., Luo, S., Jiang, B., "Differentiating the Reaction Mechanism of Three-Dimensionally Electrocatalytic System Packed with Different Particle Electrodes: Electro-Oxidation versus Electro-Fenton," *Chemosphere*, vol. 325, 2023, p. 138423.
- [6] Shen, B., Wen, X., Huang, X., "Enhanced Removal Performance of Estriol by a Three-Dimensional Electrode Reactor," *Chemical Engineering Journal*, vol. 327, 2017, pp. 597–607.
- [7] Sun, Y., Li, P., Zheng, H., Zhao, C., Xiao, X., Xu, Y., Sun, W., Wu, H., Ren, M., "Electrochemical Treatment of Chloramphenicol Using Ti-Sn/ γ -Al₂O₃ Particle Electrodes with a Three-Dimensional Reactor," *Chemical Engineering Journal*, vol. 308, pp. 1233–1242, 2017.
- [8] Li, J., Yan, J., Yao, G., Zhang, Y., Li, X., Lai, B., "Improving the Degradation of Atrazine in the Three-Dimensional (3D) Electrochemical Process Using CuFe₂O₄ as Both Particle Electrode and Catalyst for Persulfate Activation," *Chemical Engineering Journal*, vol. 361, pp. 1317–1332, 2019.
- [9] Wang, Y., Cui, C., Zhang, G., Xin, Y., Wang, S., "Electrocatalytic Hydrodechlorination of Pentachlorophenol on Pd-Supported Magnetic Biochar Particle Electrodes," *Separation and Purification Technology*, vol. 258, p. 118017, 2021.
- [10] Ren, Y., Wang, J., Qu, G., Ren, N., Lu, P., Chen, X., Wang, Z., Yang, Y., Hu, Y., "Study on the Mechanism of High Effective Mineralization of Rhodamine B in Three Dimensional Electrochemical System with γ -Fe₂O₃@CNTs Particle Electrodes," *Separation and Purification Technology*, vol. 314, p. 123616, 2023.
- [11] Wang, X., Zhao, Z., Wang, H., Wang, F., Dong, W., "Decomplexation of Cu-I-Hydroxyethylidene-1,1-Diphosphonic Acid by a Three-Dimensional Electrolysis System with Activated Biochar as Particle Electrodes," *Journal of Environmental Sciences*, vol. 124, pp. 630–643, 2023.
- [12] Zhao, H.-Z., Sun, Y., Xu, L.-N., Ni, J.-R., "Removal of Acid Orange 7 in Simulated Wastewater Using a Three-Dimensional Electrode Reactor: Removal Mechanisms and Dye Degradation Pathway," *Chemosphere*, vol. 78, no. 1, pp. 46–51, 2010.
- [13] Chowdhury, S., Saha, P., "Sea Shell Powder as a New Adsorbent to Remove Basic Green 4 (Malachite Green) from Aqueous Solutions: Equilibrium, Kinetic and Thermodynamic Studies," *Chemical Engineering Journal*, vol. 164, no. 1, pp. 168–177, 2010.
- [14] Kumar, S., Singh, S., Srivastava, V. C., "Electro-Oxidation of Nitrophenol by Ruthenium Oxide Coated Titanium Electrode: Parametric, Kinetic and Mechanistic Study," *Chemical Engineering Journal*, vol. 263, pp. 135–143, 2015.
- [15] Al-Shannag, M., Al-Qodah, Z., Bani-Melhem, K., Qtaishat, M. R., Alkasrawi, M., "Heavy Metal Ions Removal from Metal Plating Wastewater Using Electrocoagulation: Kinetic Study and Process Performance," *Chemical Engineering Journal*, vol. 260, pp. 749–756, 2015.
- [16] Tonini, G. A., Ruotolo, L. A. M., "Heavy Metal Removal from Simulated Wastewater Using Electrochemical Technology: Optimization of Copper Electrodeposition in a Membraneless Fluidized Bed Electrode," *Clean Technologies and Environmental Policy*, no. 2, 2017, pp. 403–415, vol. 19.
- [17] Gottipati, R., Mishra, S., "Preparation of Microporous Activated Carbon from Aegle Marmelos Fruit Shell and Its Application in Removal of Chromium(VI) from Aqueous Phase," *Journal of Industrial and*

Engineering Chemistry, 2016, pp. 355–363, vol. 36.

- [18] Akbal, F., Camcı, S., “Copper, Chromium and Nickel Removal from Metal Plating Wastewater by Electrocoagulation,” *Desalination*, vol. 269, no. 1–3, pp. 214–222, 2011.

- [19] Meng, H., Chen, C., Yan, Z., Li, X., Xu, J., Sheng, G., “Co-Doping Polymethyl Methacrylate and Copper Tailings to Improve the Performances of Sludge-Derived Particle Electrode,” *Water Research*, vol. 165, p. 115016, 2019.

Investigation of Light Baryons in Hot QCD

Gülşah Bozkır^{1*} 

^{1*} National Defence University, Army NCO Vocational HE School, Department of Basic Sciences, Balıkesir, Türkiye, gbozkir@msu.edu.tr

*Corresponding Author

ARTICLE INFO

ABSTRACT

Keywords:
Light Baryons
Thermal QCD Sum Rules
Mass
Residue

We investigate the behavior of light baryons in hot QCD. To this aim, we evaluate the light baryons mass and residue in hot medium using the thermal correlation function with two-point by means of the thermal QCD sum rule. In sum rule calculations, we consider the additional thermal condensates appearing in Wilson expansion at $T \neq 0$. We determine the thermal continuum threshold using obtained sum rules expressions to analyze numerically. We observe that the masses and residues of light baryons stay approximately the same until the temperature reaches a certain value and then they fall with the temperature increase. We see that vacuum values of parameters in our calculations are in good consistency with other studies in the literature. Also, we define the fit functions that show how the spectroscopic parameters for light baryons behave at $T \neq 0$.

Article History:
Received: 27.04.2023
Accepted: 23.11.2023
Online Available: 27.02.2024

1. Introduction

The determination of the behaviour of light baryons at $T \neq 0$ is among the important research topics of recent years in hadron physics. Such studies have a crucial role in commenting on the non-perturbative and perturbative nature of the hadronic matter in a hot medium. They can allow us to have more ideas about neutron stars' compact internal structure.

One of the most reliable and practicable phenomenological approaches to evaluate the spectroscopic parameters of light baryons at $T \neq 0$ is the thermal QCD sum rules method (TQCDSR). TQCDSR is the extended form to the finite temperature of QCD sum rules first proposed by Shifman, Vainshtein, and Zakharov for particles at $T=0$ [1, 2]. It was firstly given by Bochkarev and Shaposhnikov for particles in hot medium [3]. In TQCDSR, the Lorentz invariance is disrupted at $T \neq 0$ and some operators different

from vacuum operators arise in the operator product expansion (OPE) [4, 5]. Also, condensates in vacuum are changed placed by their thermal expectation values, and the four-vector velocity in the hot QCD is used.

In TQCDSR, the thermal correlation function (TCF), which forms the starting point of the method, is defined and the spectroscopic parameters of hadrons, such as mass and residue, are obtained by calculating this function in two different ways. The first calculation is to obtain the TCF in hadron language using the dispersion relationship.

The other calculation is to write the TCF in quark language using OPE. The coefficients with the same structures of these correlation functions obtained from two different ways are equalized to each other using quark-hadron duality. Finally, after the undesirable terms arising in the dispersion relationship are eliminated with the

Borel transformation, the spectroscopic parameters of hadrons in a hot medium are extracted.

Spectroscopic parameters of mesons at non-zero temperature by the TQCDSR have been widely studied in the literature [6-31], but there are comparatively lesser works about the thermal behaviour of light baryons via different phenomenological methods [32-49]. In the present paper, we calculate the $N, \Sigma, \Lambda, \Xi, \Delta, \Sigma^*, \Xi^*, \Omega^-$ light baryons mass and residue at $T \neq 0$ using the thermal light quark propagator by means of TQCDSR. In numerical calculations, we use the energy density and thermal versions of quark and gluon condensates obtained by lattice QCD.

This work is planned as follows: In Section 2, the thermal QCD sum rules for the masses and residues of light baryons at non-zero temperature are obtained. In Section 3, numerical calculations are presented for the considered light baryon. Section 4 is devoted to our discussions and conclusions.

2. Material and Method

In this part, QCD sum rules for light baryons mass and residue at non-zero temperature are presented. The starting point of the calculations is the following the TCF introduced as

$$\Pi_{(\mu\nu)}(p, T) = i \int d^4x e^{ip \cdot x} \times \langle \mathcal{T} \left(\eta_{(\mu)}^{o(D)}(x) \eta_{(\nu)}^{+o(D)}(0) \right) \rangle, \quad (1)$$

where p is the four-momentum, T represents temperature and \mathcal{T} denotes time ordering product. Also, $\eta^o(x)$ and $\eta_{\mu}^D(x)$ are interpolating currents for N, Σ, Λ, Ξ octet and $\Delta, \Sigma^*, \Xi^*, \Omega^-$ decuplet light baryons, respectively. We take the following expressions for these interpolating currents:

$$\eta^o(x) = N \varepsilon_{abc} \sum_{i=1}^2 \left[K \left(q_1^{T,a}(x) C A_1^i q_2^b(x) \right) \right.$$

$$\times A_2^i q_3^c(x) \left. \right] + L \left[\left(q_2^{T,a}(x) C A_1^i q_3^b(x) \right) A_2^i q_1^c(x) \right] + M \left[\left(q_1^{T,a}(x) C A_1^i q_3^b(x) \right) A_2^i q_2^c(x) \right], \quad (2)$$

$$\eta_{\mu}^D(x) = N \varepsilon_{abc} \left[\left(q_1^{T,a}(x) C \gamma_{\mu} q_2^b(x) \right) \times q_3^c(x) + \left(q_2^{T,a}(x) C \gamma_{\mu} q_3^b(x) \right) q_1^c(x) + \left(q_3^{T,a}(x) C \gamma_{\mu} q_1^b(x) \right) q_2^c(x) \right]. \quad (3)$$

Here a, b, c denote color indices, $A_1^1 = I, A_1^2 = A_2^1 = \gamma^5$ and $A_2^2 = t$. C and t are the charge conjugation operator and arbitrary auxiliary parameter, respectively. We take as $t = -1$ that accords to Ioffe current. The normalization constant N and the coefficients K, L, M as well as quark fields q_1, q_2 and q_3 for $N, \Sigma, \Lambda, \Xi, \Delta, \Sigma^*, \Xi^*, \Omega^-$ light baryons are presented in Table 1.

Table 1. N, K, L, M coefficients as well as quark fields q_1, q_2 and q_3 for $N, \Sigma, \Lambda, \Xi, \Delta, \Sigma^*, \Xi^*, \Omega^-$ light baryons

	N	K	L	M	q_1	q_2	q_3
N	2	1	0	0	u	d	u
Σ	$-1/\sqrt{2}$	1	-1	0	u	d	s
Λ	$1/\sqrt{6}$	1	1	2	u	d	s
Ξ	-2	1	0	0	u	d	s
Δ	$1/\sqrt{3}$	-	-	-	d	d	u
Σ^*	$\sqrt{2/3}$	-	-	-	u	d	s
Ξ^*	$1/\sqrt{3}$	-	-	-	s	s	u
Ω^-	1/3	-	-	-	s	s	s

To obtain desired sum rules, TCF given in Eq. (1) is evaluated in two different forms: In a first form, the hadronic side, the obtained expression includes observable hadronic states like mass and residue. In a second form, the QCD side, TCF is evaluated in the way of light quark fields by Wick's theorem. The sum rules for hadronic states are eventually reached by equating the determined structures' coefficients from both sides help of the dispersion relation. To suppress the terms arising from continuum and the higher states, it is necessary to apply the Borel transformation to on both parts of the equation.

The hadronic part of TCF is determined by inserting a full set of hadronic states into Eq. (1) and performing the four-dimensional integral. Therefore, we can write the hadronic part of TCF as

$$\begin{aligned} \Pi_{(\mu\nu)}^{HAD}(p, T) &= -\langle 0 | \eta_{(\mu)}^{O(D)}(0) | L(p, s) \rangle_T \\ &\times \frac{\langle L(p, s) | \bar{\eta}_{(\nu)}^{O(D)}(0) | 0 \rangle_T}{p^2 - m_{O(D)}^2(T)} + \dots, \end{aligned} \quad (4)$$

where $m_{O(D)}(T)$ is the thermal mass of octet or decuplet light baryon at $T \neq 0$, $|L(p, s)\rangle$ is the light baryon state and the dots represents the contributions of the higher states and continuum. The matrix elements for octet and decuplet baryon can be taken respectively as

$$\langle 0 | \eta^O(0) | L(p, s) \rangle_T = \lambda_O(T) u(p, s), \quad (5)$$

$$\langle 0 | \eta_\mu^D(0) | L(p, s) \rangle_T = \lambda_D(T) u_\mu(p, s), \quad (6)$$

Here, $\lambda_O(T)$ and $\lambda_D(T)$ are thermal residues of octet and decuplet baryon at $T \neq 0$, respectively. As $u(p, s)$ represents Dirac spinor, $u_\mu(p, s)$ denotes the Rarita–Schwinger spinor. After we insert the matrix elements given in Eqs. (5), (6) into Eq. (4) and sum over the spins for considered light baryon, we find the hadronic part of TCF with respect to the Borel parameter in two different Lorentz structures as

$$\hat{B}\Pi_{1(\mu\nu)}^{HAD}(p^2, p_0, T) = -\lambda_{O(D)}(T) e^{-\frac{m_{O(D)}^2(T)}{M^2}}, \quad (7)$$

$$\begin{aligned} \hat{B}\Pi_{2(\mu\nu)}^{HAD}(p^2, p_0, T) &= -\lambda_{O(D)}(T) \\ &\times m_{O(D)}(T) e^{-\frac{m_{N,H(D)}^2(T)}{M^2}}, \end{aligned} \quad (8)$$

where M^2 indicates the Borel parameter, p_0 denotes the quasi-particle energy, Π_1 and Π_2 are coefficients of Lorentz structures \not{p} and I for nucleon/hyperon as they are coefficients of $\not{p}g_{\mu\nu}$ and $g_{\mu\nu}$ for decuplet baryons, respectively.

The next aim is to obtain the QCD part of TCF with respect to quark fields by operator product expansion (OPE). TCF in this representation can be separated to the different Lorentz structures as hadronic side. We select \not{p} and I Lorentz structures for nucleon/hyperon as well as $\not{p}g_{\mu\nu}$ and $g_{\mu\nu}$ structures for decuplet baryons. By inserting the interpolating currents given in Eqs. (2) and (3) for considered light baryon into TCF and then contracting out all quark pairs by Wick's theorem, we find the QCD part of the TCF in connection with the thermal light quark propagators $S_q(x)$:

$$\begin{aligned} \Pi^{QCD,N}(p, T) &= 4i\varepsilon_{abc}\varepsilon_{\dot{a}\dot{b}\dot{c}} \int d^4x e^{ip.x} \\ &\times \left\{ \left\{ \left(\gamma_5 S_u^{c\dot{b}}(x) \hat{S}_d^{b\dot{a}}(x) S_u^{a\dot{c}}(x) \gamma_5 \right. \right. \right. \\ &\quad \left. \left. \left. - \gamma_5 S_u^{c\dot{c}}(x) \gamma_5 Tr[S_u^{a\dot{b}}(x) \hat{S}_d^{b\dot{a}}(x)] \right) \right. \right. \\ &\quad \left. \left. + t(\gamma_5 S_u^{c\dot{b}}(x) \gamma_5 \hat{S}_d^{b\dot{a}}(x) S_u^{a\dot{c}}(x) + \right. \right. \\ &\quad \left. \left. S_u^{c\dot{b}}(x) \hat{S}_d^{b\dot{a}}(x) \gamma_5 S_u^{a\dot{c}}(x) \gamma_5 - \right. \right. \\ &\quad \left. \left. \gamma_5 S_u^{c\dot{c}}(x) Tr[S_u^{a\dot{b}}(x) \gamma_5 \hat{S}_d^{b\dot{a}}(x)] - \right. \right. \\ &\quad \left. \left. S_u^{c\dot{c}}(x) \gamma_5 Tr[S_u^{a\dot{b}}(x) \hat{S}_d^{b\dot{a}}(x) \gamma_5] \right) \right. \\ &\quad \left. \left. + t^2(S_u^{c\dot{b}}(x) \gamma_5 \hat{S}_d^{b\dot{a}}(x) \gamma_5 S_u^{a\dot{c}}(x) - \right. \right. \\ &\quad \left. \left. S_u^{c\dot{c}}(x) Tr[S_d^{b\dot{a}}(x) \gamma_5 \hat{S}_u^{a\dot{b}}(x) \gamma_5] \right) \right\} \Big|_T, \end{aligned} \quad (9)$$

$$\begin{aligned} \Pi^{QCD,\Sigma}(p, T) &= \frac{i}{2} \varepsilon_{abc}\varepsilon_{\dot{a}\dot{b}\dot{c}} \int d^4x e^{ip.x} \\ &\left\{ \left(\gamma_5 S_d^{c\dot{c}}(x) \gamma_5 Tr[S_u^{a\dot{b}}(x) \hat{S}_s^{b\dot{a}}(x)] \right. \right. \\ &\quad \left. \left. + \gamma_5 S_d^{c\dot{a}}(x) \hat{S}_s^{b\dot{b}}(x) S_u^{a\dot{c}}(x) \gamma_5 \right. \right. \\ &\quad \left. \left. + \gamma_5 S_u^{c\dot{b}}(x) \hat{S}_s^{a\dot{a}}(x) S_d^{b\dot{c}}(x) \gamma_5 \right. \right. \\ &\quad \left. \left. + \gamma_5 S_u^{c\dot{c}}(x) \gamma_5 Tr[S_s^{a\dot{b}}(x) \hat{S}_d^{b\dot{a}}(x)] \right) \right. \\ &\quad \left. \left. + t(\gamma_5 S_d^{c\dot{a}}(x) \gamma_5 \hat{S}_s^{b\dot{b}}(x) S_u^{a\dot{c}}(x) \right. \right. \\ &\quad \left. \left. + \gamma_5 S_d^{c\dot{c}}(x) Tr[\gamma_5 \hat{S}_s^{b\dot{a}}(x) S_u^{a\dot{b}}(x)] \right. \right. \\ &\quad \left. \left. + S_u^{c\dot{b}}(x) \hat{S}_s^{a\dot{a}}(x) \gamma_5 S_d^{b\dot{c}}(x) \gamma_5 \right. \right. \\ &\quad \left. \left. + S_u^{c\dot{c}}(x) \gamma_5 Tr[\hat{S}_d^{b\dot{a}}(x) \gamma_5 S_s^{a\dot{b}}(x)] \right. \right. \\ &\quad \left. \left. + \gamma_5 S_u^{c\dot{c}}(x) Tr[\gamma_5 \hat{S}_d^{b\dot{a}}(x) S_s^{a\dot{b}}(x)] \right) \right\} \Big|_T, \end{aligned}$$

$$\begin{aligned}
& +\gamma_5 S_u^{cb}(x) \gamma_5' S_s^{aa}(x) S_d^{bc}(x) \\
& + S_d^{cc}(x) \gamma_5 Tr[S_s^{ba}(x) \gamma_5 S_u^{ab}(x)] \\
& + S_d^{ca}(x) \hat{S}_s^{bb}(x) \gamma_5 S_u^{ac}(x) \gamma_5 \\
& + t^2 (S_u^{cc}(x) Tr[\gamma_5 \hat{S}_s^{ab}(x) \gamma_5 S_d^{ba}(x)]) \\
& + S_u^{cb}(x) \gamma_5 \hat{S}_s^{aa}(x) \gamma_5 S_d^{bc}(x) \\
& + S_d^{ca}(x) \gamma_5 \hat{S}_s^{bb}(x) \gamma_5 S_u^{ac}(x) \\
& + S_d^{cc}(x) Tr[\gamma_5 \hat{S}_u^{ab}(x) \gamma_5 S_s^{ba}(x)]) \Big\} \Big\}_T,
\end{aligned}$$

(10)

$$\begin{aligned}
\Pi^{QCD,\Xi}(p, T) &= i \varepsilon_{abc} \varepsilon_{abc} \int d^4x e^{ip \cdot x} \\
&\times \left\{ \left((\gamma_5 S_s^{cc}(x) \gamma_5 Tr[S_s^{ab}(x) \hat{S}_u^{ba}(x)] \right. \right. \\
&- \gamma_5 S_s^{cb}(x) \hat{S}_u^{ba}(x) S_s^{ac}(x) \gamma_5) + \\
&t (\gamma_5 S_s^{cc}(x) Tr[\gamma_5 \hat{S}_u^{ba}(x) S_s^{ab}(x)] - \\
&\gamma_5 S_s^{cb} \gamma_5(x) \hat{S}_u^{ba}(x) S_s^{ac}(x) + \\
&S_s^{cc}(x) \gamma_5 Tr[\hat{S}_u^{ba}(x) \gamma_5 S_s^{ab}(x)] - \\
&S_s^{cb}(x) \hat{S}_u^{ba}(x) \gamma_5 S_s^{ac}(x)) + \\
&t^2 (S_s^{cc}(x) Tr[\gamma_5 \hat{S}_s^{ab}(x) \gamma_5 S_u^{ba}(x)] - \\
&S_s^{cb}(x) \gamma_5 \hat{S}_u^{ba}(x) \gamma_5 S_s^{ac}(x)) \Big\} \Big\}_T,
\end{aligned}$$

(11)

$$\begin{aligned}
\Pi^{QCD,\Lambda}(p, T) &= \frac{i}{6} \varepsilon_{abc} \varepsilon_{abc} \int d^4x e^{ip \cdot x} \\
&\times \left\{ \left((4\gamma_5 S_s^{cc}(x) \gamma_5 Tr[S_u^{ab}(x) \hat{S}_d^{ba}(x)] \right. \right. \\
&- 2\gamma_5 S_s^{ca}(x) \hat{S}_u^{ab}(x) S_d^{bc}(x) \gamma_5 \\
&- 2\gamma_5 S_s^{cb}(x) \hat{S}_d^{ba}(x) S_u^{ac}(x) \gamma_5 \\
&- 2\gamma_5 S_d^{ca}(x) \hat{S}_u^{ab}(x) S_s^{bc}(x) \gamma_5 \\
&+ \gamma_5 S_d^{cc}(x) \gamma_5 Tr[\hat{S}_s^{ba}(x) S_u^{ab}(x)] \\
&- \gamma_5 S_d^{ca}(x) \hat{S}_s^{bb}(x) S_u^{ac}(x) \gamma_5 \\
&- 2\gamma_5 S_u^{cb}(x) \hat{S}_d^{ba}(x) S_s^{ac}(x) \gamma_5 \\
&- \gamma_5 S_u^{cb}(x) \hat{S}_s^{aa}(x) S_d^{bc}(x) \gamma_5 \\
&+ \gamma_5 S_u^{cc}(x) \gamma_5 Tr[\hat{S}_d^{ba}(x) S_s^{ab}(x)]) \Big\} \Big\}_T,
\end{aligned}$$

$$\begin{aligned}
& + t(4\gamma_5 S_s^{cc}(x) Tr[\gamma_5 \hat{S}_d^{ba}(x) S_u^{ab}(x)] \\
& - 2\gamma_5 S_s^{ca} \gamma_5(x) \hat{S}_u^{ab}(x) S_d^{bc}(x) \\
& - 2\gamma_5 S_s^{cb}(x) \gamma_5 \hat{S}_d^{ba}(x) S_u^{ac}(x) \\
& + 4S_s^{cc}(x) \gamma_5 Tr[\hat{S}_d^{ba}(x) \gamma_5 S_u^{ab}(x)] \\
& - 2S_s^{ca}(x) \hat{S}_u^{ab}(x) \gamma_5 S_d^{bc}(x) \gamma_5 \\
& - 2S_s^{cb}(x) \hat{S}_d^{ba}(x) \gamma_5 S_u^{ac}(x) \gamma_5 \\
& - 2\gamma_5 S_d^{ca}(x) \gamma_5 \hat{S}_u^{ab}(x) S_s^{bc}(x) \\
& + \gamma_5 S_d^{cc}(x) Tr[\gamma_5 \hat{S}_s^{ba}(x) S_u^{ab}(x)] \\
& - \gamma_5 S_d^{ca}(x) \gamma_5 \hat{S}_s^{bb}(x) S_u^{ac}(x) \\
& - 2S_d^{ca}(x) \hat{S}_u^{ab}(x) \gamma_5 S_s^{bc}(x) \\
& + S_d^{cc}(x) \gamma_5 Tr[\hat{S}_s^{ba}(x) \gamma_5 S_u^{ab}(x)] \\
& - S_d^{ca}(x) \hat{S}_s^{bb}(x) \gamma_5 S_u^{ac}(x) \gamma_5 \\
& - 2\gamma_5 S_u^{cb}(x) \gamma_5 \hat{S}_d^{ba}(x) S_s^{ac}(x) \\
& - \gamma_5 S_u^{cb}(x) \gamma_5 \hat{S}_s^{aa}(x) S_d^{bc}(x) \\
& + \gamma_5 S_u^{cc}(x) Tr[\gamma_5 \hat{S}_d^{ba}(x) S_s^{ab}(x)] \\
& - 2S_u^{cb}(x) \hat{S}_d^{ba}(x) \gamma_5 S_s^{ac}(x) \gamma_5 \\
& - S_u^{cb}(x) \hat{S}_s^{aa}(x) \gamma_5 S_d^{bc}(x) \gamma_5 \\
& + S_u^{cc}(x) \gamma_5 Tr[\hat{S}_d^{ba}(x) \gamma_5 S_s^{ab}(x)]) \\
& + t^2 (4S_s^{cc}(x) Tr[\gamma_5 \hat{S}_u^{ab}(x) \gamma_5 S_d^{ba}(x)] - \\
& 2S_s^{ca}(x) \gamma_5 \hat{S}_u^{ab}(x) \gamma_5 S_d^{bc}(x) - \\
& 2S_s^{cb}(x) \gamma_5 \hat{S}_d^{ba}(x) \gamma_5 S_u^{ac}(x) - \\
& 2S_d^{ca}(x) \gamma_5 \hat{S}_u^{ab}(x) \gamma_5 S_s^{bc}(x) + \\
& S_d^{cc}(x) Tr[\gamma_5 \hat{S}_u^{ab}(x) \gamma_5 S_s^{ba}(x)] - \\
& S_d^{ca}(x) \gamma_5 \hat{S}_s^{bb}(x) \gamma_5 S_u^{ac}(x) - \\
& 2S_u^{cb}(x) \gamma_5 \hat{S}_d^{ba}(x) \gamma_5 S_s^{ac}(x) - \\
& S_u^{cb}(x) \gamma_5 \hat{S}_s^{aa}(x) \gamma_5 S_d^{bc}(x) - \\
& S_u^{cc}(x) Tr[\gamma_5 \hat{S}_s^{ab}(x) \gamma_5 S_d^{ba}(x)]) \Big\} \Big\}_T,
\end{aligned}$$

$$- \gamma_5 S_d^{ca}(x) \gamma_5 \hat{S}_s^{bb}(x) S_u^{ac}(x)$$

$$- 2S_d^{ca}(x) \hat{S}_u^{ab}(x) \gamma_5 S_s^{bc}(x)$$

$$+ S_d^{cc}(x) \gamma_5 Tr[\hat{S}_s^{ba}(x) \gamma_5 S_u^{ab}(x)]$$

$$- S_d^{ca}(x) \hat{S}_s^{bb}(x) \gamma_5 S_u^{ac}(x) \gamma_5$$

$$- 2\gamma_5 S_u^{cb}(x) \gamma_5 \hat{S}_d^{ba}(x) S_s^{ac}(x)$$

$$- \gamma_5 S_u^{cb}(x) \gamma_5 \hat{S}_s^{aa}(x) S_d^{bc}(x)$$

$$+ \gamma_5 S_u^{cc}(x) Tr[\gamma_5 \hat{S}_d^{ba}(x) S_s^{ab}(x)]$$

$$- 2S_u^{cb}(x) \hat{S}_d^{ba}(x) \gamma_5 S_s^{ac}(x) \gamma_5$$

$$- S_u^{cb}(x) \hat{S}_s^{aa}(x) \gamma_5 S_d^{bc}(x) \gamma_5$$

$$+ S_u^{cc}(x) \gamma_5 Tr[\hat{S}_d^{ba}(x) \gamma_5 S_s^{ab}(x)]$$

$$+ t^2 (4S_s^{cc}(x) Tr[\gamma_5 \hat{S}_u^{ab}(x) \gamma_5 S_d^{ba}(x)] -$$

$$2S_s^{ca}(x) \gamma_5 \hat{S}_u^{ab}(x) \gamma_5 S_d^{bc}(x) -$$

$$2S_s^{cb}(x) \gamma_5 \hat{S}_d^{ba}(x) \gamma_5 S_u^{ac}(x) -$$

$$2S_d^{ca}(x) \gamma_5 \hat{S}_u^{ab}(x) \gamma_5 S_s^{bc}(x) +$$

$$S_d^{cc}(x) Tr[\gamma_5 \hat{S}_u^{ab}(x) \gamma_5 S_s^{ba}(x)] -$$

$$S_d^{ca}(x) \gamma_5 \hat{S}_s^{bb}(x) \gamma_5 S_u^{ac}(x) -$$

$$2S_u^{cb}(x) \gamma_5 \hat{S}_d^{ba}(x) \gamma_5 S_s^{ac}(x) -$$

$$S_u^{cb}(x) \gamma_5 \hat{S}_s^{aa}(x) \gamma_5 S_d^{bc}(x) -$$

$$S_u^{cc}(x) Tr[\gamma_5 \hat{S}_s^{ab}(x) \gamma_5 S_d^{ba}(x)]) \Big\} \Big\}_T, \quad (12)$$

$$\Pi_{\mu\nu}^{QCD,\Delta}(p, T) = \frac{i}{3} \varepsilon_{abc} \varepsilon_{abc} \int d^4x e^{ip \cdot x}$$

$$\begin{aligned}
 & \times \left\{ \left\{ 2S_d^{c\acute{a}}(x)\gamma_\nu\acute{S}_d^{ab}(x)\gamma_\mu S_u^{b\acute{c}}(x) \right. \right. \\
 & - 2S_d^{c\acute{b}}(x)\gamma_\nu\acute{S}_d^{a\acute{a}}(x)\gamma_\mu S_u^{b\acute{c}}(x) \\
 & + 4S_d^{c\acute{b}}(x)\gamma_\nu\acute{S}_u^{b\acute{a}}(x)\gamma_\mu S_d^{a\acute{c}}(x) \\
 & + 2S_u^{c\acute{a}}(x)\gamma_\nu\acute{S}_d^{ab}(x)\gamma_\mu S_d^{b\acute{c}}(x) \\
 & - 2S_u^{c\acute{a}}(x)\gamma_\nu\acute{S}_d^{bb}(x)\gamma_\mu S_d^{a\acute{c}}(x) \\
 & \left. \left. - S_u^{c\acute{c}}(x)Tr[S_d^{b\acute{a}}(x)\gamma_\nu\acute{S}_d^{ab}(x)\gamma_\mu] \right. \right. \\
 & \left. \left. + S_u^{c\acute{c}}(x)Tr[S_d^{bb}(x)\gamma_\nu\acute{S}_d^{a\acute{a}}(x)\gamma_\mu] - \right. \right. \\
 & \left. \left. S_u^{c\acute{c}}(x)Tr[S_d^{bb}(x)\gamma_\nu\acute{S}_d^{a\acute{a}}(x)\gamma_\mu] \right\} \right\}_T \quad (13)
 \end{aligned}$$

$$\begin{aligned}
 \Pi_{\mu\nu}^{QCD,\Omega^-}(p,T) &= \varepsilon_{abc}\varepsilon_{\acute{a}b\acute{c}} \int d^4x e^{ip.x} \\
 & \times \left\{ \left\{ S_s^{c\acute{a}}(x)\gamma_\nu\acute{S}_s^{ab}(x)\gamma_\mu S_s^{b\acute{c}}(x) \right. \right. \\
 & - S_s^{c\acute{a}}(x)\gamma_\nu\acute{S}_s^{bb}(x)\gamma_\mu S_s^{a\acute{c}}(x) \\
 & - S_s^{c\acute{b}}(x)\gamma_\nu\acute{S}_s^{a\acute{a}}(x)\gamma_\mu S_s^{b\acute{c}}(x) \\
 & + S_s^{c\acute{b}}(x)\gamma_\nu\acute{S}_s^{b\acute{a}}(x)\gamma_\mu S_s^{a\acute{c}}(x) \\
 & \left. \left. - S_s^{c\acute{c}}(x)Tr[S_s^{b\acute{a}}(x)\gamma_\nu\acute{S}_s^{ab}(x)\gamma_\mu] \right. \right. \\
 & \left. \left. + S_s^{c\acute{c}}(x)Tr[S_s^{bb}(x)\gamma_\nu\acute{S}_s^{a\acute{a}}(x)\gamma_\mu] \right\} \right\}_T. \quad (14)
 \end{aligned}$$

$$\begin{aligned}
 \Pi_{\mu\nu}^{QCD,\Xi^*}(p,T) &= \frac{i}{3}\varepsilon_{abc}\varepsilon_{\acute{a}b\acute{c}} \int d^4x e^{ip.x} \\
 & \times \left\{ \left\{ 2S_s^{c\acute{a}}(x)\gamma_\nu\acute{S}_s^{ab}(x)\gamma_\mu S_u^{b\acute{c}}(x) \right. \right. \\
 & - 2S_s^{c\acute{b}}(x)\gamma_\nu\acute{S}_s^{a\acute{a}}(x)\gamma_\mu S_u^{b\acute{c}}(x) \\
 & + 4S_s^{c\acute{b}}(x)\gamma_\nu\acute{S}_u^{b\acute{a}}(x)\gamma_\mu S_s^{a\acute{c}}(x) \\
 & + 2S_u^{c\acute{a}}(x)\gamma_\nu\acute{S}_s^{ab}(x)\gamma_\mu S_s^{b\acute{c}}(x) \\
 & - 2S_u^{c\acute{a}}(x)\gamma_\nu\acute{S}_s^{bb}(x)\gamma_\mu S_s^{a\acute{c}}(x) \\
 & \left. \left. - S_u^{c\acute{c}}(x)Tr[S_s^{b\acute{a}}(x)\gamma_\nu\acute{S}_s^{ab}(x)\gamma_\mu] \right. \right. \\
 & \left. \left. + S_u^{c\acute{c}}(x)Tr[S_s^{bb}(x)\gamma_\nu\acute{S}_s^{a\acute{a}}(x)\gamma_\mu] \right. \right. \\
 & \left. \left. - 4S_s^{c\acute{c}}(x)Tr[S_u^{b\acute{a}}(x)\gamma_\nu\acute{S}_s^{ab}(x)\gamma_\mu] \right\} \right\}_T, \quad (15)
 \end{aligned}$$

$$\Pi_{\mu\nu}^{QCD,\Sigma^*}(p,T) = -\frac{2i}{3}\varepsilon_{abc}\varepsilon_{\acute{a}b\acute{c}} \int d^4x e^{ip.x}$$

$$\begin{aligned}
 & \times \left\{ \left\{ S_d^{c\acute{a}}(x)\gamma_\nu\acute{S}_u^{bb}(x)\gamma_\mu S_s^{a\acute{c}}(x) \right. \right. \\
 & + S_d^{c\acute{b}}(x)\gamma_\nu\acute{S}_s^{a\acute{a}}(x)\gamma_\mu S_u^{b\acute{c}}(x) \\
 & + S_s^{c\acute{a}}(x)\gamma_\nu\acute{S}_d^{bb}(x)\gamma_\mu S_u^{a\acute{c}}(x) \\
 & + S_s^{c\acute{b}}(x)\gamma_\nu\acute{S}_u^{a\acute{a}}(x)\gamma_\mu S_d^{b\acute{c}}(x) \\
 & + S_u^{c\acute{a}}(x)\gamma_\nu\acute{S}_s^{bb}(x)\gamma_\mu S_d^{a\acute{c}}(x) \\
 & + S_u^{c\acute{b}}(x)\gamma_\nu\acute{S}_d^{a\acute{a}}(x)\gamma_\mu S_s^{b\acute{c}}(x) \\
 & \left. \left. + S_s^{c\acute{c}}(x)Tr[S_d^{b\acute{a}}(x)\gamma_\nu\acute{S}_u^{ab}(x)\gamma_\mu] \right. \right. \\
 & \left. \left. + S_u^{c\acute{c}}(x)Tr[S_s^{b\acute{a}}(x)\gamma_\nu\acute{S}_d^{ab}(x)\gamma_\mu] \right. \right. \\
 & \left. \left. + S_d^{c\acute{c}}(x)Tr[S_u^{b\acute{a}}(x)\gamma_\nu\acute{S}_s^{ab}(x)\gamma_\mu] \right\} \right\}_T, \quad (16)
 \end{aligned}$$

Here $\acute{S} = CS^T C$ and $S_q(x)$ is given as

$$\begin{aligned}
 S_q^{ij}(x) &= i\frac{x_\mu\gamma_\mu}{2\pi^2x^4}\delta_{ij} - \frac{m_q}{4\pi^2x^2}\delta_{ij} - \frac{\langle\bar{q}q\rangle}{12}\delta_{ij} \\
 & - \frac{x^2}{192}m_0^2\langle\bar{q}q\rangle\left[1 - i\frac{m_q}{6}x_\mu\gamma_\mu\right]\delta_{ij} \\
 & + \frac{i}{3}\left[x_\mu\gamma_\mu\left(\frac{m_q}{16}\langle\bar{q}q\rangle - \frac{1}{12}\langle u\Theta^f u\rangle\right) \right. \\
 & \left. + \frac{1}{3}(u \cdot x u_\mu\gamma_\mu\langle u\Theta^f u\rangle)\right]\delta_{ij} \\
 & - \frac{ig_s\lambda_A^{ij}}{32\pi^2x^2}G_{\mu\nu}^A(x_\mu\gamma_\mu\sigma^{\mu\nu} + \sigma^{\mu\nu}x_\mu\gamma_\mu), \quad (17)
 \end{aligned}$$

where $\langle\bar{q}q\rangle$ shows the thermal quark condensate, m_q represents the light quark mass, $G_{\mu\nu}^A$ is the gluon field strength tensor at non-zero temperature. To proceed, we insert the above-given $S_q(x)$ into the QCD part of TCF for each light baryon.

After we perform the standard Borel transformation and continuum subtraction, we obtain the QCD side of TCF in the Borel system for each light baryon in terms of the functions Π_1 and Π_2 as the hadronic side. In the final step, we match the coefficients of these two different forms of TCF with the same structures and obtain the thermal sum rules in terms of spectroscopic parameters of considered light baryon:

$$\hat{B}\Pi_1^{QCD}(p_0, T) = -\lambda_{O(D)}^2(T)e^{-m_{O(D)}^2(T)/M^2}, \quad (18)$$

$$\hat{B}\Pi_2^{QCD}(p_0, T) = -\lambda_{O(D)}^2(T) m_{O(D)} \times e^{-m_{O(D)}^2(T)/M^2}. \quad (19)$$

From Eqs. (18) and (19), we extract masses and residues for considered light baryons.

3. Numerical Results

The starting point of the numerical analysis is the determination of some input parameters required in calculations. These input parameters which the vacuum values of quark masses, quark condensates and gluon condensates are gathered in Table 2.

Aside from these input parameters presented for $T = 0$, there are three more that the thermal quark condensate $\langle \bar{q}q \rangle$, the thermal gluon condensate $\langle G^2 \rangle$ and energy density of hot medium $\langle \Theta_{00}^f \rangle$. For $\langle \bar{q}q \rangle$, we use the following expression [50]

$$\langle \bar{q}q \rangle = \langle 0 | \bar{q}q | 0 \rangle \frac{1}{1 + e^{A(BT^2 + C[\frac{1}{GeV}]^{T-1})}}, \quad (20)$$

where fit parameters are $A = 18.10042$, $B = 1.84692 \frac{1}{GeV^2}$, $C = 4.99216 \frac{1}{GeV}$, and this expression is consistent with the Lattice QCD studies presented in [51, 52].

$\langle G^2 \rangle$ is given by

$$\langle G^2 \rangle = \langle 0 | G^2 | 0 \rangle \left[1 - 1.65 \left(\frac{T}{T_c} \right)^{8.735} + 0.04967 \left(\frac{T}{T_c} \right)^{0.7211} \right], \quad (21)$$

where T_c is the critical temperature and $\langle 0 | G^2 | 0 \rangle$ being gluon condensate at $T = 0$. Using the graphics drawn in the framework lattice QCD [52], we can describe the following fit formula for energy density of hot medium

$$\langle \Theta_{00}^f \rangle = \langle \Theta_{00}^g \rangle = T^4 e^{(DT^2 - ET)} - FT^5, \quad (22)$$

where D, E and F are fit parameters that $D = 113.867 \frac{1}{GeV^2}$, $E = 12.190 \frac{1}{GeV}$, $F = 10.141 \frac{1}{GeV}$, and this formula is valid at temperatures up to $130 MeV$.

Table 2. Vacuum values of input parameters involved in calculations [53-56]

Parameter	Vacuum Value	Unit
p_0^N	1	[GeV]
p_0^Σ	1.192	[GeV]
p_0^Λ	1.15	[GeV]
p_0^{Ξ}	1.314	[GeV]
p_0^{Λ}	1.231	[GeV]
$p_0^{\Sigma^*}$	1.383	[GeV]
$p_0^{\Xi^*}$	1.531	[GeV]
$p_0^{\Omega^-}$	1.672	[GeV]
m_u	$2.3_{-0.5}^{+0.7}$	[MeV]
m_d	$4.8_{-0.3}^{+0.5}$	[MeV]
m_s	95 ± 5	[MeV]
m_0^2	0.8 ± 0.2	[GeV] ²
$\langle 0 \bar{u}u 0 \rangle = \langle 0 \bar{d}d 0 \rangle$	$-(0.24 \pm 0.01)^3$	[GeV] ³
$\langle 0 \bar{s}s 0 \rangle$	$-0.8(0.24 \pm 0.01)^3$	[GeV] ³
$\langle 0 \frac{1}{\pi} \alpha_s G^2 0 \rangle$	(0.012 ± 0.004)	[GeV] ⁴

To complete the numerical calculations, we need to determine the three auxiliary parameters, the Borel parameter M^2 , the thermal version of the continuum threshold $s_0(T)$ and the parameter x ($x = \cos\theta, t = \tan\theta$). According to the QCD sum rule principle, physical quantities should be roughly independent with respect to these parameters in suitable working ranges. To determine the suitable working ranges for M^2 and x , we investigate the behaviour of the physical parameters of the corresponding light baryon according to these auxiliary parameters in vacuum. We realize that they weakly depend on these parameters for selected regions.

Therefore, we take the working ranges of x [$\pm 0.6 \mp 0.2$] and [$\pm 0.8, \mp 0.4$] for nucleon and hyperon, respectively. The working ranges of M^2 are taken as $[0.8GeV^2 - 1.2GeV^2]$, $[1.0GeV^2 - 1.6GeV^2]$, $[1.0GeV^2 - 1.6GeV^2]$,

$[1.2\text{GeV}^2 - 1.8\text{GeV}^2]$, $[1.5\text{GeV}^2 - 3.0\text{GeV}^2]$,
 $[1.7\text{GeV}^2 - 3.5\text{GeV}^2]$, $[2.0\text{GeV}^2 - 3.8\text{GeV}^2]$,
 $[2.2\text{GeV}^2 - 4.0\text{GeV}^2]$ for the
 $N, \Sigma, \Lambda, \Xi, \Delta, \Sigma^*, \Xi^*, \Omega^-$, respectively.

At the end of this section, we would like to show the thermal behaviour of spectroscopic parameters of light baryons and residue at non-zero temperatures. For this aim, we display the mass and residue at selected s_0 and M^2 values versus temperature for the corresponding light baryon in Figure 1 and Figure 2, respectively. Selected s_0 and M^2 values in these graphs are given in Table 3. It is seen that masses and residues of $N, \Sigma, \Lambda, \Xi, \Delta, \Sigma^*, \Xi^*, \Omega^-$ light baryons remain approximately unchanged until the temperature reaches $T \cong 0.13 - 0.15 \text{ GeV}$ and then they start to rapidly fall with the temperature increases. By using Figs. 1 and 2, we also obtain the following fit functions for the thermal mass and residue as

$$m_L[\lambda_L](T) = \Gamma(1 - \delta T^n), \quad (23)$$

Here, Γ , δ and n are fitting parameters and their values are given in Table 4 and 5 for mass and residue of the corresponding light baryon, respectively. At $T \rightarrow 0$ limit, it is shown that above our fit function for both mass and residue of corresponding light baryon are consistent with other studies and experimental results in vacuum.

4. Discussion and Conclusion

In this article, we wanted to determine the thermal behaviour of light baryons at $T \neq 0$. To this aim, we evaluated the mass and residue of light baryons by means of the TQCDSR in hot medium. In these calculations, we used the selected interpolating current for the corresponding light baryon and determined working ranges of auxiliary parameters partaken sum rules. We also obtained the thermal continuum threshold for considered light baryon in terms of their vacuum values.

Using the additional thermal condensates at $T \neq 0$, we numerically analyzed for $N, \Sigma, \Lambda, \Xi, \Delta, \Sigma^*, \Xi^*, \Omega^-$ light baryons masses and residues. We see that the physical parameters of light baryons stay approximately the same until the temperature reaches $T \cong 0.13 - 0.15 \text{ GeV}$ and then they fall with the temperature increases. If we compare this thermal reduction behavior with other studies in the literature, we see that the behaviour with respect to temperature on the mass and residue of N, Σ, Λ, Ξ octet baryons is rapport with studies given in [32, 33, 35, 47]. On the other hand, the behaviour of the $\Delta, \Sigma^*, \Xi^*, \Omega^-$ decuplet baryon's mass with respect to the temperature in this work is agreed with results given in [44,45].

As a result, this melting of physical parameters of light baryons with increasing temperature may be interpreted as a transition to the quark-gluon plasma phase from the hadron phase. Also, it is seen that the vacuum values of physical parameters in this study are in good conform with other studies in the literature.

We obtained the fit functions at non-zero temperature for the mass and residue of light baryons in this article. These fit functions may be used to investigate other spectroscopic parameters of light baryons in a hot medium. We hope that our results may help analyses of heavy ion collision experiments in later times.

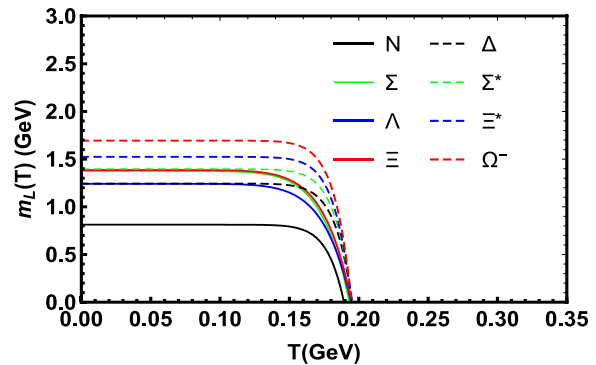


Figure 1. Mass-temperature graph for the corresponding light baryon at selected s_0 and M^2

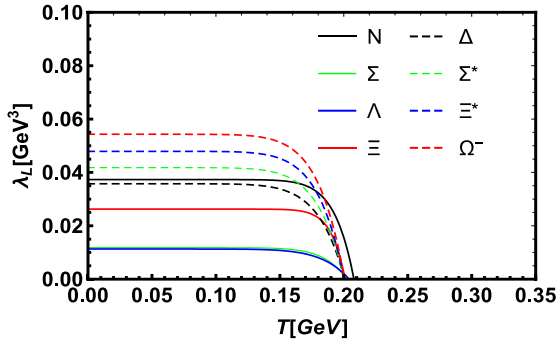


Figure 2. Residue-temperature graph for the corresponding light baryon at selected s_0 and M^2

Table 3. Selected s_0 and M^2 values in Figs. 1 and 2

particle	$s_0(\text{GeV}^2)$	$M^2(\text{GeV}^2)$
N	1.5	1.0
Σ	2.8	1.3
Λ	2.6	1.3
Ξ	3.2	1.5
Δ	2.9	1.5
Σ^*	3.5	1.7
Ξ^*	4.1	2.0
Ω^-	4.7	3.0

Table 4. The values of parameters Γ , δ and n in the fit function defined for $m_L(T)$

particle	$\Gamma(\text{GeV})$	$\delta\left(\frac{1}{\text{GeV}}\right)^n$	n
N	0.81	3.67×10^{11}	16
Σ	1.37	1.37×10^7	16
Λ	1.24	1.29×10^7	10
Ξ	1.38	1.27×10^7	10
Δ	1.24	2.23×10^{11}	10
Σ^*	1.39	2.32×10^{11}	16
Ξ^*	1.52	2.34×10^{11}	16
Ω^-	1.69	2.31×10^{11}	16

Table 5. The values of parameters Γ , δ and n in the fit function defined for $\lambda_L(T)$

particle	$\Gamma(\text{GeV})$	$\delta\left(\frac{1}{\text{GeV}}\right)^n$	n
N	0.03	3.55×10^9	14
Σ	0.01	2.14×10^8	12
Λ	0.01	2.14×10^8	12
Ξ	0.02	1.80×10^8	12
Δ	0.03	9.42×10^6	10
Σ^*	0.04	9.68×10^6	10
Ξ^*	0.04	9.63×10^6	10
Ω^-	0.05	9.50×10^6	10

Article Information Form

Acknowledgments

The authors would like to thank the editors and anonymous referees for their contributions.

Funding

The author have no received any financial support for the research, authorship or publication of this study.

The Declaration of Conflict of Interest/ Common Interest

No conflict of interest or common interest has been declared by the authors.

The Declaration of Ethics Committee Approval

This study does not require ethics committee permission or any special permission.

The Declaration of Research and Publication Ethics

The authors of the paper declare that they comply with the scientific, ethical and quotation rules of SAUJS in all processes of the paper and that they do not make any falsification on the data collected. In addition, they declare that Sakarya University Journal of Science and its editorial board have no responsibility for any ethical violations that may be encountered, and that this study has not been evaluated in any academic publication environment other than Sakarya University Journal of Science.

Copyright Statement

Authors own the copyright of their work published in the journal and their work is published under the CC BY-NC 4.0 license.

References

- [1] M. A. Shifman, A. I. Vainstein, V. I. Zakharov, "QCD and resonance physics. Theoretical foundations," Nuclear Physics B, vol. 147, pp. 385-447, 1979.
- [2] M. A. Shifman, A. I. Vainstein, V. I. Zakharov, "QCD and resonance physics, applications," Nuclear Physics B, vol. 147, pp. 448-518, 1979.

- [3] A. I. Bochkarev, M. E. Shaposhnikov, "The spectrum of hot hadronic matter and finite-temperature QCD sum rules," *Nuclear Physics B*, vol. 268, pp. 220-252, 1986.
- [4] E. V. Shuryak, "Correlation functions in the QCD vacuum," *Reviews of Modern Physics*, vol. 65, pp. 1-46, 1993.
- [5] T. Hatsuda, Y. Koike, S. H. Lee, "Finite-temperature QCD sum rules reexamined: ρ , ω and A_1 mesons," *Nuclear Physics B*, vol. 394, pp. 221-266, 1993.
- [6] S. Mallik, S. Sarkar, "Vector and axial-vector mesons at finite temperature," *The European Physical Journal C-Particles and Fields*, vol. 25, no. 3, pp. 445-452, 2002.
- [7] K. Morita, S. H. Lee, "Mass Shift and Width Broadening of J/ψ in hot gluonic plasma from QCD Sum Rules," *Physical Review Letter*, vol. 100, 022301, 2008.
- [8] P. Gubler, K. Morita, M. Oka, "Charmonium spectra at finite temperature from QCD sum rules with the maximum entropy method," *Physical Review Letter*, vol. 107, 092003, 2011.
- [9] E. V. Veliev, H. Sundu, K. Azizi, M. Bayar, "Scalar quarkonia at finite temperature," *Physical Review D*, vol. 82, 056012, 2010.
- [10] K. Azizi, A. Türkan, E. Veli Veliev, H. Sundu, "Thermal properties of light tensor mesons via QCD sum rules," *Advances in High Energy Physics*, vol. 2015, 794243, 2015.
- [11] E. V. Veliev, K. Azizi, H. Sundu, G. Kaya, "Thermal Properties of the Heavy Axial Vector Quarkonia," *Romanian Journal of Physics*, vol. 59, pp. 140-154, 2014.
- [12] E. Yazici, H. Sundu, E. V. Veliev, "B_cB_c J/ψ vertex form factor at finite temperature in the framework of QCD sum rules approach," *The European Physical Journal C*, vol. 76, no. 2, 89, 2016.
- [13] K. Azizi, H. Sundu, A. Türkan, E. Veli Veliev, "Thermal properties of $D_2^*(2460)$ and $D_{s2}^*(2573)$ tensor mesons using QCD sum rules," *Journal of Physics G: Nuclear and Particle Physics*, vol. 41, 035003, 2015.
- [14] E. Veli Veliev, G. Kaya, "Leptonic decay constants of D_s and B_s Mesons at finite temperature", *The European Physical Journal C*, vol. 63, pp. 87-91, 2009.
- [15] E. Veli Veliev, G. Kaya, "The mass and leptonic decay constant of $D_{s0}(2317)$ meson in the framework of thermal QCD sum rules", *Acta Physica Polonica B*, vol. 41, pp. 1905-1916, 2010.
- [16] E. Veli Veliev, K. Azizi, H. Sundu, G. Kaya, A. Türkan, "Thermal QCD sum rules study of vector charmonium and bottomonium states", *The European Physical Journal A*, vol. 47, 110, 2011
- [17] K. Azizi, A. Türkan, H. Sundu, E. Veli Veliev, E. Yazıcı, "Thermal behaviors of light unflavored tensor mesons in the framework of QCD sum rule," *Journal of Physics: Conference Series*, vol. 562, 012016, 2014.
- [18] E Veli Veliev, S Günaydın, H Sundu, "Thermal properties of the exotic X(3872) state via QCD sum rule," *The European Physical Journal Plus*, vol. 133, pp. 1-8, 2018.
- [19] K. Azizi, B. Barsbay, H. Sundu, "Light scalar $K_0^*(700)$ meson in vacuum and a hot medium," *Physical Review D*, vol. 100, 094041, 2019.
- [20] E. V. Veliev, K. Azizi, H. Sundu, N. Akşit, "Investigation of heavy-heavy pseudoscalar mesons in thermal QCD sum rules," *Journal of Physics G*, vol. 39, no. 1, 015002, 2012.

- [21] C. A. Dominguez, M. Loewe, J. C. Rojas, “Heavy-light quark pseudoscalar and vector mesons at finite temperature,” *Journal of High Energy Physics*, vol. 2007, no. 8, 040, 2007.
- [22] Z. B. Wang, Z. G. Wang, “Analysis of the Heavy Pseudoscalar Mesons with thermal QCD sum rules,” *International Journal of Theoretical Physics*, vol. 55, pp. 3137–3146, 2016.
- [23] C.A. Dominguez, M. S. Fetea, M. Loewe, “Pions at finite temperature from QCD sum rules,” *Physics Letter B*, vol. 387, no. 1, pp. 151-154, 1996.
- [24] C. A. Dominguez, M. Loewe, Y. Zhang, “The $a_1(1260)$ meson and chiral symmetry restoration and deconfinement at finite temperature QCD,” *Nuclear Physics B*, vol. 234, pp. 305-308, 2013.
- [25] C. A. Dominguez, M. Loewe, Y. Zhang, “Chiral symmetry restoration and deconfinement in QCD at finite temperature,” *Physical Review D*, vol. 90, pp. 039903, 2014.
- [26] R. Gao, Z. H. Guo, J. Y. Pang, “Thermal behaviors of light scalar resonances at low temperatures,” *Physical Review D*, vol. 100, pp. 114028, 2019.
- [27] E. Veli Veliev, T. M. Aliev, “Thermal QCD sum rules for $\sigma(600)$ meson,” *Journal of Physics G: Nuclear and Particle Physics*, vol. 35, 125002, 2008.
- [28] S. Mallik, S. Sarkar, “Thermal QCD sum rules for mesons,” *Physical Review D*, vol. 66, 056008, 2002.
- [29] A. Türkan, H. Dağ, J. Y. Süngü, E. Veli Veliev, “Light D-wave axial-tensor $K_2(1820)$ meson at finite temperature,” *Europhysics Letters*, vol. 126, 51001, 2019.
- [30] J. Y. Süngü, A. Türkan, E. Sertbakan, E. Veli Veliev, “Axial-tensor Meson family at $T \neq 0$,” *The European Physical Journal C*, vol. 80, 943, 2020.
- [31] J. Y. Süngü, A. Türkan, H. Sundu, E. Veli Veliev, “Impact of a thermal medium on newly observed $Z_{cs}(3985)$ resonance and its b -partner,” *The European Physical Journal C*, vol. 82, 453, 2022.
- [32] H. Leutwyler, A. V. Smilga, “Nucleons at finite temperature,” *Nuclear Physics B*, vol. 342, pp. 302-316, 1990.
- [33] C. Adami, I. Zahed, “Finite-temperature QCD sum rules for the nucleon,” *Physical Review D*, vol. 45, pp. 4312-4322, 1992.
- [34] M. Kacir, I. Zahed, “Nucleons at Finite Temperature,” *Physical Review D*, vol. 54, pp. 5536-5544, 1996.
- [35] S. Mallik, S. Sarkar, “Spectral representation and QCD sum rules for the nucleon at finite temperature,” *Physical Review D*, vol. 65, No. p. 016002, 2001.
- [36] M. Abu-Shady, “Nucleon properties below the critical point temperature,” *International Journal of Theoretical Physics*, vol. 50, pp. 1372-1381, 2010.
- [37] M. Abu-Shady, H. M. Mansour, “Quantized linear σ model at finite temperature, and nucleon properties,” *Physical Review C*, vol. 85, p. 055204, 2012.
- [38] M. Abu-Shady, A. K. Abu-Nab, “Nucleon Properties at Finite Temperature in the Extended Quark-Sigma Model,” *American Journal of Physics and Applications*, vol. 2, pp. 46-51, 2014.
- [39] C. Y. Ryu, C. H. Hyun, M.-K. Cheoun, “Magnetic moments of octet baryons at finite density and temperature,” *Journal of Physics G: Nuclear and Particle Physics*, vol. 37, pp. 105002, 2010.
- [40] Y. Koike, “Octet Baryons at finite temperature: QCD sum rules vs. Chiral

- symmetry,” *Physical Review D*, vol. 48, pp. 2313, 1993.
- [41] G. F. Burgio, H.-J. Schulze, A. Li, “Hyperon stars at finite temperature in the Brueckner theory,” *Physical Review C*, vol. 83, pp. 025804, 2011.
- [42] A. Rios, A. Polls, A. Ramos, I. Vidana, “Bulk and single-particle properties of hyperonic matter at finite temperature,” *Physical Review C*, vol. 72, pp. 024316, 2005.
- [43] P. F. Bedaque, “Chiral perturbation theory analysis of baryon temperature mass shifts,” *Physics Letter B*, vol. 387, pp. 1-8, 1996.
- [44] J. M. Torres-Rincon, B. Sintes, J. Aichelin, “Flavor dependence of baryon melting temperature in effective models of QCD,” *Physical Review C*, vol. 91, pp. 065206, 2015.
- [45] Y. Xu, Y. Liu, M. Huang, “The temperature dependence of the decuplet baryon masses from thermal QCD sum rules,” *Communications in Theoretical Physics*, vol. 63, pp. 209-214, 2015.
- [46] S. Ghosh, S. Mitra, S. Sarkar, “ Δ self-energy at finite temperature and density and the πN cross-section,” *Physical Review D*, vol. 95, pp. 056010, 2017.
- [47] K. Azizi, G. Kaya, “Modifications on nucleon parameters at finite temperature,” *The European Physical Journal Plus*, vol. 130, pp. 172-183, 2015.
- [48] K. Azizi, G. Kaya, “Thermal Behavior of the mass and residue of hyperons,” *Journal of Physics G: Nuclear and Particle Physics*, vol. 43, pp. 055002, 2016.
- [49] K. Azizi, G. Bozkır, “Decuplet baryons in a hot medium,” *European Physical Journal C*, vol. 76, pp. 521-183, 2016.
- [50] A. Ayala, A. Bashir, C. A. Dominguez, E. Gutierrez, M. Loewe, A. Raya, “QCD phase diagram from finite energy sum rules,” *Physical Review D*, vol. 84, pp. 056004, 2011.
- [51] A. Bazavov, T. Bhattacharya, M. Cheng, N. H. Christ, C. DeTar, S. Ejiri, Steven Gottlieb, R. Gupta, U. M. Heller, K. Huebner, C. Jung, F. Karsch, E. Laermann, L. Levkova, C. Miao, R. D. Mawhinney, P. Petreczky, C. Schmidt, R. A. Soltz, W. Soeldner, R. Sugar, D. Toussaint, P. Vranas, “Equation of state and QCD transition at finite temperature,” *Physical Review D*, vol. 80, pp. 014504, 2009.
- [52] M. Cheng, S. Ejiri, P. Hegde, F. Karsch, O. Kaczmarek, E. Laermann, R. D. Mawhinney, C. Miao, S. Mukherjee, P. Petreczky, C. Schmidt, W. Soeldner, “Equation of state for physical quark masses,” *Physical Review D*, vol. 81, pp. 054504, 2010.
- [53] P. A Zyla, R. M. Barnett, J. Beringer, O. Dahl, D. A. Dwyer, D. E. Groom, C.-J. Lin, K. S. Lugovsky, E. Pianori, D. J. Robinson, C. G. Wohl, W. -M Yao, K. Agashe, G. Aielli, B. C. Allanach, C. Amshler, M. Antonelli, E. C. Aschenauer, D. M. Asner, H. Baer, Sw. Banerjee, L. Baudis, C. W. Bauer, J. J. Beatty, V. I. Belousov, S. Bethke, A. Bettini, O. Biebel, K. M. Black, E. Blucher, O. Buchmuller, V. Burkert, M. A. Bychkov, R. N. Cahn, M. Carena, A. Ceccucci, A. Cerri, D. Chakraborty, R. Sekhar Chivukula, G. Cowan, G. D'Ambrosio, T. Damour, D. de Florian, A. de Gouvêa, T. DeGrand, P. de Jong, G. Dissertori, B. A. Dobrescu, M. D'Onofrio, M. Doser, M. Drees, H. K. Dreiner, P. Eerola, U. Egede, S. Eidelman, J. Ellis, J. Erler, V. V. Ezhela, W. Fetscher, B. D. Fields, B. Foster, A. Freitas, H. Gallagher, L. Garren, H. -J. Gerber, G. Gerbier, T. Gershon, Y. Gershtein, T. Gherghetta, A. A. Godizov, M. C. Gonzalez-Garcia, M. Goodman, C. Grab, A. V. Griksan, C.

- Grojean, M. Grünewald, A. Gurtu, T. Gutsche, H. E. Haber, C. Hanhart, S. Hashimoto, Y. Hayato, A. Hebecker, S. Heinemeyer, B. Heltsley, J. J. Hernández-Rey, K. Hikasa, J. Hisano, A. Höcker, J. Holder, A. Holtkamp, J. Huston, T. Hyodo, K. F. Johnson, M. Kado, M. Karliner, U. F. Katz, M. Kenzie, V. A. Khoze, S. R. Klein, E. Klempt, R. V. Kowalewski, F. Krauss, M. Kreps, B. Krusche, Y. Kwon, O. Lahav, J. Laiho, L. P. Lellouch, J. Lesgourgues, A. R. Liddle, Z. Ligeti, C. Lippmann, T. M. Liss, L. Littenberg, C. Lourenço, S. B. Lugovsky, A. Lusiani, Y. Makida, F. Maltoni, T. Mannel, A. V. Manohar, W. J. Marciano, A. Masoni, J. Matthews, U.-G. Meißner, M. Mikhasenko, D. J. Miller, D. Milstead, R. E. Mitchell, K. Mönig, P. Molaro, F. Moortgat, M. Moskvic, K. Nakamura, M. Narain, P. Nason, S. Navas, M. Neubert, P. Nevski, Y. Nir, K. A. Olive, C. Patrignani, J. A. Peacock, S. T. Petcov, V. A. Petrov, A. Pich, A. Piepke, A. Pomarol, S. Profumo, A. Quadt, K. Rabbertz, J. Rademacker, G. Raffelt, H. Ramani, M. Ramsey-Musolf, B. N. Ratcliff, P. Richardson, A. Ringwald, S. Roesler, S. Rolli, A. Romaniouk, L. J. Rosenberg, J. L. Rosner, G. Rybka, M. Ryskin, R. A. Ryutin, Y. Sakai, G. P. Salam, S. Sarkar, F. Sauli, O. Schneider, K. Scholberg, A. J. Schwartz, J. Schwiening, D. Scott, V. Sharma, S. R. Sharpe, T. Shutt, M. Silari, T. Sjöstrand, P. Skands, T. Skwarnicki, G. F. Smoot, A. Soffer, M. S. Sozzi, S. Spanier, C. Spiering, A. Stahl, S. L. Stone, Y. Sumino, T. Sumiyoshi, M. J. Syphers, F. Takahashi, M. Tanabashi, J. Tanaka, M. Taševský, K. Terashi, J. Terning, U. Thoma, R. S. Thorne, L. Tiator, M. Titov, N. P. Tkachenko, D. R. Tovey, K. Trabelsi, P. Urquijo, G. Valencia, R. Van de Water, N. Varelas, G. Venanzoni, L. Verde, M. G. Vinciter, P. Vogel, W. Vogelsang, A. Vogt, V. Vorobyev, S. P. Wakely, W. Walkowiak, C. W. Walter, D. Wands, M. O. Wascko, D. H. Weinberg, E. J. Weinberg, M. White, L. R. Wiencke, S. Willocq, C. L. Woody, R. L. Workman, M. Yokoyama, R. Yoshida, G. Zanderighi, G. P. Zeller, O. V. Zenin, R.-Y. Zhu, S.-L. Zhu, F. Zimmermann, J. Anderson, T. Basaglia, V. S. Lugovsky, P. Schaffner, W. Zheng, “Review of Particle Physics,” *Progress of Theoretical and Experimental Physics*, vol. 8, pp. 083C01, 2020.
- [54] H. G. Dosch, M. Jamin, S. Narison, “Baryon masses and flavour symmetry breaking of chiral condensates,” *Physics Letter B*, vol. 220, pp. 251-257, 1989.
- [55] B. L. Ioffe, “QCD at low Energies,” *Progress in Particle and Nuclear Physics*, vol. 56, pp. 232-277, 2006.
- [56] V. M. Belyaev, B. L. Ioffe, “Determination of Baryon and Baryonic resonance masses from QCD sum rules 1. Nonstrange Baryons,” *Soviet Physics Journal of Experimental and Theoretical Physics*, vol. 56, pp. 493-501, 1982.

Distributed Control of a Vibrating String in Response to Pointwise Force Application

Sule Kapkin¹ , Mehmet Sirin Demir^{1*} , Erol Uzal¹ 

¹ Istanbul University-Cerrahpaşa, Faculty of Engineering, Department of Mechanical Engineering, Istanbul, Türkiye, skapkin@iuc.edu.tr, demirms@iuc.edu.tr, euzal@iuc.edu.tr

*Corresponding Author

ARTICLE INFO

ABSTRACT

Keywords:
Pointwise Control
Vibrations
Control of Partial Differential Equations
Analytical Solution

Article History:
Received: 07.09.2023
Accepted: 13.11.2023
Online Available: 27.02.2024

The problem of controlling the vibrations of a string by a discrete applied force is considered. The vibrations of the string are modeled by the linear wave equation and the control is provided by an added force term. The wave equation is solved for controlled and uncontrolled cases with and without control force term. The applied force is chosen to be proportional to string displacement at some specified point. In the controlled case; the wave equation involves a control parameter (gain) and related terms involving the value of the displacement at a single point and a delta function. This makes the equation quite different from the usual wave equation. The problem is solved analytically using a modified (compared to usual wave equation) solution procedure and an equation relating the string eigenfrequencies to the proportionality constant (gain) is derived. This allows the observation of the change in eigenfrequencies with the gain. Finally, examples of uncontrolled and controlled responses are presented, graphically. The results show that the resonances can be avoided by the applied control procedure.

1. Introduction

Distributed control conceivably has important applications in many areas including aerospace technology. For example, the problem of controlling the panel flutter is receiving attention due to its occurrence at high speeds. The specific difficulty of distributed control comes from its being modeled by partial differential equations. One way of circumventing this is to discretize the system by some numerical method and apply the well-known methods of lumped-parameter control. This, however, has the danger of losing some of the physics in the problem.

Pointwise control refers to the measurement and actuation processes being performed at certain points (and not at continuous intervals) within the problem domain. This type of control design is more realistic to be implemented in real-life problems. Several problems relating to the pointwise control on elastic structures, parabolic

equations and the wave equation were considered by You [1], Sadek [2], Wang [3], Cherid et al. [4], Droniou and Raymond [5], Sadek et al. [6], Guo and Xie [7], Beauchard [8] and Ouzahra [9]. Nguyen and Raymond [10] attempted to apply pointwise control concept to a fluid mechanics problem. Recently, Sirota and Halevi [11] investigated the control of a membrane (two-dimensional wave equation) using Laplace transforms and transfer functions. In a more recent study, Latas [12] investigated the suppression of the waves traveling along a moving string by distributed force.

In this article, we will consider a control problem related to the one-dimensional wave equation which might be thought of as governing the vibrations of a string (among other things). Measurement and actuation will be performed on two points on the string, which may be identical. The controlled wave equation will involve one (or possibly more) control term that includes the

value of the physical variable (displacement of string) to be controlled, measured at one point.

Therefore, the resulting mathematical problem (Eq.(5)) is not the usual wave equation since it involves the value of the displacement at one point combined with a delta function as an extra term. To solve this problem, the usual solution procedure of expanding the displacement field in terms of the eigenfunctions of the spatial part of the problem will be modified as explained in the next section. The controlled problem still has eigenfrequencies and eigenfunctions, but the eigenfunctions may no longer be orthogonal. In that case, the eigenfunctions will be orthogonalized using the Gram-Schmit procedure. The controlled eigenfrequencies are also different from the usual wave equation eigenfrequencies, and the values of the controlled eigenfrequencies can be modified by inserting a control parameter (a constant, gain) into the control term. This procedure makes it possible to avoid any possible resonances by simply changing the control parameter.

The paper is organized as follows. In Chapter 2, the problem description and the response of the string both with and without the control term are given. In Chapter 3, the response of the string under an external force, both without the control term and with the control term are presented. Finally, in Chapter 4, graphical solutions for all mentioned cases will be provided.

2. Problem Formulation and Solution

Consider a string of length one pinned at both ends, at $x = 0$ and $x = 1$ as shown in Figure 1.

We assume that the problem is suitably nondimensionalized so we do not have to worry about certain parameters like the length of the string, material properties, and applied forces.

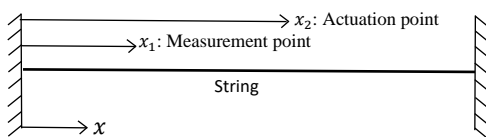


Figure 1. Geometry of the structure.

The small vibrations of the string are governed by

$$\frac{\partial^2 u}{\partial t^2} - \frac{\partial^2 u}{\partial x^2} = 0 \tag{1}$$

where $u(x, t)$ denotes the displacement of the string. We set the wave velocity equal to one because of nondimensionalisation. The boundary conditions at the pinned ends are

$$u(0, t) = u(1, t) = 0 \tag{2}$$

To find the eigenfrequencies, one makes the substitution

$$u(x, t) = U(x)e^{i\omega t} \tag{3}$$

and this gives the eigenfrequencies and the mode shapes as

$$\omega_n = n\pi, U_n(x) = \sin n\pi x, n = 1,2,3, \dots \tag{4}$$

We apply control to this problem in the following manner: displacement u is measured at some point x_1 , at all times, and a force proportional to $u(x_1, t)$ is applied at another point x_2 . Thus the vibration equation in the controlled case becomes

$$\frac{\partial^2 u}{\partial t^2} - \frac{\partial^2 u}{\partial x^2} + K u(x_1, t)\delta(x - x_2) = 0 \tag{5}$$

where δ is the Dirac delta function, and K is a constant which can be considered as a gain. We want to investigate the changes in the system as K is changed. In passing, we note that a related problem

$$\frac{\partial^2 U}{\partial t^2} - \frac{\partial^2 U}{\partial x^2} + K \frac{\partial U}{\partial t}(x_1, t) \delta(x - x_2) = 0 \tag{6}$$

in which the control is proportional to the velocity, rather than displacement, was considered in [13-15]. For this problem, the total energy of the string

$$E = \frac{1}{2} \int_0^1 \left[\left(\frac{\partial U}{\partial t} \right)^2 + \left(\frac{\partial U}{\partial x} \right)^2 \right] dx$$

satisfies

$$\frac{dE}{dt} = - \left[\frac{\partial U}{\partial t}(x_1, t) \right]^2 < 0 \tag{7}$$

Thus, total energy decreases and therefore the control term in Eq. (6) stabilizes the string. However, in the present problem (Eq.(5)) the control is proportional to displacement rather than velocity and no result similar to Eq. (7) is known. Thus, it is important to investigate the solution of Eq.(5). Again, making the substitution $u(x, t) = U(x)e^{i\omega t}$,

$$\frac{d^2U}{dx^2} + \omega^2U + K U(x_1) \delta(x - x_2) = 0 \quad (8)$$

This equation must be solved with the boundary conditions

$$U(0) = U(1) = 0 \quad (9)$$

Since $U(x_1)$ is (an unknown) constant, assuming

$$U(x) = C_1(x) \cos \omega x + C_2(x) \sin \omega x \quad (10)$$

where $C_1(x)$ and $C_2(x)$ are functions to be found, we obtain the solution satisfying the boundary conditions as

$$U(x) = \frac{K}{\omega} U(x_1) \left[\sin \omega(x_2 - x) h(x - x_2) + \frac{\sin \omega(1-x_2)}{\sin \omega} \sin \omega x \right] \quad (11)$$

where h is the unit step function. Setting $x = x_1$ in the above solution gives the eigenvalue equation,

$$1 = \frac{K}{\omega} \left[\sin \omega(x_2 - x_1) h(x_1 - x_2) + \frac{\sin \omega(1-x_2)}{\sin \omega} \sin \omega x_1 \right] \quad (12)$$

Roots ω_n of this equation are eigenvalues with the corresponding eigenfunctions given by Eq.(11), ignoring the factor in front,

$$U_n(x) = \sin \omega_n(x_2 - x) h(x - x_2) + \frac{\sin \omega_n(1-x_2)}{\sin \omega_n} \sin \omega_n x \quad (13)$$

From Eqs. (8) and (9), we obtain

$$\int_0^1 U_m(x)U_n(x)dx = K \frac{U_m(x_1)U_n(x_1)}{\omega_n^2 - \omega_m^2} \left(\frac{\sin \omega_n x_2}{\sin \omega_n x_1} - \frac{\sin \omega_m x_2}{\sin \omega_m x_1} \right) \text{ for } n \neq m \quad (14)$$

so that $U_n(x)$ are not orthogonal unless measurement and actuation are at the same point, i.e., $x_1 = x_2$. To clarify further discussion, assume that $x_1 < x_2$ thus $h(x_1 - x_2) = 0$ and the eigenvalue equation becomes

$$\omega \sin \omega - K \sin \omega x_1 \sin \omega(1 - x_2) = 0 \quad (15)$$

For $K = 0$ this gives the same eigenvalues as in Eq.(4), the uncontrolled case, while for $K = \infty$, the eigenvalues are

$$\omega_n = \frac{n\pi}{x_1}, \omega_m = \frac{m\pi}{1-x_2}, \quad m, n = 1, 2, 3, \dots \quad (16)$$

Eigenvalues change smoothly between Eqs.(4) and (16) as K takes values between 0 and ∞ . This allows us to shape the output of the system.

3. Uncontrolled and Controlled Response

In this section we will compute the response of the string to an external force with and without the control action under zero initial conditions. For the uncontrolled string

$$\frac{\partial^2 u}{\partial t^2} - \frac{\partial^2 u}{\partial x^2} = \cos \pi t \sin \pi x \quad (17)$$

with the boundary and initial conditions

$$\begin{aligned} u(0, t) &= u(1, t) = 0, \\ u(x, 0) &= u_t(x, 0) = 0 \end{aligned} \quad (18)$$

The solution of Eqs. (17) and (18) is:

$$u(x, t) = \frac{1}{4\pi} [\cos \pi t - \cos 3\pi t - 2t \sin \pi t] \sin \pi x \quad (19)$$

The presence of $\cos \pi t$ in the external forcing term (Eq.(17)) causes a resonance and the response, Eq.(19), blows up with time. The aim of control, in this case, will be to suppress the unboundedly growing vibrations of the string. The controlled response is governed by

$$\frac{\partial^2 u}{\partial t^2} - \frac{\partial^2 u}{\partial x^2} + K u(x_1, t) \delta(x - x_2) = \cos \pi t \sin \pi x \quad (20)$$

with the same conditions Eq.(18). We will take the gain constant as $K = 2$ and examine the

response for two different cases of measurement and actuation:

- (1) Measurement and actuation are at the same point: $x_1 = x_2 = 1/3$

In this case the eigenfunctions, Eq.(13), are orthogonal; expanding the solution as

$$u(x, t) = \sum_{n=0}^{\infty} p_n(t) U_n(x) \tag{21}$$

we find that the time factors satisfy

$$\frac{d^2 p_n}{dt^2} + \omega_n^2 p_n = -\alpha_n \cos \pi t \tag{22}$$

$$p_n(0) = \frac{dp_n}{dt}(0) = 0 \tag{23}$$

where

$$\alpha_n = \frac{\int_0^1 \sin \pi x U_n(x) dx}{\int_0^1 [U_n(x)]^2 dx} \tag{24}$$

The solution is, unless $\omega_n = \pi$,

$$p_n(t) = \frac{\alpha_n}{\omega_n^2 - \pi^2} (\cos \omega_n t - \cos \pi t) \tag{25}$$

- (2) Measurement and actuation are at different points: $x_1 = 1/3, x_2 = 2/3$

In this case the eigenfunctions are not orthogonal. But we can orthogonalize them using the Gram-Schmidt procedure. Naming the orthogonalized eigenfunctions $\varphi_n(x)$; these satisfy the same Eqs.(8) and (9). Expanding the solution as

$$u(x, t) = \sum_{n=0}^{\infty} p_n(t) \varphi_n(x) \tag{26}$$

The time factors again satisfy Eqs.(22), (23) and, (24) with U_n replaced by φ_n , and the solution is given by Eq.(25) with U_n replaced by φ_n .

4. Results and Discussion

For both cases (1) and (2), five mode shapes were used in evaluating the response. The calculations are performed analytically using Wolfram Mathematica. The calculations for case (2) are shown in Figure 2 as an example. Table 1 lists the eigenvalues for the uncontrolled and the two

controlled cases mentioned above for comparison.

```

K = 2;
x1 = 1 / 3;
x2 = 2 / 3;
w = ww /. NSolve[ww Sin[ww] ==
  -K Sin[ww/3] Sin[ww/3] && 0 < ww < 16, ww]
u = Sin[w[[k]] (x2 - x)] HeavisideTheta[x - x2]
  + Sin[w[[k]] (1 - x2)] Sin[w[[k]] x];
A = {};
For[k := 1, k < Dimensions[w][[1]] + 1, k++,
  Print["k=", k];
  vk = u - Sum[
    (int_0^1 ((u) * (vj)) dx) / (int_0^1 ((vj) * (vj)) dx) * (vj);
  bb = DSolve[{p''[t] + (w[[k])^2 p[t] ==
    -Cos[Pi * t] * (int_0^1 Sin[Pi * x] * vk dx) / (int_0^1 vk * vk dx),
    p[0] == 0, p'[0] == 0}, p[t], t];
  sol = p[t] /. bb;
  pk[t] = sol[[1]];
  AppendTo[A, {k, vk, pk[t]}];]
U = Sum[A[[n, 2]] * A[[n, 3]]

```

Figure 2. A Sample calculation.

Table 1. Eigenfrequencies for uncontrolled and controlled string

Uncontrolled	Case 1	Case 2
3.141593	2.67206	3.64467
6.283185	6.49607	6.00458
9.424778	9.42478	9.42478
12.566371	15.6081	12.4511
15.707963	18.8496	15.7996

Figure 3 shows the uncontrolled time-response for the mid-point of the string which blowsup while making sinusoidal vibrations.

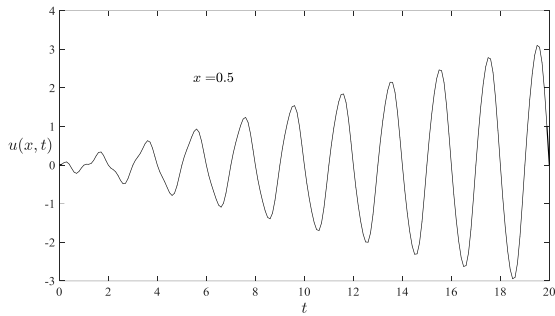


Figure 3. Uncontrolled response to sinusoidal forcing

Figure 4 shows the displacement in time of the mid-point of the string when the measurement and the actuation are at the same point $x_1 = x_2 = 1/3$. The unbounded growth has been suppressed and the mid-point makes periodical vibrations in time.

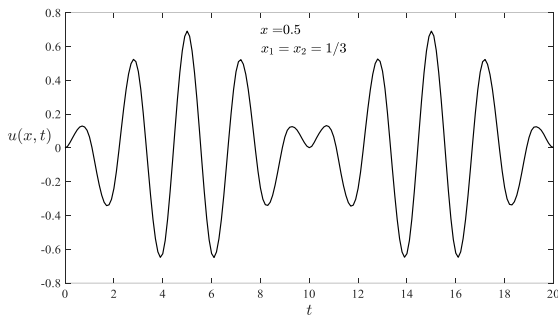


Figure 4. Controlled response when measurement and actuation are at the same point

Figure 5 and Figure 6 show the shape of the string at various times; there is a sharp change in slope at $x = x_1 = x_2 = 1/3$.

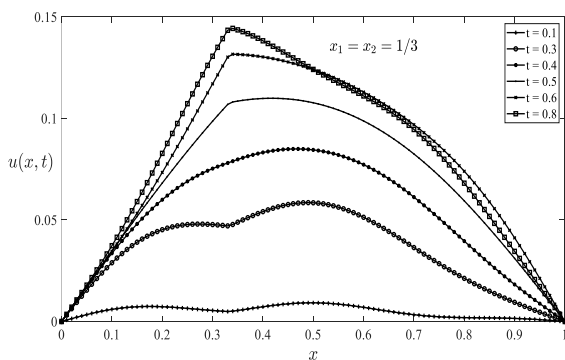


Figure 5. Shape of string at various times; controlled case ($t < 1$)

Figure 7 shows the displacement in time of the mid-point of the string when the measurement is at $x_1 = 1/3$ and the actuation is at $x_2 = 2/3$. The response is similar to the case (1).

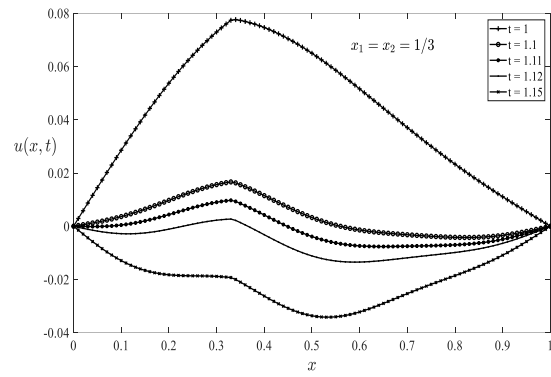


Figure 6. Shape of string at various times; controlled case ($t \geq 1$)

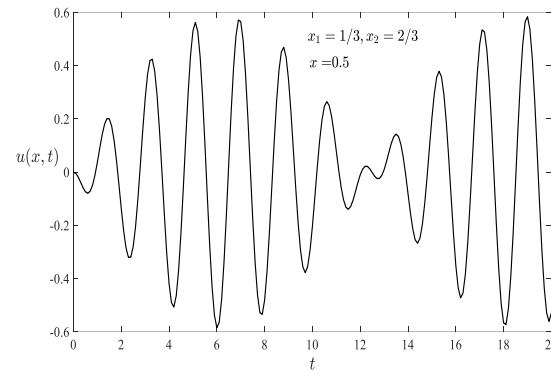


Figure 7. Controlled response when measurement and actuation are at different points

Similarly, Figure 8 and Figure 9 show the shape of the string at various times. In this case, there is a sharp change in slope at $x = x_2 = 2/3$ where the control is applied. But the string shape is smooth at $x = x_1 = 1/3$ where the measurement is made.

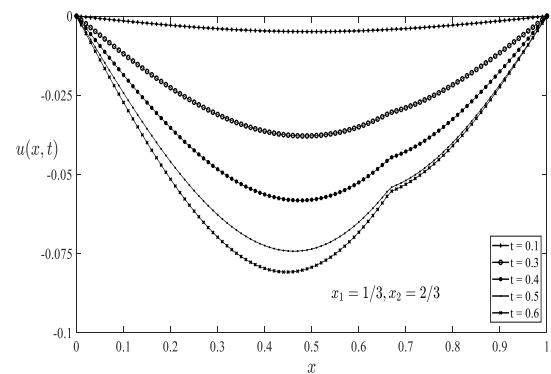


Figure 8. Shape of string at various times; controlled case ($t < 1$)

Finally, a few remark concerning the control effort (the size of the controlling force) should be made. This quantity is $K u(x_1, t)$ and K was taken to be 2. Fig. 10 shows this for the case measurement and actuation points are the same,

i.e., $K u\left(\frac{1}{3}, t\right)$. Control force is basically twice the displacement, but since the controlled displacement is smaller, the control effort also gets smaller.

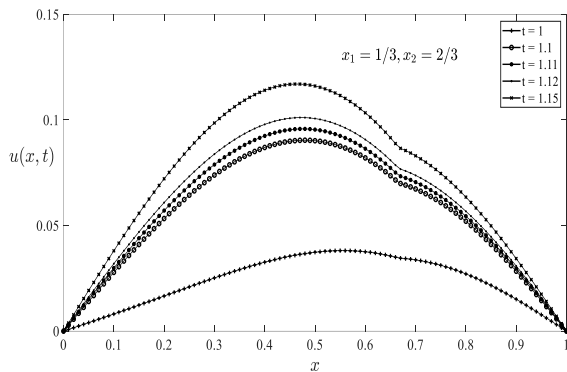


Figure 9. Shape of string at various times; controlled case ($t \geq 1$)

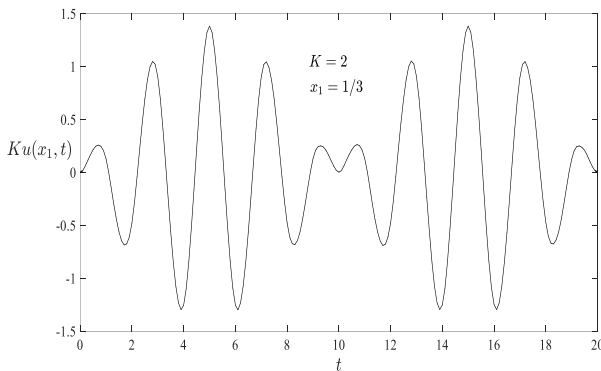


Figure 10. Control force as a function of time when actuation and measurement are at $x=1/3$

The controlled response can further be shaped by varying the constant K , the measurement and actuation points and more importantly, utilizing pointwise velocity-feedback, i.e., adding another control term to the right-hand side of Eq. (5) or (20) proportional to the time derivative of the displacement at possibly another point.

5. Conclusion

The vibrations of a string were controlled by applying the pointwise control concept: the string displacement was measured at a single point and a force proportional to this displacement is applied at another (or the same) point. The resulting controlled wave equation was solved analytically. The usual solution procedure namely, eigenfunction-expansion method modified and resulting non-orthogonal

eigenfunctions were orthogonalized using the Gram-Schmit procedure. This analytical solution allows to carry out numerical experiments on the system for various input forms. As an example, the system was forced by an input that drives the uncontrolled system to resonance, causing growing sinusoidal vibrations. The controlled system suppresses the growth in vibrations and results in a bounded periodic output. As a result, it can be inferred that resonances can be avoided by the control procedure outlined here. Furthermore, it should be emphasized that pointwise control is a more realistic method to control such distributed parameter systems as considered here since it is impossible to actually measure the displacement field, as well as apply control forces, in a continuous interval. Only one measurement and one actuation point were considered here. By measurement and actuation at more points, better results may be obtained

Article Information Form

Funding

The author (s) has no received any financial support for the research, authorship or publication of this study.

Authors' Contribution

The authors contributed equally to the study.

The Declaration of Conflict of Interest/ Common Interest

No conflict of interest or common interest has been declared by the authors.

The Declaration of Ethics Committee Approval

This study does not require ethics committee permission or any special permission.

The Declaration of Research and Publication Ethics

The authors of the paper declare that they comply with the scientific, ethical and quotation rules of SAUJS in all processes of the paper and that they do not make any falsification on the data collected. In addition, they declare that Sakarya University Journal of Science and its editorial board have no responsibility for any ethical

violations that may be encountered, and that this study has not been evaluated in any academic publication environment other than Sakarya University Journal of Science.

Copyright Statement

Authors own the copyright of their work published in the journal and their work is published under the CC BY-NC 4.0 license.

References

- [1] Y. You, "Controllability and stabilizability of vibrating simply supported plate with pointwise control," *Advances in Applied Mathematics*, vol. 10, no. 3, pp. 324-343, 1989.
- [2] S. Sadek, "Optimal pointwise control of flexible structures," *Mathematical and Computer Modelling*, vol. 17, no. 9, pp. 89-99, 1993.
- [3] C. M. Wang, "Linear quadratic optimal control of a wave equation with boundary damping and pointwise control input," *Journal of Mathematical Analysis and Applications*, vol. 192, no. 2, pp. 562-578, 1995.
- [4] A. Cherid, Y. A. Fiagbedzi, I. S. Sadek, "Stabilization of structurally damped systems by pointwise time-delayed feedback control," *Journal of the Franklin Institute*, vol. 336, no. 7, pp. 1175-1185, 1999.
- [5] J. Droniou, J. P. Raymond, "Optimal pointwise control of semilinear parabolic equations," *Nonlinear Analysis: Theory, Methods Applications*, vol. 39, no. 2, pp. 135-156, 2000.
- [6] I. Sadek, M. Abukhaled, T. Abualrub, "Optimal pointwise control for a parallel system of Euler–Bernoulli beams," *Journal of Computational and Applied Mathematics*, vol. 137, no. 1, pp. 83-95, 2001.
- [7] B. Z. Guo, Y. Xie, "Basis property and stabilization of a translating tensioned beam through a pointwise control force," *Computers and Mathematics with Applications*, vol. 47, no. 8-9, pp. 1397-1409, 2004.
- [8] K. Beauchard, "Local controllability and non-controllability for a 1D wave equation with bilinear control," *Journal of Differential Equations*, vol. 250, no.4, pp. 2064-98, 2011.
- [9] P. A. Nguyen, J. P. Raymond, "Pointwise control of the Boussinesq system," *Systems and Control Letters*, vol. 60, no. 4, pp. 249-255, 2011.
- [10] M. Ouzahra, "Controllability of the wave equation with bilinear controls," *European Journal of Control*, vol. 20, no. 2, pp. 57-63, 2014.
- [11] L. Sirota, Y. Halevi, "Fractional order control of the two-dimensional wave equation," *Automatica*, vol. 59, pp. 152-163, 2015.
- [12] W. Latas, "Active vibration suppression of axially moving string via distributed force," *Vibrations in Physical Systems*, vol. 31, no. 2020215, pp. 1-8, 2020.
- [13] M. Tucsnak, "On the pointwise stabilization of a string," in *Control and Estimation of Distributed Parameter Systems: International Conference in Vorau, Vorau, Austria, 1996*, pp. 287-295.
- [14] G. Chen, M. Coleman, H. H. West, "Pointwise stabilization in the middle of the span for second order systems, nonuniform and uniform exponential decay of solutions," *SIAM Journal on Applied Mathematics*, vol. 47, no. 4, pp. 751-780, 1987.
- [15] L. F. Ho, "Controllability and stabilizability of coupled strings with control applied at the coupled points," *SIAM Journal on Control and Optimization*, vol. 31, no. 6, pp. 1416-1437, 1993.

Evaluation of The Effect of Outer Skin Slope on Fire Safety in Double-Skin Façade Systems

Mehmet Akif Yıldız^{1*}, Figen Beyhan²

¹ Ministry of Environment Urbanization and Climate Change, Ankara, Türkiye, makif.yildiz@csb.gov.tr

² Gazi University, Faculty of Science, Department of Architecture, Ankara, Türkiye, fbeyhan@gazi.edu.tr

*Corresponding Author

ARTICLE INFO

Keywords:

Double Skin Façade
Outer Skin Slope
Fire Safety
Smoke Spread
Computational Fluid Dynamic



Article History:

Received: 13.10.2023

Accepted: 24.11.2023

Online Available: 27.02.2024

ABSTRACT

In order to increase energy efficiency and user comfort, double skin façade designs are becoming increasingly popular in the built environment as an alternative to traditional façade and curtain walling systems. The vertical cavity between the outer and inner skins of double skin façade systems, which is critical for natural ventilation, can destroy the effectiveness of façade designs by creating fire hazards due to the creation of uninterrupted areas between spaces. It is essential for the sustainability of the buildings to make appropriate fire safety designs for the risks of spreading toxic gases released in a possible fire through the double skin façade cavity to monitor the design before the building is built and to take the necessary precautions. Therefore, that paper developed a numerical model using computational fluid dynamics to monitor the smoke propagation through the cavity of the double skin façade and the temperature changes in the building. As a contribution to the physical modeling studies of double skin façade systems in the literature, the effect of changing the slope of the outer skin on smoke propagation and temperature changes was investigated. A design model was created by developing 9 scenarios: 4 wide angles, 4 acute angles, and a right angle, each with an angle varying by 3 degrees. While acute-angle cavity designs increased the flue effect in the cavity and increased the direction speed and density of the smoke towards the cavity, wide-angle cavity designs reduced the ambient temperature.

1. Introduction

The energy and economic crises emerging in the globalizing world have affected the building design and the effect of developing technology, the building envelope has gone beyond being a cover separating the interior and exterior spaces and has become a building element that improves building performance. Thus, in addition to aesthetic concerns, the shell has turned into a design element that provides energy conservation and healthy living spaces by allowing climatic elements to be taken into the interior space in a controlled manner. Double skin façade systems, which have developed as an alternative to traditional and single-layer curtain wall systems, have been preferred in built environments in recent years because they allow

controlled intake of climatic data such as wind, sun, humidity, and external pressure. Double skin façade systems consist of an outer skin, an inner skin, and the air cavity between these two layers. In double skin façade systems, the outer skin protects the building from adverse environmental conditions and provides control of natural ventilation with the help of vents on it. These vents provide air to be drawn into the cavity and, thanks to the open windows, allow natural, fresh air to enter the interior. In the inner layer, window can be opened as desired with the opportunity given by the outer layer. However, as this façade system creates uninterrupted areas between internal spaces through vertical and horizontal cavities, it poses fire risks if the necessary measures are not taken.

Predicting the development and hazards of fires is an excellent opportunity to prevent and extinguish fires in time effectively. In fire safety research, it is inefficient to carry out actual fire testing because the cost of fire testing is high, the experimental environment preparation time is long, and the experiment process has hazards. Therefore, using computer simulation to analyze fire problems is also valuable research. The key point of the computer model is to build a fire model so that the development process of fire can be analyzed and understood without building construction. For the fire model, computational fluid dynamics is widely used, which uses numerical methods and algorithms to analyze and solve fluid mechanics (CFD) and heat transfer problems.

In the physical model studies with CFD, studies examining the fire problems caused by double-skin facades, the resistance of the glass in the outer and inner skin, smoke propagation in the cavity, and the effect of blind elements on fire have been investigated. In recent years, physical model studies of double skin façades have generally investigated the effect on fire of blinds placed in the cavity or glazing of the double skin façade.

It has been demonstrated that the blind angle and position have a significant effect on the fire propagation characteristics and temperature distribution in the double skin façade and should be taken into account [1-3]. The risks posed by smoke and flame clouds moving parallel to the airflow in naturally ventilated double-skin facades were among the research areas numerically analyzed in the literature. In these studies, smoke, temperature, pressure, and flame cloud analyses were carried out with scenarios consisting of the type of double skin façade, cavity width, physical properties of the spaces facing the cavity, position and size of window openings, air inlet, and outlet properties [4-11].

It has been observed that the parameters that affect smoke propagation and temperature in double-shell facades are cavity width and ventilation openings. It has been shown that the decrease in the cavity width increases the chimney effect in the cavity and increases the smoke velocity and temperature in the cavity. It

has been shown that the air outlets opening out of the double shell facade cavity are dimensionally larger than the ventilation openings in the spaces, which increases the efficiency of smoke evacuation through the cavity.

In the studies analyzing the performance of the glass of the outer skin and inner skin due to high temperature and pressure in a fire, scenarios were created from the glass's physical and mechanical properties and the cavity's properties [12-16]. Experiments and numerical analyses were carried out to measure the surface temperature and heat flow in the outer and inner glass panes and to investigate the cracking patterns, breakage and collapse of the glass panels. As the cavity width increases, smoke and flame move towards the outer glass, making the inner glass safer. As the cavity width decreased, the temperature inside the cavity increased and cracking and breakage occurred in the glass.

2. Material and Methods

Within the scope of the study, the effect of outer skin geometry on fire propagation in double skin façade cavities was numerically investigated using (CFD). Unlike the physical modeling studies in the literature, this study investigated the effect of the slope of the façade on the spread of smoke and temperature rise in the building due to the fire starting in the spaces adjacent to the double skin façade.

2.1. Prototype building design

Based on the relevant studies in the literature, a prototype building was designed to investigate smoke movement and temperature levels in the double skin cavity, neglecting the effect of climatic elements such as the environment and prevailing wind. Each floor of the three-story prototype building has a 400 x 600 x 350 cm (width x length x height) space with a double-skin façade cavity on one side and an atrium on the other. The working principle of the double skin façade was to provide an air inlet on the lower surface of the outer skin and an air outlet on the upper surface. Air inlets and outlets were designed with dimensions of 350x50 cm, while

100x150 cm window openings and 100x210 cm door openings were placed in the rooms. The cavity width in the double skin façade was designed to be 250 cm, but the cavity width and volume changed as the slope of the outer skin changed. The dimensions of the atrium, which had a 200 x 100 cm ceiling vent, were 350 x 400 x 1050 cm (width x length x height). As the material design is not the subject of the study, the walls, ceilings, and floors of the entire building have been designed as concrete with a thermal inertia $k\rho c$ of approximately 2 kW/s /m² k² (Figure 1).

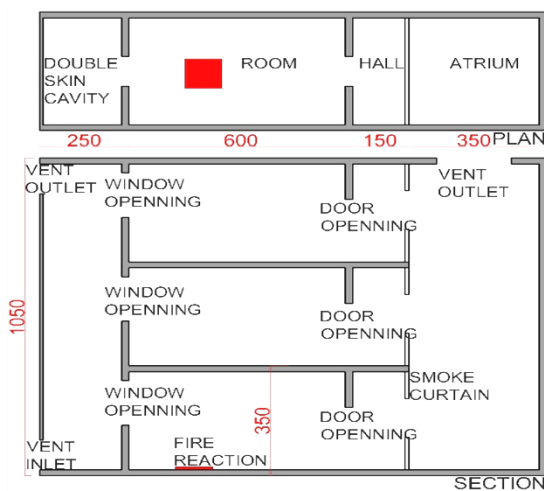


Figure 1. Prototype building plan and section

2.2. Design fire and numerical model features

Studies that provide performance-based approaches through CFD use the t-squared fire model, where the combustion rate varies with the square of time. The curve expressing the ratio of the combustion rate to the square of time for a T-squared fire shows the time required to reach the highest heat release rate. If the heat release rate is known, which gives the most crucial information about how much heat is released when combustible materials burn, temperature, smoke layer thickness, smoke flow rate, and radiant heat flux are also known. The equation giving the heat release rate for a T square fire is given below:

$$Q = \alpha t^p \tag{1}$$

Q: Heat release rate Btu/s (kW)

α : Fire growth coefficient Btu/s³ (kW/s²)

t: Time from ignition (s)

p: Positive exponent

While the NFPA 92 Smoke Control Systems Standard classifies the fire growth rate as slow, medium, fast, and ultra-fast, it calculates the reference heat release rate as 1055 kW for physical model studies. Figure 2 shows the fire growth curve for slow, medium, fast, and ultra-fast growth rates according to the above equation to reach the reference heat release rate of 1055 kW [19].

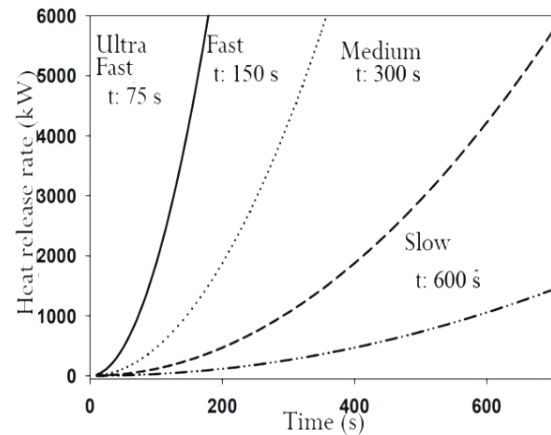


Figure 2. Fire growth rate for the reference heat release rate [20]

According to Figure 2, the time to reach the reference heat release rate was 150 seconds and the fire growth coefficient (α) was calculated as 0.047 kW/s² from Equation 1. The 100 x 100 cm reaction source was selected as polyurethane GM27 consisting of 1.00 carbon, 1.7 hydrogen, 0.3 oxygen and 0.08 nitrogen atoms. For this reaction source, smoke production is 0.198 g/g and carbon monoxide (CO) production is 0.042 g/g. Table 1 shows the features of the design fire [21].

Table 1. Design fire features

Feature	Value
Reaction type	Polyurethane GM27
Fire growth	Fast
Smoke production	0.198 g/g
CO production	0.042 g/g
Heat release rate	1055
Fire growth coefficient	0.047
Ignition start time	10 s
Simulation duration	160 s
Ambient temperature	10 °C

The study used the Pyrosim program, which includes FDS functions and Smokeview visualization, to create geometry and define boundaries. To create the three-dimensional model in Pyrosim, the lengths of the cell network structure in which the boundaries were determined were set to 0.2x0.2x0.2m. direction to be used for measuring temperature, smoke movement, and velocity, a total of 3 thermocouples, in the double-skin facade cavity, in the atrium cavity, and the last floor room, were placed to measure the temperature (Figure 3).

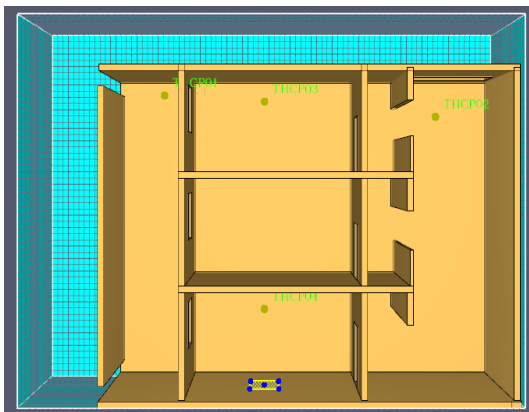


Figure 1. Computer model features

In order to examine the effect of changing the slope of the outer skin of the double-skin facade on fire, a total of 9 scenarios were determined as a result of changing the outer skin slope by 3 degrees, considering that all conditions are constant (Figure 4). As a result of modeling 9 scenarios, numerical analyses were performed,

and the findings were discussed in the context of smoke propagation and temperature levels.

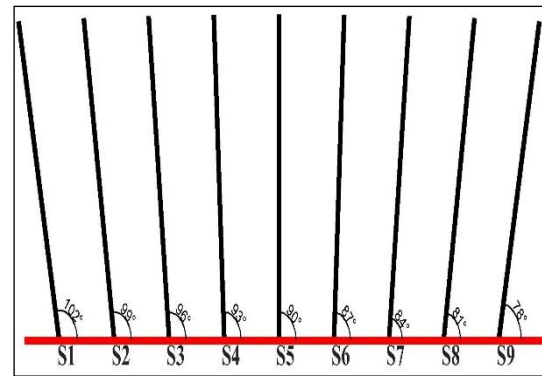


Figure 4. Scenarios with changing the slope of the outer skin of the design model

3. Findings

Based on the design fire' characteristics and prototype building design, the findings of 9 scenarios consisting of outer skin slopes were analysed.

The smoke views during the Scenario 1 simulation process were shown in Figure 5. In the double skin cavity, the smoke reached the first floor window level at 40. seconds and the air outlet in the cavity at 75. seconds. The smoke passed into the atrium cavity at 80 seconds. Smoke also entered the room on the last floor at 72. seconds, and was filled with smoke at 110. seconds.

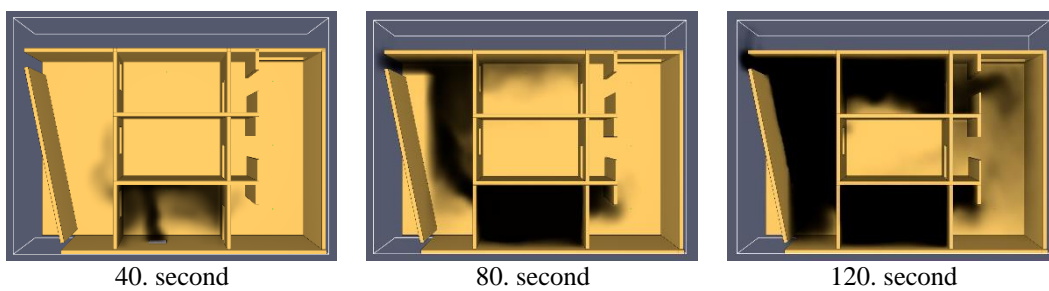


Figure 5. Scenario 1 smoke view

In scenario 1, the temperature values measured at the thermocouples were 46.04 °C at the top floor room, 73.52 °C at the upper level of the double skin cavity and 27.14 °C at

the upper level of the atrium. The highest ambient temperature during the simulation period was 145.8 °C (Figure 6).

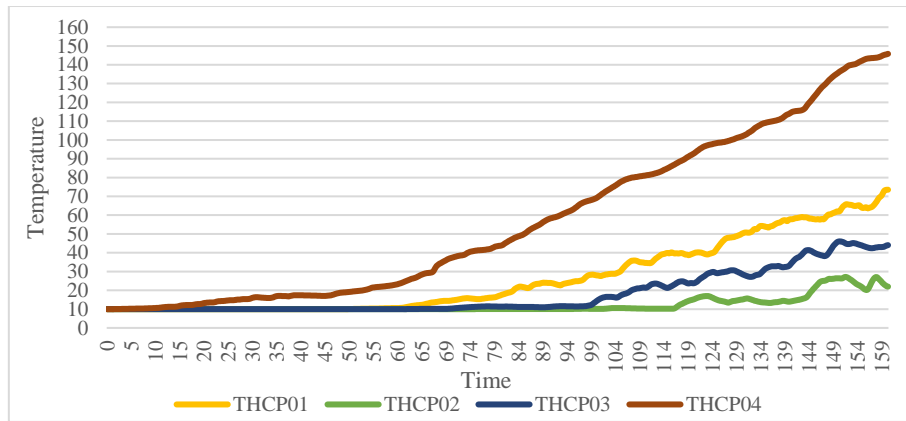


Figure 6. Scenario 1 time dependent -temperature values

The smoke views during the Scenario 2 simulation process were shown in Figure 7. In the double skin cavity, the smoke reached the first floor window level at 40. seconds and the air outlet in the cavity at 72. seconds. The

smoke passed into the atrium cavity at 80. seconds. Smoke also entered the room on the last floor at 70. seconds, and was filled with smoke at 110. seconds.

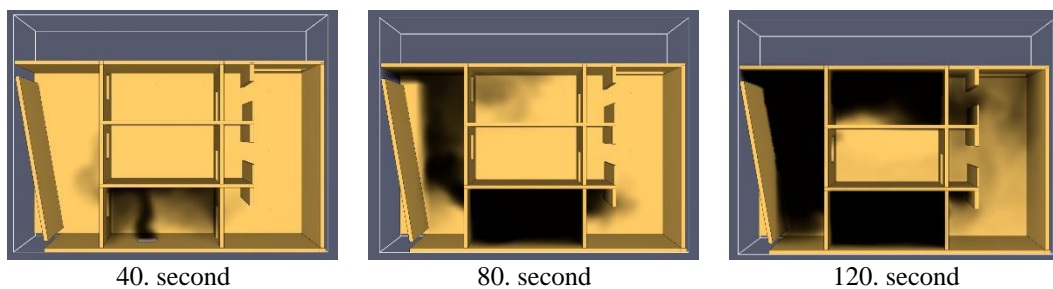


Figure 7. Scenario 2 smoke view

In scenario 2, the temperature values measured at the thermocouples were 42.52 °C at the top floor room, 69.31 °C at the upper level of the double skin cavity and

27.46 °C at the upper level of the atrium. The highest ambient temperature during the simulation period was 142.33 °C (Figure 8).

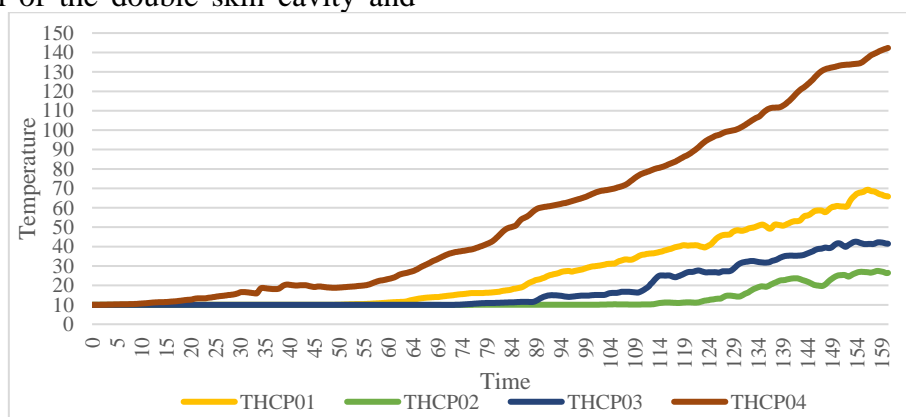


Figure 8. Scenario 2 time-dependent temperature values

The smoke views during the Scenario 3 simulation process were shown in Figure 9. In the double skin cavity, the smoke reached the first floor window level at 40. seconds and the

air outlet in the cavity at 70. seconds. The smoke passed into the atrium cavity at 75. seconds. Smoke also entered the room on the

last floor at 70. seconds, and was filled with smoke at 115. seconds.

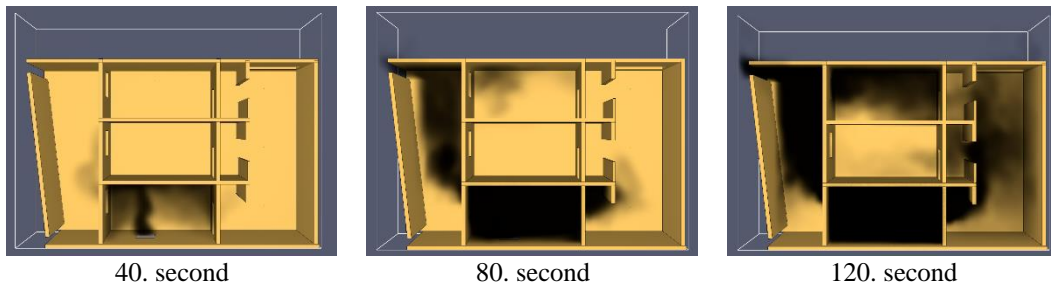


Figure 9. Scenario 3 smoke view

In scenario 3, the temperature values measured at the thermocouples were 31.80 °C at the top floor room, 41.28 °C at the upper level of the double skin cavity and 22.98 °C at

the upper level of the atrium. The highest ambient temperature during the simulation period was 227.82 °C (Figure 10).

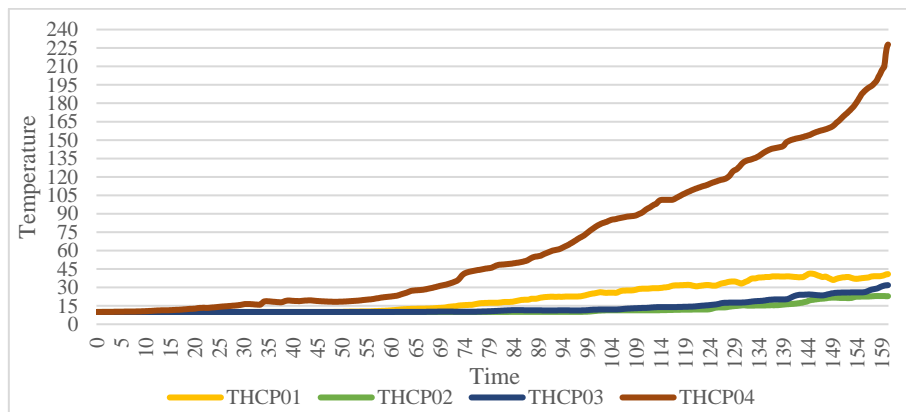


Figure 10. Scenario 3 time-dependent temperature values

The smoke views during the Scenario 4 simulation process were shown in Figure 11. In the double skin cavity, the smoke reached the first floor window level at 40. seconds and the air outlet in the cavity at 65. seconds. The

smoke passed into the atrium cavity at 72. seconds. Smoke also entered the room on the last floor at 68. seconds, and was filled with smoke at 115. seconds.

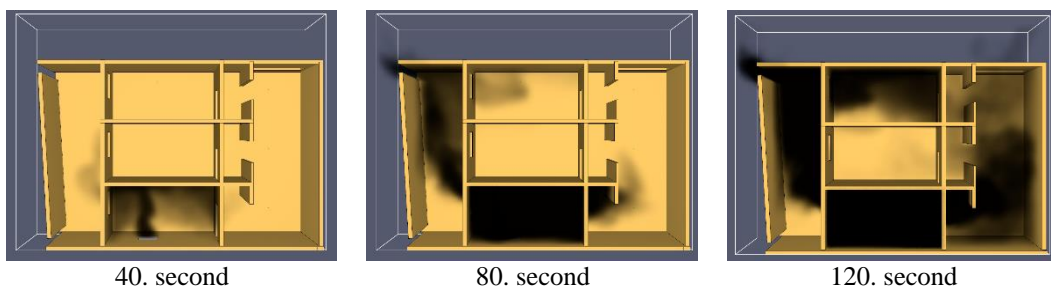


Figure 11. Scenario 4 smoke view

In scenario 4, the temperature values measured at the thermocouples were 24.64 °C at the top floor room, 41.99 °C at the upper

level of the double skin cavity and 27.48 °C at the upper level of the atrium. The highest

ambient temperature during the simulation period was 263.07 °C (Figure 12).

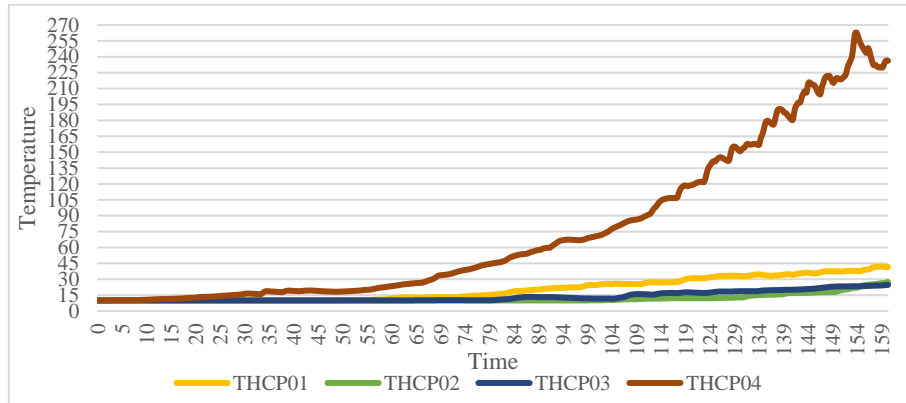


Figure 12. Scenario 4 time-dependent temperature values

The smoke views during the Scenario 5 simulation process were shown in Figure 13. In the double skin cavity, the smoke reached the first floor window level at 40. seconds and the air outlet in the cavity at 60. seconds. The

smoke passed into the atrium cavity at 78. seconds. Smoke also entered the room on the last floor at 110. seconds.

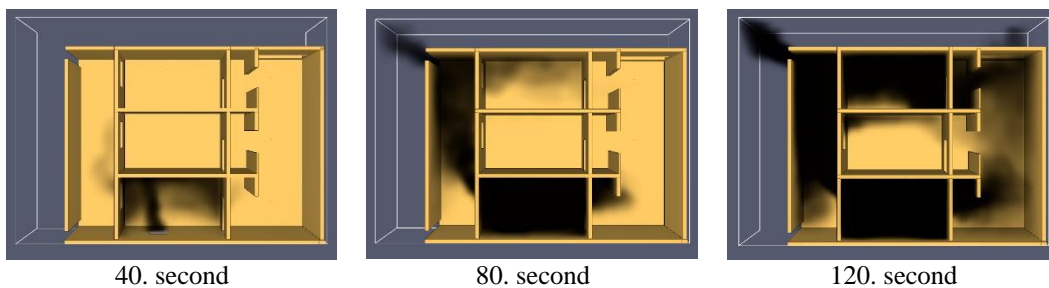


Figure 13. Scenario 5 smoke view

In scenario 5, the temperature values measured at the thermocouples were 42.18 °C at the top floor room, 60.72 °C at the upper level of the double skin cavity and 26.23 °C at

the upper level of the atrium. The highest ambient temperature during the simulation period was 206.94 °C (Figure 14).

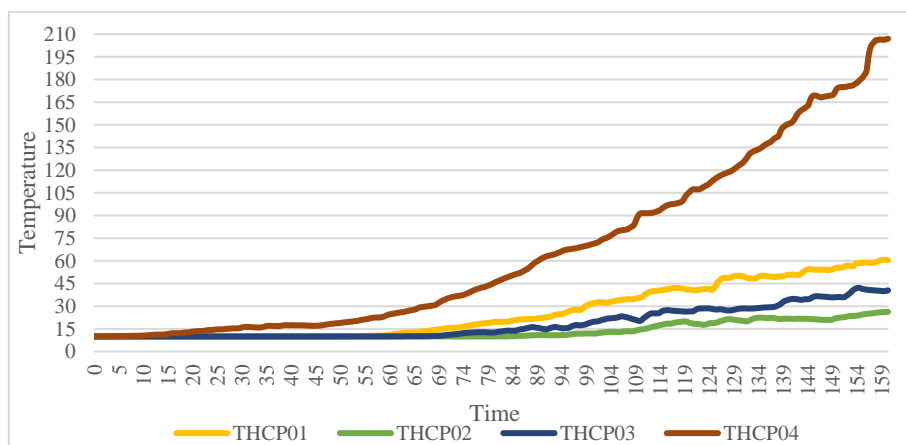


Figure 14. Scenario 5 time dependent temperature values

The smoke views during the Scenario 6 simulation process were shown in Figure 15. In the double skin cavity, the smoke passed the first floor window level at 40. seconds and the air outlet in the cavity at 57. seconds. The

smoke passed into the atrium cavity at 80. seconds. Smoke also entered the room on the last floor at 62. seconds, and was filled with smoke at 105. seconds.

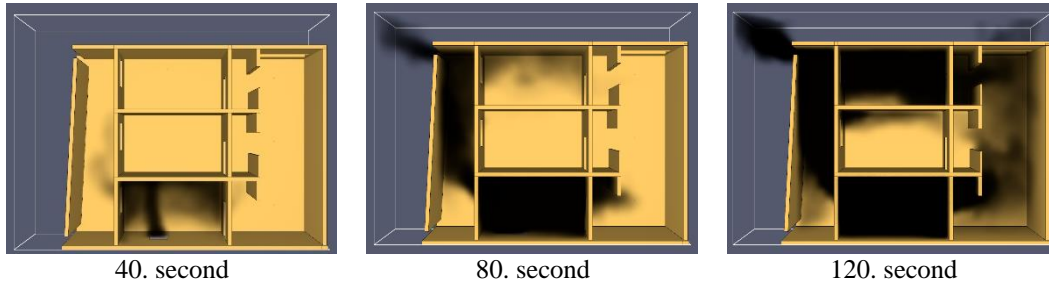


Figure 15. Scenario 6 smoke view

In scenario 6, the temperature values measured at the thermocouples were 41.75 °C at the top floor room, 57.69 °C at the upper level of the double skin cavity and 27.74 °C at the upper level of the atrium. The highest

ambient temperature during the simulation period was 194.22 °C (Figure 16).

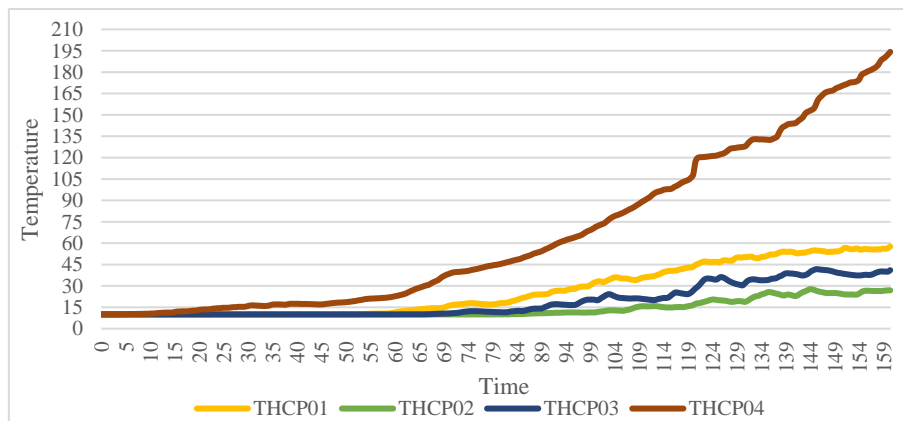


Figure 16. Scenario 6 time dependent temperature value

The smoke views during the Scenario 7 simulation process were shown in Figure 17. In the double skin cavity, the smoke passed the first floor window level at 40. seconds and the air outlet in the cavity at 55. seconds. The

smoke passed into the atrium cavity at 80. seconds. Smoke also entered the room on the last floor at 60. seconds, and was filled with smoke at 103. seconds.

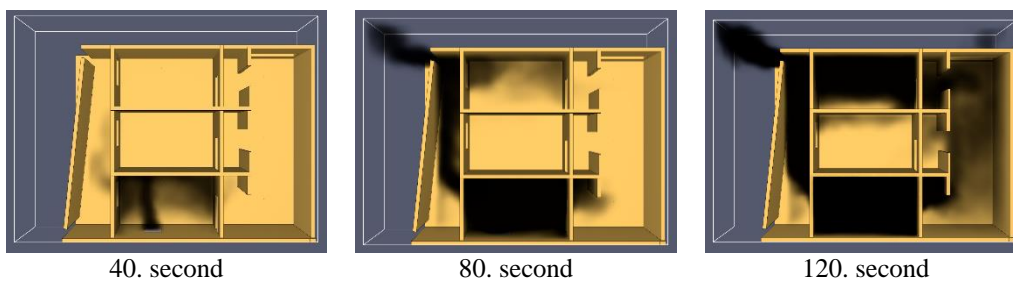


Figure 17. Scenario 7 smoke view

In scenario 7, the temperature values measured at the thermocouples were 43.83 °C at the top floor room, 63.35 °C at the upper level of the double skin cavity and 26.66 °C at

the upper level of the atrium. The highest ambient temperature during the simulation period was 181.86 °C (Figure 18).

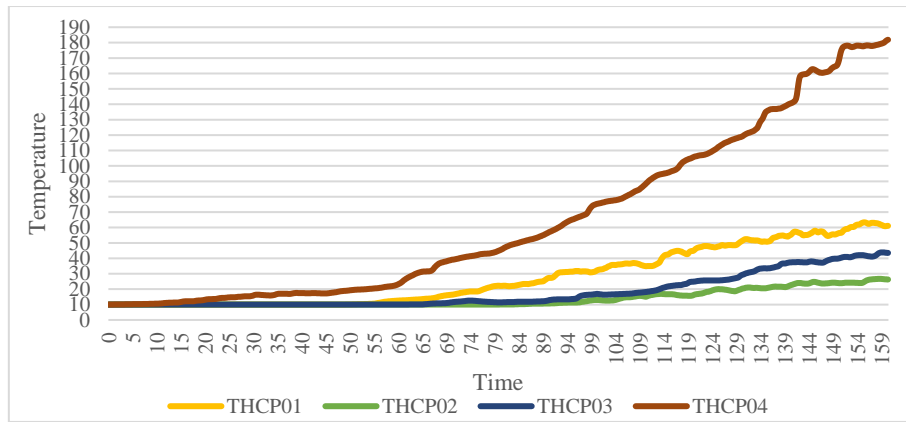


Figure 18. Scenario 7 time dependent temperature values

The smoke views during the Scenario 8 simulation process were shown in Figure 19. In the double skin cavity, the reached the first floor ceiling level at 40. seconds and the air outlet in the cavity at 52. seconds. The smoke

passed into the atrium cavity at 83. seconds. Smoke also entered the room on the last floor at 107. seconds.

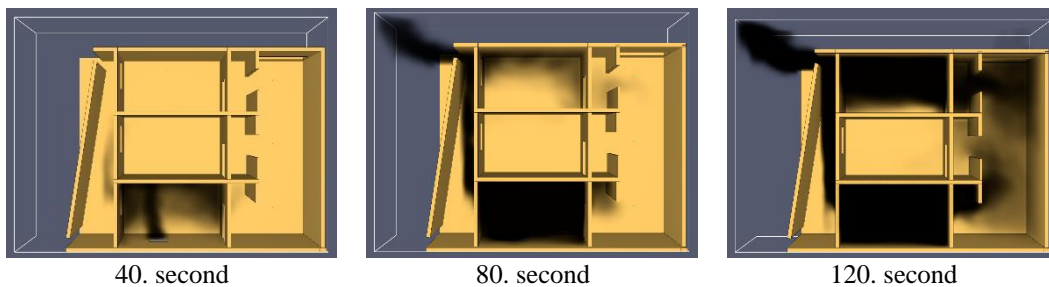


Figure 19. Scenario 8 smoke view

In scenario 8, the temperature values measured at the thermocouples were 42.68 °C at the top floor room, 75.14 °C at the upper level of the double skin cavity and 28.57 °C at

the upper level of the atrium. The highest ambient temperature during the simulation period was 179.57 °C (Figure 20).

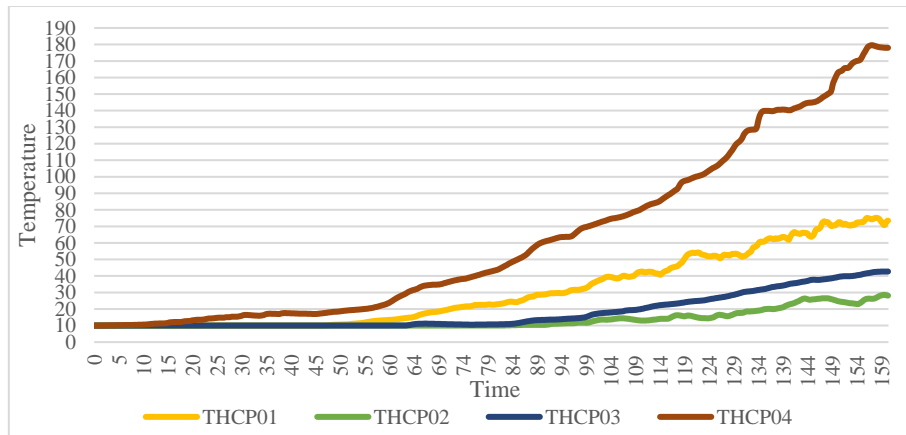


Figure 20. Scenario 8 time dependent temperature values

The smoke views during the Scenario 9 simulation process were shown in Figure 21. In the double skin cavity, the reached the first floor ceiling level at 40. seconds and the air outlet in the cavity at 50. seconds. The smoke

passed into the atrium cavity at 88. seconds. Smoke also entered the room on the last floor at 60. seconds, and was filled with smoke at 120. seconds.

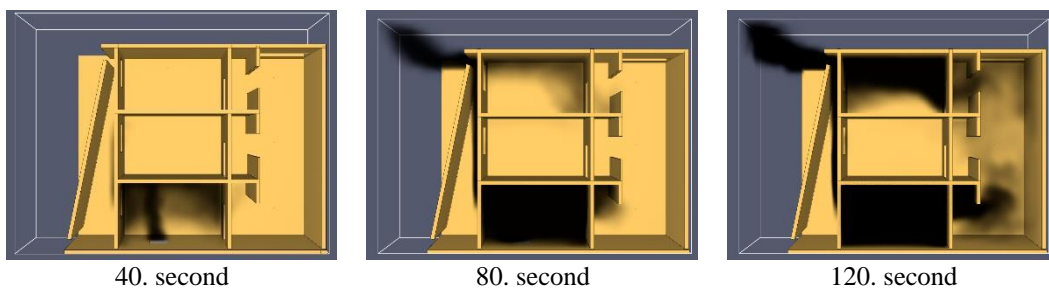


Figure 21. Scenario 9 smoke view

In scenario 9, the temperature values measured at the thermocouples were 36.78 °C at the top floor room, 80.42 °C at the upper level of the double skin cavity and 18.89 °C at

the upper level of the atrium. The highest ambient temperature during the simulation period was 193.62 °C (Figure 22).

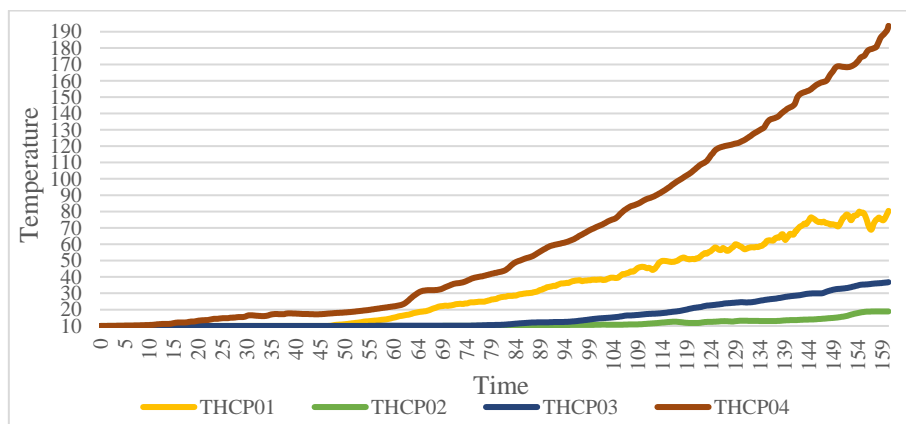


Figure 22. Scenario 9 time dependent temperature values

4. Discussion and Conclusion

The academic studies on double skin façade systems in the literature analyzed numerical models of cavity dimensional properties, ventilation conditions properties, construction, and glass material properties. As a contribution to the literature physical model studies, the effect of the outer shell slope of the double skin façade on smoke extraction and indoor temperature was investigated in this study. In a naturally ventilated double skin façade system, it was observed that changing the slope of the façade by designing the ventilation conditions in the same way in all scenarios significantly affects the smoke extraction from the cavity air outlet and indoor temperature values.

As a result of the cavity slope decreasing and being designed in an upward narrowing structure, the time for the smoke to reach the outside air outlet decreased, and the smoke density in the cavity increased. The smoke filling time in the last floor space was longer in the wide angle cavity designs than in the acute angle cavity designs. Exceptionally, in the S9 scenario, smoke diffusion decreased in areas other than the last cavity due to the high chimney effect in the cavity.

When the slope of the outer shell was increased, and the cavity volume increased by expanding the cavity upwards, the level of smoke in the atrium has decreased compared to the scenario of the right-angled outer shell. Similarly, the smoke density in the atrium decreased in the scenarios with an outer shell inclination of less than 90° compared to the right-angled shell scenario. Still, the smoke density has been higher than the wide-angle scenarios. As a result, an outer or inner sloping shell design instead of a right-angled shell design provided the appropriate design criteria for reducing the spread of smoke into the spaces.

While the ambient temperature decreased in the wide-angle scenarios S1 and S2, the highest ambient temperature of 263.07°C was reached in the S4 scenario. In the other scenarios, a similar time-dependent temperature increase curve was observed, and in general, a negative correlation

was observed, where the temperature increased as the angle decreased.

According to the temperatures measured from the thermocouple in the last floor room, as the slope angle decreased, the temperature decreased compared to the right-angle scenario, and the temperature was measured 36.79°C in the S9 scenario, where the slope was the lowest. As the slope angle increased, the temperature has decreased significantly in the first place, but as the width increased more, the temperature level has reached the same level as the right angle. In the S4 scenario with 93° slope, the temperature measured in the last floor room has been the lowest among the scenarios, with 24.64°C . This model showed no correlation between the inclination angle and the temperature levels in the last floor room, and a shell inclination increasing by 3 degrees showed the most favorable temperature level at the last floor room.

Since the chimney effect increases as the temperature rises due to the increase in pressure, one of the methods used to determine the strength of the chimney effect in the cavity of the double-skin façade is to measure the temperature levels in the cavity. While the temperature level in the cavity increased in the acute slope skin scenarios, the chimney effect increased as the angle decreased. However, while no negative or positive correlation was observed for the chimney effect temperature relationship for the wide-angle outer shell designs, the cavity temperature was lowest value for the S3 and S4 scenarios compared to the other scenarios.

In this study, the effect of the slope of the outer surface of the double-shell façade on smoke propagation and temperature was investigated, and appropriate cavity design criteria for fire safety were put forward. In addition to ensuring that climatic data can be efficiently taken indoors with appropriate cavity design, smoke extraction can be done through the cavity in case of a fire.

The smoke and other gases generated in the fire will be extracted through the cavity with appropriate cavity designs, and the temperature and smoke levels in other areas of the building will be provided in suitable conditions for evacuating people. Only the effect of the slope of

the outer skin on the fire safety design has been investigated, and it is considered that other design criteria, such as natural ventilation conditions and space dimensions, can be examined by further academic research.

Article Information Form

Acknowledgments

The authors express their gratitude to the reviewers whose valuable input significantly enhanced the quality of this manuscript.

Funding

The authors have not received any financial support for the research, authorship or publication of this study.

Authors' Contribution

The authors contributed equally to the study.

The Declaration of Conflict of Interest/ Common Interest

No conflict of interest or common interest has been declared by the authors.

The Declaration of Ethics Committee Approval

This study does not require ethics committee permission or any special permission.

The Declaration of Research and Publication Ethics

The authors of the paper declare that they comply with the scientific, ethical and quotation rules of SAUJS in all processes of the paper and that they do not make any falsification on the data collected. In addition, they declare that Sakarya University Journal of Science and its editorial board have no responsibility for any ethical violations that may be encountered, and that this study has not been evaluated in any academic publication environment other than Sakarya University Journal of Science.

Copyright Statement

Authors own the copyright of their work published in the journal and their work is published under the CC BY-NC 4.0 license.

References

- [1] D. A. Abdoh, V. K. R. Kodur, K. M. Liew, "Smoothed particle hydrodynamics modeling of the thermal behavior of double skin facades in fires considering the effects of venetian blinds," *Applied Mathematical Modelling*, vol. 84, pp. 357-376, 2020.
- [2] Y. Huang, S. Yeboah, J. Shoa, "Numerical data on fire in the cavity of naturally ventilated double skin façade with venetian blinds," *Data in Brief*, vol. 46, pp. 108859-108863, 2023a.
- [3] Y. Huang, S. Yeboah, J. Shoa, "Numerical investigation of fire in the cavity of naturally ventilated double skin façade with venetian blinds," *Building Services Engineering Research and Technology*, vol. 44, pp. 45-61, 2023b.
- [4] W. K. Chow, W. Y. Hung, "Effect of cavity depth on smoke spreading of double-skin façade," *Building and Environment*, vol. 41, pp. 970-979, 2006.
- [5] J. Ji, Y. F. Li, W. X. Shi, J. H. Sun, "Numerical studies on smoke spread in the cavity of a double-skin façade," *Journal of Civil Engineering and Management*, vol. 22, pp. 470-479, 2016.
- [6] L. Miao, C. L. Chow. "A study on window plume from a room fire to the cavity of a double-skin façade," *Applied Thermal Engineering*, vol. 129, pp. 230-241, 2017.
- [7] J. Li, X. Xing, C. Hu, Y. Li, S. Liu, "Numerical studies on effects of cavity width on smoke spread in double-skin façade," *Procedia Engineering*, vol. 45, pp.695-699, 2012.
- [8] G. Thomas, M. Al-Janabi, Donn, M, "Designing double skin facade venting regimes for smoke management," *Fire and Materials*, vol. 42, pp. 549-560, 2018.
- [9] J. Shoa, S. Yeboah, T. Zhu, Y. Li, "Simulation study on the spreading of fire-induced smoke in natural-ventilated double-skin facade buildings," in *Proceedings of the 11th International Symposium on Heating, Ventilation and*

- Air Conditioning Singapore, 2019, pp. 1011-1018.
- [10] R. Wang, S. He, H. Yue, "Numerical study of smoke spread upon shaft-box type double skin facades," *Procedia Engineering*, vol. 211, pp. 755-761, 2018.
- [11] C. L. Chow, "Full-scale burning tests on double skin façades fires," *Fire and Materials*, vol. 37, pp. 17-34, 2013.
- [12] W. K. Chow, W. Y. Hung, Y. Gao, G. Zou, H. Dong, "Experimental study on smoke movement leading to glass damages in double-skinned façade," *Construction and Building Materials*, vol. 21, pp. 556-566, 2007.
- [13] A. Vedrtam, C. Bedon, M. A. Youssef, M. Wamiq, A. Sabsabi, S. Chaturvedi, "Experimental and numerical structural assessment of transparent and tinted glass during fire exposure," *Construction and Building Materials*, vol. 250, pp. 118918, 2020.
- [14] Y. Wang, Y. Zhang, Q Wang, Y. Yang, J. Sun, "The effect of glass panel dimension on the fire response of glass façades," *Construction and Building Materials*, vol. 181, pp. 588-597, 2018.
- [15] Z. Ni, X. Huang, "Experimental and numerical study of fire spread upon double-skin glass facades," in *MATEC Web of Conferences 9*, Paris, France, 2013, pp. 3009-3019.
- [16] C. L. Cheuk, "Spread of smoke and heat along narrow air cavity in double-skin façade fires," *Thermal Science*, vol. 18, pp. 405-416, 2014.
- [17] K. Grewolls, "Computer simulation of fire hazards and evacuation," *Fire Toxicity*, vol. 12, pp. 607-618, 2010.
- [18] K. McGrattan, "Fire Dynamics Simulator-Technical Reference Guide," Washington: NIST, 2006.
- [19] NFPA, "NFPA 92: Standard for Smoke Control Systems," Quincy: National Fire Protection Association, 2021.
- [20] A. C. Bwalya, M. A. Sultan, N. Benichou, "Design fires for fire safety engineering: a state-of-the-art review," in *CIB World Building Congress*, Rotterdam, Netherlands, pp. 1-13, 2014.
- [21] J. M. Hurley, "SFPE Handbook of Fire Protection Engineering," Fifth Edition New York: Springer, 2016.

A Rapid DMeyer-CWT Method Application to the Spectrophotometric Data for the Quantification of Losartan Potassium and Hydrochlorothiazide in a Binary Mixture

Özgür Üstündağ^{1*} , Erdal Dinç² 

^{1*} Ankara University Faculty of Pharmacy Department of Analytical Chemistry, Ankara, Türkiye, ustundag@pharmacy.ankara.edu.tr

² Ankara University Faculty of Pharmacy Department of Analytical Chemistry, Ankara, Türkiye, dinc@ankara.edu.tr

*Corresponding Author

ARTICLE INFO

ABSTRACT

Keywords:
Spectrophotometric
Determination
Continuous Wavelet Transform
Losartan Potassium
Hydrochlorothiazide
Simultaneous Determination

This paper outlines a precise, swift, and convenient spectrophotometric method based on the continuous wavelet transform methodology for the estimation of losartan potassium and hydrochlorothiazide in tablets. The continuous wavelet transform method is based on the use of DMeyer (DMEY-CWT). When the original UV spectra of losartan potassium and hydrochlorothiazide are studied, it is clear that their spectra closely overlap. The analysis was completed successfully without any pre-separation using the created DMEY-CWT approach. The calibration equations for losartan potassium measurement and hydrochlorothiazide determination were obtained at 257.6 nm and 268.4 nm for losartan potassium, 250.1 nm and 263.8 nm for hydrochlorothiazide. The developed approaches were evaluated for their validity and practicality.

Article History:

Received: 20.09.2023

Accepted: 27.11.2023

Online Available: 27.02.2024

1. Introduction

Researchers today are attempting to meet the demands of better scientific measurements and to evolve more efficient processes to boost the accuracy of existing analytical methods in order to attain the desired analytical results across a range of disciplines, such as those noted above. [1-3].

To get more chemical data and minimize the complexity of multicomponent substance analysis, LC and CE procedures were utilized in combination with various spectroscopic systems (independent approaches, notably LC-MS and CE-MS). Furthermore, these combined unit approaches are expensive and time consuming to analyze [4-6]. For analytical purposes, analytical

procedures such as spectrophotometry [7], mass-spectrometry [8], chromatography [9], electrophoresis [10], electrochemistry [11], and their combined devices have been utilized. Because of the difficulties of the aforementioned separation techniques or combination analyzers, analytical chemists prefer to employ spectroscopic methods (rather than separation techniques) to enable rapid and low-cost analysis. Continuous wavelet transform (CWT) approaches for spectrophotometric data are becoming increasingly popular since they may be employed in the study of components in complicated systems without the requirement for any separation step.

As a result, CWT approaches can provide appropriate answers in such instances. [12-14].

The aim of this study is to propose a new signal processing approach based on the simultaneous quantitative detection of losartan potassium (LOS) and hydrochlorothiazide (HCT) in tablets without the usage of a separation step using CWT and zero crossing methodology [15]. In pharmacological and biological investigations, several analytical techniques for the determination of LOS and HCT have been published, including spectrophotometric methods [16-19], spectrofluorometric methods [20], and chromatographic methods [21-25].

2. General Methods

A Shimadzu UV-1601 dual-beam UV-VIS spectrophotometer with a constant gap width of 2 nm was used to analyze the absorption spectra of mixes and tablet solutions in the spectral range 200-305 nm.

2.1. Commercial tablet

A pharmaceutical tablet (HYZAAR® Tablet, MSD Ind., Istanbul, Türkiye, batch no:401042301) including 50 mg LOS and 12.5 mg HCT per tablet was gathered from the Turkish market.

2.2. Standard solutions

By dissolving 25 mg of each drug in 100 mL of methanol, standard LOS and HCT stock solutions were created, respectively. From standard stock solutions for each active component, a calibration with a range of 4.0-26.0 $\mu\text{g mL}^{-1}$ for LOS and 2.0-24 $\mu\text{g mL}^{-1}$ HCT in solvent was made for spectrum analysis.

2.3. Sample solutions preparation

Twenty LOS and HCT tablets were weighed and pulverized for testing. Add methanol to a 100 ml volumetric flask along with an equal amount of powder. The flask's contents were swirled mechanically. The supernatant is diluted with methanol to its final concentration after filtering. Ten times this process was carried out.

3. Results and Discussion

Applying the DMEY-Continuous wavelet transform (DMEY-CWT) approach to the spectra of LOS and HCT in mixtures and preparations for the simultaneous assay is the goal of this work. The UV spectra of the tablet solution and the LOS and HCT standards were measured between 200 and 305 nm, as shown in Figure 1.

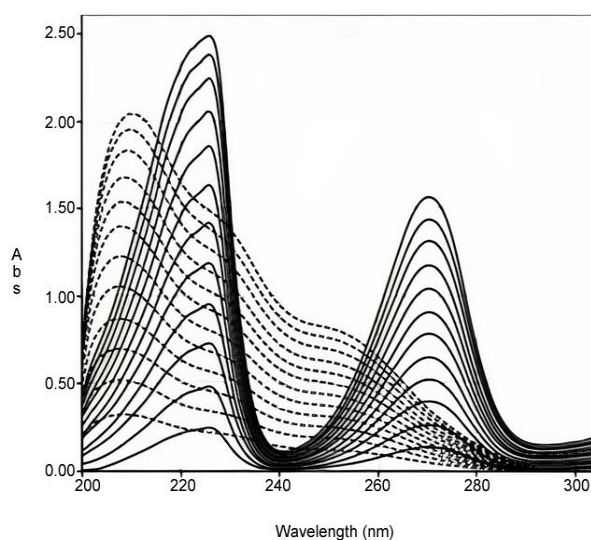


Figure 1. The UV-Absorption spectra of 4.0-26 $\mu\text{g mL}^{-1}$ LOS (---) and 2.0-24 $\mu\text{g mL}^{-1}$ HCT (—) in methanol

3.1. DMEY continuous wavelet transform method (DMEY-CWT)

Using methanol as the solvent, calibration mixtures were prepared with linear concentration ranges of 4.0–26 $\mu\text{g mL}^{-1}$ for LOS and 2.0–24 $\mu\text{g mL}^{-1}$ for HCT in order to analyze artificial mixtures and tablets containing LOS and HCT compounds by the DMEY–CWT technique. These calibration solutions' initial UV spectra were captured at wavelengths between 200 and 305 nm, with = 0.1 nm intervals. The LOS and HCT spectra were subjected to the DMEY-CWT technique (Figure 2). Table 1 displayed the regression equation, correlation coefficient, and associated statistical information.

The quantitative analysis of synthetic mixtures was used to validate the calibration equation for the DMEY-CWT technique. Table 2 displays the recovery outcomes together with the relative standard deviation. In the application of these methods, DMEY-CWT method was applied

directly to UV spectra and DMEY-CWT amplitudes were measured at 257.6 nm and 268.4 nm for LOS and 250.0 nm and 263.8 nm for HCT in the concentration range of 4.0-26.0 µg/mL for LOS and 2.0-24.0 µg/mL for HCT by using zero-cut technique in the obtained DMEY-CWT spectra and calibration graphs were obtained by linear regression. Table 1 displays the results of the regression analysis.

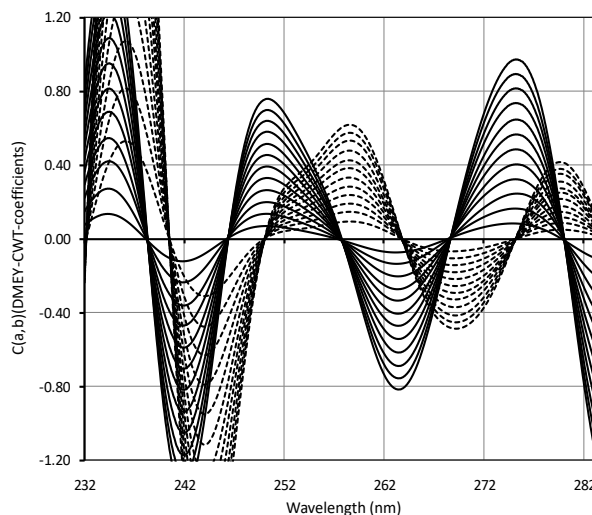


Figure 2. DMEY-CWT spectra obtained by transforming the UV absorption spectra of LOS (---) and HCT (—)

Table 1. Statistical outcome for the DMEY-CWT method

Method Parameter	DMEY-CWT			
	LOS	HCT	250.1	263.8
λ (nm)	257.6	268.4	250.1	263.8
m	2.34×10^{-2}	-1.86×10^{-2}	3.14×10^{-2}	-3.41×10^{-2}
n	-1.67×10^{-3}	8.64×10^{-3}	1.12×10^{-2}	2.32×10^{-3}
r	0.9999	0.9997	0.9999	0.9998
SE(m)	1.43×10^{-3}	1.37×10^{-3}	1.27×10^{-4}	1.83×10^{-4}
SE(n)	1.17×10^{-4}	1.43×10^{-4}	1.39×10^{-3}	1.69×10^{-3}
SE(r)	2.80×10^{-3}	3.43×10^{-3}	3.03×10^{-3}	4.37×10^{-3}
OD	0.69	0.82	0.50	0.56
LOQ	2.29	2.75	1.65	1.85

3.2. Validation of the Proposed Methods

A validation set consisting of 24 artificial mixture solutions in methanol at different concentrations within the linear working range of 4.0-26.0 µg/mL for LOS and 2.0-24.0 µg/mL for HCT was prepared. This validation set evaluated the DMEY-CWT method's precision and accuracy. Table 2 displays the results obtained after using the DMEY-CWT approach to synthetic combinations produced as a verification set.

The prepared solutions were utilized for intra-day and inter-day tests in order to evaluate the accuracy and precision of the DMEY-CWT technique. Precision and accuracy evaluations were applied daily at three different concentrations. The results can be seen in Table 3.

Table 2. Recovery outcome calculated by using artificial mixtures

DMEY-CWT									
Added ($\mu\text{g mL}^{-1}$)		Found ($\mu\text{g mL}^{-1}$)				Recovery (%)			
LOS	HCT	LOS ($\mu\text{g mL}^{-1}$)		HCT ($\mu\text{g mL}^{-1}$)		LOS		HCT	
		257.6 nm	268.4 nm	250.1 nm	263.8 nm	257.6 nm	268.4 nm	250.1 nm	263.8 nm
4	6	3.94	4.18	5.94	5.99	98.4	104.5	99.0	99.9
6	6	5.65	5.92	5.97	5.86	94.2	98.7	99.6	97.7
8	6	7.78	8.07	5.98	5.80	97.2	100.9	99.7	96.6
10	6	9.80	10.03	6.04	5.86	98.0	100.3	100.7	97.7
12	6	11.77	12.01	5.97	5.80	98.1	100.1	99.5	96.7
14	6	13.94	14.15	5.88	5.76	99.6	101.1	97.9	96.0
16	6	15.97	16.22	6.02	5.82	99.8	101.4	100.4	97.0
18	6	18.18	18.50	6.11	5.81	101.0	102.8	101.8	96.9
20	6	20.02	20.40	5.87	5.91	100.1	102.0	97.8	98.5
22	6	22.06	22.45	5.94	6.00	100.3	102.0	99.0	99.9
24	6	24.04	24.48	5.98	5.88	100.2	102.0	99.6	98.1
26	6	25.94	26.42	5.98	5.87	99.8	101.6	99.7	97.8
24	2	24.02	24.01	2.17	2.04	100.1	100.0	108.7	101.8
24	4	24.15	24.19	4.11	4.05	100.6	100.8	102.8	101.2
24	6	24.18	24.40	6.19	5.95	100.8	101.6	103.1	99.2
24	8	24.00	24.02	8.12	7.92	100.0	100.1	101.5	99.0
24	10	24.20	24.46	10.15	9.76	100.8	101.9	101.5	97.6
24	12	23.96	24.22	12.14	11.58	99.8	100.9	101.1	96.5
24	14	24.35	24.85	14.00	13.52	101.5	103.6	100.0	96.6
24	16	24.27	24.65	15.96	15.49	101.1	102.7	99.7	96.8
24	18	24.26	24.80	17.72	17.12	101.1	103.3	98.4	95.1
24	20	24.36	24.43	19.84	19.05	101.5	101.8	99.2	95.3
24	22	25.24	24.09	21.73	20.75	105.2	100.4	98.8	94.3
24	24	24.73	24.11	23.26	23.85	103.1	100.4	96.9	99.4
					Mean	100.1	101.5	100.3	97.7
					SD	2.06	1.31	2.36	1.87
					RSD	2.35	1.30	2.35	1.91

Table 3. Intra-day and inter-day outcome by the DMEY-CWT method

Intra-day Results						
	Added ($\mu\text{g mL}^{-1}$)	Found ($\mu\text{g mL}^{-1}$)	SD	RSD	RE	Recovery (%)
LOS	4	4.08	0.04	1.09	2.12	103.0
257.6 nm	16	16.20	0.38	2.36	1.26	101.8
	20	20.32	0.41	2.01	1.62	101.9
HCT	4	3.94	0.09	2.38	-1.54	98.9
250.1 nm	16	16.17	0.36	2.23	1.06	99.4
	20	20.03	0.30	1.48	0.14	99.6
LOS	4	3.95	0.07	1.76	-1.37	98.3
268.4 nm	16	15.87	0.22	1.39	-0.81	100.0
	20	20.13	0.29	1.42	0.63	100.2
HCT	4	3.89	0.17	4.35	-2.80	99.5
263.8 nm	16	15.96	0.15	0.95	-0.22	100.3
	20	19.80	0.45	2.28	-1.01	98.2
Inter-day Results						
LOS	4	4.12	0.04	1.04	3.00	98.3
268.4 nm	16	16.28	0.21	1.32	1.77	100.0
	20	20.39	0.38	1.86	1.94	100.2
HCT	4	3.96	0.06	1.54	-1.08	99.5
263.8 nm	16	15.90	0.24	1.52	-0.62	100.3
	20	19.92	0.25	1.25	-0.41	98.2
LOS	4	3.93	0.07	1.78	-1.70	98.3
268.4 nm	16	16.00	0.16	1.00	0.00	100.0
	20	20.03	0.23	1.14	0.16	100.2
HCT	4	3.98	0.07	1.76	-0.53	99.5
263.8 nm	16	16.05	0.14	0.90	0.28	100.3
	20	19.64	0.44	2.26	-1.80	98.2

The interfering effects of tablet excipients on LOS and HCT were tested using a standard addition methodology before the DMEY-CWT

method was used to the commercial tablet composition. Table 4 presents the findings.

No.	Added ($\mu\text{g mL}^{-1}$)											
	LOS						HCT					
	2		6		10		2		8		12	
	Found ($\mu\text{g mL}^{-1}$)						Found ($\mu\text{g mL}^{-1}$)					
	257.6	268.4	257.6	268.4	257.6	268.4	250.1	263.8	250.1	263.8	250.1	263.8
1	1.99	2.03	5.71	5.84	10.04	9.92	1.96	2.05	7.83	8.03	11.95	12.02
2	1.94	2.08	5.85	5.90	10.24	9.86	1.93	2.07	7.83	7.84	11.94	12.27
3	1.98	2.09	5.89	5.84	10.22	9.75	1.93	1.96	8.19	8.06	11.84	12.18
4	2.01	2.07	5.96	6.06	10.31	9.86	1.93	1.98	7.84	8.09	12.02	12.11
5	2.00	2.02	6.06	5.95	10.35	9.96	1.91	2.01	7.80	7.90	11.79	11.99
No.	Recovery (%)											
	LOS						HCT					
	257.6	268.4	257.6	268.4	257.6	268.4	250.1	263.8	250.1	263.8	250.1	263.8
1	99.6	101.3	95.2	97.3	100.4	99.2	98.1	102.6	97.9	100.3	99.6	100.2
2	97.1	103.9	97.5	98.3	102.4	98.6	96.3	103.7	97.8	98.0	99.5	102.3
3	98.8	104.3	98.2	97.4	102.2	97.5	96.6	98.1	102.4	100.7	98.6	101.5
4	100.6	103.6	99.3	101.0	103.1	98.6	96.5	99.1	98.0	101.1	100.2	100.9
5	99.9	101.0	101.0	99.2	103.5	99.6	95.6	100.5	97.5	98.7	98.2	100.0
Mean	99.2	102.8	98.2	98.6	102.3	98.7	96.6	100.8	98.7	99.8	99.2	101.0
SD	1.32	1.6	2.16	1.5	1.21	0.8	0.91	2.3	2.05	1.3	0.78	0.9
RSD	1.33	1.5	2.20	1.5	1.18	0.8	0.94	2.3	2.08	1.3	0.79	0.9
RE	-0.79	2.8	-1.76	-1.4	2.33	-1.3	-3.39	0.8	-1.29	-0.2	-0.78	1.0

Table 4. Standard addition results for DMEY-CWT method

By subtracting the amount of LOS and HCT from the tablets, recovery and other calculations for LOS and HCT were carried out. Five replicas were used for these surveys, with three different concentration grades.

3.3. Tablet Analysis

Table 5 displays the results obtained by applying the suggested technique to the LOS-HCT commercial preparation solutions. Results have been obtained successfully for quantifying tablets containing LOS and HCT. When the DMEY-CWT method was applied to commercially accessible tablets, there was no interaction with the tablet excipients in the determination of the concerned substances.

Table 5. Tablet assay by the DMEY-CWT method (50.0 mg LOS and 12.5 mg HCT per tablet)

	mg/tablet			
	LOS		HCT	
	257.6 nm	268.4 nm	250.1 nm	263.8 nm
Mean	49.82	50.04	12.65	12.44
SD	0.47	0.81	0.11	0.15
RSD	0.93	1.63	0.83	1.18
SE	0.15	0.26	0.03	0.05
CL	0.29	0.50	0.07	0.09

4. Conclusion

CWT offers new possibilities and alternative ways for the resolution of mixtures of active compounds with overlapping absorption spectra. One of the main advantages of CWT approach is the simultaneous data reduction and de-noising for the signal analysis.

In our case, this DMEY-CWT approach provides higher peak amplitude, less noise, and sharper peaks than the other wavelet families and having flexible and versatile properties gives a good resolution for mentioned binary pharmaceutical dosage form. The spectrum analysis of synthetic mixtures and tablet formulations comprising LOS and HCT has been successfully carried out using the DMEY-CWT method that we have developed, to briefly explain the study.

When the spectra overlap in the same spectral region, as they do in this study, this newly developed approach can be used without the need for pre-separation (see Figure 1). To demonstrate the reliability and practicality of the method, it was carried out using analytical validation parameters. We believe that the DMEY-CWT method that has been developed is a promising approach for the measurement of related compounds.

Article Information Form

Funding

The authors have not received any financial support for the research, authorship or publication of this study.

Authors' Contribution

The authors contributed equally to the study.

The Declaration of Conflict of Interest/ Common Interest

No conflict of interest or common interest has been declared by the authors.

The Declaration of Ethics Committee Approval

This study does not require ethics committee permission or any special permission.

The Declaration of Research and Publication Ethics

The authors of the paper declare that they comply with the scientific, ethical and quotation rules of SAUJS in all processes of the paper and that they do not make any falsification on the data collected. In addition, they declare that Sakarya University Journal of Science and its editorial board have no responsibility for any ethical violations that may be encountered, and that this study has not been evaluated in any academic publication environment other than Sakarya University Journal of Science.

Copyright Statement

Authors own the copyright of their work published in the journal and their work is published under the CC BY-NC 4.0 license.




References

- [1] M. Siddiqui, Z. AlOthman, N. Rahman, "Analytical techniques in pharmaceutical analysis: A review," *Arabian Journal of Chemistry*, vol. 10, pp. 1409-1421, 2017.
- [2] R. Valagaleti, P. Burns, M. Gill, "Analytical support for drug manufacturing in the United States—from active pharmaceutical ingredient synthesis to drug product shelf life," *Drug Information Journal*, vol. 37, pp. 407-438, 2003.
- [3] H. Ju, "Grand challenges in analytical chemistry: towards more bright eyes for scientific research, social events and human health," *Frontiers in Chemistry*, vol. 1, no. 5, pp. 1-6, 2013.
- [4] Y. Chhonker, C. Edi, D. Murry, "LC-MS/MS method for simultaneous determination of diethylcarbamazine, albendazole and albendazole metabolites in human plasma: Application to a clinical pharmacokinetic study," *Journal of Pharmaceutical and Biomedical*

- Analysis, vol. 20, no. 151, pp. 84–90, 2018.
- [5] J. Sáiz, C. García-Ruiz, B. Gómara, “Comparison of different GC-MS configurations for the determination of prevalent drugs and related metabolites,” *Analytical Methods*, vol. 9, pp. 2897-2908, 2017.
- [6] H. Maurer, “Toxicological analysis of drugs: GC-MS screening and confirmation,” *Acta Medicinæ Legalis*, vol. XLIV, pp. 489-492, 1994.
- [7] F. Rocha, L. Teixeira, “Strategies to increase sensitivity in UV-VIS spectrophotometry,” *Quimica Nova*, vol. 27, no. 5, pp. 807-812, 2004.
- [8] T. Thiem, “Comparison of optical-emission mass-spectroscopy utilizing laser vaporization of solid samples for inorganic analysis,” *American Laboratory*, vol. 26, no. 3, pp. 48-52, 1994.
- [9] Z. Deyl, J. Janak, V. Schwarz V. “Bibliography section - Liquid column chromatography - Gas chromatography - Planar chromatography - Gel chromatography - Capillary electrophoresis and electrokinetic chromatography,” *Journal of Chromatography A*, vol. 940, no. 2, pp. 119-219, 2001.
- [10] A. Otieno, S. Mwangela S, “Capillary electrophoresis-based methods for the determination of lipids - A review,” *Analytica Chimica Acta*, vol. 624, no. 2, pp. 163-174, 2008.
- [11] A. Naggar, A. Kotb, A. Abdelwahab, “Graphite studded with facile-synthesized cu₂o nanoparticle-based cubes as a novel electrochemical sensor for highly sensitive voltametric determination of mebeverine hydrochloride,” *Chemosensors*, vol. 9, no. 2, pp. 35-40, 2021.
- [12] I. Daubechies, “Ten Lectures on Wavelets, Society for Industrial and Applied Mathematics,” Philadelphia, pp. 1-357, 1992.
- [13] E. Dinç, D. Baleanu, “Continuous wavelet transform applied to the overlapping absorption signals and their ratio signals for the quantitative resolution of mixture of oxfendazole and oxyclozanide in bolus,” *Journal of Food and Drug Analysis*, vol. 15, no. 2, pp. 109-117, 2007.
- [14] Ö. Üstündağ, E. Dinç, “Continuous wavelet transforms and ultra performance liquid chromatography applied to the simultaneous quantitative determination of candesartan cilexetil and hydrochlorothiazide in tablets,” *Monatshefte für Chemie*, vol. 152, no. 9, pp. 1097-1106, 2021.
- [15] Ö. Üstündağ, E. Dinç, “Spectrophotometric determination of losartan potassium and hydrochlorothiazide in tablets by wavelet transform approach” *Sakarya University Journal of Science*, vol. 25, no. 6, pp. 1432-1437, 2021.
- [16] M. Toral, O. Saldias, C. Soto, “Strategies used to develop analytical methods for simultaneous determination of organic compounds by derivative spectrophotometry,” *Quimica Nova*, vol. 32, no. 1, pp. 257-282, 2009.
- [17] D. Nagavalli, V. Vaidhyalingam, O. Divya, “Simultaneous spectrophotometric determination of losartan potassium, amlodipine besilate and hydrochlorothiazide in pharmaceuticals by chemometric methods,” *Acta Pharmaceutica*, vol. 60, no. 2, pp. 141-152, 2010.
- [18] C. Vetuschi, A. Giannandrea, “Anti-beer evaluation of Hydrochlorothiazide and Losartan by UV derivative spectrophotometry,” *Analytical Letters*, vol. 36, no. 5, pp. 1051-1064, 2003.

- [19] T. Binh, L. Tram, N. Trang, “Simultaneous Determination of Hydrochlorothiazide and Losartan Potassium in Pharmaceutical Product by UV-Vis Spectrophotometric Method with Kalman Filter Algorithm,” *Journal of Analytical Methods in Chemistry*, vol. 27, no. 5, pp. 1-8, 2021.
- [20] A. Youssef, “Spectrofluorimetric assessment of hydrochlorothiazide using optical sensor nano-composite Terbium Ion Doped in Sol-Gel Matrix,” *Journal of Fluorescence*, vol. 22, no. 3, pp. 827-834, 2012.
- [21] K. Marghany, R. Abdelsalam, G. Haddad, “HPLC method transfer study for simultaneous determination of seven angiotensin II receptor blockers,” *Journal of Separation Science*, vol. 43, no. 8, pp. 1398-1405, 2020.
- [22] S. Rahaman, K. Micheal, “A new RP-HPLC method for the simultaneous estimation of hydrochlorothiazide and losartan potassium in bulk and pharmaceutical dosage forms,” *International Journal of Life Science and Pharma Research*, vol. 10, pp. 648-653, 2020.
- [23] N. Mohammed, H. Abdo, H. Hassan, “Method development and validation of simultaneous determination of hydrochlorothiazide and losartan in tablet dosage form by RP-HPLC,” *International Journal of Pharmaceutical Sciences and Research*, vol. 10, no. 1, pp. 227-231, 2019.
- [24] C. Vishnuvardhan, P. Radhakrishnanand, N. Satheeshkumar, “RP-HPLC Method for the Simultaneous Estimation of Eight Cardiovascular Drugs,” *Chromatographia*, vol. 77, no. 3-4, pp. 265-275, 2014.
- [25] R. Maggio, P. Castellano, T. Kaufman, “A multivariate approach for the simultaneous determination of losartan potassium and hydrochlorothiazide in a combined pharmaceutical tablet formulation,” *Analytical and Bioanalytical Chemistry*, vol. 391, no. 8, pp. 2949-2955, 2008.

Development of NGR-GelMA Hydrogels for PC3 Prostate Cancer Cells

Ziyan Buse Yaralı Çevik^{1*} , Meryem Zeybekoğlu² , Ozan Karaman^{1,2} 

¹ Biomedical Test, Calibration, Application and Research Center, Izmir Katip Çelebi University, Türkiye, ziyanbuse.yarali@ikcu.edu.tr

² Biomedical Engineering, Faculty of Engineering And Architecture, Izmir Katip Çelebi University, Türkiye, meryemzeybekoglu@gmail.com, ozan.karaman@ikcu.edu.tr

*Corresponding Author

ARTICLE INFO

ABSTRACT

Keywords:

Prostate Cancer

GelMA

NGR

3 Dimensional (3D)



Article History:

Received: 08.08.2023

Accepted: 04.12.2023

Online Available: 27.02.2024

Prostate cancer is one of the most common cancer for men. Current therapies such as chemotherapy or radiotherapy non-specifically affect cancerous cells. Current therapies need more targeted delivery approaches such as peptide. Asn-Gly-Arg (NGR) is a tool for cancer targeting therapy. To mimic more natural cancer microenvironment, peptide treatment approaches are examined in 3 Dimensional (D) hydrogels. GelMA is one of the hydrogels that permits to construct 3D microenvironment of PC3 prostate cancer cells. The goal of the study was to evaluate characteristic of GelMA to model prostate cancer environment and to determine the effects of NGR peptides for PC3 line. pH values of different concentrations NGR (1 μ M, 10 μ M and 100 μ M)-GelMA were measured. To analyze biodegradation capacity of different concentrations NGR (1 μ M, 10 μ M and 100 μ M)-GelMA, weight measurements were performed. Live and Dead analysis was performed on days 1, 4, and 7. The findings revealed that GelMA hydrogels created a relatively stable and neutral pH, making them potentially valuable for drug delivery systems. Furthermore, the NGR-GelMA hydrogels incorporated exhibited the capacity to absorb liquids, resulting in an increase in weight. Notably, these hydrogels allowed for the observation of the dynamic 3D microenvironment of prostate cancer, which was influenced by the concentration of the targeted drug in the GelMA matrix. This suggests promising implications for developing targeted therapies for prostate cancer using GelMA-based drug delivery systems. As a conclusion, GelMA and NGR-GelMA hydrogels may be useful platform for further studies to progress on prostate cancer treatment.

1. Introduction

Cancer has affected multicellular living organisms for more than 200 million years, and evidence of cancer among modern human progenitors dates back well over a million years [1]. Prostate cancer is the most frequent cancer among males in the Western world and the second largest cause of cancer mortality [2]. Prostate cancer is described as malignant tumoral formations caused by aberrant and uncontrolled growth of prostate gland cells, which are part of the male reproductive system [3]. Current

chemotherapy and radiotherapy are used to fight cancers [4]. However, current therapeutic approaches have some disadvantages because of their high side effects and non-specific to target cells [5-7]. Thus, new methodologies have been developed to catch more specificity for cancerous region.

Peptides can specifically recognize the complex of antibody and cell surface [7, 8]. One of the first generation of tumor targeting peptides is the Asn-Gly-Arg (NGR) peptide [9]. The NGR peptide recognizes to aminopeptidase N (CD13),

which is a receptor that is expressed on only tumor neovasculature [10]. To increase the anticancer action of several antitumor drugs as doxorubicin (dox), cisplatin, proapoptotic peptides, and tumor necrosis factor (TNF), NGR peptides have been utilized for their target delivery. Garde et. al. showed that NGR based dox showed reduction of tumor vasculature rather than only dox in PC3 prostate cancer cell line [11].

Anticancer targeting compounds including NGR motif can demonstrate higher affinity to tumor and promote higher efficacy. A study showed that only NGR can also affect and exhibit antitumor effect [12]. NGR peptides may also attach to CD13-v3+ tumor cells, including MDA-MB-435 breast cancer cells, and prevent them from migrating and proliferating in vitro condition [12].

Complex in vitro techniques are needed to mimic microenvironment of cancer tissues. 3 Dimensional (D) cell culture supports more natural biochemical signals and mimics tissue-specific architecture in terms of forced polarity, flattened cell shape, and subsequent cellular communication [13-16]. In recent years, the combination of hydrogel and peptide has been frequently used in 3D systems [17]. Hydrogel models may be successful in mimicking the tumour environment so hydrogel and peptide combination is a promising method for cancer studies [18]. Gelatin methacrylate (GelMA)-based hydrogels provide bioengineered, semi-synthetic 3-D platform for spheroid growth of ovarian cancer cells in vitro and in vivo [19].

Being unique features, such as biocompatibility, biodegradability, and adjustable mechanical properties, GelMA has a potential biomaterial for cancer therapy [20]. GelMA-based systems provide an excellent platform for the creation of cancer therapeutics and drug delivery systems. Since the effects of only NGR peptide and its different concentrations have not clarified, yet.

In this proof of the concept, the study aimed to examine usage of GelMA for PC3 prostate cancer modelling application and find the optimum concentration of different NGR peptide, one of the most important peptide for

cell targeted approach, for PC3 prostate cancer cell line.

2. General Methods

All chemical and peptide products were purchased from Aapptec (Louisville, USA). GelMA was commercially taken from Zetamatrix, Türkiye. All cell culture materials were taken from Sigma Aldrich (St. Louis, Missouri, USA). Live and Dead was purchased from Dojindo (Munich, Germany).

2.1. NGR peptide synthesis

The Asn-Gly-Arg (NGR) peptide was synthesized on the Rink Amide NovaGel resin (0.62 mmol/g) [14, 16]. The resin was swollen with 3 mL dimethylformamide (DMF) solution for 30 min. Fmoc protected amino acid derivative (2 eq), HBTU (1.95 eq), and DIEA (3 eq) were dissolved in DMF. To remove the peptide sequence from the resin, the resin was then left in a trifluoroacetic acid (TFA)-based solution for 2 hours. The product was precipitated into cold ether and lyophilised.

2.2. Fabrication of GelMA and GelMA: NGR hydrogels

Lyophilised GelMA was dissolved in 45 °C deionised water to obtain 10% concentration prepolymer solution [21]. A photoinitiator (Irgacure-2959) at 0.5% concentration was added to the GelMA solution and the mixture was stirred at 70°C for 4 h to dissolve GelMA. Only GelMA hydrogel was used as the control group. 1 µM, 10 µM and 100 µM concentrations of NGR peptide were dissolved in GelMA.

After removing air bubbles, the solutions were poured into a disposable 90 mm diameter culture. They were exposed to UV light for 2 min to cross-link only GelMA and NGR-GelMA. They were stored at 4 °C for further characterization as presented in Figure 1.

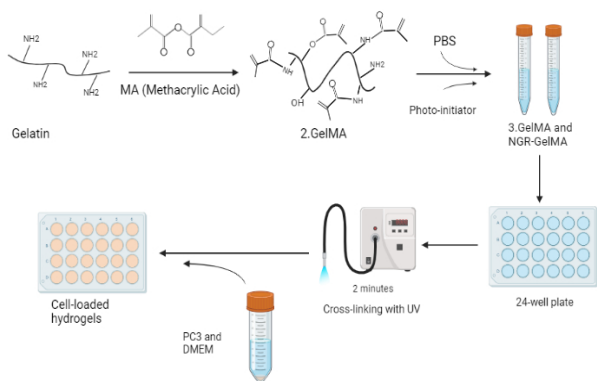


Figure 1. Basic experimental procedure for PC3 prostate cancer in GelMA and NGR- GelMA

2.3. pH and swelling analysis of GelMA

pH values in different concentrations NGR (1 μ M, 10 μ M and 100 μ M)-GelMA were measured on days 1, 3, 5, 7, 9 and 12 to test acidity properties of these hydrogels. The dry weights of GelMA and NGR (1 μ M, 10 μ M and 100 μ M)-GelMA hydrogels were measured on day 0 before placement in SBF. Then, the weights of GelMA and NGR (1 μ M, 10 μ M and 100 μ M)-GelMA hydrogels were measured on days 1, 4 and 7.

2.4. Cell culture

PC3 cells were grown in DMEM medium including 10% FBS and 1% penicillin-streptomycin [14-16]. Cells were seeded in a 12-well plate at the density of 1×10^5 cells per well and maintained in an incubator with a humidified atmosphere containing 5% CO₂ at 37°C. The culture medium was refreshed every two days. Cells were washed three times with DPBS and harvested by trypsinization.

2.5. Live and dead analysis of PC3 prostate cancer cells

The Double Staining Kit was used to evaluate the viability analysis of PC3 prostate cancer. 1 mmol/L solution A-green (Calcein-AM/DMSO) and 1.5 mmol/L solution B-red (PI/pure water) were used to get qualitative viability analysis of PC3 prostate cancer cells. The red colour represents dead cells and the green colour represents living cells. While the red colour

represents dead cells, the green colour represents living cells.

2.6. Statistical analysis

All data are statistically evaluated using two-way ANOVA (SPSS 12.0, SPSS GmbH, Germany) and post hoc test. p values less than 0.05 were used to evaluate if there were significant differences between groups. (*p<0.05, **p<0.01, ***p<0.001).

3. Results And Discussion

GelMA is a biocompatible material which supports mechanical tuning [22, 23]. Bock et. al. utilized from GelMA, PEG and GelSH to create an organoid form for cancer cell lines [22]. They conjugated peptides to these hydrogels and concluded that functionalization of hydrogel with peptides may provide ex vivo organoid growth of cancer cells.

The pH values of NGR (1 μ M, 10 μ M and 100 μ M)-GelMA hydrogels were measured. pH is important for gelation and cross-linking. Crosslinking of GelMA molecules is responsible for the formation of GelMA hydrogels. The pH value of the control group GelMA hydrogel showed values of 7.65 ± 0.2 , 7.70 ± 0.2 , 7.75 ± 0.2 , 7.75 ± 0.2 , 7.77 ± 0.2 , and 7.80 ± 0.2 on days 1, 3, 5, 7, 9 respectively as given in Figure 2.

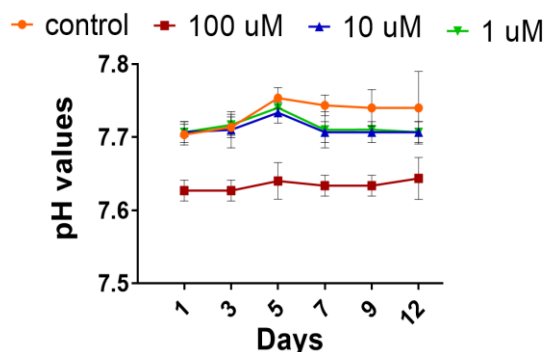


Figure 2. pH changing of only GelMA and NGR (1 μ M, 10 μ M and 100 μ M)-GelMA hydrogels

pH of GelMA hydrogel increased depending on time, but remained constant at 7.80 after day 9. pH values of NGR (100 μ M)-GelMA showed values of 7.63 ± 0.2 , 7.63 ± 0.2 , 7.63 ± 0.2 , 7.63 ± 0.2 , 7.63 ± 0.2 , 7.63 ± 0.2 , 7.65 ± 0.2 on days 1, 3, 5, 7, 9, and

12, respectively. pH values of NGR (100 μM)-GelMA remained constant over time, but started to increase on day 12. pH values of NGR (10 μM)-GelMA showed a higher pH value than the other experimental groups until day 7. On day 9, pH values of NGR (10 μM)-GelMA was observed as 7.77, while it was observed as 7.76 in NGR (10 μM)-GelMA.

On the 12 days, it was observed that the pH value of the control group and NGR (10 μM)-GelMA remained constant at 7.80. This showed that the pH values of only GelMA hydrogel and NGR (10 μM)-GelMA continued to increase until the 9th day. pH values of NGR (1 μM)-GelMA were 7.70 ± 0.2 , 7.75 ± 0.2 , 7.76 ± 0.2 , 7.77 ± 0.2 , 7.76 ± 0.2 , 7.76 ± 0.2 , 7.80 ± 0.2 on days 1, 3, 5, 7, 9, and 12, respectively. This showed that the pH value of NGR (10 μM)-GelMA increased over time but remained at a constant value (7.80) after day 9. In this study, pH measurements of GelMA hydrogels and NGR (1 μM , 10 μM and 100 μM)-GelMA hydrogels fluctuated over time, the pH value stabilised at 7.70 on the 12nd day. The pH value of NGR (1 μM)-GelMA hydrogel was 7.63 on day 1, which was lower than the other experimental groups. The pH value gradually increased over time and reached 7.70 on day 12. GelMA in the control group and different concentration NGR (1 μM , 10 μM and 100 μM)-GelMA hydrogels created a slightly basic environment.

GelMA and NGR-GelMA hydrogels have been investigated for drug delivery applications. The pH sensitivity of the hydrogel can be utilised to design pH-sensitive drug delivery systems [24, 25]. For example, the hydrogel can undergo controlled degradation for tumour tissue or cause the release of charged therapeutic agents. pH values of GelMA clearly affects drug release kinetics, possibly as a result of the requirement for extra diffusion across the GelMA layer, which lengthens the duration of the release [25].

Gelation kinetics and crosslinking efficiency can be affected by the pH of the GelMA precursor solution. Proper hydrogel formation and mechanical stability can be achieved by optimising the pH during gelation. Moghdatari concluded that high acidity promotes drug releasing. In addition, Pan et al. also showed that

the pH values of GelMA changed between 6.4 and 8.4 [24]. Literature also concluded that pH can affect the stability and activity of proteins and enzymes in hydrogels [24, 26].

However, healthy cell viability and behavior can also be affected by the pH of the hydrogel [24]. It is critical to maintain a suitable pH range to promote cell adhesion, proliferation and differentiation within the hydrogel matrix [24, 25].

pH values should be compatible with the physiological environment and promote the integration of the hydrogel into the host system. The basic pH of environment can suppress the growth and proliferation of cancer cells while promoting the growth of healthy cells [27]. Raghunand et al. concluded that pH and drug resistance associated each other in tumours and mentioned that low extracellular pH in tumours contributes to drug resistance [28]. Gu et al. showed that pH values of liposomes hardly ever change when NGR peptide bond the liposomes [29].

As peptides are able to change biodegradability of modified materials, dry weights of NGR-GelMA were measured on days 0, 1, 4 and 7 as shown in Figure 3.

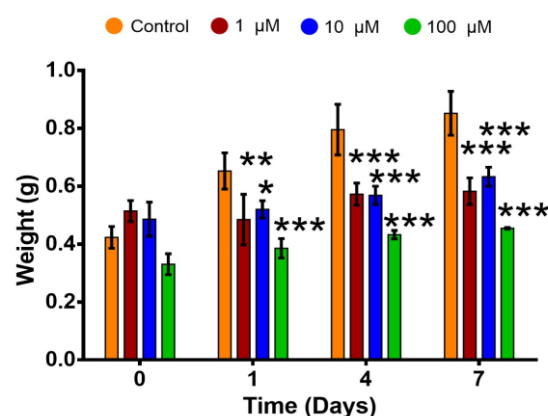


Figure 3. Weight measurements of only GelMA and NGR-GelMA hydrogels

Briefly, the initial weights of the hydrogel scaffolds were measured. The weights of the control group GelMA hydrogel were measured as 0.423 ± 0.02 g, 0.653 ± 0.04 g, 0.796 ± 0.09 g and 0.852 ± 0.00 g on days 0, 1, 4 and 7, respectively. This shows that the weight of GelMA hydrogel increases with time depending

on liquid absorbing capacity. The weights of NGR (100 μM)-GelMA were measured as 0.331 ± 0.2 g, 0.386 ± 0.2 g, 0.433 ± 0.2 g and 0.455 ± 0.2 g on days 0, 1, 4 and 7, respectively. This showed that NGR (100 μM)-GelMA absorbed into the liquid and increased its weight. The control group was found that it had the lowest weight compared to GelMA and other experimental groups.

The weight of NGR (100 μM)-GelMA was initially less than the other experimental groups so it may be the reason. It was also thought that the absorption potential of NGR (100 μM)-GelMA was less than the other experimental groups. The weights of NGR (10 μM)-GelMA were measured as 0.486 ± 0.2 g, 0.520 ± 0.2 g, 0.569 ± 0.2 g, 0.633 ± 0.2 g on days 0, 1, 4 and 7, respectively. This indicated that the weight of NGR (10 μM)-GelMA increased with time. The results showed that the NGR (10 μM)-GelMA was absorbed by the liquid and increased its weight. The weights of NGR (1 μM)-GelMA were measured as 0.514 ± 0.2 g, 0.485 ± 0.2 g, 0.573 ± 0.2 g, 0.583 ± 0.2 g on days 0, 1, 4 and 7, respectively. The weight of NGR (1 μM)-GelMA increased with time. The results showed that NGR (1 μM)-GelMA increased its weight by absorbing into the liquid. The results show the variation of the weights of GelMA hydrogels and NGR (1 μM , 10 μM and 100 μM)-GelMA over a period of time (on days 0, 1, 4 and 7).

The weights increased continuously with time, indicating that the hydrogels absorbed liquid from the surrounding medium. The reason of these weight changes is the hydrophilic nature of GelMA hydrogel [30]. When GelMA hydrogel was incubated in simulated body fluid for this study, it started to absorb the fluid through a process called imbibition. The porous structure of the hydrogel allows it to absorb and retain water, the weight increased. This absorption occurs due to the presence of hydrophilic functional groups in the GelMA structure that have affinity for water molecules. NGR (1 μM , 10 μM and 100 μM)-GelMA also show their ability to absorb liquid by showing weight increase over time. However, it was observed that the NGR (100 μM)-GelMA had the lowest weight compared to the control group GelMA and other experimental groups.

This may be due to the relatively low initial dry weight of the NGR (100 μM)-GelMA, suggesting that the GelMA material had a lower mass before the absorption process begins. Overall, the weight changes in GelMA hydrogels and NGR (1 μM , 10 μM and 100 μM)-GelMA were primarily due to the hydrophilic nature of GelMA and its ability to absorb liquid by sorption. Specific concentrations of NGR can affect the initial weight and absorption potential to some extent as observed in the experiment.

On days 1, 4 and 7, PC3 prostate cancer cell line was encapsulated into NGR (1 μM , 10 μM and 100 μM)-GelMA. Live/Dead staining analysis was performed to determine the viability. As a result of the analysis the images obtained with the microscope are shown in Figure 4.

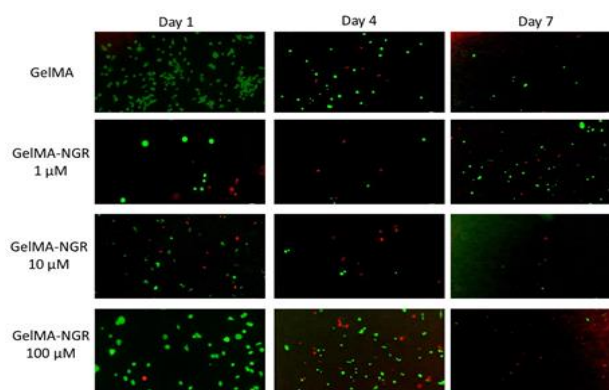


Figure 4. Images of the live and dead analysis of PC3 cell line in the control group GelMA and NGR (1 μM , 10 μM and 100 μM)-GelMA on days 1, 4 and 7

In Figure 4, green colour represents living cells and red colour represents dead cells. Only GelMA was used as a control group. The control group observed higher green colour intensity and less red colour intensity compared to NGR-GelMA hydrogel on days 1 and 4. It indicated that the number of living cells was higher as the green colour was higher in NGR-GelMA. However, the green colour intensity in only GelMA hydrogel was relatively less than NGR (1 μM)-GelMA hydrogels at day 7.

At day 7, NGR (1 μM)-GelMA hydrogels showed that the the number of viable cells was less than the control group. In NGR (100 μM)-GelMA, the green colour intensity at day 1 and day 4 was relatively higher than the red colour

intensity. However, on day 7, the red colour intensity was higher than the green colour intensity. This indicated that NGR (100 μM)-GelMA relatively proliferated on day 1, but the number of dead cells increased after day 4. These results show that NGR (100 μM)-GelMA hydrogel did not provide a favorable environment for the survival of the cells, it contained and increased the number of dead cells.

Changes in PC3 cell viability over time were observed in the results of live/dead staining analysis of GelMA and NGR (1 μM , 10 μM and 100 μM)-GelMA hydrogels. The only GelMA hydrogel provided a favorable environment for cells. Cell surviving and growing, which is reflected in living cells, observed on days 1 and 4. However, the green colour intensity in GelMA hydrogels decreased on day 7. This may be due to limitations in nutrient diffusion or accumulation of metabolic waste within the hydrogel over time. Similarly, Shih et al. in 2019 investigated the effect of oxygen diffusion on cell viability in the hydrogel [31].

The results showed that the transportation ability of oxygen and nutrients in the hydrogel to cells and removing metabolic wastes are limited so cell viability decreased over time due to the limitations of oxygen diffusion in the hydrogel [32]. Miri et. al. used MCF-7 line to model the breast cancer in GelMA [32]. They proved that nutrients are able to diffuse into breast cancer cell line. The conclusion was coincided with the behavior of control group GelMA [33]. Fusion proteins within different concentration of NGR sequence demonstrated cytotoxic effects on cancer cell lines and reduced cell survival [34]. Since NGR (1 μM)-GelMA included the highest red cells and lowest green cells on day 7, the concentration may have been effective in promoting cell apoptosis and suppressing cell viability in the hydrogel. The dynamic nature of cell behavior and the microenvironment within hydrogels may explain the observed differences in cell viability between time points. The decrease of cell viability in NGR (1 μM)-GelMA hydrogels may indicate prolonged exposure to the hydrogel environment at day 7. GelMA presented high producibility and controllability for PC3 prostate cancer cells. It is possible to

observe changing 3D microenvironment of PC3 prostate cancer depending on targeting drug concentration in GelMA.

The results appeared the effects of different concentration NGR (1 μM , 10 μM and 100 μM)-GelMA in terms of PC3 prostate cancer viability. These findings suggested that it is important to optimize NGR (1 μM , 10 μM and 100 μM)-GelMA hydrogels to achieve the desired results in PC3 prostate cancer cell studies. Further research is needed to understand the underlying mechanisms and explore the potential of NGR-GelMA hydrogels as a therapeutic approach for prostate cancer treatment.

4. Conclusion

GelMA hydrogels provide a neutral pH environment that remains relatively stable, which may be effective for drug releasing systems. NGR-GelMA hydrogels were able to absorb liquid and their weight increased. GelMA hydrogels showed promise as a suitable matrix for PC3 prostate cancer cells. To calibrate model constants, experimental factors like cell line, testing duration, and peptide modification should be changed to match the intended volume of GelMA. In case of usage of NGR (100 μM) may contribute to PC3 prostate cancer death.

Further research and optimisation is required to fully understand the underlying mechanisms and potential applications of GelMA and NGR-GelMA hydrogels in PC3 prostate cancer therapy.

Article Information Form

Acknowledgments

The authors thank to Gülşah Sunal for supporting peptide synthesis, Dilek Kaya for providing cell line and Assoc. Prof. Dr. Mustafa Şen for providing Irgacure-2959 and fluorescence microscope

Funding

The authors thank to TUBITAK 2209-B Project.

Authors' Contribution

Z.B.Y.Ç. designed the study. Z.B.Y.Ç. and M.Z. performed all experiments. Z.B.Y.Ç. and O.K.

concluded and funded the experiments. All authors wrote, proofread, revised and approved the manuscript.

The Declaration of Conflict of Interest/ Common Interest

No conflict of interest or common interest has been declared by the authors.

The Declaration of Ethics Committee Approval

This study does not require ethics committee permission or any special permission.

The Declaration of Research and Publication Ethics

The authors of the paper declare that they comply with the scientific, ethical and quotation rules of SAUJS in all processes of the paper and that they do not make any falsification on the data collected. In addition, they declare that Sakarya University Journal of Science and its editorial board have no responsibility for any ethical violations that may be encountered, and that this study has not been evaluated in any academic publication environment other than Sakarya University Journal of Science.

Copyright Statement

Authors own the copyright of their work published in the journal and their work is published under the CC BY-NC 4.0 license.

References

- [1] W. Bijoux, E. C. Duverger, S. Balbolia, P. J. Lamy, X. Rebillard, B. Tretarre, S. Cenee, F. Menegaux "Occupation and prostate Cancer risk: results from the epidemiological study of prostate cancer (EPICAP)," *Journal of Occupational Medicine and Toxicology*, vol. 17, no. 1, p. 5, 2022/02/07 2022.
- [2] M. S. Litwin, H. J. Tan, "The Diagnosis and Treatment of Prostate Cancer: A Review," *JAMA*, vol. 317, no. 24, pp. 2532-2542, 2017.
- [3] V. Sailer, G. Amsberg, S. Duensing, J. Kirfel, V. Lieb, E. Metzger, A. Offermann, K. Pantel, R. Schuele, H. Taubert, S. Wach, S. Perner, S. Werner, A. Aigner "Experimental in vitro, ex vivo and in vivo models in prostate cancer research," *Nature Reviews Urology*, vol. 20, no. 3, pp. 158-178, Mar 2023.
- [4] M. Thomsen, L. Vitetta, "Adjunctive Treatments for the Prevention of Chemotherapy- and Radiotherapy-Induced Mucositis," *Integrative Cancer Therapies*, vol. 17, no. 4, pp. 1027-1047, Dec 2018.
- [5] K. Nurgali, R. T. Jagoe, R. Abalo, "Editorial: Adverse Effects of Cancer Chemotherapy: Anything New to Improve Tolerance and Reduce Sequelae?," *Frontiers in Pharmacology*, vol. 9, p. 245, 2018.
- [6] Q. Zhang, L. Li, "Photodynamic combinational therapy in cancer treatment," *Journal of the Balkan Union of Oncology*, vol. 23, no. 3, pp. 561-567, May-Jun 2018.
- [7] E. Nezir, M. P. Khalily, S. Gulyuz, S. Ozcubukcu, Ş. G. Küçükgülzel, O.Yilmaz, D. Telci, "Synthesis and evaluation of tumor-homing peptides for targeting prostate cancer," *Amino Acids*, vol. 53, no. 5, pp. 645-652, 2021/05/01 2021.
- [8] T. You, Y. Ding, H. Chen, G. Song, L. Huang, M. Wang, X. Hua, "Development of competitive and noncompetitive immunoassays for clothianidin with high sensitivity and specificity using phage-displayed peptides," *Journal of Hazardous Materials*, vol. 425, p. 128011, 2022/03/05/ 2022.
- [9] F. Curnis, G. Arrigoni, A. Sacchi, L. Fischetti, W. Arap, R. Pasqualini, A. Corti, "Differential binding of drugs containing the NGR motif to CD13 isoforms in tumor vessels, epithelia, and myeloid cells," *Cancer Research*, vol. 62, no. 3, pp. 867-74, Feb 1 2002.
- [10] L. Zhu, Z. Ding, X. Li, H. Wei, Y. Chen, "Research Progress of Radiolabeled Asn-Gly-Arg (NGR) Peptides for Imaging and

- Therapy," *Molecular Imaging*, vol. 19, p. 1536012120934957, Jan-Dec 2020.
- [11] S. V. Garde, A. J. Forté, M. Ge, E. A. Lepekhn, C. J. Panchal, S. A. Rabbani, J. J. Wu, "Binding and internalization of NGR-peptide-targeted liposomal doxorubicin (TVT-DOX) in CD13-expressing cells and its antitumor effects," *Anti-Cancer Drugs*, vol. 18, no. 10, pp. 1189-1200, 2007.
- [12] Z. Zhang, L. Hou, L. Feng, S. Huang, M. Luo, S. Shao, X. Zhang, S. Gu, X. Zhao, "An antimicrobial peptide containing NGR motif has potent antitumor activity against CD13+ and CD13- tumor cells," *Tumor Biology*, vol. 36, no. 10, pp. 8167-8175, 2015/10/01 2015.
- [13] J. Hoarau-Véchet, A. Raffi, C. Touboul, J. Pasquier, "Halfway between 2D and Animal Models: Are 3D Cultures the Ideal Tool to Study Cancer-Microenvironment Interactions?," *International Journal of Molecular Sciences*, vol. 19, no. 1, p. 181, 2018.
- [14] Z. B. Yaralı Çevik, O. Karaman, N. Topaloğlu, "Synergistic effects of integrin binding peptide (RGD) and photobiomodulation therapies on bone-like microtissues to enhance osteogenic differentiation," *Biomaterials Advances*, vol. 149, p. 213392, 2023/06/01/ 2023.
- [15] Z. B. Yaralı Çevik, O. Karaman, N. Topaloğlu, "Photobiomodulation therapy at red and near-infrared wavelengths for osteogenic differentiation in the scaffold-free microtissues," *Journal of Photochemistry and Photobiology B: Biology*, vol. 238, p. 112615, 2023/01/01/ 2023.
- [16] Z. B. Yaralı, G. Onak, O. Karaman, "Effect of Integrin Binding Peptide on Vascularization of Scaffold-Free Microtissue Spheroids," *Tissue Engineering and Regenerative Medicine*, vol. 17, no. 5, pp. 595-605, Oct 2020.
- [17] H. Huang, Y. Ding, X. S. Sun, T. A. Nguyen, "Peptide hydrogelation and cell encapsulation for 3D culture of MCF-7 breast cancer cells," *PLoS One*, vol. 8, no. 3, p. e59482, 2013.
- [18] F. Gelain, Z. Luo, S. Zhang, "Self-Assembling Peptide EAK16 and RADA16 Nanofiber Scaffold Hydrogel," *Chemistry Reviews*, vol. 120, no. 24, pp. 13434-13460, Dec 23 2020.
- [19] E. Kaemmerer, F. P. W. Melchels, B. M. Holzapfel, T. Meckel, D. W. Hutmacher, D. Loessner, "Gelatin methacrylamide-based hydrogels: An alternative three-dimensional cancer cell culture system," *Acta Biomaterialia*, vol. 10, no. 6, pp. 2551-2562, 2014/06/01/ 2014.
- [20] M. Vigata, C. Meinert, S. Pahoff, N. Bock, D. W. Hutmacher, "Gelatin Methacryloyl Hydrogels Control the Localized Delivery of Albumin-Bound Paclitaxel," *Polymers (Basel)*, vol. 12, no. 2, Feb 24 2020.
- [21] K. Yue, G. Trujillo-de Santiago, M. M. Alvarez, A. Tamayol, N. Annabi, A. Khademhosseini, "Synthesis, properties, and biomedical applications of gelatin methacryloyl (GelMA) hydrogels," *Biomaterials*, vol. 73, pp. 254-71, Dec 2015.
- [22] N. Bock, F. Forouz, L. Hipwood, J. Clegg, P. Jeffery, M. Gough, T. V. Wyngaard, C. Pyke, M. N. Adams, L. J. Bray, L. Croft, E. W. Thompson, T. Kryza, C. Meinert, "GelMA, Click-Chemistry Gelatin and Bioprinted Polyethylene Glycol-Based Hydrogels as 3D Ex Vivo Drug Testing Platforms for Patient-Derived Breast Cancer Organoids," *Pharmaceutics*, vol. 15, no. 1, Jan 12 2023.
- [23] H. Wang, Y. Feng, B. An, W. Zhang, M. Sun, Z. Fang, W. Yuan, M. Khan, "Fabrication of PU/PEGMA crosslinked hybrid scaffolds by in situ UV photopolymerization favoring human endothelial cells growth for vascular tissue engineering," *Journal of Materials Science:*

- Materials in Medicine, vol. 23, no. 6, pp. 1499-1510, 2012/06/01 2012.
- [24] Q. Pan, R. Fan, R. Chen, J. Yuan, S. Chen B. Cheng, "Weakly acidic microenvironment of the wound bed boosting the efficacy of acidic fibroblast growth factor to promote skin regeneration," *Frontiers in Bioengineering and Biotechnology*, vol. 11, p. 1150819, 2023.
- [25] M. Moghtaderi, S. Bazzazan, S. Bazzazan, G. Sorourian, M. Sorourian, Y. Akhavanzanjani, H. Noorbazargan, Q. Ren, "Encapsulation of Thymol in Gelatin Methacryloyl (GelMa)-Based Nanoniosome Enables Enhanced Antibiofilm Activity and Wound Healing," *Pharmaceutics*, vol. 15, no. 6, Jun 9 2023.
- [26] K. Wang, Q. Fu, X. Chen, Y. Gao, K. Dong, "Preparation and characterization of pH-sensitive hydrogel for drug delivery system," *RSC Advances*, 10.1039/C2RA20989F vol. 2, no. 20, pp. 7772-7780, 2012.
- [27] S. Lee, A. Shanti, "Effect of Exogenous pH on Cell Growth of Breast Cancer Cells," *International Journal of Molecular Science*, vol. 22, no. 18, Sep 14 2021.
- [28] N. Raghunand, R. Martínez-Zaguilán, S. H. Wright, R. J. Gillies, "pH and drug resistance. II. Turnover of acidic vesicles and resistance to weakly basic chemotherapeutic drugs," *Biochemical Pharmacology*, vol. 57, no. 9, pp. 1047-58, May 1 1999.
- [29] Z. Gu, M. Chang, Y. Fan, Y. Shi, G. Lin, "NGR-modified pH-sensitive liposomes for controlled release and tumor target delivery of docetaxel," *Colloids and Surfaces B Biointerfaces*, vol. 160, pp. 395-405, Dec 1 2017.
- [30] Y. Piao, H. You, T. Xu, H. P. Bei, I. Z. Piwko, Y. Y. Kwan, X. Zhao, "Biomedical applications of gelatin methacryloyl hydrogels," *Engineered Regeneration*, vol. 2, pp. 47-56, 2021/01/01/ 2021.
- [31] H. C. Shih, T. A. Lee, H. M. Wu, P. L. Ko, W. H. Liao, Y. C. Tung, "Microfluidic Collective Cell Migration Assay for Study of Endothelial Cell Proliferation and Migration under Combinations of Oxygen Gradients, Tensions, and Drug Treatments," *Scientific Reports*, vol. 9, no. 1, p. 8234, 2019/06/03 2019.
- [32] K. Miri, H. G. Hosseinabadi, B. Cecen, S. Hassan, Y. S. Zhang, "Permeability mapping of gelatin methacryloyl hydrogels," *Acta Biomaterials*, vol. 77, pp. 38-47, Sep 1 2018.
- [33] Valentinis, S. Porcellini, C. Asperti, M. Cota, D. Zhou, P. D. Matteo, G. Garau, C. Zucchelli, N. R. Avanzi, G. P. Rizzardi, M. Degano, G. Musco, C. Traversari, "Mechanism of Action of the Tumor Vessel Targeting Agent NGR-hTNF: Role of Both NGR Peptide and hTNF in Cell Binding and Signaling," *International Journal of Molecular Science*, vol. 20, no. 18, Sep 12 2019.
- [34] Mohammadi-Farsani, M. Habibi-Roudkenar, M. Golkar, M. A. Shokrgozar, A. J. Najafabadi, H. KhanAhmad, S. Valiyari, S. Bouzari, "A-NGR fusion protein induces apoptosis in human cancer cells," *Excli Journal*, vol. 17, pp. 590-597, 2018.

Analysis of Türkiye's Cybersecurity Strategies: Historical Developments, Scope, Content and Objectives

Hasan Çifci^{1*} 

^{1*} İstanbul Aydın University, Faculty of Engineering, Department of Software Engineering, İstanbul, Türkiye, hasancifci@aydin.edu.tr

*Corresponding Author

ARTICLE INFO

ABSTRACT

Keywords:
Cybersecurity
Turkish Cybersecurity
Cybersecurity Strategy
National Cyber Strategy
Cybersecurity Objectives



Article History:
Received: 10.02.2023
Accepted: 05.12.2023
Online Available: 27.02.2024

Cybersecurity is regarded as a crucial part of overall national security. A national cybersecurity strategy (NCSS) offers direction and a framework for national cybersecurity-related concerns and initiatives. Many nations have devised their own plans to defend against attacks, reduce risks, discourage attackers, and provide a secure and accessible cyberspace to promote innovation, the economy, commerce, and wealth. In order to assist the countries in developing their plans, organizations like the ITU, ENISA, OECD, NATO, e-Governance Academy and Oxford University issued research and advice publications based on the best practices from various countries. The assessment of the scope, objective, and content of Turkish national cybersecurity strategies is limited in academic literature. The studies in the literature that gathered multinational NCSS attributes from various countries and served as a guide for the development of national cybersecurity strategies were examined through a comprehensive literature review in order to assess Türkiye's strategies in terms of scope, content, and objectives. Following the development of assessment criteria based on these studies and research, a qualitative study was carried out to evaluate and ascertain the degree of conformity of Turkish cybersecurity strategies with the criteria. The historical context of Türkiye's cybersecurity strategies was explored in this article, along with strategy revisions, evaluations of the strategies' scope, content, and objectives, and gaps that should be filled to make the strategies more effective.

1. Introduction

Information and communication technology (ICT) is becoming increasingly vital in contemporary life. Ensuring continual access to and providing integrity and confidentiality of the ICT systems and contained data is defined as “cybersecurity” [1] and it focuses on the process of protecting information by monitoring, blocking, and dealing with cyber threats [2]. Cybersecurity is provided not only by technical means but also by establishing and applying best practices, training, concepts, guidelines, policies and strategies [1]. Cybersecurity is much more complex than just computer security. Rather, it should be viewed as a national security issue

since improper use of the online services might compromise national security, safety and services that are provided for the nation's benefit [3].

Several significant cyberattacks threatened the assets and systems in cyberspace and national security [4]. For instance, in 2007, Estonia faced a series of coordinated cyberattacks that targeted wide range of the services in internet. Iran's nuclear facilities was targeted by the Stuxnet worm in 2010 [5]. Ukraine has repeatedly been targeted by Russia before and during the war. Most recently, the United States experienced a significant breach with the ransomware attack on the Colonial Pipeline in 2021, resulting in a

temporary shutdown of the largest fuel pipeline. These incidents demonstrate the danger of cybersecurity threats, emphasizing the necessity for comprehensive national cybersecurity strategies.

Assuring the cybersecurity of a country's cyberspace, cyberspace systems, information and communication infrastructure, and the information processed therein, particularly critical infrastructures, is of critical importance [6]. Online services are used in a variety of ways, from entertainment to education, from law enforcement and military services to banking services, and from e-commerce to international logistics services. Today, the maintenance of economic life, the continuation of the public services provided by a state, the provision of social and individual safety, security and privacy are highly dependent on the uninterrupted continuation of online services.

For this reason, ensuring the cybersecurity of critical infrastructures and ICT systems in a country, including the internet infrastructure, is one of the most critical national security challenges. National cybersecurity can be defined as the establishment of particular governmental instruments and information security guidelines for important ICT systems and content within these systems [7]. National cybersecurity strategy (NCSS) is a broad and high-level strategy for identifying and prioritizing a set of national objectives that must be met within a particular time frame in order to secure cybersecurity at a national level [8].

Analyzing and evaluating cybersecurity strategies and policies in terms of content will ensure that the steps to be taken based on them are consistent and holistic. Various studies have been carried out by international organizations such as ITU (International Telecommunication Union), ENISA (The European Union Agency for Cybersecurity), OECD (Organization for Economic Co-operation and Development), NATO (North Atlantic Treaty Organization), e-GA (e-Governance Academy) and Oxford University for the creation of cybersecurity strategies. These studies cover various topics, such as guidance on how an NCSS lifecycle should be, how an NCSS should be evaluated,

what its content should cover, and what objectives should be included in an NCSS.

It can be suggested that studies on the national cybersecurity strategy in Türkiye were initiated with the publication of the OECD Guidelines for the Security of Information Systems and Networks [9] with the now-abolished Prime Ministry Circular in the early 2000s, followed by the e-Transformation Türkiye Project [4]. On the other hand, the strategy document focused directly on national-level cybersecurity, was first published in 2013 and was renewed in 2016 and 2020.

In this article, scope, content and objectives of Türkiye's cybersecurity strategies were analyzed based on the criteria drawn from international research and studies. Based on the results of the studies carried out by reputable organizations such as ITU, ENISA, OECD, NATO, e-GA and Oxford University, the contents of NCSSs and the objectives that were and should be addressed in the NCSSs of various countries in the world were determined, and evaluation criteria were established. Then, Türkiye's national cybersecurity strategies were examined, and their compatibility with the determined criteria was revealed in detail. In this circumstance, Türkiye's cybersecurity strategies were examined in the historical context, strategy changes were determined, strategies were evaluated in terms of scope, content and objectives, and gaps identified to improve the strategies.

The significance of this study comes from its evaluation criteria, which were extracted through an extensive literature survey from the research and guidance documents created by notable organizations. Another contribution is the evaluation results of the comprehensiveness of Türkiye's cybersecurity strategies, which provides guidance to scholars and decision-makers. In addition, by using the approach in this study, it would be easier to carry out similar studies for other countries.

2. Methodology

In the first phase of the study, an extensive literature review was undertaken to gather relevant multinational NCSS attributes and

guidance on creating national cybersecurity strategies. The review included sources such as academic journals, conference papers, reports from international organizations like ITU, ENISA, OECD, NATO, e-GA, and Oxford University, and other scholarly literature. Based on these findings, specific assessment criteria were established to evaluate the content, scope, and objectives of Türkiye's national cybersecurity strategies, reflecting best practices, international standards, and widely recognized principles in the field of cybersecurity.

The next phase involved data collection and qualitative analysis. Primary data were collected from Türkiye's official national cybersecurity strategy documents, as well as associated regulations, guidelines, and related governmental publications. Secondary data were gathered from scholarly works, reports, and analyses relating to Türkiye's cybersecurity strategies. The analysis process included careful examination of the collected documents to identify key themes, patterns, and elements that align with or diverge from the assessment criteria.

The study concluded with summarizing the findings, drawing conclusions, and developing recommendations for enhancing Türkiye's cybersecurity strategies.

3. Important Guidance Documents for Creating NCSS

A nation's welfare and the sustainability of a business have long depended on reliable ICT systems, infrastructures and services. The importance of cybersecurity to the nation as a whole is being recognized to a greater extent. An NCSS is a mechanism for enhancing the security and robustness of national infrastructure and services and offers a comprehensive and overarching approach [8]. Even though the nations develop strategies and take actions to provide cybersecurity nationwide, United States is one of the first countries which published its national cybersecurity strategy which was part of homeland security strategy [10]. Then, other nations published their strategies by highlighting the importance of national-level strategy settings.

There are various research and studies in the literature that provide guidance for developing NCSS in terms of scope and objectives. In this context, the documents in Table 1 were analyzed to create assessment criteria for Turkish national cybersecurity strategies.

National Cybersecurity Strategy Guide [3] was developed with ITU sponsorship. The document mainly focuses on the issues that should be considered when creating or reviewing national-level cybersecurity strategies. The principles in the document were gathered from the multiple stakeholders and formulated in ends-ways-means approach. The guide comprises elements of the national cybersecurity program, and it provides a template for the strategy.

The National Cyber Security Strategies document by ENISA [8] summarizes the common objectives that need to be addressed to prepare national cybersecurity strategies with sufficient content. The document also presents a brief analysis of the current state of cybersecurity strategies, common themes and differences between EU countries and the US, Canada and Japan.

ENISA's National Cyber Security Strategies-Practical Guide on Development and Execution [11] intends to provide appropriate stakeholders with practical assistance on the formulation, execution, and maintenance of cybersecurity strategies. In addition to the strategy development stages, the practices and recommendations for these stages, the basic strategic themes that need to be addressed are included.

The National Cybersecurity Framework Manual, created by NATO Cooperative Cyber Defense Center of Excellence (CCD COE) [7], highlights various aspects of national cybersecurity rather than giving the steps to follow for strategy development at the national level. Detailed information is given about the issues that need to be addressed in the strategies and the issues that need to be balanced.

Table 1. Important Guidance Documents for Creating NCSS

No	Year	Institution	Document
G1	2011	ITU	National Cybersecurity Strategy Guide
G2	2012	ENISA	National Cyber Security Strategies
G3	2012	ENISA	National Cyber Security Strategies-Practical Guide on Development and Execution
G4	2012	NATO	National Cyber Security Framework Manual
G5	2012	OECD	Cybersecurity Policy Making at a Turning Point
G6	2014	ENISA	An Evaluation Framework for National Cyber Security Strategies
G7	2016	ENISA	NCSS Good Practice Guide: Designing and Implementing National Cyber Security Strategies
G8	2018	ITU	Guide to Developing a National Cyber Security Strategy-Strategic Engagement in Cybersecurity
G9	2019	ENISA	Good Practices in Innovation Under NCSS
G10	2020	ENISA	National Capabilities Assessment Framework (NCAF)
G11	2020	e-GA	National Cyber Security in Practice
G12	2021	GCSCC	Cybersecurity Capacity Maturity Model for Nations (CMM)

Cybersecurity Policy Making at a Turning Point report, created by OECD [12], includes an analysis of a total of ten voluntary OECD countries (Australia, Canada, France, Germany, Japan, Netherlands, UK, USA, Finland and Spain) that published their cybersecurity policies between 2009 and 2011. The report provides insights on commonalities and variances between nations, as well as significant changes between policy generations.

An Evaluation Framework for National Cyber Security Strategies, developed by ENISA [13], includes the analysis of the strategies of 18 EU member states and 8 other countries and the findings obtained as a result of 11 interviews. The framework document aims to conduct an inventory of approaches used for evaluating strategies, provide recommendations on the implementation and evaluation of strategies, identify good practices, develop an evaluation framework, and support the framework with key performance indicators.

NCSS Good Practice Guide: Designing and Implementing National Cyber Security Strategies created by ENISA [14] is the updated version of the guide prepared in 2012 [11]. The original guide's various processes, objectives, and best practices were reassessed, and the strategies of EU member states and European Free Trade Association members (Norway, Switzerland, Iceland and Liechtenstein) were analyzed. The document's goal is to assist these countries in developing and updating their national cybersecurity strategies.

Guide to Developing a National Cyber Security Strategy-Strategic Engagement in Cybersecurity, created under the coordination of ITU [15], aims to establish a set of guidelines and best practices for developing, formulating, and implementing national cybersecurity strategies. In this context, the stages for all phases of the strategy were explained in detail. Additionally, general principles and the areas to focus on were specified in the document.

The main purpose of the Good Practices in Innovation Under NCSS document by ENISA [16] is to analyze the cybersecurity innovation environment in EU member states and present the challenges and good practices in innovation when implementing national cybersecurity strategies. In the document, the main objectives that should be included in the national strategies, which were determined as a result of the interviews with the member countries, are included.

In accordance with the EU Network and Information Security Directive [17], each EU member country is required to have a national cybersecurity strategy. In this context, the National Capabilities Assessment Framework (NCAF) document by ENISA [18] provides a model for member countries to measure the maturity level of strategies.

National Cyber Security in Practice [19] is a handbook developed by e-Governance Academy (e-GA) and supported by Estonian Ministry of Foreign Affairs. It defines the key elements of a country's cybersecurity architecture.

The Cybersecurity Capacity Maturity Model for Nations (CMM) is a maturity framework developed by Oxford University's Global Cybersecurity Capacity Center (GCSCC) with over 200 experts worldwide to determine the level of cybersecurity maturity of countries [20]. The model was developed in 2014, and the most recent iteration was released in 2021. The CMM lists five factors that must be addressed at the national level in order to properly handle cybersecurity. These are legal and regulatory measures, cybersecurity policy and strategy, cybersecurity culture and society, creating cybersecurity knowledge and capabilities and technology and standards.

Academic literature is lacking regarding assessment of the content, scope and objectives of the Turkish NCSSs. Çakır and Arınmış [21] evaluated the strategies and action plans by using 11 criteria (continuity, protection of critical infrastructures, research and development supports, leadership, national and international cooperation, human resources development, education and training, legislation, budget allocation, cyber deterrence, and monitoring of action plan results) derived from the European Union and ENISA documents. The study suggested that the number of criteria can be increased but kept concise since they are sufficient to assess the strategies. On the other hand, the study lacks explanations as to why the mentioned criteria were chosen and extracted from which exact sources.

4. Important Turkish Cybersecurity Strategy Initiatives and Historical Developments

It is possible to trace the beginning of the most important studies on cybersecurity in Türkiye to the establishment of TUBITAK National Electronics and Cryptology Institute and especially to the production of the first national crypto device in 1978 [22]. On the other hand, it is seen that studies on the strategy started in the early 2000s.

The historical development of Turkish cybersecurity strategies demonstrates the country's increasing focus on protecting its citizens, businesses, and critical infrastructure from cyber threats. The first strategy document,

Prime Ministry Circular No. 2003/10, was released in 2003 [4] on the security guideline [9] published by the OECD laid the foundation for the country's cybersecurity efforts. This was followed by the E-Transformation Türkiye Project [23] and its action plans [24], which aimed to create a more secure and efficient digital environment. The Information Society Strategy and Action Plan 2006-2010 [25] further advanced these efforts by defining a comprehensive framework for promoting the growth of the information society.

In 2013, the National Cybersecurity Strategy and 2013-2014 Action Plan [26] marked a new phase in the country's cybersecurity efforts, with a focus on strengthening national cybersecurity and improving the resilience of critical infrastructure. This was followed by the Information Society Strategy and Action Plan 2015-2018 [27], which continued to prioritize cybersecurity while also emphasizing the importance of access to digital services for all citizens. The National Cybersecurity Strategy and 2016-2019 Action Plan [28] further expanded on these efforts, focusing on cyber defense, cybercrime, cybersecurity ecosystem, and national security integration with cybersecurity.

In 2019, the Presidential Circular on Information Security Measures [29] reinforced the importance of cybersecurity for the country and outlined the measures necessary to protect sensitive information. The most recent strategy document, the National Cybersecurity Strategy and 2020-2023 Action Plan [30], focuses on critical infrastructures, improving national capabilities, combating cybercrime, promoting the use of secure digital technologies, and establishing international cooperation.

In conclusion, the historical development of Turkish cybersecurity strategies reflects the country's growing recognition of the importance of protecting its citizens, businesses, and critical infrastructure from cyber threats. The successive strategy documents have evolved to address changing threats and technologies, reflecting the country's commitment to staying ahead of the curve in the rapidly evolving world of cybersecurity.

Türkiye's efforts to strengthen its cybersecurity posture have been reflected in the numerous initiatives launched over the years. In the following sub-titles, brief information is given for initiatives to better understand the evolution of Türkiye's cybersecurity strategies.

4.1. Prime ministry circular no. 2003/10 (2003)

Prime Ministry Circular dated 17 February 2003 and numbered 2003/10 can be accepted as one of the first initiatives to set a strategy for communication and information security and the protection of personal privacy in Türkiye [4]. Adoption of the guidelines prepared by the OECD was adopted by the Circular.

The Guidelines recommend establishing a culture of security among users of information and communication technologies, raising awareness on this issue, establishing a general reference framework for security, developing security practices, measures and procedures, and establishing standards by performing risk management [9].

4.2. E-Transformation Türkiye project (2003)

e-Transformation Türkiye Project was initiated by the former Prime Ministry to make maximum use of ICT in the country, to provide citizens with fast and quality public service, and to rearrange the relevant legislation in line with the EU acquis [23].

In the project, the basic steps that Türkiye should take in the EU membership candidacy process were discussed. It is aimed to contribute to the transparent management of the public administration, to develop and expand the use of information and communication infrastructure and technologies, to prevent waste by carrying out investment projects in a coordinated manner and to use these technologies safely and securely.

4.3. E-Transformation Türkiye project action plans (2003 and 2005)

The first short-term action plan in the purview of e-Transformation Türkiye Project was put into practice with the Prime Ministry Circular dated 4 December 2003 and numbered 2003/48 [24]. The

second short-term action plan was published on March 24, 2005 [31].

Short-term action plans are discussed under eight headings (Information Society Strategy, Information Security and Technical Infrastructure, Human Resources and Education, Legal Framework, Standards, e-Government, e-Health and e-Commerce). The topic titled "Technical Infrastructure and Information Security" is directly related to cybersecurity. However, there are action clauses on cybersecurity under other headings as well. In this context, actions for cybersecurity are listed below:

- Conducting information security risk analysis to public institutions
- Working on the use of smart cards in public
- Development of pilots for testing and ensuring network security
- Expanding the internet infrastructure and producing solutions for its security
- Examining the usage of open-source software in government
- Raising awareness in society about safe internet use
- Enactment of the law on cyber crimes
- Combating unwanted electronic communications
- To carry out legal studies in order to protect sensitive information for national security (enactment of the National Information Security Law)
- Public information systems emergency management

4.4. Information society strategy and action plan 2006-2010 (2006)

Information Society Strategy and Action Plan 2006-2010 was published in the Official Gazette on July 28, 2006, and entered into force [25]. A total of seven main themes in the strategy (Social

Transformation, Impact of ICT in the Business World, Citizen-Oriented Service Transformation, Modernization in Public Administration, Global Competitive Information Technologies Sector, Competitive, Widespread and Cheap Communication Infrastructure and Services, Development of R&D and Innovation) with 111 action items were targeted.

Among the action plans, those related to cybersecurity are listed below:

- Internet Security
- e-Commerce Security Infrastructure
- Public Website Standardization and Hosting Service
- Public Safety Net
- Public Utilization Open-Source Software
- Information Systems Disaster Management Center
- Increasing the Use of e-Signature
- Legal Regulations Regarding Information Security
- National Information Systems Security Program

Ensuring a secure internet environment, establishing a secure communication network between public institutions, safeguarding the protection of national security information, legislative efforts for the protection of personal data, establishing a central structure (Computer Emergency Response Team-CERT) under TUBITAK to respond to computer incidents across the country, determining the cybersecurity levels of public institutions and eliminating their deficiencies and determining the minimum security levels on the basis of public organizations are among the most important targets for cybersecurity.

4.5. National cybersecurity strategy and 2013-2014 action plan (2013)

The previous strategy documents mainly contain objectives for the dissemination of ICT, and cybersecurity is considered as one of the secondary steps. The National Cyber Security Strategy and 2013-2014 Action Plan is the first nationwide document on cybersecurity on its own. The Cyber Security Council was established prior to the publication of this document by a Council of Ministers Decision released in Official Gazette No. 28447 on October 20, 2012 [26].

The Cyber Security Council, in collaboration with public and non-governmental organizations (NGOs), developed the strategy and action plan, which were publicized in the Official Gazette with the resolution of the Council of Ministers dated June 20, 2013, and numbered 28683 [32].

The action plan's goal is to create the legislative foundation for cybersecurity to maintain the security of critical infrastructures run by the public or private sectors, to protect the systems used in the services provided by public organizations and the data kept here, to develop cybersecurity technologies and to train human resources in this field.

The action plan includes 29 action items and 95 sub-action items under seven main topics. The main topics in the action plan are:

1. Making legal arrangements
2. Carrying out studies to assist the judicial processes
3. Creating a national-level organization for cyber incident response
4. Increasing the resiliency of the national cybersecurity infrastructure
5. Human resource development in the field of cybersecurity
6. Development of domestic cybersecurity technologies

7. Increasing the breadth of national security safeguards

With this strategy and action plan, it has been decided to establish the National Cyber Incidents Response Center (Turkish: Ulusal Siber Olaylara Müdahale Merkezi-USOM), which works on a 7x24 basis, instead of CERT, which was decided to be established within TÜBİTAK. USOM was established under the Information and Communication Technologies Authority (Turkish: Bilgi ve İletişim Teknolojileri Kurumu-BTK) according to the Communiqué on the Procedures and Principles Regarding the Establishment, Duties and Operations of Cyber Incidents Response Teams dated 11 November 2013 and numbered 28818 [33].

4.6. Information society strategy and action plan 2015-2018 (2015)

Türkiye's Information Society Strategy and Action Plan covering the period of 2015-2018 was released in the Official Gazette dated 6 March 2015 and numbered 29287 [27]. In the strategy and action plan, under eight main objectives (ICT sector, Sectoral competitiveness and broadband connectivity, Skilled manpower, ICT uptake, User trust and information security, ICT-enabled innovative techniques, Digital entrepreneurship and e-commerce, Public service efficiency), a total of 72 action items were arranged. Action items with cybersecurity are:

- Enactment of the Cyber Security Law
- Enactment of personal data protection legislation
- Creation of Cybercrime Strategy and Action Plan
- Raising awareness on secure internet use
- Establishment of Specialized Computer Crimes Courts

It is seen that the action plan focuses on legal issues in terms of cybersecurity, apart from the issue of secure internet use.

4.7. National cybersecurity strategy and 2016-2019 action plan (2016)

A committee comprised of members from government organizations, academia, NGOs, and private sector officials produced the National Cybersecurity Strategy and Action Plan 2016-2019 under the direction of the defunct Ministry of Transport, Maritime Affairs, and Communications. Even though the strategy document was published, since the action plan was classified, it was not shared with the public but relevant government organizations [28].

The strategic objectives determined to minimize the risks in the cyberspace and to provide a secure national cyberspace are as follows [28]:

- Creating a national critical infrastructure catalog, achieving critical infrastructure security criteria, and having these critical infrastructures audited by the regulatory organizations with whom they are affiliated.
- Establishment of legislation in line with international standards, including the audit approach in the field of cybersecurity.
- Developing the awareness and competencies with respect to regulatory and supervisory capabilities of organizations such as sector regulatory bodies and ministries.
- Creating regulations to safeguard organizations' information systems not just from cyberattacks, but also from human mistakes and mishaps.
- The ability of any organization to conduct its own information security management procedures.
- Increasing cybersecurity awareness among business leaders.
- Educating competent individuals in cybersecurity and encouraging workers, academics, and students that desire to specialize in this sector.
- Increasing cybersecurity awareness throughout society by conducting awareness campaigns in

the written and visual media, in addition to the actions of educational institutions.

- Providing legislative support for the employment of expert personnel in cybersecurity in government institutions and improving the personnel rights of the employees.

- Increasing the efficiency of institutional and sectoral CERTs by supplying assistance, producing financial adjustments, satisfying the need for skilled staff, setting up information infrastructure, and enhancing information exchange within the purview of the national incident response institution.

- Establishing a strong central governmental power to enforce cybersecurity coordination.

- Establishing a national cybersecurity ecosystem with wide participation from all of the stakeholders.

- Dissemination of best practices across the ecosystem for national cybersecurity, establishing consultancy services, vulnerability and threat information sharing, and application sharing.

- Conducting vulnerability research and certification studies to avoid the exploitation of vulnerabilities in local or foreign software and hardware items utilized in crucial components of computer systems.

- Establishing a culture of secure software development and supply management.

- Developing domestic products by attaching importance to R&D activities in order to reduce foreign dependency in cybersecurity.

- Development of national proactive cyber defense capabilities to prevent attackers before they strike.

- Deploying effective event management and IPv6 technology to prevent anonymity.

Actions to be taken to achieve the stated strategic goals are grouped under five strategic action titles:

1. Improving Cyber Defense and Critical Infrastructure Protection: It was planned to take actions to threats that may affect society, infrastructures and national economy.

2. Fighting Against Cybercrime: It was planned to take actions aimed at eliminating the threats causing financial losses that affect citizens and organizations.

3. Awareness and Human Resources Development: It was planned to carry out actions aimed at bringing a culture of cybersecurity to all segments of society, from corporate managers to computer users, and to train cybersecurity experts.

4. Developing a Cybersecurity Ecosystem: It was planned to take actions to determine and implement the requirements for all aspects of cybersecurity with the participation of all necessary stakeholders.

5. Integration of Cybersecurity into National Security: It was planned to take actions to reduce the damage that can be caused by deliberate attacks.

4.8. Presidential circular on information security measures (2019)

The Presidential Circular on Information Security Measures was published in the Official Gazette No. 30823 on July 6, 2019, with the goal of reducing and neutralizing security risks for information and information systems in the digital environment, as well as ensuring the security of key data types that may lead to serious consequences or disrupt social stability, especially when their security is compromised [29].

The circular consists of 21 articles in total. It was decided to create an Information and Communication Security Guide. Apart from the duties and activities performed for protecting national security and confidentiality, it was obligatory to comply with the procedures and principles included in the guide in the information systems to be established in all government organizations and enterprises providing critical infrastructure services. The

systems should be audited at least once a year, and the results should be reported to the Presidency Digital Transformation Office.

4.9. National cybersecurity strategy and 2020-2023 action plan (2020)

National Cybersecurity Strategy and 2020-2023 Action Plan was enacted with the Presidential Circular No. 2020/15 and the Official Gazette dated 29 December 2020 and numbered 31349 [30]. The strategy was released under the supervision of Ministry of Transport and Infrastructure, and the action plan was shared with only accountable and relevant government entities and organizations [34]. The following eight strategic objectives have been adopted in the document:

1. Securing critical infrastructure and enhancing resiliency
2. Building national capability
3. Creating an organic cybersecurity infrastructure
4. Providing security for emerging technologies
5. Combating cybercrime
6. Creation and promotion of national cybersecurity technologies
7. Integrating cybersecurity into national security
8. Developing international cooperation

According to the strategy document, cybersecurity is accepted as an essential component of national security, it was emphasized that transparency, accountability and ethical values should be taken into account while fulfilling the responsibilities for cybersecurity. It was also stated that the services provided through critical infrastructures should be provided uninterruptedly and effectively. Providing legal framework and the principle of using national products and services have been adopted by making the necessary investments.

The objectives set in the strategy are:

- Protecting critical infrastructures continuously.
- Possessing state-of-the-art cybersecurity technology.
- Creating in-house technological opportunities to meet operational requirements.
- Adopting proactive cyber defense and taking steps against cyber incidents.
- Measuring and monitoring the competency levels of CERTs.
- Improving the capabilities of cybersecurity manpower for incident response.
- Adopting risk analysis-based planning and enhancing the institutional, sectoral and national capabilities to deal with cyber incidents.
- Providing data sharing mechanisms within the cybersecurity ecosystem.
- Keeping the traffic domestic whenever the source and target of the data are domestic.
- Development of a cybersecurity approach based on regulation and supervision in critical infrastructure sectors.
- Preventing manufacturer dependency in IT products in critical infrastructure sectors.
- Determining the requirements for ensuring the security of emerging technologies.
- Incentivizing R&D and innovation to create national technologies and products.
- Maintaining secure use of cyberspace by society.
- Increasing citizens' cybersecurity awareness.
- Creating information security culture within organizations.
- Protecting children in the online environment.
- Enhancing the skills of cybersecurity manpower.

- Expanding cybersecurity education in formal and non-formal education and enriching the educational content.
- Creating venue for national and international secure information sharing.
- Reducing cybercrime and boosting cyber deterrence.
- Creating systems to ensure the distribution of correct and up-to-date information on social media and the internet.

5. Findings and Discussion

As mentioned in the literature review, research and guidance documents from leading organizations were analyzed to determine the scope, content and objectives of the NCSSs around the world. In the analysis for Türkiye, only the documents that directly target the cybersecurity strategy were included for the comparison. These documents are National Cybersecurity Strategy and 2013-2014 Action Plan, National Cybersecurity Strategy and 2016-2019 Action Plan, and National Cybersecurity Strategy and 2020-2023 Action Plan.

In terms of scope and content of the Turkish NCSSs, 10 criteria have been extracted from the referenced sources as shown in Table 2.

Table 2. Comparison of Content and Scope of the Turkish NCSSs

No	Topic	International Guides	Str2013	Str2016	Str2020
1	Standards and Technical Measures	G2-G12	+	+	+
2	Legal and Regulatory Measures	G1-G4, G6-G8, G10, G12	+	+	+
3	Cyber Incident Response	G1-G8, G10-G12	+	+	+
4	Developing Cybersecurity Capacity	G1-G3, G5-G12	+	+	+
5	Raising Cybersecurity Awareness	G1-G3, G5-G12	+	+	+
6	Organizational Measures	G1-G4, G6-G8, G10, G12		+	
7	R&D and Innovation	G2, G3, G6-G10, G12	+	+	+
8	Cybersecurity Sector	G2-G10, G12			+
9	International Cooperation and Partnership	G1-G12	+	+	+
10	Domestic Cooperation and Partnership	G1-G10, G12	+	+	+

According to the results of the comparison, the first strategy (Str2013) covers all but organizational measures and cybersecurity sector. The second strategy (Str2016) covers all but the cybersecurity sector. The last strategy (Str2020) covers all but organizational measures and actions for cybersecurity sector were addressed in this strategy. In short, it can be suggested that Turkish NCSSs cover most of the scope and content of the contemporary NCSSs, while there are shortcomings in terms of organizational measures and cybersecurity sector-related actions.

In terms of the objectives given in the Turkish NCSSs, 28 criteria have been extracted from the referenced sources as shown in Table 3.

The objectives in Table 3 were sorted out based on the number of referenced sources. Even if the number of sources is only one for the last six objectives, it should not be overlooked that these sources contain the common objectives of many countries. Therefore, one should not be mistaken that objectives from fewer sources are less important. According to the results of the comparison, Str2013 covers 16 (57%) of the common objectives, while Str2016 covers 18 (64%) and Str2020 covers 20 (71%).

Table 3. Comparison of Objectives of the Turkish NCSSs

No	Objective	International Guides	Str2013	Str2016	Str2020
1	Raise awareness	G1-G3, G5-G11	+	+	+
2	Strengthen training and educational programs	G1-G3, G-11	+	+	+
3	Engage in international cooperation	G1-G3, G5-G10	+	+	+
4	Establish a public-private partnership	G1-G3, G5-G8, G10	+	+	+
5	Establish incident response capacity	G2, G3, G5-G8, G10, G11	+	+	+
6	Address cyber crime	G2, G3, G5-G8, G10, G11		+	+
7	Foster R&D and innovation	G2, G3, G6-G10	+	+	+
8	Protect critical infrastructures	G2, G5-G8, G10, G11	+	+	+
9	Develop cybersecurity contingency plans	G2, G3, G6-G8, G10			
10	Organize cybersecurity exercises	G3, G5, G7-G10	+		+
11	Establish baseline security measures	G3, G6-G10			
12	Develop a clear governance structure	G1-G3, G5, G8		+	
13	Follow a national risk assessment approach	G2, G3, G7, G8	+	+	+
14	Recognize and protect individual rights (Balance security with privacy)	G3, G7, G8, G10	+	+	
15	Identify and engage stakeholders	G2, G3, G5, G7		+	+
16	Support private cybersecurity sector	G5, G7, G9, G10	+	+	+
17	Respect for fundamental values	G1, G5, G6	+	+	+
18	Establish and implement legislative framework	G1, G2, G6	+	+	+
19	Increase national cooperation	G7, G8, G10	+	+	+
20	Set the vision, scope, objectives and priorities	G2, G3	+	+	+
21	Establish trusted information sharing mechanisms	G3, G8			+
22	Protect national digital information resources	G6, G10			+
23	Adjust the national cybersecurity strategy	G3	+	+	+
24	Protect children online	G5			+
25	Allocate dedicated budget and resources	G8			
26	Create compliance mechanisms	G8			
27	Improve cybersecurity supply chain	G10			
28	Evaluate security level	G3			

In Turkish NCSSs, there are some objectives that were not captured in the referenced sources but are unique and specific to Türkiye, which are given in Table 4.

As it is seen in Table 4, integrating cybersecurity into broader national security is a common unique objective of all three NCSSs, and the most recent strategy covers several unique objectives while also covering the majority of the common objectives. Even though some of the objectives were not directly mentioned in the Turkish NCSSs, there are still regulations and actions taken to address those objectives. Developing cybersecurity contingency plans [35], establishing baseline security measures [29],

supply chain security, evaluation and compliance [29] are all addressed by government regulations.

It is suggested that a good strategic plan, if implemented with adequate budget and sufficient resources, provides significant benefits to organizations [35, 36]. Similarly, since the level of cybersecurity capabilities at a national level is a result of national strategies and action plans, it can be suggested that good strategies directly affect the success of the cybersecurity posture, together with the will and aspiration to perform written actions.

The Global Cybersecurity Index (GCI), developed by the ITU to assess the countries' commitment to cybersecurity, is one of the

measures to assess the success of national level cybersecurity strategies. GCI is a composite index with five pillars: 1) Legal measures, 2) Technical measures, 3) Organizational measures, 4) Capacity building, and 5) Cooperation [37]. Türkiye, which was 22nd in 2014 [38] but regressed to 43rd in 2017 [39]. It rose to the 20th rank in 2018 [40] and achieved the success of rising to the 11th rank among 194 countries in the latest GCI index, which was conducted in 2020 [41]. Since the content and scope of the common NCSSs as given in Table 2 cover the pillars of GCI, Türkiye's approach to cybersecurity strategies can be deemed successful from the scope and content perspectives.

Table 4. Unique and Specific Objectives in Turkish NCSSs

NCSS	Objectives
Str2013	Integration of the cybersecurity into national security
Str2016	Recruiting specialists in government organizations with better rights Creating national cybersecurity ecosystem Secure software development and procurement Improving proactive cyber defense capability Deployment of IPv6 protocol Integration of the cybersecurity into national security
Str2020	Improving proactive defense mindset Keeping domestic internet traffic within country Preventing manufacturer dependency in IT products in critical infrastructures Determining the requirements for ensuring the security of new generation technologies Minimizing cybercrime and increasing deterrence Organic cybersecurity network Security of new generation technologies Integration of the cybersecurity into national security Development and support of domestic and national technologies

6. Conclusion

National cybersecurity strategies provide guidance and framework for cybersecurity related actions and issues in countries. A lot of countries developed their strategies to prevent attacks, decrease risks, deter attackers, and

provide secure and available cyberspace to foster technology, economy, business and prosperity.

Organizations such as ITU, ENISA, OECD, e-GA, NATO and Oxford University published research and guidance documents by eliciting the best practices from several countries to assist the nations in developing their strategies. Based on the criteria derived from the worldwide research and studies, the scope, content and objectives of Türkiye's cybersecurity plans were examined in this article.

Turkish cybersecurity related strategies appeared in the early 2000s under the strategies addressing e-transformation and information society. The first strategy directly dedicated to cybersecurity was published in 2013 and then updated in 2016 and 2020. All three strategies cover most of the scope and content of the common NCSSs while lacking organizational and cybersecurity sector-related measures.

From the perspective of common objectives, Turkish strategies include most of the common objectives, while some of them (establishing trusted information sharing, protecting national digital information resources, budget and resource allocation, compliance mechanisms, supply chain security and evaluation) are not directly cited in the documents. Apart from the common objectives, Türkiye has specific objectives and supplementary directives that improve the cybersecurity posture.

National cybersecurity is such a complicated subject that no single solution can be viewed as a universally applicable across all countries and all local situations [7], and therefore there isn't a single policy solution for cybersecurity that works in every circumstance [13]. Based on the comparisons in this paper and Türkiye's rankings in ITU's GCI, it can be concluded that Turkish cybersecurity strategies are among the examples of successful ones in terms of scope, content and objectives, even though there are topics, as identified in this paper, that should be addressed.

This study does not evaluate either the outcomes of the strategies and action plans or whether the actions were performed successfully or not. A further study should be conducted to find out the

success of the implementation of the actions aimed in the strategies.

Article Information Form

Funding

The author has not received any financial support for the research, authorship or publication of this study.

Authors' Contribution

This article was written by the single author.

The Declaration of Conflict of Interest/ Common Interest

No conflict of interest or common interest has been declared by the authors.

The Declaration of Ethics Committee Approval

This study does not require ethics committee permission or any special permission.

The Declaration of Research and Publication Ethics

The authors of the paper declare that they comply with the scientific, ethical and quotation rules of SAUJS in all processes of the paper and that they do not make any falsification on the data collected. In addition, they declare that Sakarya University Journal of Science and its editorial board have no responsibility for any ethical violations that may be encountered, and that this study has not been evaluated in any academic publication environment other than Sakarya University Journal of Science.

Copyright Statement

Authors own the copyright of their work published in the journal and their work is published under the CC BY-NC 4.0 license.

References

- [1] ITU, "Definition of cybersecurity," 2022. <https://www.itu.int/en/ITU-T/studygroups/com17/Pages/cybersecurity.aspx>
- [2] NIST, "Cybersecurity," 2022. <https://csrc.nist.gov/glossary/term/cybersecurity>

- [3] F. Wamala, "ITU National Cybersecurity Strategy Guide," 2011. [Online]. Available: <https://www.itu.int/ITU-D/cyb/cybersecurity/docs/itu-national-cybersecurity-guide.pdf>
- [4] H. Çifci, Her Yönüyle Siber Savaş, 3rd ed. Ankara, Türkiye: TÜBİTAK, 2023.
- [5] E. Abdurahmanlı, "Siber İstihbarat Kapsamında: Echelon İstihbarat Sistemi," Academic Journal of History and Idea, vol. 8, no. 3, pp. 1212–1234, 2021.
- [6] D. Štililis, P. Pakutinskas, U. Kinis, and I. Malinauskaite, "Concepts and principles of cyber security strategies," Journal of Security Sustainability Issues, vol. 6, no. 2, pp. 199–210, 2016.
- [7] NATO CCD COE, "National Cyber Security Framework Manual," NATO CCD COE Publications, Tallinn, 2012.
- [8] ENISA, "National Cyber Security Strategies," 2012. [Online]. Available: <https://www.enisa.europa.eu/publications/cyber-security-strategies-paper>
- [9] OECD, "OECD Guidelines for the Security of Information Systems and Networks: Towards a Culture of Security," 2002. [Online]. Available: <https://www.oecd.org/sti/ieconomy/15582260.pdf>
- [10] The White House, "The National Strategy to Secure Cyberspace." 2003. [Online]. Available: <https://georgewbush-whitehouse.archives.gov/pcipb/>
- [11] ENISA, "National Cyber Security Strategies - Practical Guide on Development and Execution," 2012. [Online]. Available: <https://www.enisa.europa.eu/publications/national-cyber-security-strategies-an-implementation-guide>
- [12] OECD, "Cybersecurity Policy Making at a Turning Point - Analyzing a new generation of national cybersecurity

- strategies for the internet economy,” 2012. doi: 10.1787/5k8zq92vdgtl-en.
- [13] ENISA, “An Evaluation Framework for National Cyber Security Strategies,” 2014.
- [14] ENISA, “NCSS Good Practice Guide: Designing and Implementing National Cyber Security Strategies,” 2016
- [15] ITU, “Guide to Developing a National Cyber Security Strategy - Strategic Engagement in Cybersecurity,” Geneva, 2018. [Online]. Available: https://www.itu.int/dms_pub/itu-d/opb/str/D-STR-CYB_GUIDE.01-2018-PDF-E.pdf
- [16] ENISA, “Good Practices in Innovation Under NCSS,” 2019.
- [17] The European Parliament, Network and Information Security Directive, no. July. EU, 2016. [Online]. Available: <https://www.enisa.europa.eu/topics/nis-directive>
- [18] ENISA, “National Capabilities Assessment Framework,” The European Union Agency for Cybersecurity (ENISA), 2020.
- [19] T. Vaks, E. Maaten, O. Gross, E. Neeme, L. Luht, and K. Rousku, “National Cyber Security in Practice.” e-Governance Academy, Tallinn, 2020. [Online]. Available: https://ega.ee/wp-content/uploads/2020/05/Kuberturvalisuse_kasiraamat_ENG.pdf
- [20] Oxford GCSCC, “Cybersecurity Capacity Maturity Model for Nations (CMM),” 2021. [Online]. Available: <https://gcsc.ox.ac.uk/the-cmm>
- [21] H. Çakır and S. A. Uzun, “Türkiye’nin siber güvenlik eylem planlarının değerlendirilmesi,” Ekon. İşletme Siyaset ve Uluslararası İlişkiler Dergisi, vol. 7, no. 2, pp. 353–379, 2021.
- [22] TÜBİTAK-BİLGEM, “Tarihçe,” 2022. <https://uekae.bilgem.tubitak.gov.tr/tr/kurumsal/tarihce>
- [23] Prime Ministry of the Republic of Türkiye, Circular No. 2003/12: e-Transformation Türkiye Project. 2003. [Online]. Available: http://www.bilgitoplumu.gov.tr/Document s/1/Mevzuatlar/BasbakanlikGenelge_2003-12.pdf
- [24] Prime Ministry of the Republic of Türkiye, Circular No. 2003/48: e-Transformation Türkiye Short-Term Action Plan 2003-2004. 2003. [Online]. Available: <https://www.resmigazete.gov.tr/eskiler/2003/12/20031204.htm#3>
- [25] Prime Ministry of the Republic of Türkiye, 2006/38 Numbered Information Society Strategy and Action Plan 2006-2010. 2006. [Online]. Available: <https://www.resmigazete.gov.tr/eskiler/2006/07/20060728-7.htm>
- [26] Council of Ministers, Decision on the Execution, Management and Coordination of National Cybersecurity Studies. 2012. [Online]. Available: <https://www.resmigazete.gov.tr/eskiler/2012/10/20121020-18-1.pdf>
- [27] Ministry of Development, 2015-2018 Information Society Strategy and Action Plan. 2015. [Online]. Available: <https://www.resmigazete.gov.tr/eskiler/2015/03/20150306M1-2.htm>
- [28] Ministry of Transport Maritime and Communication, 2016-2019 National Cyber Security Strategy. 2016. [Online]. Available: <https://hgm.uab.gov.tr/uploads/pages/siber-guvenlik/2016-2019guvenlik.pdf>
- [29] Presidency of the Republic of Türkiye, Information and Communication Security Measures No. 2019/12. 2019. [Online]. Available: <https://www.mevzuat.gov.tr/MevzuatMeti n/CumhurbaskanligiGenelgeleri/20190706-12.pdf>

- [30] Presidency of the Republic of Türkiye, National Cyber Security Strategy No. 2020/15 and Action Plan for 2020-2023. 2020. [Online]. Available: <https://www.mevzuat.gov.tr/MevzuatMetin/CumhurbaskanligiGenelgeleri/20201229-15.pdf>
- [31] Prime Ministry of the Republic of Türkiye, 2005/5 Numbered e-Transformation Türkiye Project Action Plan for 2005. 2005. [Online]. Available: <https://www.resmigazete.gov.tr/Eskiler/2005/04/20050401-12.htm>
- [32] Council of Ministers, National Cyber Security Strategy and Action Plan 2013-2014. 2013. [Online]. Available: <https://www.resmigazete.gov.tr/eskiler/2013/06/20130620-1.htm>
- [33] Ministry of Transport and Infrastructure, Communique on Procedures and Principles Regarding the Establishment, Duties and Operations of Cyber Incidents Response Teams. 2013. [Online]. Available: <https://www.mevzuat.gov.tr/mevzuat?MevzuatNo=19004&MevzuatTur=9&MevzuatTertip=5>
- [34] Ministry of Transport and Infrastructure, 2020-2023 National Cyber Security Strategy. 2020. [Online]. Available: <https://hgm.uab.gov.tr/uploads/pages/strateji-eylem-planlari/ulusal-siber-guvenlik-stratejisi-ve-eylem-planlari-2020-2023.pdf>
- [35] Ministry of Transport and Infrastructure, “Minimum Information Security Criteria That Public Institutions Must Comply with,” 2013. [Online]. Available: <https://hgm.uab.gov.tr/uploads/pages/siber-guvenlik/asbk.pdf>
- [36] M. J. B. Kabeyi, “Organizational strategic planning, implementation and evaluation with analysis of challenges and benefits for profit and nonprofit organizations,” *International Journal of Applied Research*, 2019.
- [37] ITU, “GCI scope and framework,” 2019. [Online]. Available: https://www.itu.int/en/ITU-D/Cybersecurity/Documents/GCIv4/New_Reference_Model_GCIv4_V2.pdf
- [38] ITU, “Global Cybersecurity Index (GCI) 2014,” 2014. [Online]. Available: https://www.itu.int/dms_pub/itu-d/opb/str/D-STR-SECU-2015-PDF-E.pdf
- [39] ITU, “Global Cybersecurity Index (GCI) 2017,” 2017. [Online]. Available: https://www.itu.int/dms_pub/itu-d/opb/str/D-STR-GCI.01-2017-R1-PDF-E.pdf
- [40] ITU, “Global Cybersecurity Index (GCI) 2018,” 2019. [Online]. Available: https://www.itu.int/dms_pub/itu-d/opb/str/D-STR-GCI.01-2018-PDF-E.pdf
- [41] ITU, “Global Cybersecurity Index (GCI) 2020,” 2021. [Online]. Available: https://www.itu.int/dms_pub/itu-d/opb/str/D-STR-GCI.01-2021-PDF-E.pdf

Effect of Adhesion and Corrosion Performance of Geomet Basecoat (321)- Topcoat (ML Black) Applications on Cathophoretic Coating

İbrahim Usta^{1,2*} , Oğuz Yılmaz^{1,3} , Minel Gül^{1,4} , Ahmet Can¹ , Harun Gül² 

¹Uzman Kataforez Yüzey Kaplama San. ve Tic. A.Ş., Bursa, Türkiye, b16.ibrahim@gmail.com, oguzyilmaz@uzmankataforez.com, minelgul@uzmankataforez.com, ahmetcan@uzmankataforez.com

² Sakarya University of Applied Sciences, Metallurgy and Materials Engineering, Sakarya, Türkiye, b16.ibrahim@gmail.com, harungul@subu.edu.tr

³ Bilecik Şeyh Edebali University, Chemical Engineering, Bilecik, Türkiye, oguzyilmaz@uzmankataforez.com

⁴ Bursa Technical University, Department of Chemical, Bursa, Türkiye, minelgul@uzmankataforez.com

*Corresponding author

ARTICLE INFO

ABSTRACT

Keywords:

Cataphoresis

Geomet

Zinc Lamellar

Coating

Corrosion

Article History:

Received: 21.08.2023

Accepted: 05.12.2023

Online Available: 25.02.2024

This study aimed to improve corrosion resistance and adhesion of metallic materials typically used in automotive application. A combination of cathophoretic and Geomet coatings has been used to improve corrosion resistance. Firstly, cathophoretic coating was applied and then the coating process was completed with Geomet 321 and ML Black respectively. The results of the corrosion tests were classified into different categories such as adhesion, water resistance, moisture resistance, salt resistance and cyclic tests. The corrosion properties of the two- and three-layer coatings were found to improve as a function of both the sandblast pre-treatment and the post-cathophoresis curing temperature. The findings show that the adhesion strength and corrosion properties of Geomet 321 increases with curing temperature and sandblasting. This study will be a contribution to the future of protective coatings in the automotive industry by describing the process steps necessary to achieve optimum results.

1. Introduction

Metallic materials are widely used in automotive, aerospace, and chemical applications because of their strength, melting point, and hardness. However, corrosion resistance is poor in some metallic materials. Corrosion occurs when metal loses electrons or interacts with air, water, and chemicals. It may also affect the appearance and structural integrity of the metal [1]. Globally, the annual cost of corrosion is estimated to be approximately US \$2.5 trillion [2]. Therefore, improving corrosion properties are an important issue, especially for materials used in corrosive environments [3, 4].

Electrochemical, electrophoretic, galvanic, zinc, chromium, phosphate coatings have been proposed as the best, cheapest and most effective industrial methods of improving metallic corrosion properties [5–11]. Coatings provide a

physical barrier to metal surfaces, extending substrate life [12]. Electroplating and electroless coatings are generally used in the spacecraft and aerospace industry due to their high wear and corrosion properties and high cost [13,14]. Cathophoresis and Geomet coatings offer a more economical option than other coatings, as well as high corrosive resistance. That's why, these coating methods have become increasingly popular in the automotive industry. Cathophoresis coatings are widely used for corrosion protection of metal surfaces. In this method, the metal substrate is immersed in an electrolyte coating bath and an electric current form a thin film [15]. A cathophoretic coating offers an aesthetic appearance, a long service life and resistance to corrosion. Cathophoresis can also be used as a primer before many applications, and superior properties can be achieved with different coating techniques.

Cite as: I. Usta, O. Yılmaz, M. Gül, A. Can, H. Gül (2024). Effect of Adhesion and Corrosion Performance of Geomet Basecoat (321)- Topcoat (ML Black) Applications on Cathophoretic Coating, *Sakarya University Journal of Science*, 28(1), 220-236. <https://doi.org/10.16984/saufenbilder.1345904>

Zinc is the most used metal for corrosion protection. It exhibits a lower electrochemical potential than other metals [16–18]. Zinc does not corrode as toxic as cadmium and is suitable for anti-corrosive coatings [19]. The organic zinc lamellar coating (Geomet) is ideal for use in automotive materials. It provides impact, friction, chemical and corrosion resistance for bolts, nuts, hinges, and discs. Therefore, the second and third layers were Geomet 321 and Geomet ML Black after cataphoresis coating. These coatings contain metal oxide, zinc, and lamellar aluminium in their structure [20].

Philip et al. used accelerated corrosion tests (ACT) to investigate the differences between Zn-Fe and Geomet coatings. They observed that Zn-Fe coated screws developed white rust within one week, and after four weeks, significant red rust [21]. However, Geomet-coated screws showed much better corrosion resistance. No rust residues were observed after even eight weeks of exposure to ACT.

Another study compared the corrosion resistance of mechanical, hot-dip and Geomet coatings on a bolt using salt spray. The hot dip and mechanical zinc coatings corroded in a 750-hour corrosion environment while Geomet coatings showed no red-white rusting even after 1000 hours of corrosion [22]. It is also ideal for use on bolted joints, particularly where the bolt is subject to constant friction. It also eliminates the risk of hydrogen absorption associated with many electroplated zinc and zinc alloy coatings. Another advantage over electroplating is that the process is low cost and has significantly less environmental impact [23].

Geomet coatings are completely resistant to inorganic and organic solvents. They provide long term corrosion resistance due to their ability to withstand thermal shock [24]. Geomet coatings have been reported to not only improve the corrosion properties of the bolt coating, but also to provide lubricity, reduce bolt friction and extend service life [22, 25]. In combination with cataphoresis coatings, certain coating types can reduce high wear rates and maximise corrosion

resistance [26]. Non-hydrogen embrittlement lamellar coatings consist of a combination of zinc and aluminium flakes with a water-based inorganic coating. During application, the liquid is applied to the substrate and excess liquid is removed by centrifugal action. A final passivation process enhances the corrosion protection properties of the coating [27].

In this study two different pre-treatment methods, with and without sandblasting, were applied to the surface of the low carbon steel to develop a three-layer corrosion resistant coating process. The first layer was cataphoresis (I), the second layer was base coat (Geomet 321) (II) and the last layer was top coat (Geomet ML Black) (III). To optimise the corrosion resistance, different curing temperatures were used in the cataphoresis process. Adhesion and corrosion resistance of Basecoat 321 and Topcoat ML Black were investigated using water, humidity, salt and cycling tests to assess post-paint corrosion. The combined use of [C+B] and [C+B+T] coatings, the applicability of sandblasting pre-treatment and the effect of different curing temperatures (150, 175, 200, 210, 220, 230 °C) on the coatings were investigated, unlike other studies in the literature. Corrosion resistance was 50% better than other literature studies. The results showed that the best corrosion resistance was achieved with a three-layer coating (C+B+T) in combination with sandblasting pre-treatment and curing at 210°C.

2. Experimental Process

2.1. Materials

Low carbon steel (AISI 1040) substrates (75x50x5 mm) were used for the experimental coating. All Geomet and Cataphoresis coating chemicals were purchased from PPG and NOF Metal Coating. The coding system shown in Table 1 was used to product 2-layer and 3-layer coatings in the publication. After the necessary pre-treatments, the coatings were applied in two layers [C+B] and three layers [C+B+T].

Table 1. Coding of two- and three-layer coatings

COATING TYPE	CODE	LAYER
Cataphoresis+ Basecoat Geomet 321	[C+B]	Two Layer
Cataphoresis+ Basecoat Geomet 321+ Topcoat ML Black	[C+B+T]	Three Layer

To better understand the coating methods used in the paper, both coatings are presented in the form of a model in Figure 1. Figure 1(a) shows the two-layer coating, while Figure 1(b) shows the three-layer coating. All coating procedures and tests were carried out at "Uzman Kataforez San. ve Tic. Ltd. Şti".

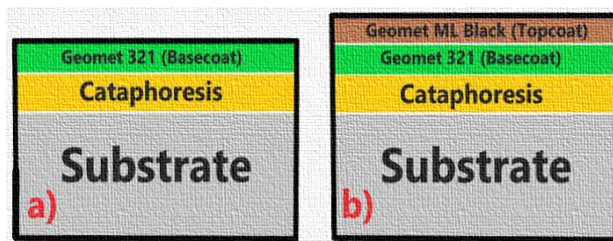


Figure 1. Cross-sectional model of the coatings (a: [C+ B] b: [C+ B+ T]).

2.2. Method and process

The effect of different curing temperatures applied to the cataphoresis coatings on the adhesion and corrosion properties of Basecoat and Topcoat was investigated. Figure 2 details the surface preparation of the specimens prior to cataphoresis and the application of Geomet Basecoat 321 and Topcoat ML Black. The variable parameters used in the experimental study, sandblasting, and degree of curing, are shown in different colours. Figure 2 shows the coatings applied to the substrate sample from top to bottom. First step two coats [C+B] and then three coats [C+B+T] were applied.

The first step in the pre-treatment process was an acid degreasing process to remove oil and contaminants from the sample surface. This gives the coating a better bond strength and then followed by rinsing and sandblasting.

Two different cataphoresis coatings were produced with the same parameters with and without sandblasting pre-treatment. Sandblasting is a mechanical method of roughening a material surface. Sandblasting can produce nanocrystalline surfaces, just like surface

treatment [28, 29]. Cast steel granular (S-70) powder with a density of 7 g/cm³ with a hardness of 40-50 HRC was used for the sand blasting process (12A; 10 min. blasting). The cutting action of the abrasive grit completely cleans the surface of the substrate and improves the surface quality. Sandblasting makes the surface rougher and cataphoresis coatings adhere better to the rough surface and provide better adhesion. After sandblasting, rinsing starts again; the necessary pre-treatments are shown in Figure 2.

Activation pre-treatment affects phosphate crystal structure and size [30]. The crystal grains in the coating are thick, especially in zinc phosphate baths. Excessive phosphorus in the coating structure makes the structure porous, greatly reducing corrosion resistance [31]. An activation process is necessary to reduce the size of the phosphate coating crystals. When zinc phosphate crystals are small and thin, a denser and more homogeneous coating forms. Therefore, prior to cataphoresis coating, the activation process plays an essential role in terms of bond strength and corrosion properties.

Phosphating is a process which is widely used for the improvement of corrosion resistance and materials surface structure like steel [31].

The phosphating process creates a thin, rough, and porous layer of phosphate on the surface. This layer ensures that the cataphoresis coating harmonises with the surface. For this reason, phosphating is considered a fundamental step in surface preparation for cataphoresis coating.

The formation of a zirconium passivation layer after phosphating provided greater corrosion resistance by filling the high porosity areas on the sample surface. It also improved the surface properties by increasing the adhesion of the organic coating to be applied (Geomet 321/ML Black). The phosphate film is not uniform on the surface. Passivation homogenises the phosphate and minimises the amount of air that can remain under the cataphoresis. After pre-treatment of the substrate, the first layer of cataphoretic coating was applied. The cataphoresis coating bath was prepared by selecting the concentration and parameters from a previous study [32, 33]. After cataphoresis coating, the paint on the sample surface was filtered twice, and curing processes

were performed at different temperatures (150, 175, 200, 210, 220, 230 °C) for 20 min.

curing window showing various curing times and temperatures at different panel temperatures.

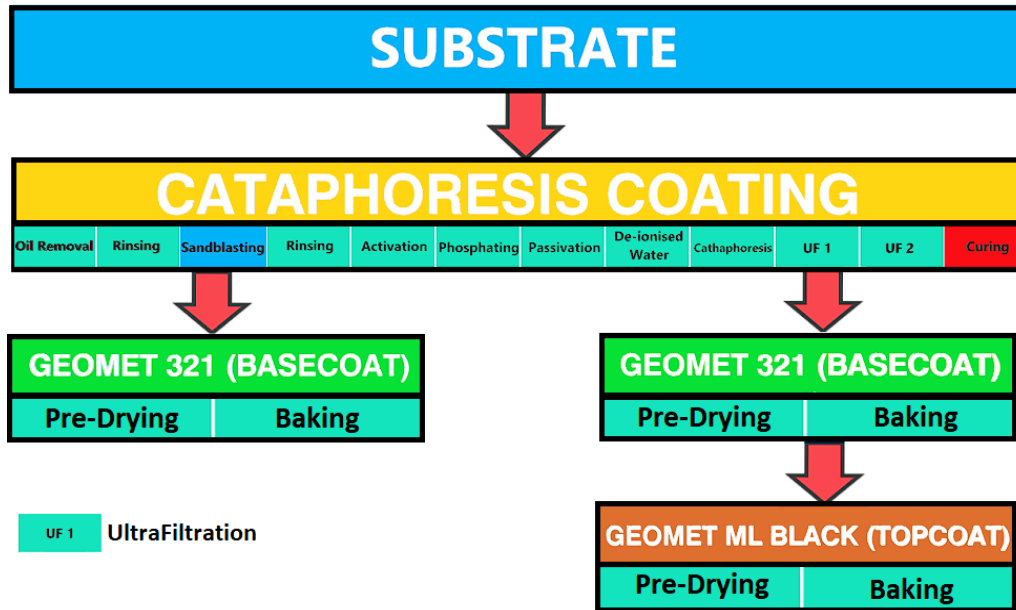


Figure 2. The pre-treatments and coating processes for [C+B] and [C+B+T]

After curing of the cataphoresis coatings, the Geomet coating process was started. Table 2 shows the parameters of the bath for the Basecoat 321 and the Topcoat ML Black coatings.

Table 2. Bath parameters of Geomet 321 and Geomet ML Black coatings

	PARAMETERS	
BASECOAT GEOMET 321	Temperature	20 °C
	Viscosity	90 s (DIN 4 Cup)
	Density	1,32 g/cm ³
	pH	8
	Solids Amount	%40
PRE-DRYING	Temperature	80-100 °C
	Time	6-10 min.
CURING	Temperature	300-320 °C
	Time	20 min.
	PARAMETERS	
	Temperature	24 °C
	Density	1,10
	Solids Amount	%25
	Coating Time	10 min.
	Temperature	80-100 °C
	Time	6-10 min.
	Temperature	300-320 °C
	Time	20 min.

The NOF chemicals concentration was adjusted using the chemical analyses methods presented by the company to achieve the optimum coating concentration for Geomet coating.

A curing window was used to evaluate the curing quality after cataphoresis. Figure 3 shows a

To produce a quality coating, the values in the curing temperature/time regions containing the inner regions of the red, blue, and black lines should be selected. For example, the curing time at 180 °C should be between 20 and 80 min in Figure 3. The curing window is used to prevent the formation of defects on the surface from being coated.

Increasing the curing temperature after cataphoresis may improve corrosion resistance by providing less permeability on the performance of anti-corrosion primers, or delamination and crack zones may occur due to stress and high hardness [34]. Thus, the degree of curing applied after cataphoresis coating is critical. In addition, a defect on the surface of the cataphoresis coating will adversely affect different types of coating to be applied to it.

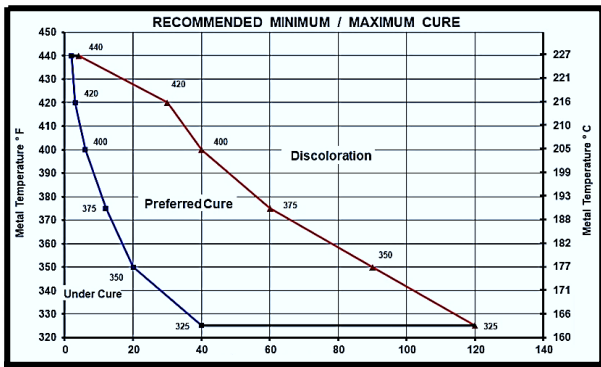


Figure 3. Curing window used for determining coating quality after drying [35]

Curing below 155 °C will cause the primer/metallic substrate interphase to become more active, increasing the coating's tendency to delamination. Too low a curing temperature reduces the bond strength of the coating to the substrate. The low binding density increased the delamination areas on the coating surface. The bond density of the coating to the substrate is very fast at very high curing temperatures. The speed of this binding density makes the cathoretic coating more brittle and reduces its corrosion performance [36]. In both cases, the cathoresis coating shows poor performance in corrosive environments. Therefore, the determination of the optimum curing temperature prior to Geomet coating is very important.

After cathoresis coating, Geomet 321 and then Geomet ML Black topcoats were applied on top of each other, using different pre-drying and curing degrees (150, 175, 200, 210, 220, 230) to obtain the optimum corrosion and adhesion result.

2.3. Testing process

The thickness of the cathoresis coating was measured using an Elcometer 456 Probe, while the weight of the Geomet coating was measured using a Fischerscope Hybrid System X Ray instrument. Contact angle measurements were performed with Theta Flex Contact Angle Measurement Device. Each sample was photographed with Canon EOS 600D camera for comparison of sample images after the test.

All the post-coating tests are shown in Figure 4. Adhesion testing is generally used to determine the bond strength and the force required to peel the coating from the substrate on surfaces such as painted surfaces. All samples were tested using a Qualtech Cross Cutting Tester (REF DIN ISO 2409) (6-blade system at 1mm pitch). Tests were performed at room temperature, $50 \pm 5\%$ relative humidity and constant pressure, with a tape width of 25 mm and an adhesive force of 6 - 10 N on glass. In the adhesion test, the coating surface to be tested is first cleaned and degreased, then cut

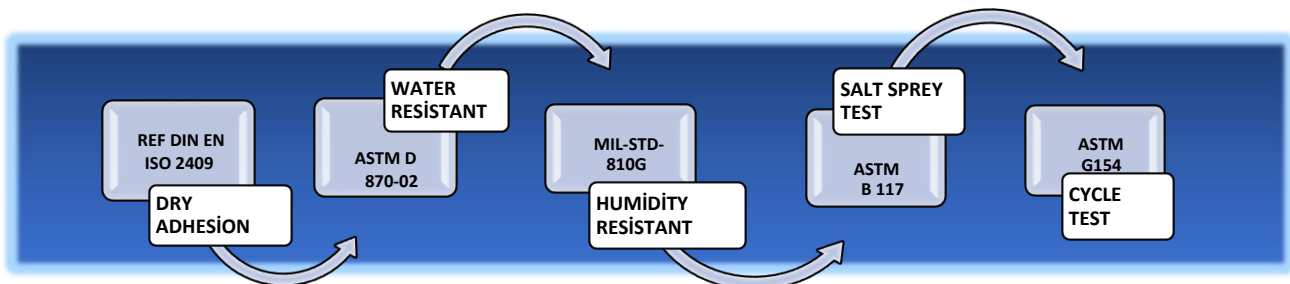


Figure 4. Tests applied after coatings are produced

Geomet 321 coatings were applied for 10 minutes at room temperature, pH 8. The speed of the centrifuge was 280 rpm for Geomet coatings. The Geomet 321 coatings were pre-dried at 90 °C and curing at 300 °C for 30 minutes. The application of the coating was carried out for 10 minutes at room temperature. The pre-drying and curing parameters used for the [C+B] coating was applied to the [C+B+T] coating, and the coatings were prepared for testing.

with a sharp tool (knife, razor blade) down to the substrate material (two cuts at 30-45°) to create edges where the coating can be removed.

Adhesive tape is applied over the cut area and pressed to the coating surface diagonally along the pattern. The tape is then pulled back in a parallel direction to the surface. When the coating peels off because of removing the tape; it will be concluded that the coating adhesion strength is insufficient.

The test area is visually inspected, and the adhesion strength is graded based on the amount of peel from the substrate surface [37]. Figure 5 shows a detailed model of the peel test.

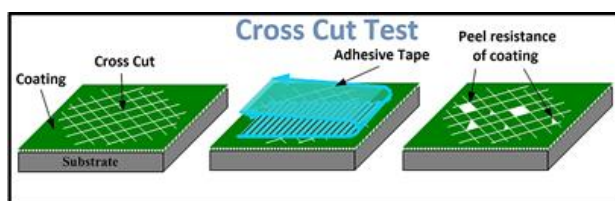


Figure 5. Cross-Cut Band Test Model [38]

The degree of peeling of coatings can be determined according to the ISO standard shown in Table 3. ISO 0-5 represents the peel rates of the coatings from the best to the worst.

Dry adhesion tests were first carried out on Geomet 321, and Geomet ML Black coatings pre-treated with and without sandblasting. The samples that passed the dry adhesion test were subjected to water and moisture resistance testing and then adhesion testing. After these tests, the adhesion and corrosion properties of the coatings were investigated by performing salt spray and cycle tests on the coatings that passed the adhesion test. Table 4 shows all tests and parameters. All adhesion tests were scored using the conditions shown in Table 3. "0" and "1" were considered successful and tested further, while "2", "3", "4" and "5" were considered failed and not tested further.

Table 3. Conditions for evaluating the amount of peeled coating after the Cross-Cut Tape Test [37]

Peel Type	Definition	Peel Degree
	Perfectly straight cut edges. No abrasions on the coating.	0
	Flaking of coatings in the crosscut mid-section. Less than 5%, no significant peeling visible.	1
	Intermediate areas and edges of the coating have peeling. (5- 15%)	2
	Partial or total breakage along the peel edges, partial or total breakage of individual pieces in wide strips and trims (15-35 %).	3
	Partial or total breakage of wide strips or individual squares. (35- 65%)	4
	Over 65% peel of coating from surface.	5

The water resistance tests (according to ASTM D 870-02 standard) of the coating samples produced within the scope of the study were

carried out in a BM 402 water bath (Figure 6) [39]. The samples were kept in deionised water at a constant temperature of $60\pm 2^\circ\text{C}$ in a water bath for 24 hours. After 24 hours, samples were removed from water bath and dried. Samples were kept at room temperature for two hours and adhesion tested. As a result of the peel test, no deformation (peeling) and no change in coating colour is expected.

The moisture resistance of the coating samples was also examined in a hot atmosphere (according to MIL-STD-810G Method 507.5) using a BM 402 water bath (Figure 6) [40]. It is relatively important for applications where the coating material is exposed to changes in different pressure or temperature.

Table 4. Test and parameters performed after coating

Test	Device	Temperature	Time (hours)
Water Resistant	BM 402	$60 \pm 2^\circ\text{C}$	24h
Humidity Resistant	BM 402	$40\pm 1^\circ\text{C}$	150h
Salt Spray (%5 NaCl)	ASCOT	35°C	1000h at 24h intervals
Cycle Test	Scania/STD4319	35°C	A single cycle lasts for 24h and there are 63 cycles to be completed (1512h.) (Fig 7).

This is because moisture in the atmosphere can react with the metal components on the coating, which can disrupt the coating integrity structure. To determine the moisture resistance, moisture testing was performed on the produced samples. Moisture can cause oxidation of the coating structure and chemical or electrochemical degradation of organic and inorganic surface coatings. The coating sample was kept at 40°C for 150 h for the moisture test.



Figure 6. Water and moisture resistance test (BM 402)

The resistance of a coating to corrosive environments is evaluated by salt spray testing. This test is performed by spraying salt on the coating surfaces placed in the test chamber and observing the corrosive effect on the material and the corrosion process. To ensure the correct application of this test, the ISO 9227 has been implemented in the ASTM B 117 standard [41]. The study used ASCOT as a corrosion chamber. The salt spray test creates a highly corrosive atmosphere using a standard 5% NaCl solution.

After testing, surface corrosion is evaluated according to standards and acceptance criteria. At the end of the test, the surface is expected to be free from staining, deformation, red rust (a max. of 5% rust [42].) and white rust due to corrosion. Figure 7 shows the cabinet in which the salt spray and corrosion cycle tests are conducted.

A method of evaluating the performance of a coating in a corrosive environment is corrosion cycle testing. It is then subjected to a series of temperature, moisture, and chemical tests. Cycle testing is performed using the Scania/STD4319 device according to ASTM G 154 and lasts 24 hours. A total of 63 cycles are completed by returning to the start after five repetitions. The parameters used in the cycle tests are detailed in Figure 8. These cycles evaluate coating material durability by examining corrosion, rusting and other material effects. After corrosion cycles, specimens are inspected for corrosion severity, coating quality, surface deformation, and other characteristics.



Figure 7. Cabinets for salt spray test (a) and cycle tests (b)

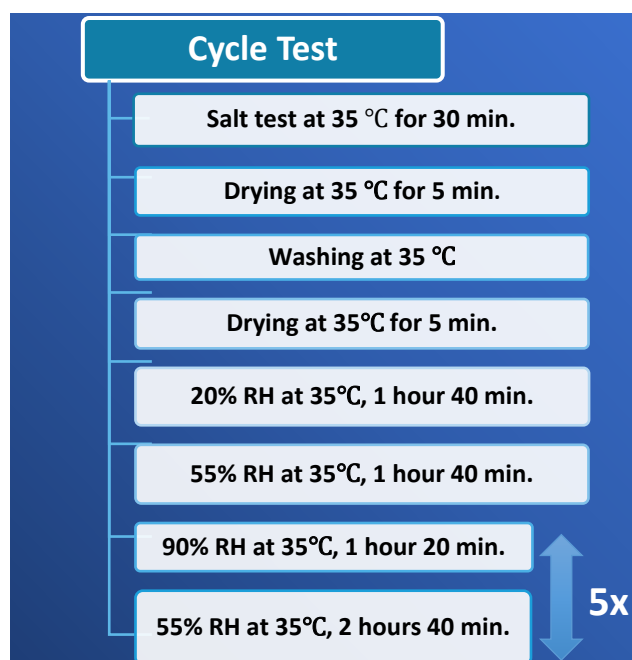


Figure 8. Cycle test parameters applied to coatings.

3. Conclusions and Discussion

It was observed that the average coating thickness after cataphoresis coating was 20 μm . The amount of coating per m^2 after Geomet coatings was obtained by dividing the weight difference before and after coating by the surface area. Densities of Geomet Basecoat and ML Black are presented in Table 5 as g/m^2 . Because of Geomet coatings are dip-spin processes, a homogeneous coating is not formed on the surface and therefore the coating thickness is given in gram per m^2 . For visual inspection, images of (a) C+B (white) and (b)C+B+T (black) samples after coating are shown in Figure 9.

Table 5. Geomet 321 and ML Black coating density (g/m^2)

Curing Degree ($^{\circ}\text{C}$)	Geomet 321 (g/m^2) (Basecoat)	ML Black (g/m^2) (Topcoat)
150	15.1	2.64
175	18.8	2.14
200	17.5	1.87
210	26.3	2.14
220	20.4	2.34
230	18.2	1.25

Firstly, surface images of Geomet 321 (Basecoat) were examined in Figure 9. The adhesion strength of Geomet 321 is low due to the low curing temperatures of 150 and 175 $^{\circ}\text{C}$ after cataphoresis. This is because the low curing

temperature creates delamination areas in the coating. As a first observation, curing at higher temperatures gives better adhesion to Geomet 321. Good adhesion was observed at all curing temperatures prior to Geomet ML Black (Topcoat) testing.

problem, and the sample was prepared for the next test.

Figure 10b shows the surface images of Geomet 321 coatings without sandblasting pre-treatment after dry adhesion test. Comparing the Geomet 321 coatings with and without sandblasting pre-

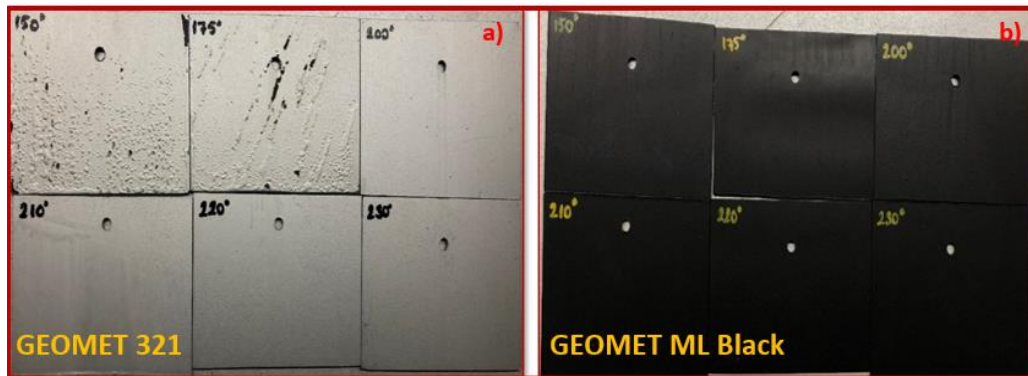


Figure 9. Surface images of after coating. (a: C+B b: C+B+T)

3.1.Dry adhesion test

The dry adhesion tests were carried out without any post coating corrosion test. Figure 10a shows the images of sandblasted C+B coatings after dry adhesion test. Table 6 shows the degree of peeling of Geomet 321 (Basecoat) coatings. The amount of peeling decreased with increasing curing temperatures. A high degree of peeling of the coating was clearly visible at a curing temperature of 150°. The coatings curing at 175, 200, 210, 220° were unsuccessful, although the amount of coating passing to the tape decreased with increasing curing temperatures. The coating curing at 230° has not been observed any peeling

treatment, the first impression is that the adhesion of the sandblasted samples is much better. In particular, the coatings at 150, 175 and 200° cured without sandblast pre-treatment were judged unsuccessful in the dry adhesion test due to excessive peeling. No peeling was observed at 210° curing temperature, and the test was therefore successfully passed.

Due to the low peel of the coatings, the samples treated at 220° and 230° were also eliminated. As a result, all second layer samples [C+B] that were not sandblasted except 210° were eliminated in the adhesion test.

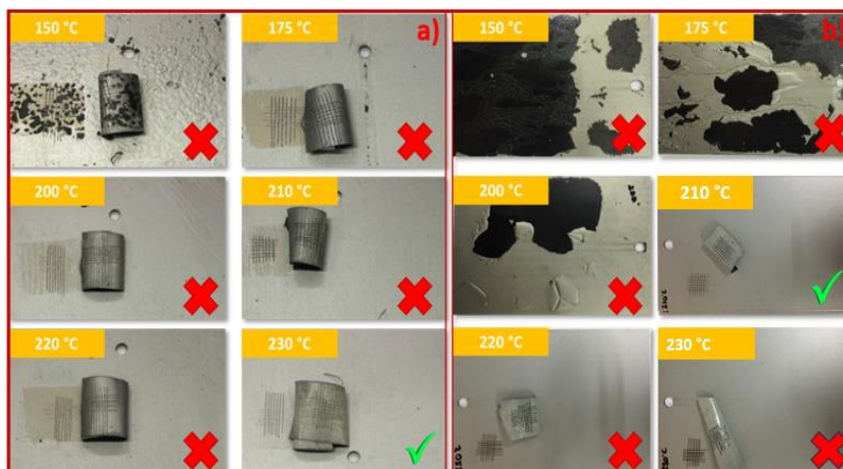


Figure 10. Surface images of Geomet 321 (Basecoat) coatings with different degrees of cure after cathaphoresis coating with (a) and without (b) sandblasting pre-treatment after dry adhesion test

Table 6. Dry adhesion test results of Geomet 321 (Basecoat) coatings with different degrees

Coating Type	Sandblasting Pre-treatment	Curing Degree (°C)	Peel Degree	Test Results
CATAPHORESIS + GEOMET 321 (BASECOAT)	APPLIED	150	5	FAIL
		175	4	FAIL
		200	3	FAIL
		210	3	FAIL
		220	3	FAIL
		230	0	PASSED
	NOT APPLIED	150	5	FAIL
		175	5	FAIL
		200	4	FAIL
		210	0	PASSED
		220	2	FAIL
		230	3	FAIL

Due to the low peel of the coatings, the samples treated at 220° and 230° were also eliminated. As a result, all second layer samples [C+B] that were not sandblasted except 210° were eliminated in the adhesion test.

dry adhesion test and were approved for water resistance testing. It can be said that the dry adhesion strength of ML Black topcoats is much higher than C+B coatings at all curing temperatures.

This is due to the silicate material contained in the ML Black coating. Zinc based coatings offer a higher level of adhesion due to their formation with an epoxy resin binder and an inorganic silicate [43]. Silicate material has been reported to be a good binder in previous studies [44]. In addition, reducing the grain size of the coating material can both improve the properties of the coating and provide better adhesion of the coating to the surface as a suitable binder [45]. Determination of solid-liquid interfacial tensions is essential in terms of corrosion properties. For this reason, contact angles of Geomet ML Black

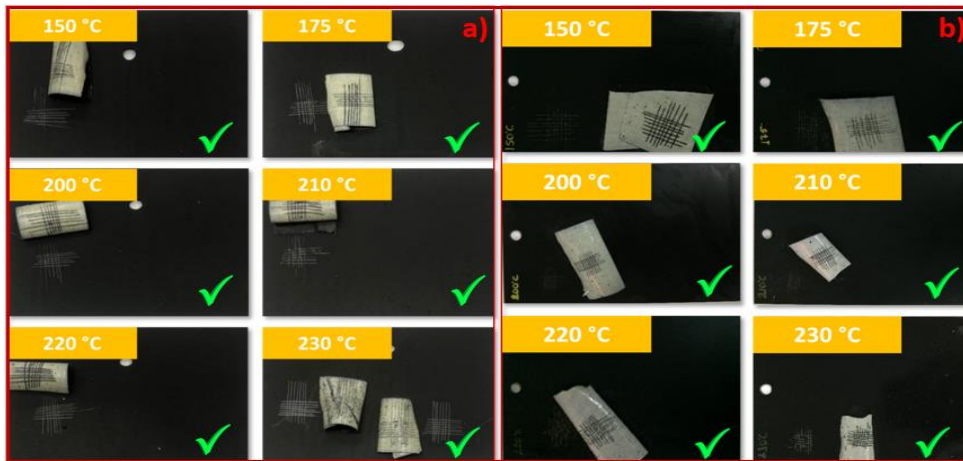


Figure 11. Surface images after dry adhesion test of Geomet 321 + ML Black coatings produced at different degrees of cure after cataphoresis coating with (a) and without (b) sandblasting

The images after the dry adhesion tests of C+B+T coatings with sandblasting pre-treatment at different curing degrees are presented in Figure 11a, and the test results are presented in Table 7.

The coatings passed the dry adhesion test at all curing temperatures. ML Black coatings were found not to peel from the surface and to adhere well when all surface images were analysed.

Figure 11b shows the surface images of Geomet ML Black coatings without sandblasting pre-treatment and with different degrees of curing. As with sandblasted coatings, no peeling was observed at all cure levels; all samples passed the

(Topcoat) coatings were measured before water, humidity, salt fog and cycling tests.

Table 7. Dry adhesion test results of C+B+T coatings with different degrees of cure after cataphoresis

Coating Type	Sandblasting Pre-treatment	Curing Degree (°C)	Peel Degree	Test Results
CATAPHORESIS + GEOMET 321 (BASECOAT) + GEOMET ML Black (TOPCOAT)	APPLIED	150	1	PASSED
		175	1	PASSED
		200	0	PASSED
		210	0	PASSED
		220	0	PASSED
		230	1	PASSED
	NOT APPLIED	150	1	PASSED
		175	1	PASSED
		200	1	PASSED
		210	0	PASSED
		220	0	PASSED
		230	1	PASSED

Contact angle measurements were performed with Theta Flex Contact Angle Measurement Device. The contact angle is determined according to a certain standard in a material where corrosion resistance is required. Typically, the aim is to create a hydrophobic (water-repellent) effect on the coating surface to improve corrosion resistance. This is the way in which a drop of water spreads or collects on the surface of a material [46]. Increasing the contact angle allows the water droplet to spread and flow more, rather than collecting in a small area on the surface. Therefore, the effect of after coating curing on the contact angle was investigated.

Figure 12 shows a graph of the contact angles on the coating surface. This shows a progression from a spreading (most wettable) to a non-wetting contact angle with increasing contact angle. Increasing the contact angle reduces the liquid penetration on the coating sample surface. It increases the corrosion resistance of coatings by reducing the surface defect/corrosion rate that will occur over time [47].

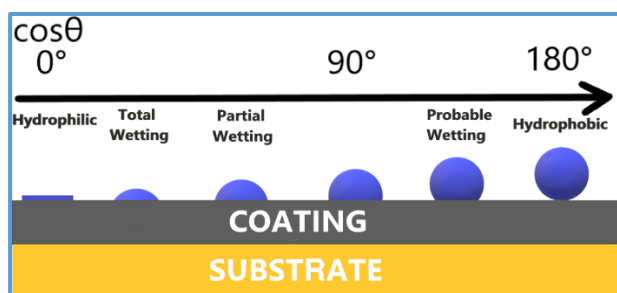


Figure 12. Hydrophobicity and hydrophilicity varying with contact angle. (Adapted from Tylkowski B. and Tsihranska I.) [47].

The contact angles of the coatings increased according to the contact angle of the substrate. The contact angle of the low carbon steel substrate was reported to be 49.5° in previous studies [48]. Compared to the contact angles after coating and substrate, the contact angles increased by an average of 42% according to substrate (Figure 13). It can be said that the coatings tend from a hydrophilic to a hydrophobic structure with an increase in the contact angle. This increased contact angle reduced liquid retention on the coating surface and improved corrosion resistance. The coating samples were observed to increase to a contact angle of 73° with an increasing degree of curing.

A whole wetting angle is observed in the substrate, and a partial wetting angle is observed in the coatings when this contact angle is evaluated on the graph. This result proves that the coating with high wetting angle provides the best corrosion properties.

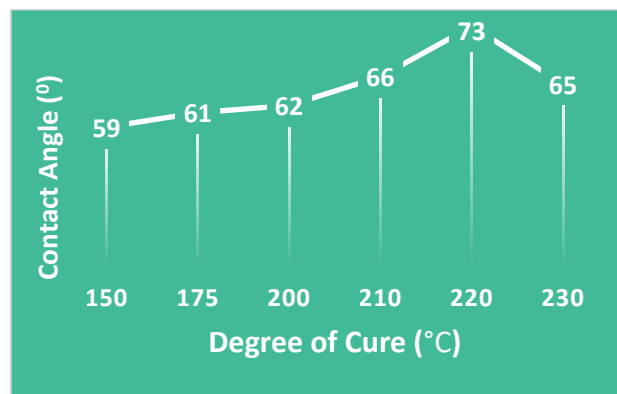


Figure 13. Effects of curing degrees after cataphoresis on coating contact angles (C+B+T)

3.2. Water resistance test

After the water resistance test, adhesion tests were performed on the with (a) without (b) sandblasted C+B+T and C+B (indicated in yellow) coatings produced at different curing temperatures and their surface images are presented in Figure 14. Table 8 shows the adhesion test results graded according to the standard. After the water resistance test, the samples produced at 150, 175, and 200 curing degrees in sandblasted (a) coatings after the water resistance test have not been pass the test as some of the coating layer passed into the adhesion band after the adhesion test. It was concluded that this situation affected the adhesion resistance due to the low bond density of the coatings on the substrate surface at low curing temperatures.

No peeling was observed at 210 and 220° curing degrees and these samples passed the test. In the case of the non-sandblasted coatings, the samples produced at high cure rates (210° (C+B), 220°(C+B+T) were not stripping from the surface after the water test and prepared for the moisture resistance test. The non-sandblasted coatings at 150, 175 and 200° curing failed the adhesion test after the water test. The coatings peeled off the surface at low curing temperatures with a water resistance effect. According to the

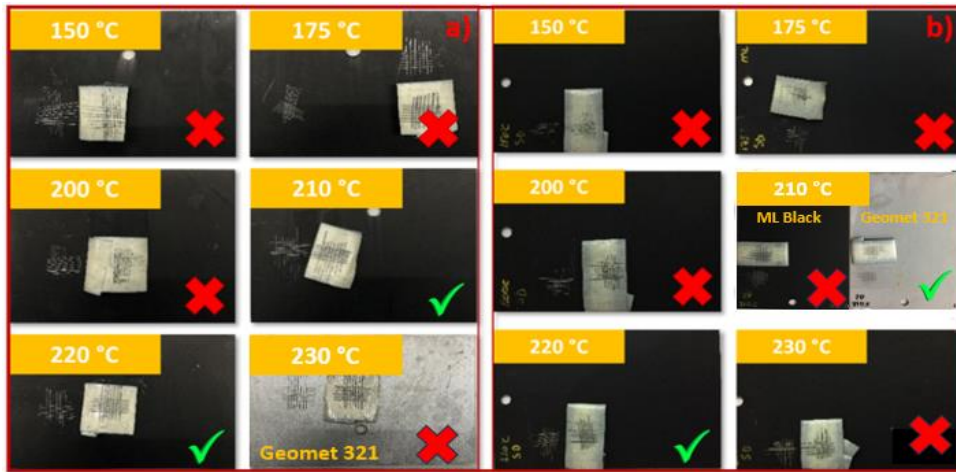


Figure 14. C+B+T (three layer) coatings surface image of after water resistance

test results, curing temperatures above 200°C increased corrosive performance and adhesion resistance. However, there was surface shrinkage due to rapid drying and a reduction in bond strength when cured at 230°C with and without sandblasting.

Table 8. Adhesion test results after water resistance of Geomet ML Black

Coating Type	Sandblasting Pre-Treatment	Curing Time (°C)	Peel Degree	Test Results
CATAPHORESIS + GEOMET 321 (BASECOAT) + GEOMET ML Black (TOPCOAT)	APPLIED	150	3	FAIL
		175	2	FAIL
		200	2	FAIL
		210	1	PASSED
		220	0	PASSED
		230	4	FAIL
		230 (Geomet 321)	4	FAIL
	NOT APPLIED	150	3	FAIL
		175	3	FAIL
		200	2	FAIL
		210	3	FAIL
		210 (Geomet 321)	1	PASSED
		220	0	PASSED
		230	2	FAIL

3.3. Moisture resistance test

In order to investigate the reaction of the sandblasted (a) and non-sandblasted (b) coatings in a hot and humid atmosphere, a moisture resistance test was carried out on Geomet 321 and Geomet ML Black coatings. The tape adhesion tests of the coatings with (a) and without (b) sandblasting after moisture resistance test is presented in Figure 15. The adhesion test results determined according to the standard are given in Table 9.

Table 9. Adhesion test results after moisture resistance of Geomet ML Black coatings

Coating Type	Sandblasting Pre-treatment	Curing Degree (°C)	Peel Degree	Test Results
CATAPHORESIS + GEOMET 321 (BASECOAT)	APPLIED	210	0	PASSED
		220	4	FAIL
CATAPHORESIS + GEOMET ML Black (TOPCOAT)	NOT APPLIED	210 (Geomet 321)	0	PASSED
		220	0	PASSED

After the moisture resistance test, the sandblasted C+B+T coating curing at 220° failed the moisture resistance test, while the curing at 210° and passed the test successfully. This is because to the brittle structure of the coatings after cataphoresis with the increase in bond density with high curing temperature. In addition, the surface contact area decreases with the increase in the lamellar structure of Geomet coatings [49]. The 2-layer [C+B] and 3-layer [C+B+T] coatings at 210° without sandblasting pre-treatment passed the test. Curing at 220° without sandblasting [C+B+T], coatings passed the test, and the samples that passed the test were prepared for salt testing.

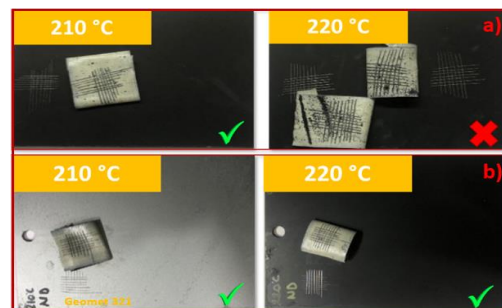


Figure 15. Adhesion test surface images of Geomet ML Black coatings with (a) and without (b) sandblasting after moisture resistance

3.4. Salt spray test

Illustrated in Figure 16 are the surface images after the salt test, depicting coatings both with (a) and without (b) prior to sandblasting pre-treatment. Following the conclusion of the test, an absence of corrosion indications was noted on the ML Black topcoat, which had undergone curing at 210° after the cataphoresis process. The cataphoresis + Geomet 321 coating cured at 210°, and the ML Black topcoat cured at 220° failed this test due to corrosion. The non-sandblasted Geomet 321 coating at 210°C has not been pass the salt test due to the formation of too many red rust patches. Due to the formation of red and white rust patches, the non-sandblasted ML Black coating surface (220) also failed the test.

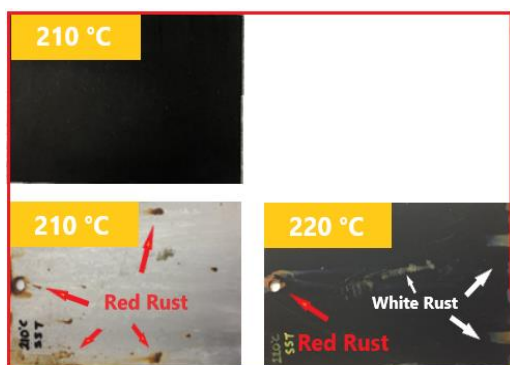


Figure 16. Surface images of Geomet ML Black coatings with (a) and without (b) sandblasting after salt test

3.5. Cycle test

The surface image of C+B+T coating curing at 220° after sandblasted cataphoresis coating is given in Figure 17a. The surface images of the 321-coating curing at 210° without sandblasting and the C+B+T coating curing at 220° are presented in Figure 17b. Since the cycle test is more aggressive than the salt test, C+B curing at 210° and Topcoat Geomet ML Black coating

curing at 210, and 220° were retaken into the cycle test after the salt test.

The best corrosion performance was obtained by curing at 210 and 220°C. The basecoat Geomet 321 coating without sandblasting passed the cycle test as no red rust formation was observed, although white rust residue was formed at 210°C curing condition. Topcoat ML Black coatings curing at 210°C with sandblasting and 220°C without sandblasting successfully passed the cycle test as no red rust formation was observed. As a result, all the coating samples shown in Figure 17 passed the cyclic corrosion test for 1512 hours.

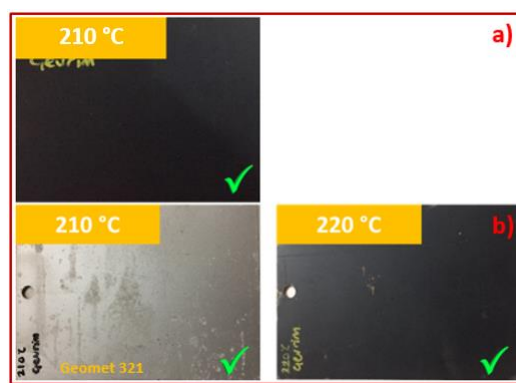


Figure 17. Post-cycle surface images of C+B+T coatings

The cycle results of the zinc coatings, Geomet coating, and the results obtained in the study after the salt test are shown in Table 10 for comparison with the study. According to these results in the literature, alkaline Zn, Zn-Fe, and Zn-Ni coatings withstood the cyclic salt test for 300 hours, 360 hours, and 720 hours, respectively [50, 51]. These values were increased to 1008 hours with more innovative Geomet coatings. In this study, Basecoat 321 and Topcoat ML Black coatings applied on cataphoresis have not been observed red and white rust formation even in the 1512 hours (63 cycles) salt test. It was concluded that

Table 10. Comparison of corrosion properties of coating after Salt Spray

	Alkaline Zn Coating [50]	Alkaline Zn-Fe Coating [50]	Alkaline Zn-Ni Coating[50]	Cataphoresis Coating [51]	[Basecoat 321] + [Topcoat ML Black] [52]	[Cataphoresis] + [Basecoat 321] + [Topcoat ML Black] (This paper)
Corrosion Resistance	300 hours	360 hours	720 hours	720 hours	1008 hours	1512 hours
Cyclic Corrosion Resistance	13 cycles	15 cycles	30 cycles	30 cycles	42 cycles	63 cycles

the cathaphoretic intermediate coat applied prior to the Geomet coating increased the corrosion resistance of the Geomet (321 + ML Black) coatings by 50 percent.

As a result, Cataphoresis and Geomet coating, which have superior corrosion resistance, were deposited together on a similar substrate, resulting in much higher corrosion resistance to corrosion environments.

Low curing temperatures which led to delamination and reduced bond strength. The first test applied to the coating samples, water resistance, was successful at 210 and 220 °C. The coating layer shrinkage due to rapid drying and had a brittle structure at the high curing temperature (230°C).

In addition, the rapid drying of the cataphoresis coating resulted in a rough and inhomogeneous

Table 11. Comparative test results of [C+B] and [C+B+T]

		✓	Samples passing the test					
		X	Sample that failed the test					
		-	Untested sample (Sample that failed to pass the previous test)					
Coating Type	Sandblasting Pre-treatment	Cure Degree (°C)	Dry Adhesion Test	Water Resistant Test	Moisture Resistance	Salt Test	Cycle Test	RESULT
Cataphoresis + GEOMET 321 (2 Layer)	APPLIED	150	X	-	-	-	-	FAIL
		175	X	-	-	-	-	FAIL
		200	X	-	-	-	-	FAIL
		210	X	-	-	-	-	FAIL
		220	X	-	-	-	-	FAIL
		230	✓	X	-	-	-	FAIL
	NOT APPLIED	150	X	-	-	-	-	FAIL
		175	X	-	-	-	-	FAIL
		200	X	-	-	-	-	FAIL
		210	✓	✓	✓	X	✓	PASSED
		220	X	-	-	-	-	FAIL
		230	X	-	-	-	-	FAIL
Cataphoresis + GEOMET 321 + ML Black (3 Layer)	APPLIED	150	✓	X	-	-	-	FAIL
		175	✓	X	-	-	-	FAIL
		200	✓	X	-	-	-	FAIL
		210	✓	✓	✓	✓	✓	PASSED
		220	✓	✓	X	-	-	FAIL
		230	✓	X	-	-	-	FAIL
	NOT APPLIED	150	✓	X	-	-	-	FAIL
		175	✓	X	-	-	-	FAIL
		200	✓	X	-	-	-	FAIL
		210	✓	X	-	-	-	FAIL
		220	✓	✓	✓	X	✓	PASSED
		230	✓	X	-	-	-	FAIL

Analysing the dry adhesion results in Table 11, Geomet ML Black topcoat shows much better adhesion than Geomet 321 basecoat. This is due to the silicate material in the Geomet ML Black topcoat. The sandblast effect was positive for the topcoats, while it was negative for the 321 coatings. According to corrosive test results, increasing curing temperatures obtained good results for both two- and three-layer coatings.

structure, which adversely affected the corrosion properties due to the uneven deposition of the Geomet coatings on the surface.

4. Conclusion

In summary, the study evaluated the performance of the Geomet coatings, specifically the Geomet 321 basecoat and the Geomet ML Black topcoat, applied by means of a cataphoresis process. The results showed that the adhesion strength of

Geomet 321 is influenced by the curing temperature, with higher temperatures resulting in better adhesion. Dry adhesion tests showed that using sandblasting as pre-treatment significantly improved adhesion, especially at higher curing temperatures.

The contact angle measurements showed that an increase in the curing temperature resulted in a transition of the coatings from a hydrophilic to a hydrophobic structure, thus improving the corrosion resistance. The water resistance tests confirmed the effectiveness of the coatings cured at 210°C and 220°C, while the adhesion and performance at lower curing temperatures were found to be inadequate. The moisture resistance test highlighted the embrittlement of coatings at high curing temperatures, which affected adhesion and performance.

The salt spray tests identified the optimum curing conditions for corrosion resistance, with coatings cured at 210°C showing superior performance.

The cycle test, a more aggressive assessment, confirmed the corrosion resistance of Cataphoresis + Geomet321 + ML Black lasting 1512 hours (63 cycles) without red or white rust formation. As a result, 50% superior corrosion resistance was obtained compared to other studies in the literature.

Article Information Form

Acknowledgments

The authors would like to thank UZMAN Kataforez for providing laboratory and analysis facilities.

Funding

The authors have not received any financial support for the research, authorship, or publication of this study.

Authors' Contribution

Conceptualization, İ.U. and O.Y.; methodology, M.G.; validation, İ.U.; writing—original draft preparation, İ.U.; writing—review and editing, İ.U, M.G, and O.Y; supervision, M.G.; project administration, A.C. All authors have read and agreed to the published version of the manuscript.

The Declaration of Conflict of Interest/ Common Interest

No conflict of interest or common interest has been declared by the authors.

The Declaration of Ethics Committee Approval

This study does not require ethics committee permission or any special permission.

The Declaration of Research and Publication Ethics

The authors of the paper declare that they comply with the scientific, ethical and quotation rules of SAUJS in all processes of the paper and that they do not make any falsification on the data collected. In addition, they declare that Sakarya University Journal of Science and its editorial board have no responsibility for any ethical violations that may be encountered, and that this study has not been evaluated in any academic publication environment other than Sakarya University Journal of Science.

Copyright Statement

Authors own the copyright of their work published in the journal and their work is published under the CC BY-NC 4.0 license.

References

- [1] G. Koch, "Cost of corrosion," Trends in oil and gas corrosion research and technologies: Production and transmission, Elsevier Inc., A. M. El-Sherik, 2017, pp. 3–30.
- [2] J. Kinugasa, F. Yuse, M. Tsunazawa, M. Nakaya, "Effect of corrosion resistance and rust characterization for hydrogen absorption into steel under an atmospheric corrosion condition," ISIJ International, vol. 56, pp. 459–464, 2016.
- [3] H. Li, Y. He, P. Luo, Y. Fan, H. Yu, Y. Wang, T. He, Z. Li, H. Zhang, "Influence of pulse frequency on Corrosion Resistance and Mechanical Properties of Ni-W/B₄C Composite Coatings," Colloids

- Surface A Physicochemical Engineering Asp, vol. 629, 127406, 2021.
- [4] A. Karadag, E. Duru, M. Uysal, H. Akbulut, "Tribological performance of Ni-W/PTFE composite coating," vol. 26, no. 4A, pp. 2885–2893, 2022.
- [5] H. Gül, M. Uysal, H. Akbulut, A. Alp, "Effect of PC electrodeposition on the structure and tribological behavior of Ni-Al₂O₃ nanocomposite coatings," Surface Coating Technology, vol. 258, pp. 1202–1211, 2014.
- [6] Y. Yang, L. Qu, L. Dai, T. S. Kang, M. Durstock, "Electrophoresis coating of titanium dioxide on aligned carbon nanotubes for controlled syntheses of photoelectronic nanomaterials," Advanced Materials, vol. 19, no. 9, pp. 1239–1243, 2007.
- [7] S. M. A. Shibli, B. N. Meena, R. Remya, "A review on recent approaches in the field of hot dip Zinc Galvanizing process," Surface Coating Technology, vol. 262, pp. 210–215, 2015.
- [8] A. R. Marder, "The metallurgy of Zinc-Coated steel," Progress in Materials Science, vol. 45, no. 3, pp. 191–271, 2000.
- [9] H. Cheng Yu, B. Zhen Chen, X. Shi, X. Sun, B. Li, "Investigation of the Trivalent-Chrome Coating on 6063 Aluminum Alloy," Materials Letters, vol. 62, no. 17–18, pp. 2828–2831, 2008.
- [10] P. K. Sinha, R. Feser, "Phosphate coating on steel surfaces by an electrochemical method," Surface Coating Technology, vol. 161, no. 2–3, pp. 158–168, 2002.
- [11] H. Gul, İ. Usta, "Effect of Alumina Concentration on morphology, wear, and corrosion: Electroless Ni-W-P/Al₂O₃ composite coatings on aluminum surfaces," Journal of Materials Engineering and Performance, vol. 32, no. 13, pp. 6107–6122, 2023.
- [12] A. López-Ortega, R. Bayón, J. L. Arana, "Evaluation of protective coatings for offshore applications. Corrosion and tribocorrosion behavior in synthetic seawater," Surface Coating Technology, vol. 349, pp. 1083–1097, 2018.
- [13] J. R. Lince, "Effective application of solid lubricants in spacecraft mechanisms," Lubricants, vol. 8, p. 74, 2020.
- [14] H. C. Barshilia, "Surface modification technologies for aerospace and engineering applications: Current trends, challenges and future prospects," Transactions of the Indian National Academy of Engineering, vol. 6, no. 2, pp. 173–188, 2021.
- [15] W. Skotnicki, D. Jędrzejczyk, "The Comparative analysis of the coatings deposited on the automotive parts by the cataphoresis method," Materials, vol. 14, no. 20, p. 6155, 2021.
- [16] M. Doerre, L. Hibbitts, G. Patrick, N. K. Akafuah, "Advances in automotive conversion coatings during pretreatment of the Body Structure: A Review," Coatings, vol. 8, no. 11, p. 405, 2018.
- [17] N. Sorour, W. Zhang, E. Ghali, G. Houlachi, "A review of organic additives in Zinc Electrodeposition process" Hydrometallurgy, vol. 171, pp. 320–332, 2017.
- [18] "Home | ZINC. International Zinc Association. (2023, Jul. 17). Zinc essential for modern life [Online]. Available: <https://www.zinc.org/>
- [19] N. Rawal. (2023). The Characteristics, Toxicity and Effects of Cadmium [Online]. Available: <https://www.researchgate.net/publication/305778858>
- [20] R. Ding, S. Chen, J. Lv, W. Zhang, X. Zhao, J. Liu, X. Wang, T. Gui, B. Li, Y.

- Tang, W. Li, "Study on graphene modified organic anti-corrosion coatings: A comprehensive review," *Journal of Alloys and Compounds*, vol. 806, pp. 611–635, 2019.
- [21] B. Philip (2011). Evaluation of Corrosion in Crevices in Screw Joints Mats Thörnqvist [Online]. Available: <https://www.diva-portal.org/smash/get/diva2:441388/FULLTEXT01.pdf>
- [22] D. Zhmurkin, "Corrosion Resistance of Bolt Coatings Technical Paper," Tyco Electronics Harrisburg, PA, pp. 1-7, 2009.
- [23] Benseler. (2023). New Dip-Spin System for Zinc Flake Coatings on Rack Parts All-Over Coating [Online]. Available: <https://www.benseler.de/en/verfahren/beschichtung/geomet.php>
- [24] "Geomet Coating. (2023). Keys & Clamps." [Online]. Available: <https://www.keytechno.com/service/geomet-coating/>
- [25] K. Westphal, "An optimized coating system for fasteners with metric threads," *ATZ Worldwide*, vol. 107, no. 5, pp. 8–10, 2005.
- [26] R. B. Egêa, A. Primolini, B. I. Da Maia, "Development of friction coefficient controller for E-coat (KTL)," *SAE Technical*, 2018-36-0200, 2018.
- [27] B. Oleksiak, K. Kołtało, R. Poloczek, "Application methods and selected properties of Zinc Flake coatings," *Metalurgija*, vol. 60, pp. 162–164, 2021.
- [28] M. R. Isa, O. S. Zaroog, M. A. Yunus, V. R. Sanny Bavu, N. Rosmi, "Effect of sandblasting process on mechanical properties of ASTM A516 Grade 70 Steel," *Key Engineering Materials*, vol. 765, pp. 222–226, 2018.
- [29] A. Rudawska, I. Danczak, M. Müller, and P. Valasek, "The effect of sandblasting on surface properties for adhesion," *International Journal of Adhesion and Adhesives*, vol. 70, pp. 176–190, 2016.
- [30] B. Herbáth, K. Kovács, M. Jakab, É. Makó, "Crystal structure and properties of Zinc Phosphate Layers on aluminium and steel alloy surfaces," *Crystals*, vol. 13, p. 369, 2023.
- [31] L. Kwiatkowski, "Phosphate coatings porosity: Review of new approaches," *Surface Engineering*, vol. 20, no. 4, pp. 292–298, 2013.
- [32] M. Kiliç, L. Akyalcın, "Kataforez kaplamalı çelik yüzeylere uygulanan dubleks kaplamanın korozyon dayanım performansı üzerindeki etkisinin incelenmesi," *Eskişehir Osmangazi Üniversitesi Mühendislik ve Mimarlık Fakültesi Dergisi*, vol. 30, pp. 68–78, 2022.
- [33] A. Ş. Yargıç, B. Eren, N. Özbay, "Enhancement of coating features by supporting Zinc-Based coating with cataphoresis process: Effect of acidity and coating thickness on the coating Quality," *Journal of Polytechnic*, pp. 1, 2023.
- [34] Yellow Powder Coating (2023). PPG Powder Coating Colors | PPG Powder Coatings [Online]. Available: <https://powdercoatings.ppg.com/products/pctz39104-yellow>
- [35] S. J. García, J. Suay, "A comparative study between the results of different electrochemical techniques (EIS and AC/DC/AC) application to the optimisation of the cataphoretic and curing parameters of a primer for the automotive industry," *Progress in Organic Coatings* vol.59, pp. 251–258, 2007.
- [36] S. J. García, M. T. Rodríguez, R. Izquierdo, J. Suay, "Evaluation of cure temperature effects in cataphoretic automotive primers by electrochemical techniques," *Progress in Organic Coatings*, vol.60, no.4, pp. 303–311, 2007.

- [37] “Cross Hatch Method. (2023). [Online]. Available: <https://www.elcometer.com/en/cross-hatch-method>
- [38] “Adhesion tests (2023). [Online]. Available: https://www.substech.com/dokuwiki/doku.php?id=adhesion_tests
- [39] “ASTM D 870: 2002 Standard (2023). Practice for testing water resistance.” [Online]. Available: https://infostore.saiglobal.com/en-us/standards/astm-d870-02-151549_SAIG_ASTM_ASTM_357357/
- [40] “MIL-STD-810 Test Method 507 Humidity-Crystal group.” (2023). [Online]. Available: <https://www.crystalrugged.com/mil-std-810-test-method-507-humidity/>
- [41] DIN EN ISO 9227 – (2023) European Standards. [Online]. Available: <https://www.en-standard.eu/din-en-iso-9227-corrosion-tests-in-artificial-atmospheres-salt-spray-tests-iso-9227-2022/>
- [42] SIST EN ISO 9227:2006 – (2023) Corrosion Tests in Artificial Atmospheres - Salt Spray Tests [Online]. Available: <https://standards.iteh.ai/catalog/standards/sist/6e82d425-e4fd-4579-a86d-d94eddd1cb36/sist-en-iso-9227-2006>
- [43] B. Chatterjee, (2017) “Science and industry of processes for Zinc-based coatings with improved properties,” *Jahrbuch Oberflächentechnik Band*, pp 1-30, [Online]. Available: <https://www.researchgate.net/publication/311793888>
- [44] L. Zaretskiy, “Modified silicate binders new developments and applications,” *International Journal of Metal Casting*, vol. 10, no. 1, pp. 88–99, 2016.
- [45] L. Zaretskiy, “Modified Silicate Binders New developments and applications,” *International Journal of Metal Casting*, vol. 10, no. 1, pp. 88–99, 2016.
- [46] L. Feng, H. Zhang, “Superhydrophobic aluminium alloy surface: Fabrication, structure, and corrosion resistance,” *Physicochemical Engineering Aspects*, vol. 441, pp. 319–325, 2014.
- [47] B. Tylkowski, I. Tsibranska, “Overview of main techniques used for membrane characterization,” *Journal of Chemical Technology and Metallurgy*, vol. 50, 1 pp. 3-12, 2015.
- [48] M. Mantel, J. P. Wightman, “Influence of the surface chemistry on the wettability of stainless steel,” *Surface and Interface Analysis*, vol. 21, pp. 595–605, 1994.
- [49] A. R. Luz, L. S. Santos, C. M. Lepienski, P. B. Kuroda, “Characterization of the morphology, structure and wettability of phase dependent lamellar and nanotube Oxides on Anodized Ti-10Nb Alloy,” *Applied Surface Science*, vol. 448, pp. 30–40, 2018.
- [50] D. Crotty, “Zinc alloy plating for the automotive industry,” *Metal Finishing*, vol. 94, pp. 56-58, 1996.
- [51] Teknorot (2023). Cataphoresis [Online]. Available: <https://www.teknorot.com/en/cataphoresis/>
- [52] GEOMET® (2023) Protection Principals,. [Online]. Available: www.nofmetalcoatings.com